GEOTHERMAL CHARACTERISTICS OF THE ROOSEVELT HOT SPRINGS SYSTEM AND ADJACENT FORGE EGS SITE, MILFORD, UTAH

edited by Rick Allis[1] and Joseph N. Moore[2]

[1]Utah Geological Survey, Salt Lake City, Utah
[2]Energy & Geoscience Institute, University of Utah, Salt Lake City, Utah

MISCELLANEOUS PUBLICATION 169
UTAH GEOLOGICAL SURVEY
a division of
UTAH DEPARTMENT OF NATURAL RESOURCES
2019

Blank pages are intentional for printing purposes

GEOTHERMAL CHARACTERISTICS OF THE ROOSEVELT HOT SPRINGS SYSTEM AND ADJACENT FORGE EGS SITE, MILFORD, UTAH

edited by

Rick Allis and Joseph N. Moore

Contributing Authors – Rick Allis, John M. Bartley, Aleta Finnila, Tobias P. Fischer, Bryan Forbes, Mark Gwynn, David A. Handwerger, Christian Hardwick, Adam Hiscock, Will Hurlbut, Paul C. Inkenbrandt, Clay G. Jones, Stefan Kirby, Emily Kleber, Tyler Knudsen, Fan-Chi Lin, John D. McLennan, John Miller, Joseph N. Moore, Siavash Nadimi, Peter Nielsen, Kristine L. Pankow, Robert Podgorney, Stephen Potter, Kristen Rahilly, Amy S. Record, Stuart Simmons, Stan Smith, Andy J. Trow, Yadong Wang, and Hao Zhang

Cover photo: *Drill rig on the FORGE site during the drilling of well 58-32, which proved that the site had granite at 200° C at about 2 km depth. The town of Milford is in the background.*

Editors' note:

The valley immediately west of the Mineral Mountains, containing the town of Milford and the FORGE project site, comprises Milford Flat (southern part) and Beaver Bottoms (northern part). The name Milford Valley is not a formal geographic name recognized by the U.S. Board on Geographic Names, but is used locally to refer to this area, and is used as such in this publication.

FORGE—Frontier Observatory for Research in Geothermal Energy (https://www.energy.gov/eere/forge/forge-home)

EGS—Enhanced Geothermal System

Bibliographic citation for this report:

Allis, R., and Moore, J.N., editors, Geothermal characteristics of the Roosevelt Hot Springs system and adjacent FORGE EGS site, Milford, Utah: Utah Geological Survey Miscellaneous Publication 169, 245 p., 8 appendices, 2 plates, scale 1:24,000, https://doi.org/10.34191/MP-169.

UTAH FORGE U.S. Department of Energy

MISCELLANEOUS PUBLICATION 169
UTAH GEOLOGICAL SURVEY
a division of
Utah Department of Natural Resources
2019

STATE OF UTAH
Gary R. Herbert, Governor

DEPARTMENT OF NATURAL RESOURCES
Brian Steed, Executive Director

UTAH GEOLOGICAL SURVEY
R. William Keach II, Director

PUBLICATIONS
contact
Natural Resources Map & Bookstore
1594 W. North Temple
Salt Lake City, UT 84116
telephone: 801-537-3320
toll-free: 1-888-UTAH MAP
website: mapstore.utah.gov
email: geostore@utah.gov

UTAH GEOLOGICAL SURVEY
contact
1594 W. North Temple, Suite 3110
Salt Lake City, UT 84116
telephone: 801-537-3300
website: geology.utah.gov

CONTENTS

GEOTHERMAL CHARACTERISTICS OF THE ROOSEVELT HOT SPRINGS SYSTEM AND ADJACENT FORGE EGS SITE, MILFORD, UTAH

PREFACE

This volume captures the research completed as part of the characterization of a field laboratory near Milford, Utah, to advance technologies to develop an Enhanced Geothermal System (EGS). An EGS involves the creation of a fracture network in hot, low-permeability rock so that water can be circulated through the rock, sweeping out the heat for power generation (https://www1.eere.energy.gov/geothermal/pdfs/egs_basics.pdf). In 2014, the U.S. Department of Energy (DOE) initiated a program known as FORGE (Frontier Observatory for Research in Geothermal Energy) for characterizing, creating, and sustaining an EGS reservoir. Five sites were initially considered. The DOE concluded the ideal site for a FORGE laboratory would be in low-permeability crystalline rock having temperatures between 175° and 225°C at depths between 1.5 and 4 km. Additional criteria included water availability, minimal environmental issues, easy access, and low potential of seismic hazards.

In 2018 the DOE selected the site near Milford, Utah, for the field laboratory. Led by the Energy & Geoscience Institute at the University of Utah, the considerable, diverse research that was carried out during the previous two years to characterize the site is summarized in the 14 papers presented in this publication. Each paper has been given its own link and digital object identifier (doi) to facilitate search engines directly accessing the paper. We have been flexible on the system of units used in the papers because of differing conventions across disciplines, as long as there is consistency within each paper. Supporting data from the research can be accessed through the Geothermal Data Repository maintained by DOE: https://gdr.openei.org/search?kw[]=Utah+FORGE. More general information and news about the site is available at the project website: http://www.utahFORGE.com/.

The FORGE site is located 250 km south of Salt Lake City and 16 km north of Milford (Figure 1), a small community with a population of 1400. The site is unpopulated and covers an area of about 5 km^2. It is situated within Utah's Renewable Energy Corridor adjacent to a 306 MWe wind farm, a 240 MWe solar array, and PacifiCorp Energy's 36 MWe Blundell geothermal plant at Roosevelt Hot Springs. Blundell was commissioned in 1984 as a traditional flash steam plant with production wells tapping 250°–270°C (~ 500°F) water in naturally fractured granitic rock at 1–2 km (3000–6000 ft) depth. A binary power plant was commissioned in 2006 to generate additional power from the separated water prior to being reinjected. The cooled waste water is reinjected in several wells to the east and north of the production borefield to help sustain the reservoir pressure (wells 14-2, 82-33 and 71-10 are shown on Figure 1).

A very large volume of hot, unfractured rock surrounds the Blundell production borefield, as indicated by the 250°C isotherm at 3 km depth in Figure 1. The quantity of heat stored in this low-permeability rock has a power potential many times greater than the generation capacity of the naturally fractured rock volume at Roosevelt Hot Springs (hundreds of MW).

In 2017, a deep vertical well, 58-32, was drilled to a depth of 2297 m (7536 ft) on the FORGE site to demonstrate the necessary characteristics of temperature, rock type, and low permeability for an EGS reservoir. A complete suite of geophysical, image, and temperature logs was obtained, and injection tests were conducted to evaluate the permeabilty and stress regime. Several papers in this volume refer to the analysis of the rock samples, logs, measurements, and testing of the well. Complementary seismic monitoring and three-dimensional reflection seismic, gravity, lidar, geochemical, geological, and resistivity investigations provide supporting information on the characteristics and geometry of the reservoir.

Figure 2 is a simplified block diagram extending northwest-southeast through the FORGE site. The blue and red wells are the two deep, deviated wells that will be drilled during the main phase of the project. After the rock is fractured, water will be circulated between the wells, with cool water exiting the open portion of the injection well and being heated as it flows through the fracture network to the production well. The heat swept from the granitic basement at about 2.5 km depth will be extracted at the FORGE test site with a heat exchanger. The cooled water will then be returned to the injection well. A complete application of an EGS would have the heat removed in a power plant.

A bibliography of past research carried out near the FORGE site is given at the end of this publication with active links to each paper. Much of the data was generated under DOE funding during the late 1970s and early 1980s to assist the development of the Roosevelt Hot Springs hydrothermal reservoir. These publications, together with the research described in this volume, form a knowledge platform for the technology development that will occur at the Milford FORGE site.

We are grateful for the numerous reviewers who improved the clarity of the papers. Finally Utah Geological Survey (UGS) technical reviews of all papers were carried out by Stephanie Carney and Mike Hylland. The UGS Editorial Section arranged the page layout and produced the final version of this publication.

Rick Allis and Joseph Moore
Editors, August 2019

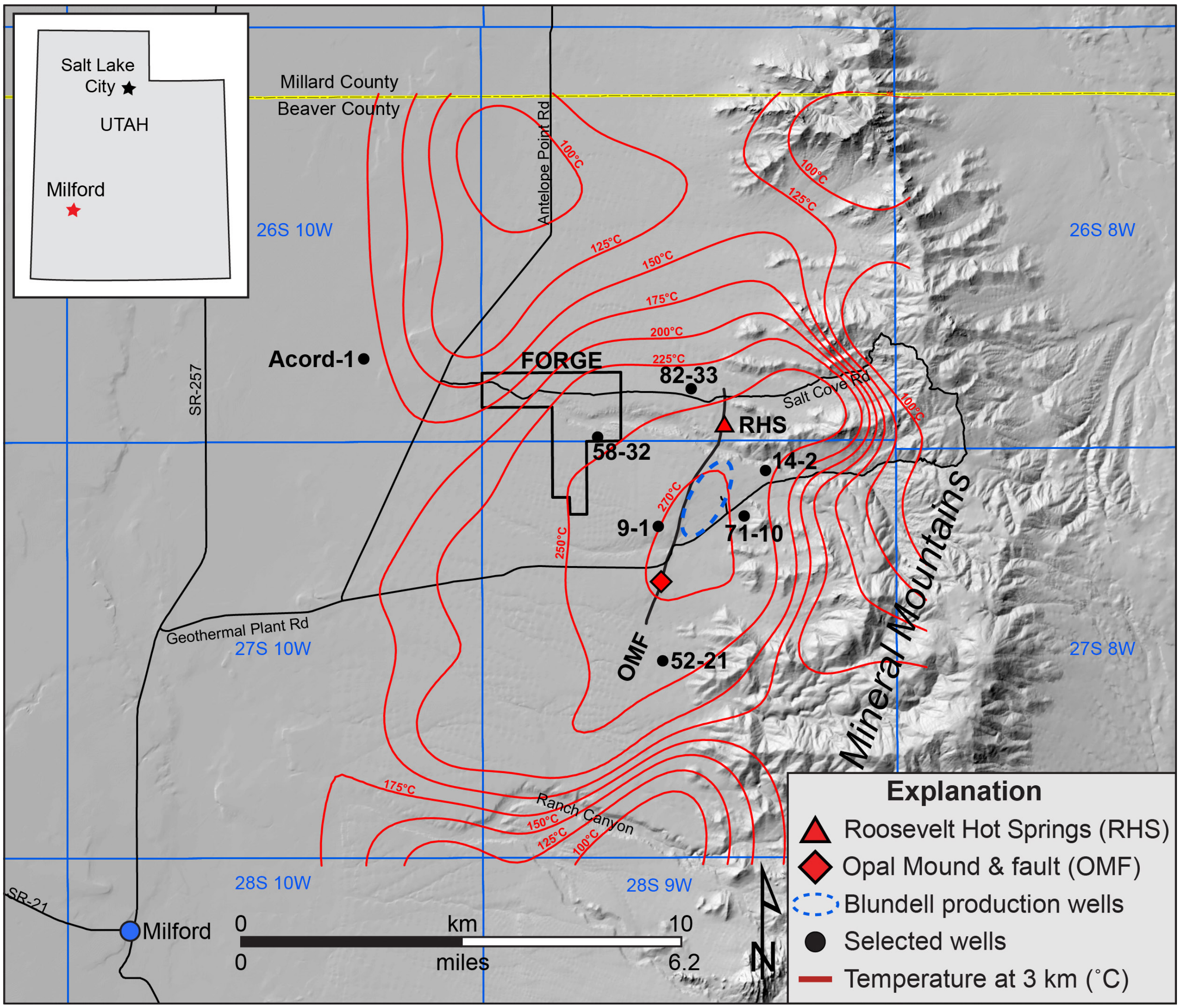

Figure 1. *Relationship of the FORGE site (heavy black outline containing well 58-32) to the thermal anomaly of the Roosevelt Hot Springs system at 3 km depth. The isotherms are from Allis et al. (this volume).*

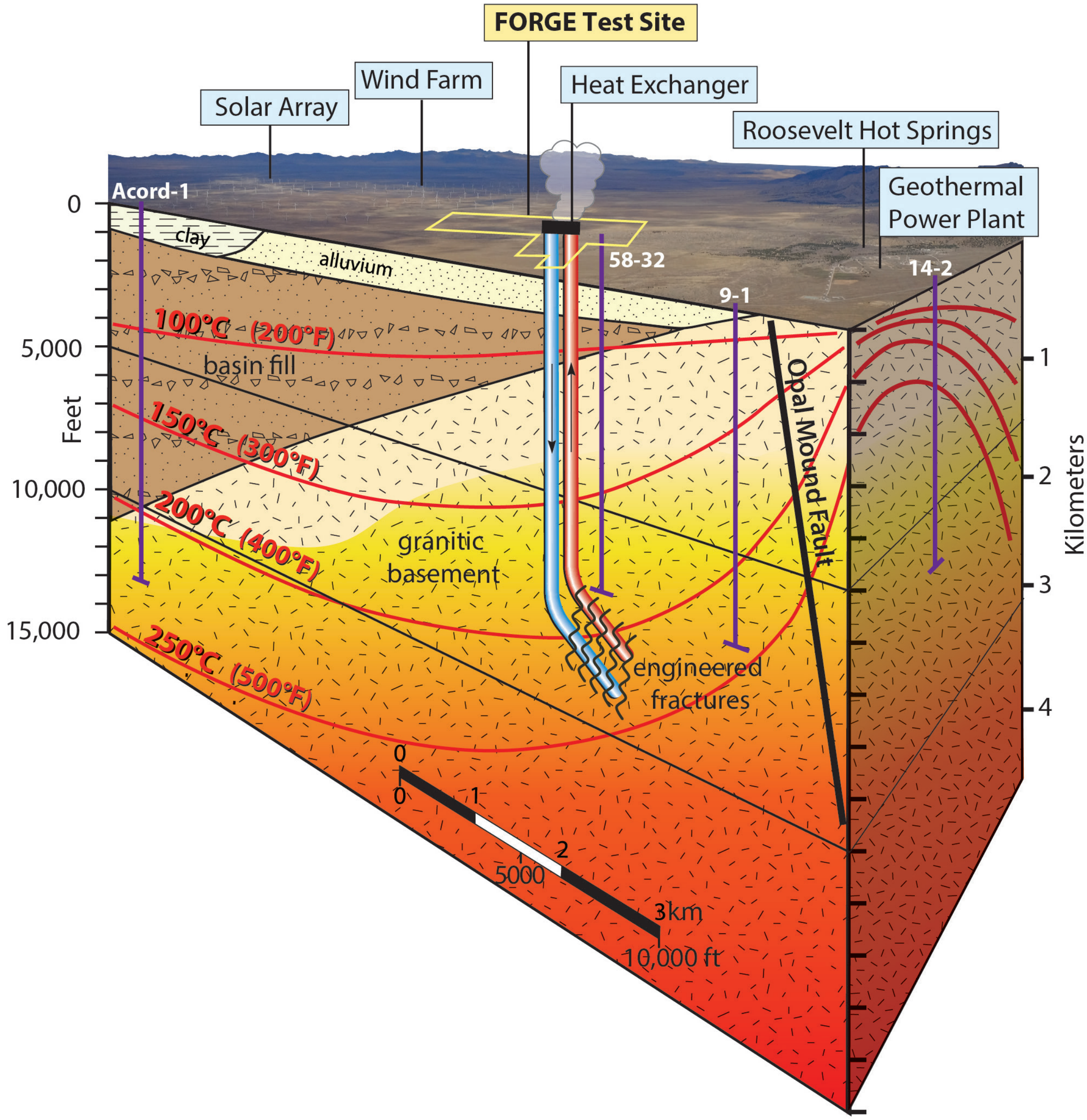

Figure 2. *Block diagram highlighting the thermal regime in the granitic basement beneath the FORGE test site. The goal of the project is to improve techniques for creating a fracture network which allows water to circulate between an injection and production well. The distance between the two wells is expected to be about 100 m (330 ft).*

REVISED MAPPING OF BEDROCK GEOLOGY ADJOINING THE UTAH FORGE SITE

by Stefan M. Kirby

Utah Geological Survey, Salt Lake City, Utah

Link to supplemental data download: https://ugspub.nr.utah.gov/publications/misc_pubs/mp-169/mp-169-a.zip
Plates 1 & 2

Miscellaneous Publication 169-A
Utah Geological Survey
a division of
UTAH DEPARTMENT OF NATURAL RESOURCES

This paper is part of *Geothermal Characteristics of the Roosevelt Hot Springs System and Adjacent FORGE EGS Site, Milford, Utah*. https://doi.org/10.34191/MP-169

Bibliographic citation:

Kirby, S.M., 2019, Revised mapping of bedrock geology adjoining the Utah FORGE site, *in* Allis, R., and Moore, J.N., editors, Geothermal characteristics of the Roosevelt Hot Springs system and adjacent FORGE EGS site, Milford, Utah: Utah Geological Survey Miscellaneous Publication 169-A, 6 p., 2 plates, scale 1:24,000, https://doi.org/10.34191/MP-169-A.

REVISED MAPPING OF BEDROCK GEOLOGY ADJOINING THE UTAH FORGE SITE

by Stefan M. Kirby

ABSTRACT

The bedrock of the central Mineral Mountains is dominated by an Oligocene through Miocene intrusive batholith emplaced in older Precambrian metamorphic rocks and a series of Paleozoic sedimentary rocks. Most exposed rocks consist of a variety of granitoid intrusives and a few exposures of related diorites, and adjoining gneiss, schist, and quartzite. All of these rocks are intruded by late-stage dikes that range from felsic to mafic in composition. Paleozoic wall rocks are exposed along the north and southeast parts of the intrusive complex. A significant series of Quaternary rhyolite and tuff, consisting of high-standing domes and drainage-filling flows, occurs across the central Mineral Mountains. The intrusive and metamorphic rocks exposed in the central Mineral Mountains are directly analogous to reservoir rocks at the Utah FORGE site.

Precambrian metamorphic rocks form screens and wall rocks along the western margin of the batholith. These rocks consist primarily of Precambrian banded gneiss (~1720 Ma) and minor associated quartzite and sillimanite schist. Intrusions of Oligocene granodiorite (~ 26 Ma) occur along the western flank and at the northern end of the batholith. Most of the exposed batholith consists of Miocene (~17–18 Ma) intrusions of granitoid rocks that include granite, quartz monzonite, syenite and diorite. The oldest of these rocks is a locally comingled series of hornblende-bearing granite, quartz monzonite, and diorite. Most of this phase of hornblende-bearing intrusives consists of medium- to coarse-grained granite that contains potassium feldspar, quartz, biotite, and hornblende. A series of smaller syenite intrusions occurs along the western flank of the Mineral Mountains. Map relations and chilled margins along contacts indicate the unit was emplaced between 17.5 and 18 Ma. A medium-grained biotite granite makes up most of the eastern part of the batholith. This unit intrudes older hornblende-bearing units forming a large contiguous body in the central Mineral Mountains. A series of late Miocene (~11 Ma) intrusive dikes that consist of granite, porphyritic rhyolite, diabase, and andesite, cross-cut the older intrusive and metamorphic rocks across the range.

INTRODUCTION

This chapter summarizes the revised mapping of the bedrock geology of the central Mineral Mountains adjoining the Utah Frontier Observatory for Research in Geothermal Energy (FORGE) site. The metamorphic and intrusive bedrock exposed in the Mineral Mountains is contiguous and directly analogous to the bedrock at the Utah FORGE site. The proximity and correlation between reservoir and exposed bedrock represents a unique opportunity to study and quantify rocks and processes at outcrop scale that are likely to be observed in the borehole.

This mapping was completed as part of FORGE project phase 2b in 2017. The bedrock geologic map presented in this section is based on the digitized version of Sibbett and Nielson (1980) and the subsequent unit correlations and age information presented by Coleman (1991) and McDowell (2004). Map alterations and adjustments were made based on fieldwork during the summer of 2017.

Previous bedrock mapping includes early work by Sibbett and Nielson (1980), who mapped the entire central Mineral Mountains and defined basic geologic units. Their mapping was completed as part of Department of Energy (DOE)-funded geothermal investigations related to development of the Roosevelt Hot Springs hydrothermal system. Lipman et al. (1978) mapped and subdivided the Quaternary rhyolites of the Mineral Mountains and other nearby extrusive volcanic units. Alienikoff et al. (1987) mapped and subdivided Precambrian metamorphic rocks and intrusive rocks on the northern and western margins of the central Mineral Mountains. Coleman (1991) and Coleman and Walker (1992) present localized detailed mapping and new unit correlations for intrusive rocks of the central Mineral Mountains. McDowell (2004) presents detailed mapping of a strip of bedrock along the western flank of the Mineral Mountains. Regional scale (1:100,000) geologic mapping by Hintze et al. (2003) and Rowley et al. (2005) provide detail on the Paleozoic wall rocks that adjoin the batholith to the north and southeast.

METHODS

Previous bedrock mapping by Sibbett and Nielson (1980) was digitized and turned into a GIS product in spring 2017 and released as a Utah Geological Survey Miscellaneous Publication (Sibbett and Nielson, 2017). This mapping is contiguous across the

Mineral Mountains and the geologic units are accurately described. The mapping of Sibbett and Nielson (2017) was therefore used as the basis for the bedrock geology. Subsequent work by Aleinikoff et al. (1987), Coleman (1991), Coleman and Walker (1992, 1994), and McDowell (2004) has better defined age and lithologic correlations of the bedrock in the Mineral Mountains. These age data and unit correlations were applied to the Sibbett and Nielson (2017) map following the scheme presented by Coleman (1991) (Table 1). The resulting map was edited and checked based on several weeks of fieldwork in the summer of 2017. Plates 1 and 2 present the revised bedrock geology merged with a simplified and expanded version of Quaternary mapping by Knudsen et al. (2019) completed as a part of FORGE project phase 2b. Plate 2 presents a correlation diagram of map units based on the revised bedrock mapping. Map units are described in detail on Plate 2 and a discussion of these units is presented below.

Table 1. *Correlation matrix used to revise bedrock nomenclature for intrusive and metamorphic rocks of the central Mineral Mountains. Correlation largely follows the schema presented by Coleman (1991).*

Coleman (1991) Unit	Age (Ma)	Rock Type	Sibbett and Nielson (2017) Unit	Rock Type
Mpr	11	Porphyritic Rhyolite	Tpr	porphyritic rhyolite dikes
			Trd	rhyolite dikes
Mhd	11	Hornblende Diabase Dikes	Tds	diabase dikes
			Tmd	microdiorite dikes
Mg	11	Granite Dikes	Tgr	granite dikes
Mbg	17	Biotite Granite	Tg	granite
			Tg?	granite?
Mbhs	<18	Biotite-Hornblende Syenite	Ts	syenite
Mbhg	18	Biotite-Hornblende Granite	Tbg	biotite granite
			Tqm	quartz monzonite
Mbhm	18	Biotite-Hornblende Monzonite	Ti	porphyritic quartz monzonite
Mbhd	18	Biotite-Hornblende Diorite	Td	diorite
			gd	biotite granodiorite
			Tdb	diorite breccia
Ohg	26	Hornblende Granodiorite	hd	hornblende granodiorite
			hgn	hornblende gneiss
PCss	1720	Sillimanite Schist	Xs	sillimanite schist
PCq	1720	Quartzite	Xq	quartzite
PCbg	1720	Biotite Gneiss	Xbg	banded gneiss

GEOLOGIC BACKGROUND

The Utah FORGE site is in the eastern Basin and Range Province of south-central Utah. Late Cenozoic unconsolidated deposits in the map area consist of coarse-grained alluvial deposits of late Tertiary to Holocene age, and coarse- and fine-grained lacustrine sediment deposited during at least two Quaternary lake cycles. Quaternary hot-spring deposits are common along the western margin of the Roosevelt geothermal area. Scarps of the Mineral Mountain West, NM, and Opal Mound faults offset pre-Holocene alluvial-fan deposits.

The bedrock in the Mineral Mountains, east of the Utah FORGE site, consists primarily of a Miocene- to Oligocene-age batholith complex and adjoining Precambrian metamorphic and Paleozoic sedimentary wall rocks. Exposures of the batholith cover an area of more than 200 km^2 in the central Mineral Mountains. Precambrian metamorphic rocks form screens and wall rocks along the western margin of the batholith. These rocks consist of Precambrian (~1720 Ma) banded gneiss and associated quartzite and schist (Alienikoff et al., 1987; Coleman, 1991). Small intrusions of Oligocene (~26 Ma) granodiorite occur along the western flank and at the northern end of the batholith. Most of the exposed batholith consists of Miocene (~17–18 Ma) intrusions of granitoid rocks that include granite, quartz monzonite, syenite and diorite. A series of late Miocene (~11 Ma) intrusive dikes that consists of granite, porphyritic rhyolite, diabase, and andesite cross-cut the older intrusive and metamorphic rocks throughout the range. The northern edge of the batholith intrudes Lower and Middle Cambrian quartzite, shale, and limestone (Coleman, 1991; Hintze et al., 2003). The southeast margin of the batholith intrudes upper Paleozoic wall rocks that include sandstone, limestone, dolomite, and shale (Rowley et al., 2005).

Thermochronologic, mineralogic, and textural relations in the batholithic rocks support emplacement at mid-crustal depths greater than 5 km (Nielson et al., 1986; Coleman and Walker, 1992; Coleman et al., 2001). Thermochronology also supports rapid exhumation and cooling of the batholith between 11 and 8 Ma (Coleman et al., 2001). Exhumation was likely localized along regionally extensive detachment faults (Coleman and Walker, 1994). Paleomagnetic data, dike orientations, and fracture data from various phases of the Miocene intrusions support eastward rotation of the Mineral Mountains (Coleman and Walker, 1994; Coleman et al., 2001; Kirby et al., 2017). Exhumation likely followed a rolling hinge model (Buck, 1988) whereby uplift of the igneous bedrock of the Mineral Mountains was accommodated by a combination of fault slip, rotation, and flexural rebound of the footwall of a regional detachment fault (Coleman and Walker, 1994; Coleman et al., 2001).

Volcanism began following or during active exhumation. The oldest extrusive unit is a Miocene (6.2 Ma) porphyritic quartz-latite flow that overlies Tertiary alluvial-fan deposits southwest of the Mineral Mountains. This flow and its relationship with underlying fan deposits provide basic age constraint on basin formation and consequent sedimentation immediately adjoining the Mineral Mountains.

Quaternary volcanism in the central Mineral Mountains began just after 1 Ma with the eruption of several small basaltic cones and flows along the northeastern flank of the Mineral Mountains (Hintze et al., 2003). An extended period of rhyolitic volcanism also began just after 1 Ma and continued to 0.5 Ma (Lipman et al., 1978). Age control on the rhyolites is based on a small number of older K-Ar ages presented by Lipman et al. (1978). These rocks are exposed over an area of more than 50 km^2 and they overlie intrusive and metamorphic rocks and, locally, older alluvial-fan deposits. The mapped rhyolites form a series of at least 10 distinct high-standing domes and related tuffaceous deposits that fill adjoining drainages. The rhyolitic units locally overlie the oldest Quaternary alluvial deposits and constrain the age of the oldest exposed Quaternary deposits to the middle Pleistocene.

GEOLOGY OF THE MINERAL MOUNTAINS BATHOLITH

The Oligocene through Miocene intrusive rocks of the Mineral Mountains batholith, and Precambrian metamorphic rocks, are directly analogous to the rocks beneath the Utah FORGE site. Faults exposed in the Mineral Mountains may be similar to faults encountered at depth in the reservoir rocks of the Utah FORGE site. To facilitate better understanding and correlation of these rocks, and associated faults, across the various FORGE project tasks, the exposed geology of the Mineral Mountains batholith is described in detail below.

Tertiary Intrusive Rocks

Intrusions of Oligocene granodiorite occur along the western flank and at the northern end of the batholith (Plate 1). This granodiorite is coarse- to medium-grained and consists of plagioclase, potassium feldspar, hornblende, quartz, and biotite with accessory minerals including sphene, apatite, magnetite, and thorite. Large hornblende and potassium feldspar crystals up to 1 cm are common. Coleman (1991) and McDowell (2004) note that individual potassium feldspar crystals commonly contain abundant fractures. This unit intrudes Cambrian rocks on the northern end of the batholith and intrudes Precambrian metamorphic rocks along the western flank of the batholith. The granodiorite commonly displays planar foliation. The age of the granodiorite is 26 Ma based on U-Pb zircon analyses of Alienikoff et al. (1987).

Most of the exposed batholith consists of Miocene (~17–18 Ma) intrusions of granitoid rocks that include granite, quartz monzonite, syenite, and diorite. The oldest of these rocks is a locally comingled series of hornblende-bearing granite, quartz monzonite, and diorite. Most of this phase of hornblende-bearing intrusives consists of medium- to coarse-grained granite that contains potassium feldspar, quartz, biotite, and hornblende. The quartz monzonite is medium-grained and porphyritic, and contains large potassium feldspar phenocrysts with plagioclase mantles in a matrix of plagioclase, quartz, biotite, and hornblende (Coleman, 1991). The diorite is medium- to fine-grained and contains plagioclase, potassium feldspar, quartz, biotite, and hornblende. Coleman (1991) states sphene is commonly observed in the core of plagioclase crystals in the diorite. Accessory minerals are similar amongst the hornblende-bearing suite of intrusives and commonly include sphene, apatite, zircon, and magnetite. Mineralogic composition is commonly variable across these units, and where these units are mapped adjoining one another there is locally extensive mixing of the various lithologies on a scale of less than 10 m (Coleman, 1991; McDowell, 2004). The age of the hornblende-bearing monzonite, granite, and diorite is 18 Ma based on U-Pb zircon analyses (Coleman, 1991).

Syenite is mapped as a series of smaller intrusions along the western flank of the Mineral Mountains. The syenite is medium- to coarse-grained and consists primarily of potassium feldspar with lesser amounts of plagioclase, quartz, biotite, and hornblende. Accessory minerals include sphene, magnetite, zircon, and apatite. The syenite has no direct age control. Map relations and chilled margins along contacts indicate the unit is younger than the hornblende-bearing units and older than the biotite granite and was likely emplaced between 17.5 and 18 Ma (Coleman, 1991).

A medium-grained biotite granite makes up most of the eastern part of the batholith. This granite contains potassium feldspar, quartz, plagioclase, and biotite. Accessory minerals include sphene, apatite, zircon, magnetite, and hematite, and locally the granite contains beryl, garnet, and hornblende. This unit intrudes older hornblende-bearing units forming a large contiguous body in the central Mineral Mountains. Coleman (1991) distinguished this unit from slightly older biotite-hornblende granite by the presence of abundant early resorbed quartz, late-stage interstitial quartz, and significantly less hornblende. The age is 17.5 Ma based on U-Pb zircon analyses (Coleman, 1991).

A series of young Miocene (~11 Ma) intrusive dikes that consist of granite, porphyritic rhyolite, diabase, and andesite cross-cut the older intrusive and metamorphic rocks throughout the range. The granite dikes consist of coarse- to fine-grained, typically resistant granite containing quartz, potassium feldspar, plagioclase, and biotite. Accessory minerals include sphene, apatite, and zircon. The unit includes fine-grained and coarse-grained dikes mapped as unit Tgr by Sibbett and Nielson (1980). The granite dikes intrude older rocks along the western flank of the Mineral Mountains. The current map unit correlation yields a wide zone of these dikes north of Negro Mag Wash. Individual dikes may be up to 10 m thick. Age is ~11 Ma based on U-Pb zircon analyses (Coleman and Walker, 1992). Porphyritic rhyolite dikes contain phenocrysts of quartz, potassium feldspar, hornblende, and biotite in a groundmass of potassium feldspar and quartz. Accessory minerals include magnetite and sphene. Porphyritic rhyolite dikes range in thickness from several meters to tens of meters and are oriented from sub-horizontal to sub-vertical. The age of the porphyritic rhyolite is 11 Ma based on data presented by Nielson et al. (1986) and Coleman and Walker (1994). Dark colored, fine-grained, hornblende-bearing diabase dikes contain plagioclase microlites (Sibbett and Nielson, 1980). Accessory minerals include biotite and magnetite. Individual diabase dikes are up to 10 m thick. Diabase dikes commonly co-occur with granite dikes and porphyritic rhyolite dikes and have similar orientations. The diabase dikes have no direct age data. Coleman (1991) and McDowell (2004) correlate this unit with 11 Ma granite dikes and porphyritic rhyolite dikes based on proximity and similar orientations. Porphyritic andesite dikes with phenocrysts of plagioclase and hornblende in a fine-grained glassy groundmass intrude biotite granite on the southeast flank of the Mineral Mountains. Coleman and Walker (1992) give an age of ~11 Ma based on field relations and similar orientations with other dike units.

Select whole-rock geochemical samples from the Mineral Mountains batholith are presented on Plate 2. These data are taken from geochemistry presented by Alienikoff et al. (1987) and Coleman and Walker (1992). For each sample, a map unit based on the available sample location and sample description information was added to the geochemical samples based on the correlation scheme discussed above. A simple total alkali versus silica plot displays significant compositional overlap among geologic units (Plate 2). This plot defines broad zones of geochemistry for the various units and implies that whole-rock geochemistry is variable and not necessarily sufficient to determine geologic map units. This result is broadly consistent with the observable variation in lithology at outcrop scale and the genetic relationships described between the various units (Coleman, 1991; Coleman and Walker, 1992). Alternately, whole-rock geochemistry may be under-characterized by the existing sample data and revised bedrock geology.

Precambrian Metamorphic Rocks

Precambrian metamorphic rocks form screens and wall rocks along the western margin of the batholith. These rocks consist primarily of Precambrian banded gneiss and minor associated quartzite and sillimanite schist (Alienikoff et al., 1987; Coleman, 1991). The banded gneiss consists of light-colored bands of potassium feldspar, quartz, and biotite, and dark-colored bands of biotite, plagioclase, quartz, and hornblende. Gneissic banding is commonly folded and ptygmatic in character. Accessory minerals include rounded zircon and apatite. Muscovite is locally present and useful for distinguishing this unit from the granodiorite. The gneiss also contains no sphene, whereas sphene is common in all younger intrusive units. The age of the gneiss is ~1720 Ma based on U-Pb zircon and Rb-Sr model ages presented by Alienikoff et al. (1987). Nielson et al. (1978) suggest the protolith for the gneiss may be the quartzite and schist associated with the gneiss.

Faults

Previously mapped faults in the bedrock of the Mineral Mountains (Sibbett and Nielson, 2017) consist of structures that range from steeply dipping normal faults along the western margin to gently dipping faults mapped in the central part of the Mineral Mountains. Field examination of the gently dipping faults suggest these features have offsets of less than several meters. The scale of the mapping does not allow depiction of these faults. These gently dipping faults are discussed in greater detail in a companion paper that examines fracturing in the Mineral Mountains (Bartley, 2019). The steeply dipping faults along the western margin of the Mineral Mountains commonly offset Precambrian metamorphic rocks and various intrusive phases. In outcrop these faults commonly contain discrete damage zones and defined fault planes that occur over a width of several meters. Secondary mineralization along the fault planes is common and includes quartz, calcite, and epidote. Observable slickensides indicate dip slip in most cases. Similar steeply dipping faults may exist in the reservoir rocks of the Utah FORGE site.

CONCLUSION

The bedrock of the central Mineral Mountains is dominated by an Oligocene- to Miocene-age batholith emplaced in Precambrian metamorphic rocks and a series of Paleozoic sedimentary rocks. The bedrock of the central Mineral Mountains is directly analogous to reservoir rocks at the Utah FORGE site. Most of the exposed rocks east of the site consist of Miocene (~17–18 Ma) intrusions of granitoid rocks that include granite, quartz monzonite, syenite and diorite. The oldest of these rocks is a locally comingled series of hornblende-bearing granite, quartz monzonite, and diorite. All of these rocks are intruded by late-stage dikes that range from felsic to mafic in composition. A significant series of Quaternary rhyolite and tuff, consisting of high-standing domes and drainage-filling flows, occurs across the central Mineral Mountains. The steeply dipping bedrock faults along the western margin of the Mineral Mountains offset Precambrian metamorphic rocks and various intrusive phases. In outcrop these faults commonly contain discrete damage zones and defined fault planes that occur over a width of several meters. Secondary mineralization along the fault planes is common and includes quartz, calcite, and epidote. Observable slickensides indicate dip slip in most cases. Similar steeply dipping faults may exist in the reservoir rocks of the Utah FORGE site.

ACKNOWLEDGMENTS

John Bartley of the University of Utah provided insightful comments and in-depth understanding of the intrusive geology of the Mineral Mountains during several field excursions and at various points during the preparation of this map. Stuart Simmons of EGI provided thought provoking comments and oversight both in the field and during preparation of the map. Martha Jensen of the Utah Geological Survey assisted with the GIS, cartography, and layout of the plates. This chapter and accompanying plates benefitted from timely and concise reviews by Hugh Hurlow and Mike Hylland, both of the Utah Geological Survey.

REFERENCES

Alienikoff, J.N., Nielson, D.L., Hedge, C.E., and Evans, S.H., 1987, Geochronology of Precambrian and Tertiary rocks in the Mineral Mountains, south-central Utah: U.S. Geological Survey Bulletin 1622, p. 1–12.

Bartley, J.M., 2019, Joint patterns in the Mineral Mountains intrusive complex and their roles in subsequent deformation and magmatism, *in* Allis, R., and Moore, J.N., editors, Geothermal characteristics of the Roosevelt Hot Springs system and adjacent FORGE EGS site, Milford, Utah: Utah Geological Survey Miscellaneous Publication 169-C, 13 p., 1 appendix, https://doi.org/10.34191/MP-169-C.

Buck, R.W., 1988, Flexural rotation of normal faults: Tectonics, v. 7, p. 959–973.

Coleman, D.S., 1991, Geology of the Mineral Mountains batholith, Utah: Lawrence, University of Kansas, unpublished Ph.D. thesis, 219 p.

Coleman, D.S., and Walker, J.D., 1992, Evidence for the generation of juvenile granitic crust during continental extension, Mineral Mountains batholith, Utah: Journal of Geophysical Research, v. 97, p. 11011–11024.

Coleman, D.S., and Walker, J.D., 1994, Modes of tilting during extensional core complex development: Science, v. 263, p. 215–218.

Coleman, D.S., Walker, J.D., Bartley, J.M., and Hodges, K.V., 2001, Thermochronologic evidence for footwall deformation during extensional core complex development, Mineral Mountains, Utah, *in* Erskine, M.C., Faulds, J.E., Bartley, J.M., and Rowley, P.D., editors, The geologic transition, High Plateaus to Great Basin—a symposium and field guide (The Mackin Volume): Utah Geological Association and Pacific Section of the American Association of Petroleum Geologists, Utah Geological Association Publication, v. 30, p. 155–168.

Hintze, L.H., Davis, F.D., Rowley, P.D., Cunningham, C.G., Steven, T.A., and Willis, G.C., 2003, Geologic map of the Richfield 30′ x 60′ quadrangle, southeast Millard County, and parts of Beaver, Piute, and Sevier Counties, Utah: Utah Geological Survey Map 195.

Kirby, S.M., Bartley, J., and Simmons, S., 2017, Revised geologic mapping and fracture analysis of bedrock adjoining the Utah FORGE site: Geothermal Resources Council Transactions, v. 41, p. 34.

Knudsen, T., Kleber, E., Hiscock, A., and Kirby, S.M., 2019, Quaternary geology of the Utah FORGE site and vicinity, Millard and Beaver Counties, Utah, *in* Allis, R., and Moore, J.N., editors, Geothermal characteristics of the Roosevelt Hot Springs system and adjacent FORGE EGS site, Milford, Utah: Utah Geological Survey Miscellaneous Publication 169-B, 21 p., 2 appendices, https://doi.org/10.34191/MP-169-B.

Lipman, P.W., Rowley, P.D., Mehnert, H.H., Evans S.H., Jr., Nash, W.P., and Brown F.H., 1978, Pleistocene rhyolite of the Mineral Mountains, Utah—geothermal and archeological significance: U.S. Geological Survey Research Journal, v. 6, p. 133–147.

McDowell, S.M., 2004, Construction of the Mineral Mountains Sheet Complex, Mineral Mountains Batholith, Southwestern Utah: Chapel Hill, University of North Carolina, unpublished M.S. thesis, 79 p.

Nielson D. L., Evans, S.H., Jr., and Sibbett, D.S., 1986, Magmatic, structural, and hydrothermal evolution of the Mineral Mountains intrusive complex, Utah: Geological Society of America Bulletin, v. 97, no. 6, p. 765–777.

Nielson, D.L., Sibbett, B.S., McKinney, D.B., Hulen J.B., Moore, J.N., and Samberg, S.M., 1978, Geology of Roosevelt Hot Springs KGRA, Beaver County, Utah: unpublished report prepared by Earth Science Laboratory, for U.S. Department of Energy, Division of Geothermal Energy, University of Utah Research Institute, Salt Lake City, Utah, 120 p.

Rowley, P.D., Vice, G.E., McDonald, R.E., Anderson, J.J., Machette, M.N., Maxwell, D.J., Ekren, E.B., Cunningham, C.G., Steven, T.A., and Wardlaw, B., 2005, Interim geologic map of the Beaver 30′ x 60′ quadrangle, Beaver, Piute, Iron, and Garfield Counties, Utah: Utah Geological Survey Open-File Report 454, 27 p.

Sibbett, B.S., and Nielson, D.L., 1980, Geology of the central Mineral Mountains, Beaver County, Utah: University of Utah Research Institute, Earth Science Laboratory Report 33, 42 p.

Sibbett, B.S., and Nielson, D.L., 2017, Geologic map of the central Mineral Mountains (GIS of 1980 map), Beaver County, Utah: Utah Geological Survey Miscellaneous Publication 17-2DM.

QUATERNARY GEOLOGY OF THE UTAH FORGE SITE AND VICINITY, MILLARD AND BEAVER COUNTIES, UTAH

by Tyler Knudsen, Emily Kleber, Adam Hiscock, and Stefan M. Kirby

Utah Geological Survey, Salt Lake City, Utah

Miscellaneous Publication 169-B
Utah Geological Survey
a division of
UTAH DEPARTMENT OF NATURAL RESOURCES

This paper is part of *Geothermal Characteristics of the Roosevelt Hot Springs System and Adjacent FORGE EGS Site, Milford, Utah*. https://doi.org/10.34191/MP-169

Bibliographic citation:

Knudsen, T., Kleber, E., Hiscock, A., and Kirby, S.M., 2019, Quaternary geology of the Utah FORGE site and vicinity, Millard and Beaver Counties, Utah, *in* Allis, R., and Moore, J.N., editors, Geothermal characteristics of the Roosevelt Hot Springs system and adjacent FORGE EGS site, Milford, Utah: Utah Geological Survey Miscellaneous Publication 169-B, 21 p., 2 appendices, https://doi.org/10.34191/MP-169-B.

QUATERNARY GEOLOGY OF THE UTAH FORGE SITE AND VICINITY, MILLARD AND BEAVER COUNTIES, UTAH

by Tyler Knudsen, Emily Kleber, Adam Hiscock, and Stefan M. Kirby

ABSTRACT

We present new Quaternary geologic mapping, geomorphic analysis, and luminescence geochronology to better understand the Quaternary geologic history of the Utah FORGE site near Milford, Utah. Late Cenozoic unconsolidated deposits in the map area are predominantly coarse-grained alluvial-fan deposits sourced from the Mineral Mountains. Boulder-rich basin-fill deposits are the oldest mapped unconsolidated unit (Taf) representing debris shed from the rapidly rising ancestral Mineral Mountains during Miocene to Pliocene time. Erosion of the Mineral Mountains continued into the early Pleistocene, forming the deeply embayed canyons and generally mature topography of the range today. In early middle Pleistocene time (~0.7–0.5 Ma), rhyolitic lava flows and domes partially filled pre-existing canyons. By the late middle Pleistocene (~0.5–0.1 Ma), alluvial fans began aggrading east, deep into the canyons and abutting against the rhyolitic flows. The distal ends of the alluvial fans were extensively reworked and etched by shorelines of Lake Bonneville, which occupied Milford Valley from about 20 to 18 ka. The recession of Lake Bonneville about 18 ka and resultant lowering of base level may have spurred the deep incision of Negro Mag Wash (NMW), Ranch Canyon, and Corral Canyon that has rendered older alluvial fans inactive.

We mapped three fault zones near the Utah FORGE site that had apparent Quaternary displacement: the Negro Mag fault (NMF), the Opal Mound fault (OMF), and the Mineral Mountains West fault zone (MMWFZ). The steeply dipping NMF trends east-west across much of the Mineral Mountains and bounds the northern margin of the Roosevelt Hot Springs geothermal area. We found no definitive evidence for displacement of Quaternary deposits along the inferred trace of the NMF and suspect the fault may be pre-Quaternary in age.

The steeply east-dipping, north-trending OMF defines the western boundary of the Roosevelt Hot Springs geothermal system. The fault displaces late Pleistocene alluvial-fan deposits as much as 18 m. Hot springs emanating from the fault zone have deposited abundant siliceous sinter along the fault. Sinter deposition and faulting have been contemporaneous as evidenced by buried horizons of sinter detected in well logs, and by possible fault-rotated blocks of sinter mapped in the fault zone. However, Holocene sinter as young as 1.6 to 1.9 kyr covers the southern end of the fault and appears unbroken. Development of the OMF scarp has been greatly influenced by differential erosion of siliceous sinter exposed along the fault. Latest movement on the OMF was in the late Pleistocene (12–126 kyr), but its resultant scarp appears older than scarps formed by the nearby Lake Bonneville shoreline (>18 ka) and scarps formed by the MMWFZ.

The north-south-trending MMWFZ extends for about 40 km from near the Utah FORGE site to south of Minersville. The fault zone has produced a series of east- and west-dipping scarps on late Pleistocene alluvial fans that are less than 5 m high. South of Corral Canyon, multiple strands of the fault zone converge into a single fault that has produced a scarp as high as about 12 m. MMWFZ scarps are deeply dissected and display similar scarp morphologies as the nearby Bonneville shoreline that formed about 18 ka. Unfaulted latest Pleistocene to Holocene alluvium covers parts of the fault zone, indicating that the most recent movement on the fault zone is late Pleistocene.

INTRODUCTION

The Utah FORGE site is in the eastern Basin and Range Province (Figure 1), a region of east-west extension that covers much of the southwestern United States. The province consists of north-south-striking, range-bounding normal faults that define a series of bedrock horst blocks and corresponding basins. Basin and Range extension began in the early Miocene (ca. 17.5 Ma) and continues today (Dickinson, 2006). Within the Basin and Range, most developed geothermal systems are fault controlled (Faulds and others, 2011). In the Sevier Desert of southwestern Utah, several geothermal systems may have magmatic sources (Faulds and others, 2011), and deep-seated faults allow for hydrothermal circulation. Some late Quaternary normal faulting in the Sevier Desert about 75 km north of the FORGE site may be related to rift-assisted magmatism (Stahl and Niemi, 2017; Figure 1).

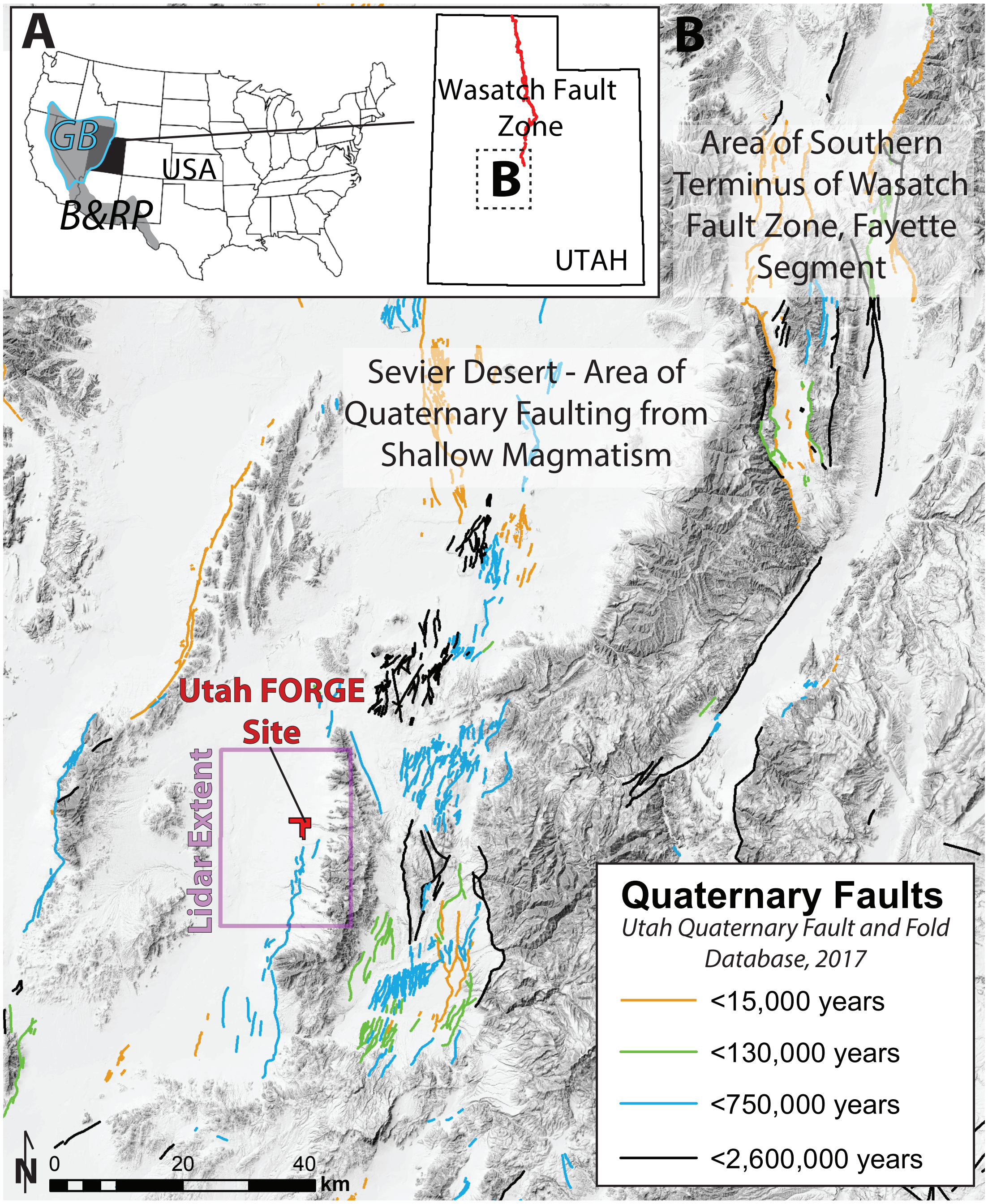

Figure 1. (A) *Regional overview of the study area relative to the Great Basin (GB), Basin and Range Province (B&RP), and the Wasatch fault zone (WFZ) in Utah.* ***(B)*** *Regional Quaternary faults near the Utah FORGE site include the southern terminus of the WFZ and faulting that may be driven by shallow magmatism in the Sevier Desert (Stahl and Niemi, 2017); colored fault lines indicate age of the most recent surface-rupturing movement.*

The Utah FORGE site is on the western flank of the Mineral Mountains, a 45-km-long, north-south-trending mountain range consisting primarily of late Oligocene to late Miocene intrusive rocks (Nielson and others, 1986; Kirby, 2019). Late Cenozoic unconsolidated deposits in the map area consist of coarse-grained alluvial deposits of late Tertiary to Holocene age, and coarse- and fine-grained lacustrine sediment deposited during at least two Quaternary lake cycles. The FORGE site is 2 km west of the Roosevelt Hot Springs (RHS) hydrothermal system that currently generates up to 35 MWe of gross power at the Blundell Power Plant (Simmons and others, 2016) (Figure 2). Quaternary hot spring deposits are common along the western margin of the RHS geothermal area. Thin eolian sand deposits are present throughout the study area, and form dunes and partially stabilized sand sheets and sand mounds. Late Tertiary and Quaternary rhyolitic lava flows and domes are present in the central Mineral Mountains. Three fault zones within the study area having suspected Quaternary movement are the north-south-trending Mineral Mountains West fault zone (MMWFZ), the Opal Mound fault (OMF), and the east-west-trending Negro Mag fault (NMF; Figure 2).

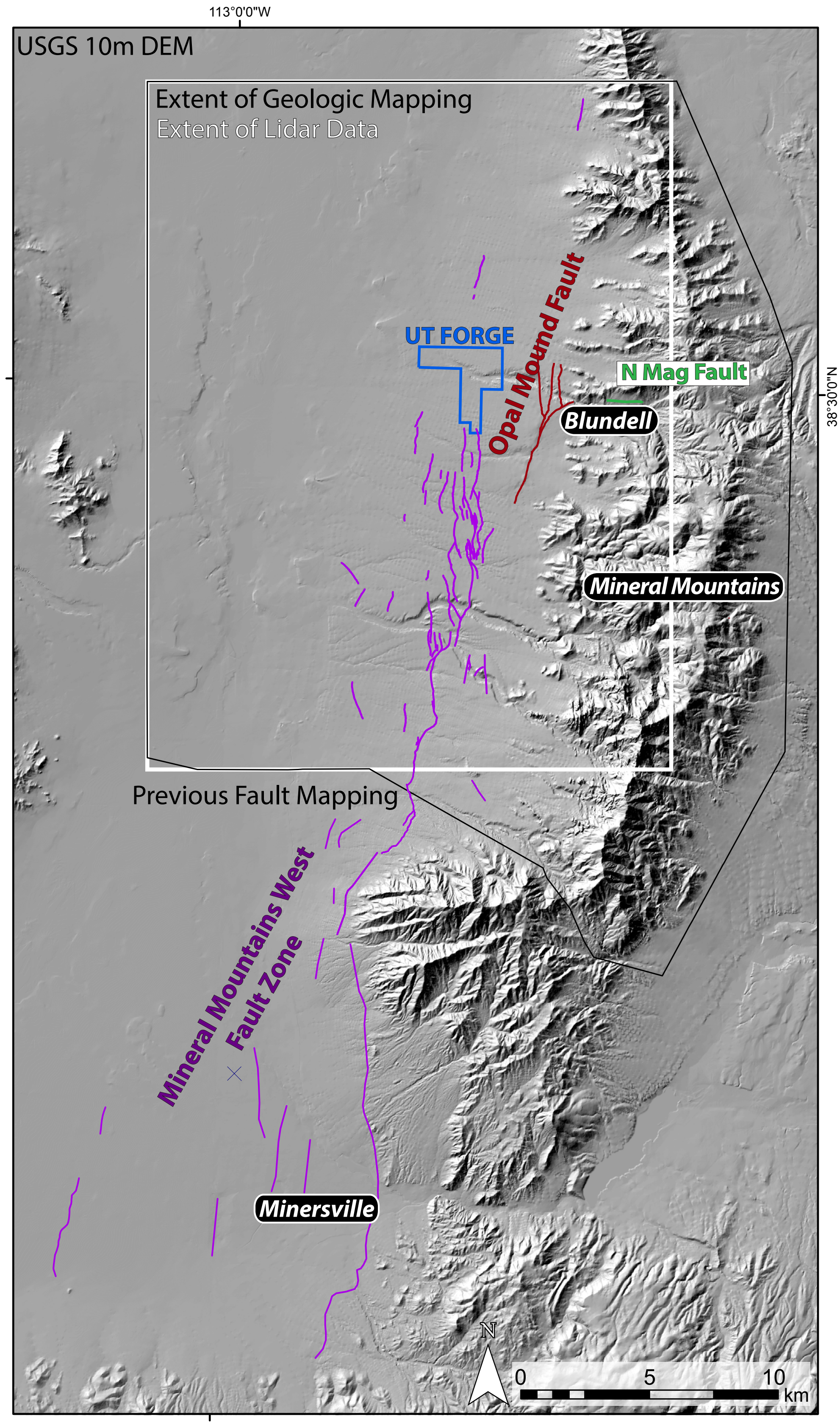

Figure 2. *Extent of Quaternary geologic mapping based on available lidar elevation data and the extent of the combined bedrock Quaternary geologic map presented in Kirby (2019). The surface traces of the OMF and the MMWFZ are also shown. The location of the MMWFZ south of the lidar-mapping area is depicted at a reconnaissance level based on previously published mapping (Rowley and others, 2005; Utah Geological Survey, 2017), satellite data, and aerial photographs.*

Petersen (1975) produced one of the earliest geologic maps of the RHS geothermal area that focused on Quaternary unconsolidated deposits and faulting. Anderson and Bucknam (1979) investigated fault scarps along the eastern margin of Milford Valley as part of a larger study of Quaternary fault scarps in the Richfield 1° x 2° quadrangle. Brogan and Birkhahn (1981) completed detailed surficial mapping, topographic profiling, and paleoseismic trench investigations along Quaternary faults near the RHS geothermal area. Geologic mapping by Hintze and others (2003; 1:62,500 scale) and Rowley and others (2005; 1:100,000 scale) subdivided unconsolidated units in the Richfield and Beaver 30′ x 60′ quadrangles, respectively, that collectively cover the Mineral Mountains and eastern Milford Valley.

Our mapping provides new information on the distribution and relative age of Quaternary unconsolidated deposits near the Utah FORGE site. This mapping also greatly improves information on the location, extent, and relative age of Quaternary-active fault traces. These data may be used to update geologic models and to provide updated information for seismic-hazard analyses.

METHODS

Geologic Mapping

We mapped late Cenozoic surficial deposits and Quaternary fault traces in an area encompassing 850 km^2 centered on the Utah FORGE site and the adjacent RHS geothermal area. The map encompasses an area that extends from Milford in the southwest corner to nearly the northern end of the Mineral Mountains in the northeast corner (Figure 2). Geologic mapping was based primarily on the interpretation of a digital elevation model (DEM) derived from 0.5-m airborne lidar (light detection and ranging) data acquired in the fall of 2016. Black-and-white and color aerial photography having various dates and scales (1953 AMS, 1:63,300 scale; 1955 GS-VJI, 1:37,400 scale; 1979 CSR-F, 1:25,000 scale) was also reviewed. We discovered that many prominent lineaments and tonal changes on the photos—some of which were mapped as fault scarps by some previous mappers—are the result of extensive range-management and fire-suppression/mitigation efforts in the area that have spanned several decades. Mapping was performed at 1:10,000 scale, but for convenience, is here combined with recently mapped bedrock geology at 1:24,000 scale (Kirby, 2019, Plates 1 and 2). We performed field mapping intermittently from August to December of 2017. We distinguished the relative age of alluvial-fan deposits based on surface morphology and degree of pedogenic carbonate development.

Geochronology

Infrared Stimulated Luminescence (IRSL) is a technique that uses infrared light to release trapped electrons within a crystal lattice to calculate an age. The infrared luminescence signal from potassium feldspar sand grains yields an estimate for the last time the grains were exposed to sunlight and thus infer a burial age (Rittenour, 2008; Rhodes, 2011). Before deposition, the grains are "bleached" by exposure to the sun. The bleaching process removes any trapped electron charge by brief natural light exposure during the transport of grains on the surface. The sand grains are deposited, buried, and then begin the process of being exposed to ionizing radiation from the surrounding soil. Over time, the ionizing radiation creates a charge by energizing electrons and moving them out of their normal orbits and into the crystal lattice of the potassium feldspar crystal. IRSL stimulates aliquots (i.e., samples) of sand grains that have not been exposed to light since burial using intense infrared light (880 ± 80 nm). These aliquots then luminesce from electrons being released from the crystal lattice. The luminescence decays until there is no more signal. From measuring the amount of luminescence from the sand grain, the equivalent dose (D_E), or amount of radiation energy the crystal has been exposed to since burial, is calculated. Another measurement of the ionizing radiation in the surrounding soil is taken to calculate the amount of radiation the sample has been exposed to over time (i.e., dose rate). The burial age of the deposit is calculated by dividing the D_E by the dose rate of the deposit sampled.

In August 2017 we excavated five test pits into various alluvial-fan deposits to better understand the composition and age of the sediments. In addition to detailed descriptions of sediment composition, texture, and soil development, we collected and submitted eight samples for IRSL dating at the Utah State University Luminescence Laboratory (https://www.usu.edu/geo/luminlab/). Based on geologic mapping, the burial ages of feldspar sand on the footwall of normal fault scarps will give maximum ages for fan-surface abandonment by vertical fault offset. We collected samples in light-safe tubes of sand-size grains in buried sheet flow deposits within mapped alluvial-fan units. Special care was taken when sampling to avoid poorly sorted deposits where sand grains may have not been completely bleached during deposition. Quartz and feldspar grains from 63 to 250 µm were separated and analyzed at the Utah State University Luminescence Lab. IRSL sample locations are shown on Figure 3 and final IRSL results are in Table 1. Soil logs with IRSL ages are in Appendix 1.

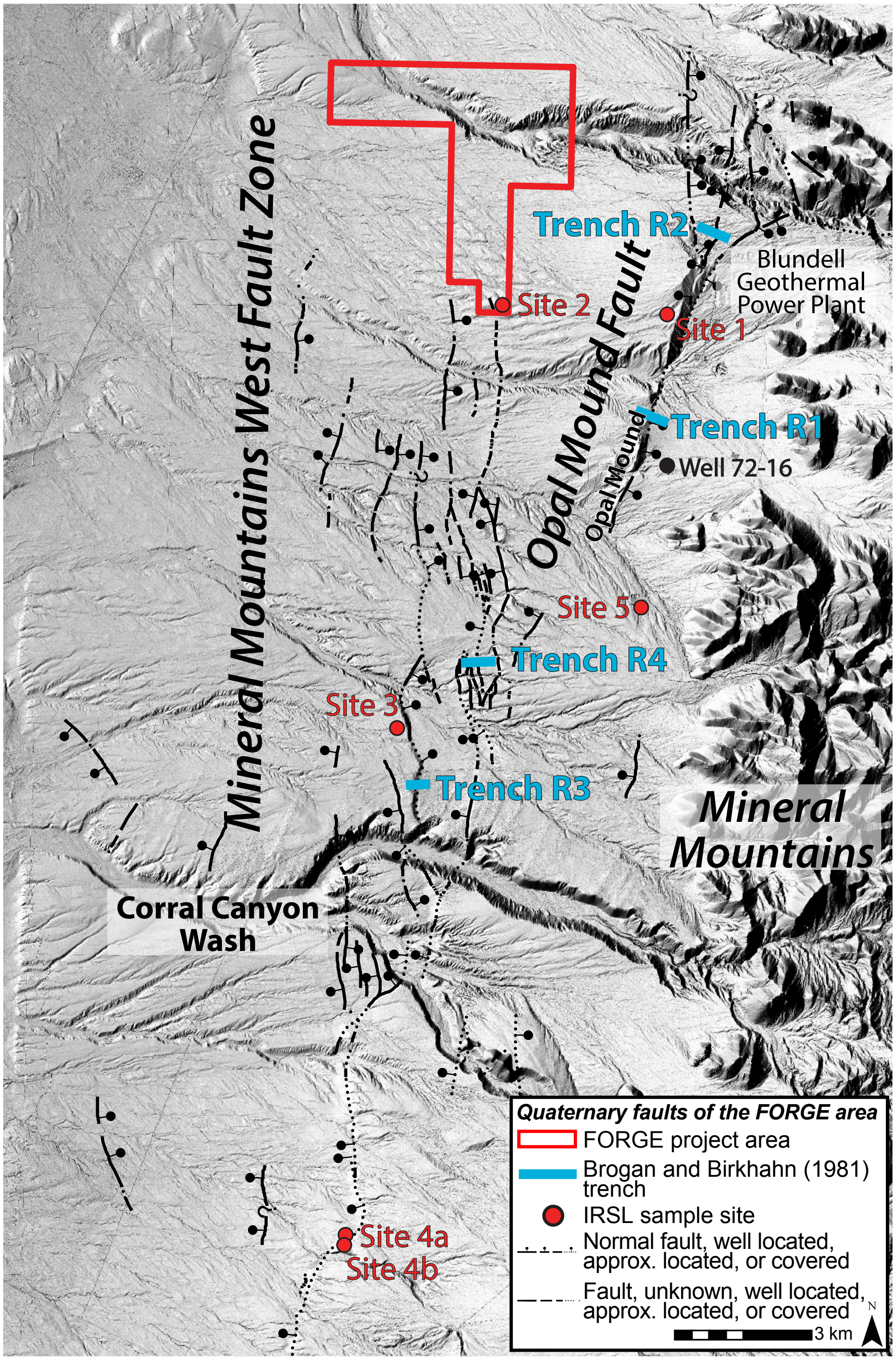

Figure 3. Half-meter slope-shade image derived from lidar of the fault systems around the RHS. The east-dipping OMF is considered a hydrologic barrier to geothermal fluid flow. The northern extent of the MMWFZ is a graben system that initiates 8 km south of the FORGE project area. The graben has internal horsts and grabens, with some discontinuous faults outside of the surface expression of the main graben.

Geomorphic Analysis

We used slope and aspect maps, hillshade models, and elevation contours derived from the 0.5-m lidar DEM to describe fault-scarp morphologies. To compare fault scarps along strike, we generated elevation profiles from the DEM using Global Mapper v.14. Using a slope map, we collected elevation profiles perpendicular to fault scarps. Elevation profiles were sufficiently long to ensure complete capture of undeformed alluvial-fan surfaces on the hanging wall and footwall of the faults (Figure 4).

Table 1. *Final IRSL age information results received January 31, 2018 from the Utah State University Luminescence lab.*

Sample num.	USU num.	Num. of aliquots[1]	Dose rate (Gy/ka)	D_E[2] ± 2σ (Gy)	Fading Rate[3] ± 1σ g_{2days} (%/decade)	**IRSL age ± 2σ (ka)**
FORGE 1 – OSL2	USU-2680	19 (19)	7.43 ± 1.24	255.85 ± 21.81	4.8 ± 0.9	**55.55 ± 12.07**
FORGE 2 – OSL3	USU-2681	14 (16)	9.13 ± 1.67	272.54 ± 25.13	8.9 ± 2.4	**80.12 ± 22.60**
FORGE 5 – OSL1	USU-2682	15 (16)	10.45 ± 2.09	161.43 ± 24.00	6.8 ± 1.7	**30.67 ± 9.25**
FORGE 3 – OSL7	USU-2683	20 (23)	11.29 ± 2.25	153.87 ± 27.94	9.8 ± 2.1	**41.41 ± 12.89**
FORGE 4a – OSL4	USU-2684	17 (17)	5.99 ± 0.77	45.76 ± 4.78	11.7 ± 2.74	**25.26 ± 6.40**
FORGE 4a – OSL5	USU-2685	17 (17)	6.34 ± 0.92	42.71 ± 3.21	10.8 ± 1.74	**21.53 ± 4.31**
FORGE 4a – OSL8	USU-2686	12 (12)	6.58 ± 0.85	39.34 ± 2.87	10.7 ± 1.94	**14.95 ± 4.33**
FORGE 4b – OSL6	USU-2687	13 (13)	8.22 ± 2.36	58.12 ± 5.77	6.9 ± 1.4	**>14.48 ± 5.43**

[1] Age analysis using the IRSL (50°C) and elevated temperature (225°C) pIR IRSL protocol of Buylaert et al. (2009). Number of aliquots used in age calculation and number of aliquots analyzed in parentheses.

[2] Equivilent dose (DE) and IRSL age calculated using the Central Age Model (CAM) of Galbraith and Roberts (2012).

[3] IRSL age on each aliquot corrected for fading following the method by Auclair et al. (2003) and correction model of Huntley and Lamothe (2001).

[4] Average fading rate from all site 4a samples (9.9±1.3%/decade) is likely underestimating true fading rate values, maximum fading rate for Huntley and Lamothe (2001) model of 10.0±1.0%/decade applied to all aliquots for fading-corrected IRSL ages.

We used Scarp Offset (v. 4g) (DuRoss, in preparation) in MatLab (v. R2017a) to analyze the fault-scarp profiles for the MMWFZ and OMF within the airborne lidar coverage area (Figure 4). This script uses a graphical user interface (GUI) that displays elevation versus distance and slope versus distance to allow the user to select the upper and lower bounds (i.e., fault offset surfaces) and the fault-scarp slope. The GUI plots and displays elevation vs. distance as well as slope vs. distance. Once the upper and lower bounds of the scarp are defined by the user, the script produces multiple measurements of the scarp to determine a preferred mean, or midpoint offset, value for the scarp and a minimum-maximum range. For each elevation profile, we made three measurements of the upper and lower bounds of the fault scarp based on (1) slope change in the topographic profile, (2) slope changes in the slope vs. distance plot, and (3) all profile data on the hanging-wall and footwall surfaces, except for the scarp (Appendix 2). The value used in each scarp height and scarp slope measurement is the mean value of these three measurements. These measurements were combined along strike to show the distribution of first-order measurements of scarp morphology of the OMF and MMWFZ (Figure 4).

LATE NEOGENE–QUATERNARY STRATIGRAPHY

Pre-Quaternary Volcanic Rocks and Alluvium

The oldest unconsolidated deposits exposed in the map area are Tertiary basin-fill deposits (map unit Taf) that crop out in two small areas: one area is north of Opal Mound and the other area is along the northern rim of Corral Canyon (see Kirby, 2019, Plate 1). North of Opal Mound, the east-dipping OMF has exhumed Taf deposits that are well exposed in a roadcut (Figure 5). Taf deposits consist of coarse, poorly sorted, non-stratified debris with boulders as large as 5 m in greatest dimension. Clasts are predominantly Precambrian banded gneiss and granitic intrusive rocks sourced from the Mineral Mountains. The abundance of large boulders of Precambrian metamorphic rocks on Taf slopes north of Opal Mound led Petersen (1975) to map much of the outcrop as Precambrian bedrock. Taf material was likely deposited on alluvial fans as debris flows and debris floods, although no original fan morphology remains. Boulder-rich Taf deposits are strikingly different than adjacent gruss-dominated, middle-fan alluvial units (Qaf_2 and Qaf_3) that were deposited in a comparatively low-energy environment. Obsidian, derived from ~0.8 to 0.5 Ma rhyolite flows (Lipman and others, 1978) in the Mineral Mountains, is common in all mapped Quaternary fan deposits except Taf, indicating that Taf predates the early to middle Pleistocene rhyolite eruptions. At Corral Canyon, Taf sediment is clearly overlain by a 7.9 Ma quartz-latite flow (Lipman and others, 1978; Sibbett and Nielson, 1980; Kirby, 2019, map unit Ml on Plates 1 and 2). Therefore, the age of Taf is loosely constrained between about 0.8 Ma to older than 8 Ma. However, because the transport of very coarse Taf sediment could not have occurred in the modern, low-relief landscape that characterizes the area today, we suggest that deposition occurred in late Tertiary time when the Mineral Mountains were substantially more prominent. Rapid uplift of the Mineral Mountains began about 11–8 Ma (Evans and Nielson, 1982; Coleman and others, 2001) and the range acquired most of its relief by the end of the Pliocene (Machette, 1985). We interpret that Taf deposits represent coarse debris shed from the ancestral Mineral Mountains that was deposited on the margin of the developing Milford Valley in late Miocene to Pliocene time.

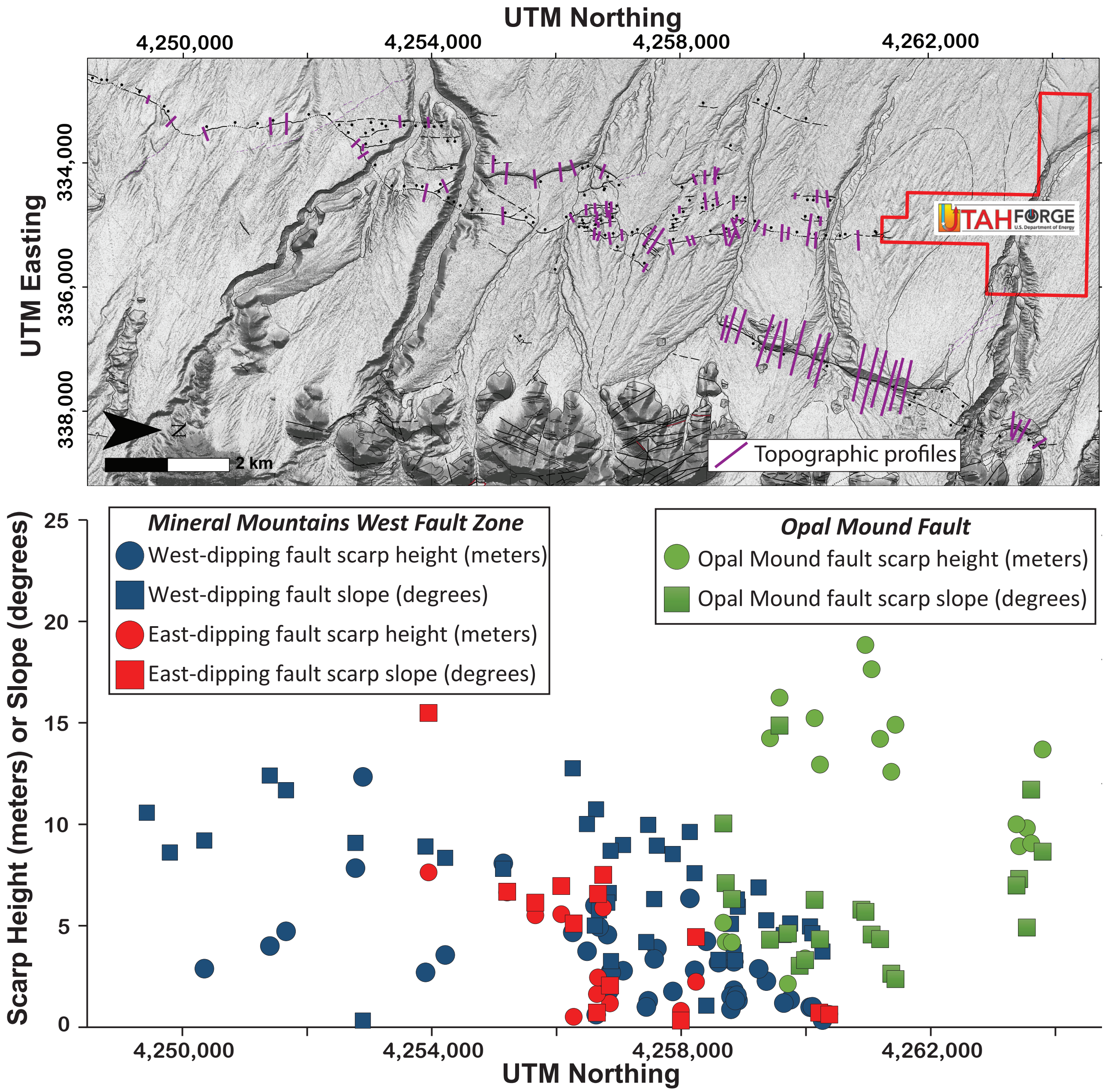

Figure 4. *Lidar-derived slope-shade image of the western Mineral Mountains showing location and extent of fault-scarp elevation profiles. Graph shows fault scarp height and slope along strike of the MMWFZ and the OMF.*

Quaternary Volcanic Rocks

Rhyolitic domes, lava flows, and air-fall and ash-flow tuffs were deposited from about 0.5 to 0.8 Ma (Lipman and others, 1978) on eroded bedrock surfaces and in canyons cut into the central Mineral Mountains (Rowley and others, 2005). The paleotopography preserved beneath the rhyolitic flows appears to be unchanged from the modern topography (Lipman and other, 1978). This indicates that the deeply embayed, low-gradient, and generally mature topography that characterizes the western flank of the central Mineral Mountains was likely established during the early Pleistocene, shortly after the range reached its maximum relief in the late Pliocene (Machette, 1985). The rhyolite flows in NM Wash (NMW; Bailey Ridge flow) and Wildhorse Canyon are well known for containing abundant implement-grade obsidian (Lipman and others, 1978). The distribution of obsidian clasts derived from the rhyolite helps constrain the relative ages of deposits that contain the clasts.

Figure 5. *Coarse debris-flow deposits exposed in a road cut north of Opal Mound that are part of map unit Taf. The road cut is about 4 m high; photo taken September 7, 2017.*

Quaternary Alluvial Deposits

Alluvial-fan deposits blanket much of the area near the Utah FORGE site (Kirby, 2019, Plate 1). The alluvium consists principally of pea-size gruss with minor cobbles and boulders derived from granitic intrusive and metamorphic rocks of the Mineral Mountains. Many fan surfaces are largely inactive and are incised by modern drainages. These older, dissected fan deposits are mapped as Qaf_3 and Qaf_2, where the subscript indicates relative age—Qaf_2 is younger and Qaf_3 is older. Older fan deposits typically extend from the valley interior upslope (at a remarkably consistent and relatively gentle 3° to 6° slope) into embayments cut deep into the Mineral Mountains. Modern drainages incise Qaf_2 alluvium as much as 9 m. Qaf_3 fan surfaces are incised as much as 45 m at NMW (Figure 6), and as much as 60 m at Ranch Canyon. Qaf_3 alluvium laps against the toe of the ~0.8-Ma Bailey Ridge flow, indicating that Qaf_3 is younger than ~0.8 Ma. Additionally, obsidian derived from the Bailey Ridge and Wildhorse Canyon flows is commonly intercalated with Qaf_3 and younger alluvial-fan deposits. The distal ends of Qaf_3 and Qaf_2 fans have been reworked by late Pleistocene Lake Bonneville and are deeply etched by the Bonneville highstand shoreline formed about 18 ka (Oviatt, 2015). Therefore, the age of $Qaf_{2\text{-}3}$ alluvium is broadly constrained between about 0.8 Ma and 18 ka. However, based on weakly to moderately developed pedogenic carbonate observed in test pits excavated in older alluvial-fan deposits, we consider the sediment to be mostly late Pleistocene in age (~126–18 ka). IRSL burial ages for sediment collected from $Qaf_{2\text{-}3}$ fans mostly support this conclusion. We obtained burial ages of 80.12 ± 22.60 ka, 55.55 ± 12.07 ka, and 41.41 ± 12.89 ka for samples collected from mapped Qaf_3 fan deposits (Figure 3 and Table 1). A single sample from a Qaf_2 fan yielded a 30.67 ± 9.25 ka burial age. A sample collected from a Qaf_2 fan surface at site 4b in the southern part of the map area yielded an anomalously young IRSL age of 14.48 ± 5.43 ka (Figure 3). The Qaf_2 fan surface having the anomalously young age is incised as much as 6 m and is surrounded by younger alluvium (Qafy and Qaf_1) (Figure 7). Less than 700 m east of site 4b, young, active-fan deposition (Qafy) is occurring at a higher elevation and is advancing downslope toward site 4b, burying the Qaf_2 surface. The fan surface at site 4b was possibly inundated by the distal end of some larger floods that discharged onto the active fan to the east.

Deep entrenchment of NMW, Ranch Canyon, and Corral Canyon of underlying alluvium has largely rendered older fan surfaces (Qaf_2 and Qaf_3) in the map area inactive. The excavation and down-gradient redistribution of alluvium driven by this period of incision resulted in the deposition of young fan alluvium (Qaf_1) at the mouths of the entrenched drainages. Young alluvial-fan deposits (Qaf_1) lack Bonneville shoreline etchings and clearly bury the Bonneville highstand shoreline and therefore are latest Pleistocene to Holocene in age. At about the same latitude of the entrenched drainages discussed above, the Beaver River is

Figure 6. *View to the west into NMW near RHS. The wash is incised about 45 m into older alluvial-fan deposits (Qaf$_3$); photo taken September 18, 2017.*

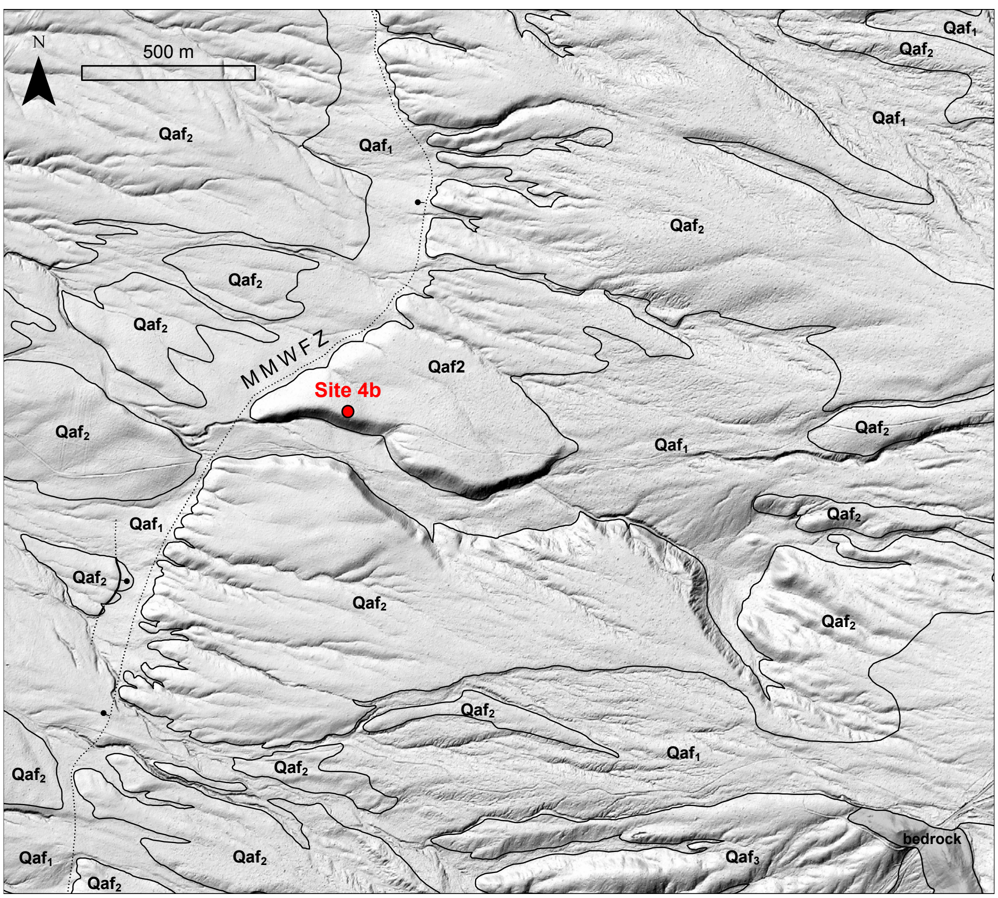

Figure 7. *Lidar-derived hillshade image of MMWFZ scarp and Quaternary surficial units near IRSL sample site 4b. Bar and ball on downthrown side of fault; Qaf$_1$=latest Pleistocene to Holocene alluvial-fan deposits; Qaf$_2$, Qaf$_3$=older late Pleistocene alluvial-fan deposits; Qafy=undivided Qaf$_1$ and Qaf$_2$ alluvial-fan deposits.*

similarly incised into underlying lacustrine deposits as much as 18 m. This period of incision could be the result of local uplift, as proposed by Mower and Cordova (1974). Or, perhaps more likely, the incision is the result of the lowering of base level following the regression of Lake Bonneville from Milford Valley at about 18 ka (Hintze and Davis, 2003; Oviatt, 2015) (see Lacustrine Deposits section below). Since the intermittent streams that now occupy the entrenched washes are conspicuously underfit, the channels were probably cut by more substantial streams that flowed during a wetter and cooler climate. The wetter and cooler climate that contributed to the Bonneville lake cycle continued for approximately 3000 years following the regression of Lake Bonneville (Hintze and Davis, 2003; Oviatt, 2015). Therefore, deep incision of the fans may have largely occurred in latest Pleistocene to early Holocene time.

Additional younger, mostly Holocene fan alluvium (Qaf_1) fills small grabens and other low areas formed along the OMF and MMWFZ. The alluvial deposits locally bury strands of the fault zones and are not displaced by the faults.

Hot Spring Deposits

Hot spring deposits are common along the OMF where it defines the western boundary of the RHS geothermal area. We subdivided hot spring deposits into two units: siliceous-sinter-cemented alluvium (map unit Qafs) and primary, banded opaline sinter (Qs) (Kirby, 2019, Plates 1 and 2). Siliceous sinter was deposited by hot spring water emanating from vents along and closely parallel to the OMF. Unit Qafs consists principally of silica-cemented, pea-size gruss that resembles adjacent uncemented fan alluvium. Locally, the cement also contains calcium carbonate. Qafs tends to preserve geomorphic surfaces, such as fan surfaces and fault scarps, as they appeared at the time of spring activity and cementation. For example, stratified, sinter-cemented alluvium (Qafs) in the NE 1/4 section 4, T. 27 S., R. 9 W., Salt Lake Base Line and Meridian (SLBM), dips as steeply as 25° to the east even though the modern fan surface dips west (Figure 8). The discordant deposits may represent preserved slope-wash deposits that mantled an east-facing fault scarp formed along a strand of the OMF. Alternatively, the east-dipping Qafs could be cemented fan deposits that originally dipped west, but were later back-rotated to the east by faulting.

The most significant deposits of primary opaline sinter (Qs) are at Opal Mound along the southern end of the OMF, where laminated tan, red, white, and brown opaline sinter have a thickness of at least 5 m. Laminations are vertical along narrow, north-trending vents (Figure 9), but more commonly, the laminations dip gently away from the vents.

Hot spring mineral deposition along the OMF has been periodic and has likely spanned several thousand years. Discordant and/or elevated and dissected sinter-cemented alluvium is likely late Pleistocene in age. Cemented alluvium mapped on modern, undissected surfaces, such as the deposits found along the active drainage bottom in NMW (Kirby, 2019, Plate 1), are likely Holocene in age. Well 72-16, drilled 400 m east of Opal Mound (Figure 3), encountered sinter-cemented alluvium horizons at depths of 90 m and 130 m (Glenn and Hulen, 1979), indicating that additional aprons of sinter-cemented alluvium are interbedded with late Pleistocene fans (Qaf_2 and Qaf_3) on the OMF hanging wall. Faulder (1991) reported that paleomagnetic studies conducted at Opal Mound yielded a minimum age of 12,000 years for opal found there. Radiocarbon ages of ~1900 and ~1600 ^{14}C yr B.P. reported by Lynne and others (2004, 2005) for the opal indicate that at least some opal deposition continued into the late Holocene, although spring activity at Opal Mound has not occurred historically.

Lacustrine Deposits

Lacustrine deposits are widely distributed in the central Milford Valley, and are exposed within 1.5 km to the west of the Utah FORGE site. The oldest exposed lacustrine deposit in the map area is a massive freshwater limestone (Qln) (Figure 10) that caps a series of low bluffs at an approximate elevation of 1510 m near the Beaver-Millard County line. The limestone is light tan to light gray and is partially covered by a thin veneer (<1 m thick) of gruss sourced from nearby alluvial fans. Several linear ground cracks, apparent in aerial photography and lidar-derived elevation models and observed in the field as vegetation lineaments (Figure 11), are developed on unit Qln in sections 1 and 12, T. 26. S., R. 10 W (SLBM). The origin of the cracks is unknown. We traced outcrops of the limestone northeast nearly to Antelope Spring in the Black Rock 7.5-minute quadrangle, where Oviatt (1991) mapped the unit as pre-Lake Bonneville lacustrine limestone. Hintze and Davis (2003) informally named this unit the “limestone of Twin Peaks,” and we apply this usage on our map. Although we have identified only a single 2- to 5-m-thick limestone bed in the map area, the limestone of Twin Peaks elsewhere commonly consists of several limestone beds interbedded with relatively soft marlstone that is up to 80 m thick (Zimmerman, 1961; Hintze and Davis, 2003). At Lava Ridge in the Black Point 7.5-minute quadrangle, the limestone of Twin Peaks is interbedded with basalt flows dated to about 2.5 Ma (Oviatt, 1991; Hintze and Davis, 2003). About 2.5 km southeast of Antelope Spring, limestone of Twin Peaks clearly overlies the ~1.3 Ma (Crecraft and others, 1981) Black Rock lava flow (Oviatt, 1991; this report), indicating that periodic limestone deposition by pre-Bonneville lakes spanned much of the early Pleistocene.

Figure 8. *View to the south of east-dipping (~20°) sinter-cemented alluvium south of NMW; photo taken September 11, 2017.*

Figure 9. *View to the south of a spring vent on Opal Mound. White arrow points to hammer placed in the vent neck where banded opal is vertical. Note that opal laminations dip gently away from either side of the vent. Photo taken September 8, 2017.*

Figure 10. *Outcrop of pre-Lake Bonneville limestone (Qln) just south of the Millard-Beaver County line. The limestone is tentatively correlated with the limestone of Twin Peaks of Hintze and Davis (2003). Photo taken August 30, 2017.*

Lake Bonneville began forming in the Great Salt Lake basin about 30 ka (Oviatt and others, 1992; Oviatt, 2015), but did not inundate the higher Sevier basin, Black Rock Desert, and Milford Valley until about 20 ka (Hintze and Davis, 2003). About 18 ka, Lake Bonneville reached its highest level, the Bonneville shoreline (Oviatt, 2015), at an elevation of about 1560 m in the map area. Prominent wave-cut escarpments formed on $Qaf_{2\text{-}3}$ surfaces at the Bonneville shoreline reach a maximum height of about 6 m south of Ranch Canyon wash. Shortly after the highstand, failure of the Red Rock Pass threshold in southeastern Idaho caused a rapid drop of lake level to an elevation of 1445 m (Provo shoreline) (Hintze and Davis, 2003), which is well below the elevation of Milford Valley. During Lake Bonneville's approximately 2000 years of occupation in Milford Valley, wave action and currents extensively reworked the gruss-dominated alluvial fans at and below the Bonneville shoreline. We mapped sand (map unit Qls) and gravel (Qlg) deposited in shore-zone beaches (Figure 12), spits, shoreline embankments, and cuspate barrier beaches (v-bars). Fine-grained, deep-water lacustrine deposits consisting principally of silt, clay, and marl are common at lower elevations in the northwestern part of the map area.

QUATERNARY FAULTING

N. Mag Fault

The east-west-trending NMF is thought to play an important role in localizing the NMW canyon, and as a controlling structure for the RHS geothermal system (Nielson and others, 1978). The presence and geometry of the NMF is primarily based on displaced bedrock features (Petersen, 1975; Nielson and others, 1978) and geophysical data that indicate displacement is down to the south (Crebs and Cook, 1976; Ward and others, 1978). The fault may be pre-Quaternary (Simmons and others, 2016; this report), but a conspicuous east-west-trending scarp formed on late Pleistocene fan alluvium (Qaf_3) is near the inferred trace of the NMF, and therefore is discussed here. The north-facing, 1.5-km-long scarp is adjacent to, and closely parallels, the bottom of NMW, the linear toe of the Bailey Ridge lava flow, and the inferred trace of the NMF (Kirby, 2019). The discontinuous scarp faces uphill and is as much as 5 m high. Mapping by Nielson and others (1978), Sibbett and Neilson (1980), Rowley and others (2005), and Kirby (2019) show a north-dipping strand of the NMF associated with the scarp that implies late Pleistocene surface faulting. We found no additional scarps formed on Qaf_3 deposits or bedrock to the west or east along the inferred trace of the NMF.

Figure 11. *One of several vegetation lineaments just south of the Millard-Beaver County line that mark ground cracks formed on the underlying limestone of Twin Peaks (Qln); photo taken September 25, 2017.*

Figure 13 presents an alternative interpretation that explains the scarp in NMW as resulting from differential erosion along a geologic contact rather than due to surface faulting. The scarp is formed on gruss- and obsidian-rich alluvium identical to Qaf_3 alluvium that forms the broad fan surface underlying the Blundell power plant. The scarp appears to be a remnant of this once-continuous Qaf_3 fan that extended up NMW and abutted against the 0.8-Ma Bailey Ridge lava flow and the north canyon wall. Later incision of NMW in latest Pleistocene to Holocene time along the toe of the Bailey Ridge lava flow isolated a remnant of the Qaf_3 fan along the northern canyon wall. Erosion along the linear contact between the more resistant Qaf_3 remnant and adjacent slope-wash (Qafy) deposits on the canyon wall (Figure 13), rather than surface faulting, may have formed the north-facing scarp. Brogan and Birkhahn (1981) also suggested that erosion along a geologic contact may be responsible for the scarp.

The prominent line of sinter deposits that delineates the north-south-trending OMF (discussed in next section) appears to be undeflected by the intersecting NMF (Kirby, 2019, Plate 1), indicating that the NMF is the older structure. If scarp formation on late Pleistocene alluvium in NMW is non-tectonic in origin, then the latest movement on the NMF was likely pre-Quaternary since the fault is in an unfavorable orientation to accommodate east-west Basin and Range extension (Nielson, 1989; Faulder, 1994).

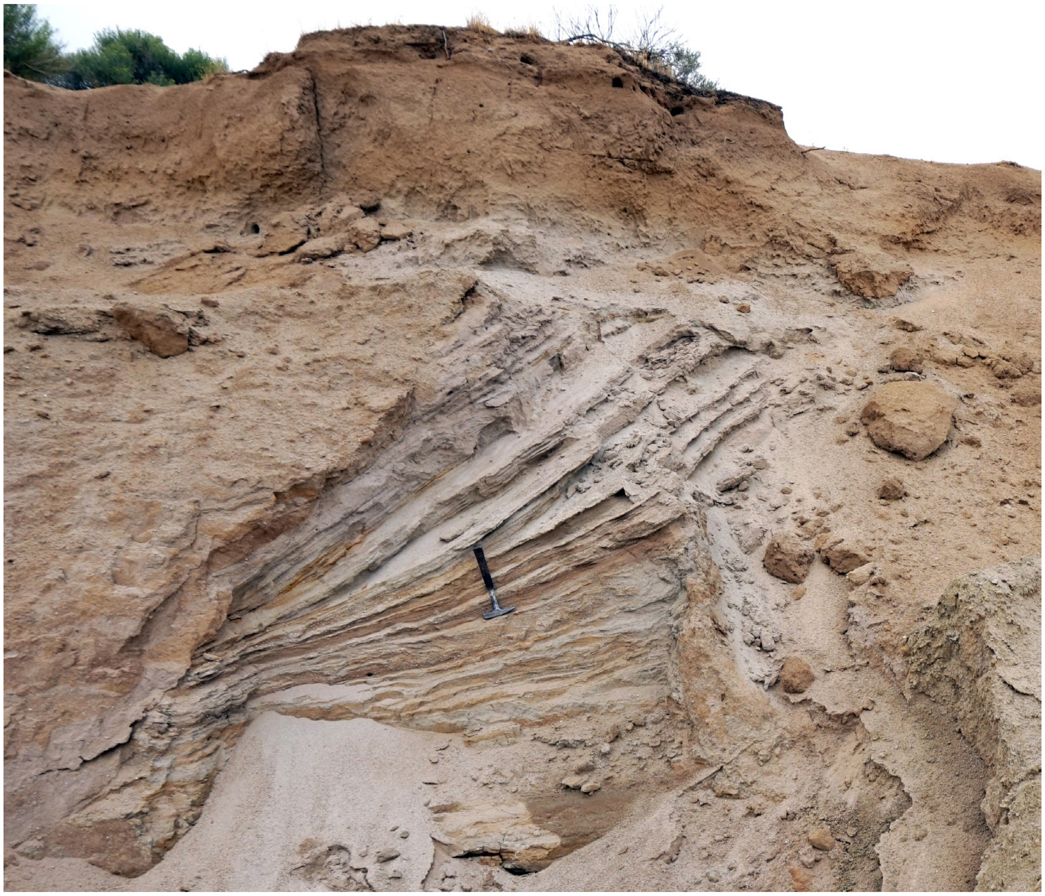

Figure 12. *View to the east into a sand and gravel pit excavated into a Lake Bonneville shoreline beach deposit east of Milford (SW1/4 section 9, T. 28 S., R. 10 W. [SLBM]); photo taken August 30, 2017.*

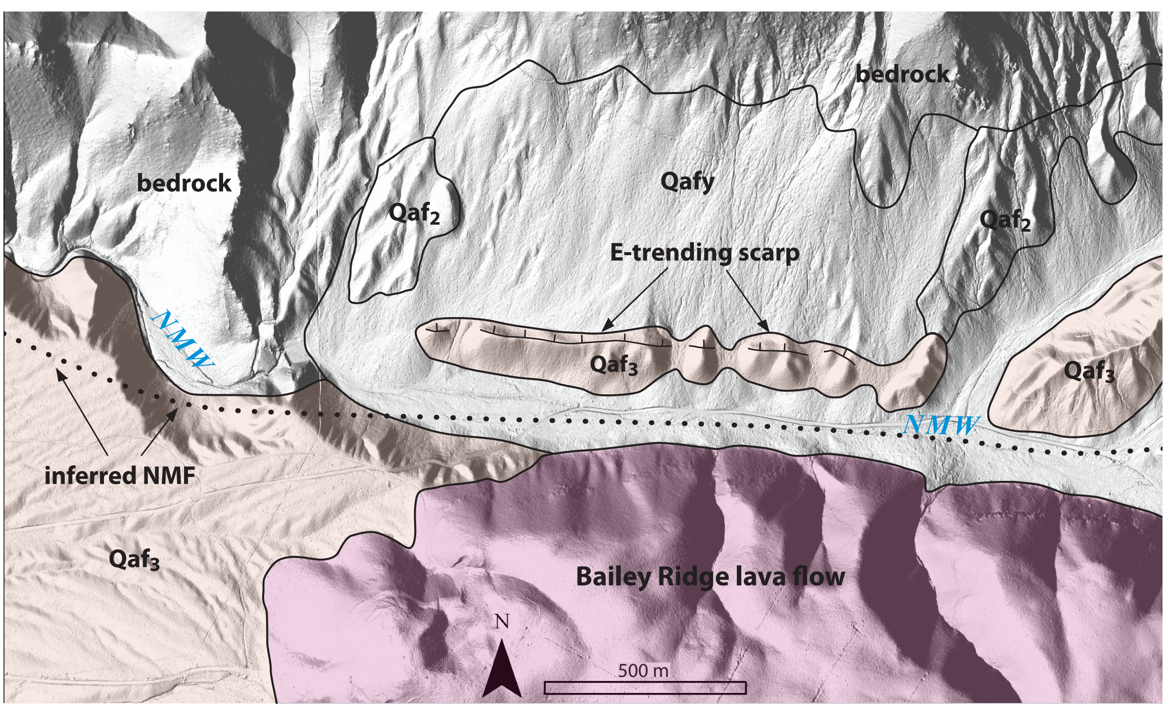

Figure 13. *Lidar-derived hillshade image of a prominent east-trending scarp oriented parallel to NMW and the toe of the Bailey Ridge lava flow. This geologic mapping varies from the mapping of Kirby (2019) and presents an alternative interpretation of the relation between the east-trending scarp and the NMF. Qaf$_3$, Qaf$_2$=old (late Pleistocene) fan alluvium, Qafy=young (Holocene to latest Pleistocene) fan alluvium and slope wash.*

Opal Mound Fault

The north-northeast-striking OMF extends for at least 7 km near the western margin of the Mineral Mountains (Figure 3). The OMF dips east toward the Mineral Mountains and defines the western boundary of the RHS geothermal area (Nielson and others, 1978, 1986; Faulder, 1991). Near NMW, the OMF consists of both east- and west-dipping splays (Figure 14). The fault is up to 1.5 km distant from the Mineral Mountains range front. Scarp height varies widely from about 18 m where the fault juxtaposes units Taf and Qaf$_3$ southwest of the power plant, to 0 m where the scarp has been removed by erosion (Figure 4). Burial ages (IRSL) from fault-isolated alluvial-fan deposits (Qaf$_3$) just west of the OMF indicate aggradation west of the OMF ceased at about 56 ka (Figure 14). Scarps measured in alluvium along the 7 km fault length averaged ~11 m high with an average slope of ~6° (Kleber and others, 2017).

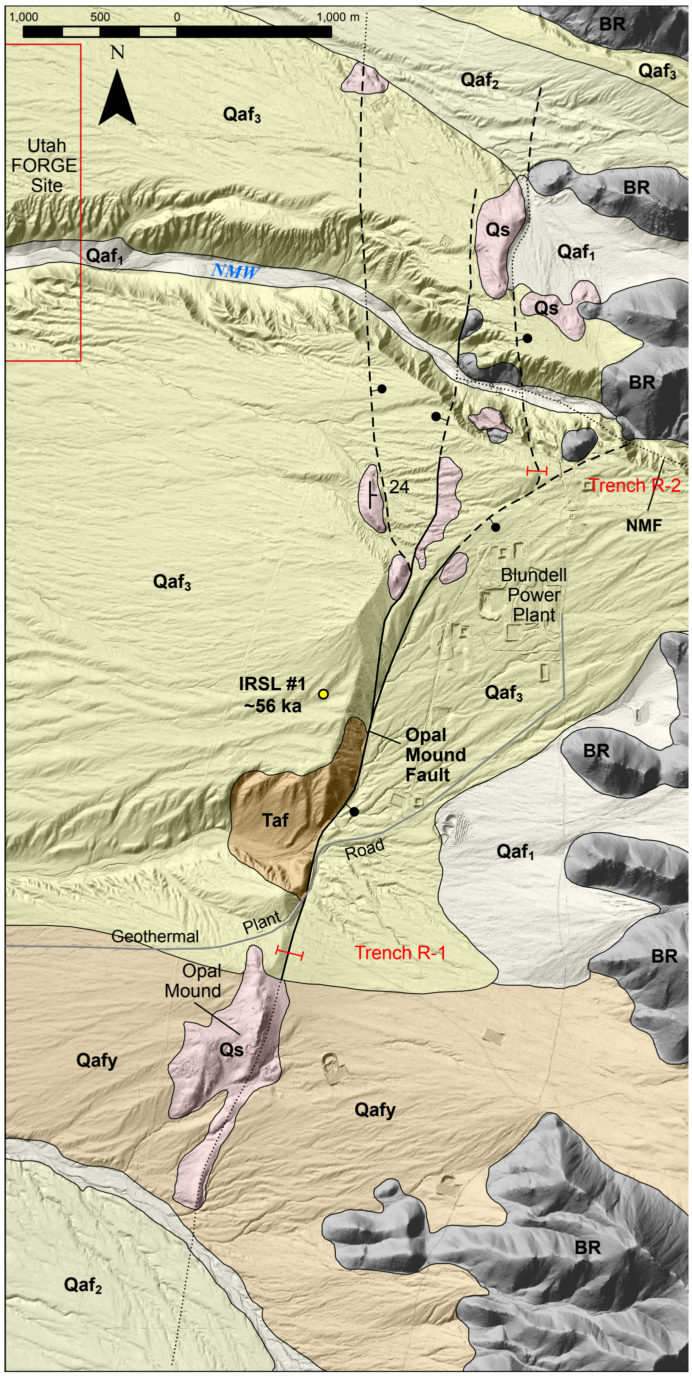

Figure 14. *Simplified Quaternary geology on a lidar-derived hillshade image of the area near the OMF. Taf=late Tertiary basin-fill deposits; Qaf$_3$, Qaf$_2$=late Pleistocene alluvial fans; Qaf$_1$=latest Pleistocene to Holocene alluvial fans; Qafy=undivided young (Holocene to late Pleistocene) fan alluvium; Qs=primary siliceous sinter and sinter-cemented alluvium, undivided; BR=bedrock.*

Hot springs have periodically emanated from fissures along the OMF and have resulted in the deposition of primary, laminated opaline sinter and cementation of adjacent alluvium. Hot spring mineral deposition has been contemporaneous with faulting along the OMF. As previously discussed in the Hot Spring Deposits section, buried horizons of sinter-cemented fan alluvium east of the OMF and the possible fault-rotated sinter-cemented alluvium indicate that some older spring deposits have been displaced by the fault. Previous workers have suggested that primary banded opal as young as about 1.6 kyr (Lynne and others, 2004, 2005) exposed on the surface at Opal Mound is displaced by the OMF (e.g., Petersen, 1975; Lynne and others, 2005). However, we could not find evidence for the displacement of either sinter or alluvium of Holocene age along the OMF. A reconnaissance investigation of the OMF by Anderson and Bucknam (1979) likewise failed to find evidence for Holocene faulting. We believe that if resistant siliceous sinter deposits were displaced by surface faulting on the OMF in the Holocene, fault scarps would be easily detected in both high-resolution (0.5 m) lidar elevation data and in the field. It is more likely that the youngest (Holocene) sinter deposits were sourced from vents along the crest of Opal Mound and that they simply drape over a preexisting scarp and are unbroken by the underlying OMF. Likewise, recent mapping (see Kirby, 2019, Plate 1) shows that young, mostly Holocene, alluvial deposits cover the OMF at many locations and that the deposits are not displaced.

Paleoseismic Data

Paleoseismic trench logs are available from a 1981 Woodward–Clyde study completed for the U.S. Geological Survey investigating faults and geothermal anomalies in the Great Basin (Brogan and Birkhahn, 1981). Woodward–Clyde excavated a paleoseismic trench (R-1) near the intersection of Geothermal Plant Road and the southern end of the OMF (Figure 14). Depositional units exposed included older bedded alluvium, colluvium, mudflows, and younger alluvium (Figure 15). There was evidence that hydrothermal fluids had circulated within more permeable parts of a mudflow. Dames and Moore identified a 10-m-wide fault zone in the trench. The fault zone had apparent down-to-the-east movement, cemented shear fabrics, and discrete normal-sense displacements of 5–33 cm. Trench R-2, excavated across a suspected fault scarp just south of NMW (Figure 14), exposed an unfaulted sequence of older alluvium.

We interpret that scarp development along the OMF is largely influenced by differential erosion of resistant, siliceous sinter exposed along the fault. The steeper, most prominent scarps are coincident with significant spring deposits and resemble fault-line scarps (Figure 14). Similarly, a well-defined scarp north of Opal Mound formed where the OMF juxtaposes rela-

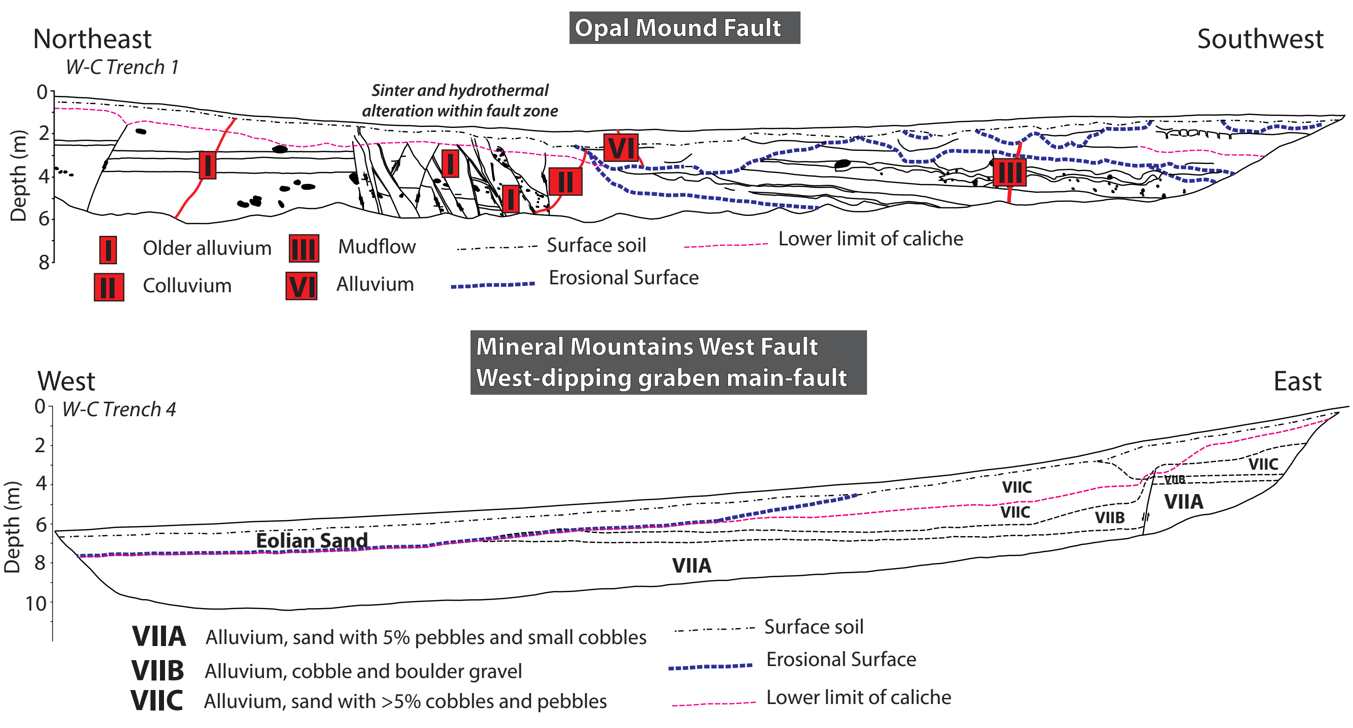

Figure 15. *Reproduced paleoseismic trench logs from Woodward-Clyde investigation (Brogan and Birkhahn, 1981). Approximate trench locations are on Figure 3. Trench 1 was excavated on the OMF and trench 4 was on a strand of the MMWFZ. No geochronology samples were analyzed.*

tively resistant late Neogene basin-fill deposits (Taf) with grussy Qaf_3 deposits (Figure 14). Relatively steep escarpments, particularly near Opal Mound, have formed on both the east and west sides of north-trending spring vents adjacent to the fault (Figure 14). If scarps near Opal Mound were formed only by surface faulting along the east-dipping OMF, we would expect to see scarp formation only on the east side of the spring deposits. Where not armored by sinter deposits, the OMF scarp has either been degraded by erosion to a very low angle or has been completely removed. One of the few OMF scarps not influenced by spring deposits is formed solely on alluvial-fan deposits in the NW corner of section 9, T. 27 S., R. 9 W. (SLBM) (Kirby, 2019, Plate 1). There, the scarp has degraded to a gentle 4° slope angle.

Spring deposits are generally absent along a 1-km-long section of the OMF near NMW—this section also lacks any detectable topographic expression of the fault (Figure 14). Additionally, several west-flowing drainages, including minor drainages with drainage basins less than 1.5 km^2, pass through the OMF scarp (Figure 14), indicating significant time has elapsed since the most recent surface displacement on the fault (Petersen, 1975). Where not influenced by sinter deposits, the morphology and degree of dissection of the OMF scarp appear more mature than Bonneville shoreline scarps formed on alluvial-fan material of similar age and texture. Figure 16 shows scarp height plotted against scarp slope measured along the OMF and the MMWFZ (discussed in next section) in the study area. We did not measure scarps formed on sinter or opal deposits. Scarp profile data from regional Basin and Range faults (Anderson and Bucknam, 1979) are included on the graph for comparison. The graph shows that the OMF scarp has a significantly lower slope than other regional Basin and Range faults and the MMWFZ (Figure 16).

Based on cross-cutting relations with both late Pleistocene and Holocene alluvial deposits, IRSL ages from fault-isolated fan deposits, degree of dissection, scarp slope degradation, development of through-going drainages, and the development of fault-line scarp morphology, we deduce a late Pleistocene age for the most recent movement on the OMF.

Mineral Mountains West Faults

Movement on a complex zone of north-south-trending normal faults has formed a series of scarps on late Pleistocene alluvial fans (map units Qaf_2 and Qaf_3) (see Kirby, 2019, Plate 1; Figure 17) about midway between the Mineral Mountains range front and the Bonneville shoreline. The fault zone begins near the southern boundary of the Utah FORGE site, where it consists of several west- and east-dipping strands, and continues south for about 40 km to near Minersville (Rowley and others, 2005; Figure 2). There are no definitively mapped fault scarps within the Utah FORGE site. The fault zone is named the Mineral Mountains (West Side) faults in the *Quaternary Fault and Fold Database of the United States* (U.S. Geological Survey, 2018) and the *Utah Quaternary Fault and Fold Database* (Utah Geological Survey, 2018). We simplify this name to the Mineral Mountains West fault zone (MMWFZ).

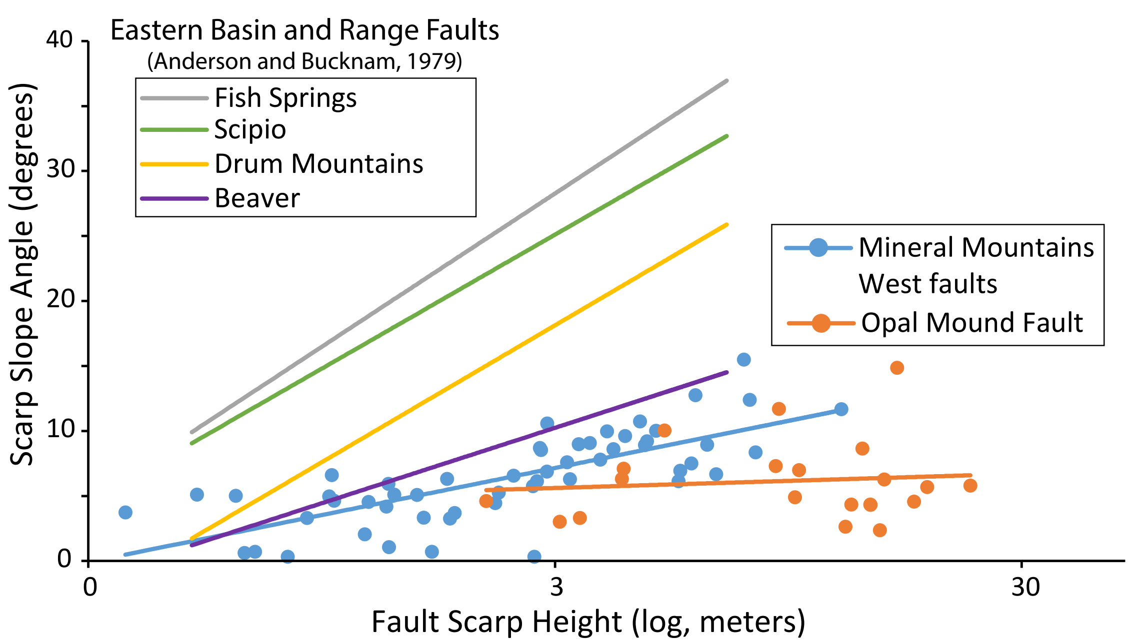

Figure 16. *Scarp height (log, meters) plotted against scarp slope (degrees) measured on MMW faults and the OMF with a logarithmic regression. Regression functions from other Basin and Range faults are from Anderson and Bucknam (1979).*

Figure 17. *Low-sun angle (a.m.) photo of a low MMWFZ scarp (<5 m high) formed on late Pleistocene alluvial-fan deposits north of Ranch Canyon. The Mineral Mountains range front is 2 km distant from the scarp. View is to the southeast; photo taken September 11, 2017.*

Scarps associated with the multi-strand MMWFZ south of the FORGE site have a mean height of 3.5 m and some are less than 1.5 m high. The faults form a prominent graben that varies in width from ~700 to 1200 m with internal horst and graben blocks. Throughout the graben, the highest and most continuous scarps are west-dipping and displace alluvial deposits 1 to 8 m with a normal sense of motion. Within the graben, east-dipping scarps have an average height and slope of 3.18 m and 5°, respectively, and west-dipping faults have an average height and slope of 3.16 m and 7°, respectively. Both east- and west-dipping scarps increase in height and slope south of the FORGE site. South of Corral Canyon, multiple strands of the fault converge into a single fault that has produced a scarp as high as 13 m (Figure 7). The larger average displacement on the fault south of Corral Canyon has resulted in higher rates of erosion on the upthrown Qaf_{2-3} fan surface. Substantial alluvium (Qaf_1, Qafy) derived from the upthrown block has buried much of the downthrown Qaf_{2-3} surface south of Corral Canyon and conceals the MMWFZ (Kirby, 2019, Plate 1).

Brogan and Birkhahn (1981) and Rowley and others (2005) mapped short faults (<2 km long) several kilometers west of the MMWFZ in central Milford Valley, where they possibly displace Lake Bonneville deposits. Our mapping produced no evidence for fault-displaced Lake Bonneville sediment.

Paleoseismic Data

Paleoseismic data are available for two trenches excavated on MMWFZ graben faults by Brogan and Birkhahn (1981). Trench R-3 crossed a prominent east-dipping graben fault north of Ranch Canyon (Kirby, 2019, Plate 1; Figure 3). The trench exposed a series of mudflows displaced about 0.5 m down-to-the-east. Trench R-4, excavated across a west-dipping graben fault about 2 km north of trench R-3 (Kirby, 2019, Plate 1; Figure 3), exposed alluvium interpreted to be intermediate in age with the older alluvium exposed in trench R-1 across the OMF. Brogan and Birkhahn (1981) identified 2.2 m of down-to-the-west displacement of alluvium in trench R-4 (Figure 15), but did not interpret the number of surface-faulting earthquakes associated with these displaced deposits. After reviewing the R-4 trench log, we interpret the presence of at least one, and possibly two scarp-derived colluvial wedges, providing evidence for one or two surface-rupturing earthquakes on this strand of the MMWFZ. Trench R-4 is within a complicated graben, and there are several other east- and west-facing graben faults close to this site that may complicate interpretations of the number of earthquakes and the amount of slip-per-earthquake for the entire fault zone.

MMWFZ scarps are deeply dissected, locally discontinuous, and generally display similar scarp morphologies as nearby Bonneville shorelines that formed about 18 ka. Latest Pleistocene to Holocene alluvial deposits (map unit Qaf_1) have filled several grabens and other low areas adjacent to the MMWFZ. The young alluvium conceals the faults and has not been displaced. Although the MMWFZ is the major western range-bounding fault for the Mineral Mountains, Quaternary slip rates on the fault zone in the map area have been insufficient to form a range front; the mountain front lies 3 to 5 km to the east. We deduce a latest Pleistocene age for the most recent surface faulting on the MMWFZ.

SUMMARY OF LATE NEOGENE TO QUATERNARY GEOLOGY

Uplift and maximum relief of the Mineral Mountains likely occurred in late Miocene to Pliocene time (Evans and Nielson, 1982; Machette, 1985; Coleman and others, 2001). Erosion of the rapidly uplifting mountain block resulted in coarse sedimentation into the incipient Milford Valley. Erosion of the Mineral Mountains block continued into the early Pleistocene, forming deeply embayed canyons and other gently dipping erosional surfaces that graded to the adjacent valley floor. At least one early Pleistocene freshwater lake occupied the central part of Milford Valley and deposited limestone. Starting in the early middle Pleistocene (~0.8 Ma), volcanism along the crest of the Mineral Mountains deposited rhyolitic lava flows that partially filled NMW, Wildhorse, and Ranch Canyons. By late-middle Pleistocene time, alluvial fans began aggrading eastward into the Mineral Mountains, resulting in the burial of low-relief bedrock foothills and the partial infilling of the deeply embayed canyons. In NMW, the aggrading fans lapped against the toe of the ~0.8-Ma Bailey Ridge lava flow. In late Pleistocene time, movement on the OMF and the MMWFZ displaced alluvial-fan surfaces several meters but were not sufficiently active to form mountain fronts. The east-dipping OMF is in a favorable position and orientation to form the western boundary of the RHS geothermal system. Periodic hot spring activity throughout the late Pleistocene and into the Holocene deposited abundant siliceous sinter along the OMF. Differential erosion of the sinter deposits has greatly influenced the OMF's scarp morphology. Sand and gravel at the distal ends of coalesced alluvial fans were extensively reworked—locally, into prominent barrier bars and v-embankments—by late Pleistocene Lake Bonneville, which occupied Milford Valley from about 20 to 18 ka. Perhaps driven by local uplift, or the lowering of base level following the recession of Lake Bonneville (~18 ka), NMW, Ranch Canyon, Corral Canyon, and the Beaver River incised their channels, thus rendering many fan surfaces inactive. This period of incision contributed to latest Pleistocene to Holocene deposition of alluvium near the mouths of the entrenched drainages, where the deposits obscure and bury the Bonneville shoreline. Latest Pleistocene to Holocene deposits, including opaline sinter and young alluvium, locally conceal the OMF and MMWFZ and are not faulted. A highly degraded and dissected OMF scarp morphology indicates a late Pleistocene age for the most recent surface displacement. Scarp morphologies of the MMW fault zone appear younger than those of the OMF, and are similar to those formed by Lake Bonneville shorelines (~18 ka), indicating a latest Pleistocene age for most recent movement on the MMW fault zone.

ACKNOWLEDGMENTS

We would like to thank Dr. Tammy Rittenour, Michelle Nelson, and Carlie Ideker of Utah State University (USU) for assistance with sample collection in the field and sample processing at the USU Luminescence lab (http://www.usu.edu/geo/luminlab/). We would also like to thank Brendon Quirk of the University of Utah for his insights on dating methods and processing. Reviews from William Lund, Michael Hylland, and Stephanie Carney of the Utah Geological Survey contributed to this manuscript.

REFERENCES

Anderson, R.E., and Bucknam, R.C., 1979, Map of fault scarps in unconsolidated sediments, Richfield 1° x 2° quadrangle, Utah: U.S. Geological Survey Open-File Report 79-1236, 15 p., scale 1:250,000.

Brogan, G., and Birkhahn, P., 1981, Faults and occurrence of geothermal anomalies: Woodward-Clyde Consultants final report to the U.S. Geological Survey Geothermal Research Program, Contract 14-08-0001-16310, variously paginated.

Crebs, T.J., and Cook, K.L., 1976, Technical report—gravity and ground magnetic surveys of the central Mineral Mountains, Utah, volume 6, final report: unpublished report prepared by Department of Geology and Geophysics, University of Utah, Salt Lake City, 129 p.

Crecraft, H.R., Nash, W.P., and Evans, S.H., Jr., 1981, Late Cenozoic volcanism at Twin Peaks, Utah, geology and petrology: Journal of Geophysical Research, v. 86, p. 10,303–10,320.

Coleman, D.S., Walker, J.D., Bartley, J.M., and Hodges, K.V., 2001, Thermochronologic evidence for footwall deformation during extensional core complex development, Mineral Mountains, Utah, *in* Erskine, M.C., Faulds, J.E., Bartley, J.M., and Rowley, P.D., editors, The geologic transition, High Plateaus to Great Basin—a symposium and field guide (The

Mackin Volume): Utah Geological Association and Pacific Section of the American Association of Petroleum Geologists, Utah Geological Association Publication 30, p. 155–168.

Dickinson, W.R., 2006, Geotectonic evolution of the Great Basin: Geosphere, v. 2, p. 353–368, doi: 10.1130/GES00054.1.

DuRoss, C., in preparation, Scarp offset v4g, MATlab script.

Evans, S.H., Jr., and Nielson, D.L., 1982, Thermal and tectonic history of the Mineral Mountains intrusive complex: Geothermal Resources Council Transactions, v. 6, p. 15–18.

Faulder, D.D., 1991, Conceptual geologic model and native state model of the Roosevelt Hot Springs hydrothermal system: Proceedings, 16th Workshop on Geothermal Reservoir Engineering, Stanford University, p. 131–142.

Faulder, D.D., 1994, Long-term flow test #1, Roosevelt Hot Springs, Utah: Geothermal Resources Council Transactions, v. 18, p. 583–590.

Faulds, J.E., Hinz, N.H., Coolbaugh, M.F., Cashman, P.H., Kratt, C., Dering, G., Edwards, J., Mayhew, B., and Mclachlan, H., 2011, Assessment of favorable structural settings of geothermal systems in the Great Basin, Western USA: Geothermal Resources Council Transactions, v. 35, p. 777–783.

Hintze, L.F., and Davis, F.D., 2003, Geology of Millard County, Utah: Utah Geological Survey Bulletin 133, 305 p.

Hintze, L.F., Davis, F.D., Rowley, P.D., Cunningham, C.G., Steven, T.A., and Willis, G.C., 2003, Geologic map of the Richfield 30′ x 60′ quadrangle, southeast Millard County, and parts of Beaver, Piute, and Sevier Counties, Utah: Utah Geological Survey Map 195, scale 1:62,500.

Glenn, W.E., and Hulen, J.B., 1979, Interpretation of well log data from four drill holes at Roosevelt Hot Springs KGRA: unpublished report prepared by Earth Science Laboratory, University of Utah Research Institute, Salt Lake City, Utah, for U.S. Department of Energy, Division of Geothermal Energy, 74 p.

Kirby, S.M., 2019, Revised mapping of bedrock geology adjoining the Utah FORGE site, *in* Allis, R., and Moore, J.N., editors, Geothermal characteristics of the Roosevelt Hot Springs system and adjacent FORGE EGS site, Milford, Utah: Utah Geological Survey Miscellaneous Publication 169-A, 6 p., 2 plates, scale 1:24,000, https://doi.org/10.34191/MP-169-A.

Kleber, E., Kirby, S.M., Hiscock, A.I., and Bowman, S., 2017, Preliminary assessment of Quaternary faulting based on high resolution topographic data near the FORGE geothermal site, Mineral Mountains, Utah, USA: Proceedings for the 8th international INQUA Meeting on Paleoseismology, Active Tectonics and Archaeoseismology (PATA), November 12–15, 2017, New Zealand.

Lipman, P.W., Rowley, P.D., Mehnert, H.H., Evans S.H., Jr., Nash, W.P., and Brown F.H., 1978, Pleistocene rhyolite of the Mineral Mountains, Utah—geothermal and archeological significance: U.S. Geological Survey Journal of Research, v. 6, p. 133–147.

Lynne, B.Y., Campbell, K.A., Moore, J.N., and Browne, P.R.L., 2004, Siliceous sinter diagenesis at the Opal Mound, Roosevelt Hot Springs, Utah, USA: Proceedings, 26th New Zealand Geothermal Workshop, p. 12–17.

Lynne, B.Y., Campbell, K.A., Moore, J.N., and Browne, P.R.L., 2005, Diagenesis of 1900 year-old siliceous sinter (opal-A to quartz) at Opal Mound, Roosevelt Hot Springs, Utah: Sedimentary Geology, v. 179, p. 249–278.

Machette, M.N., 1985, Late Cenozoic geology of the Beaver Basin, southwestern Utah: Brigham Young University Geology Studies, v. 32, pt. 1, p. 19–37.

Mower, R.W., and Cordova, R.M., 1974, Water resources of the Milford area, Utah, with emphasis on ground water: Utah Department of Natural Resources Technical Publication no. 43, 99 p.

Nielson, D.L., 1989, Stress in geothermal systems: Geothermal Resources Council Transactions, v. 13, p. 271–276.

Nielson D. L., Evans, S.H., Jr., and Sibbett, B.S., 1986, Magmatic, structural, and hydrothermal evolution of the Mineral Mountains intrusive complex, Utah: Geological Society of America Bulletin, v. 97, no. 6, p. 765–777.

Nielson, D.L., Sibbett, B.S., McKinney, D.B., Hulen J.B., Moore, J.N., and Samberg, S.M., 1978, Geology of Roosevelt Hot Springs KGRA, Beaver County, Utah: unpublished report prepared by Earth Science Laboratory, University of Utah Research Institute, Salt Lake City, Utah, for U.S. Department of Energy, Division of Geothermal Energy, 120 p.

Oviatt, C.G., 1991, Quaternary geology of the Black Rock Desert, Millard County, Utah: Utah Geological and Mineral Survey Special Study 73, 23 p., scale 1:100,000.

Oviatt, C.G., 2015, Chronology of Lake Bonneville, 30,000 to 10,000 yr B.P.: Quaternary Science Review, v. 110, p. 166–171.

Oviatt, C.G., Currey, D.R., and Sack, D., 1992, Radiocarbon chronology of Lake Bonneville, eastern Great Basin, USA: Palaeogeography, Palaeoclimatology, Palaeoecology, v. 99, p. 225–241.

Petersen, C.A., 1975, Geology of the Roosevelt Hot Springs area, Beaver County, Utah: Utah Geology, v. 2, no. 2, p. 109–116.

Rhodes, E.J., 2011, Optically stimulated luminescence dating of sediments over the past 200,000 years: Annual Review of Earth and Planetary Sciences, v. 39, p. 461–488.

Rittenour, T.M., 2008, Luminescence dating of fluvial deposits: applications to geomorphic, paleoseismic, and archaeological research: Boreas, v. 37, p. 613–635.

Rowley, P.D., Vice, G.E., McDonald, R.E., Anderson, J.J., Machette, M.N., Maxwell, D.J., Ekren, E.B., Cunningham, C.G., Steven, T.A., and Wardlaw, B., 2005, Interim geologic map of the Beaver 30′ x 60′ quadrangle, Beaver, Piute, Iron, and Garfield Counties, Utah: Utah Geological Survey Open-File Report 454, 27 p., 1 plate, scale 1:100,000.

Sibbett, B.S., and Nielson, D.L., 1980, Geology of the central Mineral Mountains, Beaver County, Utah: University of Utah Research Institute, Earth Science Laboratory Report 33, 42 p. (under DOE contract no. DE-AC07-78ET28392).

Simmons, S., Kirby, S., Jones, C., Moore, J., Allis, R., Brandt, A., and Nash, G., 2016, The geology, geochemistry, and geohydrology of the FORGE deep well site, Milford, Utah: Proceedings, 41st Workshop on Geothermal Reservoir Engineering, 10 p.

Stahl, T., and Niemi, N.A., 2017, Late Quaternary faulting in the Sevier Desert driven by magmatism: Scientific Reports, v. 7, article no. 44372, doi: 10.1038/srep44372.

Utah Geological Survey, 2018, Utah Quaternary fault and fold database: Online, https://geology.utah.gov/resources/data-databases/qfaults/.

U.S. Geological Survey, 2018, Quaternary fault and fold database of the United States: U.S. Geological Survey Earthquake Hazards Program, Online, https://earthquake.usgs.gov/hazards/qfaults/.

Ward, S.H., Parry, W.T., Nash, W.P., Sill, W.R., Cook, K.L., Smith, R.B., Chapman, D.S., Brown, F.H., Whelan, J.A., and Bowman, J.R., 1978, A summary of the geology, geochemistry, and geophysics of the Roosevelt Hot Springs thermal area, Utah: Geophysics, v. 43, p. 1515–1542.

Zimmerman, J.T., 1961, Geology of the Cove Creek area, Millard and Beaver Counties, Utah: Salt Lake City, University of Utah, M.S. thesis, 91 p., scale 1:24,000.

Appendix A: IRSL Soil Pit Logs by E. Kleber

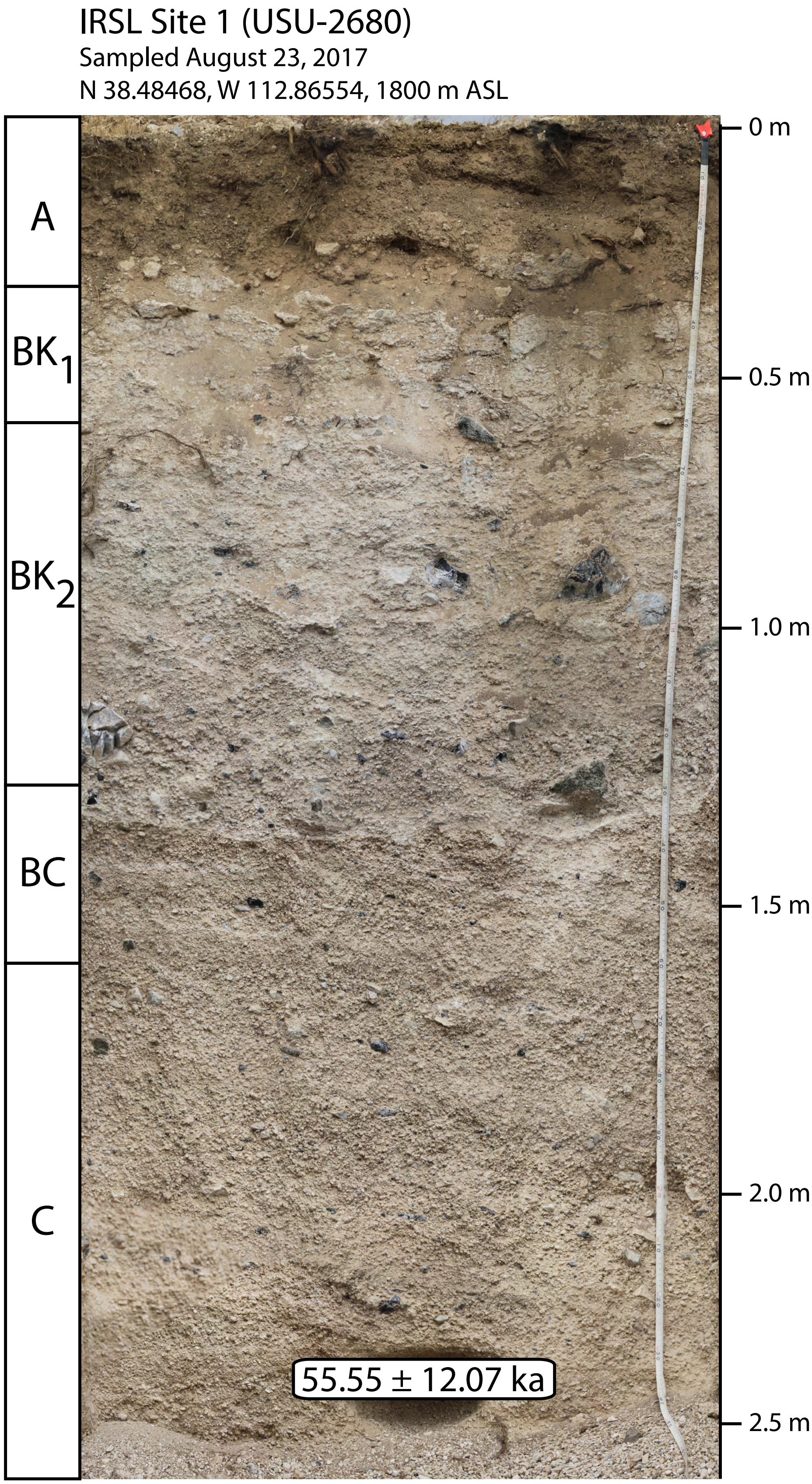

IRSL Site 2 (USU-2681)
Sampled August 23, 2017
N 38.48514, W 112.88897, 1703 m ASL

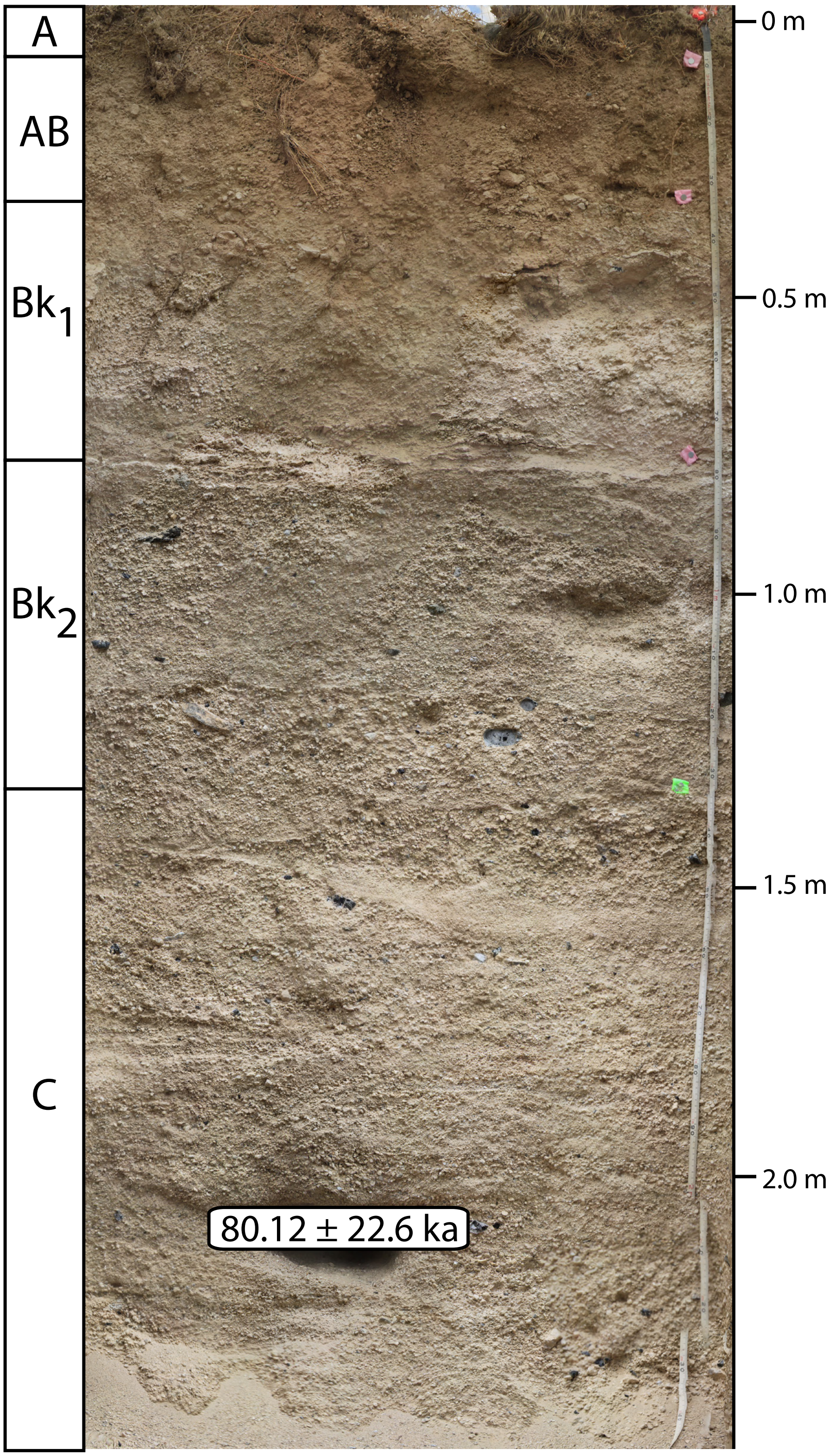

IRSL Site 3 (USU-2683)
Sampled August 23, 2017
N 38.43803, W 112.90150, 1171 m ASL

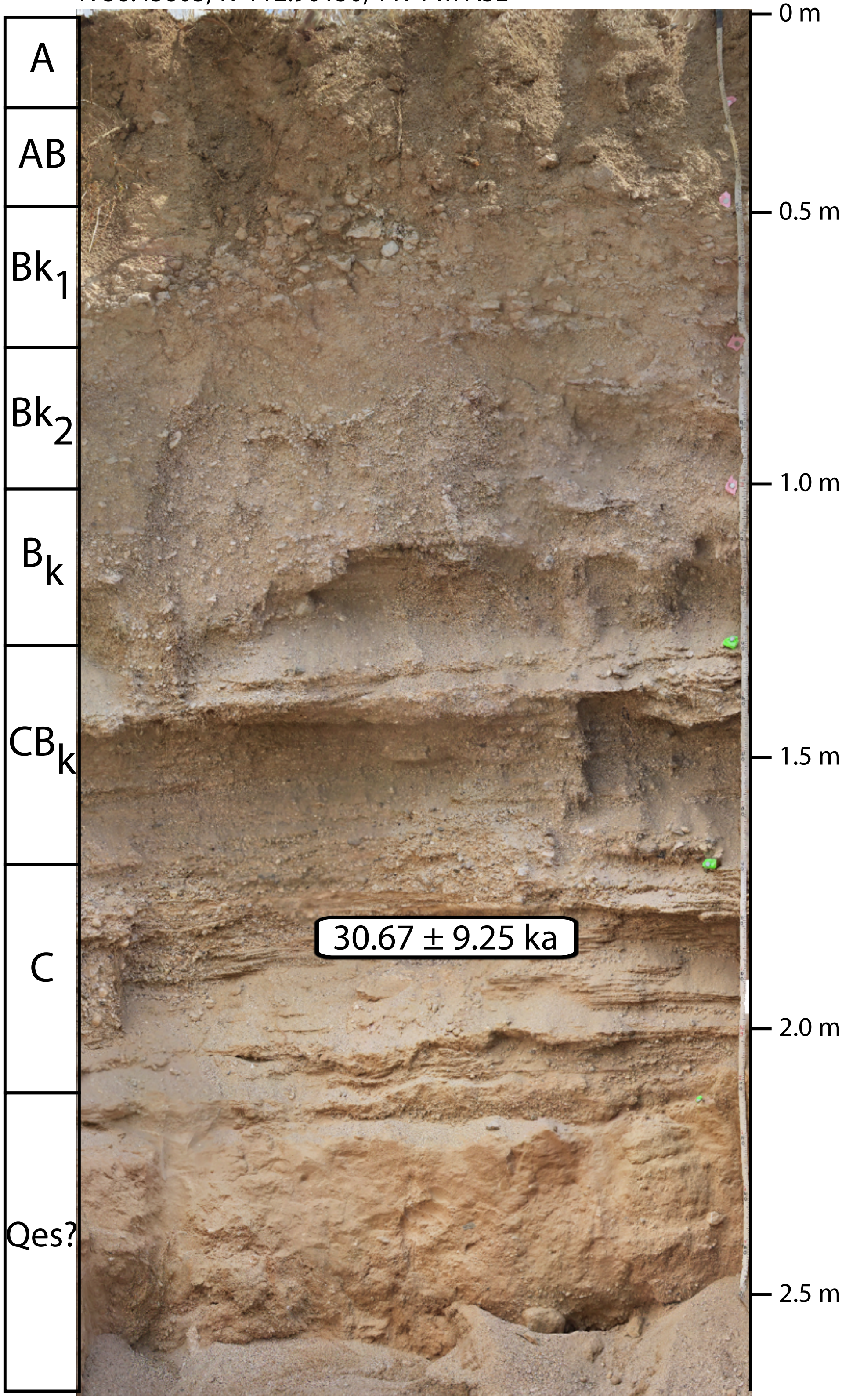

IRSL Site 4a (USU-2684, 2685, 2686)
Sampled August 23 and 24, 2017
N 38.38123, W 112.90760, 1744 m ASL

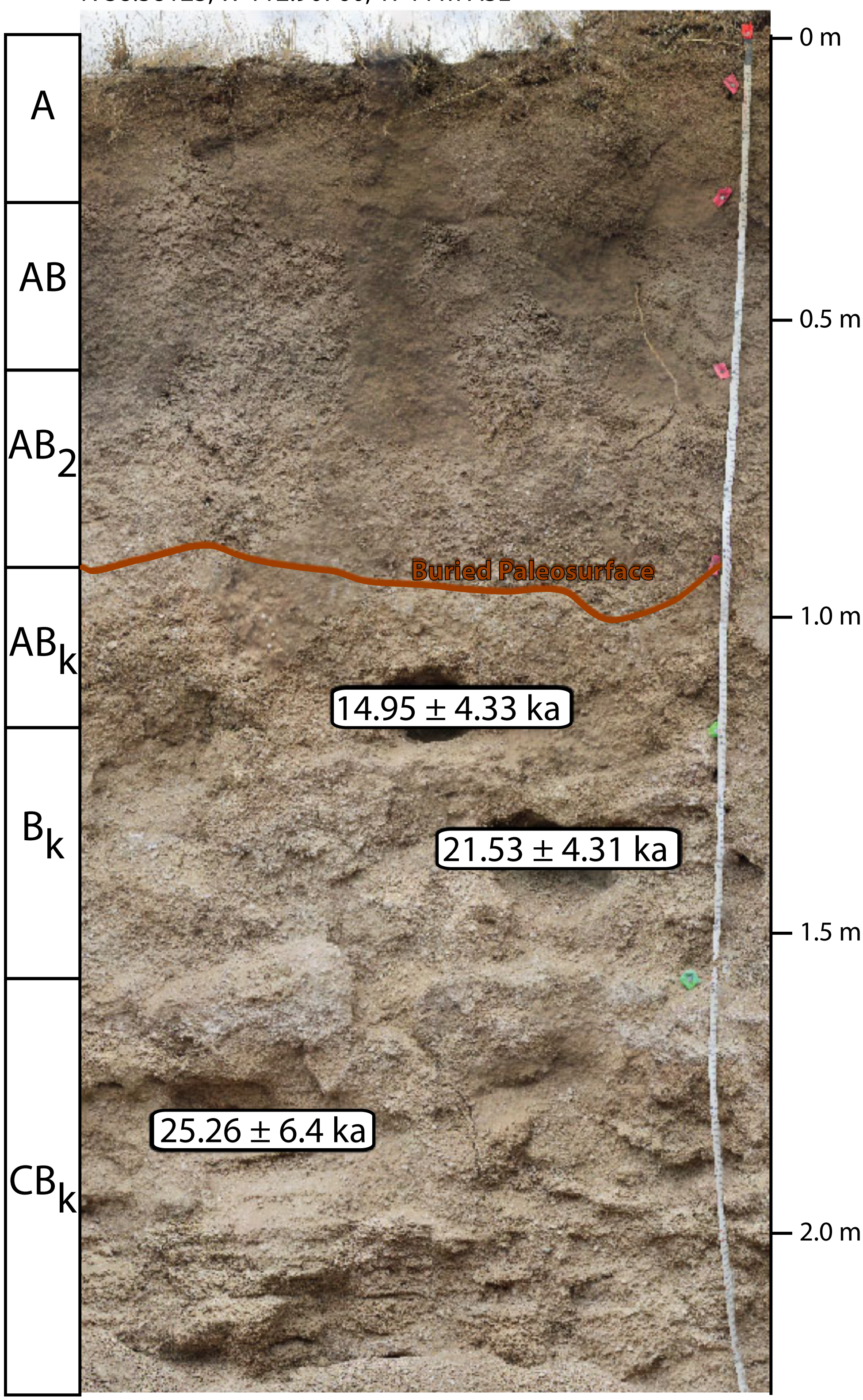

IRSL Site 4b (USU-2684)
Sampled August 24, 2017
N 38.37970, W 112.90788, 1738 m ASL

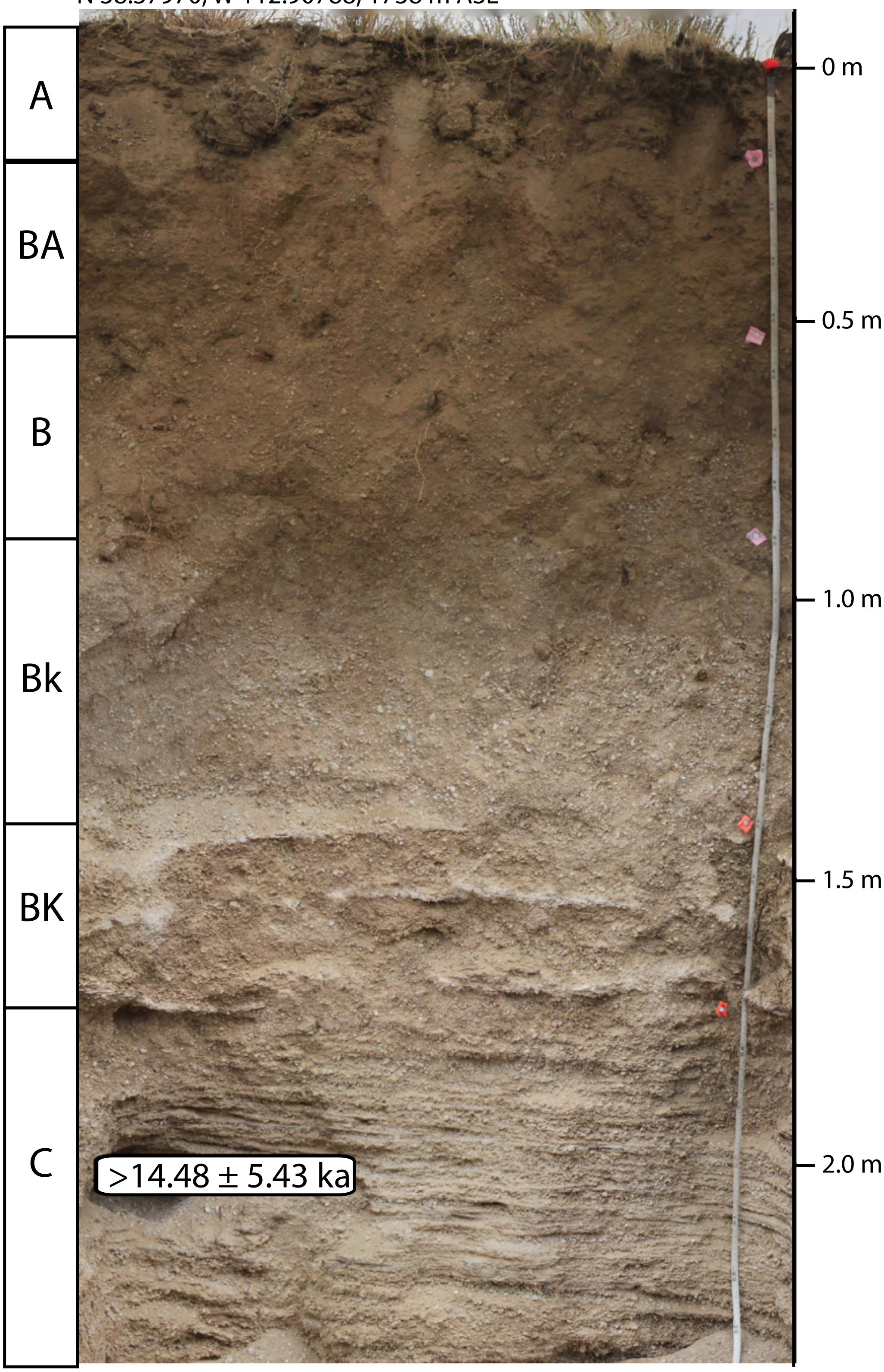

IRSL Site 5 (USU-2682)
Sampled August 23, 2017
N 38.45210, W 112.86866, 1791 m ASL

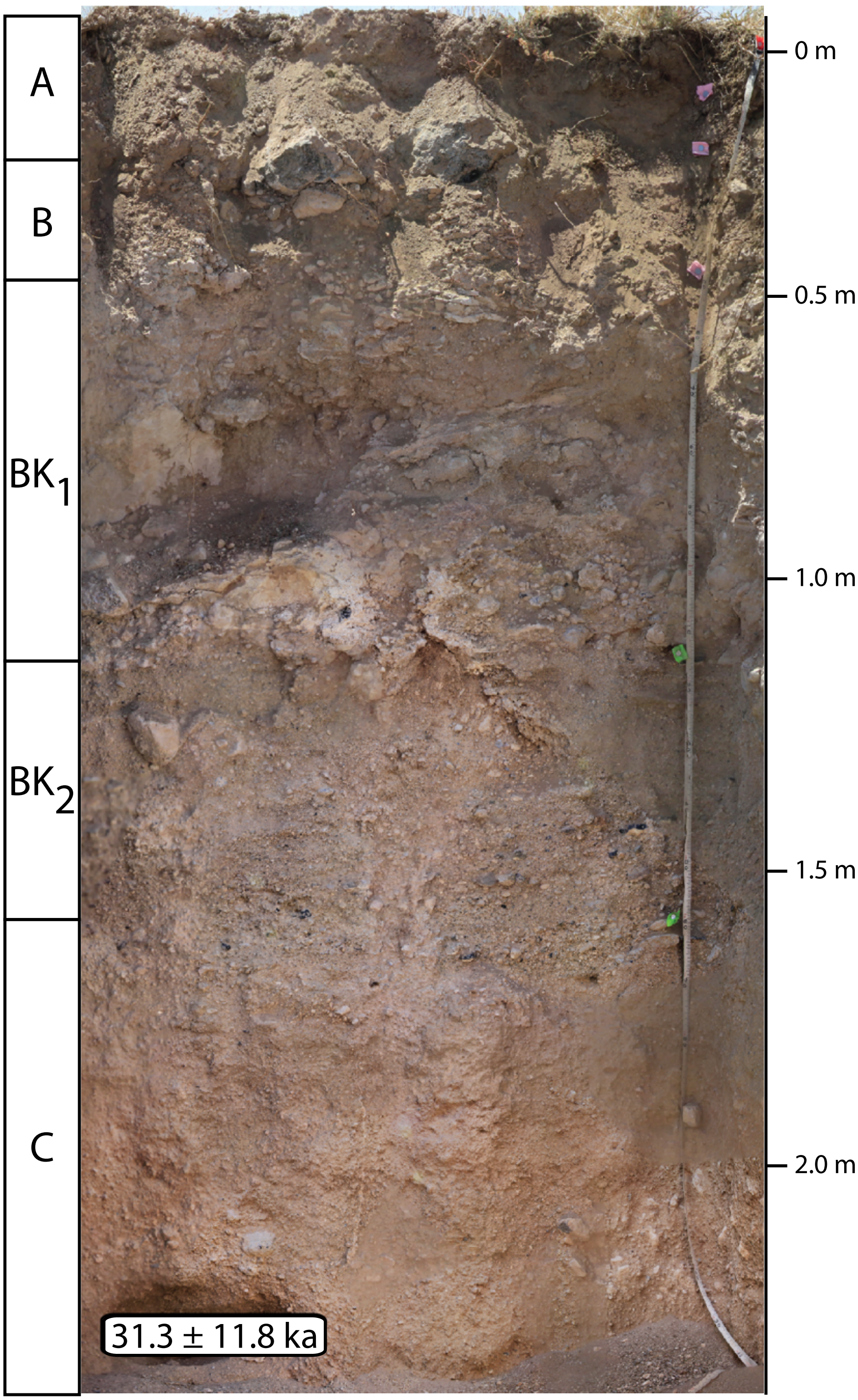

Appendix B: Scarp Offset Selection

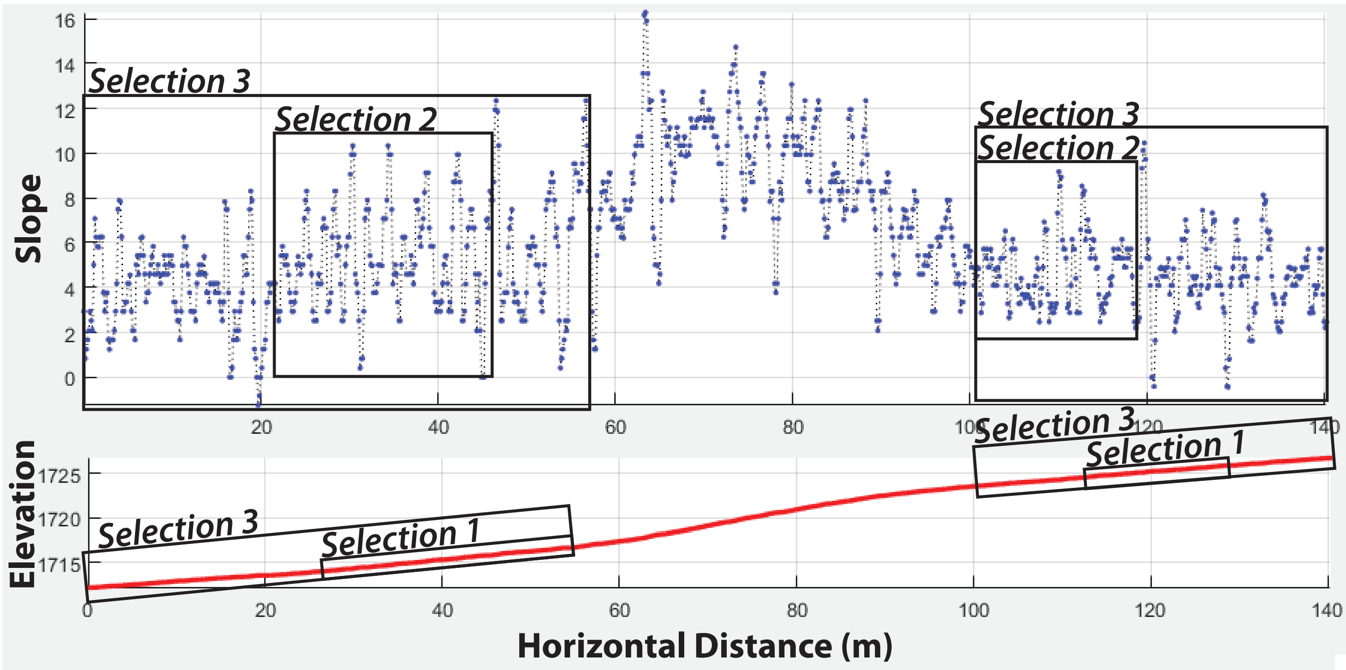

Figure B1. Explanation of methods for selecting the slope defining a fault scarp for geomorphic analysis. The reported fault scarp characteristics are shown in Figure 4 for the OMF and MMWFZ.

JOINT PATTERNS IN THE MINERAL MOUNTAINS INTRUSIVE COMPLEX AND THEIR ROLES IN SUBSEQUENT DEFORMATION AND MAGMATISM

by John M. Bartley

Department of Geology and Geophysics, University of Utah, Salt Lake City, Utah

Link to supplemental data download: https://ugspub.nr.utah.gov/publications/misc_pubs/mp-169/mp-169-c.zip
Appendix

Miscellaneous Publication 169-C
Utah Geological Survey
a division of
UTAH DEPARTMENT OF NATURAL RESOURCES

This paper is part of *Geothermal Characteristics of the Roosevelt Hot Springs System and Adjacent FORGE EGS Site, Milford, Utah*. https://doi.org/10.34191/MP-169

Bibliographic citation:

Bartley, J.M., 2019, Joint patterns in the Mineral Mountains intrusive complex and their roles in subsequent deformation and magmatism, *in* Allis, R., and Moore, J.N., editors, Geothermal characteristics of the Roosevelt Hot Springs system and adjacent FORGE EGS site, Milford, Utah: Utah Geological Survey Miscellaneous Publication 169-C, 13 p., 1 appendix, https://doi.org/10.34191/MP-169-C.

JOINT PATTERNS IN THE MINERAL MOUNTAINS INTRUSIVE COMPLEX AND THEIR ROLES IN SUBSEQUENT DEFORMATION AND MAGMATISM

by John M. Bartley

ABSTRACT

Granitic rocks intersected by drill holes in the Utah FORGE site in Milford Valley strongly resemble the Oligocene-Miocene Mineral Mountains batholith and belong to the same structural block as the Mineral Mountains. Thus, the Mineral Mountains batholith and the FORGE reservoir may share the same joint pattern. Fractures in the Mineral Mountains plutonic complex were mapped in seven 0.03–0.08 km^2 areas in the northern half of the range to document orientations, spacing, continuity, intersection relationships, and orientations of slickenlines where present. To compare the patterns to those in the granitic rocks, fractures also were measured in four Pleistocene rhyolite bodies.

Fractures in batholithic rocks exposed near the FORGE area consist of three main sets: 1) strike ~090–110, dip 70°–90°; 2) strike ~010–040, dip 70°–90°; and 3) strike ~180±30, dip 30°±30° toward the west. All three sets formed either before or early during Basin-Range faulting. Slickenlines are sparse and mainly found on gently W-dipping set 3 fractures. Riedel shears consistently indicate top-west slip. Fracture patterns in the Pleistocene rhyolites differ both from those in adjacent granitic rocks and from one body to another, indicating that they reflect local near-surface stresses and are unrelated to deeper joint patterns.

Fracture sets 2 and 3 are inferred to be a conjugate set formed with a vertical maximum compressive stress, followed by ~40° eastward tilt. Eastward tilting of the range is indicated by a) the wall-rock map pattern; b) eastward dips of stratified rocks exposed in the range; c) late Miocene dikes that dip 40°–50° west but probably were originally vertical; and d) paleomagnetic data that, although too scattered to reliably quantify the magnitude, indicate eastward tilt of the plutonic complex. The lack of evidence for a large-offset W-dipping normal fault on the east side of the Mineral Mountains favors the isostatic rolling-hinge mechanism for tilting, which implies that the range tilted as it was unroofed by faulting.

The fracture pattern in the batholith and other evidence suggest three further implications. First, the average orientation of slipped joints in the range parallels the bedrock-basin fill contact which most authors have interpreted to be the basin-bounding fault. This suggests that the basin-bounding fault developed by shear across set 3 fractures. Second, the NNE-striking Opal Mound fault strikes subparallel to steep N-striking set 2 fractures and probably represents shear across that fracture set. The rolling-hinge mechanism predicts this shear sense in the footwall of the basin-bounding fault, and therefore the Opal Mound fault may reflect isostatic rebound of the footwall as it was unroofed by faulting. Finally, the WNW-striking Negro Mag fault probably formed by shear across steep E-striking fractures of set 1. Geomorphic evidence suggests south-side-up displacement across the fault, and the majority of Pleistocene rhyolitic volcanism in the range is located on the upthrown side. These relations suggest the hypothesis that the Negro Mag fault is the northern boundary of a bysmalith (i.e., fault-bounded laccolith) that formed part of the shallow magmatic plumbing system during Pleistocene magmatism. This further suggests that, although the youngest intrusive rocks exposed at the surface are Miocene in age, growth of the batholith continued into the Pleistocene and may be presently ongoing.

INTRODUCTION

The Utah FORGE site is located near the eastern edge of Milford Valley, a basin formed by late Cenozoic crustal extension at the eastern margin of the Basin and Range Province (Figure 1). Because basin-filling sediment conceals the granitic bedrock of the FORGE enhanced geothermal system (EGS) reservoir, geologic questions that are important to the FORGE project include 1) what is the relationship between granitic rocks intersected by drill holes in and near the FORGE site to the bedrock exposed in the surrounding ranges, and 2) to what extent can observed characteristics of the exposed bedrock be used to predict characteristics in the FORGE EGS reservoir?

The Mineral Mountains form the eastern boundary of the Milford Valley basin and provide the bedrock exposures nearest to the FORGE site (Figure 1). The Mineral Mountains are dominated by an Oligocene-Miocene granitic batholith, and granitic rocks intersected by drill holes in Milford Valley almost certainly belong to the same intrusive complex. Seismic imaging (Smith and

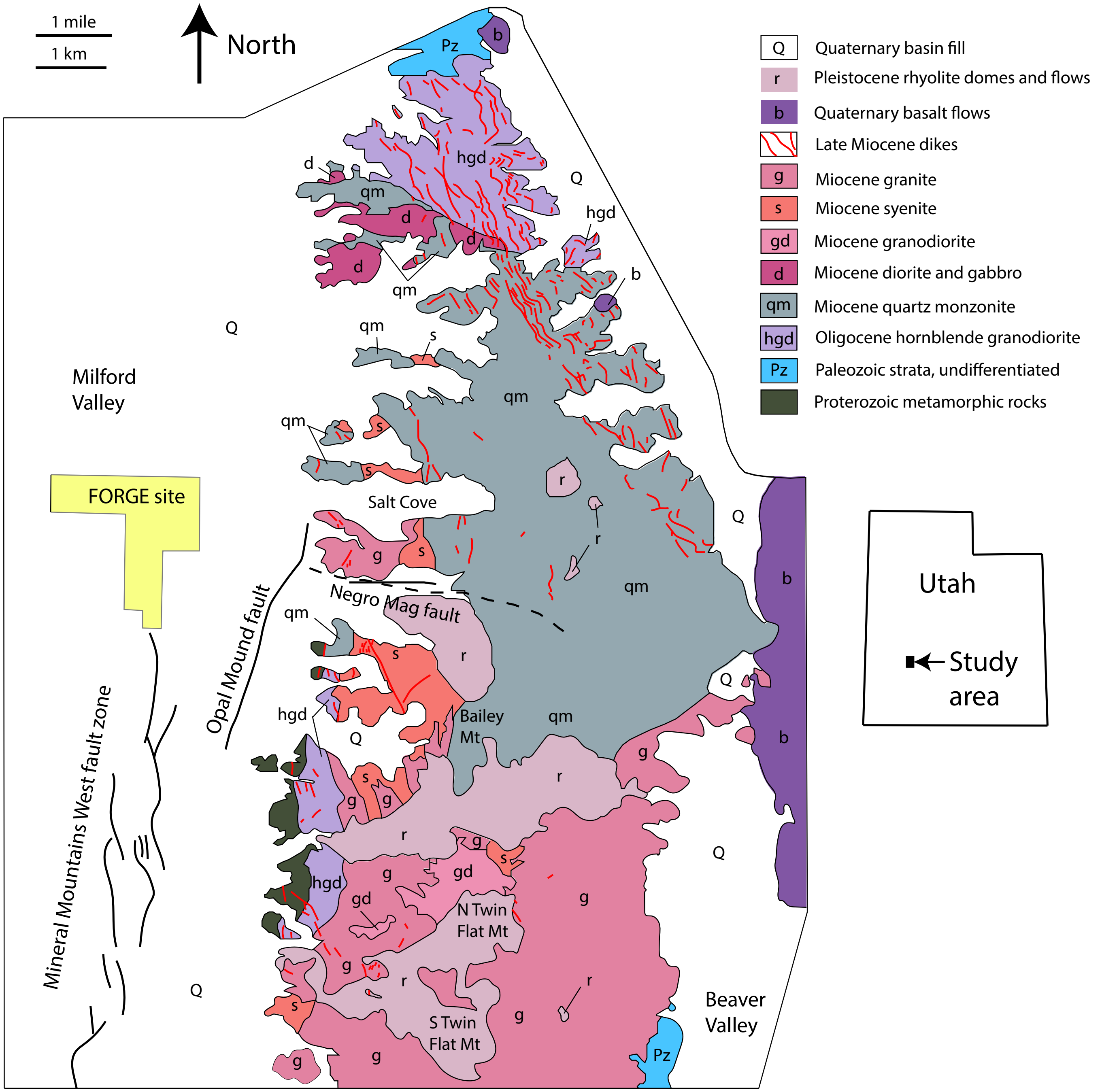

Figure 1. *Generalized geology of the north-central Mineral Mountains, simplified from Sibbett and Nielson (2017).*

Bruhn, 1984; Nielson et al., 1986; Miller et al., 2019) and inversion of gravity data (Hardwick et al., 2019) indicate that the basin fill-bedrock contact at the eastern margin of Milford Valley dips ~30° to the west. Previous investigations (e.g., Smith and Bruhn, 1984; Nielson et al., 1986; Coleman et al., 1997) interpreted the basin fill-bedrock surface to be a west-dipping normal fault that formed the Milford Valley basin. Miller et al. (2019) interpret new, more detailed seismic imaging to indicate erosion of the bedrock surface before its burial. Other evidence noted by earlier studies nonetheless favors formation of the basin by a west-dipping master fault. For example, the most likely explanation for exposure of Proterozoic basement at the western foot of the Mineral Mountains is that it was unroofed in the footwall of a major west-dipping normal fault. Practically all other outcrops of Proterozoic basement in Utah, including the Beaver Dam Mountains, Wasatch Range, Grouse Creek Mountains, Raft River Mountains, and Antelope Island, are exposed in the footwalls of major normal faults (Hintze et al., 2000). Therefore, the basin fill-bedrock contact in the FORGE area may nonetheless represent the basin-bounding fault, but the fault surface was exposed and modified by erosion before its current complete burial by basin fill. Observations of fractures in the Mineral Mountains reported here are consistent with interpretation of the basin fill-bedrock contact as a west-dipping normal fault, and this interpretation places granitic rocks in the FORGE area in the same major structural block as the Mineral Mountains. This in turn implies that field observations of granitic rocks exposed in the Mineral Mountains are apt to be useful in predicting properties of granitic rocks in the FORGE area.

Methods

Three types of structural data were collected:

1) Fracture orientations, with kinematic information where available along fractures that accommodated shear displacement. The complete fracture data set is presented in the Appendix[1] to this report.

2) Detailed fracture maps (resolution ~1 m) of small areas (0.03–0.08 km^2) of excellent exposure to document fracture lengths and continuity and their intersection relationships.

3) Field photographs to portray geometric relations of gently dipping fractures which tend to be inadequately represented by a conventional horizontal map.

All data types were collected simultaneously during mapping. The relative abundances of fractures in different sets may thus be portrayed less precisely than achievable by more objective sampling (e.g., measuring all fractures along a scanline). The importance of the other data types justifies this compromise. Reconnaissance fracture orientation data also were collected in some locations where fractures were not mapped.

Study Areas

Seven areas of exceptional exposure were mapped, in Oligocene hornblende granodiorite (1 area), Miocene quartz monzonite (4 areas), Miocene granite (1 area), and Miocene syenite (1 area). The Oligocene granodiorite is more intensely fractured and faulted than any of the Miocene granitic rocks. This may reflect early Miocene deformation that is recorded by an angular unconformity between late Oligocene and Miocene stratified rocks exposed at the southern end of the range (Price, 1998). In order to compare the fracture patterns to those found in granitic rocks, fractures also were measured in four Quaternary rhyolite bodies including the Bailey Ridge lava flow, a lava dome on the southwest flank of Bailey Mountain, and the lava domes that form North and South Twin Flat Mountains.

Fracture and Fault Data

Fracture Spacing

There is an overall northward trend of decreasing fracture spacing in the Miocene plutonic rocks (Figure 2). Fracture spacing also varies somewhat with rock type (Figure 3A). Miocene granitic rocks generally contain the sparsest macroscopic fractures, and this does not appear to vary from granite to quartz monzonite to syenite. The Oligocene granodiorite is more intensely fractured and appears to be significantly more deformed than adjacent Miocene granitic rocks. Closely spaced fractures likely contributed to the fact that only one outcrop area of Oligocene granodiorite provided sufficiently continuous exposure to undertake fracture mapping. Silicic dikes, including both aplite dikes that are cogenetic with batholithic rocks and post-batholith rhyolite dikes, are by far the most intensely fractured rocks in the range. Fracture spacings of 10 cm or less are common in the silicic dikes, making mapping fractures at the ~1:1000 scale used in this study clearly impractical.

Fracture Orientations and Continuity

Although the fracture intensity varies, Miocene granitic rocks in the northern half of the range all contain a similar fracture pattern (Figure 4). The pattern includes three fracture sets in the following general orientations: 1) strike ~090–110, dip 70°–90°; 2) strike ~010–040, dip 70°–90°; and 3) strike ~180±30, dip 30°±30° toward the west. In some stereoplots, two of the concentrations of poles to fractures that define the three sets merge into a girdle, but the overall pattern remains much the same.

The relative abundances and continuity of the three main fracture sets in the northern part of the range vary considerably (Figure 5). Set 2 fractures that strike from north to northeast and dip steeply NW and SE dominate in Miocene quartz monzonite exposures near the northern end of the range. In the central map areas that are located nearest to the FORGE area, steep E-W striking fractures of set 1 are more abundant and continuous. In these areas, the steep E-W fractures of set 1

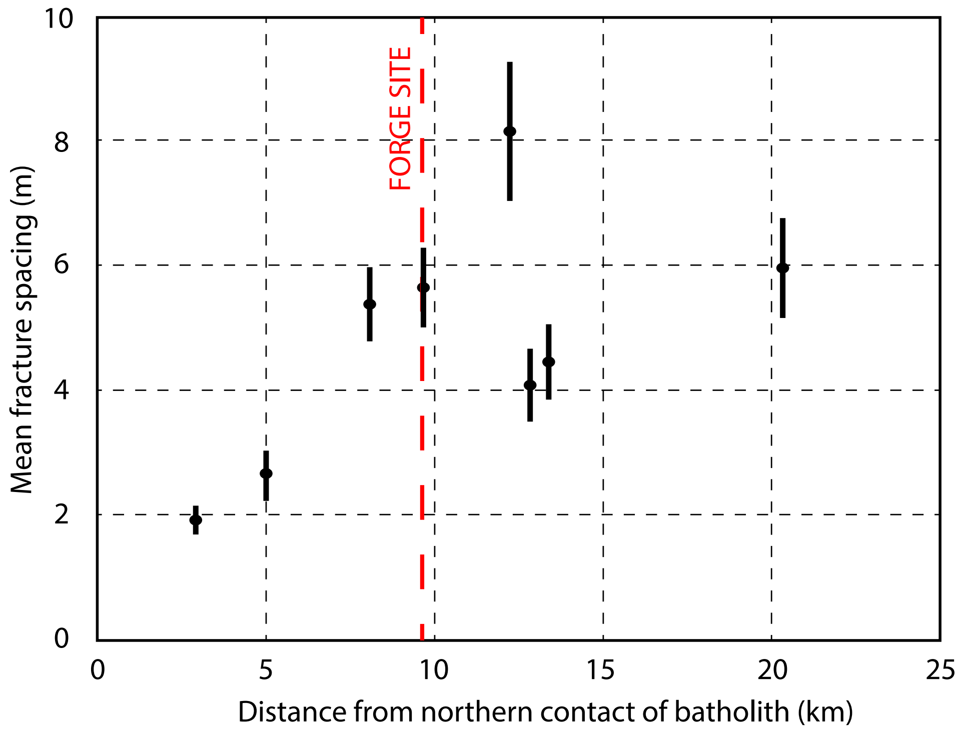

Figure 2. *Fracture spacing vs. location along the range. Fracture spacing was determined by counting mapped fractures intersected by scan lines 50–100 m in length and oriented 000°, 030°, 060°, 090°, 120°, and 150°. Three scan lines in each orientation were placed at arbitrary locations on each fracture map. Error bars are 1σ based on reproducibility of fracture counts.*

commonly bound fractures belonging to sets 2 and 3, and set 3 fractures commonly have N-S extents of only tens of meters (Figure 2B). In the southern area shown in Figure 5, gently west-dipping set 3 fractures are more abundant and longer than in the other areas shown.

Fracture sets 2 and 3 are interpreted to represent a conjugate set (Figure 2C). The fracture geometry illustrated by Figure 2C is prominent in all study areas from Salt Cove southward. As indicated in the figure, the geometry is interpreted to have formed with the maximum compressive stress vertical, as predicted for the normal fault regime in the Anderson fault theory (Anderson, 1951), followed by ~40° of west-side-up (eastward) tilt in the footwall of the normal fault that formed Milford Valley. This implies that the conjugate set formed before large displacement had accumulated across the basin-bounding fault, which probably began in late Miocene time (Coleman et al., 2001). Because fracture intersection relationships indicate that the conjugate set formed after the E-W steep fractures, all three main fracture sets appear to have formed before or early during Basin-Range faulting, and therefore in the middle Miocene shortly after the batholith was emplaced.

Several lines of evidence confirm that the Mineral Mountains block has been tilted. First, the only exposures of Proterozoic basement in the region are located on the western flank of the Mineral Mountains and, passing eastward from there, progressively shallower crustal levels are exposed, culminating in the flat-lying Cenozoic volcanic rocks that form the next range to the east, the Tushar Mountains. Second, stratified rocks in the Mineral Mountains all dip to the east. Most significant are Oligocene and Miocene strata exposed at the southern end of the range that dip from 30° to 80° eastward (Price, 1998). Third, a swarm of felsic and mafic dikes dated at 11 Ma (Coleman and Walker, 1994) is widespread in the range but is particularly prominent in the northern approximately one-third of the batholith (Figure 1). The dikes consistently dip moderately (40°–50°) westward and, if originally emplaced vertically, imply 40°–50° of eastward tilt since 11 Ma. Fourth, paleomagnetic data from Cenozoic intrusive rocks, although of uneven quality, suggest 30°–90° of eastward tilting of much of the range (Coleman, 1991).

Fracture patterns in the Pleistocene rhyolite domes and flows bear little resemblance to fracture patterns in nearby exposures of granitic rocks (Figure 6). Steep fractures predominate in all of the rhyolite bodies, but otherwise there are few similarities from one body to another. The predominance of a single fracture set in the South Twin Flat dome suggests a minimum horizontal stress trajectory along an azimuth of 045°, roughly orthogonal to in situ stress orientation inferred from hydrofracture in drill hole 58-32. Fracture patterns in the other three rhyolite bodies are more complex and not easily interpreted in terms of in situ stress. Because the rhyolite fracture patterns differ from each other as well as from patterns in the underlying granitic rocks, the fractures are inferred to reflect local near-surface stresses that are not relevant to either fracture patterns or the state of stress at depth.

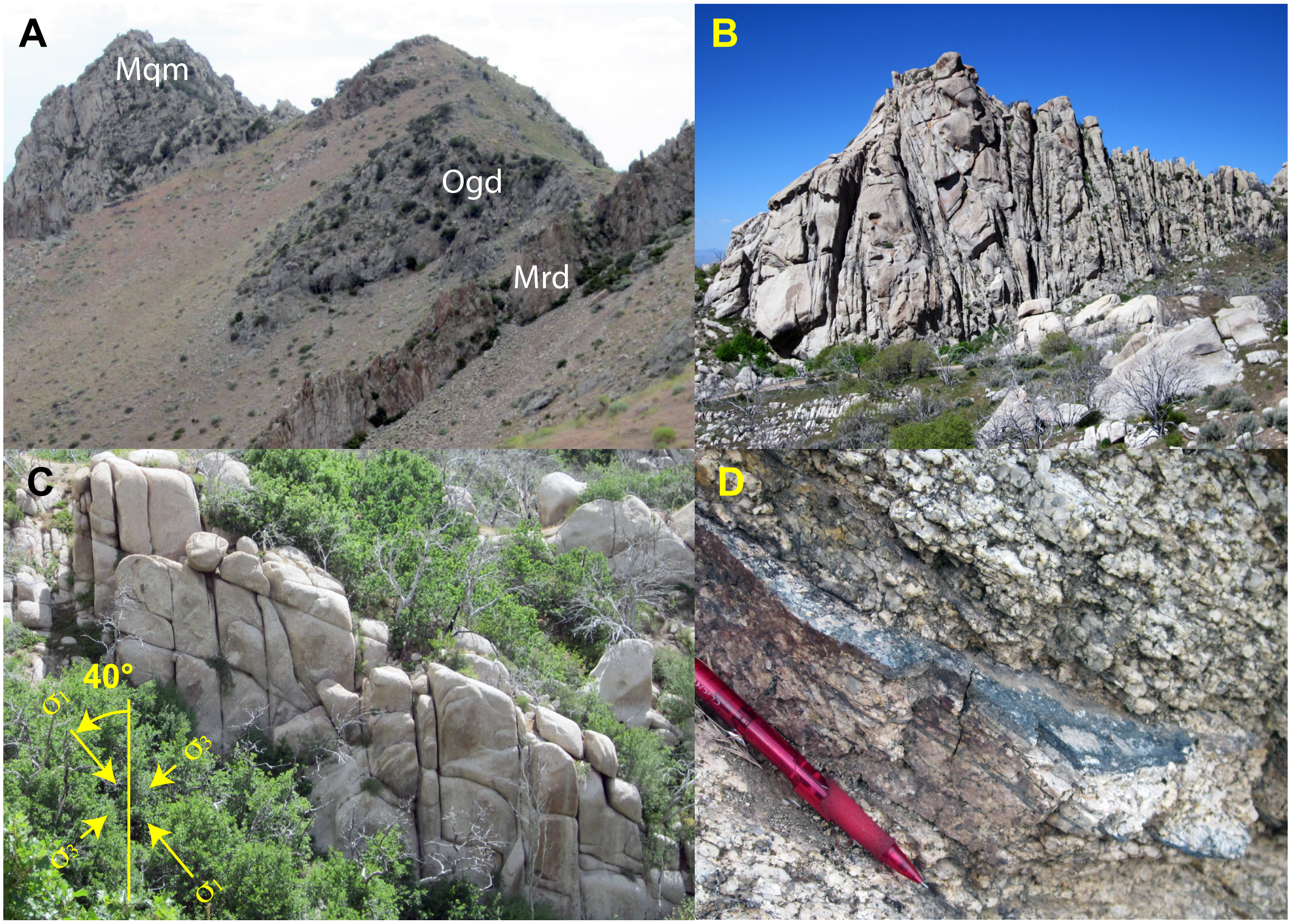

Figure 3. Field photographs of fractures and fracture patterns in the Mineral Mountains. ***(A)*** *Distant view of ridge crest northwest of Pinnacle Pass; note massive jointing of Miocene quartz monzonite (Mqm), intense jointing of Miocene rhyolite dike (Mrd), and intermediate joint density in Oligocene granodiorite (Ogd).* ***(B)*** *View westward along strike of E-W subvertical joints, Salt Cove map area. Note that gently dipping joints terminate against subvertical joints. The steep joints are interpreted to be older than, and to have been barriers to the propagation of, the gently west-dipping joint set.* ***(C)*** *View southward approximately along the strike of subvertical N to NE-striking joints and gently west-dipping joints. Based on their geometry and on independent evidence for eastward tilting of the range, these two joint sets are interpreted to be a tilted conjugate set. The conjugate set probably formed with σ1 (maximum compressive stress) vertical (i.e., normal fault stress regime) and subsequently the joints were tilted 40° eastward to their present orientations.* ***(D)*** *Cataclasite with dark greenish (probably chloritic) matrix formed by shear displacement across a west-dipping joint. Similar cataclasite is found in fractures in a variety of orientations, but mostly commonly in fractures that dip broadly westward at angles less than 40° (see Figure 5).*

Fault Geometry and Kinematics

Slickensided fault surfaces (Figures 3D, 7) are generally very sparse in the granitic rocks, with three exceptions. The Oligocene granodiorite at the northern end of the range contains numerous faults, including at least one meter-thick cataclastic zone that dips gently westward. The Miocene quartz monzonite where it is exposed on the northern wall of Negro Mag Canyon contains numerous thin (1–5 cm) cataclastic zones, as does syenite exposed on the western slopes of Bailey Mountain.

Although fractures that show evidence of shear displacement range in orientation, the majority dip gently to moderately westward with highly variable strikes (Figure 7). The average orientation of slipped fractures, determined by applying Bingham statistics to the orientations of poles to the fractures, is (173°, 30°). Slickensides and Riedel shears consistently indicate top-to-the-west shear. Such fractures exposed in Negro Mag Canyon were interpreted to be map-scale low-angle faults by Sibbett and Nielson (2017). However, the present mapping indicates that they represent slip across joints that commonly are bounded by E-W striking steep fractures and thus have small N-S extents. It therefore appears unlikely that any of the low-angle faults exposed in Negro Mag Canyon are either continuous over large areas or accommodated tectonically significant displacements.

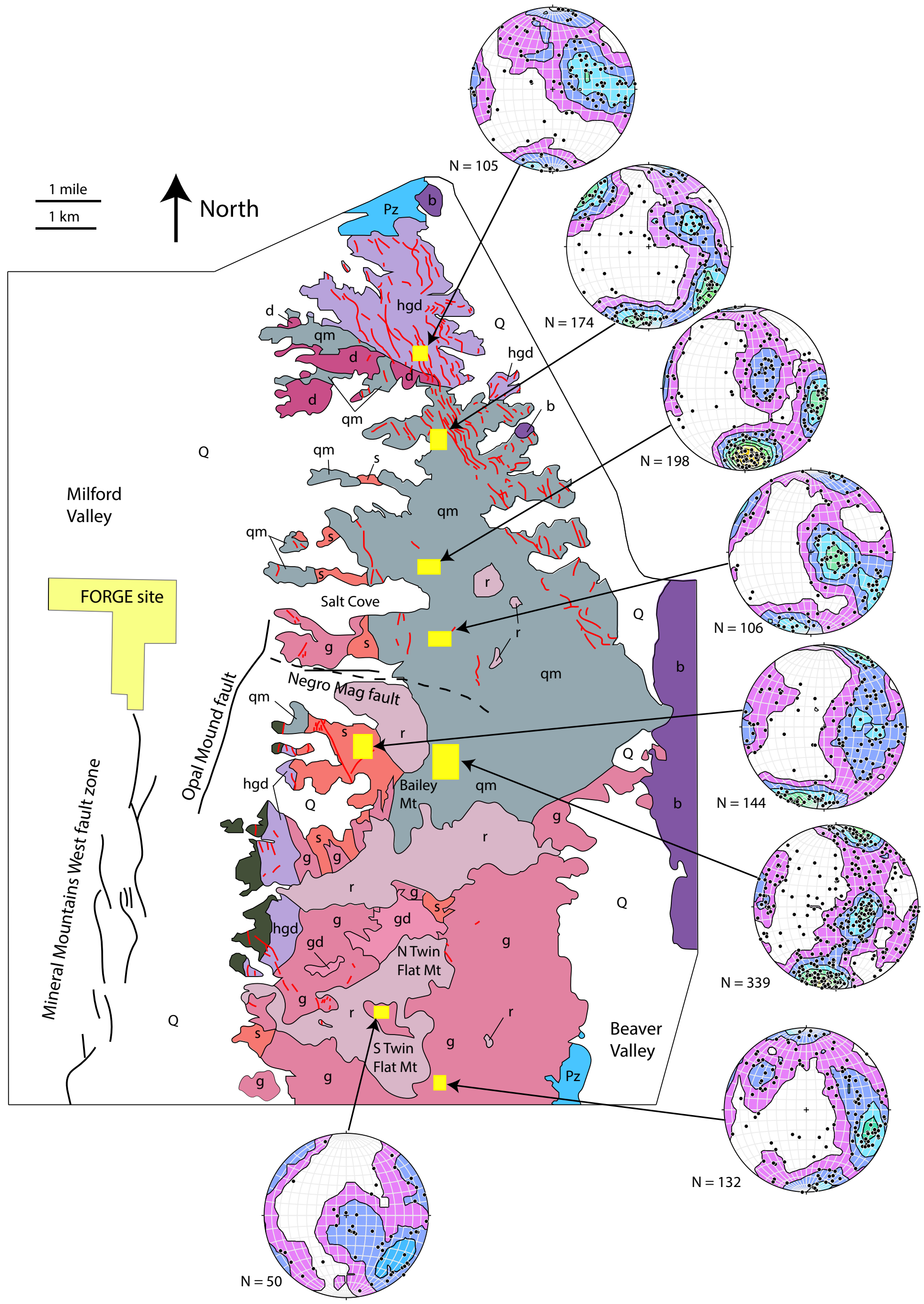

Figure 4. Lower hemisphere equal-area stereoplots of poles to fractures in Oligocene and Miocene granitic rocks. These and all subsequent stereo plots are contoured using the Kamb (1959) method. See Appendix for data on which the plots are based. Base map is the same as Figure 1. Yellow squares are areas covered by present study. All stereoplots in this paper were constructed using Stereonet v. 10.

Fracture Fillings

Fracture fillings are relatively uncommon in the study areas, although it is unclear to what extent this reflects fractures that remained open after formation versus removal of fillings by surface weathering. Where present, fillings are dominated by iron oxides, including both magnetite (based on deflection of a compass needle) and fine-grained hematite (based on its distinctive red color). The fillings occasionally are hard and resistant, probably indicative of silicification; this, however, is uncommon. Fillings have been observed in fractures belonging to all of the dominant sets, but are most common in set 1.

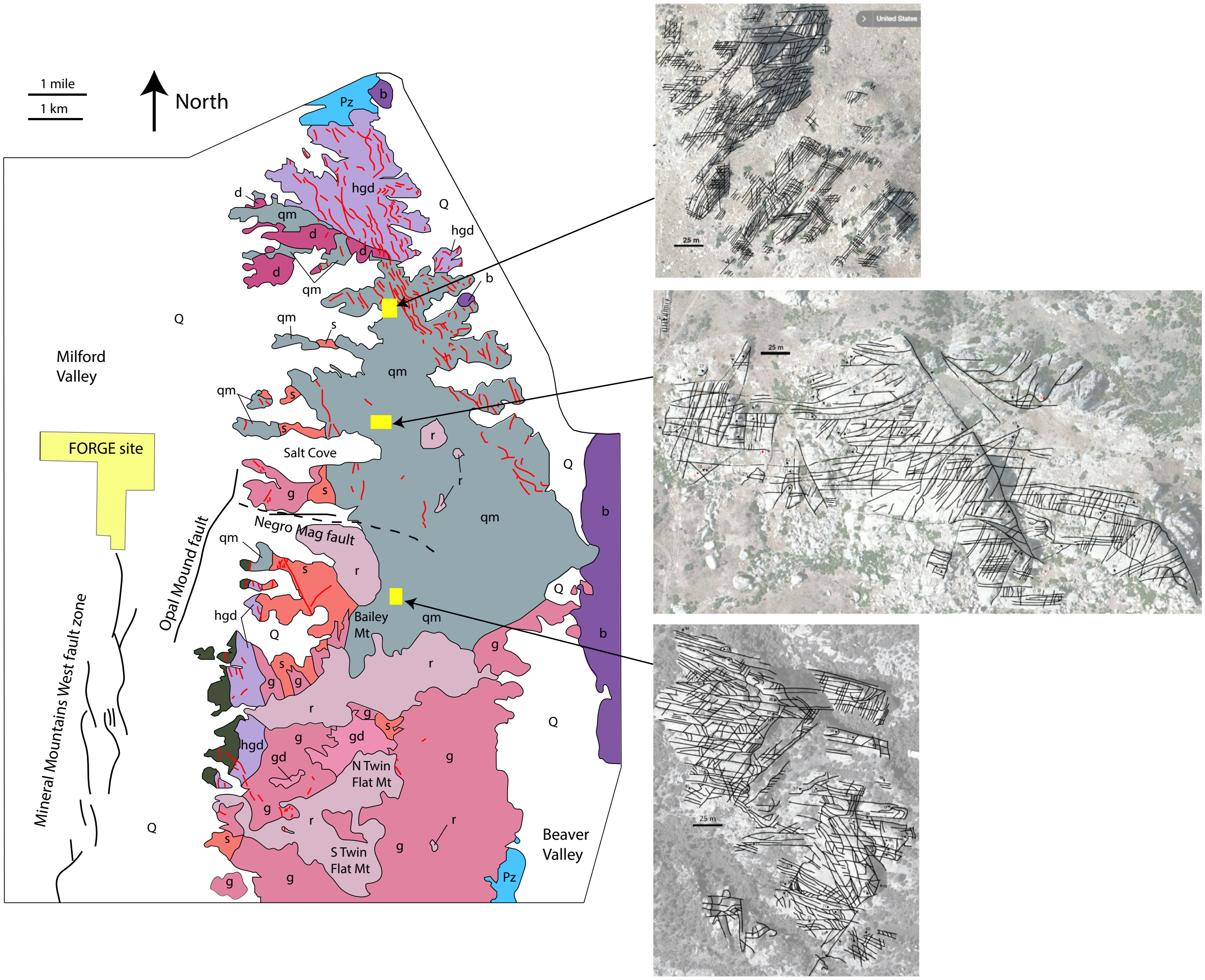

Figure 5. *Representative fracture maps, all plotted at the same scale. Photographic base was downloaded from Bing maps and is not orthorectified. Although all areas contain much the same fracture sets (Figure 4), their relative abundance and continuity vary greatly. In these examples, the northern area is dominated by steep broadly N- to NE-striking fractures of set 2; steep E-W striking fractures of set 1 are more prominent in the central (Salt Cove) area; and in the southern area, gently W-dipping fractures of set 3 (recognizable by their sinuous traces as well as measured dips) are longer and more prominent than in other areas.*

Discussion

Origin and Geometric Evolution of the Basin Boundary

Both seismic imaging and inversion of the gravity field indicate that the contact between basin fill and bedrock on the eastern side of Milford Valley dips ~30° to the west. Fracture data presented here are consistent with interpretation of that surface as the footwall side of the basin-bounding fault, perhaps somewhat modified by erosion after exposure by removal of the hanging wall (Miller et al., 2019). This dip is substantially lower than the expected 60° initial dip for a normal fault (Anderson, 1951), and lower than the 45° average dip inferred for active crustal-scale normal faults based on earthquake focal mechanisms (Thatcher and Hill, 1991). Smith and Bruhn (1984) and Nielson et al. (1986) posited a listric fault geometry (i.e., the fault dip decreases downward; e.g., Hamblin, 1965). However, observational confirmation of a listric geometry is lacking, and mechanical models for formation of listric normal faults in bedrock are problematic (e.g., Wills and Buck, 1997). In view of the abundant evidence that the range has been tilted eastward, it is more likely that the range-bounding fault formed at a high angle and has been tilted to its present orientation (Coleman and Walker, 1994; Coleman et al., 1997).

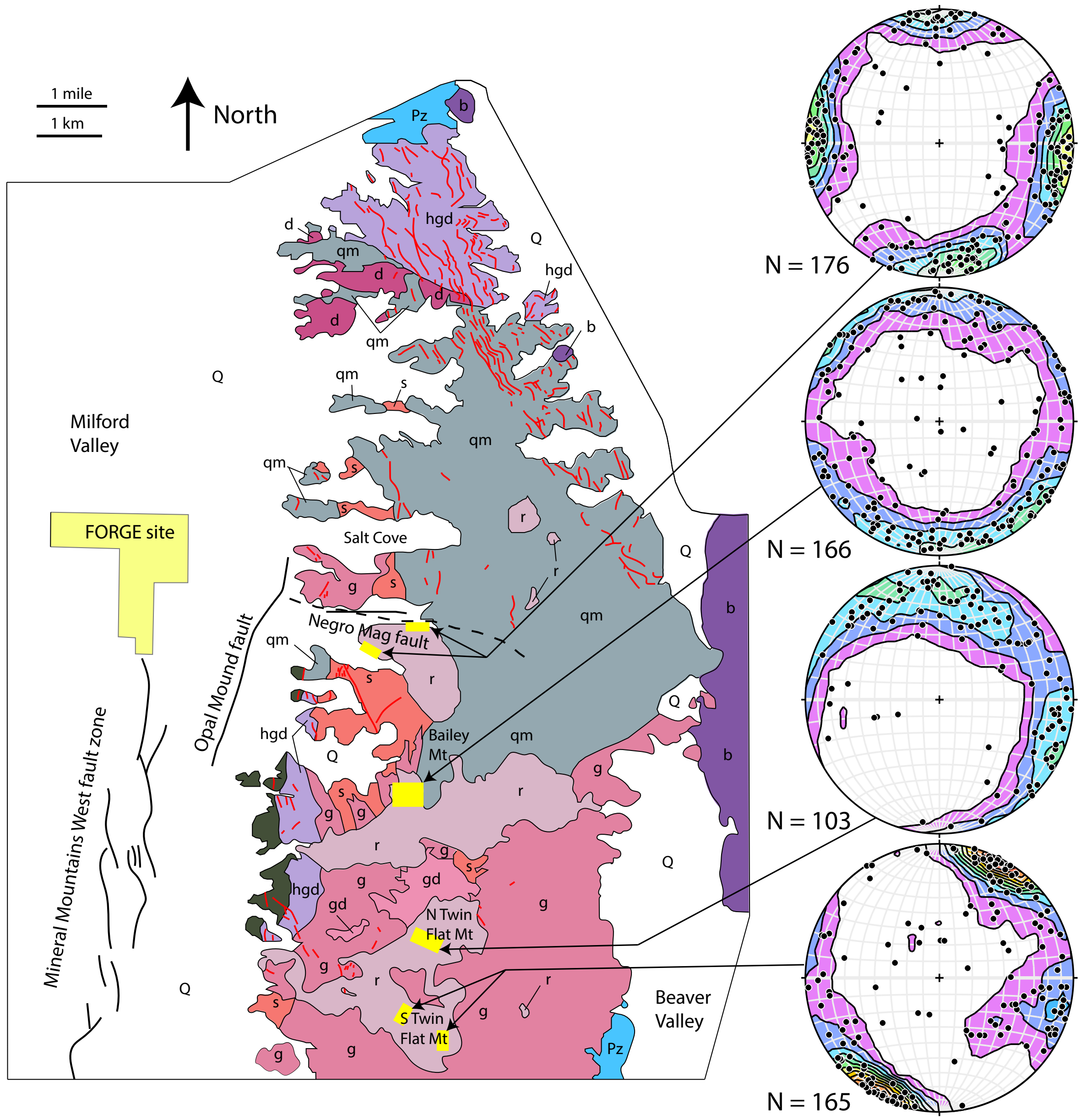

Figure 6. *Lower hemisphere equal-area stereoplots of poles to fractures in Pleistocene rhyolite domes and flows. Base map is the same as Figure 1. See Appendix for data on which the plots are based. Yellow squares are areas where fractures were measured. Note that steep fractures dominate all data sets, but that otherwise all of the patterns differ from each other. The patterns also bear little resemblance to the pattern seen in adjacent plutonic rocks (Figure 4).*

The conjugate pattern of fracture sets 2 and 3, combined with the independent evidence of eastward tilting, strongly suggests that the low-angle normal faults in the range formed as steeply west-dipping joints that during and/or after shear displacement were tilted to low dips, in rare instances through horizontal (Figure 7). The average orientation of the slipped joints (173°, 30°) is subparallel to the bedrock-basin fill surface. This suggests that the basin-bounding fault was initiated by shearing across set 3 fractures.

Tilting of the range and basin-bounding fault could have been achieved by several alternative mechanisms, including the domino model (tilting of an array of fault blocks between parallel normal faults; e.g., Proffett, 1977); reverse drag above an underlying listric normal fault (Coleman and Walker, 1994); or the rolling-hinge mechanism (isostatic upward flexure of a normal fault footwall; Spencer, 1984; Wernicke and Axen, 1988; Buck, 1988; Axen and Bartley, 1997). Both the domino model and reverse drag require a major west-dipping normal fault between the Mineral Mountains and the Tushar Mountains to the east. Whereas faults are certainly present in Beaver Valley (Machette et al., 1984), none has produced the large structural relief which would be required to significantly tilt the Mineral Mountains block. The absence of such a fault thus favors the rolling-hinge mechanism. Figure 8 schematically illustrates formation of Milford Valley and the Mineral Mountains according to the rolling-hinge model.

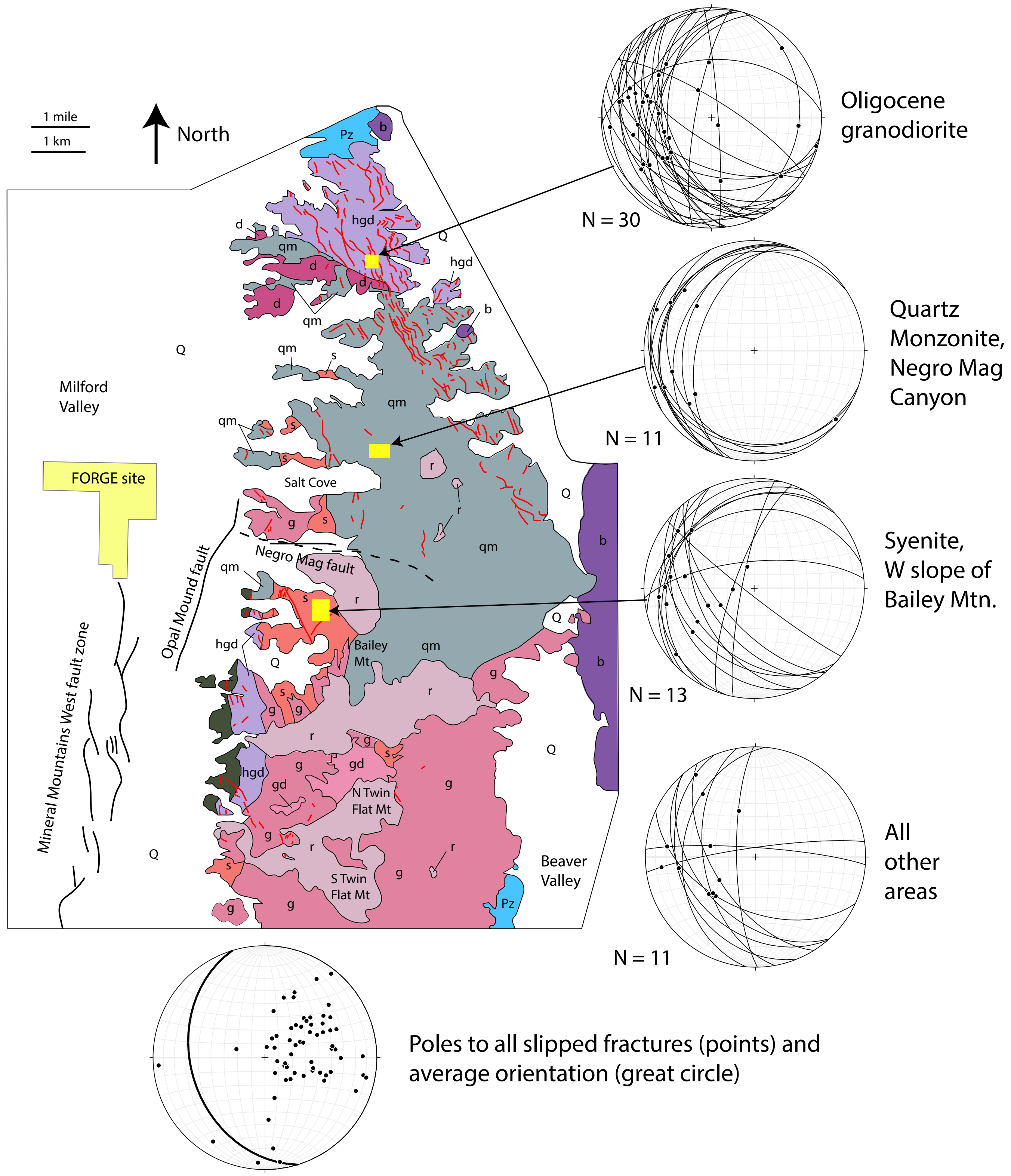

Figure 7. *Lower hemisphere equal-area stereoplots of fault kinematic data, located on the same base map as Figure 1. See Appendix for data on which the plots are based. In all but the bottom plot, great circles are fault planes. Points are slip directions based on slickenlines or, in three instances in which slickenlines were not visible, indicated by measured orientations of Riedel shears, assuming that the slip direction is normal to the intersection of Riedel shears with the fault plane. In the bottom plot, points are poles to all sheared fractures, and the great circle is their average orientation (173, 30) determined by Bingham statistical analysis in Stereonet v. 10.*

Surficial evidence of faulting at the range front is largely absent (Knudsen et al., 2019). Indications of a tectonically active range front such as fault scarps and faceted spurs are absent, and the range front is deeply embayed at drainages that issue from the range. However, the Mineral Mountains West fault zone (Figure 1; Knudsen et al., 2019) is defined by a north-trending system of fault scarps in Quaternary deposits. Along most of its length, the Mineral Mountains West fault zone is located ~2–3 km from the range front. However, south of Figure 1, the range front steps about 5 km to the west and, as a result, the fault zone and range front coincide. No offset of the bedrock surface under the basin has been detected beneath Mineral Mountains West fault scarps, yet seismic rupture of a magnitude sufficient to form surface scarps implies slip across a surface with a down-dip extent of several kilometers. Therefore, the most likely interpretation is that the Mineral Mountains West fault zone roots into the fault that forms the basin fill-bedrock contact, which therefore underwent seismic slip down-dip from where the scarp-forming fractures intersect the bedrock surface. The general lack of evidence for active faulting at the range front implies that the shallow part of the basin-forming fault that lies to the east of the Mineral Mountains West fault zone has been abandoned, as predicted by the rolling-hinge model (Figure 8).

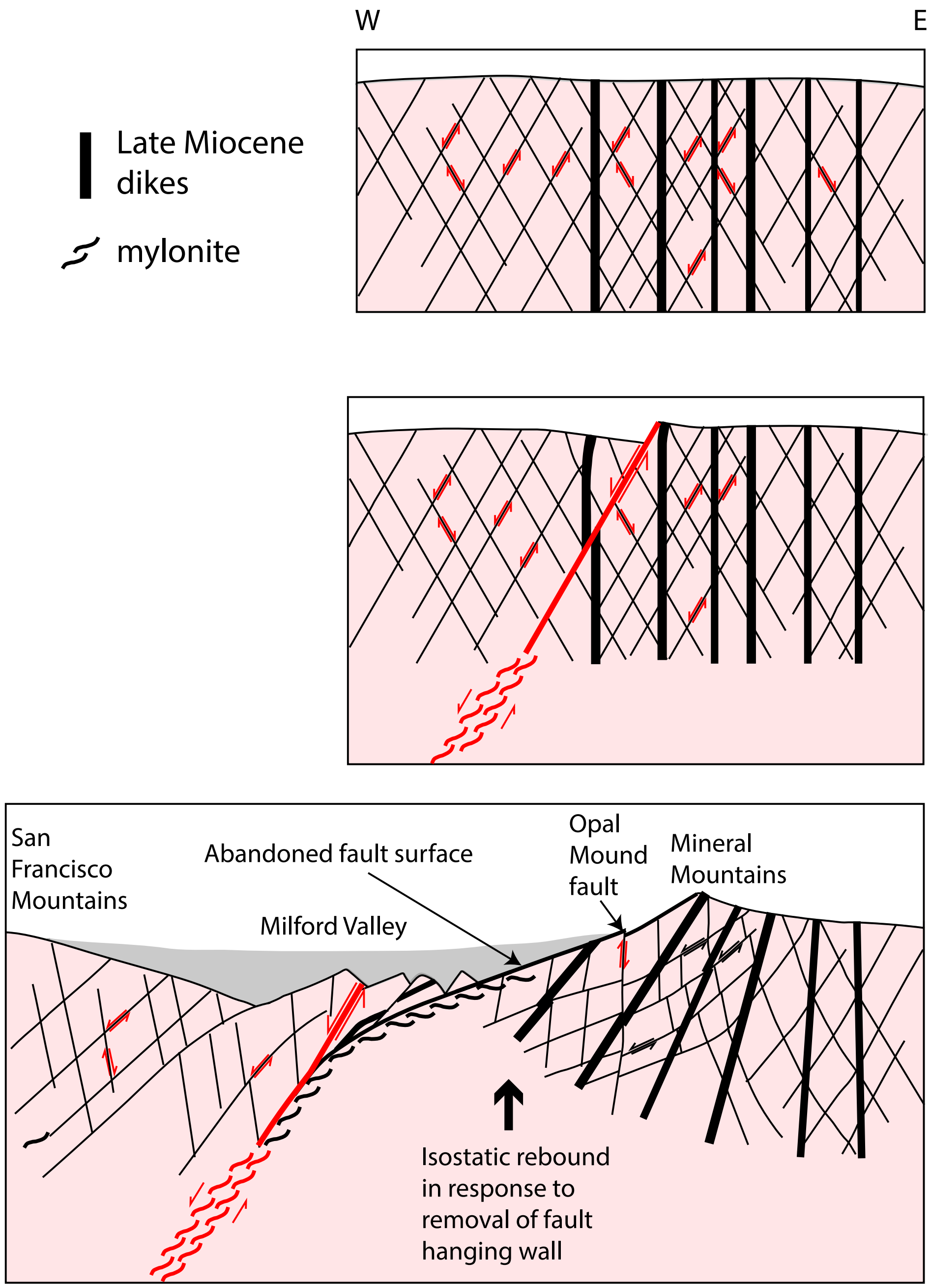

Figure 8. *Schematic east-west profiles (not to scale) illustrating orientations of the dike swarm and joint sets 2 and 3; nucleation of the basin-bounding fault on joint set 3; and fault displacement to form Milford Valley, with tilting driven by isostatic adjustment to removal of the hanging wall of the fault.*

Opal Mound Fault

The Opal Mound fault (Figure 1) is oriented similarly to steep NNE-striking fractures of set 2 within the range. Therefore, like the basin-bounding fault, the Opal Mound fault probably formed by shear across a pre-existing joint set. Surficial geology indicates west-side-up movement (Knudsen et al., 2019). This shear sense across the Opal Mound fault could be driven by the same isostatic forces that cause the geometry of the basin-bounding normal fault to evolve according to the rolling-hinge mechanism (Figure 8). Geometrically similar faulting in the footwalls of other large-displacement normal faults has been interpreted to reflect rolling-hinge deformation (e.g., central Mojave metamorphic core complex, Bartley et al., 1990; Raft River Mountains, Manning and Bartley, 1994; Tauern window in the Austrian Alps, Axen et al., 1995).

Negro Mag Fault

The Negro Mag fault also appears to reflect shear across a fracture set in the batholith, in this case the steep, broadly E-striking fractures of set 1. Geomorphic evidence suggests south-side-up displacement (Knudsen et al., 2019). Nearly all of the Pleistocene rhyolite bodies are located south of the Negro Mag fault and thus on its upthrown side. These observations suggest that motion across the Negro Mag fault may be linked to, and perhaps even driven by, Pleistocene rhyolitic magmatism.

Figure 9 illustrates one hypothesis for such a link. A bysmalith (also sometimes called a punched laccolith) is a subhorizontal tabular intrusion, space for which is made by uplift of a fault-bounded roof block. In Figure 9, the Negro Mag fault is inferred to be the northern boundary of such a roof block that would likely include all of the area characterized by Pleistocene rhyolite extrusions. No location is proposed here for the rest of the boundary of the uplifted block implied by this hypothesis. The boundaries of the uplifted roof block would be inherently difficult to locate in the massive granitic rocks that characterize most of the range, and the western and eastern boundaries could be concealed by recent sedimentation. The location and orientation of the Opal Mound fault invite speculation that it might be related to recent magma intrusion at depth, but its west-side-up offset is inconsistent with this suggestion. The Mineral Mountains West fault zone has the expected sense of offset, but the lack of offset of the basin fill-bedrock contact is difficult to reconcile with a relationship to magma intrusion under the range. As noted above, it is more likely that the Mineral Mountains West fault zone defines the up-dip limit of the most recent displacement across the basin-bounding fault.

If the bysmalith hypothesis is correct, it carries with it a broader implication for the nature and duration of batholith growth. Recent detailed geochronology of well-exposed intrusive complexes indicates that granitic plutons typically grow incrementally downward (e.g., Coleman et al., 2004; Michel et al., 2008). This implies that the age range of exposed batholithic rocks may encompass only part of the construction of the intrusive complex, and that it is particularly likely for the youngest components of an intrusive complex to remain unexposed in the subsurface. The hypothetical Pleistocene bysmalith would constitute such a younger, as-yet unexposed addition to the batholith. Although the youngest intrusive rocks presently exposed at the surface are Miocene in age, growth of the Mineral Mountains batholith may have continued into the Pleistocene, and the presence of an active high-temperature geothermal system suggests that growth of the Mineral Mountains batholith even may be ongoing.

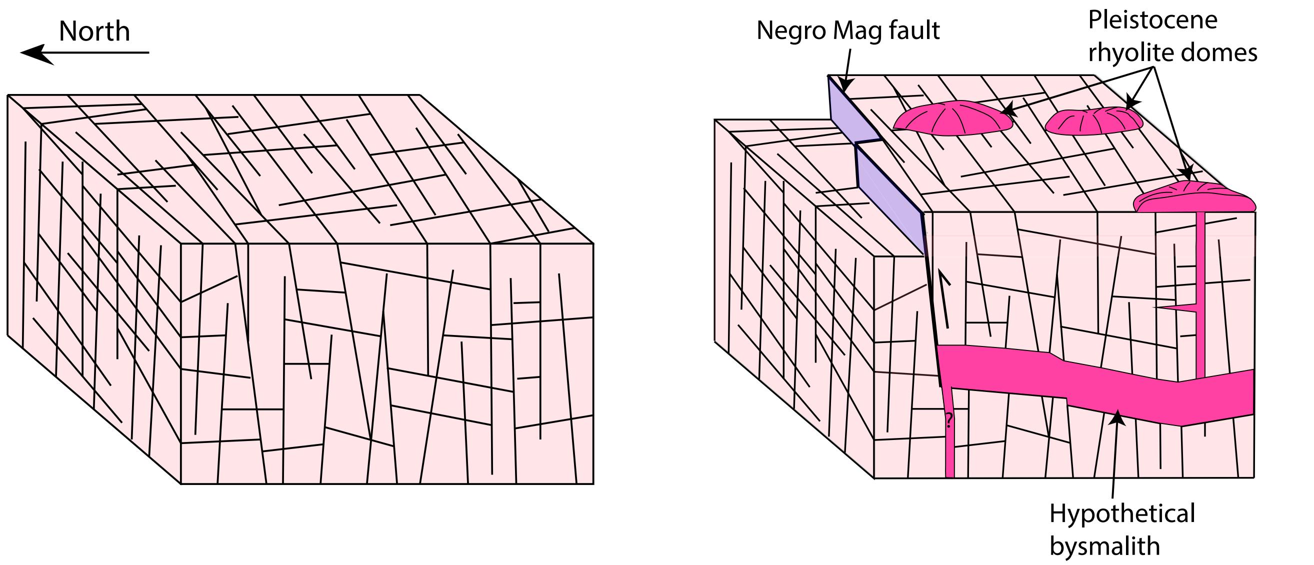

Figure 9. *Cartoon block diagram illustrating hypothetical interpretation of the Negro Mag fault as the northern boundary of a bysmalith that underlies the Pleistocene rhyolitic volcanic field.*

CONCLUSION

Miocene granitic rocks near the Utah FORGE site contain three dominant joint sets in the following orientations: 1) strike ~100±10°, dip 70°–90°; 2) strike ~025±25°, dip 70°–90°; and 3) strike ~180±30°, dip 30°±30° toward the west. Sets 2 and 3 are interpreted to form a conjugate set that formed prior to or early during Basin and Range extension. The batholith, the joints that it contains, and the west-dipping normal fault that bounds the Milford Valley basin all underwent ~40° of west-side-up tilt during Basin and Range extension. The tilting is interpreted to reflect isostatic rebound during unroofing of the range by the basin-bounding fault (rolling hinge mechanism). Each of the three significant faults in the vicinity of the FORGE site is oriented subparallel to one of the main joint sets and probably was initiated by shear across joints of that set. Most of the joints in the range that have been sheared belong to set 3. The average orientation of the sheared joints is subparallel to the basin-bounding fault, which thus is interpreted to have initiated by shear across set 3 joints. The Opal Mound fault is oriented subparallel to set 2 joints. Its west-side-up slip sense is consistent with it playing a role in rolling-hinge deformation in the footwall of the basin-bounding fault. The Negro Mag fault is oriented subparallel to set 1 joints and it appears to accommodate south-side-up displacement. The substantial majority of Pleistocene rhyolite was erupted on the upthrown side of the Negro Mag fault. These relations suggest the speculation that the Negro Mag fault represents the northern boundary of an unexposed bysmalith that could be interpreted to represent continued growth of the batholith into Quaternary time.

ACKNOWLEDGMENTS

Fieldwork in the Mineral Mountains that forms the basis of this report was supported by DOE contract DE-EE0007080. Drew Coleman shared unpublished fracture data from his Ph.D. dissertation. Discussions with members of the FORGE team, particularly Stefan Kirby, Emily Kleber, Stuart Simmons, Kris Pankow, and Rick Allis were invaluable in the development of the ideas presented here. The resulting paper benefitted from constructive reviews by Stuart Simmons, Stefan Kirby, and Drew Coleman.

REFERENCES

Anderson, E.M., 1951, The dynamics of faulting and dyke formation with applications to Britain (2nd edition): Edinburgh, Oliver and Boyd.

Axen, G.J., and Bartley, J.M., 1997, Field tests of rolling hinges: Existence, mechanical types, and implications for extensional tectonics: Journal of Geophysical Research, v. 102, No. B9, p. 20,515–20,537.

Axen, G.J., Bartley, J.M., and Selverstone, J., 1995, Structural expression of a rolling hinge in the footwall of the Brenner Line normal fault, eastern Alps: Tectonics, v. 14, p. 1380–1392.

Bartley, J.M., Fletcher, J.M., and Glazner, A.F., 1990, Tertiary extension and contraction of lower-plate rocks in the central Mojave metamorphic core complex: Tectonics, v. 9, p. 521–534.

Buck, W.R., 1988, Flexural rotation of normal faults: Tectonics, v. 7, p. 959–973.

Coleman, D.S., 1991, Geology of the Mineral Mountains batholith, Utah [unpublished Ph.D. dissertation]: University of Kansas, Lawrence, Kansas, 219 p.

Coleman, D.S., Bartley, J.M., Walker, J.D., Price, D.E., and Friedrich, A.M., 1997, Extensional Faulting, Footwall Deformation and Plutonism in the Mineral Mountains, Southern Sevier Desert, *in* Link, P., and Kowallis, B., eds., Mesozoic to Recent geology of Utah (Field Trip Guidebook, 1997 GSA Annual Meeting): Brigham Young University Geology Studies, v. 42, part 2, p. 203–233.

Coleman, D.S., Gray, W., and Glazner, A.F., 2004, Rethinking the emplacement and evolution of zoned plutons: Geochronologic evidence for incremental assembly of the Tuolumne Intrusive Suite, California: Geology, v. 32, p. 433–436.

Coleman, D.S., and Walker, J.D., 1994, Modes of tilting during extensional core complex development: Science, v. 263, p. 215–218.

Coleman, D.S., Walker, J.D., Bartley, J.M., and Hodges, K.V., 2001, Thermochronologic evidence for footwall deformation during extensional core complex development, Mineral Mountains, Utah, *in* Erskine, M., Bartley, J.M., Faulds, J., and Rowley, P.D., editors, The Geologic Transition—Colorado Plateau to Basin and Range: Guidebook - Pacific Section, American Association of Petroleum Geologists, vol. 78, p. 155–168.

Hamblin, W.K., 1965, Origin of “reverse drag” on the downthrown side of normal faults: Geological Society of America Bulletin, v. 76, p. 1145–1164.

Hardwick, C., Hurlbut, W., and Gwynn, M., 2019, Geophysical surveys of the Milford, Utah, FORGE site—gravity and TEM, *in* Allis, R., and Moore, J.N., editors, Geothermal characteristics of the Roosevelt Hot Springs system and adjacent FORGE EGS site, Milford, Utah: Utah Geological Survey Miscellaneous Publication 169-F, 15 p., https://doi.org/10.34191/MP-169-F.

Hintze, L.F., Willis, G.C., Laes, D.Y.M., Sprinkel, D.A., and Brown, K.D., 2000, Digital Geologic Map of Utah: Utah Geologic Survey, Map 179DM, 1:500,000 scale.

Kamb, W.B., 1959, Ice petrofabric observations from Blue Glacier, Washington, in relation to theory and experiment: Journal of Geophysical Research, v. 64, p. 1891–1909.

Knudsen, T., Kleber, E., Hiscock, A., and Kirby, S.M., 2019, Quaternary geology of the Utah FORGE site and vicinity, Millard and Beaver Counties, Utah, *in* Allis, R., and Moore, J.N., editors, Geothermal characteristics of the Roosevelt Hot Springs system and adjacent FORGE EGS site, Milford, Utah: Utah Geological Survey Miscellaneous Publication 169-B, 21 p., 2 appendices, https://doi.org/10.34191/MP-169-B.

Manning, A.M., and Bartley, J.M., 1994, Post-mylonitic deformation in the Raft River metamorphic core complex, northwest Utah: Evidence for a rolling hinge: Tectonics, v. 13, p. 596–612.

Machette, M.N., Steven, T.A., Cunningham, C.G., and Anderson, J.J., 1984, Geologic map of the Beaver Quadrangle, Beaver and Piute Counties, Utah: U. S. Geological Survey Miscellaneous Investigations, Map I-1520, scale 1:50,000.

Michel, J., Baumgartner, L., Putlitz, B., Schaltegger, U., and Ovtcharova, M., 2008, Incremental growth of the Patagonian Torres del Paine laccolith over 90 k.y.: Geology, v. 36, n. 6, p. 459–462.

Miller, J., Allis, R., and Hardwick, C., 2019, Interpretation of seismic reflection surveys near the FORGE enhanced geothermal systems site, Utah, in Allis, R., and Moore, J.N., editors, Geothermal characteristics of the Roosevelt Hot Springs system and adjacent FORGE EGS site, Milford, Utah: Utah Geological Survey Miscellaneous Publication 169-H, 13 p., https://doi.org/10.34191/MP-169-H.

Nielson, D.L., Evans, S.H., Jr., and Sibbett, B.S., 1986, Magmatic, structural, and hydrothermal evolution of the Mineral Mountains intrusive complex, Utah: Geological Society of America Bulletin, v. 97, p. 765–777.

Price, D.E, 1998, Timing, magnitude, and three-dimensional structure of detachment-related extension, Mineral Mountains, Utah [unpublished M.S. thesis]: University of Utah, Salt Lake City, 67 p.

Proffett, J.M., Jr., 1977, Cenozoic geology of the Yerington District, Nevada, and implications for the nature and origin of Basin and Range faulting: Geological Society of America Bulletin, v. 88, p. 247–266.

Sibbett, B.S., and Nielson, D.L., 2017, Geologic map of the central Mineral Mountains, Beaver County, Utah: Utah Geological Survey Miscellaneous Publication 17-2DM.

Smith, R.B., and Bruhn, R.L., 1984, Intraplate extensional tectonics of the eastern Basin-Range: inferences on the structural style from seismic reflection data, regional tectonics, and thermal-mechanical models of brittle-ductile deformation: Journal of Geophysical Research, v. 89, p. 5733–5762.

Spencer, J.E., 1984, Role of tectonic denudation in warping and uplift of low-angle normal faults: Geology, v. 12, p. 95–98.

Thatcher, W., and Hill, D.P., 1991, Fault orientations in extensional and conjugate strike-slip environments and their implications: Geology, v. 19, p. 1116–1120.

Wernicke, B.P., and Axen, G.J., 1988, On the role of isostasy in the evolution of normal fault systems: Geology, v. 16, p. 848–851.

Wills, S., and Buck, W.R., 1997, Stress-field rotation and rooted detachment faults; a Coulomb failure analysis: Journal of Geophysical Research, v. 102, p. 20,503–20,514.

THERMAL CHARACTERISTICS OF THE ROOSEVELT HOT SPRINGS SYSTEM, WITH FOCUS ON THE FORGE EGS SITE, MILFORD, UTAH

by Rick Allis[1], Mark Gwynn[1], Christian Hardwick[1], Will Hurlbut[1], Stefan M. Kirby[1,] and Joseph N. Moore[2]

[1]Utah Geological Survey, Salt Lake City, Utah

[2]Energy & Geoscience Institute, University of Utah, Salt Lake City, Utah

Miscellaneous Publication 169-D
Utah Geological Survey
a division of
UTAH DEPARTMENT OF NATURAL RESOURCES

This paper is part of *Geothermal Characteristics of the Roosevelt Hot Springs System and Adjacent FORGE EGS Site, Milford, Utah*. https://doi.org/10.34191/MP-169

Bibliographic citation:

Allis, R., Gwynn, M., Hardwick, C., Hurlbut, W., Kirby, S.M., and Moore, J.N., 2019, Thermal characteristics of the Roosevelt Hot Springs system, with focus on the FORGE EGS site, Milford, Utah, *in* Allis, R., and Moore, J.N., editors, Geothermal characteristics of the Roosevelt Hot Springs system and adjacent FORGE EGS site, Milford, Utah: Utah Geological Survey Miscellaneous Publication 169-D, 22 p., https://doi.org/10.34191/MP-169-D.

THERMAL CHARACTERISTICS OF THE ROOSEVELT HOT SPRINGS SYSTEM, WITH FOCUS ON THE FORGE EGS SITE, MILFORD, UTAH

by Rick Allis, Mark Gwynn, Christian Hardwick, Will Hurlbut, Stefan M. Kirby and Joseph N. Moore

ABSTRACT

The heat loss from the Roosevelt Hot Springs (RHS) system is 60–70 MW and is predominantly due to the subsurface outflow of about 60 kg/s of hot groundwater from the northern Opal Mound fault (OMF). Prior to development for geothermal power, the main surface feature was a spring close to boiling with a flow rate of 1 kg/s and a heat output of less than 500 kW. The formation of a steam zone in the reservoir due to development has caused steaming ground to replace the hot spring, and the heat loss is now about 10 MW. The high-temperature outflow to the northwest has a prominent temperature inversion below 300 m depth indicating it has been present for 100–1000 years. There is a lower-temperature outflow from the central and southern OMF that has no temperature inversion and a gradient in alluvium below the water level of about 70°C/km. This gradient is indicative of the underlying conductive heat flow and implies the outflow has been present for at least several tens of thousands of years. This southern outflow is occurring from 1–2 km north of Opal Mound up to 5 km south of the Mound. The Opal Mound and sinter deposits farther north adjacent to the OMF may have built up during periods of higher pressure in the evolution of the RHS system, perhaps during the highstand of Lake Bonneville 18,000 years ago.

The Frontier Observatory for Research in Geothermal Energy (FORGE) Milford site is situated over the flank of a granitic intrusion that outcrops to the east in the Mineral Mountains and has a temperature of more than 200°C at 2.4 km depth directly beneath the site. Integration of the thermal data from over 100 thermal gradient and deep exploration wells suggests that about 70 km^2 of the intrusion has a temperature of at least 200°C at 3 km depth. The temperature profile from the 2.3-km-deep well 58-32 that was drilled for the FORGE project confirms a predominantly conductive thermal regime within the granite, with the gradient at depth varying between 60° and 90°C/km due to thermal conductivity variations. Measurements of cuttings and core from the well show a wide range of thermal conductivity depending on the composition of the granitic rock. Values vary from 2.0 W/m°C in quartz-poor dioritic rock to 3.9 W/m°C in more quartz-rich granite. These measurements were made at room temperature and need to be reduced by about 15% for the effects of temperature at the 2–3-km-deep FORGE reservoir beneath the site. Integration of thermal conductivity and temperature gradient variations in well 58-32 yields a heat flow of 180 ± 20 mW/m^2. This value appears to be representative of the deep, thermally conductive heat flow in impermeable granite west and east of the RHS hydrothermal system. One-dimensional heat flow models of the conductive thermal regime in two deep wells adjacent to the convective RHS system suggest partial melt could exist below 7–8 km depth.

INTRODUCTION

A review of the thermal characteristics of the Roosevelt Hot Springs (RHS) system was carried out in Phase 1 of the Frontier Observatory for Research in Geothermal Energy (FORGE) project, with a summary presented by Allis et al. (2015). This review expanded the original assessment of the heat flow at RHS by Ward et al. (1978) by adding other thermal data from exploration wells drilled after 1978. The initial state and response of the Blundell borefield to production and injection was analyzed by Allis and Larsen (2012), and an update of the fluid chemistry characteristics and changes has been reviewed by Simmons et al. (2018; in preparation).

The near-surface thermal characteristics of the RHS are delineated by the temperatures at 200 m depth obtained from more than 50 thermal gradient wells drilled mostly in the late 1970s (Figure 1). The highest temperatures (> 80°C) occur over the top of the hydrothermal system on the east side of the Opal Mound fault (OMF), and this area is tapped by the Blundell geothermal power plant production wells. Temperatures at greater depth here are close to boiling-point for depth over the upper few hundred meters and the profile is near-isothermal below about 400 m depth. These wells tap what is often called the upflow zone. The northwest extension of the high-temperature zone at 200 m depth is due to an outflow of hot groundwater. The 80°C isotherm at 200 m depth is approximately equivalent to a heat flow of 1000 mW/m^2. When integrated across the entire RHS system, the total heat output is 60–70 MW. Assuming a temperature of 270°C (enthalpy of 1180 kJ/kg) in the deep upflow zone of the hydrothermal system, the pre-development mass flow of the system was 60 kg/s.

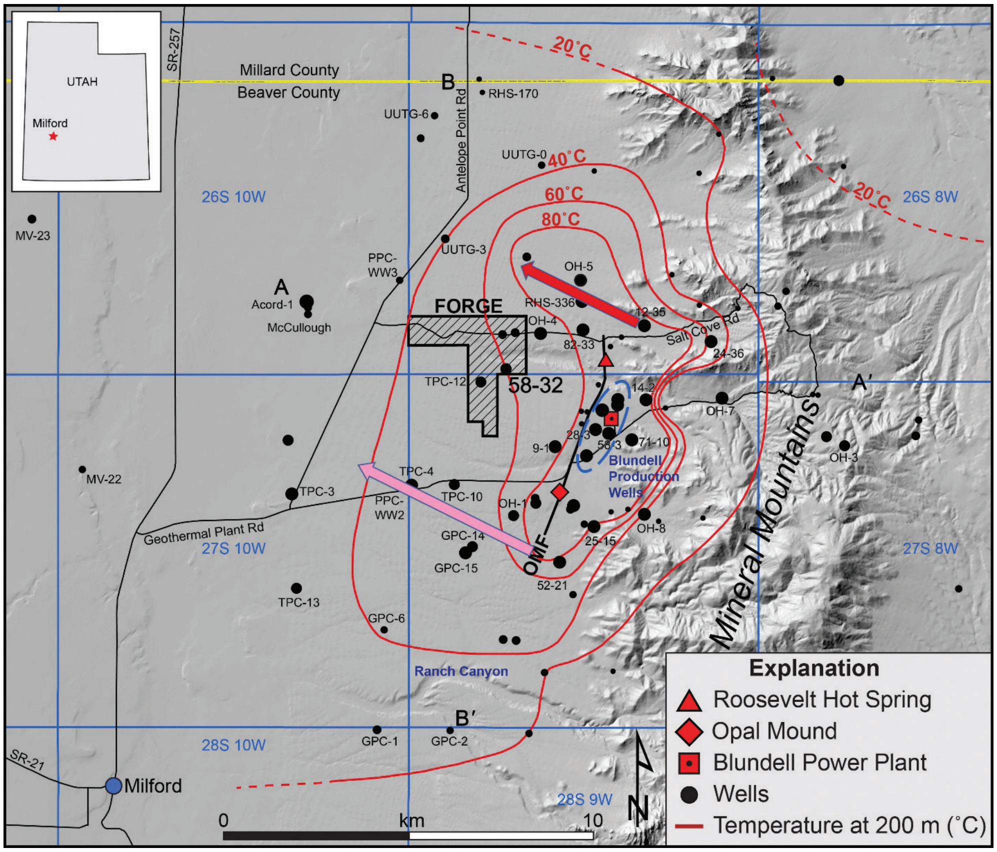

Figure 1. *Thermal regime at 200 m depth. The degree of certainty of the thermal data is indicated by the size of the dot for the well location (all wells are deeper than 50 m). The largest size is for wells greater than 200 m depth where the temperature was observed. The smallest size is for wells about 50 m deep where the temperature had to be extrapolated to a much greater depth and the temperature is considered the least certain. On the east side of the thermal anomaly, the contours represent the temperature at 200 m below the 1830 m above sea level (6000 ft asl) datum, which is the elevation of the alluvial fan near to where it laps against the Mineral Mountains. The 1830 m asl datum allows the contours beneath the flanks of the Mineral Mountains to be smoothed across the ridges and valleys, but requires that higher-elevation wells be extrapolated to greater depths (up to 405 m from the surface). West of the OMF the contours are 200 m below the surface, and near SR-257 in the middle of the valley this is at about 1325 m asl (4345 ft asl; ground surface about 5000 ft asl or 1525 m asl). See Figure 18 for cross sections A–A' and B–B'. Red and pink arrows indicate relatively young (red, ~ 1000 y) and long-lived (pink, ~ 10,000 y) outflows of geothermal groundwater.*

SURFACE THERMAL ANOMALIES

Roosevelt Hot Springs is located near the northern end of the OMF and was the only thermal feature recorded in the area prior to exploration and development of the hydrothermal system (Lee, 1908; Ward et al., 1978; Capuano and Cole, 1982). In the late 1800s and early 1900s the hot springs became a resort with a bathhouse and other facilities, and the water was used for medicinal purposes. Lee (1908) suggests a flow of at least 1 L/s (about 1 kg/s) of boiling water "strongly charged with hydrogen sulphide." The last high-temperature sample collected at the spring was in 1950 (85°C; Mundorff, 1970). By the time exploration was occurring in the 1970s, the spring had become a warm seep, but had similar chemistry to the 1950 analysis. Although there are hot spring deposits along at least a 5 km length of the OMF (Nielson et al., 1986; Kirby et al., 2018), there were no reports of associated thermal ground or seeps before development. The heat loss from the original hot spring assuming the flow rate and boiling temperature in Lee (1908) was about 300 kW, a tiny fraction of the subsurface heat output being carried by the underlying hot groundwater.

Informal comments from the operators of the Blundell power plant indicate an expansion of thermal ground occurred during the mid-1980s after the power plant was commissioned. This expansion is corroborated by comparison of aerial photos of the RHS area pre-development and more recently (Figure 2). Areas of steam-heated ground expanded, junipers and grasses died off, and areas of bare ground expanded. However, the 1955 photo shows that there was a lack of junipers in areas that subsequently became steam-heated. Growth here may have been restricted by a subtle gas flux from depth or intense hydrothermal alteration.

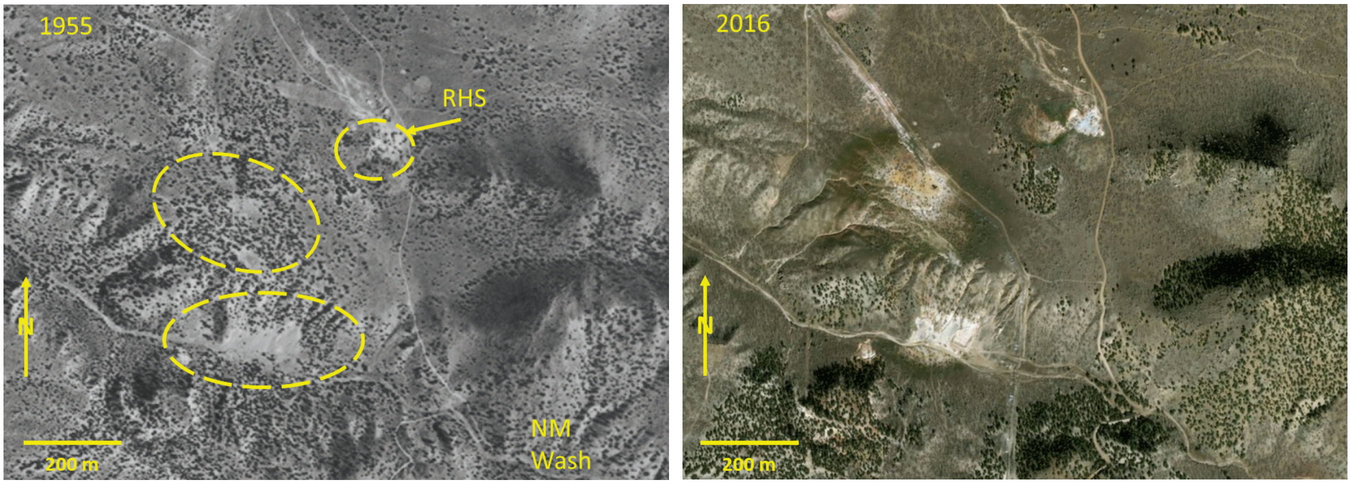

Figure 2. *Historical comparison of the vegetation patterns and thermal features around Roosevelt Hot Springs (1955 and 2016 imagery). Development of the hydrothermal system for power caused an increase in steam-heated ground and a die-off of vegetation. A major fire in 2007 (Milford Flat fire) burned much of the vegetation, so caution is required interpreting the changes. NM Wash is the Negro Mag Wash. Yellow dashed ellipses on the 1955 photo outline the areas of future steam-heated ground.*

The intensity and size of the thermal anomalies were measured in the spring of 2012 using a 20-cm dial-type thermometer (Figure 3). Measurements at different times of the day and on different days were compared to temperatures at several base stations on non-thermal ground and were adjusted to anomalies above ambient. The accuracy of the anomalies is estimated to be ±2°C. Three distinct areas have thermal ground: north of Negro Mag Wash (including the original RHS), adjacent to production well 28-3 in the production well field, and on part of the Opal Mound. A pressure decline due to production has caused a steam zone to form over the hot liquid reservoir, and steam is leaking to the surface (Allis and Larsen, 2012). A detailed assessment of the heat loss from the steaming ground has not been attempted, but a rough comparison of typical heat loss rates and the area of steaming ground elsewhere (Allis et al., 1999; Bromley at al., 2011) suggests that surface heat loss has increased to about 10 MW.

THERMAL GROUNDWATER REGIME

At 200 m depth, for a typical conductive Great Basin heat flow of 90 mW/m^2 and an average surface temperature of 12°C, the temperature should be about 24°C and the gradient in the overlying unconsolidated sediment should be about 60°C/km (assuming a thermal conductivity of 1.5 W/m°C). In low-porosity crystalline rocks (thermal conductivity of about 3 W/m°C), the equivalent temperature is about 18°C and the gradient is about 30°C/km. In the Mineral Mountains where the crystalline rocks outcrop, the elevation rises over a kilometer above the valley floor, so the mean annual surface temperature could be 5°–10°C cooler due to the adiabatic lapse rate in the atmosphere. The temperature at 200 m depth near the ridge of the Mineral Mountains, assuming thermal conduction from the surface and 90 mW/m^2, implies an ambient temperature of about 13°–15°C. Temperatures at 200 m depth greater than about 30°C in the valley, and greater than about 20°C in the Mineral Mountains, are therefore anomalously warm. Examples of thermal gradients are shown in Figure 4.

When the thermal gradient data for the central, southern, and western sectors are plotted against depth, the near-surface profiles (less than about 80 m depth) are surprisingly similar. The gradient of 270°C/km is equivalent to a heat flow of 400–500 mW/m^2 (average thermal conductivity of 1.5–1.7 W/m°C). The thermal gradients decrease by almost a factor of four at greater depth, which Wilson and Chapman (1980) attribute to a corresponding increase in thermal conductivity at the transition to water-saturated rock. If this is correct, then all wells should show the same effect at the water table. Because several wells show no change in thermal gradient at the water table (e.g., OH4, OH5, GPC15), it seems more likely that some other factor such as a cross flow of warm water at the water table may be causing this gradient change at the water table. In addition, several wells in the central part of the valley exhibit a uniform thermal gradient from the ground surface through the water table consistent with the zero-depth intercept being close to the mean annual temperature (for example, MV22, 23, McCullough). There is no evidence of cross-flowing warm water in these three wells, and they may reflect the undisturbed regional thermal regime (discussed in more detail in the Regional Heat Flow section).

When all the temperature profiles in gradient wells are plotted against elevation, the profiles are spread from warmer in the east (GPC-15) to cooler in the west (for example, TPC-3 near the intersection of Geothermal Plant Rd. and Antelope Pt. Rd.). The

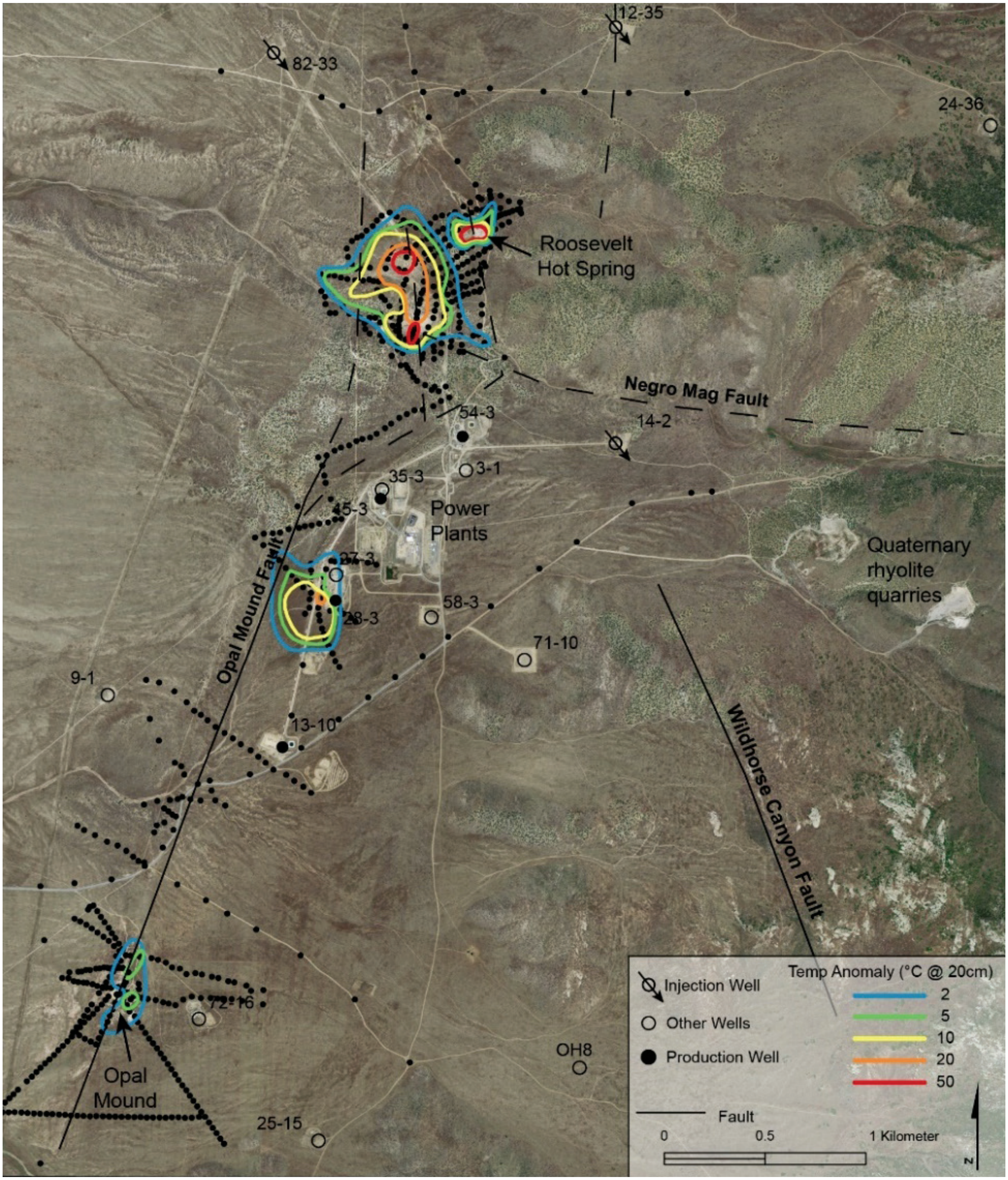

Figure 3. *Temperature anomalies at 20 cm depth (°C above ambient; small dots are measurement points) adjacent to the OMF in 2012. Well 71-10 became an injection well in 2016 and well 58-3 became a production well in 2018.*

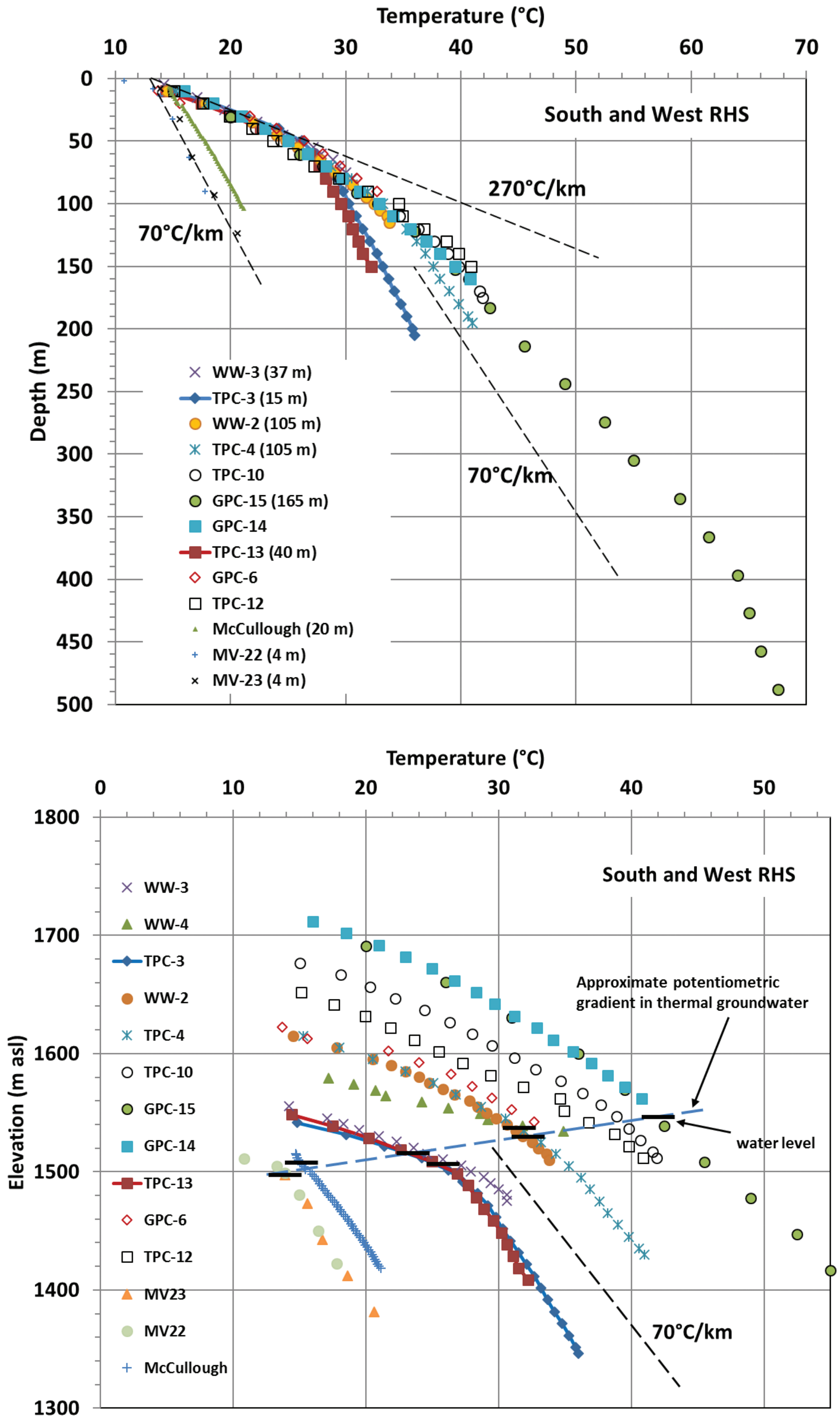

Figure 4. *Upper: Temperature profiles from thermal gradient wells around the southern and western areas of the RHS system, plotted against depth below the ground surface. Although most wells over the RHS system have shallow temperature gradients exceeding 200°C/km, the deeper thermal gradients are 70°C/km (water level in brackets, either from measurements in that well, or from a nearby well and documented by Kirby et al. [2019]). Lower: Temperature plotted against elevation (meters above sea level) shows a pattern of warm groundwater flowing from east to west, with the high thermal gradients at shallow depth in the vadose zone, and apparently conductive thermal profiles below and above the water table.*

water levels also decrease in elevation from east to west, confirming an outflow of warm groundwater (50 m of head change over 10 km; Kirby et al., 2019). The temperature of the outflow at the water table decreases from 42°C in GPC-15, to 25°C in TPC-3. This cooling of the groundwater appears to be due to both conductive heat flow through the vadose zone and mixing with infiltrating meteoric water (evidence of dilution towards the west; Kirby et al., 2019).

In the northern sector of RHS, where the northwest-directed plume flows from the northern end of the OMF, there is evidence of hot water outflow between 1300 and 1500 m asl. Well OH-5 best captures the character of the outflow plume (Figure 5). The new FORGE well 58-32 is suspected to be near the west edge of this plume, with the thermal profile suggesting a lateral flow at 40° to 45°C between 1300 and 1500 m asl. The temperature of the source of the plume probably exceeds 130°C based on the temperature in well 82-33 and may be about 200°C where it flows from the northern end of the OMF (well 12-35).

The pattern of a warm outflow in south-central RHS with an underlying uniform temperature gradient, contrasts with the inversion present beneath the hot outflow in northern RHS. The change in gradient is a phenomenon that was studied by Ziagos and Blackwell (1981, 1986). They showed that the thermal effect of a horizontal outflow of warm groundwater initially causes a temperature inversion beneath the outflow, but after a long time of continued warm outflow the underlying thermal regime heats up to reflect the regional equilibrium thermal gradient (Figure 6). The time frame for the inversion to disappear is tens of thousands of years. This type of thermal signature was used to interpret that a lateral flow of hot water on top of the Precambrian basement beneath the Fenton Hill hot dry-rock test site had been occurring for about 10,000 years (Harrison et al., 1986). A long-lived thermal outflow may help explain the fossil siliceous sinter at Opal Mound near the southern end of the OMF in contrast to the recent active hot spring area at the northern end of the OMF. Although the sinter at Opal Mound exhibits a transition from Opal-A to diagenetic quartz, and in New Zealand this transition takes about 40,000 years, the two dates from the Opal Mound are between 1000 and 2000 years (Lynne et al., 2005). Perhaps the core of the Opal Mound is significantly older than the two dates imply. In contrast, based on the thermal inversion, the hot groundwater plume northwest of the RHS maybe be relatively young (~ 1000 years). The deepest well in the south-central RHS west of the OMF, GPC-15 (580 m deep), has a second decrease in temperature gradient below 400 m depth which may be evidence of decreasing temperature with time of this long-lived thermal outflow.

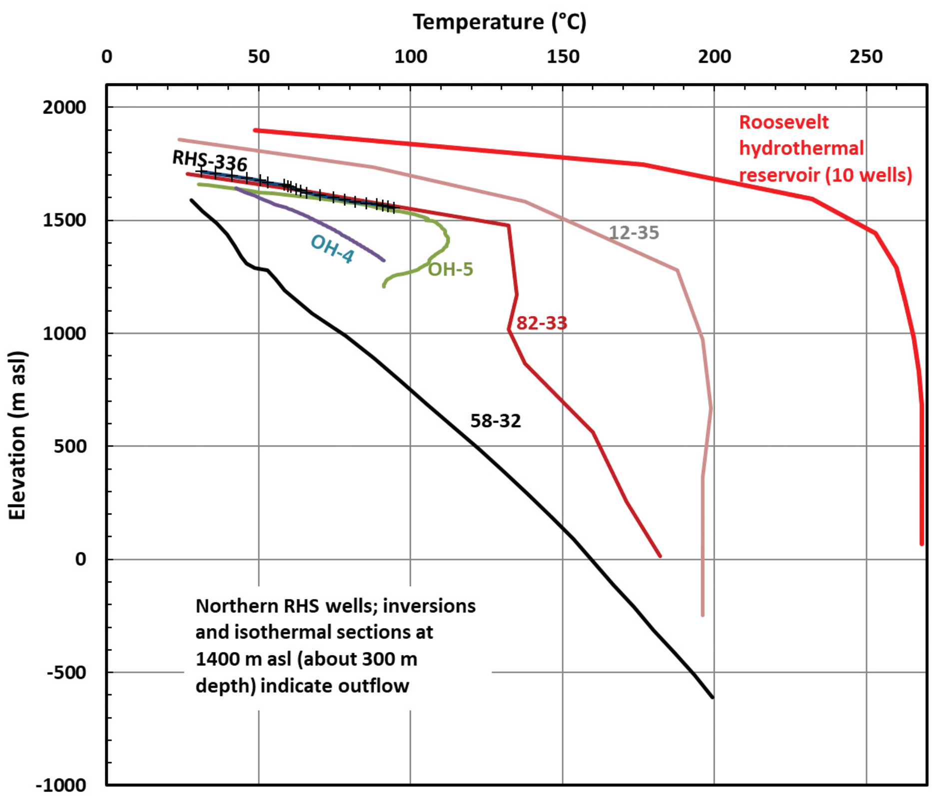

__Figure 5.__ Temperature profiles in wells around the northwest part of the RHS system near the main outflow zone of hot water. The outflow is characterized by temperature inversions (OH-5) and isothermal zones between 1500 and 1300 m asl (typically 200–400 m depth). FORGE well 58-32 appears to be outside the hot outflow but does show anomalously cooler conditions suggestive of lateral groundwater flow in this depth range.

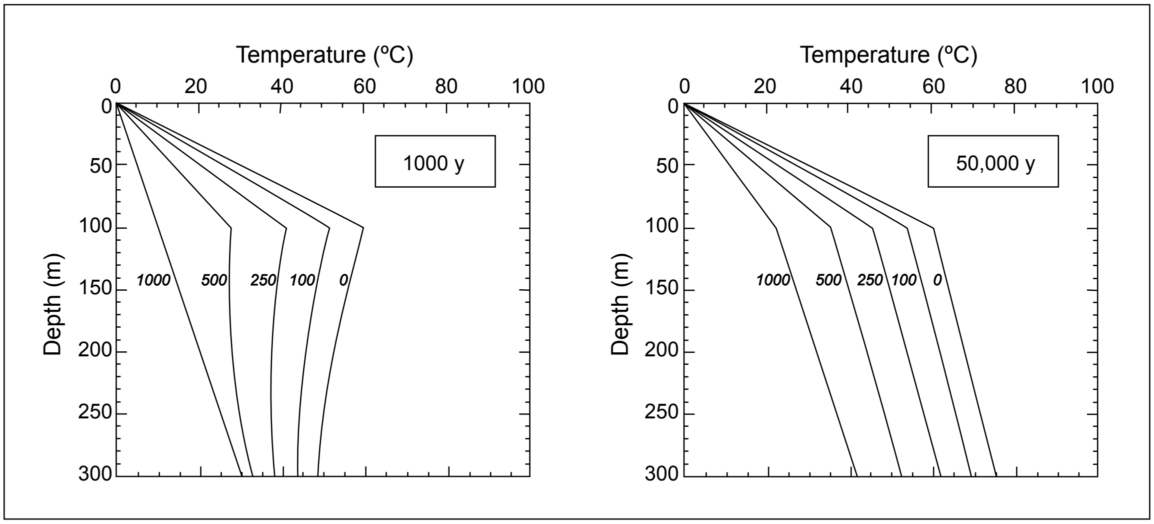

Figure 6. *Theoretical temperature-depth profiles for the thermal effects due to lateral flow in an aquifer at 100 m depth at 60°C at the recharge point (0 m) and at distances up to 1000 m from the recharge point (water flow rate of 1 m/year assumed; 100°C/km ambient gradient). On a scale of hundreds to thousands of years, there is a temperature inversion beneath the aquifer; on a scale of tens of thousands of years, the thermal regime at depth is the equilibrium gradient (Ziagos and Blackwell, 1981, 1986).*

REGIONAL THERMAL REGIME

As discussed in the previous section, the temperature gradient in the groundwater west of the OMF has a characteristic value of about 70°C/km, although over a large area the gradient is displaced to higher temperatures (Figure 4). In the Mineral Mountains east of the RHS thermal anomaly the profiles in exploration wells typically show low thermal gradients (10°–20°C/km) which extrapolate to zero-depth temperature intercepts of 8°–10°C. These low gradients are consistent with the effects of downward percolation of meteoric water into the mountainous terrain. The deepest well near the ridgeline of the Mineral Mountains (OH-3, Figure 1) is 660 m deep and has a gradient of 21°C/km (Forrest, 1994).

West of the obvious thermal groundwater anomaly in north Milford Valley several temperature gradient wells have zero-depth temperature intercepts similar to the mean annual ground-surface temperature for the elevation (13° ± 2°C) and have a gradient of 60° ± 5°C/km (Figure 7). Assuming a thermal conductivity for the basin fill of 1.5 W/m°C implies a heat flow of 90 ± 10 mW/m^2. Uncertainties in thermal conductivity will increase the uncertainties in heat flow.

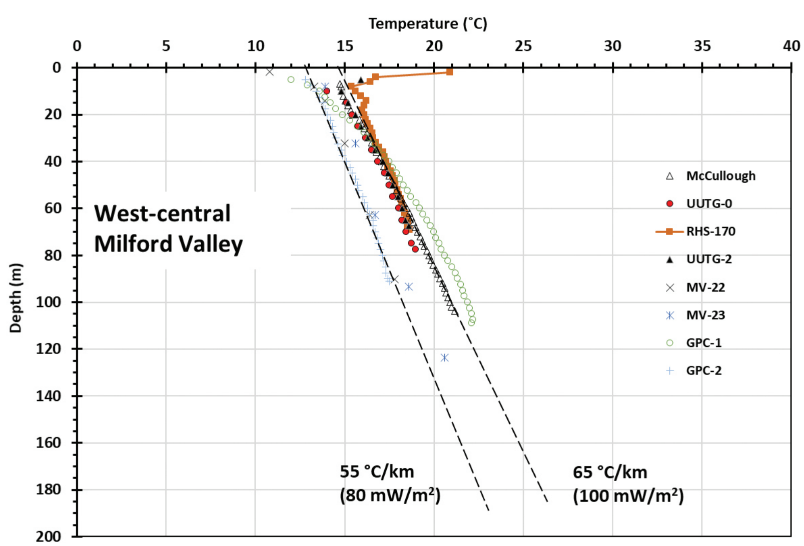

Figure 7. *Temperature profiles in thermal gradient wells in central northern Milford Valley having consistent gradients which extrapolate to the mean annual temperature of the ground surface (13°–15°C). The heat flow values assume an average thermal conductivity for the basin fill of 1.5 W/m°C.*

Acord-1

In 1979 McCullough Oil drilled a well, Acord-1, to 3.5 km depth in the same area as the gradient wells shown in Figure 7. Acord-1 (Figure 1) intercepted granitic basement at 3.0 km depth. Gwynn et al. (2016) analyzed the unusually detailed dataset of bottom-hole temperatures measured as drilling progressed. They showed for reasonable assumptions of thermal conductivity for rock type, a conductive geotherm could fit both the shallow gradient and the corrected bottom-hole temperatures (Figure 8). The heat flow that best fits both the nearby McCullough groundwater temperature profile and the corrected bottom-hole temperatures in Acord-1 is 100 ± 20 mW/m^2. Most of the uncertainty is due to assumptions about thermal conductivity.

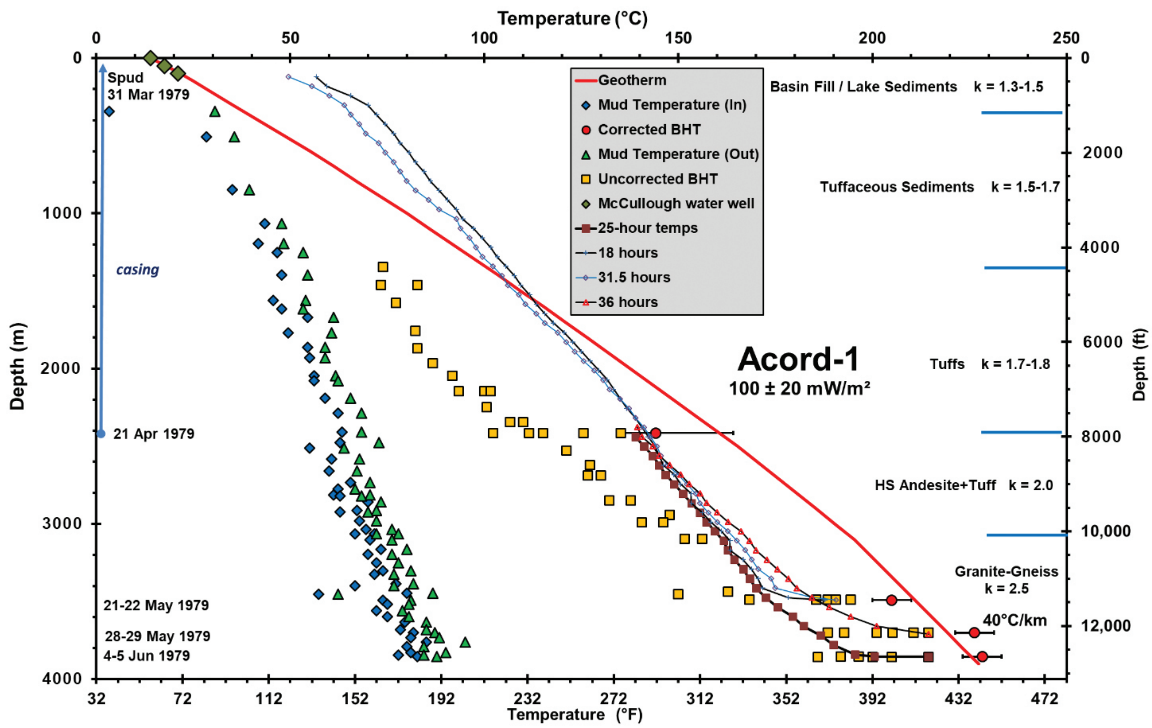

Figure 8. Temperature data from Acord-1 well during brief stops while the hole was being drilled (Gwynn et al., 2016). The corrected bottom hole temperatures (BHTs) are consistent with a conductive profile, and the best-fit geotherm has a heat flow of 100 ± 20 mW/m^2 (uncertainty due to thermal conductivity [k; units of W/m°C] assumptions; geotherm fits both the observed shallow thermal gradient at the site and the deep, corrected BHTs). The temperature gradient in the granite is 40°C/km.

Deep Wells Near the RHS Wellfield

Numerous deep exploration wells were drilled around the RHS system before the most productive zone (sometimes referred to as the "reservoir") for geothermal power generation was identified. Equilibrium profiles for these wells are shown in Figure 9 (locations on Figure 1). Wells tapping the hydrothermal reservoir are distinctive because of their high near-surface temperature gradient (typically close to a boiling point-for-depth profile) and near-isothermal zone below about 500 m depth. The near-isothermal conditions in the reservoir are consistent with the upflow of fluid at more than 265°C (Ward et al., 1978; Faulder, 1991, 1994; Allis and Larsen, 2012; Simmons et al., 2015, in preparation). Most wells outside the upflow zone are much cooler near-surface but have constant temperature gradients below about 1 km depth which can be extrapolated to greater depth. This contrast is indicative of poor permeability, lack of fluid flow, and thermal conduction as the dominant form of heat transfer. The new well drilled for the FORGE project, 58-32, is similar, with a deep gradient between 60° and 90°C/km below 800 m depth (discussed in next section). Most of these wells point to temperatures of more than 250°C at depths of 3–4 km. These deeper wells provide proxies for extrapolating nearby thermal gradient wells and enable isotherm maps to be compiled at different depths (described in a later section).

FORGE Well 58-32

FORGE well 58-32 was completed in October 2017 after two months of drilling and subsequent testing (Moore et al., 2018). Because of the volume of thermal data available, its thermal regime is discussed here in detail. Precision temperature and

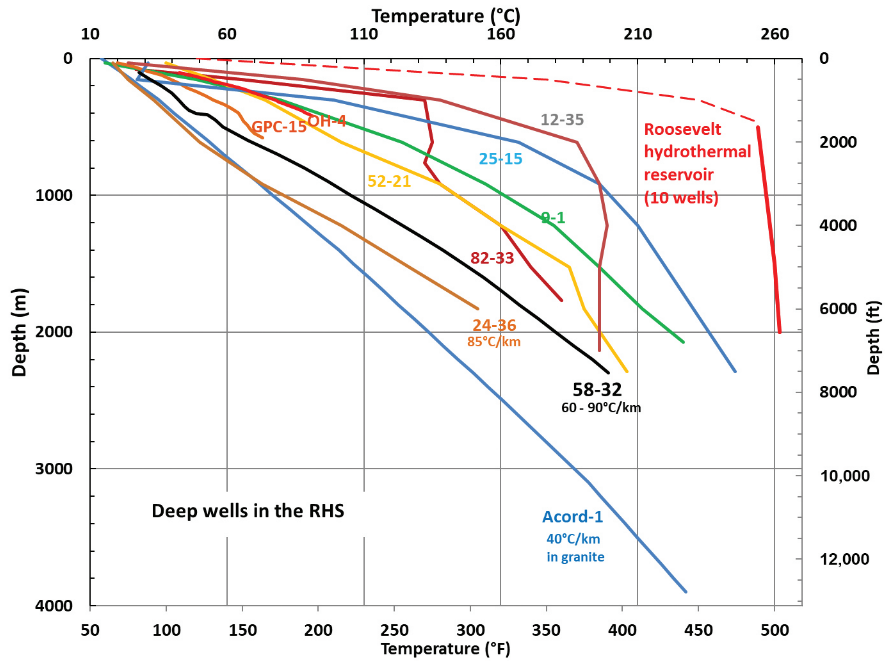

Figure 9. *Temperature profiles in deep wells mostly drilled during exploration of the RHS hydrothermal reservoir that is now tapped by the Blundell borefield. Within the production borefield, reservoir temperatures prior to development were near boiling point-for-depth, and typically in the range of 255°–265°C at greater depth. Except for well 12-35, which is at the northern end of the reservoir and close to the main outflow zone, and Acord-1, which is near the western edge of the RHS system, the profiles seem to converge on about 250°–270°C at 3–4 km depth.*

pressure profiles were run in the well 37 days after drilling and initial testing had been completed, and 13 months later when it should have been in thermal equilibrium with the host rock (Figure 10). Details of additional thermal measurements made during drilling and attempts to predict the equilibrium rock temperature during a 24-hour stoppage in drilling when the hole was at 2040 m depth are discussed by Allis et al. (2018). In all surveys, the thermal response time of the probe in water was less than 1 second and the temperature accuracy appears to be ± 0.1°C based on the typical logging speed of 15 m/minute (50 ft/minute). The 13-month pressure run showed the water level at 90 m depth, which is at similar elevation to the water level in nearby well OH4 reported by Vuataz and Goff (1987) and Kirby et al. (2019). OH4 bottomed in granite, which suggests that there may be a fracture network connecting 58-32 to the groundwater regime in the granite with sufficient permeability to allow pressure responses within a time-scale of a year.

The 37-day and 13-month logs show that the well cooled over time above 500–600 m depth and heated up below this depth. The temperature pivot of about 60°C corresponds to the typical mud circulation temperature during much of the drilling. The equilibrium temperature profile between 90 and 150 m depth matches the temperature profile in nearby gradient well TPC12, which indicates that the 1980s gradient well data in this part of the RHS system can be used to extrapolate deeper temperatures.

The maximum temperature at the bottom of well 58-32 is 199.4°C (390.8°F). The equilibrium log below about 500 m depth appears to show a conductive thermal profile, but at 90 m and 400 m depth there are jumps in temperature. The 12°C jump at 90 m coincides with the water level in the well and is an artifact of the temperature probe not having time to equilibrate in the air column with the 15 m/minute (50 feet/minute) logging rate. The unexpected thermal feature is the 7°C jump in temperature (46° to 53°C) at 400 m depth. We show below that when a conductive geotherm is fitted to the entire profile, the anomalous zone is characterized by cooler temperatures between 250 and 400 m depth. This coincides with an inversion and local minimum temperature at 300 m depth recorded in the 37-day profile. The anomaly suggests there is some permeability outside the casing and a lateral flow of groundwater between 250 and 400 m depth with a temperature between 40° and 46°C.

The temperature gradient trend with depth (Figure 11) was calculated over a moving 10 m depth interval and plotted at the midpoint. The two depths where the temperature jumped by 7°–12°C have very high gradients and are truncated on the graph. The bedrock interface near 970 m depth shows clearly as an increase in gradient with depth because of the thermal conductivity decrease from compacted granite alluvium to fractured monzodiorite. The thermal conductivity measurements on cuttings every 30 m (100 ft) and corrected to in situ conditions for porosity are shown in Figure 12 (Gwynn et al., 2019). An example of the effect of varying thermal conductivity (due mostly to varying quartz concentration) is the pronounced increase in gradient with depth at 1800 m. The gradient increases downwards from 63°C/km to 70°C/km due to the thermal conductivity decreasing

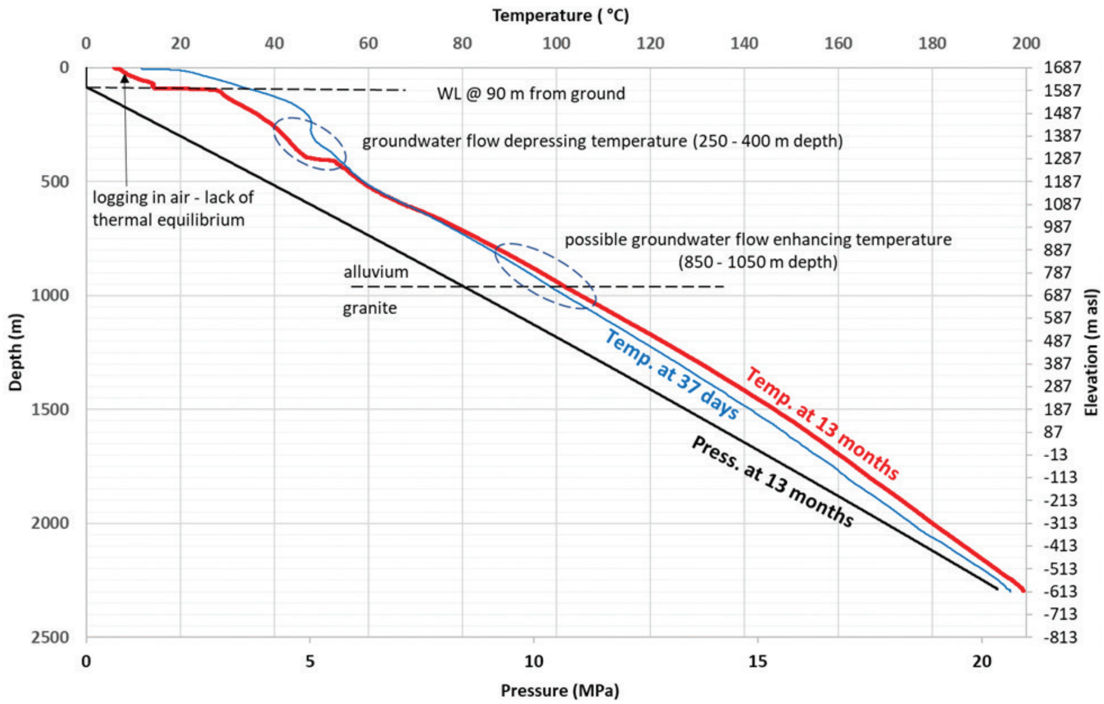

__Figure 10.__ Temperature profiles from well 58-32 measured on November 2, 2017 (blue line), and November 8, 2018 (red line). WL is water level in the well during the November 8 survey. During the November 2 survey the water level was about 1 m from the ground level (1687 m above sea level [asl]). The pressure profile measured on November 8 is shown as the black line. Dashed ellipses identify zones that do not fit a 1-D conductive geotherm.

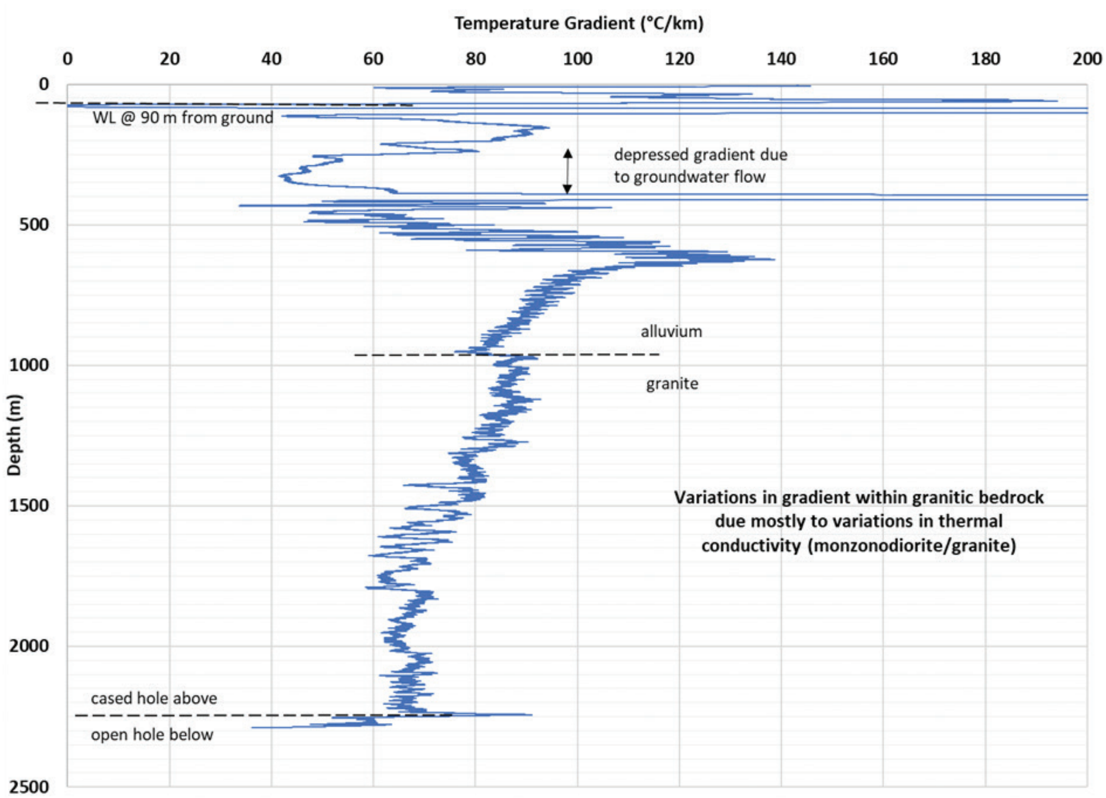

__Figure 11.__ Variation in temperature gradient with depth calculated from the temperature profile based on a moving average over 10 m.

from just over 3.5 to just under 2.5 W/m°C at that depth (Figures 11 and 12). The temperature gradient variations within the bedrock appear to be largely due to thermal conductivity effects. Gwynn et al. (2019) note from both outcrop examples and from the wireline logs in 58-32 that lithologic variations in the bedrock ranged from centimeter-scale veins, up to more than 100 m in scale with mappable geologic units. The 30 m spacing of thermal conductivity measurements on cuttings is too coarse to allow direct correlation of temperature gradient and conductivity.

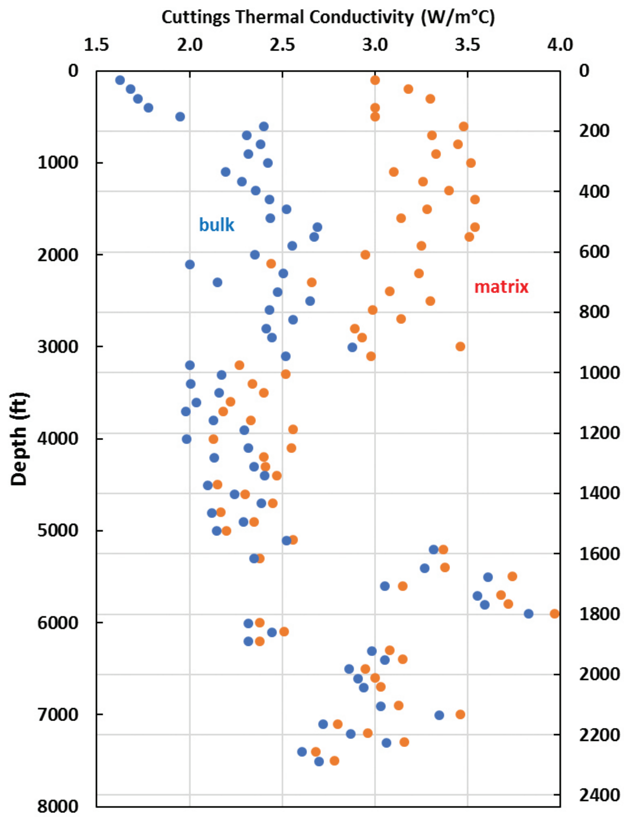

Figure 12. *Thermal conductivity data for well 58-32 based on cuttings measurements using a divided bar. Matrix thermal conductivity values are corrected for the effects of rock porosity using the wireline geophysical logs (formation density log; Gwynn et al., 2019). The variation in thermal conductivity is largely due to the quartz content of the rock. The transition from granitic basin fill to granitic bedrock occurs at 970 m.*

The temperature gradient within the granitic bedrock varies between 60° and 90°C/km and has a general trend of gradually decreasing gradient with increasing depth. The bedrock thermal conductivity (Figure 12) shows the opposite general trend increasing from 2.2 ± 0.2 W/m°C above 1600 m depth to 3.1 ± 0.6 W/m°C below 1600 m depth. One way of integrating the conductivity and gradient variations is to derive a thermal resistance plot (Bullard, 1939). The Fourier equation for conductive heat transport can be rearranged so that a temperature versus thermal resistance plot yields a line whose slope is the conductive heat flow:

$$\Delta T_i = Q * \Delta z_i / k_i ,$$

where T_i is the temperature at depth increment z_i with thermal conductivity k_i, and Q is the conductive heat flow. This plot allows departures from a uniform conductive heat flow to be highlighted. The thermal resistance plot for 58-32 using the thermal conductivity data at 30 m intervals is shown in Figure 13.

Figure 13 indicates a heat flow of 200 mW/m^2 and has an intercept of 13°C, which is similar to the mean annual ground temperature for the region, and points to a long-lived (10^4–10^5 years) thermal regime. Three zones on the plot suggest departures from uniform conductive heat flow. Temperatures are anomalously low above the water level due to the lack of thermal equilibrium from logging in air; temperatures are also several degrees low at 250–400 m depth; and there is a broader depth zone centered near the alluvium/bedrock interface where temperatures are a few degrees higher than the uniform heat flow trend. Assuming the two anomalous zones below the water table are not due to corresponding errors in the thermal conductivity measurements, the simplest explanation for both features is that groundwater flow outside the casing is the cause of the deviations from uniform conductive heat flow. In the case of the anomaly at 250–400 m depth, the thermal feature is also visible in

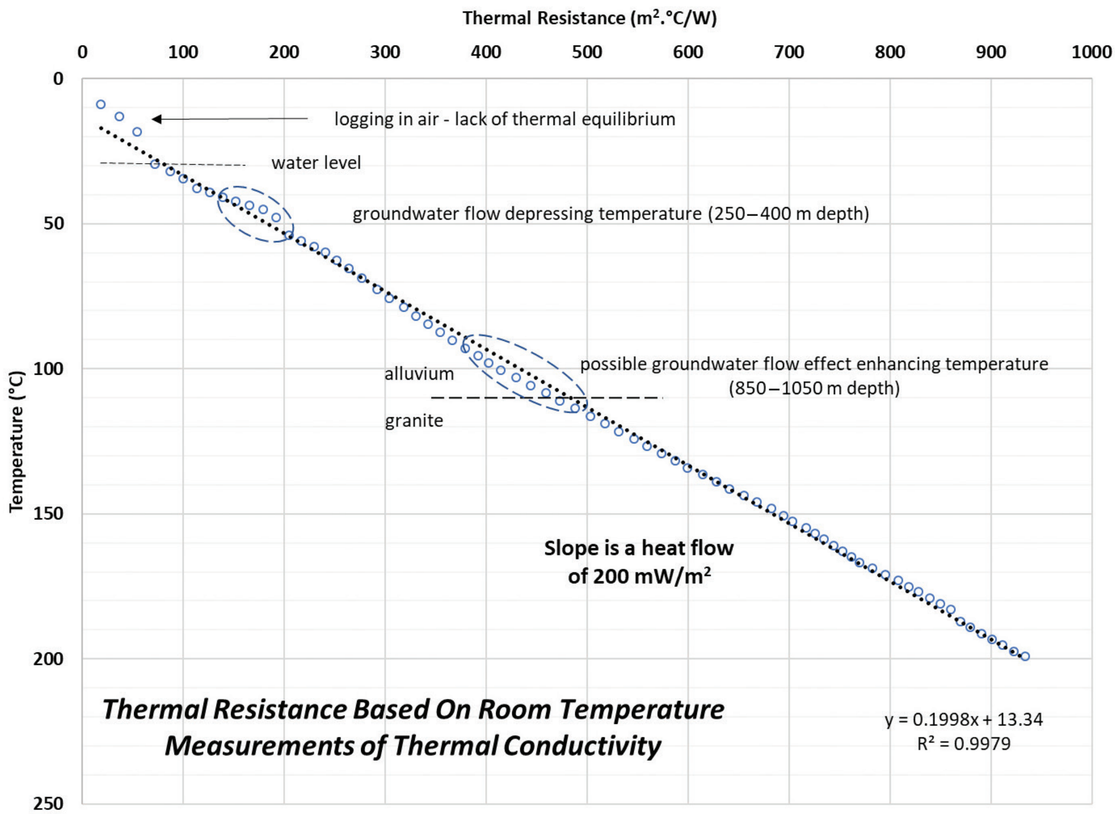

Figure 13. *Thermal resistance-temperature plot for well 58-32. A constant slope on these plots indicates one-dimensional conductive heat flow. In this case the slope is 200 mW/m^2, using the thermal conductivity measurements derived from the cuttings measurements at room temperature. The location of the water level in the well and the alluvium/granite interface are based on the temperature-depth plot of Figure 10.*

Figures 10 and 11, with its base being the jump in temperature at 400 m depth. The temperatures are up to 5°C too low and based on both the shallow thermal regime shown in Figure 4 and the potentiometric groundwater trend (Kirby et al., 2019), this flow likely to be from the east or south.

The deeper anomaly on the thermal resistance plot (Figure 13) in the temperature range of 90°–110°C (about 850 and 1050 m depth) has temperatures which are warmer than the uniform conductive heat flow trend by up to 5°C. The lowest electrical resistivities recorded in well 58-32 (that is, below top of log at 2200 ft depth) are in a 50 m thick zone at about 1000 m depth below ground level (3300–3400 ft below kelly bushing; resistivity of 5 ohm-meters; Gwynn et al., 2019). This zone is in fractured granitic rock and has the highest concentration of clay (especially illite and kaolinite) observed in the cuttings from the bedrock (Jones et al., 2019). The more intensive alteration here possibly coincides with a lateral flow of hot water which would also cause the relatively wide feature on the thermal resistance plot. It is also possible some lateral flow is occurring in the alluvium just above this clay-rich zone.

Figure 13 ignores the effect of temperature on thermal conductivity, mainly due to the sensitivity of quartz thermal conductivity to temperature. Rock with a higher quartz content has a higher thermal conductivity, but also has a 10%–15% decrease in conductivity between room temperature (about 25°C) and the temperature of 200°C at the bottom of well 58-32. To adjust the thermal resistance plot for this effect, the granitic rock in well 58-32 was assumed to be similar to the Barre granite trend shown in Figure 14. The bulk thermal conductivities in Figure 12 were adjusted based on their original downhole temperature, with the resulting thermal resistance shown in Figure 15. The effect of the temperature correction to thermal conductivity decreases the slope of the best-fit line for FORGE well 58-32 from 200 to 180 mW/m^2.

SURFACE HEAT FLOW AND ISOTHERM MAPS

The heat flow map, based on numerous thermal gradient wells at less than 200 m depth (Gwynn et al., 2016; Figure 16), delineates the conductive heat loss from the top of the RHS system and its outflow plume. For most wells, gradients were

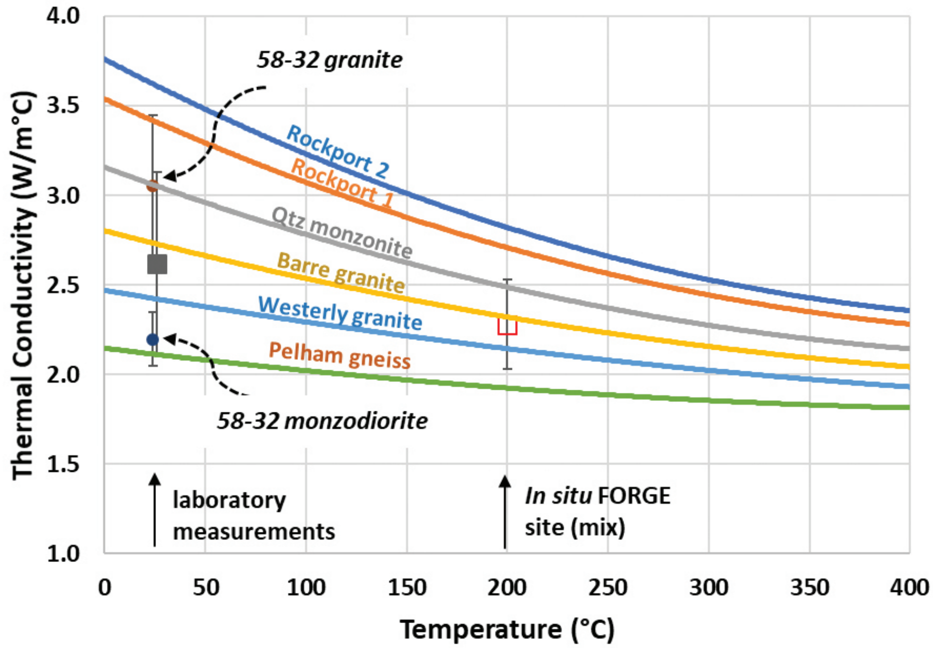

Figure 14. *Variation in thermal conductivity with temperature for granitic rocks from the northeast U.S. (Robertson, 1988). The thermal conductivity for rock in well 58-32 was corrected for the effects of increasing temperature based on the trend for the Barre granite.*

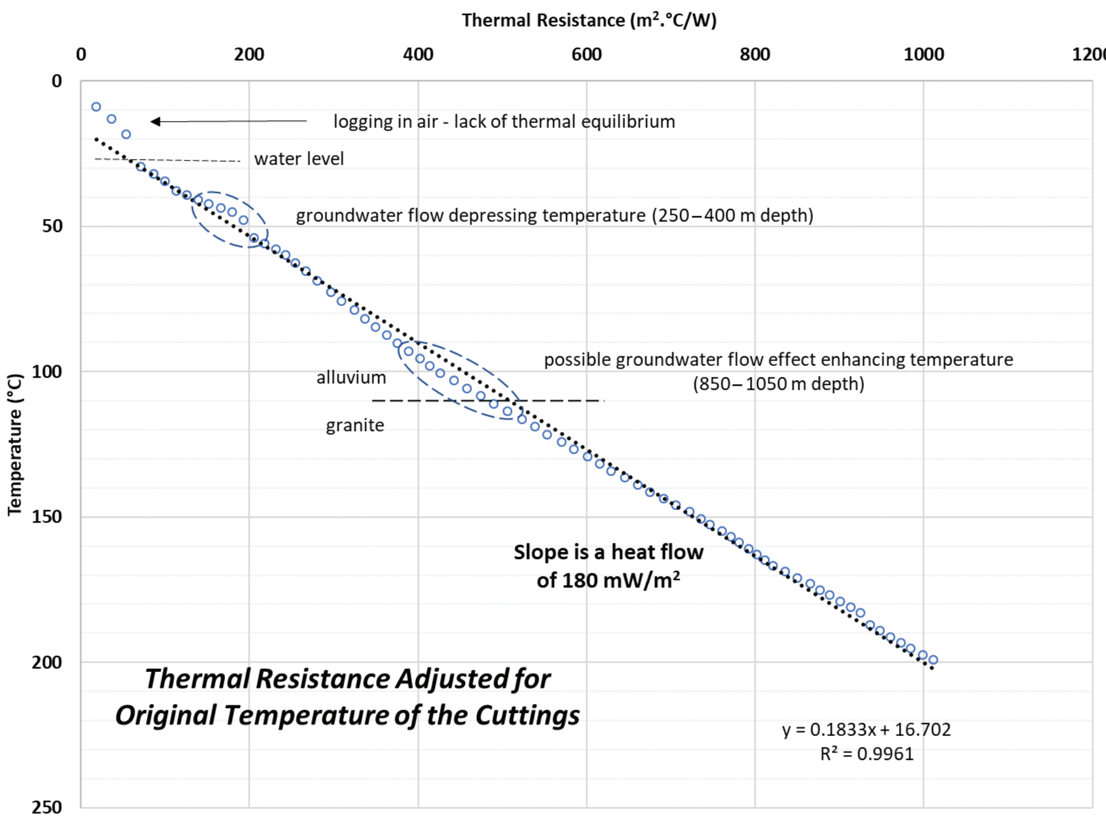

Figure 15. *Thermal resistance-temperature plot using thermal conductivities corrected for the effects of increasing temperature with depth. This reduces the heat flow from 200 mW/m^2 in Figure 13 to 180 mW/m^2.*

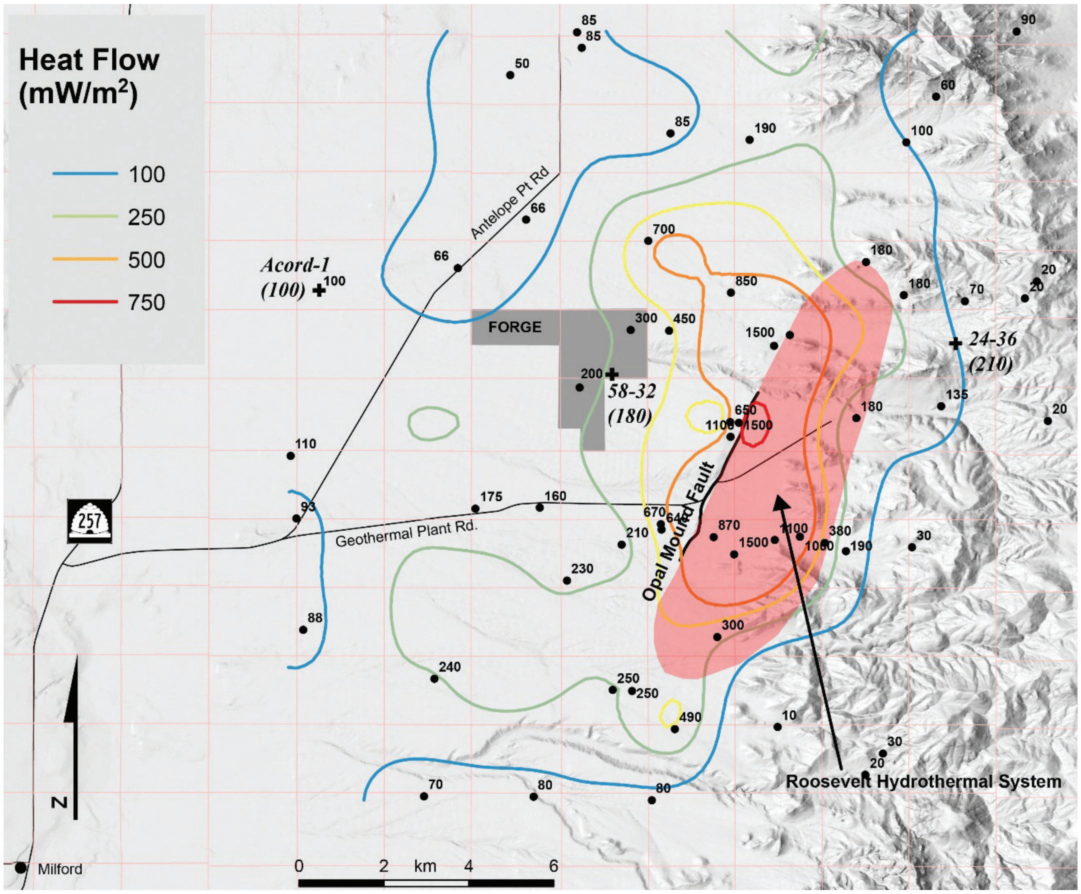

Figure 16. *Contours of conductive heat flow derived mostly from thermal gradient wells at less than 200 m depth around the Roosevelt Hot Springs hydrothermal system (mW/m^2; Gwynn et al., 2016). Very high heat flows over the hydrothermal system reflect high temperature gradients overlying upflowing hot water, which at shallow depth is constrained by boiling-point-for-depth conditions. West of the hydrothermal system (that is, the OMF) the thermal regime is conductive at depth and follows a pattern of decreasing heat flow towards the west. Three wells with deep (more than 2 km) conductive thermal gradients apparently unaffected by convective or two-dimensional heat flow are marked with a cross and have their heat flow in parentheses.*

converted to heat flows using a thermal conductivity of 1.5 ± 0.3 W/m°C for the lake sediments and alluvial-fan deposits. There is a lateral flow of thermal groundwater over most of the higher heat flow areas, and shallow temperature gradients cannot be extrapolated to depth. The west edge of thermal outflow appears to be a heat flow of 100–120 mW/m^2. Integration of the shallow heat flow data yields a total heat output of the RHS system of 60–70 MW and a mass flow of 50–60 kg/s of 265°C water (Ward et al., 1978; Allis and Larsen, 2012). The area of the hydrothermal system based on wells that have responded to the pressure drawdown from the production wellfield for the power plant extends at least from well 52-21 in the south to well 12-35 about 8 km to the north, and from the OMF in the west to wells 71-10 and 14-2 almost 1–2 km to the east (Allis and Larsen, 2012; see also Figures 1 and 14). Assuming an area of the hydrothermal system of 10 to 20 km^2, the rate of heat loss is in the range of 3–7 W/m^2. This rate is over an order of magnitude larger than the deep conductive heat flow of 100–200 mW/m^2 west and east of the RHS.

Figure 17 shows isotherm maps that integrate the shallow thermal gradient well data (for example, Figure 1) with the temperature profiles in deeper wells outside of the hydrothermal system. These maps consider the contrast in thermal conductivity between basin fill and granitic rock (Gwynn et al., 2016; Hardwick et al., 2019). As discussed with Figure 1, the datum is the ground surface of the valley floor and adjacent alluvial fan, which varies from 1525 m above sea level (asl) to 1830 m asl at the western edge of the Mineral Mountains. Beneath the Mineral Mountains, the datum is fixed at 1830 m asl so that the contours are not complicated by topography. Uncertainties increase with increasing depth and with increasing distance from deep wells. In particular, the contours at 1–3 km depth beneath the Mineral Mountains may be overly conservative (too cool) because of the effects of infiltrating groundwater depressing near-surface temperatures. There is evidence for this effect in well 24-36, as discussed in the next section. The area having a temperature of more than 200°C in these maps increases from about 25 km^2 at 2 km depth, to about 70 km^2 at 3 km depth. These estimates are minimums because of the likely increase in temperature gradient with depth beneath the western flank of the Mineral Mountains.

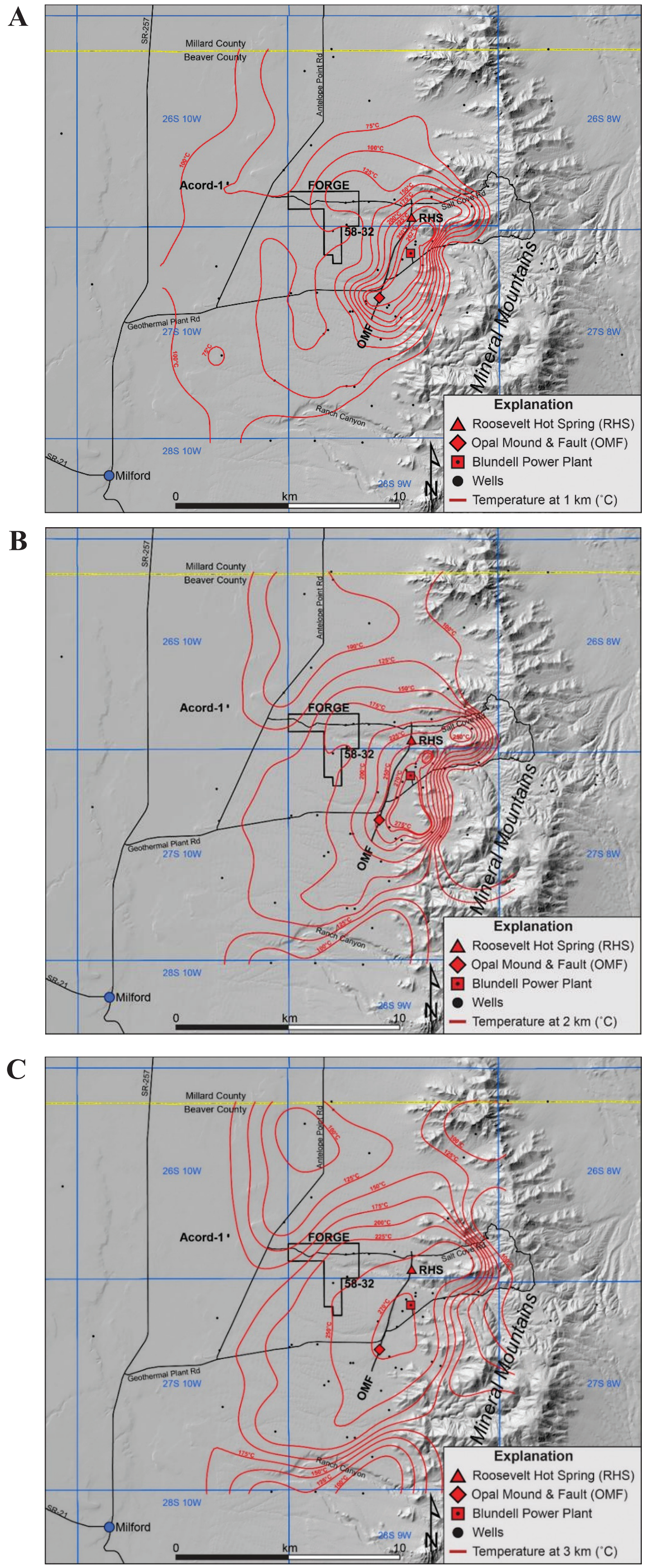

Figure 17. *Isotherm maps at **(A)** 1 km, **(B)** 2 km, and **(C)** 3 km depth based on analysis of the temperatures in thermal gradient wells and deeper exploration wells. The datum is the ground surface beneath the valley floor and adjacent alluvial fan (1525–1830 m asl), and at 1830 m asl beneath the western flank of the Mineral Mountains.*

DEEP HEAT FLOW

Although most deep wells within the RHS system (east of the OMF) are affected by the hydrothermal upflow, at least three wells seem to be outside the upflow and their deep gradients may be indicative of the underlying conductive heat flow. These wells are Acord-1, FORGE well 58-32, and 24-36 (5 km northeast of the RHS production wells). Well 9-1, about 3 km southeast of well 58-32, could also be a candidate because it has a deep gradient of 60°C/km and is likely to have a thermal conductivity similar to 58-32 because of the similarity in granitic rocks in this well. The deep heat flow is therefore 150 mW/m^2 with an uncertainty of at least ± 20 mW/m^2. The difference in deep heat flow between 58-32 and 9-1 may not be significant given the magnitude of uncertainties, but temperatures at 1–2 km depth in 9-1 are about 50°C hotter than 58-32 due to lateral heat flow effects from the nearby hydrothermal reservoir and possibly also the hot groundwater outflow near-surface. Well 9-1 temperatures between 1 and 2 km depth are extrapolated to 3 km depth but additional extrapolation is not considered justified.

As previously discussed, a conductive geotherm fits thermal data from the ground surface to the bottom of Acord-1. The gradient in the granitic bedrock below 3 km depth is 40°C/km, and assuming an in situ thermal conductivity of 2.5 W/m°C gives a heat flow of 100 ± 20 mW/m^2 (Figure 8; Gwynn et al., 2016). FORGE well 58-32 has a conductive heat flow of 180 mW/m^2 with an estimated uncertainty of ± 20 mW/m^2. In both cases the uncertainty in heat flow is based mostly on uncertainties in thermal conductivity.

The well with the highest temperature gradient below 1 km depth on Figure 9 is 24-36, which is located near the east end of a prominent valley in the Mineral Mountains (Figure 1) and encountered granite below 90 m depth. This exploration well was unproductive and was abandoned. The temperature profile in the upper portion of 24-36 is identical to gradient well OH-7 in another valley almost 2 km to the south. OH-7 had a gradient of 48°C/km (in granite) between the surface and its total depth of 600 m. The temperature gradient in 24-36 increases to 85°C/km below 750 m depth and is constant to its total depth of 1800 m. The pattern of depressed gradients near-surface is symptomatic of the effects of downward draining of groundwater beneath the eastern flank of the Mineral Mountains. This effect is more pronounced beneath the ridgeline of the Mineral Mountains where a 600 m exploration hole had a gradient of 16°C/km (OH-3, Figure 1). Assuming an in situ thermal conductivity for the granite of 2.5 W/m°C below 750 m depth in 24-36 gives a deep heat flow of 210 ± 20 mW/m^2.

Two thermal cross sections that traverse near well 58-32 have been compiled from the thermal data. Line A–A′ extends east from Acord-1, and line B–B′ extends north from Ranch Canyon and passes 1 km east of well 58-32 (Figure 18). The south end of line B–B′ is close to a possible southern extension of the OMF. The lack of deep wells here is why the contours are dashed on Figure 18. However, the thermal gradient wells in this area show an obvious transition from thermal groundwater north of Ranch Canyon to a background gradient in three wells on the south side.

The west-east cross section highlights the relatively small area of the hydrothermal system compared to the surrounding, thermally conductive, hot rock west of the OMF, and the inferred, predominantly thermally conductive regime beneath the adjacent west flank of the Mineral Mountains at 1–3 km depth. The depth to which hydrothermal waters in the RHS have circulated is unknown, and the dip of the 300°C isotherm on either side of the upflow zone is poorly constrained. Simmons et al. (in preparation) suggest the geochemical evidence points to equilibration of the waters at a temperature of 270°–310°C. Models of high-temperature, non-magmatic geothermal systems in the Basin and Range such as Dixie Valley, Nevada, require that meteoric water circulates to between 5 and 10 km depth for a regional heat flow of 90 mW/m^2 (McKenna and Blackwell, 2004; Wisian and Blackwell, 2004; McKenna et al., 2005). These models include a steeply dipping, higher permeability fault zone which focuses the upflow of hot water between about 4 km depth and the surface.

The presence of late Quaternary rhyolite adjacent to the RHS in the Mineral Mountains (Nielson et al., 1986; Kirby et al., 2018), and geophysical evidence from seismic velocity anomalies possibly consistent with partial melt in the upper crust (Robinson and Iyer, 1981; Trow et al., 2019), could indicate a significant difference to non-magmatic fluid circulation models. Higher temperatures should be present at 5–10 km depth than occurs with a regional heat flow of 90 mW/m^2 and a non-magmatic Basin and Range setting. Becker and Blackwell (1983) modeled the fluid flow of the RHS with an initial 400°C intrusion at 5 km depth. They assumed deep circulation (9 km) and a basal heat flow of 90 mW/m^2 increasing over time to 150 mW/m^2 to sustain high temperatures at depth for several hundred thousand years. Their model required low permeability on either side of the fault zone to focus the fluid upflow in the fault zone.

Improved thermal constraints to the fluid flow in the RHS from the present study provide some additional insights. The zone of high permeability representing the fractured reservoir east of the OMF is at least 1–2 km wide and 10 km in length based on the shallow heat flow map and appears to be a broad fault zone rather than a single fault. The thermal anomaly over this fault zone at 1–2 km depth has a total heat output of 60–70 MW and is equivalent to a heat flux of at least 3–7 W/m^2 assuming a horizontal

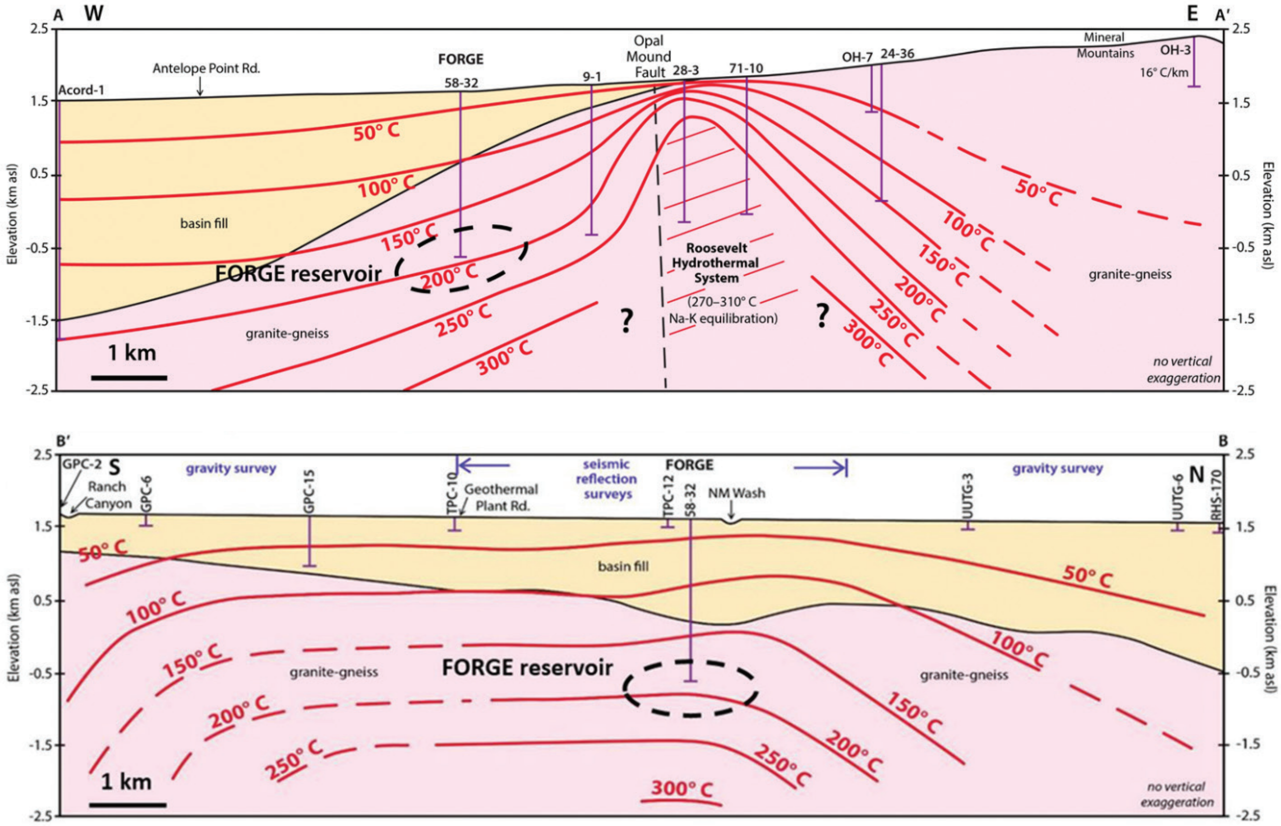

Figure 18. *Two thermal cross sections based on integration of data from many wells (locations shown on Figure 1). The contours are dashed where they are uncertain. The granite surface in B–B' is based on preliminary interpretations from the 3-D seismic reflection survey near the FORGE site (Miller et al., 2018) and from gravity models at greater distance (Hardwick et al., 2018). Well 58-32 is 1 km east of line B–B' and has been projected onto that line. The granite surface at that point is at 1.4 km depth, compared to 1.0 km depth in 58-32.*

area of 10–20 km^2. If the effective area of the high-permeability reservoir is less than this, the heat flux will be higher. The conductive heat flow at 2 km depth and 3 km west or east of the fault zone is about 0.2 W/m^2 and indicates a temperature of 300°C between 3 and 4 km depth. With the rate of heat extraction within the fault zone being so much greater than the high conductive heat flows on either side of the fault zone, it is likely that the rock-water equilibration temperature of 270°–310°C is much deeper than 3–4 km within the fault zone. The 300°C isotherms on Figure 18 may bend over and dip downwards as the fault zone is approached from the west or the east due to the high rate of heat mining by the hydrothermal system.

PRESSURE REGIME

At the time of the 37-day temperature profile, well 58-32 was liquid-filled with a wellhead pressure of about 7 bars gauge (0.7 MPa, 100 psi), which was bled-off so it could be logged as an open hole. The excess pressure was attributed to thermal recovery of the wellbore fluid after the injection testing. By the time of the 13-month logging there was zero wellhead pressure, and on opening, the sucking of air showed a vacuum was present above the water column. Logging showed the water level was at 90 m depth and the pressure in the open section of the well at 2300 m depth was 203 bars gauge (20.3 MPa; Figure 19). The pressure in the water column in 58-32 is very close to the pressure profiles at the same elevation in nearby groundwater wells which penetrated granite (OH4, OH5, OH1; Kirby et al., 2019). It appears that the pressure at the bottom of 58-32 may now be responding to the local (overlying) groundwater regime in the granite.

The nature of the connection between the groundwater regime and the open section of well 58-32 is unknown. The connection suggests there are fractures in the bedrock that are interconnected on a kilometer scale, although the connections are poor because of the sustained overpressure at the wellhead in the 37-day survey. However, over 12 months there has been apparent pressure equilibration. Assuming a 12-month time scale for equilibration, and a straight-line approximation to the Bower-Rice solution to the Theis equation, a transmissivity of 2 x 10^{-9} m/s is obtained. This value is right on the low end of reported permeabilities for fractured gneiss/granite (e.g., Freeze and Cherry, 1979).

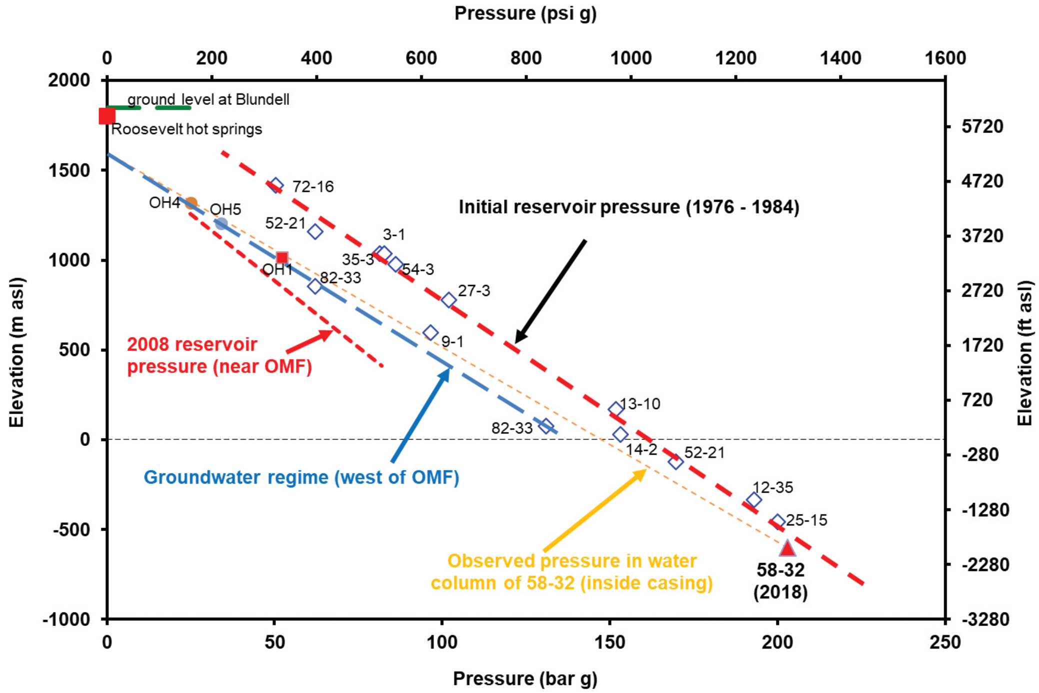

Figure 19. *Pressure trends in deep wells from the RHS reservoir east of the Opal Mound fault (OMF; modified from Allis and Larsen, 2012; 10 bars = 1 MPa), and from wells that penetrate groundwater in fractured granite west of the OMF (see Figure 1 for locations). The pressure in the open section at the bottom of well 58-32 is shown by the red triangle, and the pressure in the overlying hydrostatic column inside the casing is the dashed red line.*

CONCLUSIONS

The thermal anomaly associated with the RHS is much larger than the high-temperature upflow defined by deep productive wells drilled into the fractured granite east of the OMF. The proven zone with temperatures of more than 200°C at 1 km depth spans from well 12-15 in the south to 12-35 in the north (Figure 1), an area of at least 6 km by 2 km wide. The eastern side of this area is unconstrained due to a lack of deep wells. The shallow outflow of thermal groundwater extends at least 15 km to the north from Ranch Canyon and 10 km from east of the OMF to about Antelope Point Road. The area of hot groundwater is over ten times the area of the upflow zone. Over the southern two-thirds of this area (south of FORGE well 58-32), the temperature at the water table is lower than the outflow plume to the north (typically less than 50°C west of the OMF) and there is no evidence of a temperature inversion at greater depth (Figure 4). The temperature gradient in the alluvium-hosted groundwater here is about 70°C/km which is consistent with an underlying conductive heat flow of about 100 mW/m^2. The lack of a temperature inversion also means the thermal outflow here is relatively thin and near the water table, similar to the scenarios modeled by Ziagos and Blackwell (1981, 1986), and this outflow has persisted for at least several tens of thousands of years. The numerous patches of siliceous sinter adjacent to the OMF including the Opal Mound may have built up during periods of higher pressure in the evolution of the RHS system, such as would have occurred during the highstand of Lake Bonneville 18,000 years ago.

The northern sector of the shallow thermal regime is dominated by a high-temperature outflow plume best illustrated in well OH-5 (Figure 5), and originally recognized by Ward et al. (1978) and Wilson and Chapman (1980). The peak temperature is at about 300 m depth, and it has a temperature of at least 130°C (well 82-33) northwest of the OMF, and possibly over 200°C if well 12-35 is near where the plume exits from the upflow zone. The presence of a strong temperature inversion beneath the center of the outflow plume (OH5) shows that this is a relatively recent feature (~ 100–1000 years).

Detailed temperature and thermal conductivity measurements in FORGE well 58-32 reveal a predominantly conductive thermal profile with a heat flow of 180 ± 20 mW/m^2 when thermal conductivity is corrected for in situ temperature. The temperature at the bottom of the well (2300 m) is 199.4°C. The temperature gradient in the well varies between 60° and 90°C/km depending on bedrock thermal conductivity. Near the bottom of the well in predominantly granite the gradient is close to 70°C/km. A thermal resistance plot shows evidence of a lateral flow of groundwater outside the casing between 250 and 400 m depth. There also appears to be slightly elevated temperatures centered near the alluvium/bedrock interface which may indicate lateral flow at that depth as well.

Prior to development of geothermal power, the highest-temperature and most productive area of the reservoir had wells with boiling-point-for-depth temperature profiles from near-surface to about 400 m depth where the temperature was above about 250°C, and wells had very low thermal gradients at greater depth. The boiling point profile is typical for an upflow zone of a hydrothermal system. Outside of the productive area, all but one deep well (12-35) have conductive thermal gradients below about 1 km depth. For some of the deep wells such as 52-21 and 82-33, only one thermal profile is available, and there is uncertainty over how close to thermal equilibrium it is. The inferred deep thermal gradients in these two wells therefore also have greater uncertainty. Despite the uncertainties, the volume of the high-temperature reservoir appears to be small compared to the volume of rock having vertically extensive conductive thermal gradients. The large volume of inferred low-permeability rock highlights the need to develop technologies that can fracture the rock and greatly increase the electric power potential.

Despite the large volume of apparently thermally conductive rock around the main high-temperature upflow zone, wells within a zone about 2 km wide east of the OMF have responded rapidly to pressure drawdown from the production wellfield (Allis and Larsen, 2012). This drawdown area ranges from the southernmost deep exploration well (52-21) to the northernmost deep well (12-35), and in Figure 14 this area is referred to as the "hydrothermal system." The wells in the system had the same pressure profiles prior to development suggesting good communication with the high-temperature upflow zone. Clearly at least one fracture at some depth in each well connects to the upflow and controls the pressure regime in the well, even though the bulk of the host rock may be impermeable. The OMF itself may also be a zone of lateral and vertical permeability which allows subsurface outflow of cooler geothermal water (40°C) from the hydrothermal system into the regional groundwater as far south as Ranch Canyon (Figure 1). The permeability pattern of a relatively localized high-temperature upflow zone, surrounded by a complicated, dispersed pattern of secondary fracturing, is similar to the generalized geothermal model for Basin and Range systems described by Blackwell et al. (2012).

The uniform conductive thermal regime below 1 km depth in several of the wells outside of the hydrothermal zone may be extrapolated to much greater depth. There is diverse evidence for partial melt deeper in the crust from a low-velocity and attenuation anomaly (Robinson and Iyer, 1981; see also Trow et al., 2019), and helium anomalies (Simmons et al., in preparation). Figure 20 shows the extrapolated profiles in wells Acord-1, 58-32 and 24-36 assuming constant, one-dimensional heat flow with thermal conductivity only varying with temperature as shown in Figure 14. The effects of heat production from uranium, thorium, and potassium in the granite measured at the FORGE site have a very small effect on the extrapolated temperatures and have been ignored. Temperatures of about 600° to 700°C, often associated with the initiation of partial melting in wet granitic rocks, occur between 6 and 8 km depth beneath wells 58-32 and 24-36, and at 10–12 km in Acord-1. The 6–8 km depth is the same as a transition to lower seismic velocity inferred from recent ambient noise tomographic surveys (Trow et al., 2019). Lower heat flow in Acord-1 indicates possible melting at much greater depth in the center of north Milford Valley. There is no thermal data constraining the eastern side of the partial melt zone inferred from 24-36. The partial melt zone could extend to beneath the adjacent ridge of the Mineral Mountains where rhyolite has been extensively extruded over the last 1 million years.

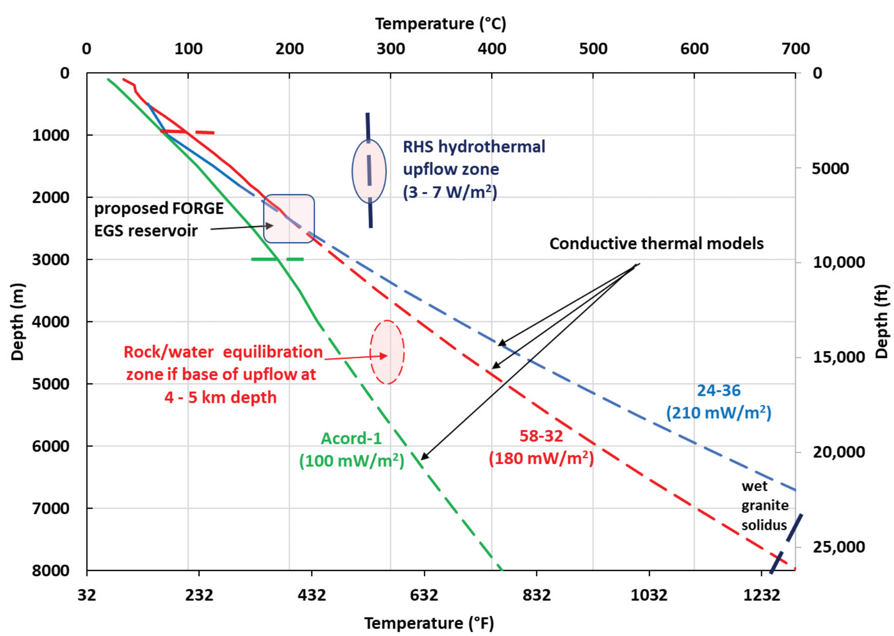

Figure 20. *Extrapolated geotherms for three wells outside the RHS hydrothermal system Thermal models assume constant, one-dimensional heat flow based on the observed thermal gradient and thermal conductivity below 1 km depth. The average thermal conductivity was assumed to be 2.5 W/m°C at 200°C in granite, and conductivity decreased with temperature based on the trends in Figure 14.*

Figure 20 also shows that if water in the RHS hydrothermal system is circulating to at least 4–5 km and this is where the 270°–310°C rock-water equilibrium chemistry is established, then the temperature at that depth could be 100°C lower than the at same depth on either side where thermally conductive conditions are the dominant form of heat loss. This is not surprising because the convective heat loss from the hydrothermal system is over an order of magnitude greater, causing more intense heat mining at depth.

ACKNOWLEDGMENTS

This worked was funded by the Geothermal Technologies Office of the U.S. Department of Energy, and by the Utah Geological Survey. PacifiCorp provided access to historical documents and well data related to the exploration of the RHS. Di Drill Survey Services ran the temperature profile in 58-32. The manuscript has benefited from discussion with Stefan Kirby and Stuart Simmons, and reviews by David Chapman, Maria Richards, Stephanie Carney, and Mike Hylland.

REFERENCES

Allis, R.G., Nash, G.D., Johnson, S.D., 1999, Conversion of thermal infrared surveys to heat flow—comparisons from Dixie valley, Nevada, and Wairakei, New Zealand: Transactions, Geothermal Resources Council, v. 23, p. 499–504.

Allis R.G. and Larsen, G., 2012, Roosevelt Hot Springs geothermal field, Utah—reservoir response after more than 25 years of power production: Proceedings, 37th Workshop on Geothermal Reservoir Engineering, Stanford University, Stanford, CA, 8 p.

Allis, R.G., Gwynn, M., Hardwick, C., Kirby, S., Moore, J., and Chapman, D., 2015, Re-evaluation of the pre-development thermal regime of Roosevelt Hot Springs geothermal system, Utah: Proceedings, 40th Workshop on Geothermal Reservoir Engineering, Stanford University, Stanford, CA., 12 p.

Allis, R., Gwynn, M., Hardwick, C., and Moore, J., 2018, The challenge of correcting bottom-hole temperatures—An example from FORGE 58-32, near Milford, Utah: Proceedings, 43rd Workshop on Geothermal Reservoir Engineering, Stanford University, Stanford, CA, 8 p.

Becker, D.J., and Blackwell, D.D., 1983, Gravity and hydrothermal modeling of the Roosevelt Hot Springs area, southwestern Utah: Journal of Geophysical Research, v. 98, B10, p. 17,787–17,800.

Blackwell, D.D., Waibel, A.F., and Richards, M., 2012, Why Basin and Range systems are hard to find—the moral of the story is they get smaller with depth!: Transactions, Geothermal Resources Council, v. 36, p. 1321–1326.

Bromley, C.J., Van Manen S.K., and Mannington, W., 2011, Heat flux from steaming ground—reducing uncertainties: Proceedings, 36th Workshop on Geothermal Reservoir Engineering, Stanford University, Stanford, CA, 7 p.

Bullard, E.C., 1939, Heat flow in South Africa: Proceedings of the Royal Society of London, Series A, v. 173, p. 474–502.

Capuano, R.M., and Cole, D.R., 1982, Fluid-mineral equilibria in a hydrothermal system: Geochimica Cosmochimica Acta, v. 46, p. 1353–1364.

Faulder, D.D., 1991, Conceptual geologic model and native state of the Roosevelt Hot Springs hydrothermal system: Proceedings, 16th Workshop on Geothermal Reservoir Engineering, Stanford University, p. 131–142.

Faulder, D.D., 1994, Long-term flow test #1, Roosevelt Hot Springs, Utah: Transactions, Geothermal Resources Council, v. 18, p. 583–590.

Forrest, R.J., 1994, Geothermal development at Roosevelt Hot Springs geothermal area Beaver County, Utah, 1972–1993: Utah Geological Association, 23, p. 37–44.

Freeze, R.A. and Cherry, J.A., 1979, Groundwater: New Jersey, Prentice-Hall Inc, 604 p.

Gwynn, M., Allis, R., Hardwick, C., Hill, J., and Moore, J., 2016, A new look at the thermal regime around Roosevelt Hot Springs, Utah: Transactions, Geothermal Resources Council, v. 40, p. 551–558.

Gwynn, M., Allis, R., Hardwick, C., Jones, C., Nielsen, P., and Hurlbut, W., 2019, Compilation of rock properties from FORGE well 58-32, Milford, Utah, *in* Allis, R., and Moore, J.N., editors, Geothermal characteristics of the Roosevelt Hot Springs system and adjacent FORGE EGS site, Milford, Utah: Utah Geological Survey Miscellaneous Publication 169-L, 36 p., https://doi.org/10.34191/MP-169-L.

Hardwick, C., Hurlbut, W., and Gwynn, M., Allis, R., Wannamaker, P., and Moore, J., 2018, Geophysical surveys of the Milford, Utah, FORGE site—gravity and TEM: Transactions, Geothermal Resources Council, v. 42, p. 1071–1083.

Harrison, M.T., Morgan, P., and Blackwell, D.D., 1986, Constraints of the age of heating at the Fenton Hill site, Valles Caldera, New Mexico: Journal of Geophysical Research, v. 91, no. B2, p. 1899–1908.

Jones, C.G., Moore, J.N., and Simmons, S., 2019, Petrography of the Utah FORGE site and environs, Beaver County, Utah, *in* Allis, R., and Moore, J.N., editors, Geothermal characteristics of the Roosevelt Hot Springs system and adjacent FORGE EGS site, Milford, Utah: Utah Geological Survey Miscellaneous Publication 169-K, 23 p., 2 appendices, https://doi.org/10.34191/MP-169-K.

Kirby, S.M., Knudsen, T., Kleber, E., and Hiscock, A., 2018, Geologic setting of the Utah FORGE site based on new and revised geologic mapping: Transactions, Geothermal Resources Council, v. 42, p. 1097–1114.

Kirby, S.M., Simmons, S., Inkenbrandt, P.C., and Smith, S., 2019, Groundwater hydrogeology and geochemistry of the Utah FORGE site and vicinity, *in* Allis, R., and Moore, J.N., editors, Geothermal characteristics of the Roosevelt Hot Springs system and adjacent FORGE EGS site, Milford, Utah: Utah Geological Survey Miscellaneous Publication 169-E, 21 p., https://doi.org/10.34191/MP-169-E.

Lee, W.T., 1908, Water resources of Beaver Valley, Utah: U.S. Geological Survey Water-Supply Paper no. 217, 55 p.

Lynne, B.Y., Campbell, K.A., Moore, J.N., and Browne, P.R.L., 2005, Diagenesis of 1900-year-old siliceous sinter (opal-A to quartz) at Opal Mound, Roosevelt Hot Springs, Utah: Sedimentary Geology, v. 179, no. 3-4, p. 249–278.

McKenna, J.R., and Blackwell, D.D., 2004, Numerical modeling of transient Basin and Range extensional geothermal systems: Geothermics, v. 33, p. 457–476.

McKenna, J.R., Blackwell, D.D., and Richards, M.C. and Swenson, D.V., 2005, Natural state modeling, structure, preliminary temperature and chemical synthesis of the Dixie Valley, Nevada geothermal field: Proceedings, 30th Workshop on Geothermal Reservoir Engineering, Stanford University, 8 p.

Miller, J., Allis, R. and Hardwick, C., 2018, Seismic reflection profiling at the FORGE, Utah EGS site: Transactions, Geothermal Resources Council, v. 42, p. 1115–1127.

Moore, J., McLennan, J., Allis, R., Pankow, K., Simmons, S., Podgorney, R., Wannamaker, P. and Rickard, B., 2018, The Utah Frontier Observatory for Geothermal Research (FORGE)—Results of Recent Drilling and Geoscientific Surveys: Transactions, Geothermal Resources Council, v. 42, p. 1128–1137.

Mundorff, J.C., 1970, Major thermal springs of Utah: Utah Geological Survey Water Resources Bulletin 14, 60 p.

Nielson, D.L., Evans, S.H., and Sibbett, B.S., 1986, Magmatic, structural, and hydrothermal evolution of the Mineral Mountains intrusive complex, Utah: Geological Society of America Bulletin, v. 97, p. 765–777.

Robertson, E., 1988, Thermal properties of rocks: U.S. Geological Survey Open File Report 88-441, 106 p.

Robinson, R. and Iyer, H.M., 1981, Delineation of a low-velocity body under the Roosevelt Hot Springs geothermal area, Utah—Using teleseismic p-wave data: Geophysics, v. 46, p. 1456–1466.

Sibbett, B.S. and Nielson, D.L., 2017, Geologic map of the central Mineral Mountains (GIS of 1980 map), Beaver County, Utah: Utah Geological Survey Miscellaneous Publication, 17-2DM.

Simmons, S.F., Kirby, S., Moore, J.N., Wannamaker, P., and Allis, R., 2015, Comparative analysis of fluid chemistry from Cove Fort, Roosevelt and Thermo—Implications for geothermal resources and hydrothermal systems on the east edge of the Great Basin: Proceedings Geothermal Resources Council, v. 39, p. 55–61.

Simmons S., Kirby, S., Allis, R., Moore, J., and Fischer, T., 2018, Update on production chemistry at Roosevelt Hot Springs, Utah: Proceedings, 43rd Workshop on Geothermal Reservoir Engineering, Stanford University, Stanford, CA, 7 p.

Simmons, S., Allis, R., Kirby, S., Moore, J., and Fisher, T., in prep., The origin and evolution of hydrothermal fluids and their flow in response to >30 years of geothermal production, Roosevelt Hot Springs, Utah, USA: manuscript not yet submitted.

Trow, A.J., Pankow, K.L., Wang, Y., and Lin, F.-C., 2019, Localized ambient noise tomography over the FORGE Utah site, *in* Allis, R., and Moore, J.N., editors, Geothermal characteristics of the Roosevelt Hot Springs system and adjacent FORGE EGS site, Milford, Utah: Utah Geological Survey Miscellaneous Publication 169-J, 15 p., https://doi.org/10.34191/MP-169-J.

Ward, S.H., Parry, W.R., Nash, W.P., Sill, W.R., Cook, K.L., Smith, R.B., Chapman, D.S., Brown, F.H., Whelan, J.A., and Bowman, J.R., 1978, A summary of the geology, geochemistry, and geophysics of the Roosevelt Hot Springs thermal area, Utah: Geophysics, v. 43, p. 1515–1542.

Wilson, W.R., and Chapman, D.S., 1980, Thermal studies at Roosevelt Hot Springs, Utah: unpublished report prepared by Department of Geology and Geophysics, University of Utah, Salt Lake City, Utah, for U.S. Department of Energy, Division of Geothermal Energy, 102 p., http://www.osti.gov/scitech/biblio/7015581.

Wisian, K., and Blackwell, D.D. 2004, Numerical modeling of Basin and Range geothermal systems: Geothermics, v. 33, p. 173–741.

Ziagos, J., and Blackwell, D., 1981, A model for the effect of horizontal fluid flow in a thin aquifer on temperature-depth profiles: Transactions, Geothermal Resources Council, v. 5, p. 221–223.

Ziagos J., and Blackwell D., 1986, A model for the transient temperature effects of horizontal fluid flow in geothermal systems: Journal of Volcanology and Geothermal Research, v. 27, no. 3-4, p. 371–397.

GROUNDWATER HYDROGEOLOGY AND GEOCHEMISTRY OF THE UTAH FORGE SITE AND VICINITY

by Stefan M. Kirby[1], Stuart Simmons[2], Paul C. Inkenbrandt[1], and Stan Smith[1]

[1]Utah Geological Survey, Salt Lake City, Utah

[2]Energy & Geoscience Institute, University of Utah, Salt Lake City, Utah

Link to supplemental data download: https://ugspub.nr.utah.gov/publications/misc_pubs/mp-169/mp-169-e.zip

Tables 1–3

Miscellaneous Publication 169-E
Utah Geological Survey
a division of
UTAH DEPARTMENT OF NATURAL RESOURCES

This paper is part of *Geothermal Characteristics of the Roosevelt Hot Springs System and Adjacent FORGE EGS Site, Milford, Utah*. https://doi.org/10.34191/MP-169

Bibliographic citation:

Kirby, S.M., Simmons, S., Inkenbrandt, P.C., and Smith, S., 2019, Groundwater hydrogeology and geochemistry of the Utah FORGE site and vicinity, *in* Allis, R., and Moore, J.N., editors, Geothermal characteristics of the Roosevelt Hot Springs system and adjacent FORGE EGS site, Milford, Utah: Utah Geological Survey Miscellaneous Publication 169-E, 21 p., https://doi.org/10.34191/MP-169-E.

GROUNDWATER HYDROGEOLOGY AND GEOCHEMISTRY OF THE UTAH FORGE SITE AND VICINITY

by Stefan M. Kirby, Stuart Simmons, Paul C. Inkenbrandt, and Stan Smith

ABSTRACT

The FORGE deep drill site is located approximately 10 miles northeast of Milford in Beaver County, Utah, on the eastern side of Milford Valley. Shallow groundwater in the study area resides in an unconsolidated basin-fill aquifer that blankets older rock units including the crystalline basement rocks that will host the FORGE EGS reservoir. The unconsolidated basin-fill aquifer supplies groundwater that is currently used for stock watering and fire suppression. The potentiometric surface slopes steeply to the west away from the Opal Mound fault from 5800 to 4900 feet in elevation over approximately 5 miles. Beneath the FORGE deep drill site, the groundwater elevation is approximately 5100 feet and the depth to water is between 200 and 600 feet. Along the valley floor west of the FORGE site, groundwater is within 150 feet of the land surface.

The chemical composition of groundwater across the study area varies according to local conditions. Springs in the Mineral Mountains are supplied by meteoric water, and the water is dilute (TDS <500 mg/L) and dominated by Ca and HCO_3. This type of water is the primary source of recharge to the basin-fill aquifer. Locally important components of groundwater are sourced from subsurface outflow from the Roosevelt Hot Springs hydrothermal system, which is 2 miles to the east of the FORGE deep drill site. This water has a high concentration of TDS (>6000 mg/L) dominated by Na and Cl. In the middle of Milford Valley near Milford, a third groundwater type with high TDS (>4000 mg/L) is dominated by Na and SO_4. Mixing trends reflected in a number of solutes and stable isotopes indicate the groundwater beneath the FORGE deep drill site is sourced primarily by subsurface outflow from the Roosevelt Hot Springs system. This water moves westward as a shallow outflow plume toward the center of the valley. Beneath the FORGE deep drill site, groundwater TDS concentrations are between 4000 and 6000 mg/L. Along the axis of Milford Valley groundwater TDS concentrations are generally less than 3000 mg/L.

To better constrain water yielding characteristics of the basin-fill aquifer near the FORGE site available aquifer test data were analyzed. Two new aquifer tests on supply wells near the FORGE site were completed by the Smithfield Corporation in the fall of 2017. Modeled results from these two tests give transmissivities of 1200 and 1600 ft^2/day. Previous aquifer tests of the basin-fill aquifer completed as part of FORGE Phase 2a and as part of earlier geothermal investigations yielded transmissivities of 240 and 1400 ft^2/day, respectively. Taken together the available aquifer test data show shallow basin fill near the FORGE site has a range of transmissivity between 240 and 1600 ft^2/day, and most shallow basin fill likely has transmissivity near 1000 ft^2/day. This transmissivity is moderate and similar to transmissivities for existing agricultural production wells nearby. Based on the available aquifer test data, the transmissivity in the basin-fill aquifer near the FORGE site is sufficient for future production wells needed to supply long-term needs of the project.

INTRODUCTION

The Frontier Observatory for Research in Geothermal Energy (FORGE) deep drill site is located just west of the Mineral Mountains, approximately 10 miles northeast of Milford in Beaver County, Utah. The project site is located west of the Roosevelt Hot Springs hydrothermal system and east of the valley axis along west-sloping alluvial fans. The FORGE project will require groundwater for various phases of drilling, completion, stimulation, and circulation testing. This paper describes the baseline hydrogeology and the groundwater availability for the FORGE project needs, based on both legacy data and new data collected as part of the FORGE project.

The groundwater system across the FORGE project area was evaluated 30 years ago as part of an initial appraisal of hot dry rock resources (Vautaz and Goff, 1987). Kirby (2012) examined the regional groundwater system including the study area to develop a groundwater budget and to examine the possibility of flow between hydrologic basins along Cove Creek and the Beaver River Valley. Other significant work has focused on the geothermal resources at Roosevelt Hot Springs (Faulder, 1991; see summaries in Moore and Nielson, 1994; Allis et al., 2015, 2016; and Simmons et al., 2016) and agricultural water and groundwater conditions in areas adjoining the study area (Mower and Cordova, 1974; Mower, 1978; Mason, 1998).

HYDROGEOLOGIC SETTING

The study area lies along the eastern margin of the Basin and Range Province in southwestern Utah. This area is characterized by a series of north-south-trending bedrock mountain ranges separated by broad basins filled with alluvium and lake sediments. Heat flow across the area is high relative to adjoining areas (Allis et al., 2015, 2016).

East of the FORGE project area, the Mineral Mountains consist primarily of Tertiary-age granitic intrusive rocks (Figure 1). Along the western margin of the range the Tertiary intrusive rocks intrude Precambrian metamorphic rocks (Nielson et al., 1986; Coleman et al., 1997). Precambrian and lower Paleozoic carbonate and clastic sedimentary rocks crop out at the northern and southern ends of the range (Nielson et al., 1986). Quaternary volcanic rocks occur west of the crest of the Mineral Mountains as well as north of the Mineral Mountains (Rowley et al., 2005). Unconsolidated basin fill covers the remainder of the study area and consists of alluvial, lacustrine, and fluvial deposits.

Figure 1 depicts the general geologic setting of the basin fill and the bedrock in the study area. Igneous and metamorphic rocks exposed in the Minerals Mountains lie beneath basin fill across the study area (e.g., Simmons et al., 2016). The thickness of basin fill increases to the west away from the Mineral Mountains as indicated by the lithologies in the Acord-1 well and other boreholes, and seismic and gravity data. Unconsolidated basin fill along the western flank of the Mineral Mountains consists primarily of sands and gravels that lie directly on fractured Tertiary intrusives (Vautaz and Goff, 1987). Along the valley floor near the Beaver River, unconsolidated basin fill is underlain by a series of consolidated to semi-consolidated Tertiary volcanic rocks and Tertiary basin fill (Hintze and Davis, 2003). The total thickness of these deposits along the valley floor is up to 9000 feet(Saltus and Jachens, 1995; Allis et al., 2016; Hardwick et al., 2016; Simmons et al., 2016). Based on well logs, groundwater in unconsolidated basin fill exists in both unconfined and confined conditions in the study area. Confined conditions exist along the valley floor where thick clay layers occur (Kirby, 2012). Unconfined conditions generally exist across the broad alluvial fans that slope to the west from the Mineral Mountains. The transition from confined to unconfined conditions correlates with the mapped position of the Lake Bonneville highstand shoreline, an elevation of approximately 5200 feet.

Unconsolidated basin fill forms the primary aquifer in the study area. The fill covers the entire study area west of the Mineral Mountains and includes a range of alluvial and lacustrine deposits. Along the west flank of the Mineral Mountains these deposits consist primarily of sand and gravel without significant confining layers (Vautaz and Goff, 1987). Within the basin -fill aquifer, particle size and sand content increases to the east up the alluvial fans. Near the western toe of these fans, the unconsolidated basin-fill aquifer is generally finer grained with significant clay layers (Figure 1).

Farther west along the valley floor, the unconsolidated basin fill includes fine grained lacustrine deposits and thick layers of clay (Mower and Cordova, 1974). Based on well logs the clay layers may be just over 100 feet thick and laterally extensive along the valley axis (Kirby, 2012). The transition between unconfined and confined conditions in the unconsolidated basin fill is likely gradational and controlled by the extent and nature of lacustrine versus alluvial deposits (Mower and Cordova, 1974). The total thickness of the unconsolidated basin-fill aquifer varies from greater than 500 feet west of the Roosevelt Hot Springs hydrothermal system to 100–400 feet thick along the valley floor (Mower and Cordova, 1974; Kirby, 2012). Current groundwater use in the study area is limited to several stock watering wells (labeled NSW, SSW, MB1, and SPW on Figure 2) and a supply well used for fire suppression at a single site (labeled FWW on Figure 2). These wells are all completed within the upper 500 feet of the basin-fill aquifer.

GROUNDWATER LEVELS

Existing groundwater elevation data was compiled and used to construct a contoured potentiometric surface across the study area (Table 1, Figure 2). Most water level data are limited to the area west of the Opal Mound fault. Two upland springs in the Mineral Mountains are shown to indicate the higher groundwater levels that occur in the bedrock of the Mineral Mountains.

Groundwater in the study area moves from areas of recharge along the upper reaches of the Mineral Mountains to areas of regional discharge along the valley floor to the north and south of the study area (Kirby, 2012). Groundwater elevations decrease to the west away from the Mineral Mountains (Table 1, Figure 2). Between the Opal Mound fault and OH-4, the potentiometric surface dips steeply westward and then flattens out towards the center of the valley. The Opal Mound fault represents the boundary of the active geothermal reservoir and is likely a lateral barrier to groundwater movement, with leakage into shallow aquifers occurring at the northern tip of the fault as indicated by chemical trends (discussed below).

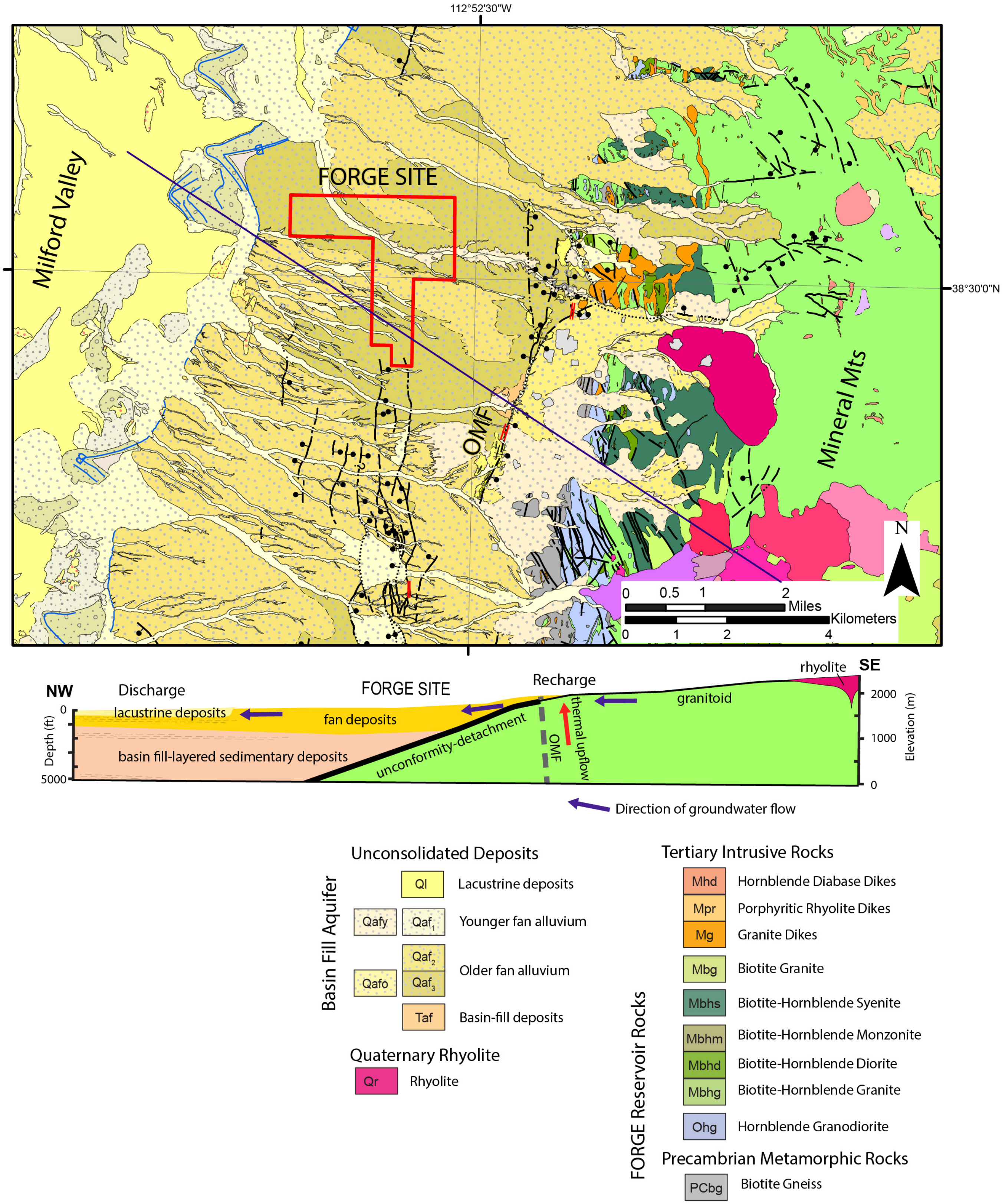

Figure 1. *Simplified geologic map of the FORGE deep well site, Milford, Utah. Geology is modified from Kirby (2019). The cross section shows simplified stratigraphy and structure across the FORGE site. The units labeled alluvium-fan deposits and lacustrine deposits compose the unconsolidated basin-fill aquifer. The zero datum for the depth axis is at 1524 m asl (5000 ft asl). Precambrian gneiss and Tertiary plutonic rocks are undifferentiated in the cross section and simply referred to as granitoid. The Roosevelt Hot Springs hydrothermal system lies east of the Opal Mound fault (OMF). The contact between granitoid and overlying basin fill is interpreted from borehole, seismic, and gravity measurements (Hardwick et al., 2019; Miller et al., 2019).*

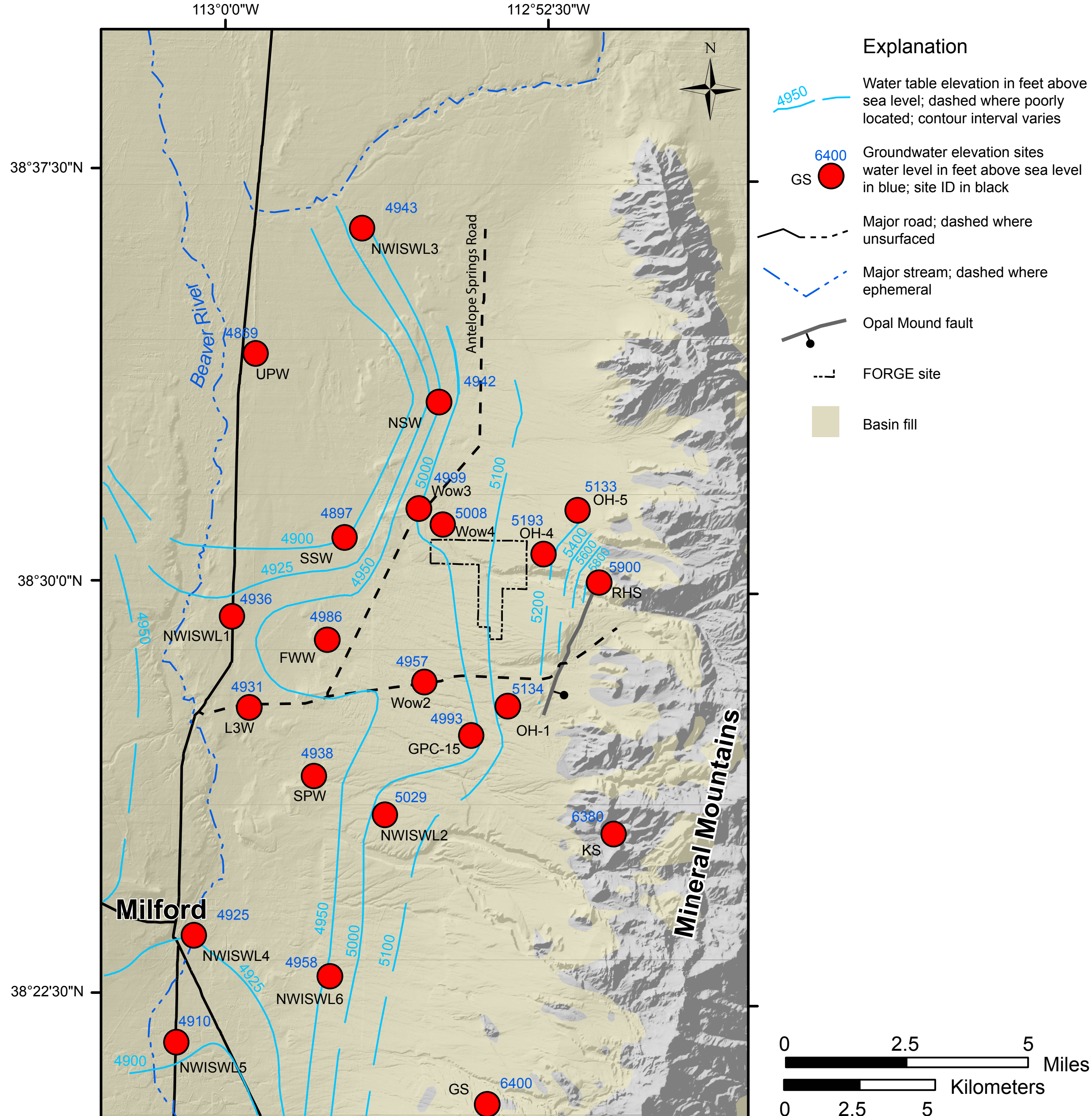

Figure 2. *Groundwater elevation map of the FORGE study area. RHS is the historic Roosevelt Hot Springs site. Site IDs correlate with Table 1.*

Table 1. *Compiled water levels for the FORGE study area.* https://ugspub.nr.utah.gov/publications/misc_pubs/mp-169/mp-169-e.zip

Name	Label[1]	Source[2]	Easting[3]	Northing	Date Measured	Land Elev (ft)	DTW (ft)[4]	Water Elev (ft)
Level 3 comm well	L3W	UGS (unpublished)	326823	4259004	8/13/14	4970.00	39.10	4930.90
First Wind Office well	FWW	UGS (unpublished)	329453	4261265	8/6/14	5035.00	49.10	4985.90
North Stock well	NSW	UGS (unpublished)	333208	4269283	8/13/14	5010.00	67.54	4942.46
UP Read siding well	UPW	UGS (unpublished)	327053	4270920	8/14/14	4882.00	12.59	4869.41
South Stock well	SSW	UGS (unpublished)	330036	4264716	8/14/14	4962.00	64.20	4897.80
Solar Panel Well	SPW	UGS (unpublished)	329007	4256688	8/13/14	5070.00	132.20	4937.80
Kirk Spring	KS	Spring	339092	4254744	--	6380.00	0.00	6380.00
Griffith Spring	GS	Spring	334829	4245644	--	6400.00	0.00	6400.00
Roosevelt Hot Springs	RHS	Spring	338216	4262751	--	5900.00	0.00	5900.00
NWIS383117112551401	Wow3	USGS (2015)	332538	4265699	3/9/15	5120.00	120.44	4999.56
NWIS382814112550101	Wow2	USGS (2015)	332721	4259849	3/9/15	5300.00	343.02	4956.98
NWIS382551112555101	NWISWL2	USGS (2015)	331398	4255382	3/9/15	5360.00	330.46	5029.54
NWIS382924112592901	NWISWL1	USGS (2015)	326254	4262060	3/6/15	4960.00	23.82	4936.18
NWIS383631112564001	NWISWL3	USGS (2015)	330628	4275136	3/9/15	4960.00	16.82	4943.18
NWIS382138113003303	NWISWL5	USGS (2015)	324382	4247736	3/5/15	4974.00	64.17	4909.83
NWIS382336113001402	NWISWL4	USGS (2015)	324961	4251331	3/6/15	4955.00	29.86	4925.14
NWIS382254112570201	NWISWL6	USGS (2015)	329547	4249940	3/6/15	5188.00	229.84	4958.16
Well OH-4	OH-4	Vautaz and Goff (1987)	336732	4264166	5/26/82	5699.00	505.25	5193.57
Well OH1	OH-1	Vautaz and Goff (1987)	335530	4259049	4/19/83	5640.00	505.25	5134.51
Well GPC-15	GPC-15	Glenn and Hulen (1979)	334304	4258057	7/25/78	5538.00	545.00	4993.00
Well Wow4	Wow4	Vautaz and Goff (1987)	333338	4265143	5/26/82	5200.00	192.26	5007.87

All location information is NAD 83 UTM zone 12N. Site ID's correlate with those on Figures 3 and 5.
[1] Labels correlate with those in Figures 3, 4, and 5.
[2] UGS measurements were collected as part of the sedimentary basins project
[3] Location coordinates are NAD 83 UTM Zone 12N.
[4] Depth to water
-- indicates no data.

Along the valley floor, groundwater elevations are generally consistent and the potentiometric surface slopes south toward areas of significant groundwater pumping near Milford or north toward areas of regional discharge (Kirby, 2012). Beneath the FORGE deep drill site groundwater elevations are near 5100 feet above sea level and between 200 and 600 feet below the land surface.

Depth to water constrains the groundwater supply and the design of new water wells. Depth to water was calculated as the difference between the potentiometric surface (Figure 2) and the surface elevation. The depth to groundwater in the unconsolidated aquifer varies sharply across the study area, from less than 20 feet near the Beaver River to over 500 feet west of the Opal Mound fault (Figure 3), decreasing to the west away from the Opal Mound fault. Near the north end of the Opal Mound fault an area of shallow groundwater correlates with historical outflow from the geothermal system. Across the FORGE deep drill site, groundwater lies within 200 feet of the ground surface along the west side and within 600 feet along the east side.

Several wells within the study area have long-term water level data (U.S. Geological Survey, 2017). These data show changes in groundwater elevation through time for the unconsolidated aquifer across the study area (Figure 4). Long-term water level change in the FORGE study area at wells WOW2 and WOW3 is less than 15 feet. Farther from the FORGE project site, NWISWL1, NWISWL2, and NWISWL3 show water level changes less than 10 feet. These data indicate that over the 70-year period in which water level data have been recorded, groundwater recharge and discharge are nearly equal across the FORGE study area. In addition, there has been little fluctuation in groundwater elevation due to current groundwater use in the area. To the south near Milford, site NWISWL5 shows a decline of 50 feet from 1985 to present, which is likely due to agricultural groundwater use.

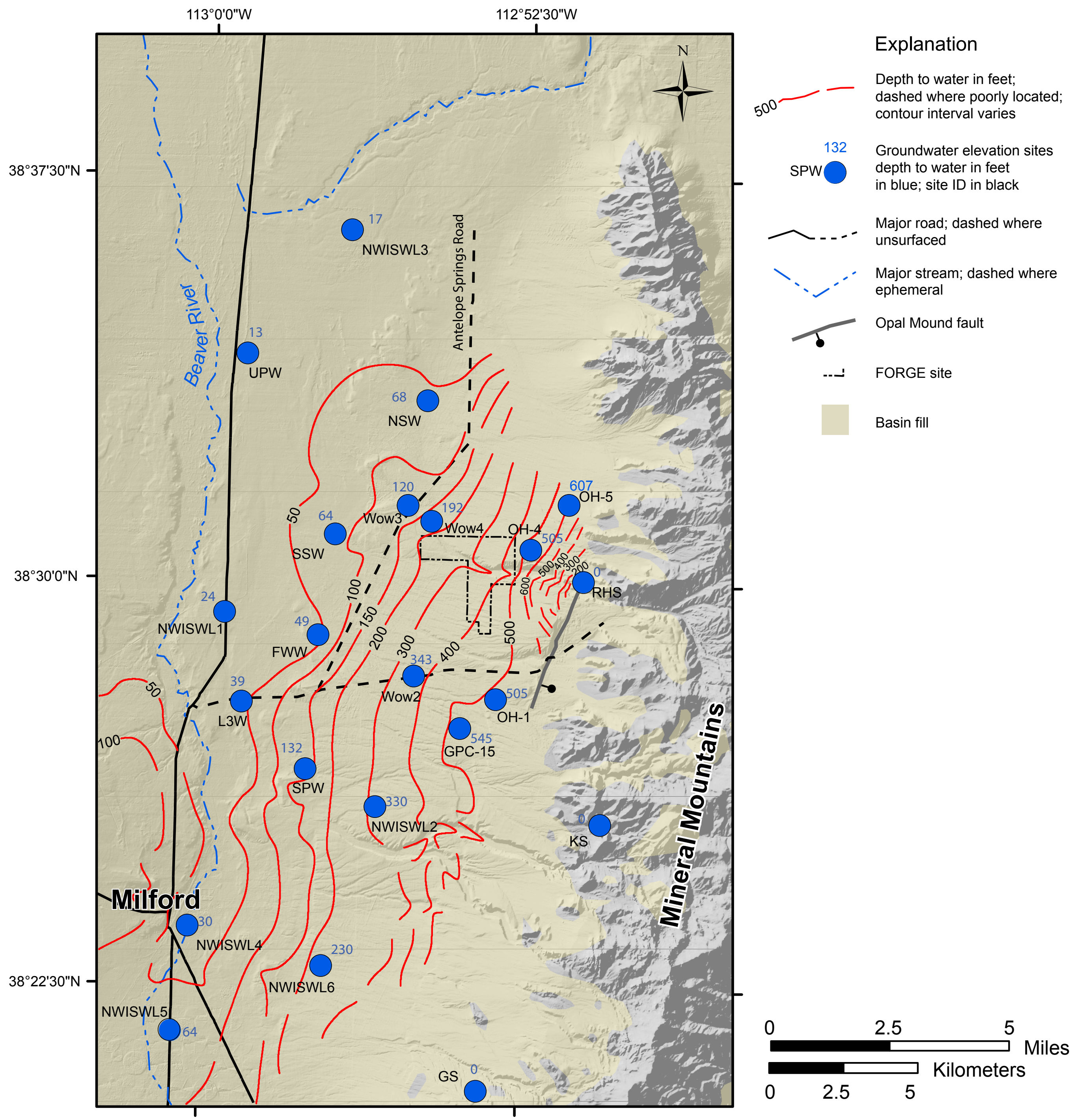

Figure 3. Depth-to-water map for the FORGE study area. Depth to water calculated as the difference between the potentiometric surface in Figure 2 and a 5-meter digital elevation model.

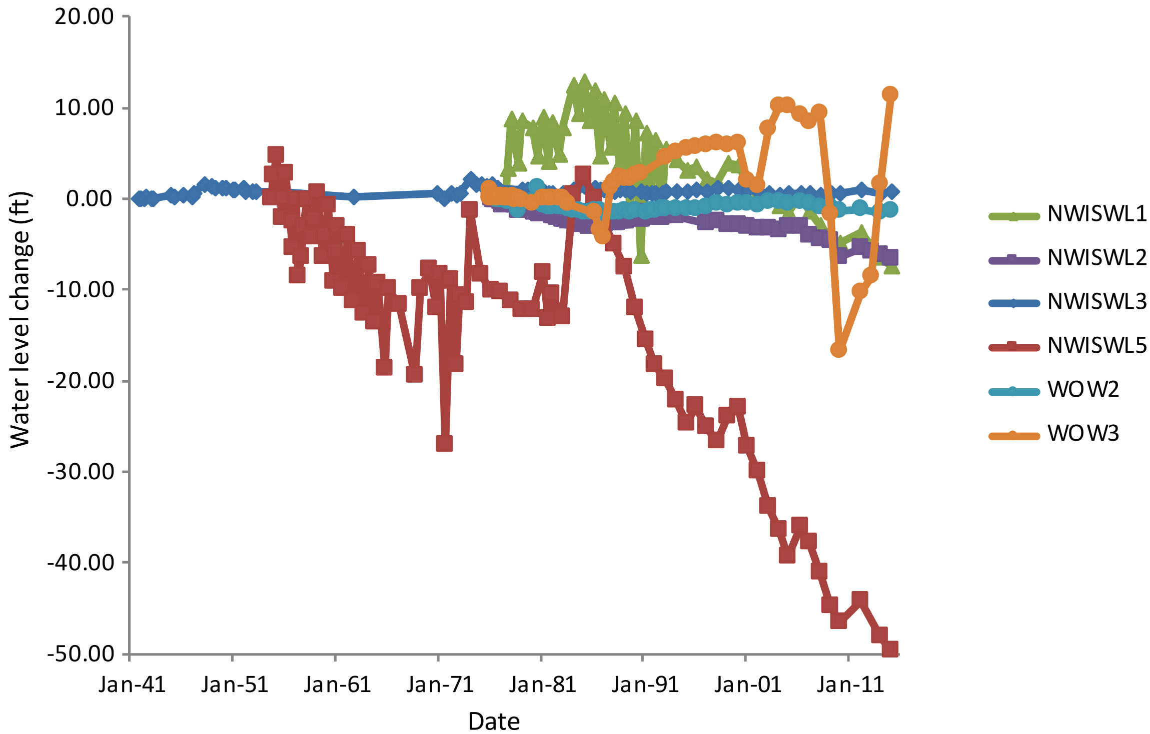

Figure 4. *Long-term water level changes in groundwater wells. Data used to construct the graph are from the USGS NWIS database (U.S. Geological Survey, 2017). Long-term water level changes near the FORGE deep drill site are less than 10 feet. To the south, near Milford, NWISWL5 shows a decline of 50 feet from 1985 to present, which is interpreted to be due to agricultural groundwater use.*

GROUNDWATER GEOCHEMISTRY AND ISOTOPES

Groundwater chemistry provides basic information concerning groundwater quality and fluid flow through the shallow aquifer. To investigate trends in groundwater chemistry, relevant chemical and isotopic data obtained in earlier investigations (e.g., Vuataz and Goff, 1987) were combined with new sampling completed as part of the FORGE project. This section examines existing chemical and isotopic data for groundwater within the FORGE project area to constrain groundwater movement and evolution and the potential for groundwater to supply water to the FORGE project.

The groundwater data comprises chemical analyses from: 1) two samples of the produced geothermal fluids and a sample from Roosevelt Hot Springs, 2) two samples from high-elevation cool springs in the Mineral Mountains, and 3) samples of cooler groundwater from wells and springs across the study area. All water samples were analyzed for the major ions Na, K, Mg, Ca, Cl, SO_4, and HCO_3, and dissolved silica (Table 2). Some samples were analyzed for other constituents including B and the stable isotopes deuterium and oxygen-18. Total dissolved solids (TDS) were calculated as the sum of dissolved constituents for each sample.

Major ion chemistry defines the dominant cation and anion in a sample based on meq/L concentrations (Kehew, 2000). Across the study area chemistry varies from Ca-HCO_3 to Na-Cl; a single sample is classified as Na-SO_4 type (Figure 5). Samples of geothermal fluids from Roosevelt Hot Springs and geothermal production wells 14-2 and 54-3 are Na-Cl waters. Nearly all samples, downgradient and west of these geothermal samples, share the Na-Cl chemistry. Samples from Kirk Springs (KS) and Bailey Springs (BS) in the Mineral Mountains, upgradient of the geothermal samples, are Ca-HCO_3, representing non-thermal water. Other Ca-HCO_3 samples are located north of the project area near Antelope Springs and to the south near Milford. A single Na-SO_4 type sample occurs in an agricultural area east of Milford. Sample NMS also consists of Na-SO_4 type water and was collected from boiling water along NMag Wash that may represent condensed steam and/or steam-heated shallow groundwater.

The groundwater compositions are differentiated using a piper diagram shown in Figure 6. Samples are categorized based on their setting relative to the general sources of groundwater in the area, including Mineral Mountain Cold Springs, Roosevelt Hot Springs upflow, geothermal outflow, and Milford Valley groundwater. Wells 14-2 and 54-3, and Roosevelt Hot Springs (RHS) plot in a corner of the diagram, and these waters are dominated by high Na and Cl, representing undiluted thermal water. Samples of upland springs BS and KS plot well to the left of the other samples with high concentrations of Ca and HCO_3. Many of the compiled samples of Milford Valley groundwater (sites NWIS11, NWIS13, NWIS14, and SPW) plot in the upper half of the piper

Table 2. *Groundwater chemistry for the FORGE study area.* https://ugspub.nr.utah.gov/publications/misc_pubs/mp-169/mp-169-e.zip

Name	Label[1]	Easting[2]	Northing	Source	Hydrogeologic setting	Sample Date	Temp (°C)	pH	Ca(mg/L)	Mg(mg/L)	Na(mg/L)	K(mg/L)	Cl(mg/L)	SO_4(mg/L)	HCO_3(mg/L)	Si(mg/L)	F(mg/L)	Br(mg/L)	B(mg/L)	NO_3(mg/L)	As(ug/L)	TDS(mg/L)	$\delta^{18}O$(‰)	$\delta^{2}H$ (‰)	Water Type	Charge Bal[3]	Cl/B	$\delta^{13}C$ (‰)	pmc[4]	Tritum (TU)
14-2	14-2	339393	4262172	Capuano and Cole (1982)	Roosevelt Hot Springs upflow	9/1/77	268	6.2	9.2	0.6	2150	390	3650	78	126.09	229	5	--	29	--	--	6667	-13.6	-116	Na-Cl	-2.62	125.9	--	--	--
382919113994701	NWIS1	324364	4261972	USGS (2017)	Milford Valley groundwater	6/27/62	13.3	8.2	25	15	203.8	--	240	20	250	22	1.2	--	2	0.158	--	779	--	--	Na-Cl	-0.82	120.0	--	--	--
383016113000101	NWIS2	325399	4263513	USGS (2017)	Milford Valley groundwater	6/21/50	--	7.36	90	92	480.4	--	980	16	304	32	0	--	--	1.6	--	1995	--	--	Na-Cl	-0.04	--	--	--	--
383123113061201	NWIS9	316574	4265946	USGS (2017)	Milford Valley groundwater	9/7/63	17.8	7.8	66	23	80	11	150	57	219	30	0.7	--	0.18	1.6	--	638	--	--	Na-Cl	-0.77	833.3	--	--	--
383138113063301	NWIS8	316076	4266420	USGS (2017)	Milford Valley groundwater	9/7/63	15	7.8	56	14	64	6.7	78	40	240	24	0.4	--	0.14	2.2	--	525	--	--	Ca-HCO_3	-0.96	557.1	--	--	--
383625112534501	NWIS5	335174	4274683	USGS (2017)	Milford Valley groundwater	3/2/71	--	8	58	22	23	5.7	53	41	200	74	2.8	--	0.14	--	--	480	-15.55	-116.8	Ca-HCO_3	0.55	378.6	--	--	--
383912112561201	NWIS7	331410	4280085	USGS (2017)	Milford Valley groundwater	5/9/71	15	7.7	45	14	30	5.2	54	43	161	61	0.3	--	0.1	0.113	--	414	--	--	Ca-HCO_3	-2.51	540.0	--	--	--
382403112592601	NWIS3	326087	4252116	USGS (2017)	Milford Valley groundwater	7/21/78	20.5	7.7	270	230	730	13	300	2300	470	43	0.6	--	1.7	2.3	--	4361	--	--	Na-SO_4	0.14	176.5	--	--	--
382254112570201	NWIS4	329572	4249956	USGS (2017)	Milford Valley groundwater	5/20/71	20.5	8	33	5.7	29	2.2	33	25	130	27	0.6	--	--	0.7	--	286	--	--	Ca-HCO_3	-2.71	--	-10.37	47.31	<0.1
382349113021101	NWIS6	322165	4251615	USGS (2017)	Milford Valley groundwater	5/6/71	20	7.9	64	23	72	4.9	86	130	200	45	1	--	0.23	--	--	626	--	--	Ca-HCO_3	-0.85	373.9	--	--	--
Roosevelt Hot Springs	RHS	338369	4263072	Capuano and Cole (1982)	Roosevelt Hot Springs upflow	9/11/57	55	7.9	22	3.3	2500	488	4240	73	156	310	7.5	3.3	38	2.48	--	7844	--	--	Na-Cl	-2.03	111.6	--	--	--
Wow 2	Wow 2	332746	4259842	Vautaz and Goff (1987)	Geothermal outflow	5/25/82	32.3	7.22	151	33	494	19	1050	3.4	229	46	0.49	0.15	7.53	--	--	2034	--	--	Na-Cl	-2.92	139.4	--	--	--
Wow 3	Wow 3	332637	4265602	Vautaz and Goff (1987)	Geothermal outflow	4/19/83	23.5	8.28	77	15.4	1540	185	2840	3.2	90	2	0.91	2	21.5	--	--	4777	-13.25	-112.7	Na-Cl	-4.29	132.1	--	--	--
Well OH-4	OH-4	336732	4264166	Vautaz and Goff (1987)	Geothermal outflow	5/26/82	48.2	6.89	260	40	1800	240	3440	84.8	104	60	1.64	2.1	30.6	--	--	6063	--	--	Na-Cl	-1.34	112.4	--	--	--
Antelope Springs	AS	337217	4280141	Kirby (2012)	Milford Valley groundwater	6/6/07	15.4	7.5	38.59	10.68	31.01	4.75	51.47	38.72	141.4	41	0.46	0.28	--	0.55	--	359	-15.67	-116.9	Ca-HCO_3	-3.8	--	--	--	--
South Stock Well	SSW	330036	4264716	This study	Geothermal outflow	11/6/17	15.8	7.2	439.1	93	1035	45.4	2365	23	341	102	0	--	17	1.1	21	4373	-13.59	-112.8	Na-Cl	-3.46	129.4	-0.35	3.27	0.1
North Stock Well	NSW	333208	4269283	Allis et al. (2015)	Geothermal outflow	8/13/14	16.8	7.4	302	13.6	882	62.2	1640	22.4	828	78.9	0	--	12.7	0.02	438.35	3842	-13.95	-106.9	Na-Cl	-4.51	129.1	-2.91	1.2	<0.1
Level 3 communications well	L3W	326823	4259004	This study	Milford Valley groundwater	11/8/17	19.1	6.7	95.1	70.8	223	12.9	657	2.5	53	23.5	0	--	1.09	0.03	4	1124	-15.3	-117.6	Na-Cl	2.99	577.1	-4.11	13.3	<0.1
BLM solar panel well	SPW	329005	4256696	Allis et al. (2015)	Milford Valley groundwater	8/14/14	24.2	7.1	117	19.4	164	7.6	411	1.5	173	36.2	0	--	2.09	0.31	1.93	932	-14.68	-109.9	Na-Cl	0.36	196.7	-4.78	14.65	<0.1
First Wind Well	FWW	329453	4261265	Allis et al. (2015)	Geothermal outflow	8/14/14	32.4	7.9	203	103	1100	45.2	1870	172	580	91.9	0	--	11.7	0.02	67.3	4177	-14.57	-115.9	Na-Cl	0.52	159.8	--	--	--
54-3	54-3	338607	4262196	Capuano and Cole (1982)	Roosevelt Hot Springs upflow	--	260	--	8	2	2320	461	3860	73	232	263	6.8	--	29.9	--	--	7256	--	--	Na-Cl	-1.76	129.1	--	--	--
Bailey Spring	BS	342471	4260408	This study	Mineral Mt cold springs	11/6/17	6.6	7.39	59.6	10.3	19.2	2.8	22	9	217	23	1.6	--	0.0014	0.4	1	350	-15.31	-114.4	Ca-HCO_3	0.92	10142.9	-12.89	98.86	4.2
Kirk Spring	KS	339092	4254744	Vautaz and Goff (1987)	Mineral Mt cold springs	5/27/82	6.1	7.6	50	11.7	33	4.6	34.5	21.8	234	23	1.15	--	0.0014	--	--	414	--	--	Ca-HCO_3	-3.02	24642.9	-12.53	91.56	0.7
382924112592901	NWIS14	326335	4262088	USGS (2017)	Milford Valley groundwater	7/21/14	18.4	7.2	63.9	24.9	67.9	2.8	146	109	101	27.1	0.28	0.193	0.183	0.7	0.014	510	--	--	Ca-Cl	1.3	797.8	--	--	--
382456113010501	NWIS12	323625	4254001	USGS (2017)	Milford Valley groundwater	9/17/70	27.1	7.9	20	6.4	74	8.4	17	31	220	70	1.2	--	0.23	0.023	--	336	-16.4	-124	Na-HCO_3	2.4	73.9	--	--	--
382506113041201	NWIS13	319253	4254308	USGS (2017)	Milford Valley groundwater	5/14/71	--	7.6	140	28	66	4.1	160	270	118	37	0.3	--	0.18	13	--	821	--	--	Ca-SO_4	0.8	888.9	--	--	--
382212112585301	NWIS10	326765	4248827	USGS (2017)	Milford Valley groundwater	5/9/71	19	7.9	65	23	50	2.6	59	160	158	26	0.6	--	0.01	2.7	--	476	--	--	Ca-SO_4	-1.4	5900.0	--	--	--
382204113002501	NWIS11	324572	4248566	USGS (2017)	Milford Valley groundwater	5/18/62	14.4	7.6	390	120	200	10	680	780	169	45	0.1	--	0.32	0.41	--	2860	--	--	Ca-SO_4	0	2125.0	--	--	--
Well OH-5	OH-5	337664	4265503	Vautaz and Goff (1987)	Geothermal outflow	5/26/82	82.7	6.56	330	41	620	34	1740	5.16	51	44	1.56	0.18	9.28	--	--	2895	-13.2	-106.8	Na-Cl	-2.4	187.5	--	--	--
Negro Mag Seep	NMS	338251	4262824	This study	Geothermal outflow	11/7/17	85	4.2	8	2.6	26.4	10	2	127	0	--	0.5	--	--	0.1	7	188	-8.69	-85.9	Na-SO_4	-15.19	--	--	--	--
Murphy-Brown Supply Well 1	MB1	328302	4259283	This study	Milford Valley groundwater	11/1/17	22.4	7.09	145.4	77.5	300	17.1	806	9	341	--	0.1	--	--	--	2	1501	-14.96	-115.9	Na-Cl	3.75	--	-6.41	5.22	<0.1

[1] Label field correlates with labels shown on figures.

[2] Location coordinates are NAD 83 UTM Zone 12N.

[3] Charge balance of meq/L of anions to cations, taken as percent of total.

[4] Percent Modern Carbon

-- indicates no data.

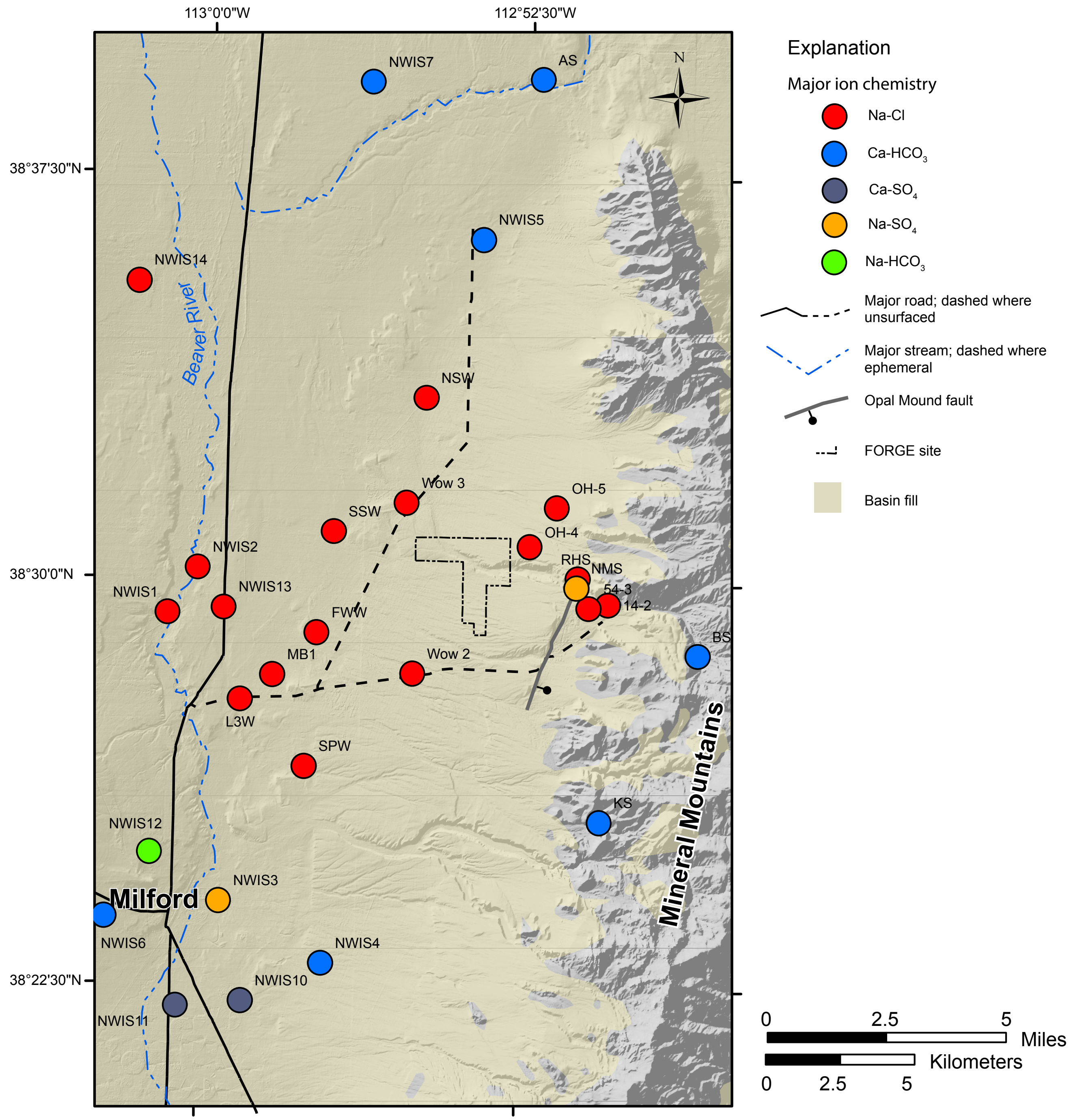

Figure 5. *Major ion chemistry for compiled groundwater samples. Site ID corresponds with those in Table 2. Most water samples near the FORGE site consist of Na-Cl type waters.*

diagram owing to increased concentrations of SO_4 relative to Cl. Samples from locations west of the Opal Mound fault that include geothermal outflow (sites WOW3, NSW, SSW, and FWW) show increasing relative concentrations of Ca, Mg, and SO_4 relative to Na and Cl, which may result from mixing between RHS thermal water, water similar to the upland springs BS and KS, and Milford Valley groundwater in the basin-fill aquifer. Based on the distribution of the different chemical types illustrated by the map (Figure 5) and the piper diagram (Figure 6), the chemistry of outflow samples is likely controlled by dilution of Roosevelt Hot Spring upflow with Milford Valley groundwater as groundwater moves to the west away from Roosevelt Hot Springs.

To better examine possible mixing trends, the ratio of major anions Cl to HCO_3 versus the TDS of each sample is shown in Figure 7. Samples appear to plot in at least two groupings which are not exclusive to a given sample's assumed setting. Samples of thermal water from wells 14-2 and 54-3, and RHS plot in a zone in the upper right part of the figure along with several of the samples of geothermal outflow including OH-4, OH-5, and Wow3. The remainder of the geothermal outflow samples plot in

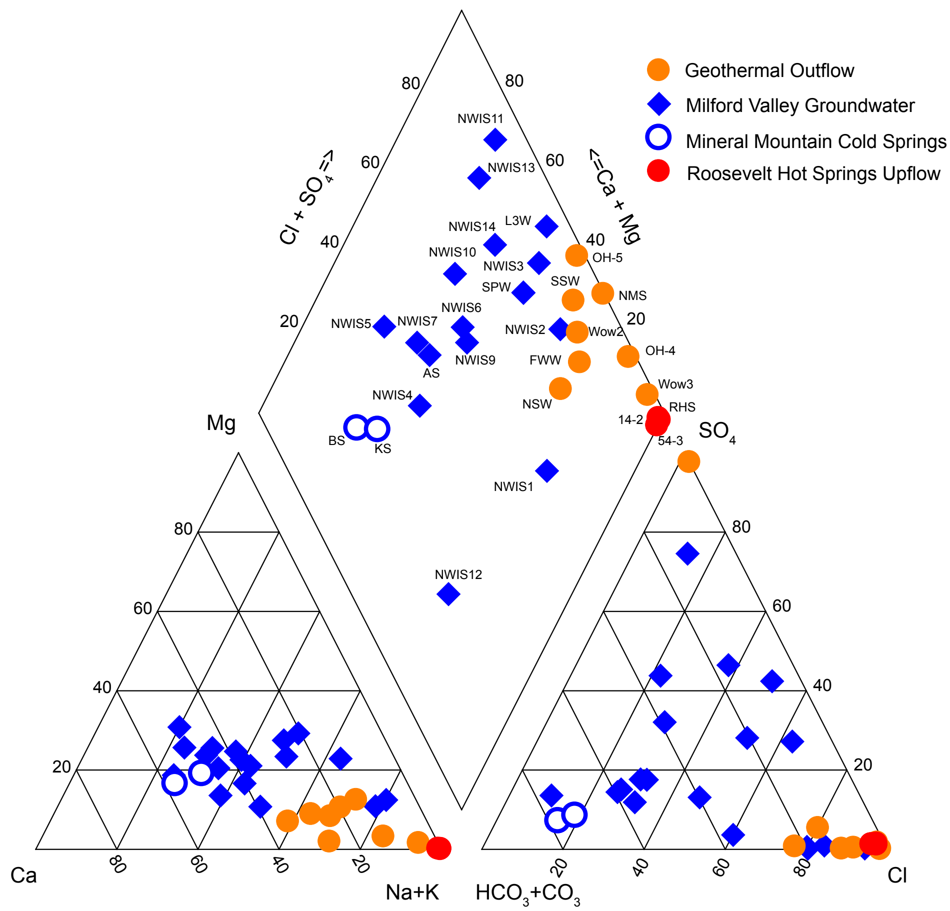

Figure 6. *Piper diagram of compiled groundwater chemistry. Site ID corresponds with those in Table 2.*

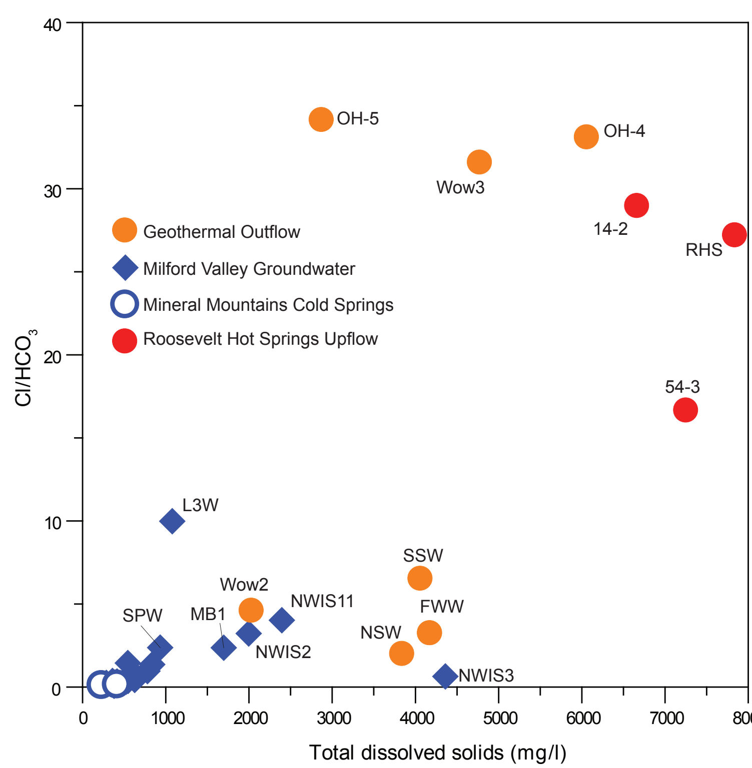

Figure 7. *Graph of the ratio of Cl and HCO_3 anions versus total dissolved solids. Samples do not lie along a simple mixing trend, implying that simple end member mixing does not control all chemical variation.*

the lower half of the diagram. The offset among samples of outflow implies that a simple linear mixing trend between Milford Valley groundwater or upland springs and Roosevelt Hot Springs upflow is insufficient to explain the variation in major ion chemistry in geothermal outflow samples.

In addition to major ion chemistry, many of the groundwater samples include B analyses that can be examined to better understand fluid flow in the groundwater system. High B concentrations are typical of many geothermal systems and comparisons of these concentrations to the relatively nonreactive Cl provides an additional perspective on groundwater mixing in the FORGE area. A plot of the ratio of Cl to B versus TDS for the sample set is shown in Figure 8. Samples of Roosevelt Hot Springs upflow have a characteristic Cl/B value of ~100 and most Milford Valley groundwater samples range from 200 to 700. Geothermal outflow samples are generally between 150 and 200 Cl/B and appear to lie along a trend of decreasing TDS and relatively consistent Cl/B. This implies that, at least with respect to Cl and B, simple dilution of Roosevelt Hot Springs upflow by groundwater with comparable Cl/B may explain observed variation in constituents. However, concentrations of the other major solutes may vary due to additional water-rock interactions and/or mixing of other sources that are not characterized by this sample set.

A map of TDS concentrations shows a plume of high-TDS thermal water emanating from the north end of the Opal Mound fault and Roosevelt Hot Springs (Figure 9). This plume broadly defines the area of thermal outflow in which TDS concentrations decrease to the west, north, and south as the plume disperses in the unconsolidated basin-fill aquifer across the FORGE deep drill site. Additional areas of high TDS (greater than 3000 mg/L) occur across Milford Valley to the northwest of the FORGE area and to the south near Milford. The extent and scale of the plume implies long-term subsurface outflow of geothermal fluids from the Roosevelt Hot Springs area.

The TDS thresholds for primary and secondary drinking water standards are 500 and 1000 mg/L, respectively. Groundwater beneath the FORGE site ranges from 4000 to >6000 mg/L, and it is unsuitable for use as drinking water supply. Potential supply wells located along the Antelope Springs Road east of the FWW well could encounter groundwater with TDS ranging from 2000 mg/L to just over 4000 mg/L.

The abundances of stable isotopes deuterium and oxygen (expressed as δ^2H and $\delta^{18}O$, respectively) in water provide information about both the source of the groundwater and the degree of high-temperature water-rock interaction (Clark and Fritz, 1997). These isotopes also provide an independent constraint on the interpretation of mixing trends. Deuterium and oxygen-18 isotope data exist for 11 samples (Table 2). Samples AS, NWIS5, SPW, BS, and NSW plot along and near the meteoric water lines and represent the compositions of local rainfall and snowmelt (Figure 10). Two samples of thermal water (14-2 and RHS) are shifted to the right from the meteoric water line by nearly 2 per mil $\delta^{18}O$. These samples show evidence of isotope exchange produced by high-temperature water-rock interaction (Bowman and Rohrs, 1981). Samples L3W, FWW, SSW and WOW3 plot in between the thermal waters and the meteoric water line, reflecting mixing as the thermal (high-TDS) plume disperses westward through the shallow aquifer.

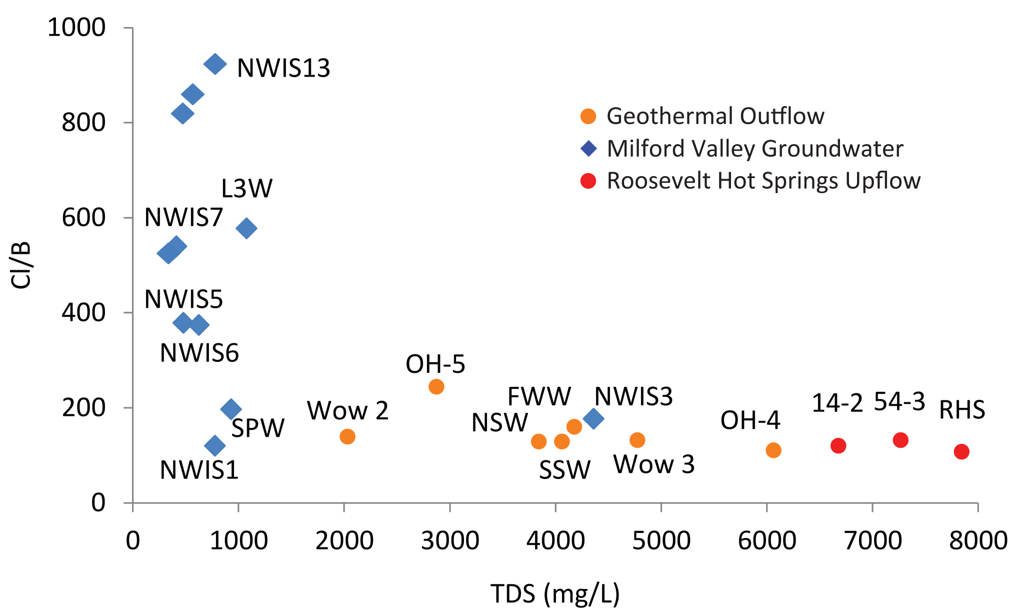

Figure 8. *Graph of Cl/B versus TDS. Most groundwater samples surrounding the FORGE deep drill site have uniform Cl/B values of ~150 with decreasing TDS resulting from mixing and dilution.*

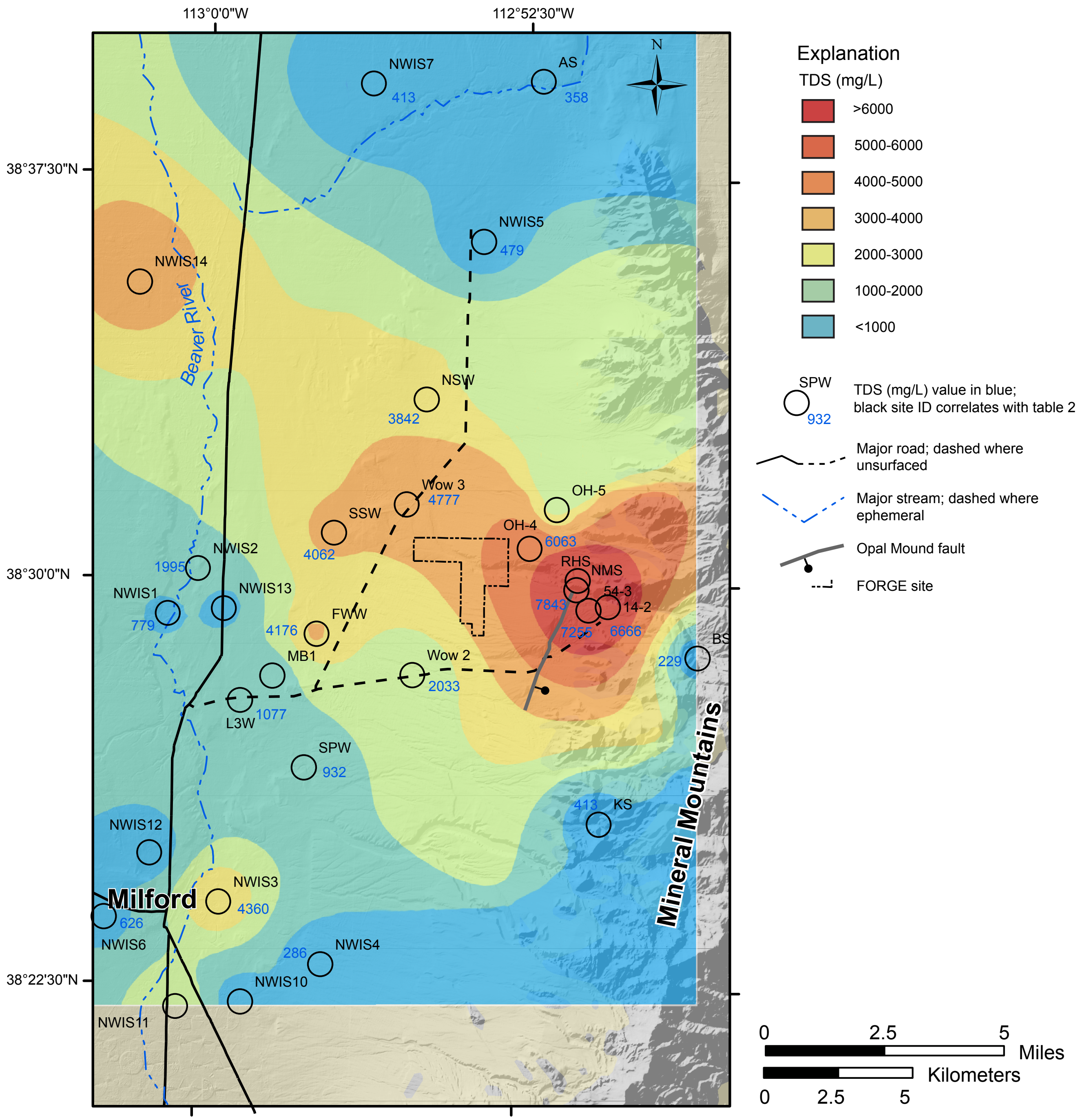

Figure 9. *Map of TDS concentrations. A high-TDS plume extends to the west from Roosevelt Hot Springs (RHS) and the north end of the Opal Mound fault.*

As part of the FORGE Phase 2b project, eight groundwater sites were sampled for the radiogenic and stable isotopes of carbon and tritium to constrain groundwater age adjoining the FORGE site (Table 2). Sample sites included the upland springs in the Mineral Mountains (sites KS and BS), geothermal outflow sites (NSW and SSW), and Milford Valley groundwater sites (MB1, L3W, SPW, and NWIS4) (Figure 11). Samples were collected in clean and rinsed HDPE bottles, carefully filled to minimize atmospheric contamination. Samples of carbon isotopes were analyzed via AMS methods at the University of Georgia CAIS laboratory. Samples of tritium were analyzed via scintillation counting at the Brigham Young University hydrogeology laboratory.

Pmc is the percent modern carbon relative to an atmospheric standard for carbon-14. Due to significant fractionation and isotopic dilution that is common to the recharge process, values typical of recently recharged water can range from 50 to 100. Low values of pmc, less than 50, indicate at least a component of the pmc concentration has been reduced via radioactive decay. Lower values tend to indicate older waters that have significant age and or may have experienced significant water-rock interaction and carbon

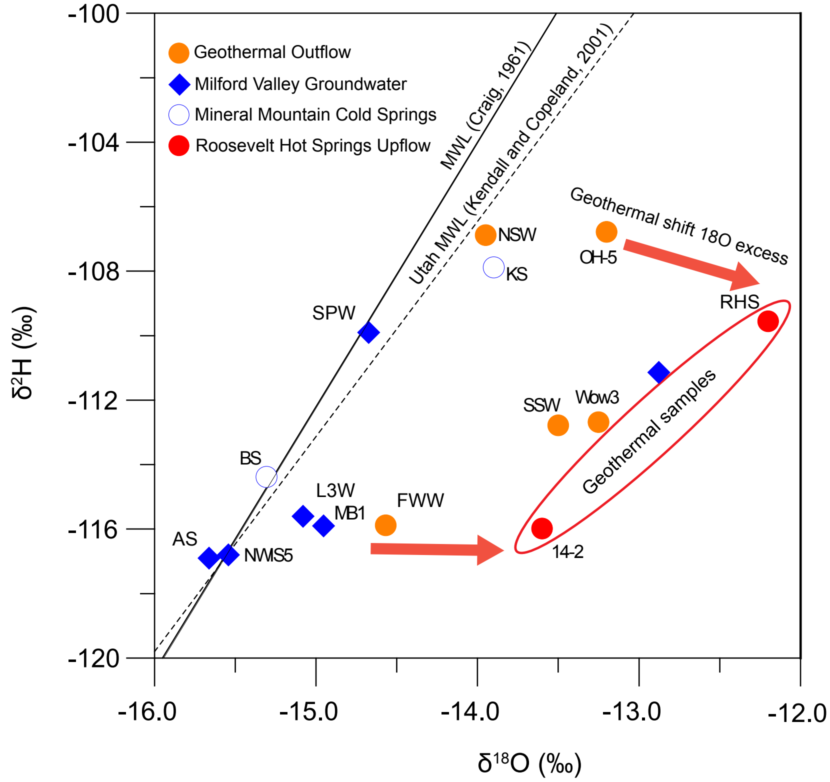

Figure 10.*Plot of stable isotope compositions (per mil) of groundwater. The meteoric water line (MWL) is defined by Craig (1961) and the Utah meteoric water line is defined by Kendall and Copeland (2001). Thermal water (14-2 and RHS) shows a significant positive shift in $\delta^{18}O$ relative to local meteoric water due to isotope exchange during high-temperature water-rock interaction.*

isotopic fractionation and exchange between the dissolved carbon and mineral carbonate (Clark and Fritz, 1997). Typical Basin and Range groundwater systems show pmc that decreases away from areas of recharge. In the case of the FORGE area, recharge of the basin-fill aquifer likely occurs along the upper reaches of the west-sloping alluvial fans. Following this conceptualization, pmc should decrease (and groundwater age increase) as groundwater flows down-gradient away from the Mineral Mountains towards the valley axis. Samples of the upland springs and sites NWIS4 and SPW follow this general pattern of decreasing sample elevation and distance from upland recharge yielding lower pmc and older water. Samples to the north show a different pattern in which the pmc and groundwater age for samples NSW, SSW, MB1, and L3W have approximately similar positions on the west-sloping fans and which appear to vary with proximity to the plume of geothermal outflow (Figures 11 and 12). The lowest pmc occurs at sites NSW and SSW which are closest to the outflow plume. Pmc increases south of SSW to L3W, away from the outflow plume. This distribution implies that the pmc concentration of these sites is controlled not by radioactive decay and water-rock interaction and instead is controlled by mixing of the geothermal plume with Milford Valley groundwater. This distribution also implies that geothermal outflow is low pmc or carbon-14 free. Groundwater ages derived from these pmc values would not represent ages of recharge and are therefore not calculated. Further sampling of the Roosevelt Hot Springs upflow is necessary to confirm the pmc content of the outflow plume.

Tritium is a radioactive isotope of hydrogen with a half-life of 12.7 years, and is generated naturally in the upper atmosphere. Precipitation, and recently recharged groundwater, typically contain concentrations between 2 and 8 TU or tritium units. Groundwater having tritium concentrations greater than 0.5 TU generally indicates recent recharge at a given site (Clark and Fritz, 1997). Of the eight samples collected, only the upland springs KS and BS have tritium greater than 0.5 TU. All other sites have low or undetectable tritium concentrations with no evidence of recent recharge at these sites. These low values correlate with the low pmc values and further support limited active recharge of groundwater near the FORGE site.

AQUIFER TESTS

Available aquifer tests constrain the water yielding characteristics of the basin-fill aquifer. Data from two single-well aquifer tests near the Utah FORGE project site were provided by the Smithfield Corporation. These aquifer tests were completed in the fall of 2017 as part of a business expansion project by the Smithfield Corporation. The results of the new aquifer tests

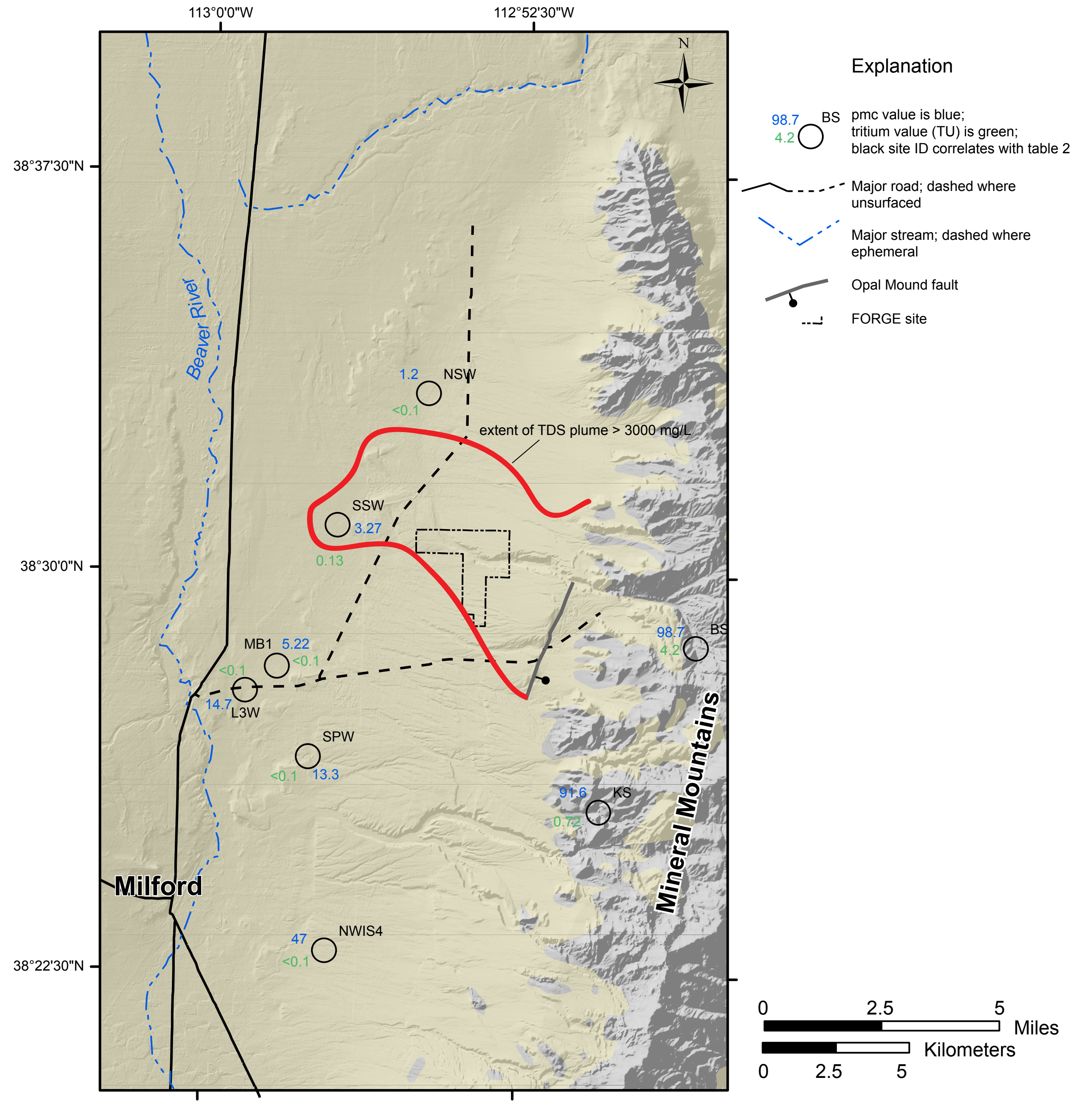

Figure 11. *Map of carbon isotope and tritium samples. Isotopic compositions typical of recharge are shown at sites KS and BS. Samples near the high-TDS plume have low pmc and tritium values.*

are summarized below. These data augment an existing aquifer test completed for the FORGE project Phase 2a and an older aquifer test presented by Vautaz and Goff (1987).

The first aquifer test was conducted on an 8-inch diameter supply well drilled in the summer of 2017 by the Smithfield corporation for agricultural supply. The well (labeled MBW-1) is located approximately 4 miles southwest of the Utah FORGE site. The MBW-1 well is completed in unconsolidated basin fill and has a total depth of 401 feet (Figure 13). Based on driller's logs, the well is screened in gravel, sand, and clay between 322 and 353 feet. The total aquifer thickness is 20 feet. This aquifer section is confined by clay between 72 and 103 feet. Static water level was 60 feet below land surface prior to pumping. Total drawdown after pumping was 3.2 feet.

The MBW-1 well was pumped at a constant rate of 50 gpm for a total of 18 hours. Drawdown was measured during the pumping period and a 4-hour recovery period (Table 3). These data were input into the modeling software AQTESOLVE

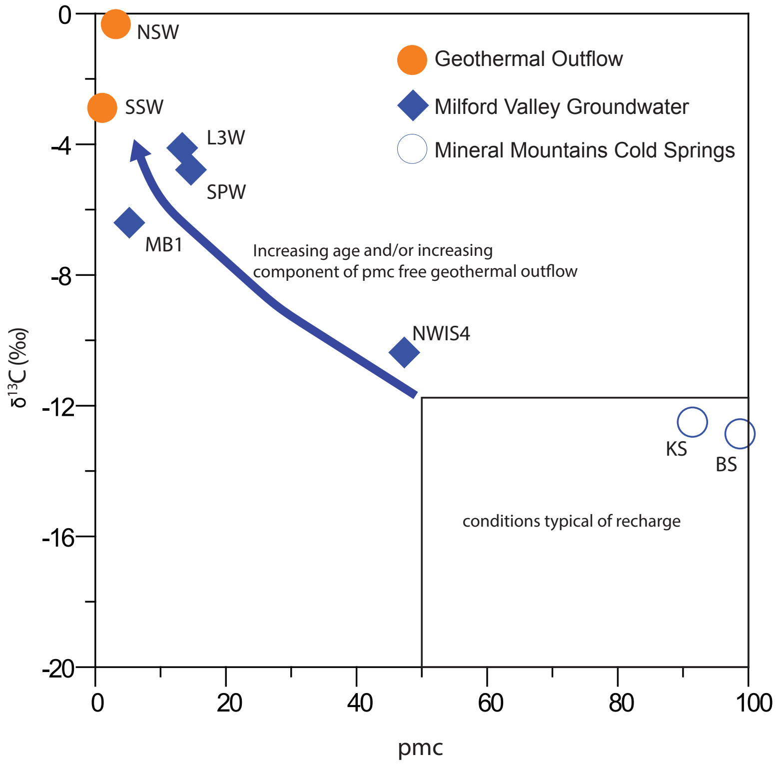

Figure 12. *Graph of pmc versus carbon-13. Graph shows carbon isotopic conditions typical of recharge in the lower right corner. Increasing amounts of water-rock interaction, time since recharge, and or increasing fractions of pmc free geothermal outflow yield a trend of increasing* ^{13}*C and decreasing pmc towards the upper left corner.*

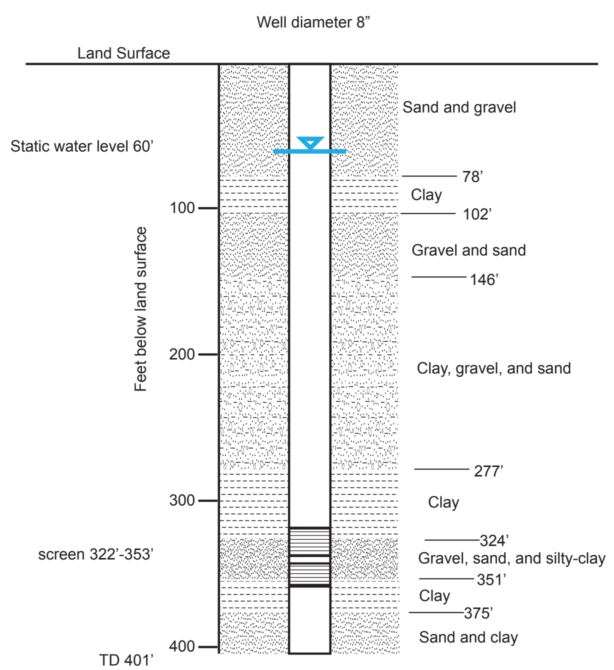

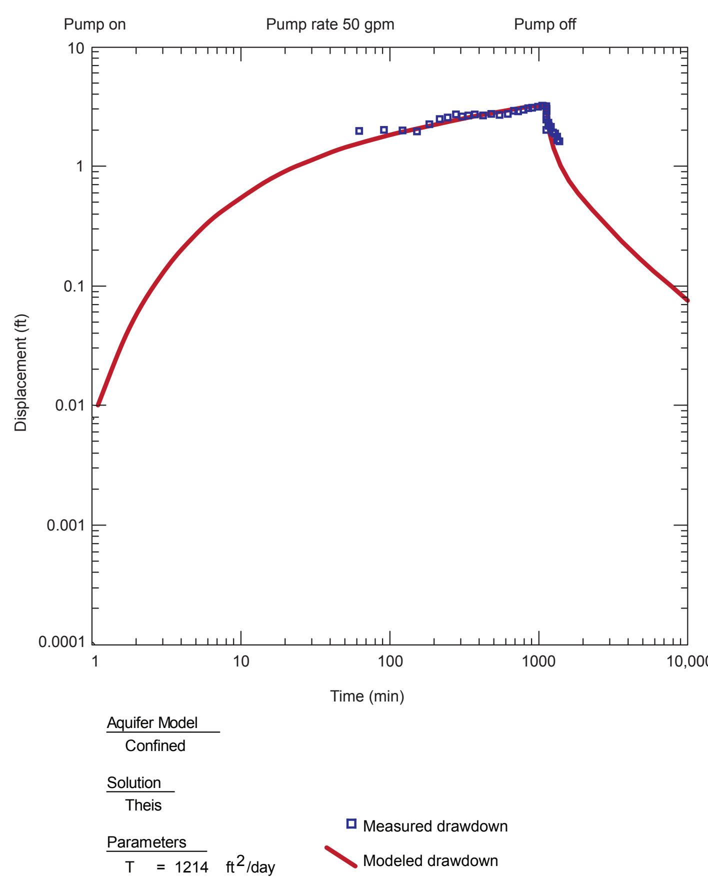

Figure 13. *Well log and aquifer test solution for well MBW-1.*

Table 3. *Aquifer test drawdown data used to model transmissivity.* https://ugspub.nr.utah.gov/publications/misc_pubs/mp-169/mp-169-e.zip

Well MBW1 (hand measurements)				Well MBW2 (hand measurements)				Well FWW (hand measurements)			
Time (min)	Change in WL (ft)	Pump Rate (gpm)	Notes	Time (min)	Change in WL(ft)	Pump Rate (gpm)	Notes	Time (min)	DTW (ft)	Discharge (gpm)	Notes
0	0	50	Pump on	0	0	300	Pump on	0	49.42	100	Pump on
30	-2	50		60	-13.6	300		1	68.74		
60	-2	50		120	-15.6	300		4	71.09		
90	-2	50		180	-18.1	300		10	73.79		
120	-2	50		240	-18.7	300		22	77.81	100	
150	-2	50		320	-19.8	300		27	78.96		
180	-2.25	50		380	-20.2	300		33	80.23		
210	-2.5	50		440	-20.7	300		43	82.14		
240	-2.6	50		500	-19.8	300		61	84.86	94.9	
270	-2.7	50		560	-20	300		77	86.67	93.4	
300	-2.7	50		620	-21.7	300		81		100	
330	-2.7	50		680	-21.9	300		96	91.25		
360	-2.7	50		740	-22	300		116	93.55		
420	-2.7	50		800	-22.1	300	Pump off	136	95.45		
480	-2.7	50		801	-17.3			166	98.09	93.3	
540	-2.7	50		802	-15.8			196	100.24	94.8	
600	-2.8	50		803	-15.75			226	102.14	93.8	
660	-2.9	50		804	-14.8			271	104.7	93.6	
720	-2.9	50		805	-14.1			316	106.98		
780	-3	50		806	-13.8			331		89.2	
840	-3.1	50		807	-13.65			713	117.81	80.8	
900	-3.1	50		808	-13.5			775	118.87	80.9	
960	-3.1	50		809	-12.9			829	119.81	79.5	
980	-3.1	50		810	-12.6			943	121.56	76	
1040	-3.1	50		812	-12			1006	122.49	74.4	
1100	-3.2	50	Pump off	814	-11.8			1066	123.15	72.6	
1101	-3.2			816	-11.4			1126	123.88	75.3	
1102	-3.1			818	-11			1186	124.52	76.1	
1103	-3			820	-10.8			1246	125.16	74.1	
1104	-3			825	-9.8			1306	125.77	73.5	
1105	-3			830	-9.4			1366	126.15	71.8	
1106	-2.9			835	-8.9			1381	126.27	71.1	
1107	-2.8			840	-8.5			1396	126.52	72.6	
1108	-2.75			850	-8.1			1411	126.66	73.3	
1109	-2.17			860	-7.7			1426	126.88	73.3	
1110	-2.6			870	-7.1			1441	127.11	74.7	
1115	-2.5			880	-6.5			1443		0	Pump off
1120	-2.03			890	-6.5			1444	116.81		
1125	-2.25			900	-6			1445	114.9		
1130	-2.25			920	-5.9			1448	113.02		
1135	-2.2			940	-5.8			1454	110.65		
1140	-2.2			960	-5.4			1459	109.1		
1150	-2.2			980	-4.9			1464	107.82		
1160	-2.15			1010	-4.6			1471	106.32		
1170	-2.1			1040	-4.3			1486	103.96		
1180	-2.05							1501	101.91		
1190	-2							1516	100.39		
1200	-1.95							1546	97.78		
1220	-1.9							1578	95.49		
1240	-1.85							1607	93.84		
1260	-1.8							1653	91.41		
1280	-1.75							2208	77.1		
1310	-1.7							2541	72.51		
1340	-1.6							2613	71.55		
								2630	71.55		

(Duffield, 2007) and used as fit points for a modeled drawdown curve. The resulting modeled drawdown was based on a single-well solution for a confined Theis aquifer having a thickness of 20 feet. Because no monitoring wells are nearby, no storativity value could be calculated. Instead, storativity is assumed to be 0.01 based on values typical of similar confined unconsolidated aquifers (Domenico and Schwartz, 1997). Calculated transmissivity based on the selected drawdown model is 1200 ft^2/day.

The second aquifer test was conducted on an existing 16-inch diameter supply well. The well (labeled MBW-2) is located approximately 8 miles north of the Utah FORGE site. Based on well logs, this well was originally drilled to a total depth of 401 feet in 1983 (Figure 14). The lithology in the well consists of a confining clay layer between 53 and 250 feet and limestone from 250 to 401 feet. The limestone is part of the Tertiary basin fill and may be correlative with the Pliocene Cove Creek limestone that is exposed 10 miles northeast of the well site. The well is screened between 101 and 401 feet and the assumed aquifer thickness is 151 feet. Static water level was 98 feet below land surface prior to pumping. Total drawdown after pumping was 22.1 feet.

The MBW-2 well was pumped at a constant rate of 300 gpm for a total of 13 hours. Drawdown was measured during the pumping period and a 4-hour recovery period. Drawdown data were modeled using AQTESOLVE software (Duffield, 2007) assuming a single-well confined Theis solution. Because there are no nearby monitoring wells, a storativity value was not calculated. Instead storativity is assumed to be 0.01 based on values typical of similar aquifers (Domenico and Schwartz, 1997). The resulting transmissivity is 1600 ft^2/day.

An aquifer test was conducted as part of FORGE project Phase 2a on the First Wind supply well (labeled FWW) located 3 miles west of the FORGE project site. The drawdown test was conducted on a 9-inch diameter supply well at the First Wind maintenance facility located approximately 1 mile west of the proposed FORGE project office site. The FWW well is completed in a confined part of the unconsolidated basin-fill aquifer with a total depth of 651 feet (Figure 15). Based on driller's logs, the well is completed in sands and gravels and has a screened interval between 567 and 651 feet and a total aquifer thickness of 440 feet. Clay between 115 and 210 feet makes up the confining layer.

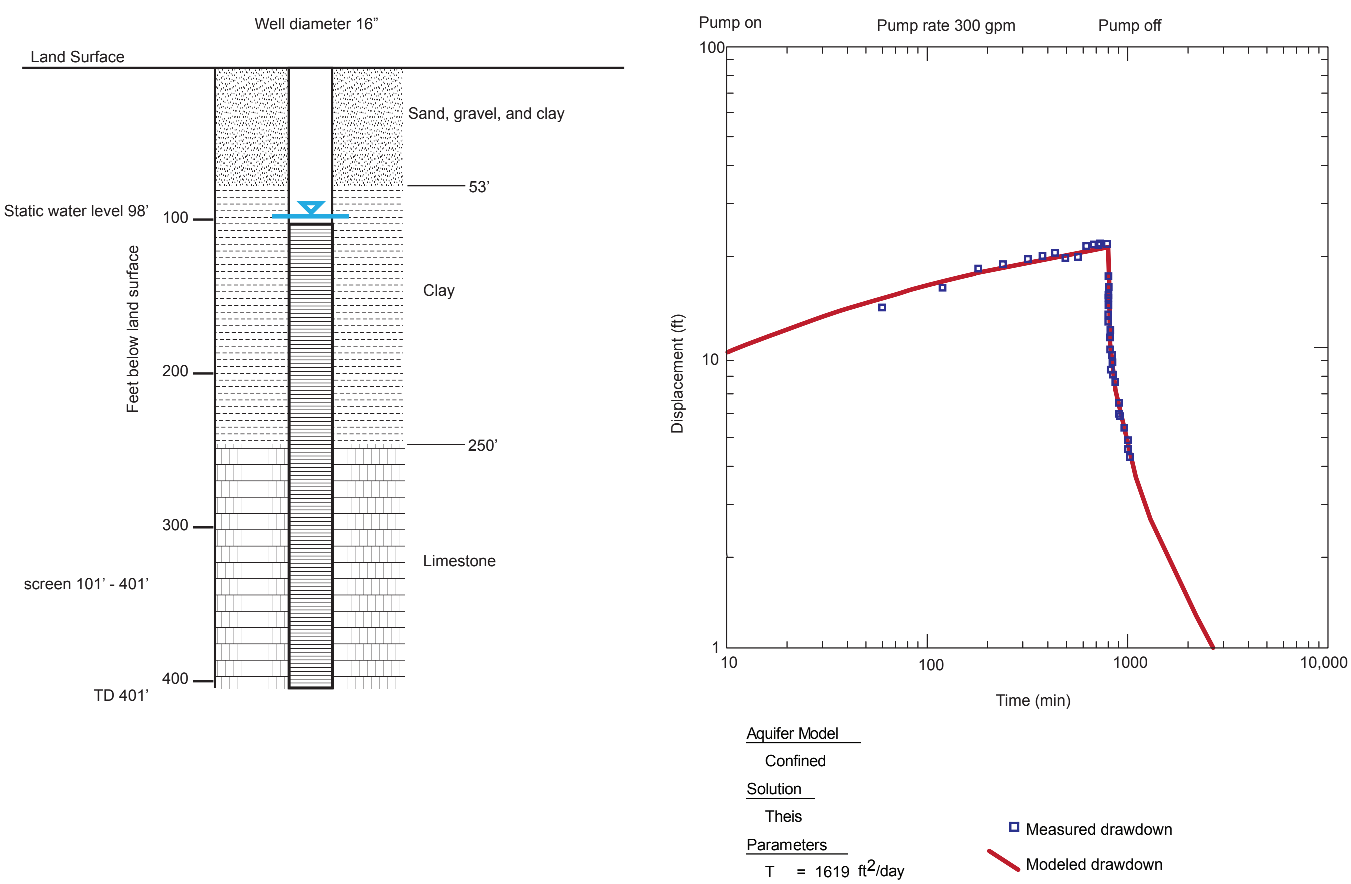

Figure 14. *Well log and aquifer test solution for well MBW-2.*

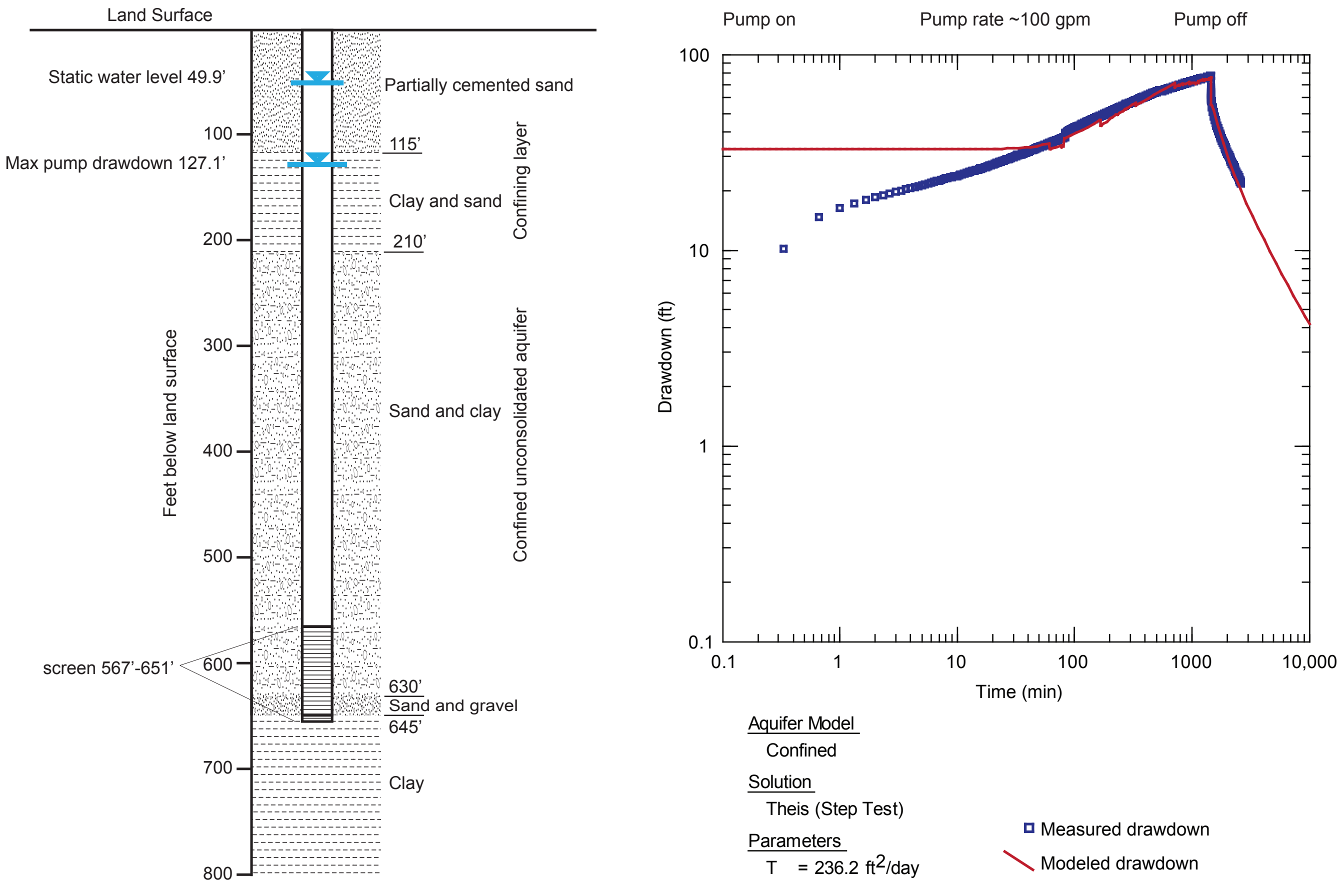

Figure 15. *Well log and aquifer test solution for well FWW.*

The well was pumped at a rate of approximately 100 gpm for 24 hours, and the flow rate and total volume pumped were measured with a clamp-on flow meter. Drawdown was measured in a sounding tube placed in the pumping well, by hand and with a downhole pressure transducer during pumping and for a recovery period following pumping. Table 3 contains the pump and drawdown data used to estimate transmissivity. Just prior to the test, the static water level was 49.1 feet below the wellhead. The water level after 24 hours of pumping was 127.1 feet and total drawdown during the test was 77.9 feet.

Transducer drawdown data and flow rate data were input into the modeling software AQTESOLVE (Duffield, 2007) and used to calculate a transmissivity of ~ 240 ft^2/ day for the FWW. Due to the changes in pump rate over time, the confined nature of the aquifer, and the partial well penetration, a Theis step solution was chosen for curve matching. Because there are no nearby monitoring wells, a storativity value was not calculated. Instead storativity is assumed to be 0.001 based on values typical of similar unconsolidated aquifers (Domenico and Schwartz, 1997). Modeled drawdown and recovery data fit well with observed data (Figure 3), and the estimated transmissivity at the FWW site appears accurate.

As part of a previous investigation of groundwater resources, a single-well aquifer test was performed on an existing supply well (labeled NSW) located approximately 3 miles north of the FORGE project site (Vautaz and Goff, 1987) (Figure 16). The aquifer test was conducted on an 8-inch-diameter supply well completed in unconsolidated basin fill with a total depth of 246 feet. The well is screened between 115 and 246 feet below land surface. No lithologic log is available for this well, and Vautaz and Goff (1987) assumed the lithology is equivalent to a well several miles to the south that was completed in unconfined interbedded sand, gravel, and clay. Estimates of aquifer thickness are not available. Static water level was 70 feet below land surface prior to pumping. Total drawdown after pumping was 24 feet.

The NSW well was pumped at five pumping steps with rates varying from 55 to 220 gpm over a total pumping period of 56 hours. Drawdown was measured during the pumping period and these data were analyzed via six separate solutions for drawdown in an unconfined aquifer. Results were broadly consistent across the solutions analyzed and transmissivity was calculated at ~1400 ft^2/day (Vautaz and Goff, 1987). Due to a lack of detailed well lithologic information for this test the transmissivity value has a much greater uncertainty than the other presented transmissivity values.

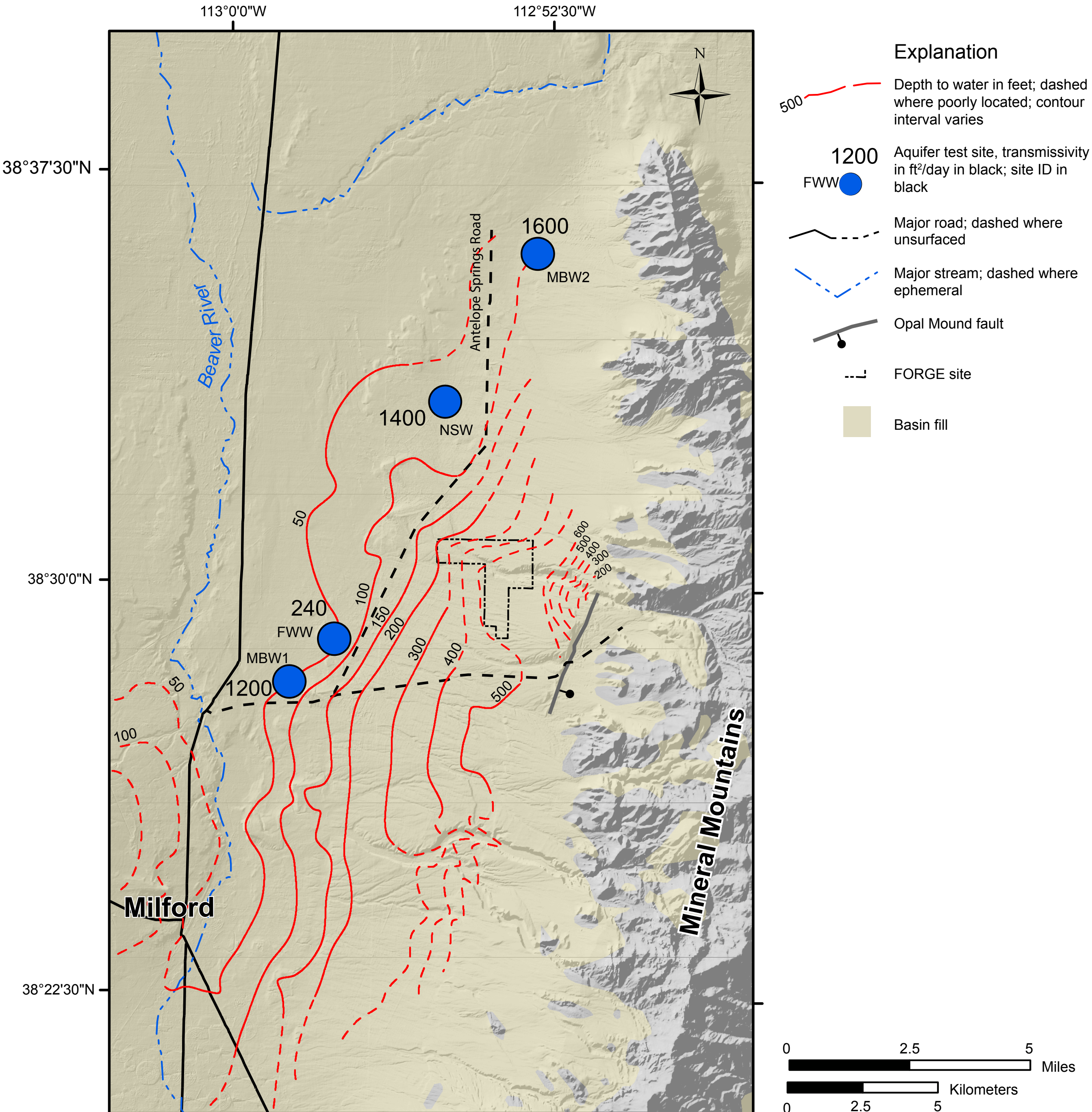

Figure 16. Summary of aquifer test data for the basin fill aquifer. Transmissivity of the basin-fill near the FORGE site ranges from 240 to 1600 ft²/day.

CONCLUSIONS

The groundwater in and around the FORGE deep drill site resides in a shallow unconsolidated basin-fill aquifer that overlies impermeable crystalline basement rock. The water in this aquifer is not potable and is not used for human consumption. Groundwater is currently used in the study area for stock watering at several wells and fire suppression.

Based on compiled water levels for groundwater in the unconsolidated basin-fill aquifer, the potentiometric surface slopes to the west away from the Opal Mound fault. Groundwater depth beneath the FORGE deep drill site is between 200 and 500 feet and at about 5100 feet in elevation. Depth to water in the unconsolidated basin fill, in areas surrounding the FORGE deep drill site, ranges from tens of feet along the valley floor to greater than 500 feet west of the Opal Mound fault. Potential supply wells are located about 2.5 miles southwest from this site, where the depth to groundwater is approximately 150 feet.

The groundwater in the study area represents a mix of geochemically distinct waters that include: 1) Roosevelt Hot Springs upflow, 2) Milford Valley groundwater, and 3) cold upland meteoric groundwater (Mower and Cordova, 1974; Vautaz and Goff, 1987; Kirby, 2012). The thermal water is dominated by Na and Cl, with TDS concentrations greater than 6000 mg/L, Cl/B ~100, and enriched $\delta^{18}O$ values. Most groundwater in the vicinity of the FORGE deep drill site represents a mixture of thermal and basinal waters. Non-thermal groundwaters have TDS concentrations less than 1000 mg/L, Cl/B >200, and stable isotope compositions that plot along the meteoric water line. Comparison of solutes other than Cl implies processes other than or in addition to dilution are required to produce the observed concentrations. The other major solutes may vary due to additional water-rock interactions and or mixing of other sources that are not characterized by this sample set. Groundwater in the geothermal outflow plume shows no evidence of recent recharge; consequently, geothermal upflow may have been recharged in the late Pleistocene.

Groundwater in the study area spans a wide range of chemical compositions from dilute (TDS <500 mg/L) to saline (TDS >6000 mg/L). The springs in the Mineral Mountains discharge dilute Ca-HCO_3 water, whereas at Roosevelt Hot Springs the groundwater is made of Na-Cl thermal water. This thermal water fills the shallow aquifer and disperses westward as it migrates downhill. Increasing dilution with Milford Valley groundwater is reflected in decreasing TDS from east to west. Groundwater TDS concentrations around the FORGE deep drill site range from 2000 to >6000 mg/L TDS, exceeding both the primary and secondary drinking water standards.

In aggregate the available aquifer test data indicate the shallow basin-fill aquifer near the FORGE site has a range of transmissivity between 240 and 1600 ft^2/day, and most shallow basin fill likely has transmissivity near 1000 ft^2/day (Figure 4). This transmissivity is moderate and similar to transmissivities for the basin fill to the south near Milford (Mower and Cordova, 1974) and to the north along the Cove Creek drainage (Kirby, 2012). Supply wells in both of these areas commonly yield several hundred gallons per minute of continuous supply and it is likely that production wells for the Utah FORGE site will have similar yields. Actual water-yielding characteristics for new production wells will be site specific. However, based on the new and existing aquifer test data presented above the transmissivity in the basin-fill aquifer near the FORGE site is sufficient for future production wells needed to supply long-term needs of the project.

ACKNOWLEDGMENTS

This paper and data presented herein were refined by helpful discussions with Rick Allis and Joe Moore. Taylor Boden of the Utah Geological Survey assisted in gathering data during the aquifer test. Mike Lowe (retired) and Hugh Hurlow of the Utah Geological Survey provided timely and thoughtful reviews that improved the presentation and focus of the paper.

REFERENCES

Allis, R.G., Gwynn, M., Hardwick, C., Kirby, S. Moore, J., and Chapman, D., 2015, Re-evaluation of the pre-development thermal regime of Roosevelt Hot Springs geothermal system, Utah: Proceedings, 40th Workshop on Geothermal Reservoir Engineering, Stanford University, California, 12 p.

Allis, R.G., Moore, J.N., Davatzes, N., Gwynn, M., Hardwick, C., Kirby, S., Pankow, K., Potter, S., and Simmons, S.F., 2016, EGS concept testing and development at the Milford, Utah FORGE site: Proceedings, 41st Workshop on Geothermal Reservoir Engineering, Stanford University, California, 13 p.

Bowman, J.R., and Rohrs, D.T., 1981, Light-stable-isotope studies of spring and thermal waters from the Roosevelt Hot Springs and Cove Fort/Sulphurdale Thermal areas and of clay minerals from the Roosevelt Hot Springs thermal area: Topical Report, U.S. Department of Energy/Division of Geothermal Energy, contract number DE-AC07-80ID12079, 40 p.

Capuano, R., and Cole, D.R., 1982. Fluid-mineral equilibria in a hydrothermal system, Roosevelt Hot Springs, Utah: Geochimica et Cosmochemica Acta, v. 46, p. 1353–1364.

Clark, I., and Fritz, P., 1997, Environmental isotopes in hydrogeology: New York, Lewis Publishers, 328 p.

Craig, H., 1961, Isotopic variation in meteoric waters: Science, v. 133, p. 1702–1703.

Coleman, D.S., Bartley, J.M., Walker, J.D., Price, D.E., and Friedrich, A.M., 1997, Extensional faulting, footwall deformation and plutonism in the Mineral Mountains, southern Sevier Desert, *in* Link, P.K., and Kowalis, B.J., editors, Mesozoic to recent geology of Utah: Brigham Young University Geology Studies, v. 42, part 2, p. 203–233.

Domenico, P.A., and Schwartz, F.W., 1997, Physical and chemical hydrogeology: New York, John Wiley and Sons, 506 p.

Duffield, G.M., 2007, AQTESOLVE: Hydrosolve Inc., Reston, Virginia.

Faulder, D.D., 1991, Conceptual geologic model and native state model of the Roosevelt Hot Springs hydrothermal system, *in* Ramey, H.J. Jr., Horne, R.N., Kruger, P., Miller, F.G., Brigham, W.E., Cook, J.W., editors, Proceedings of the Sixteenth Workshop on Geothermal Reservoir Engineering: Stanford, California, Stanford University, p. 131–142.

Glenn, W.E., and Hulen, J.B., 1979, Interpretation of well log data from four drill holes at the Roosevelt Hot Springs KGRA: DOE Earth Science Laboratory Report, Salt Lake City, University of Utah, 74 p.

Hardwick C.L., Gwynn, M., Allis, R., Wannamaker, P., and Moore, J., 2016, Geophysical signatures of the Milford, Utah FORGE site, *in* Proceedings, 41st Workshop on Geothermal Reservoir Engineering, Stanford University, Stanford, California, 11 p.

Hardwick, C., Hurlbut, W., and Gwynn, M., 2019, Geophysical surveys of the Milford, Utah, FORGE site—gravity and TEM, *in* Allis, R., and Moore, J.N., editors, Geothermal characteristics of the Roosevelt Hot Springs system and adjacent FORGE EGS site, Milford, Utah: Utah Geological Survey Miscellaneous Publication 169-F, 15 p., https://doi.org/10.34191/MP-169-F.

Hintze, L.H., and Davis, F.D., 2003, The geology of Millard County, Utah: Utah Geological Survey Bulletin 133, 305 p.

Kehew, A.E., 2000, Applied chemical hydrogeology: Upper Saddle River, New Jersey, Prentice Hall, 368 p.

Kendall, C., and Coplen, T.B., 2001, Distribution of oxygen-18 and deuterium in river waters across the United States: Hydrological Processes, v. 15, p. 1363–1393.

Kirby, S.M., 2012, Geologic and hydrologic characterization of regional nongeothermal groundwater resources in the Cove Fort area, Millard and Beaver Counties, Utah: Utah Geological Survey Special Study 140, 46 p.

Kirby, S.M., 2019, Revised mapping of bedrock geology adjoining the Utah FORGE site, *in* Allis, R., and Moore, J.N., editors, Geothermal characteristics of the Roosevelt Hot Springs system and adjacent FORGE EGS site, Milford, Utah: Utah Geological Survey Miscellaneous Publication 169-A, 6 p., 2 plates, scale 1:24,000, https://doi.org/10.34191/MP-169-A.

Mason, J.L., 1998, Groundwater hydrology and simulated effects of development in the Milford area, an arid basin in southwestern Utah: U.S. Geological Survey Professional Paper 1409-G, 69 p.

Miller, J., Allis, R., and Hardwick, C., 2019, Interpretation of seismic reflection surveys near the FORGE enhanced geothermal systems site, Utah, *in* Allis, R., and Moore, J.N., editors, Geothermal characteristics of the Roosevelt Hot Springs system and adjacent FORGE EGS site, Milford, Utah: Utah Geological Survey Miscellaneous Publication 169-H, 13 p., https://doi.org/10.34191/MP-169-H.

Moore, J.N., and Nielsen, D.L., 1994, An overview of geology and geochemistry of the Roosevelt Hot Springs geothermal area, *in* Blackett, R.E., and Moore, J.N., editors, Cenozoic geology and geothermal systems of southwestern Utah: Utah Geological Association Publication 23, p. 25–36.

Mower, R.W., 1978, Hydrology of the Beaver Valley area, Beaver County, Utah, with emphasis on groundwater: State of Utah Department of Natural Resources Technical Publication No. 63, 90 p.

Mower, R.W., and Cordova, R.M., 1974, Water resources of the Milford area, Utah, with emphasis on groundwater: State of Utah Department of Natural Resources Technical Publication No. 43, 106 p.

Nielson, D.L., Evans, S.H., and Sibbett, B.S., 1986, Magmatic, structural, and hydrothermal evolution of the Mineral Mountains intrusive complex, Utah: Geological Society of America Bulletin, v. 97, p. 765–777.

Rowley, P.D., Vice, G.E., McDonald, R.E., Anderson, J.J., Machette, M.N., Maxwell, D.J., Ekren, E.B., Cunningham, C.G., Steven, T.A., and Wardlaw, B.R., 2005, Interim geologic map of the Beaver 30′ x 60′ quadrangle, Beaver, Piute, Iron, and Garfield Counties, Utah: Utah Geological Survey Open-File Report 454, 27 p., 1 plate, scale 1:100,000.

Saltus, R.W., and Jachens, R.C., 1995, Gravity and basin-depth maps of the Basin and Range Province, western United States: U.S. Geological Survey Map GP-1012, scale 1:2,500,000.

Simmons, S., Kirby, S., Jones, C., Moore, J., Allis, R., Brandt, A., and Nash, G., 2016, The geology, geochemistry, and geohydrology of the FORGE deep well site, Milford, Utah: Proceedings, 41st Workshop on Geothermal Reservoir Engineering, Stanford University, California, 10 p.

Vuataz, F.D., and Goff, F., 1987, Water geochemistry and hydrogeology of the shallow aquifer at Roosevelt Hot Springs, southern Utah—a hot dry rock prospect: Los Alamos National Laboratory, contract report LA-11160-HDR, 63 p.

U.S. Geological Survey, 2017, National Water Information System database: Online, https://waterdata.usgs.gov/nwis, accessed December 2015.

GEOPHYSICAL SURVEYS OF THE MILFORD, UTAH, FORGE SITE: GRAVITY AND TEM

by Christian Hardwick, Will Hurlbut, and Mark Gwynn

Utah Geological Survey, Salt Lake City, Utah

Miscellaneous Publication 169-F
Utah Geological Survey
a division of
UTAH DEPARTMENT OF NATURAL RESOURCES

This paper is part of *Geothermal Characteristics of the Roosevelt Hot Springs System and Adjacent FORGE EGS Site, Milford, Utah*. https://doi.org/10.34191/MP-169

Bibliographic citation:

Hardwick, C., Hurlbut, W., and Gwynn, M., 2019, Geophysical surveys of the Milford, Utah, FORGE site—gravity and TEM, *in* Allis, R., and Moore, J.N., editors, Geothermal characteristics of the Roosevelt Hot Springs system and adjacent FORGE EGS site, Milford, Utah: Utah Geological Survey Miscellaneous Publication 169-F, 14 p., https://doi.org/10.34191/MP-169-F.

GEOPHYSICAL SURVEYS OF THE MILFORD, UTAH, FORGE SITE: GRAVITY AND TEM

by Christian Hardwick, Will Hurlbut, and Mark Gwynn

ABSTRACT

Basement geometry of the Milford, Utah, Frontier Observatory for Research in Geothermal Energy (FORGE) study area has been better defined by augmenting legacy data with 417 new, high-precision gravity measurements using a dynamic grid layout and 34 transient electromagnetic (TEM) soundings in transects. The FORGE site is situated over Tertiary-Quaternary granitic intrusions and Precambrian gneiss that crop out in the Mineral Mountains. These same rock types are also found at 3 km depth in the Acord-1 well 10 km to the west of the site, near the center of Milford Valley. Modeling of the 30 mGal gravity low, caused by basin fill overlying the granite, was accomplished using a decreasing density contrast with increasing depth. This framework was based primarily on the Acord-1 and FORGE 58-32 wells, geophysical logs, laboratory measured physical properties, and local geologic information. Two-dimensional (2D) gravity models indicate that the deepest part of the basin, approximately 4.8 km in depth, is located on the west side of the valley, 12 km from the edge of the FORGE site boundary. Basin geometry from the 2D gravity modeling shows a steeply dipping interface on the east side of Milford Valley north of the FORGE site. Electrical resistivity models from the TEM data do not indicate any anomalous structure near the surface within the study area. A TEM transect through the FORGE site delineates the depth to the groundwater table which varies from 60 to 150 m. South of the FORGE site, another TEM transect crosses the Opal Mound fault (OMF), where a distinct resistivity contrast shows conductive material to the east of the fault that is interpreted to be primarily an effect of geothermal fluids that are prevented from flowing to the west by the fault. Electrical resistivity values along the Ranch Canyon transect are relatively high compared to those to the north. The sediment-basement interface below the FORGE site appears to be moderately dipping (about 25˚) to the west, which is consistent with interpretations of 2D and 3D seismic sections.

INTRODUCTION

Geophysical data collected during the 2017 field season have been used in a preliminary characterization of the Milford, Utah, Frontier Observatory for Research in Geothermal Energy (FORGE) site in southeastern Utah. A total of 34 new transient electromagnetic method (TEM) soundings and 417 gravity stations were added in Phase 2 of the FORGE project (Figures 1 and 2). TEM soundings are sensitive to electrical properties of the subsurface, which are manifested by attenuation of the magnetic field. TEM surveys can help delineate shallow (300–400 m) subsurface features if they have a notable resistivity contrast relative to adjacent material. The gravity field is sensitive to density distribution in the subsurface which can help us delineate structures such as faults or large buried objects underground. The aim of this geophysical work is to locate and identify subsurface structures that could impact the FORGE site operations as well as obtain a better understanding of the local geology.

TEM SURVEY AND METHODS

We conducted a TEM geophysical survey to better define subsurface structures and features near the FORGE site (Figure 2). TEM is an active-source method that measures the attenuation signal of induced magnetic fields corresponding to changes in the electrical properties in the subsurface. TEM measurements were made at 34 unique locations within the FORGE study area using an ABEM WalkTEM ground loop system fitted with a 40-x-40-m transmitter antenna as well as high- and low-frequency receiver antenna coils capable of simultaneous recording. Repeat measurements were carried out at specific locations to ensure data consistency and quality for the duration of the field survey period. The time spent at each station location was less than one hour with two to three measurements completed during that time as well as subsequent checking of the field data. All TEM stations yielded high-quality data with excellent signal-to-noise ratio except for one station that was deemed less useful due to very conductive surface conditions and, perhaps, cultural noise (utility lines, etc.) at the site location.

After initial data processing, one-dimensional (1D) inversion models for every station were created (Auken et al., 2015) and improved by screening data bands until data fit was satisfactory. Using 1D TEM models and a Digital Elevation Model (DEM),

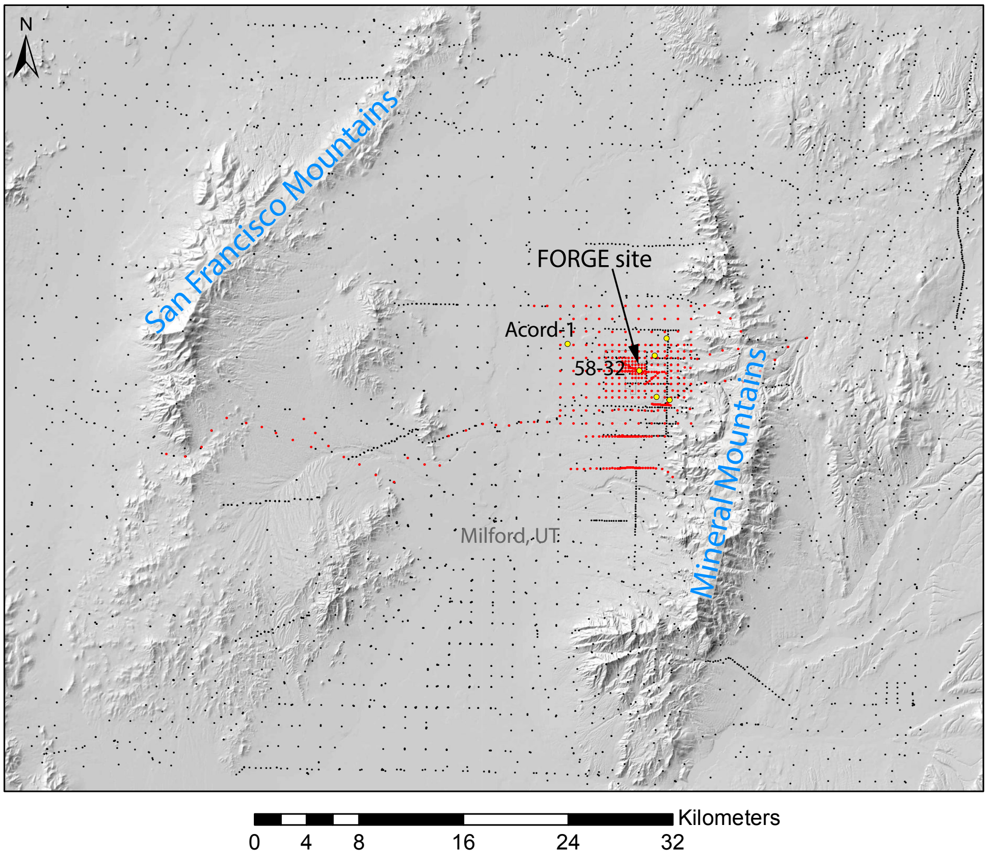

Figure 1. *Shaded elevation map of Milford Valley area showing coverage of new gravity stations (red dots), legacy gravity data (black dots), and control wells (yellow dots).*

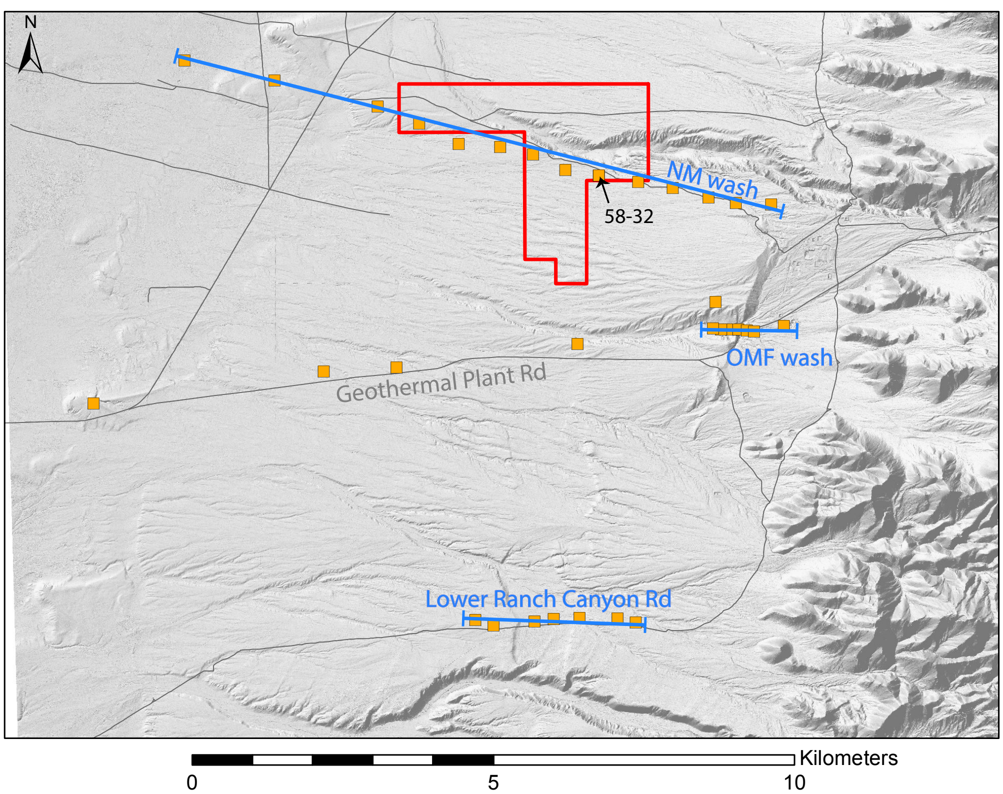

Figure 2. *Map of TEM station locations (orange squares) and transects (blue lines) for the FORGE study area (outlined in red). The transects Negro Mag (NM) wash, Opal Mound fault (OMF) wash, and Lower Ranch Canyon Rd are shown.*

pseudo two-dimensional (2D) sections of resistivity were created to aid interpretations. The pseudo 2D sections display the 1D resistivity and are constrained using the Depth of Investigation (DOI) parameter (see Spies, 1989; Christiansen and Auken, 2012). DOI is unique for each station, relies on the physical properties of subsurface material, and indicates the maximum depth of resolution with respect to modeling. When extending modeling deeper than the DOI, confidence in the resulting 1D and 2D models will subsequently decrease with increasing depth.

TEM RESULTS

The DOI values for the study area range from approximately 100 m to 400 m with an average of 300 m. The pseudo 2D sections (Figures 3 to 5) show the 1D model results from the TEM transects shown in Figure 2, as well as interpolated electrical resistivity values between the 1D models (to be used only as a visual aid). Background resistivity values within the study area range from 10 to 1000 Ohm·m, which are inferred to be the signature of fine, clay-rich valley fill (low resistivity, approximately 10 to 30 Ohm·m) as well as coarser fill on the alluvial fans consisting of sand and gravel that are closer to their sources (high resistivity, 100–1000 Ohm·m).

Resistivity model interpretations provide insight to the subsurface conditions at three areas around the FORGE site (Figure 2). Figure 3 shows the NM wash transect, which is the longest of the sections, starting in the valley and terminating near the north end of the Opal Mound fault (OMF). No significant structures were detected by TEM data on this transect. The groundwater table is well defined at the boundary where resistivity decreases from 100 to 10 Ohm·m (green-yellow transition). On the eastern end of the transect, low resistivities are detected near the surface, which are interpreted to be shallow hydrothermal outflow from Roosevelt Hot Springs (RHS).

Figure 4 shows the OMF wash transect, which crosses the OMF from west to east between stations FM19 and FM20. There is a resistivity jump between these stations from 40–50 Ohm·m to 10–20 Ohm·m. The lower resistivity values are likely due to conductive pore fluids consistent with the RHS hydrothermal system (Archie, 1942). The OMF appears to act as a flow barrier, keeping low-resistivity geothermal fluids from flowing westward. FM22, the farthest east sounding, detects shallow, higher-resistivity layers of more than 100 Ohm·m. These layers are interpreted as coarse sand and gravel near their source in the Mineral Mountains.

Figure 5 shows the Lower Ranch Canyon Road transect, where resistivity values are much higher than the northern transects. The resistivity models show no anomalous structures in the shallow subsurface and the groundwater table is detected between 1550 and 1600 m elevation above sea level (blue-green transition). The background resistivity ranges from 100 to 1000 Ohm·m in this area, which is attributed to its proximity to igneous source rocks of very high resistivity (1000 to 100,000 Ohm·m when in an unweathered state). Rapid burial of the eroded material could slow weathering and result in higher resistivity values. FM09 displays a resistive body at approximately 200–250 m depth which we believe is a result of noisy data and it is not interpreted to be real.

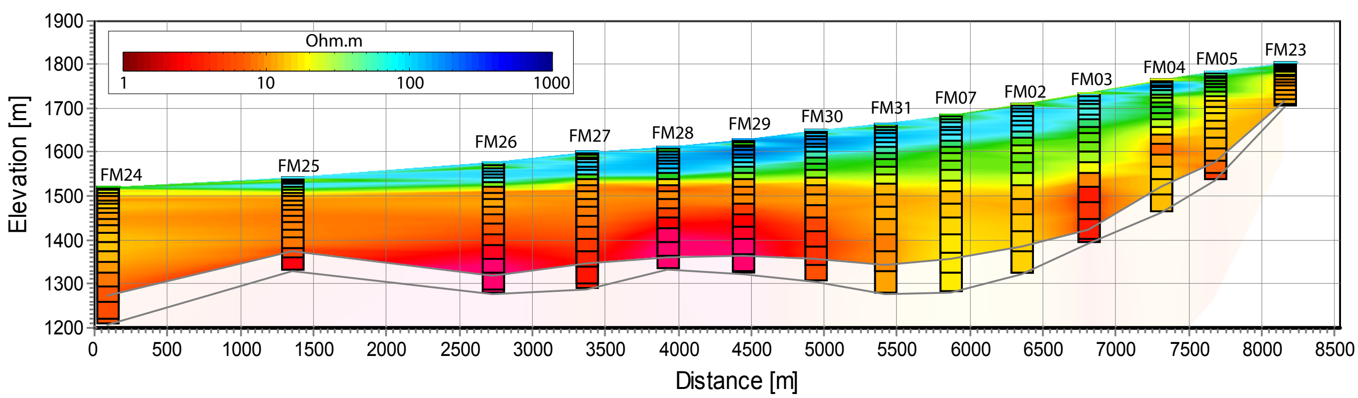

Figure 3. *Resistivity models shown as a pseudo-section for the NM wash transect. TEM station names are indicated; FORGE well 58-32 co-located with station FM07 and the gray lines show the DOI parameter. The groundwater table corresponds to the top of the 20 Ohm·m layer (yellow).*

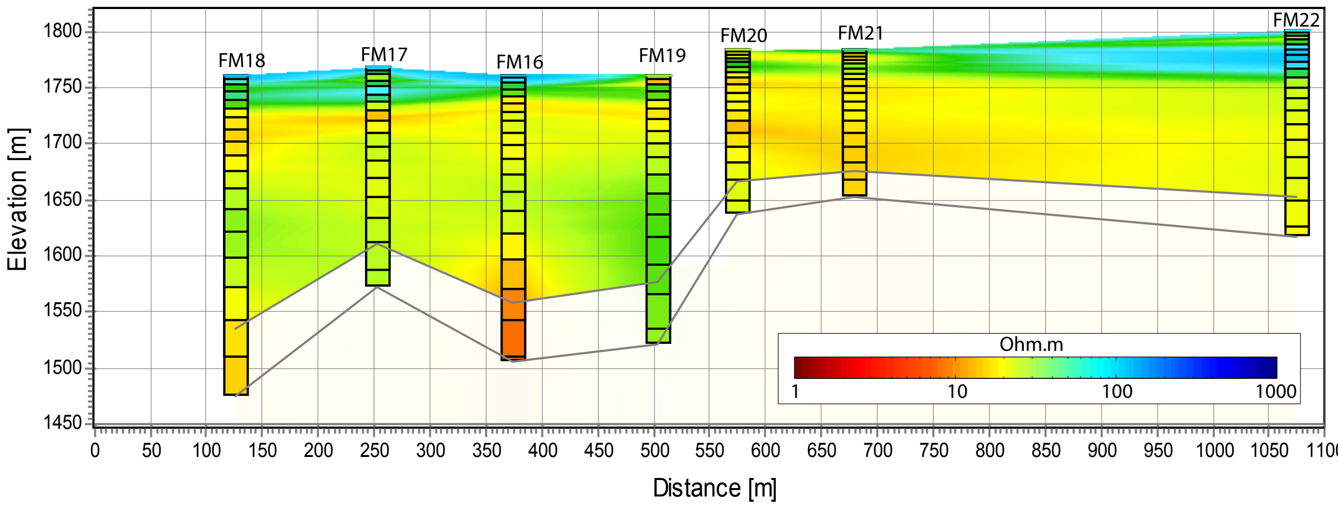

Figure 4. *Resistivity models shown as a pseudo-section for the OMF wash transect. TEM station names are indicated and gray lines show the DOI parameter. Horizontal resistivity contrasts are captured on opposite sides of the OMF; on the east side (FM20–FM22) the values are more conductive due to hydrothermal pore waters compared to the west side (FM16–FM19) where hydrothermal fluids are absent. This suggests the OMF acts as a barrier to fluid flow.*

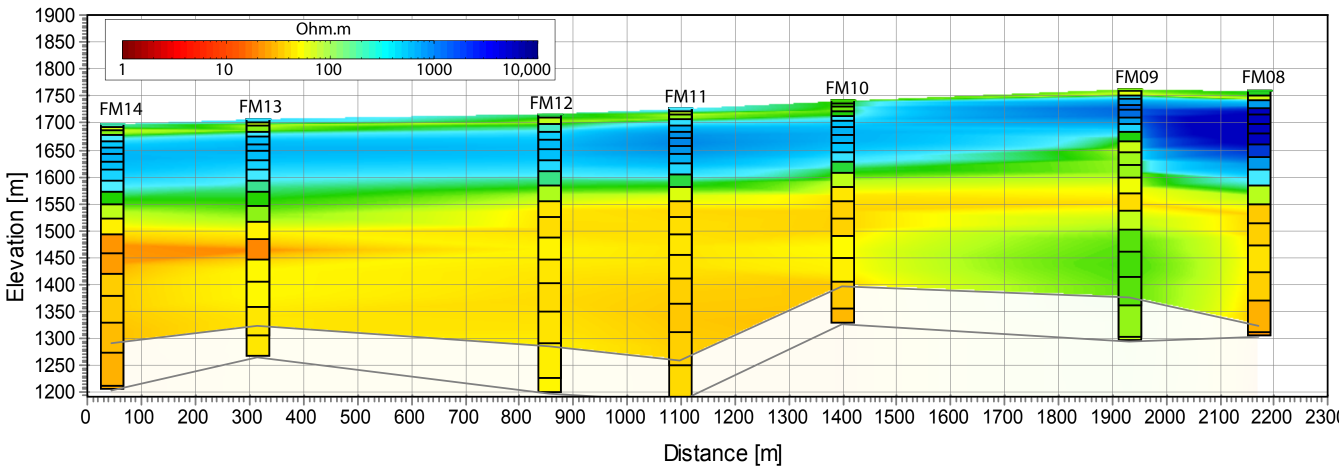

Figure 5. *Resistivity models shown as a pseudo-section for the Lower Ranch Canyon Road transect. TEM station names are indicated and gray lines show the DOI parameter. The groundwater table corresponds to the top of the 100 Ohm•m layer (green) observed between 1550 and 1600 m elevation.*

GRAVITY SURVEY AND METHODS

A total of 417 new gravity stations were combined with 3389 legacy gravity stations to achieve better coverage near the proposed drill sites and in the basin (Figure 1). A varied-offset survey grid was utilized for gravity measurements made near the proposed drill sites. Station spacing started at 250 m near the FORGE area and then stepped to 500 m and 1 km. This spacing keeps the data density high for better resolution of 3D gravity inversion models closer to the FORGE area while still providing good resolution farther from the site. Legacy gravity data is sourced from Pan American Center for Earth and Environmental Studies (PACES). Field measurements were made using two Scintrex CG-5 gravimeters following the methods of Gettings et al. (2008); we used a 10-minute time series and reoccupation of local bases only. Elevation control on most of the stations is better than 0.1 m, which was achieved through post-processing of high-precision GPS data, resulting in a gravity accuracy of better than 0.03 mGal. The Complete Bouguer Gravity Anomaly (CBGA) was computed using a reduction density of 2.67 g/cm^3 and the formulas outlined by Hinze et al. (2005). Horizontal gravity gradient fields were computed, followed by 2D gravity models of five transects using the Semi-Automated Marquardt Inversion code (SAKI; Webring, 1985). Density-depth relationships for basin-fill and rock densities were taken from existing well logs and laboratory-measured physical rock properties of field samples and drill cuttings from the FORGE well 58-32 (Gwynn et al., 2019). Initial models and densities were calibrated using wells containing both density logs and basement depth values. Calibrated density values were then used in subsequent 2D models. The basement depth values were taken from 2D gravity and 1D Magnetotelluric (MT) models (Hardwick et al., 2015) and well data, and then used to develop a depth-to-basement map.

RESULTS

The CBGA (Figures 6 and 7) shows that the dominant basin signal trends north-south. This prominent, north-trending, -30-mGal gravity low is approximately 16 km wide and is bounded by gravity highs to the east and west. 2D gravity models (Figures 8–12), transects of which are shown on Figure 6, were chosen based on the high quantity of data along the line (providing higher confidence in the gravity field values). The models use the x-coordinate of the FORGE 58-32 well as the reference in distance along each transect.

Looking at the 2D models from north to south, the steepest side of the Milford basin shifts from the east to the west side (compare Figures 8 and 10), which is suggested by the shaded CBGA map (Figure 7). Tighter contouring indicates relatively larger changes in the gravity field, which are interpreted as more steeply dipping interfaces between the less dense basin fill and higher density bedrock. There does not appear to be any significant basement structures based on the results of widely spaced 2D gravity modeling near the FORGE area. However, a subtle feature to the west of the FORGE area was observed in the horizontal gravity gradient (Figure 13), indicating slight changes in the gravity field (i.e., subsurface density changes or basement topography). This feature may be the gravity signature of the paleo valley in the surface of the granite delineated by the 3D seismic reflection survey interpretations (Miller and others, 2019). Future 3D gravity modeling and integration with the 3D seismic reflection interpretation may be able to better map this feature. Figure 14 shows the composite model of the Milford basin developed using gravity survey data, 1D MT models, and well data.

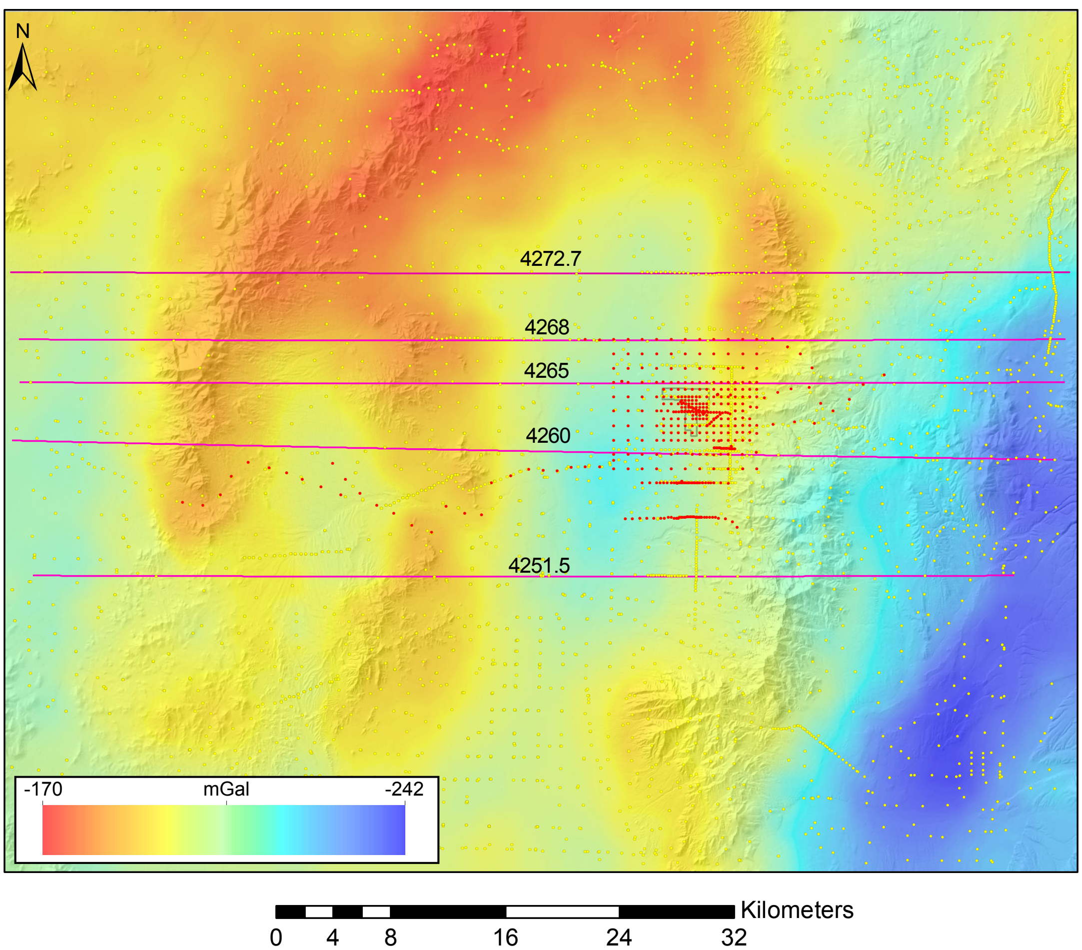

Figure 6. *The CBGA for the Milford, Utah, FORGE site overlain on shaded topography. New gravity stations are shown as red dots and the legacy gravity data area is shown as yellow-filled dots. Magenta lines are 2D model transects (see Figures 8 through 12) labeled by UTM northing in units of km.*

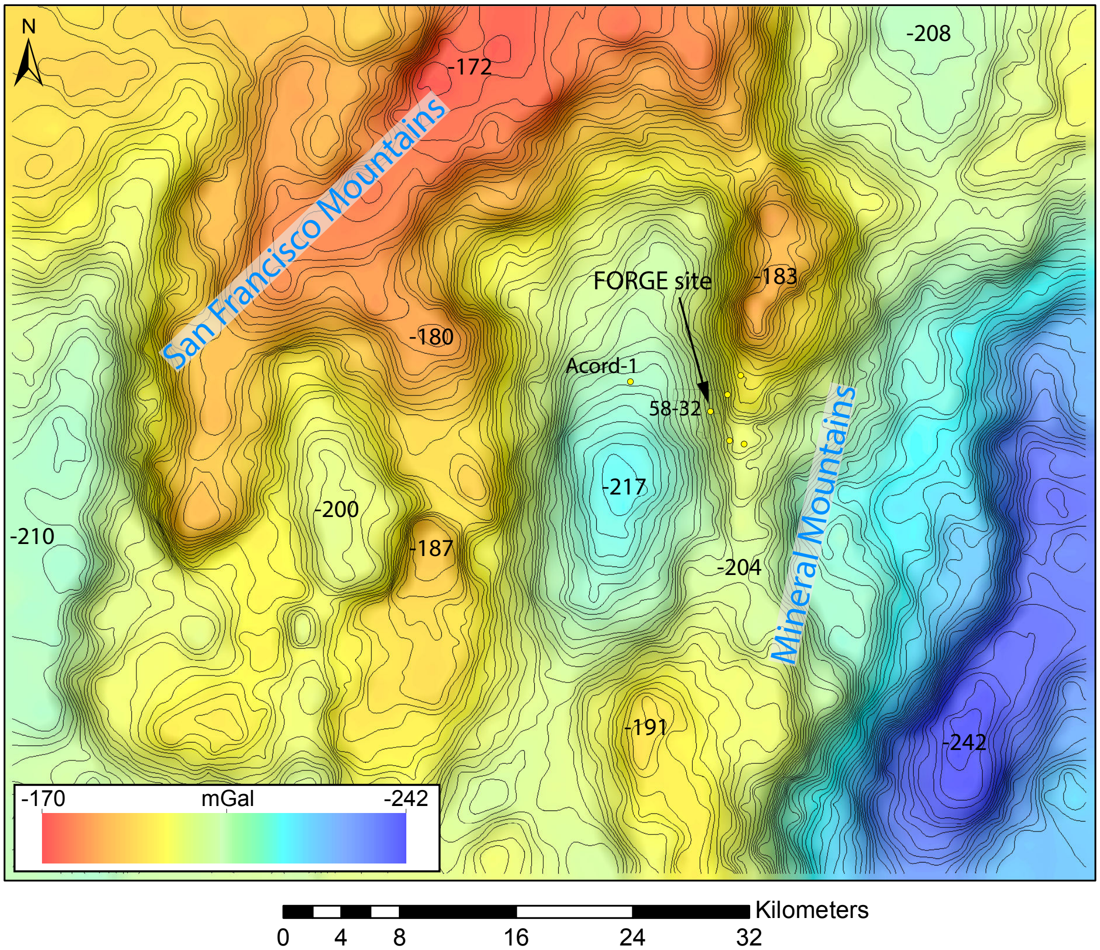

Figure 7. *Map of CBGA with shading generated from the horizontal gravity gradient. Anomaly values are in units of mGals and contours are in 1 mGal increments.*

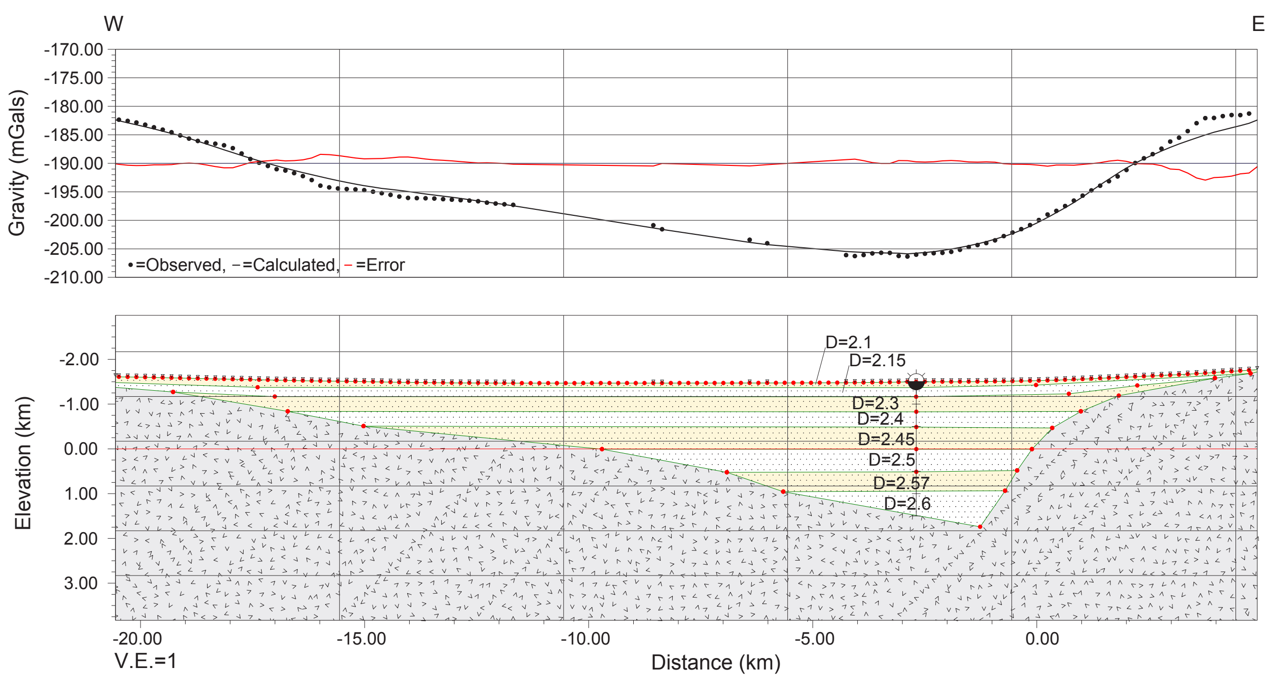

Figure 8. *2D model transect 4272.7 (see Figure 6). The model shows asymmetric basin geometry, with a gentle slope on the west side and steep slope on the east side. The maximum depth of the basin model from ground surface is 3241 m at the eastern end. Density values of the layers are given in g/cm^3.*

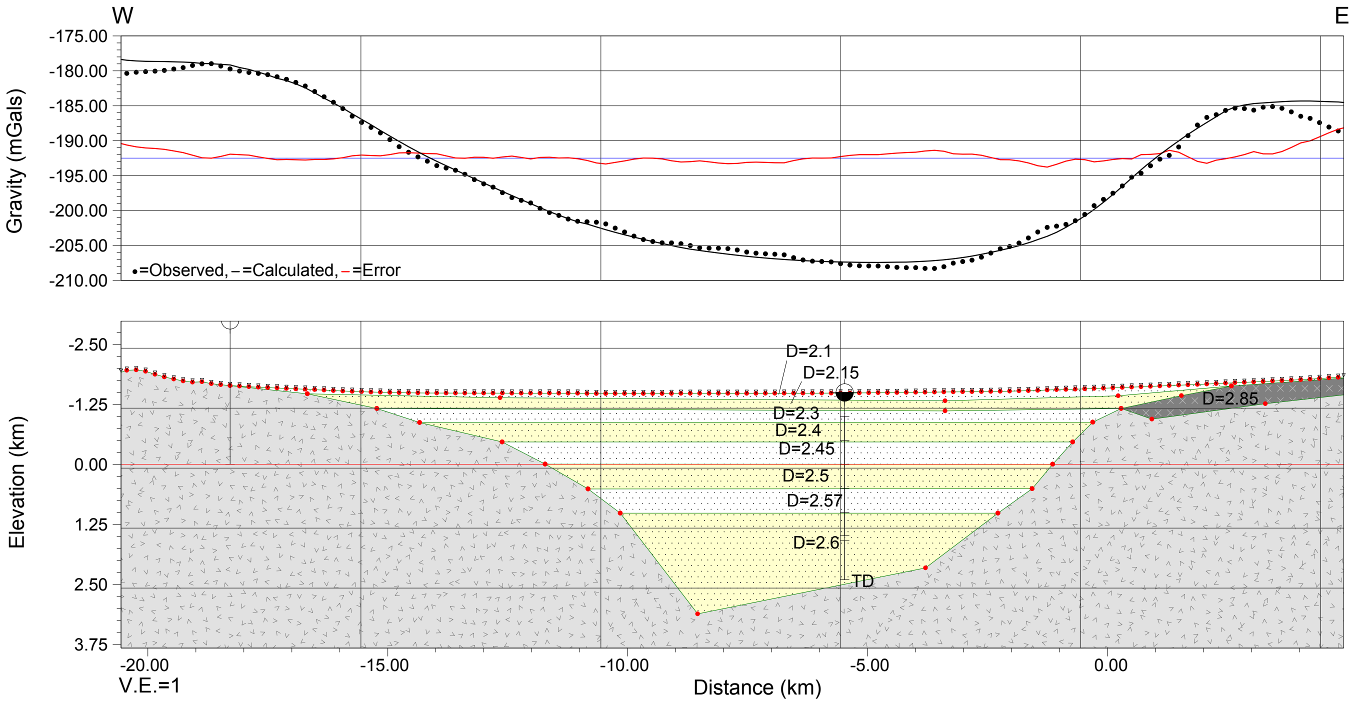

Figure 9. *2D model transect 4268 (see Figure 6). The model shows a somewhat asymmetric basin geometry, with a steep, convex-shaped slope on the west side and moderately steep slope on the east side. The maximum depth of the basin model from ground surface is 4596 m located more central in the basin. Density values of the layers are given in g/cm*^{3}.

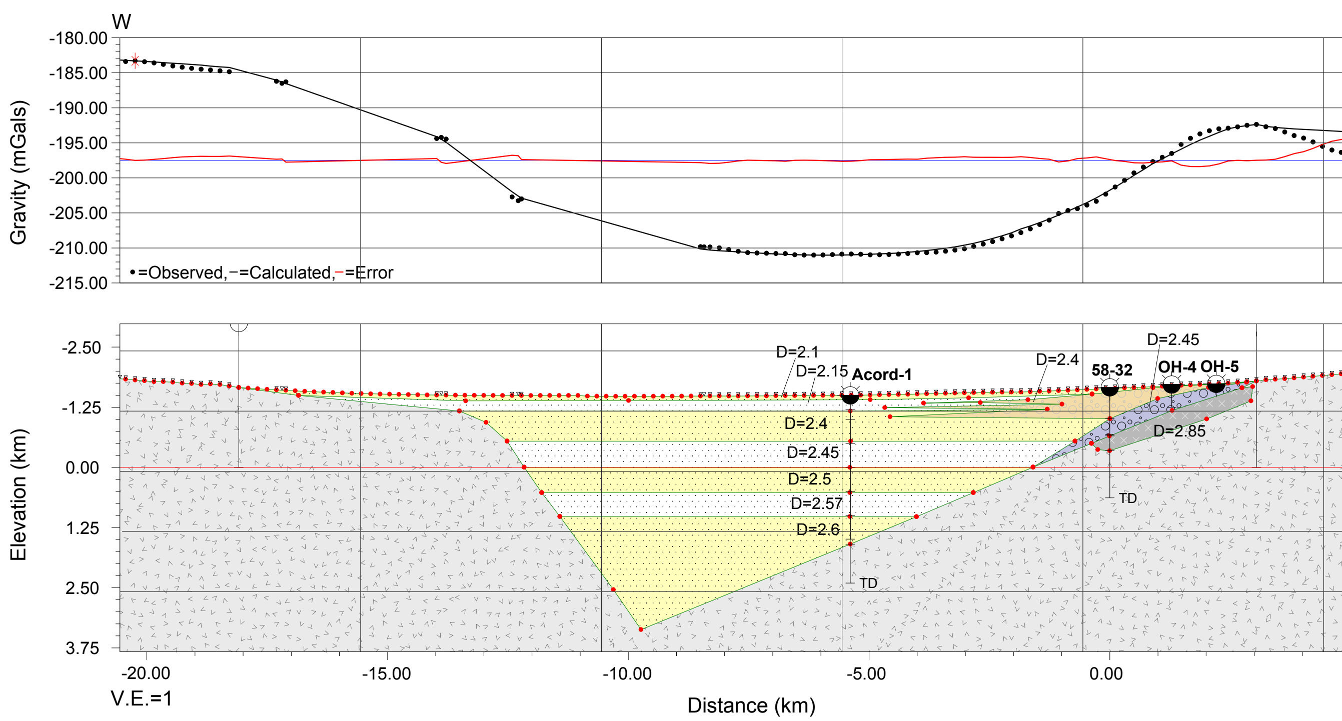

Figure 10. *2D model of transect 4265 (see Figure 6). The model shows an asymmetric basin geometry, with a steep slope on the west side and a moderate slope on the east side. The maximum depth of the basin model from ground surface is 4742 m located west of the center of the basin. Wells Acord-1, 58-32, OH-4, and OH-5 were used as control points for depth and density. Density values of the layers are given in g/cm*^{3}.

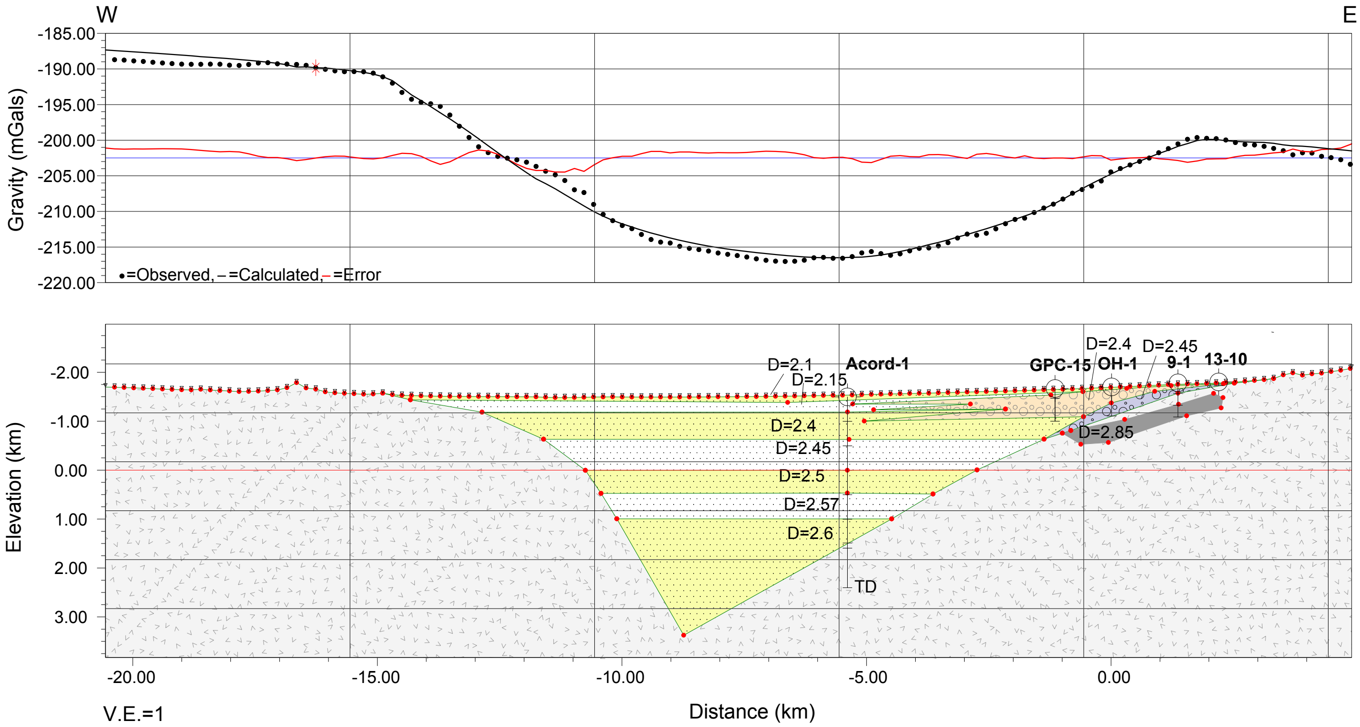

Figure 11. *2D model of transect 4260 (see Figure 6). The model shows an asymmetric basin geometry, with a steep slope on the west side and a moderate slope on the east side. The maximum depth of the basin model from ground surface is 4872 m located west of the center of the basin. Wells 9-1, 13-10, Acord-1, GPC-15, and OH-1 were used as control points for depth and density. Density values of the layers are given in g/cm³.*

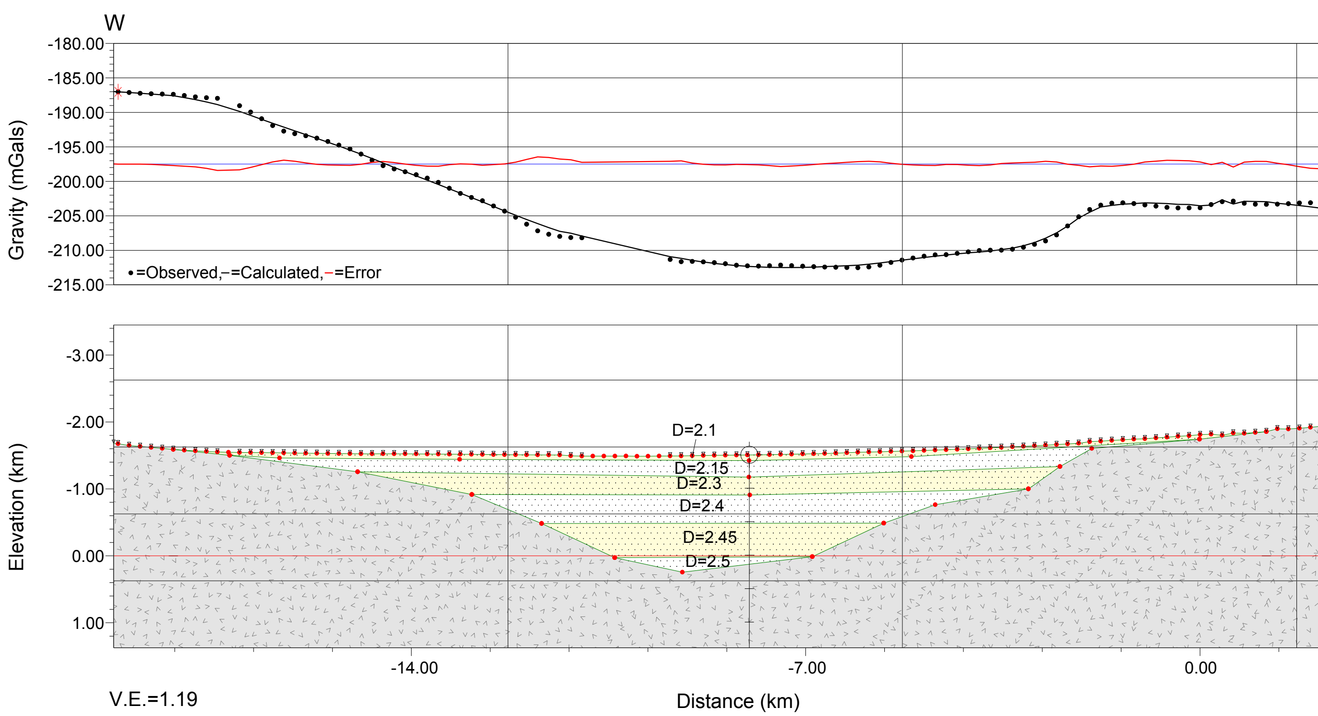

Figure 12. *2D model of transect 4251.5 (see Figure 6). The model shows near symmetric basin geometry, with gradual slopes on the west and east sides. The maximum depth of the basin model from ground surface is 1735 m located near the center of the basin. Density values of the layers are given in g/cm³.*

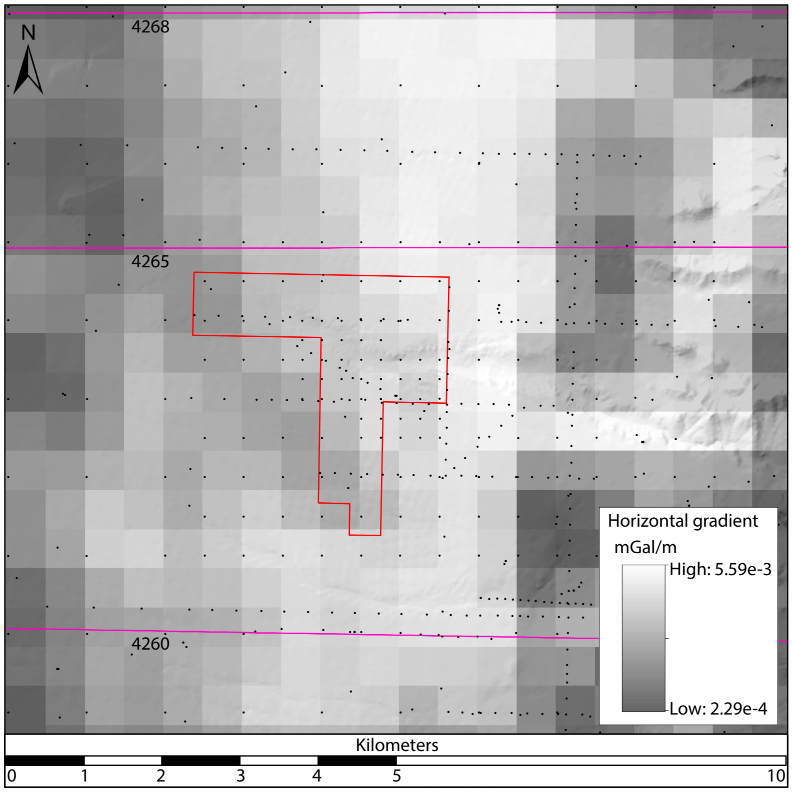

Figure 13. *Map of the local horizontal gravity gradient. The FORGE site outline is red, the 2D gravity transects are in magenta, and the gravity stations are black dots. A feature in the gradient is observed trending NW-SE to the west of the FORGE site outline.*

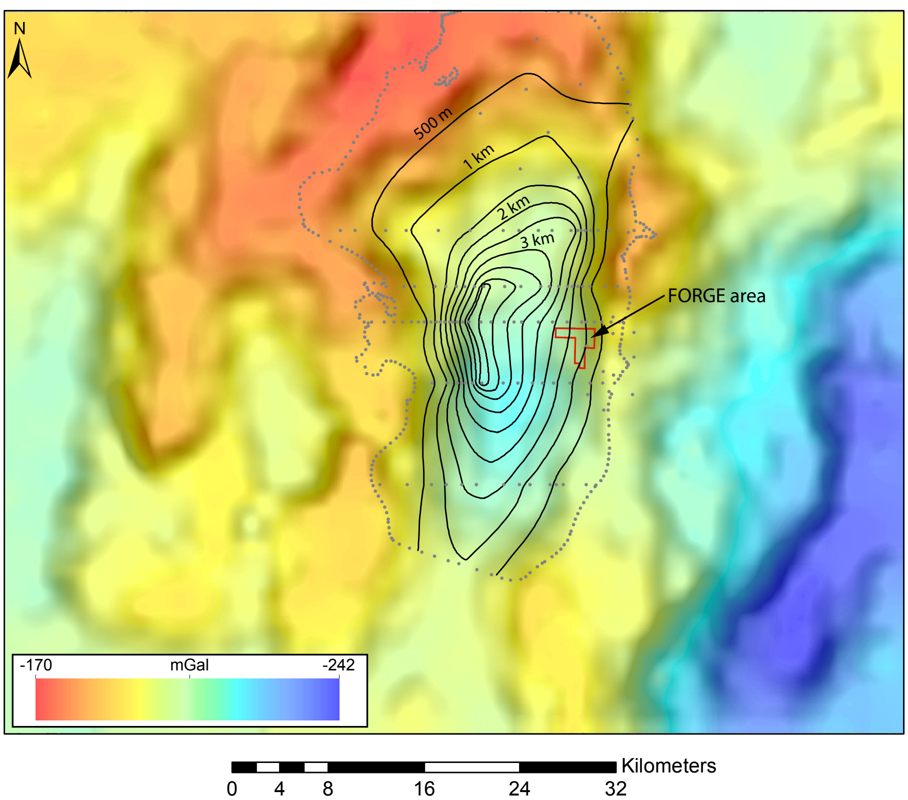

Figure 14. *Basement depth map for the Milford, Utah, FORGE site. The base map is colored by CBGA values with shading generated from the horizontal gravity gradient and overlain with contours of basement depth in Milford Valley. Contours are in 500 m increments and basement control points (gray dots) are from 2D gravity models, 1D MT models, and zero-depth picks on, or adjacent to, outcrop. The deepest part of the basin model is on the western side of the valley.*

QUANTIFICATION OF UNCERTAINTY

In gravity surveying, we consider all the following for sources of error/uncertainty: equipment precision, data processing errors, GPS precision, terrain corrections, and anomaly corrections. The Scintrex CG-5 autograv gravimeter has a measurement precision of 0.001 mGal and accuracy better than 0.005 mGal. The CG-5 gravimeter measures relative gravity using a base station loop which requires post-processing to obtain observed gravity values. Our post-processing of the FORGE gravity data resulted in 0.001 mGal of RMS error. The gravity survey conducted by the Utah Geological Survey (UGS) used high-precision GPS equipment that consistently achieved better than 0.10 m in elevation control (Figure 15, left panel, and Figure 16). Terrain corrections are computed by hand to within 0.001 mGal for each station. The gravity anomaly corrections are primarily dependent on elevation but are slightly affected by the reduction density value (assumed density of the average crustal density for the study area). The reduction density value plays a larger role in gravity modeling.

Intrinsic to the Earth's gravity field, the vertical gradient is much larger than the horizontal gradient. The vertical gradient, for example, can be approximated with the Free Air anomaly equal to 0.3086 mGal/m (formulation in Hinze et al., 2005). The horizontal gradient in the FORGE study area is calculated between 2 and 5 µGals/m, which is two orders of magnitude smaller than the vertical gradient. Because of this, the major factor affecting the accuracy of gravity measurements is elevation control. High-confidence elevation control (more difficult to achieve) is more important than horizontal control when making gravity measurements.

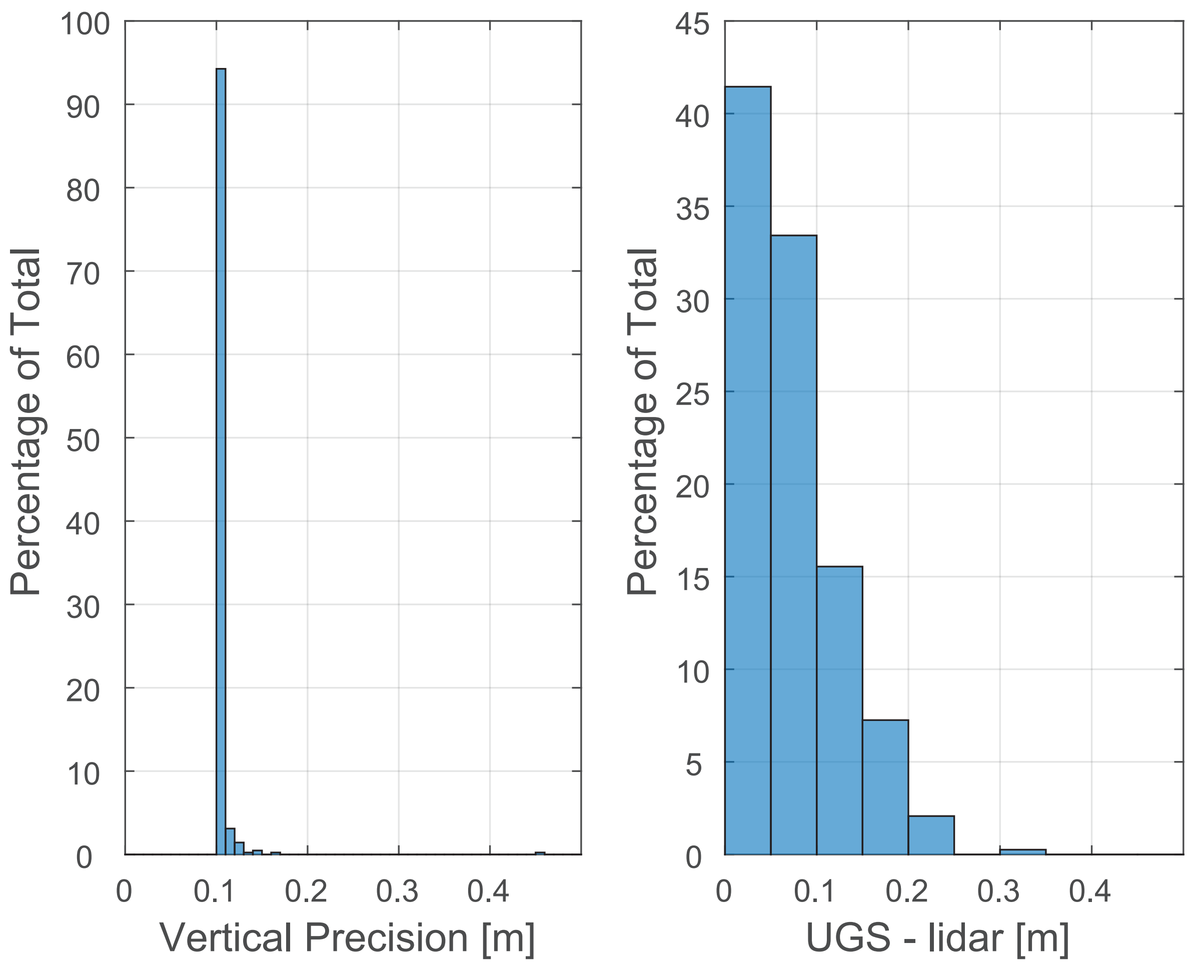

Figure 15. *Histograms of UGS gravity station elevation data. The left panel shows the vertical precision of UGS-acquired data. Vertical precision is 0.1 m or better at 394 of 418 positions (94.26%). The right panel shows differences between a subset of overlapping UGS-acquired elevation data and the lidar data collected for FORGE, where 291 of 388 UGS-acquired elevation values (75%) are within 0.10 m of the FORGE lidar values.*

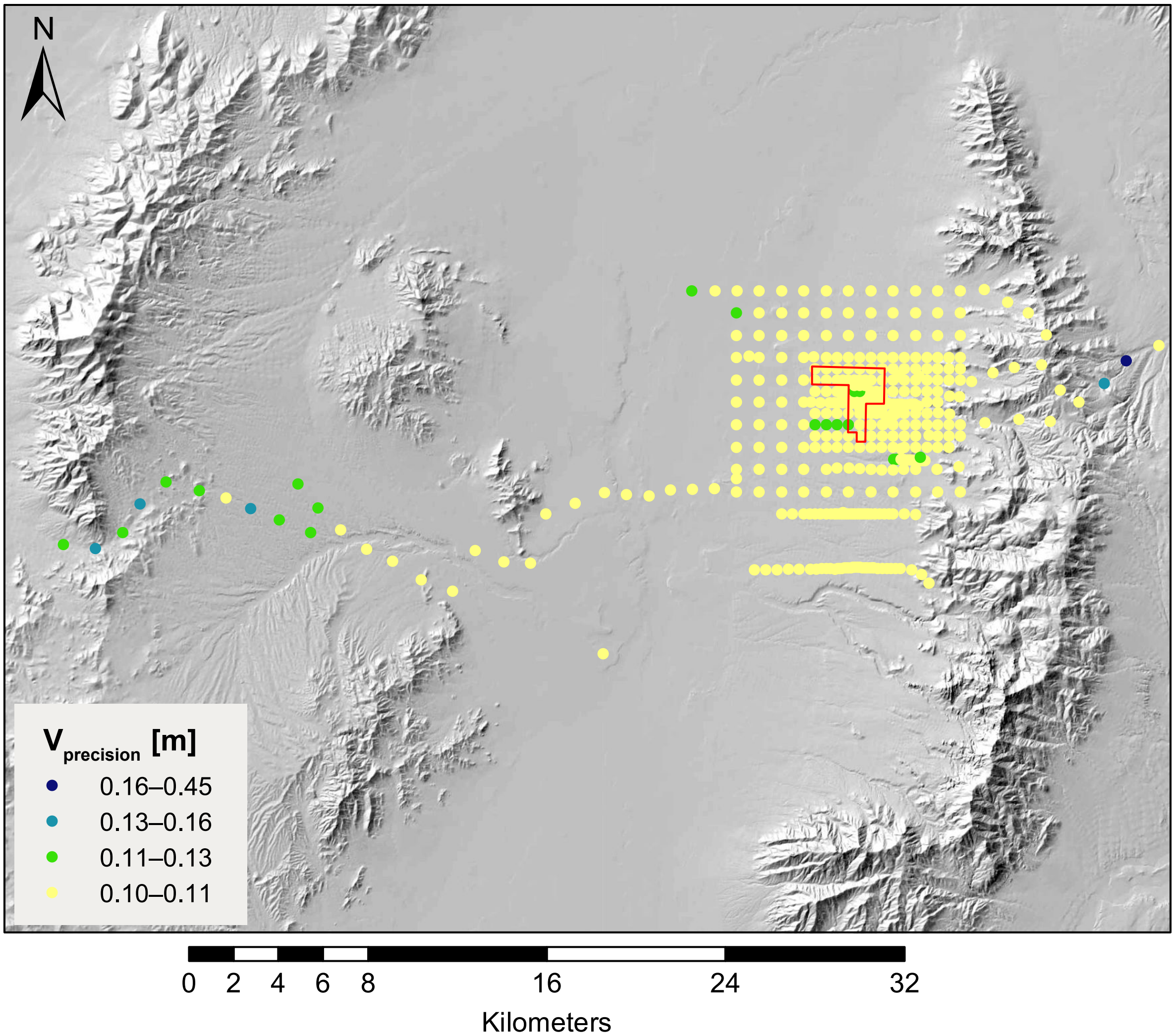

Figure 16. *Map of new FORGE gravity stations indicating vertical precision from post-processed GPS data. FORGE site outlined in red.*

For an elevation quality check, we compared UGS gravity station data to that of the lidar data acquired for FORGE (Knudsen et al., 2018), which reports vertical accuracy of 0.05 m. For the UGS gravity stations that overlap with lidar coverage, we report that 291 of 388 (75%) station elevations are within 0.10 m of the FORGE lidar values (Figure 17, right panel). The minor differences between the lidar and UGS stations are not unexpected, since the reported vertical precision of the stations is typically 0.10 m or better.

The legacy gravity data (PACES) does not have elevation control values reported in its metadata, so we compared their elevations with FORGE lidar and NED10m (if outside of the lidar coverage) to evaluate their accuracy. NED10m data is from a composite digital elevation model reported to have 3-m vertical accuracy from the U.S. Geologic Survey. A total of 3389 PACES gravity stations were used in this study, and 691 PACES stations are within the coverage area of the FORGE lidar. Figure 17 shows that 553 of 691 station elevations (80%) are within 3 m of the FORGE lidar values and 2767 of 3389 station elevations (81.4%) are within 3 m of the NED10m values (see also Figure 18). Most of the legacy gravity surveys were done prior to modern GPS equipment and survey techniques. Therefore, a 3-m vertical accuracy is assigned to the PACES data which is consistent with the vertical accuracy of older topographic maps.

Carefully considering the vertical uncertainties of each of the gravity data sets, we can propagate these uncertainties into the CBGA value and, subsequently, their estimated impact on gravity models. To do this, we computed the significant components directly related to the data elevation uncertainties. We focused on the Free Air anomaly, noted earlier, and the Bouguer Slab correction which is the approximation of the gravity effect from rock between a station and sea level using a 1D, horizontal plate. Initial 2D models of gravity transects can use a thickness-weighted mean of all the geologic layers in a basin to estimate

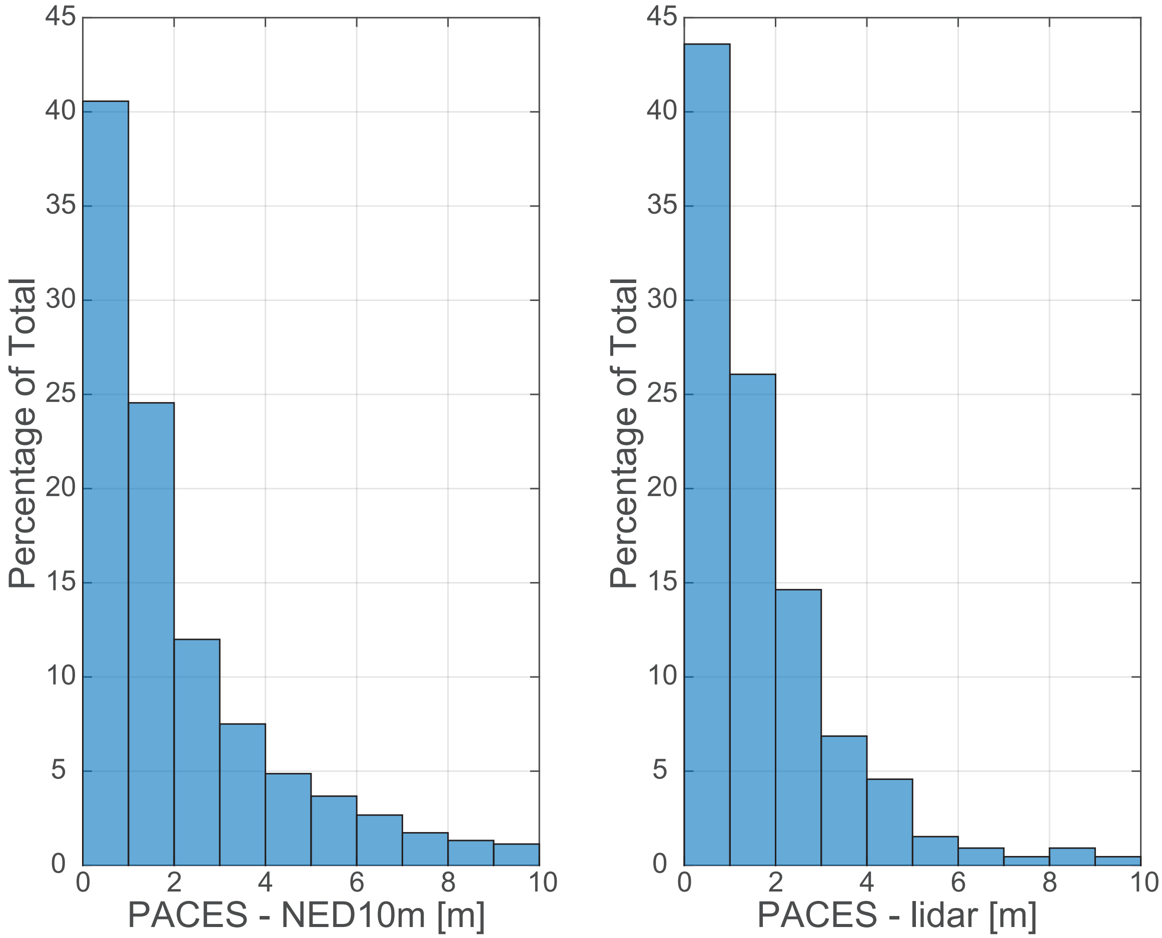

Figure 17. *Histogram of PACES gravity station elevation data comparisons. The left panel shows the differences between all PACES data and the NED10m data, where 2767 of 3389 station elevations (81.4%) are within 3 m of the NED10m values. The right panel shows the differences between a subset of overlapping PACES and lidar data collected for FORGE, where 553 of 691 station elevations (80%) are within 3 m of the FORGE lidar values.*

the depth-to-basement. For the FORGE study area, this density value is at a contrast of 0.3 g/cm^3 or the equivalent density of 2.37 g/cm^3. For the UGS gravity data, 0.1 m of vertical uncertainty equates to 0.031 mGal in the Free Air correction and 0.011 mGal in the Bouguer Slab correction, for a total of 0.042 mGal uncertainty and 3.5 m of difference in slab thickness. In the PACES data, 3 m of vertical uncertainty equates to 0.926 mGal in the Free Air correction and 0.336 mGal in the Bouguer Slab correction, for a total of 1.262 mGal uncertainty and 105 m of difference in slab thickness.

2D gravity models are most accurate when they can be tied to local density information. For the FORGE gravity models, density data from well logs, well cuttings, rock outcrops and other geologic information sources were utilized where most applicable. Gravity sections that run close to actual gravity data had the highest confidence (all other factors being the same), especially sections making use of the new FORGE gravity data. Where UGS and PACES data overlap, UGS data was given preference because it has higher confidence. For areas without modern gravity data, the confidence is lower. If the station coverage is of high spatial density, local data can be compared to determine consistency in observed gravity and elevation, and its confidence can be carefully evaluated.

It should be noted that gravity field sources decrease with an inverse-square relationship ($1/x^2$) to distance. Therefore, sources far from the observation point (larger x value) will have very small effects relative to sources closer to the observation point (smaller x values). Regarding basement structure, the implication is that it is unlikely gravity will resolve the same small-scale features at great depth compared to when they are near the surface. This results in deeper structures having the tendency to appear smooth compared to shallow features that show more detail. Furthermore, 2D gravity modeling assists in defining basin geometry, providing a better understanding of simple structure for areas where the gravity field appears to be two-dimensional. In cases where there are 3D structures, 2D gravity models will not delineate these structures with high confidence and 3D modeling will be required to further investigate these 3D features.

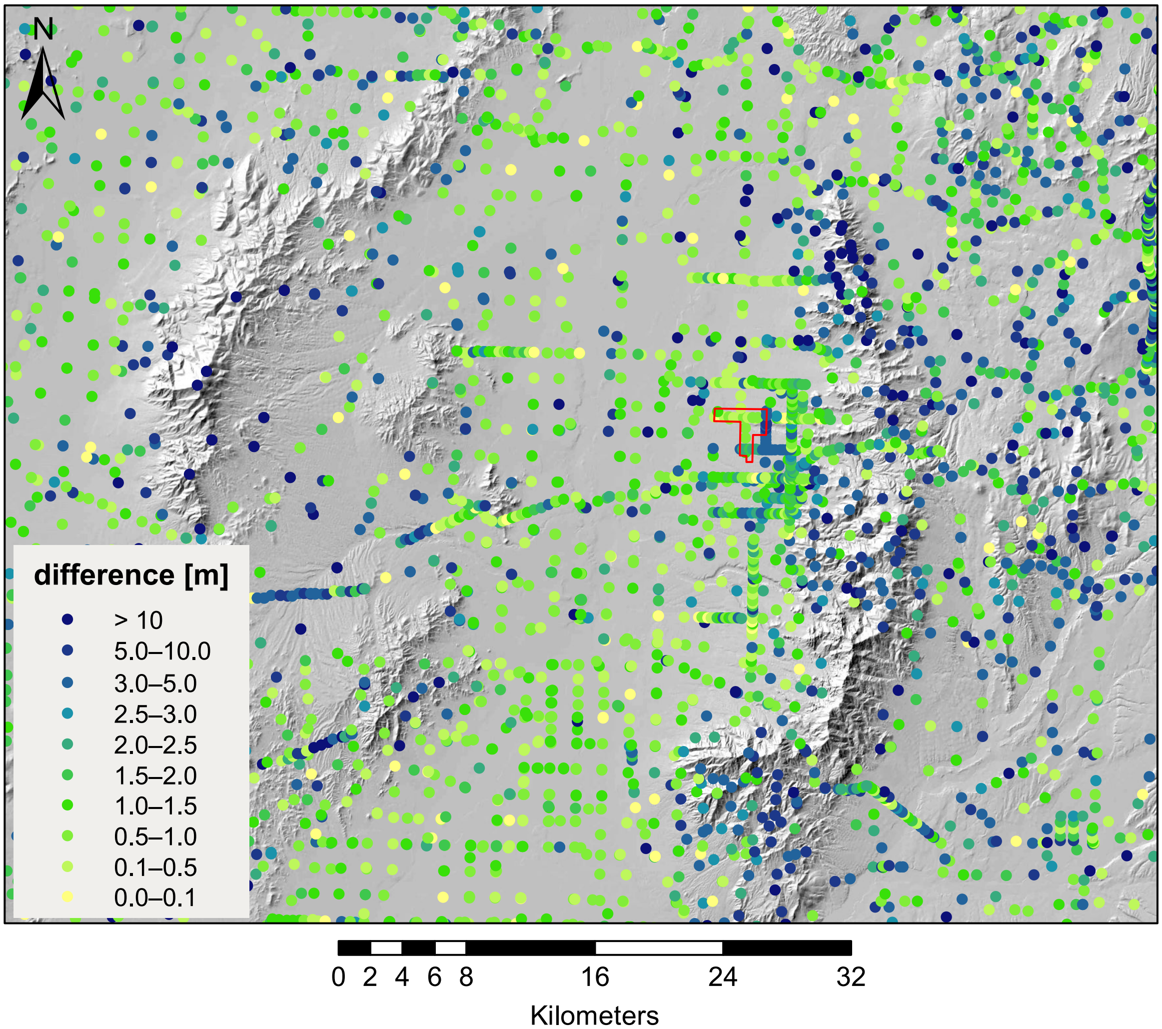

Figure 18. *Map of elevation differences between PACES station data and combined NED10m and lidar. FORGE site outlined in red.*

SUMMARY

Resistivity models from TEM sounding data better define features in the shallow subsurface near the FORGE site. A transect through the FORGE site delineates the depth to the groundwater table and does not indicate any subsurface structures are present. South of the FORGE site, a transect crosses the OMF, where a distinct resistivity contrast shows conductive material to the east of the fault that is interpreted to be primarily an effect of geothermal fluids that are prevented from flowing to the west by the fault. Resistivity along the Ranch Canyon Road transect is relatively higher compared to transects to the north, which is likely due to more resistive matrix material. The groundwater table is clearly delineated and no features consistent with a graben structure or fault are present. TEM data quality is good for nearly all stations and DOI values average 300 m. At this scale, uncertainty in depth of detected features is on the order of 5–10 m and model RMS values are typically less than 1.

Gravity surveys have better defined the basement geometry of the FORGE study area by augmenting legacy data with new, high-precision measurements using a dynamic grid layout centered on the FORGE site. 2D gravity models indicate that the deepest part of the basin, approximately 4.8 km in depth, is located on the west side of the valley, 12 km from the edge of the FORGE site boundary. Basin geometry from the 2D gravity modeling shows a steeply dipping interface on the east side of Milford Valley north of the FORGE site. The sediment-basement interface below the FORGE site appears to be moderately dipping (about 25°) to the west, which is consistent with interpretations of the 2D and 3D seismic sections. Adjacent to the FORGE site, unresolved 3D structure is suggested by the horizontal gravity gradient field. From the seismic section interpretations, this structure appears to be a paleo valley in the granite surface. This feature is located at the margin of the grid where station coverage is less dense. New data collection (improved coverage), 3D modeling, and joint interpretations with 3D seismic will be required to better image this feature.

REFERENCES

Archie, G.E., 1942, The electric resistivity log as an aid in determining some reservoir characteristics: Transactions AIME, v. 146, no. 1, p. 54–62.

Auken, E., Christiansen, A.V., Kirkegaard, C., Fiandaca, G., Schamper, C., Behroozmad, A.A., Binley, A., Nielsen, E., Efferso, F., Christensen, N.B., Sorensen, K., Foged, N., and Vignoli, G., 2015, An overview of a highly versatile forward and stable inverse algorithm for airborne, ground-based and borehole electromagnetic and electric data: Exploration Geophysics, v. 46, p. 223–235.

Christiansen, A.V., and Auken, E., 2012, A global measure for depth of investigation: Geophysics, v. 77, no. 4, p. WB171–WB177.

Gettings, P., Chapman, D.S., and Allis, R., 2008, Techniques, analysis, and noise in a Salt Lake Valley 4D Gravity experiment: Geophysics, v. 73, no. 6, p. WA71–WA82.

Gwynn, M., Allis, R., Hardwick, C., Jones, C., Nielsen, P., and Hurlbut, W., 2019, Compilation of rock properties from FORGE well 58-32, Milford, Utah, *in* Allis, R., and Moore, J.N., editors, Geothermal characteristics of the Roosevelt Hot Springs system and adjacent FORGE EGS site, Milford, Utah: Utah Geological Survey Miscellaneous Publication 169-L, 36 p., https://doi.org/10.34191/MP-169-L.

Hardwick, C.L., Allis, R., Wannamaker, P.E., 2015, Observations and implications of magnetotelluric data for resolving stratigraphic reservoirs beneath the Black Rock Desert, Utah, USA: Geothermal Resources Council Transactions, v. 39, p. 593–601.

Hintze, W.J., Aiken, C., Brozena, J., Coakley, B., Dater, D., Flanagan, G., Forsberg, R., Hildenbrand, T., Keller, G.R., Kellogg, J., Kucks, R., Li, X., Mainville, A., Morin, R., Pilkington, M., Plouff, D., Ravat, D., Roman, D., Urrutia-Fucugauchi, J., Veronneau, M., Webring, M., and Winester, D., 2005, New standards for reducing gravity data—The North American gravity database: Geophysics, v. 70, no. 4, p. J25–J32.

Knudsen, T., Kleber, E., Hiscock, A., and Kirby, S.M., 2019, Quaternary geology of the Utah FORGE site and vicinity, Millard and Beaver Counties, Utah, *in* Allis, R., and Moore, J.N., editors, Geothermal characteristics of the Roosevelt Hot Springs system and adjacent FORGE EGS site, Milford, Utah: Utah Geological Survey Miscellaneous Publication 169-B, 21 p., 2 appendices, https://doi.org/10.34191/MP-169-B.

Miller, J., Allis, R., and Hardwick, C., 2019, Interpretation of seismic reflection surveys near the FORGE enhanced geothermal systems site, Utah, *in* Allis, R., and Moore, J.N., editors, Geothermal characteristics of the Roosevelt Hot Springs system and adjacent FORGE EGS site, Milford, Utah: Utah Geological Survey Miscellaneous Publication 169-H, 13 p., https://doi.org/10.34191/MP-169-H.

Pan American Center for Earth and Environmental Studies, gravity and magnetics database: Online, https://research.utep.edu/Default.aspx?alias=research.utep.edu/paces, accessed 2012.

Spies, B., 1989, Depth of investigation in electromagnetic sounding methods: Geophysics, v. 54, no. 7, p. 872–888.

Webring, M.W., 1985, SAKI—A Fortran program for generalized linear inversion of gravity and magnetic profiles: U.S. Geological Survey Open-File Report 85-122, 104 p.

MICRO-SEISMIC CHARACTERIZATION OF THE UTAH FORGE SITE

by Kristine L. Pankow[1], Stephen Potter[2], Hao Zhang[1], Andy J. Trow[1], and Amy S. Record[1]

[1]University of Utah Seismograph Stations, Salt Lake City, Utah
[2] Cypress, Texas

Miscellaneous Publication 169-G
Utah Geological Survey
a division of
UTAH DEPARTMENT OF NATURAL RESOURCES

This paper is part of *Geothermal Characteristics of the Roosevelt Hot Springs System and Adjacent FORGE EGS Site, Milford, Utah*. https://doi.org/10.34191/MP-169

Bibliographic citation:

Pankow, K.L., Potter, S., Zhang, H., Trow, A.J., and Record, A.S., 2019, Micro-seismic characterization of the Utah FORGE site, *in* Allis, R., and Moore, J.N., editors, Geothermal characteristics of the Roosevelt Hot Springs system and adjacent FORGE EGS site, Milford, Utah: Utah Geological Survey Miscellaneous Publication 169-G, 10 p., https://doi.org/10.34191/MP-169-G.

MICRO-SEISMIC CHARACTERIZATION OF THE UTAH FORGE SITE

by Kristine L. Pankow, Stephen Potter, Hao Zhang, Andy J. Trow, and Amy S. Record

ABSTRACT

The University of Utah Seismograph Stations (UUSS) has been monitoring seismic activity in Utah and the surrounding region for over 50 years and has compiled an earthquake catalog going back to 1850. Based on this catalog and the results of a temporary seismic network operating in 1981, the Utah Frontier Observatory for Research in Geothermal Energy (FORGE) study area was characterized by small magnitude earthquakes occurring at a low seismic rate. To better understand seismic patterns and characteristics, the events in the UUSS catalog were relocated using updated velocity models, analyzed for time of day patterns, and waveforms from individual event clusters were used to identify source zones. In addition, to lower the magnitude of completeness, both a five-station local broadband network and two Nodal geophone temporary deployments were installed centered on the proposed FORGE site. Subspace detection analysis was also utilized to identify small seismic events using events from the UUSS catalog as templates. From these analyses and experiments, we identified three seismic source zones. The first source zone northwest of Milford, Utah, is located near an active quarry and contains seismic events that all occur during daylight hours. We conclude that these events are anthropogenic in origin. The second source zone is located near the Milford airport. This zone hosts the larger events in the study area, including possibly the largest event, the 1908 M 4.05 Milford earthquake. The third zone includes the Mineral Mountains. Most seismicity in this zone occurs in an east-west band to the east of the FORGE site. Notably, events detected with the local broadband and geophone arrays are located in the same source zones identified from the UUSS catalog, and no events were located within the proposed FORGE footprint.

INTRODUCTION

Seismicity induced by industrial activities has been known and studied for many years (e.g., Raleigh et al., 1976; Hsieh and Bredehoeft, 1981). With both increased and changing activity in energy sectors and the migration of some of these activities toward more populated areas, reporting and concern about induced seismicity has dramatically increased (e.g., Petersen et al., 2017). Often cited examples of the increased frequency of induced seismicity and the societal impacts resulting from these events include the rapid increase of M > 3 earthquakes in Oklahoma beginning in 2001 (Ellsworth, 2013) and the Basel, Switzerland, M 3.7 earthquake (Deichmann and Giardini, 2009; Bachmann et al., 2011). With an increase in induced seismicity worldwide (Foulger et al., 2017), it is important to assess, and make plans to mitigate, the risk of induced seismicity prior to activities that might lead to these earthquakes (e.g., Majer et al., 2012; Walters et al., 2015; Trutnevyte and Wiemer, 2017). An important step in assessing the potential risk and then for subsequent monitoring is to characterize the local seismicity prior to industrial activities, creating a baseline to which subsequent events can be compared. This paper describes the analyses used to establish the baseline for local seismicity near the Utah Frontier Observatory for Research in Geothermal Energy (FORGE).

The Utah FORGE site is located in a rural area in the West Desert of Utah in Beaver County. The nearest population center is the town of Milford, located 16 km to the southwest. The Utah FORGE site is included within the boundaries of the University of Utah Seismograph Stations (UUSS) monitoring region. UUSS has been monitoring seismic activity in Utah and the surrounding region for over 50 years and has compiled a historical earthquake catalog dating back to 1850 (Figure 1; Arabasz et al., 2015). Based on this historical record, there was only one M > 4 earthquake in the greater Milford, FORGE study area (yellow box Figure 1), namely the Milford earthquake M 4.05 event in 1908. Within ~50 km of the proposed FORGE site there are additional earthquakes M < 4.9, and one earthquake M ≥ 4.9, the 1901 M 6.6 Tushar Mountain earthquake (#2, Figure 1) located ~50 km to the east. Beginning in 1981, UUSS transitioned to cataloging digital data from the regional seismic network. Analysis of the UUSS earthquake catalog for the time period 1 January 2000 to 30 June 2003 found a minimum magnitude of completeness (M_{comp}) for the Utah FORGE site of 1.5 (Pankow et al., 2004). In subsequent work, Potter (2017) using only UUSS catalog data local to the Utah FORGE site determined an M_{comp} for the Utah FORGE site of 1.7.

In addition to regional monitoring, two local seismic studies recorded events near the Utah FORGE site. Olson (1976) analyzed the seismicity located in known geothermal resource areas (KGRA) in central Utah. For the Roosevelt Hot Springs KGRA located due east of the Utah FORGE site in the Mineral Mountains, six earthquakes were recorded on the west flank of the Mineral Mountains. Olson (1976) concluded that the Roosevelt Hot Springs KGRA is characterized by low seismic rates. They attributed these low rates to either high seismic detection levels or the result of localized high temperatures.

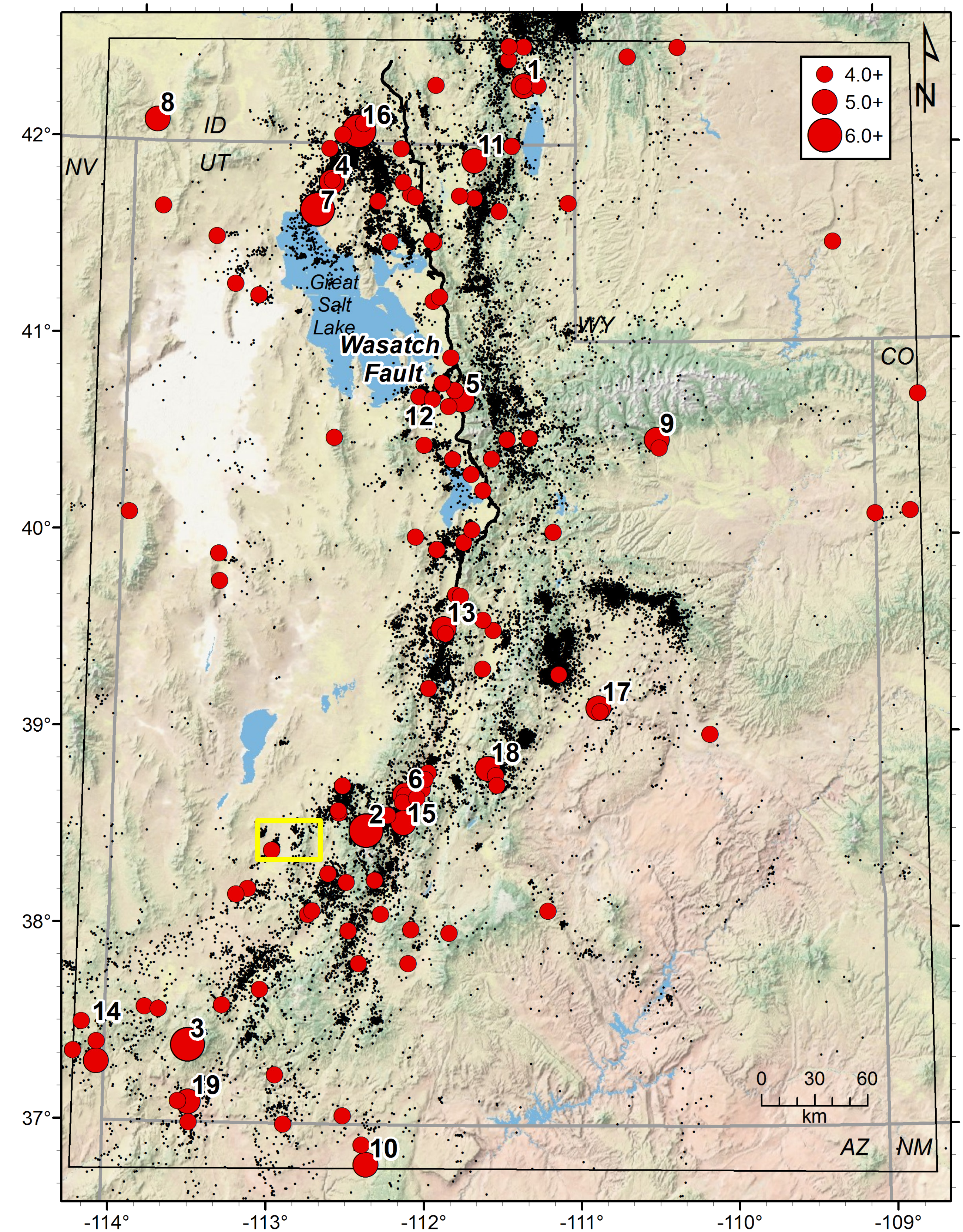

Figure 1. *Epicenter map of mainshocks of moment magnitude **M** > 4.0 in the Utah Region, 1850 through September 2012 (red dots); foreshocks, aftershocks, and mining-related seismicity are excluded. Data are from a revision of Utah's historical earthquake catalog (Arabasz et al., 2015). The small black dots show all earthquake epicenters in the UUSS earthquake catalog, July 1962 through December 2012. The numbers correspond to significant earthquakes discussed in Arabasz et al. (2015). The yellow box encompasses the FORGE study area.*

In a second experiment to characterize background seismicity prior to production at Roosevelt Hot Springs Blundell Geothermal Plant, Zandt et al. (1982) installed a local seismic array to characterize the background seismicity. During the approximate two-year deployment (September 1979–January 1982), they concluded that there are few earthquakes M > 2. However, they did capture one energetic seismic swarm (1044 earthquakes M ≤ 1.5) from June through August 1981. This swarm occurred east of the present borefield at the Blundell Power Plant, primarily in the Mineral Mountains (Figure 2). The seismicity trend of this swarm was mostly east-west. They concluded that the swarm was primarily naturally occurring and was consistent with either (or both) seismicity occurring along the projection of the east-west-trending Negro Mag fault or along northwest-trending faults mapped by Nielson et al. (1978; Kirby, 2019).

Based on these prior works, seismicity near the Utah FORGE site was known to be low-magnitude, occurring at low seismic rates with possibly a tendency for low-magnitude (below regional network detection levels) seismic swarms. To establish a baseline for these small-magnitude events, we installed a local broadband network and two stand-alone dense short-period digital Fairfield Nodal seismic arrays centered on the FORGE footprint. Additionally, we applied detection algorithms to continuous UUSS regional seismic data from 2010 through 2016.

To establish the baseline seismicity levels for the Utah FORGE site, we examined the location, magnitude, and seismic rates for earthquakes detected and located by the UUSS regional seismic network (01/01/1981–10/31/2016) and added catalogs compiled as part of the FORGE study. Consistent with previous studies, we conclude that this area is characterized by low seismic rates and low magnitudes. Additional events detected with the local networks deployed for the FORGE study and from enhanced detection methods were located in the same general areas as the events in the UUSS regional catalog. Importantly, no events were located within the areal footprint of the proposed FORGE site.

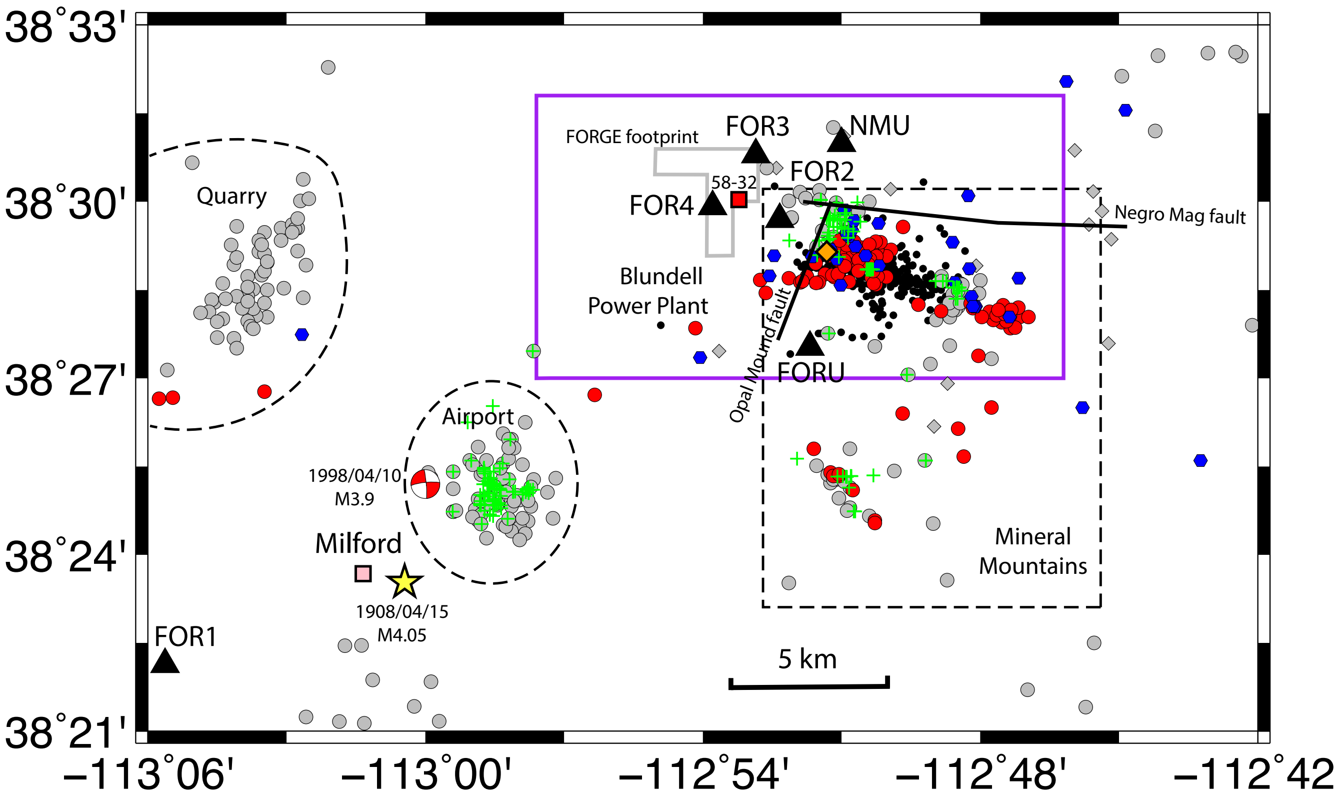

Figure 2. *Utah FORGE earthquake catalog. Gray circles, earthquakes from the UUSS catalog 1981–2016 relocated with an updated velocity model. Red circles, earthquakes located after installation of the broadband network. Blue hexagons, earthquakes detected with the Nodal array. Gray diamonds, earthquakes from Olson (1976). Black circles, earthquakes from Zandt et al. (1982). Green crosses, earthquakes identified using subspace analysis. Dashed polygons denote the three source zones discussed in the text. Black triangles, locations of seismic stations. Purple region, area shown in Figure 7. Gray polygon, region defined as FORGE footprint.*

SEISMIC MONITORING

UUSS Regional Catalog

In support of the Utah FORGE project, events in the UUSS catalog (1981–2016) were relocated using updated velocity models, with depths set relative to sea level (Figure 2). The relocation of these events caused slight changes in location, and overall resulted in tighter spatial clustering. No earthquakes, during this time period, were located within the proposed FORGE footprint (Figure 2). During the study period, earthquakes occurring outside the Utah FORGE footprint ranged in magnitude from M -0.09 to 3.91. The average horizontal and vertical 90% confidence errors for these earthquakes are 0.9 km and 4.9 km, respectively. Spatially, there are three distinct clusters: (1) northwest of Milford, (2) northeast of Milford, and (3) scattered seismicity in the Mineral Mountains (Figure 2).

Waveform analysis and event timing indicate that events in the northwest cluster (labeled Quarry, Figure 2) are quarry blasts, not tectonic earthquakes. Evidence for this conclusion includes their epicentral proximity to quarries (conspicuous on Google maps), small magnitudes (M 0.49 to 2.05), shallow depths, restricted timing (all events occur during daylight hours, Figure 3), and highly correlated waveforms implying a similar location and source mechanism.

The second cluster is located northeast of Milford near the Milford airport and is not far from the M_W 4.05 1908 Milford earthquake (Figure 2). The magnitudes in this cluster range from M 0.46 to 3.91, and the events occur throughout the day (random timing, Figure 3). This cluster seems to host the largest events in the region and the events are interpreted as tectonic in origin. The moment tensor for the M 3.9 event indicates a strike-slip mechanism and relocation of the seismicity in this cluster (Potter, 2017) is consistent with a north-south-striking fault plane.

Events in the third cluster located in the Mineral Mountains also occur throughout the day (random timing, Figure 3). Spatially, there is a clustering of events around the Opal Mound fault, distributed on the eastern edge of the Zandt swarm region and to the south of station FORU (Figure 2). While these events are most consistent with a tectonic origin, given the proximity to the Blundell Power Plant, induced seismicity may be a secondary source type.

Few events were located from April 2011 through August 2016 within the study area (Figure 4). To explore this quiescence period, we employed subspace detection analysis (Potter, 2017). Subspace analysis (Harris, 2006; Harris and Paik, 2006) uses singular value decomposition (SVD) to decompose a cluster of similar waveforms into basis vectors. These basis vectors are then scanned against continuous data in order to find new events that belong to the same family. We use the program *Detex* (Chambers et al., 2015) to implement the subspace detection analysis. For this, we created two sets of templates. For the airport region, we used 55 template events and for the Mineral Mountains 42 templates. Waveforms from each set of template events recorded at UUSS regional stations NMU, IMU, and DWU were correlated by station against all other templates in the set and linked into subspace groups using single-link clustering (Harris, 2006). Based on the cross-correlation value not all events clustered into a family, as the waveform similarity with the other waveforms in these cases was too low. These events are called singletons. Both basis vectors and singletons are correlated against continuous data for the same stations, for the time period 2010 through 2016. This analysis detected 61 seismic events in the Mineral Mountains region (M -0.55 to 1.52) and nine events in the airport region (M -1.49 to 0.91). These events are below the M_{comp} determined for the regional network.

Waveform clustering analysis (Potter, 2017) identifies several distinct clusters of seismic events in the Mineral Mountains area. Based on the different clusters and the proximity to the Blundell Power Plant, we investigated possible correlations with the pumping history at that power plant. We found no observable connection between the events cataloged in the area and the injection/withdrawal history of the power plant (Figure 5). The plant was completed in 1984 and although the pumping history is not available prior to 1992, there is only one event cataloged from 1984 (completion of the plant) to 1992. The plant opened a binary power plant in 2007, allowing more heat to be pulled from the recovered fluids. Even with this change in activity, no change is evident in the seismic activity.

Local Broadband Network

In November 2016, a five-station broadband seismic network was installed (Figure 2). Three stations were located on-top or in close proximity to the FORGE footprint. A fourth station was located on bedrock in the Mineral Mountains southeast of the FORGE footprint. The fifth station was located on bedrock southwest of Milford. The fifth station was selected to provide better azimuthal control to the seismic locations. These stations together with UUSS regional station NMU, located to the northeast of the FORGE footprint in the Mineral Mountains, form the local array for the Phase 2 FORGE project. Data from this local array

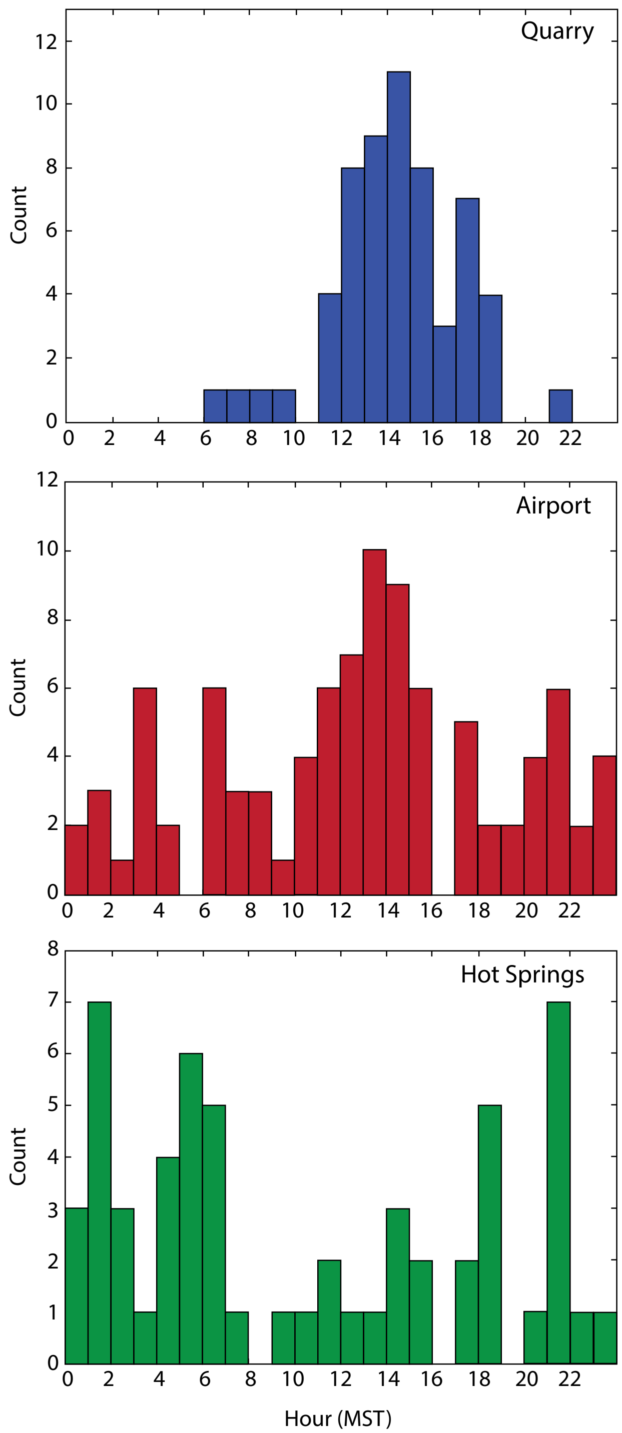

Figure 3. *Time-of-day histograms of events in each of the three source zones shown in Figure 2. Quarry, located northwest of Milford, Utah. Airport, located northeast of Milford, Utah. Hot Springs, events occurring in the Mineral Mountains.*

and from the regional seismic network were combined to locate and estimate magnitudes for new seismic events. The goal of this array was to reduce the M_{comp} to 0 or lower.

The local seismic array installed for the FORGE project combined with nearby UUSS regional seismic stations greatly improves the seismic detection level for the study area. Figure 6A shows that most detections after the installation of the broadband array are well below the regional network M_{comp} of 1.5 to 1.7. We estimate a revised M_{comp} of around 0.0 for the FORGE area (Figure 6D). Because there are stations closer to the source zones, 90% confidence location errors decreased to 0.7 and 3.9 km for horizontal and vertical, respectively. Spatially, most of the seismic events were located east of the Opal Mound fault primarily in or near to the Zandt swarm region (Figure 2). There is also a small cluster in the southern Mineral Mountains source zone.

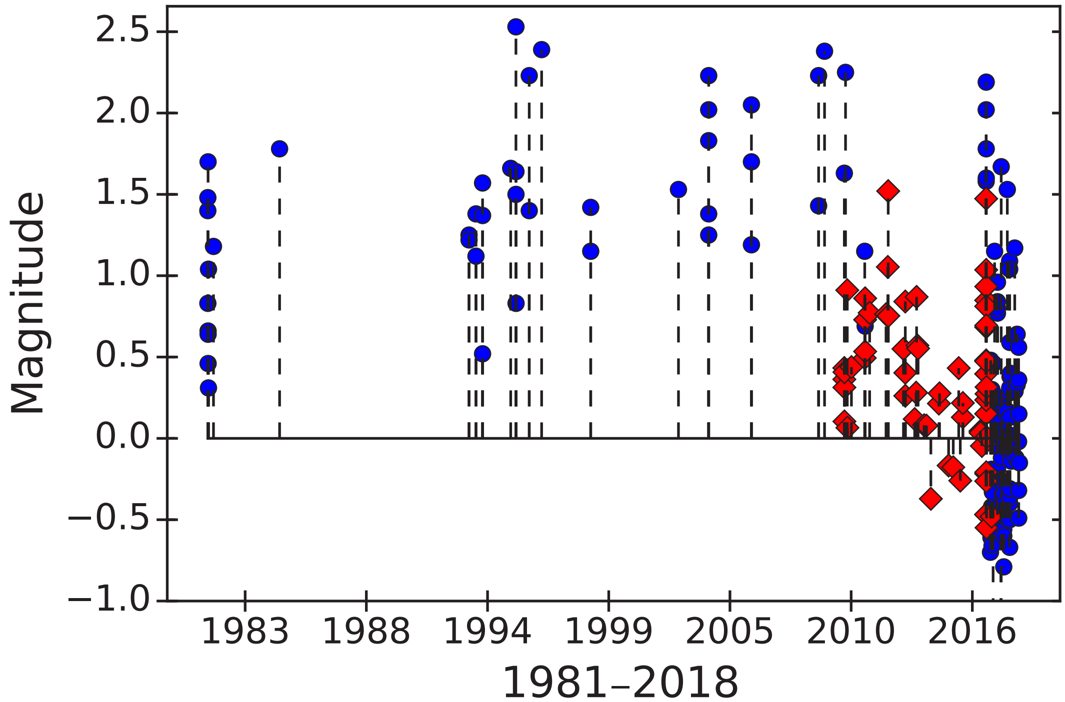

Figure 4. *Magnitude-time history for events in the UUSS catalog (blue circles). For the time period 2011 to 2016, there were no events in the regional catalog. However, 70 events below the regional* M_{comp} *were identified using subspace analysis (red diamonds).*

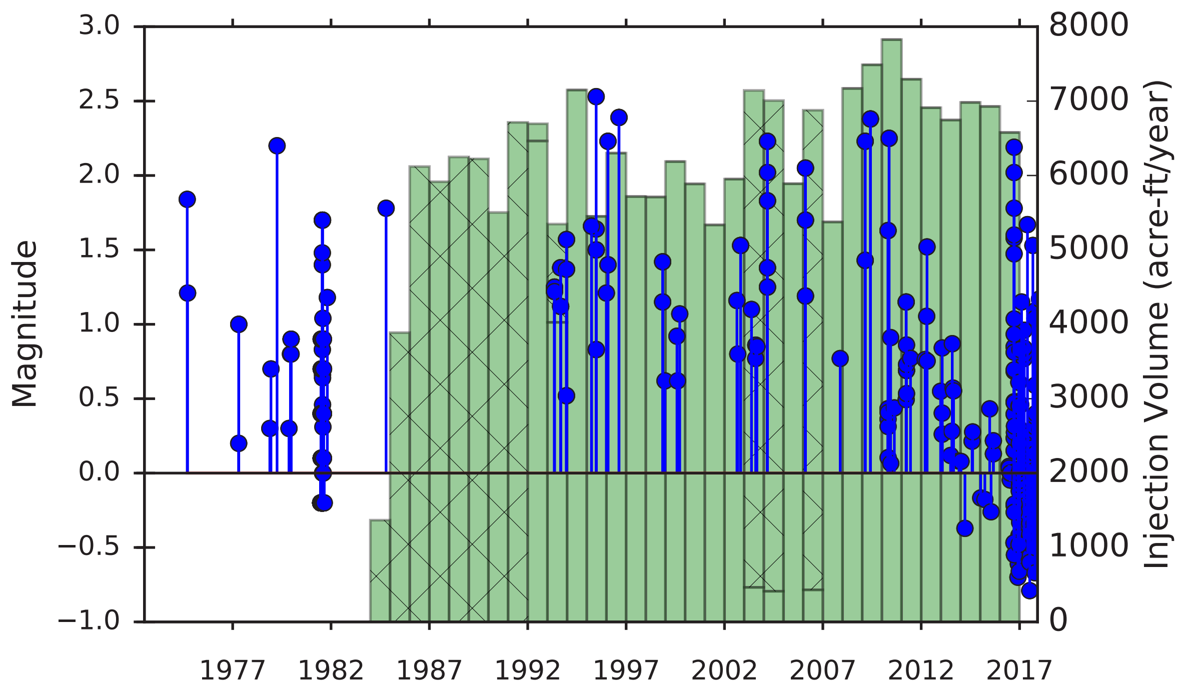

Figure 5. *Seismicity (blue circles, left axis) versus pumping history for the Roosevelt Hot Springs geothermal plant (green bars, right axis). Pumping history from published data from* [*waterrights.utah.gov*](waterrights.utah.gov)*. Hashed green bars (right axis), pumping history adjusted based on the reported power produced and discrepancies in the reported fluid production.*

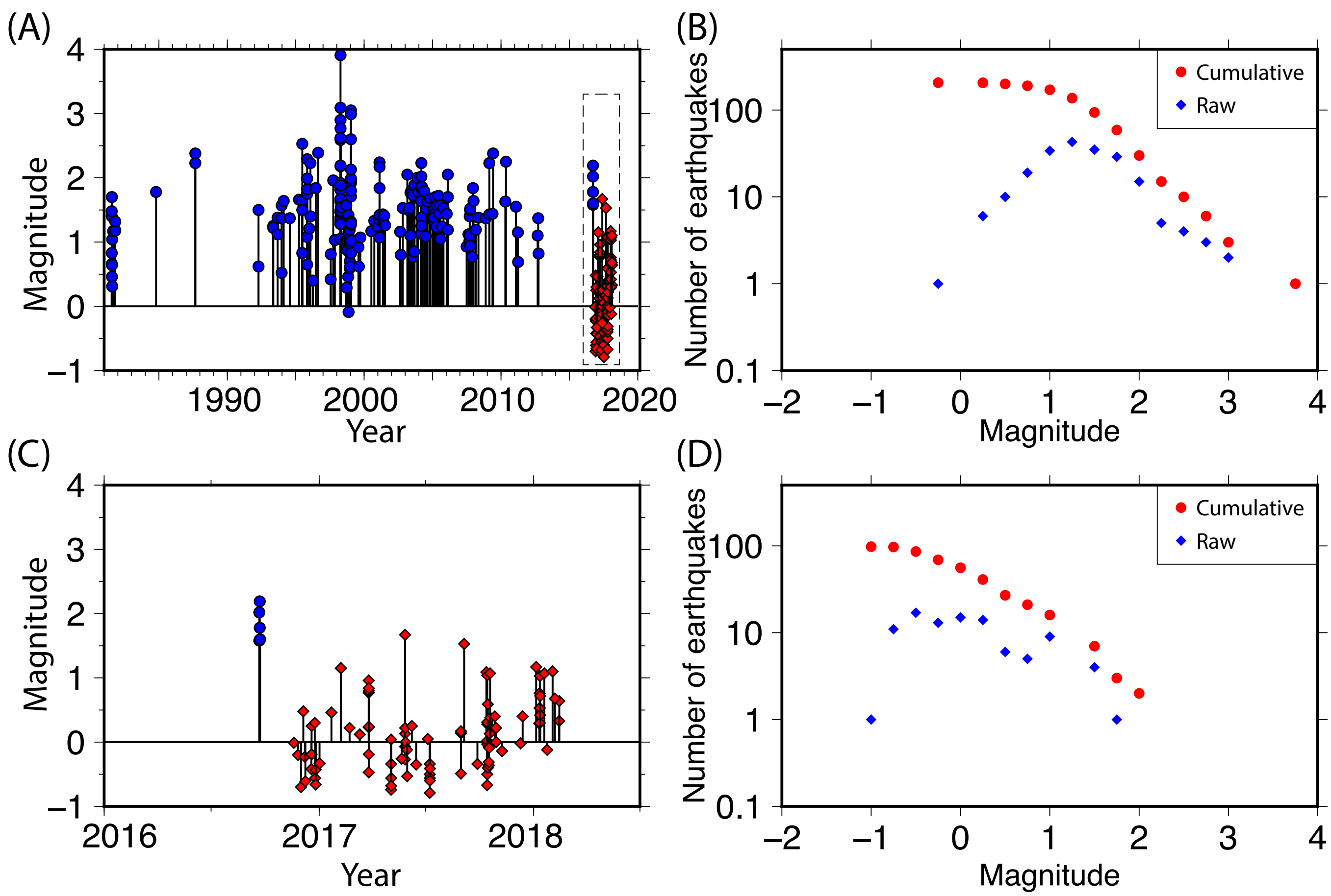

Figure 6. *Magnitude-time plot for events in the UUSS catalog before (blue) and after (red) the broadband network was installed.* ***(A)*** *Full time period of the catalog.* ***(B)*** *Magnitude distribution of numbers of events for time period shown in* ***(A)****.* ***(C)*** *Magnitude-time distribution for events since 2016.* ***(D)*** *Magnitude distribution of numbers of events for time period shown in* ***(C)****.*

Short-Term Geophone Experiments

In addition to the local broadband network, two ~one-month long deployments of three-component Fairfield Nodal geophones were installed to further enhance seismic detection levels. The first Nodal array was installed in December 2016 and consisted of 93 stations, 49 with ~650 m spacing directly above the Utah FORGE footprint and the remaining 44 distributed with ~4.5 km spacing surrounding the FORGE site. The small aperture dense array above the FORGE site was reoccupied on August 18, 2017, for 32 days. Using this dataset 42 events (M -0.5 to 0.5) were added to the FORGE catalog (Trow et al., 2018). The majority of these events were located in the region defined by the Zandt swarm zone.

RESULTS

Using multiple scales of seismic monitoring and advanced detection analysis (subspace), we identified three source zones in the larger Utah FORGE study area (Figure 2): (1) a zone located northwest of Milford, Utah, composed of primarily anthropogenic sources; (2) a zone located northeast of Milford, Utah, consistent with a roughly north-south-striking nodal plane determined from the moment tensor of an M 3.9 strike-slip earthquake; and (3) a zone located in the Mineral Mountains. Within the Mineral Mountains most events occur within a roughly 5-km-wide east-west-striking area originally identified by Zandt et al. (1982) with a smaller cluster of events located south of station FORU. The events located in the Zandt swarm zone (Figure 7) are separated into two distinct clusters: a shallow cluster located near the power plant production zone and a deeper cluster to the east, which appears to dip toward the west. No new source areas were identified as a consequence of lowering the detection level from M_{comp} 1.7 to 0.0, and no events were detected within the FORGE footprint. Additionally, no additional energetic (N > 25) swarms have been recorded since the 1982 swarm.

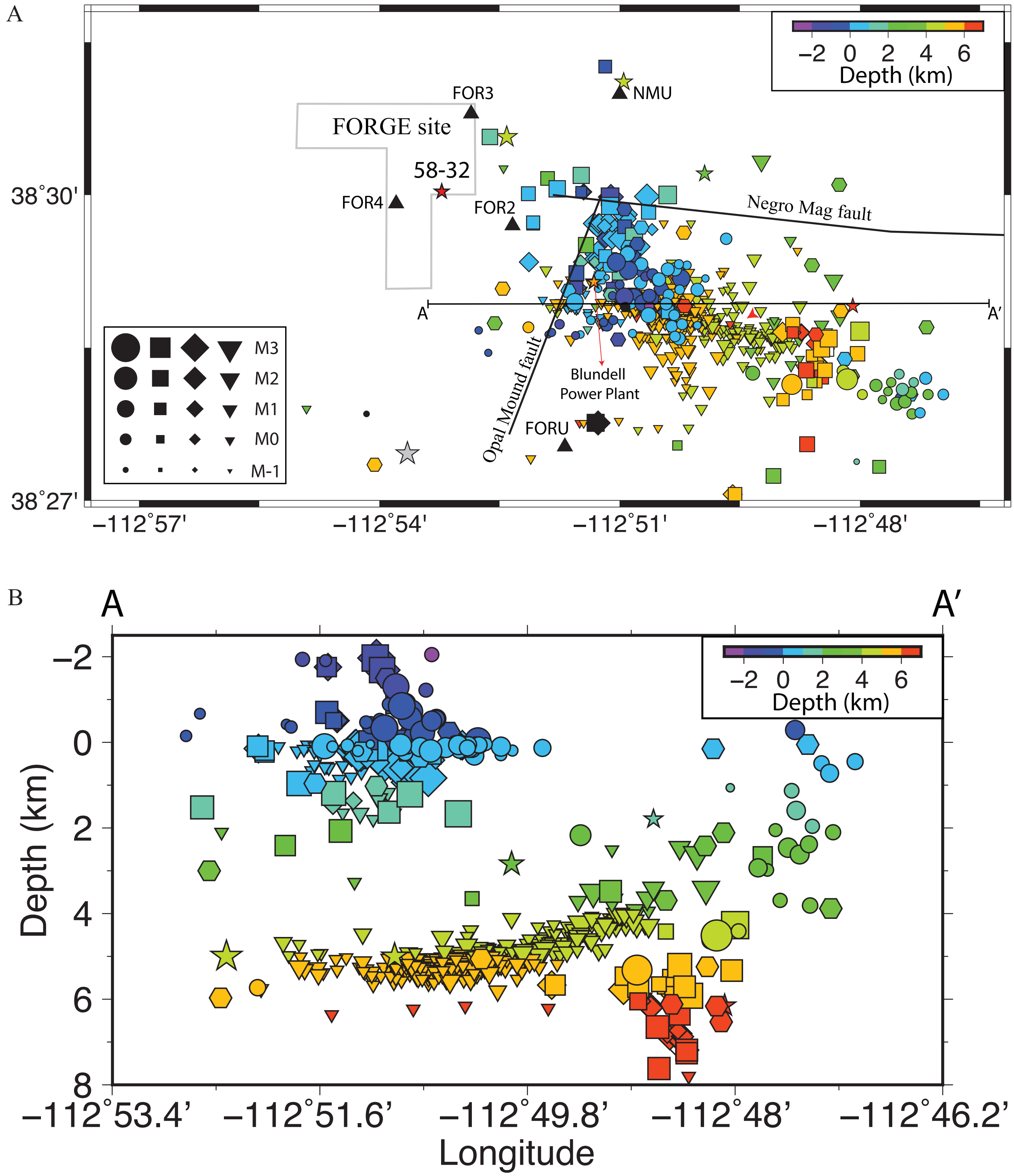

Figure 7. (A) *Utah FORGE earthquake catalog. Circles, earthquakes from the UUSS catalog 1981–2016 relocated with an updated velocity model. Squares, earthquakes located after installation of the broadband network. Hexagons, earthquakes detected with the Nodal array. Stars, earthquakes from Olson (1976). Inverted triangles, earthquakes from Zandt et al. (1982). Diamonds, earthquakes identified using subspace analysis. Black triangles, locations of seismic sensors. Gray polygon, region defined as FORGE footprint.* ***(B)*** *Seismic events shown in Figure 7****(A)*** *collapsed onto an east-west cross section (A–A′). Depth is relative to sea level.*

CONCLUSIONS

Based on the multiple levels of seismic monitoring, we conclude that (1) no naturally occurring seismic events were located within the Utah FORGE footprint; (2) seismicity occurs at low rates and events have low magnitudes, typically M < 1.5; and (3) most seismic events in the larger FORGE study area occur under the Mineral Mountains to the east of the Opal Mound fault with a less pronounced source zone near the Milford airport.

ACKNOWLEDGMENTS

We thank Relu Burlacu and Debi Kilb, for thoughtful reviews of the manuscript. Figures 2 and 7 were drawn using the Generic Mapping Tools (http://gmt.soest.hawaii.edu/; Wessel and Smith, 1995).

REFERENCES

Arabasz, W.J., Pechmann, J.C., and Burlacu, R., 2015, A uniform moment magnitude earthquake catalog for the Utah region (1850–2012) and estimation of unbiased recurrence parameters for background seismicity, *in* Lund, W.R., editor, Proceedings volume, Basin and Range Province Seismic Hazards Summit III, Utah Geological Survey Miscellaneous Publication 15-5, CD (electronic poster).

Bachmann, C.E., Wiemer, S., Woessner, J., and Hainzl, S., 2011, Statistical analysis of the induced Basel 2006 earthquake sequence—introducing a probability-based monitoring approach for enhanced geothermal systems: Geophysical Journal International, v. 186, no. 2, p. 793–807.

Chambers, D.J., Koper, K.D., Pankow, K.L., and McCarter, M.K., 2015, Detecting and characterizing coal mine related seismicity in the Western US using subspace methods: Geophysical Journal International, v. 203, no. 2, p. 1388–1399.

Deichmann, N., and Giardini, D., 2009, Earthquakes induced by the stimulation of an enhanced geothermal system below Basel (Switzerland): Seismological Research Letters, v. 80, no. 5, p. 784–798.

Ellsworth, W.L., 2013, Injection-induced earthquakes, Science, v. 341, no. 6142, https://doi.org/10.1126/science.1225942.

Foulger, G.R., Wilson, M., Gluyas, J., Julian, B.R., and Davies, R., 2017, Global review of human-induced earthquakes: Earth-Science Reviews, v. 178, p. 438–514.

Harris, D., 2006, Subspace detectors—Theory: Lawrence Livermore National Laboratory, Livermore, California, 48 p. TPI 7501398

Harris, D., and Paik, T., 2006, Subspace detectors—Efficient implementation, theory: Lawrence Livermore National Laboratory, Livermore, California, 36 p.

Hsieh, P.A., and Bredehoeft, J.D., 1981, A reservoir analysis of the Denver earthquakes—a case of induced seismicity: Journal of Geophysical Research, Solid Earth, v. 86, no. B2, p. 903–920.

Kirby, S.M., 2019, Revised mapping of bedrock geology adjoining the Utah FORGE site, *in* Allis, R., and Moore, J.N., editors, Geothermal characteristics of the Roosevelt Hot Springs system and adjacent FORGE EGS site, Milford, Utah: Utah Geological Survey Miscellaneous Publication 169-A, 6 p., 2 plates, scale 1:24,000, https://doi.org/10.34191/MP-169-A.

Majer, E., Nelson, J., Robertson-Tait, A., Savy, J., and Wong, I., 2012, Protocol for addressing induced seismicity associated with enhanced geothermal systems: U.S. Department of Energy, Office of Energy Efficiency and Renewable Energy, Washington, DC, no. DOE/EE—0662, Online, https://www1.eere.energy.gov/geothermal/pdfs/geothermal_seismicity_protocol_012012.pdf.

Nielson, D.L., Sibbett, B.S., McKinney, D.B., Hulen, J.B., Moore, J.N., and Samberg, S.M., 1978, Geology of Roosevelt Hot Springs KGRA, Beaver County, Utah: Earth Science Laboratory, University of Utah Research Institute, Salt Lake City, Utah, 120 p.

Olson, T.L., 1976, Earthquake surveys of the Roosevelt Hot Springs and the Cove Fort Areas, Utah: Salt Lake City, University of Utah, M.S. thesis, 80 p., 2 pl.

Pankow, K.L., Arabasz, W.J., Nava, S.J., Pechmann, J.C., , 2004, Triggered seismicity in Utah from the 3 November 2002 Denali fault earthquake: Seismological Society of America Bulletin 94, p. S332– S347.

Petersen, M.D., Mueller, C.S., Moschetti, M.P., Hoover, S.M., Shumway, A.M., McNamara, D.E., Williams, R.A, Llenos, A.L., Ellsworth, W.L., Michael, A.J., Rubinstein, J.L., McGarr, A.F., and Rukstales, K.S., 2017, 2017 one-year seismic-hazard forecast for the central and eastern United States from induced and natural earthquakes: Seismological Research Letters, v. 88, no. 3, p. 772–783.

Potter, S., 2017, Characterizing background seismicity in the region surrounding Milford, Utah: Salt Lake City, University of Utah, M.S. thesis, 79 p.

Raleigh, C.B., Healy, J.H., and Bredehoeft, J.D., 1976, An experiment in earthquake control at Rangely, Colorado: Science, v. 191, no. 4233, p. 1230–1237.

Trow, A.J., Zhang, H., Record, A.S., Mendoza, K.A., Pankow, K L., and Wannamaker, P.E., 2018, Microseismic event detection using multiple geophone arrays in southwestern Utah: Seismological Research Letters, v. 89, no. 5, p. 1660–1670.

Trutnevyte, E. and Wiemer, S., 2017, Tailor-made risk governance for induced seismicity of geothermal energy projects—an application to Switzerland: Geothermics, v. 65, p. 295–312.

Walters, R.J., Zoback, M.D., Baker, J.W., and Beroza, G.C., 2015, Characterizing and responding to seismic risk associated with earthquakes potentially triggered by fluid disposal and hydraulic fracturing: Seismological Research Letters, v. 86, no. 4, p. 1110–1118.

Wessel, P., and Smith, W.H.F., 1995, New version of Generic Mapping Tools released: EOS, Transactions, American Geophysical Union, v. 76, p. 329.

Zandt, G., McPherson, L., Schaff, S., and Olsen, S., 1982, Seismic baseline and induction studies—Roosevelt Hot Springs, Utah and Raft River, Idaho Earth Science Laboratory, University of Utah Research Institute, Salt Lake City, Utah, 63 p.

INTERPRETATION OF SEISMIC REFLECTION SURVEYS NEAR THE FORGE ENHANCED GEOTHERMAL SYSTEMS SITE, UTAH

by John Miller[1], Rick Allis[2], and Christian Hardwick[2]

[1]Consulting Geophysicist, Golden Colorado

[2]Utah Geological Survey, Salt Lake City, Utah

Miscellaneous Publication 169-H
Utah Geological Survey
a division of
UTAH DEPARTMENT OF NATURAL RESOURCES

This paper is part of *Geothermal Characteristics of the Roosevelt Hot Springs System and Adjacent FORGE EGS Site, Milford, Utah*. https://doi.org/10.34191/MP-169

Bibliographic citation:

Miller, J., Allis, R., and Hardwick, C., 2019, Interpretation of seismic reflection surveys near the FORGE enhanced geothermal systems site, Utah, *in* Allis, R., and Moore, J.N., editors, Geothermal characteristics of the Roosevelt Hot Springs system and adjacent FORGE EGS site, Milford, Utah: Utah Geological Survey Miscellaneous Publication 169-H, 13 p., https://doi.org/10.34191/MP-169-H.

INTERPRETATION OF SEISMIC REFLECTION SURVEYS NEAR THE FORGE ENHANCED GEOTHERMAL SYSTEMS SITE, UTAH

by John Miller, Rick Allis, and Christian Hardwick

ABSTRACT

New three-dimensional multichannel and two-dimensional seismic reflection data were acquired across, and extending eastward and westward from, the FORGE EGS site in Utah in November 2017; data were processed and interpreted between December 2017 and February 2018. These data supplement two previously existing two-dimensional seismic lines located adjacent to the south and west edges of the site that were licensed in September and October 2017 from Seismic Exchange, Inc. The data image two distinct lithofacies comprising basin fill sediments and crystalline basement rocks; the latter are mostly Miocene granitic rocks that will host the proposed EGS reservoir. The contact between these rock types forms an inclined surface that generally dips 20° to 30° west and appears as a strong reflection on all seismic lines within and to the south of the site. This paper (1) briefly describes the data acquisition effort and processing techniques used to create the seismic images, (2) focuses on the interpretation of the 2-D and 3-D surveys, (3) sufficiently images the FORGE site for detailed interpretation of basin evolution and orogenic uplift, (4) ties seismic interpretation with FMI logs and gravity surveys, and (5) reveals new interpretation of the Milford Valley and the Mineral Mountains evolution. The key finding is a west-dipping valley and ridge structure to the granitic surface. The simplest interpretation is that the granitic surface is likely an erosional feature similar in scale to the western flank of the Mineral Mountains, rather than the previously interpreted detachment fault surface. This does not preclude detachment tectonics occurring during basin evolution but the 3-D image of the granitic surface shows otherwise for this feature.

INTRODUCTION

In support of the effort by the U.S. Department of Energy (DOE) to establish an enhanced geothermal systems (EGS) laboratory in the western USA, ~7 mi^2 (~17 km^2) of new three-dimensional (3-D) multichannel seismic reflection data were acquired across the Frontier Observatory for Research in Geothermal Energy (FORGE) site, centered on the new vertical test well (58-32) near Milford, Utah. Two new ~2.5 (4 km) mile long two-dimensional (2-D) multichannel seismic reflection lines were also acquired, extending east and west from the FORGE site. In addition, two previously existing 2-D multichannel seismic reflection lines were licensed from Seismic Exchange, Inc. (SEI) with limited publication rights (referred to here as lines 5 and 11).

A location map of the seismic reflection data purchased by FORGE Utah is given in Figure 1. In the center is the 3-D area, a series of 13 source lines and 27 receiver lines resulting in 170 "inlines" oriented west-east and 213 "crosslines" oriented south-north. The two new 4-kilometer-long 2-D seismic lines (301 and 302) extend east and west from the 3-D survey area and consist of 161 receiver locations with source points at each receiver, except for points that were close to pipelines or other hazards. These lines provided ties to a 3.8-km-deep well (Acord-1) near the middle of the basin, as well as to granitic outcrops at the eastern flank of the Mineral Mountains. Lines 5 and 11 were recorded in 1979 and are oriented roughly south-north along Antelope Pt. Rd., and oriented east-west near Geothermal Plant Rd.

ACQUISITION AND PROCESSING

Lines 5 and 11 were purchased from SEI with limited publication rights (GSI-SU-5, and GSI-SU-11 on https://web.seismicexchange.com/1/). These purchases included (1) unprocessed digital field data and data reprocessed in 2016 in standard Society of Exploration Geophysicists Y format files (SEG-Y; Barry et al., 1975), (2) images of the processed cross sections in TIFF graphics format, developed by Aldus Corporation, now Adobe Systems (Murray and vanRyper, 1996), and (3) navigation and associated support data. In addition, both SEI lines were originally processed in 1979 and that version of the processing only exists as a graphic image. The reprocessed version of line 11 gave a superior image to the 1979-processed TIFF image, so we used that line and seismic- and well-derived velocities to convert the digital traces from time to depth. However, the 1979-processed TIFF image of line 5 gave a superior image to that of the 2016 reprocessing, resolving the basement reflection

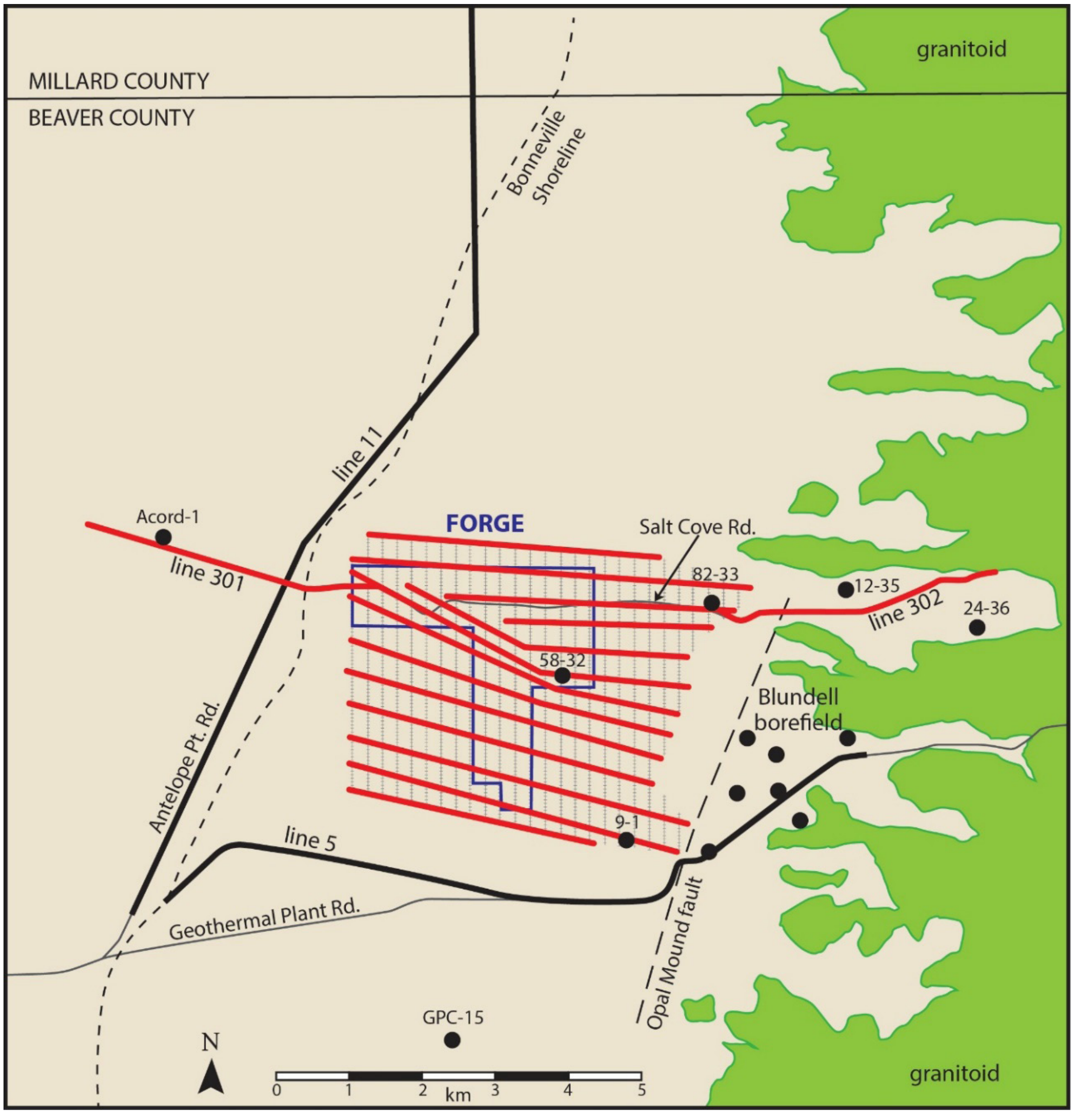

Figure 1. *Seismic survey locations. The 3-D survey area comprises red lines (vibrator point locations 50 m apart), and geophone locations (oriented north-south, 50 m apart). Red lines 301 and 302 are new 2-D seismic lines; heavy black lines are 2-D lines licensed from Seismic Exchange, Inc. with limited publication rights. Black circles are well locations. Granitic outcrop is given by the green contour.*

especially well. Because there were no digital data of the 1979 processing, we identified a contractor with specialized software that could convert the graphic image into individual digital traces by using a raster to vector conversion. Using these digital traces and a velocity model created from a combination of seismic- and well-derived velocities, we converted the digital data from time to depth.

In November 2017, Paragon Geophysical Services, Inc. of Wichita, Kansas, began work in the 3-D survey area and 2-D lines 301 and 302 (Figure 1). There were 1,114 source points and 1,741 receiver points in the 3-D area. Receivers were located at 50-m intervals and source points were energized at 50-m intervals (Figure 2). All receivers were active for each source point. The energy source used for both the 2-D and 3-D surveys was a Vibroseis method consisting of two I/O AHV IV 364 and 365 vibrators spaced 30 feet apart. Each vibrator imparts 62,000 lbs. of peak force and was operated at 70% of peak force. The Vibroseis sweep produced a 4-48 Hz linear excitation that was 12 seconds in duration with four sweeps per source location.

The new 2-D data were organized into Common Depth Point (CDP) bins along each line, spaced 12.5 m apart. The 3-D data were organized geometrically into CDP bins spaced 25 m apart and were further organized into the “inlines” and “crosslines” (details in Figure 2). All data exhibited a considerable amount of noise including ground roll and air blast from the vibrators. Extensive testing was performed to design a model-based filter to remove as much of this noise as possible. The noise was not coherent enough to be removed completely, but it was sufficient to condition the data for input to the processing flow.

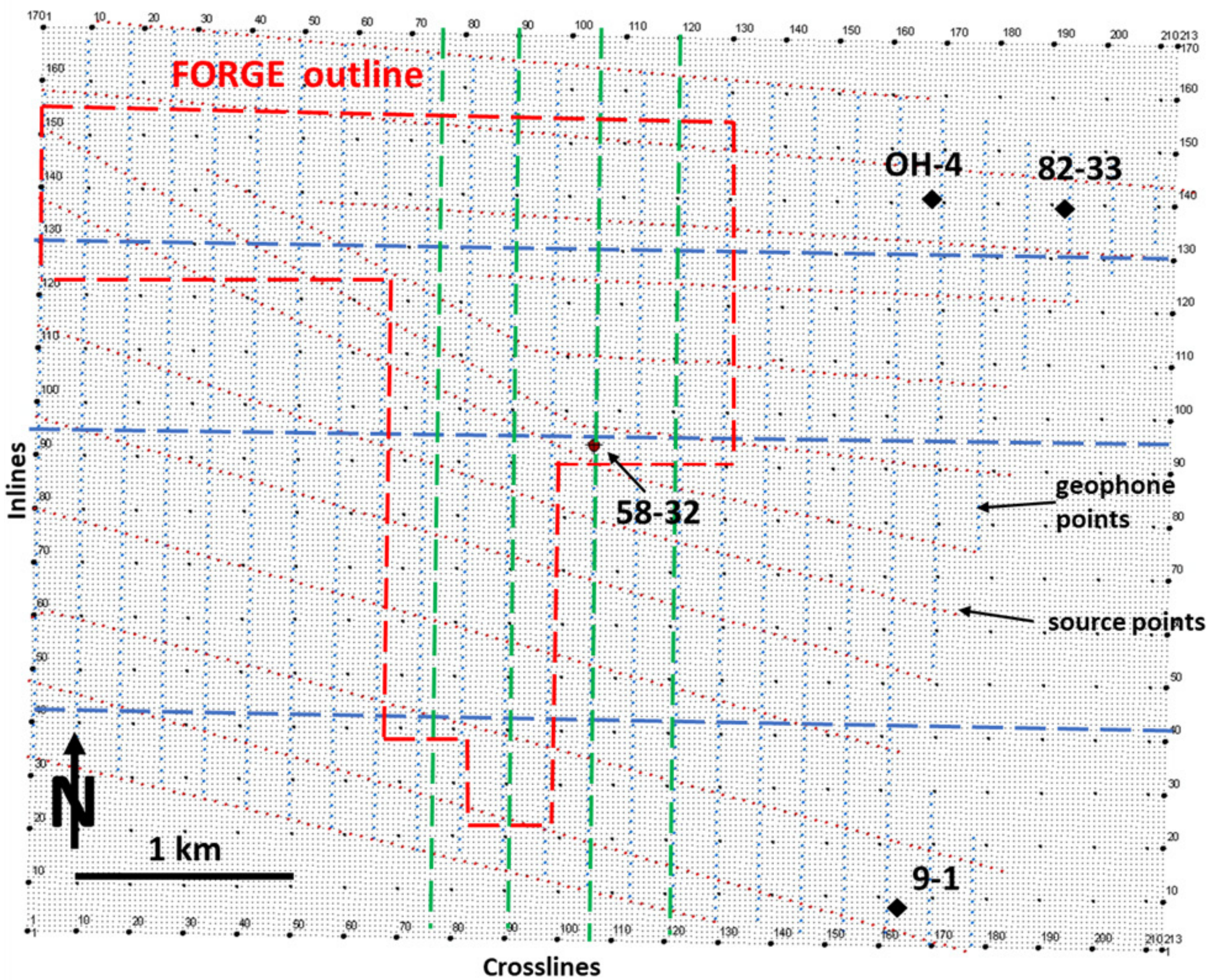

Figure 2. *Details of the source and receiver points, the FORGE boundary (red dashes), north-south crosslines (green dashes) and west-east inlines (blue dashes) chosen for discussion. Well 58-32 is the FORGE well drilled during 2017, and wells 9-1, 82-33, and OH-4 are exploration wells drilled in the late 1970s that penetrated granitic bedrock. CDP bins as well as inline and crossline numbering system are displayed around the perimeter of the figure.*

The main source of uncertainty in reflection seismic profiling rests with the determination of velocity directly from the seismic data and subsequent depth to the reflecting interfaces. Velocity determination depends on adequate source-receiver offset (the distance between the seismic source and the receiver farthest away from it) relative to the depth of the target that is to be imaged. The maximum source-receiver offset in the 3-D area, greater than 3000 m, is suitable for determining the velocity field with a high degree of confidence. In addition, we measured velocity and depth in well 58-32 which assisted in calibrating the velocity analysis. To test the accuracy, we used inline 93 which intersects the well. We converted that line from time to depth using only the well velocities, and then converted it to depth using seismic-derived velocities. The difference in depth to the granitic interface was less than 20 m, which at 1000 m total depth to the granitic interface is less than 2% difference. In addition, the velocity field away from the wellsite was quite homogeneous, and structural contours above of the granite, which were derived from the seismic data, integrate seamlessly with gravity modeling by Hardwick et al. (2019).

INTERPRETATION

All lines discussed in this report except line 302 are plotted relative to an elevation datum of 1800 m above sea level (asl) and most have no vertical exaggeration (line 302 datum is 2000 m asl because of the higher ground elevation). The ground surface generally increases from 1500 m asl near the axis of Milford Valley close to Acord-1, to about 1800 m asl on the alluvial fan adjacent to the western flank of the Mineral Mountains.

2-D Lines

Line 11, extending 13 km northward along Antelope Pt. Rd., illustrates a complex pattern of basin fill draped over granitic bedrock (Figure 3). The central portion of the line crosses a 6-km-wide sub-basin in the assumed granitic bedrock with a vertical relief of about 500 m. Truncated reflectors on the south side of this sub-basin suggest infilling sediments have been partially eroded, which indicates cycles of erosion and deposition during the evolution of Milford Valley and the Mineral Mountains. The near-surface lake sediments, which transition to underlying volcaniclastic sediments at about 1 km depth in Acord-1 (Hintze and Davis, 2003; Jones et al., 2018), dip towards the north and appear to be about 1.7 km thick at the north end of the profile (2 km below 1800 m datum). Deformation of the lake sediments, between 8 and 12 km along the profile and coinciding with a topographic high in the ground surface, appears to indicate faulting. The true dip of the faults may be obscured because the profile intersects the faults at a narrow angle.

Line 301 extended west from the 3-D survey area, crossing line 11 and tying into the known stratigraphy in Acord-1. This well is the deepest in Milford Valley (3.8 km) and penetrated granitic basement at 3.0 km. The overlying basin fill comprised lacustrine sediments near surface, and the underlying volcaniclastic sediments had several thin andesite lava flows at 2.2 km depth (Jones et al., 2018). The line is shown in Figure 4 with reflecting horizons highlighted.

The lake sediments are characterized by fine, near-horizontal layering across the entire line. Near the eastern end of the line there may be a transition to alluvial-fan deposits that dominate the upper part of the 3-D survey area. The top of the volcaniclastic unit dips eastward to a low point of 1600 m below the 1800 m asl datum where the line crosses Antelope Pt. Rd. East of this subtle basin the top surface of the volcaniclastics rises to above 1000 m below the datum near the eastern edge of the line (adjacent to the west edge of the 3-D survey area.) The andesite lavas within the volcaniclastic unit dip towards the east and appear to fade out and disappear around the middle of the line. Possibly the andesite lavas lap against the west-dipping granitic bedrock, which is not clearly imaged by seismic reflections.

According to the gravity interpretation by Hardwick et al., (2019), the earliest phase of basin filling had a depocenter about 4 km west of Acord-1. Thus, the center of the valley may have been beneath Antelope Pt Rd. by the time the lake sediments began to be deposited. Today the center of the valley is again to the west of Acord-1.

A minimally processed version of line 302 is also included here because it reveals a surprisingly deep buried valley beneath the western flanks of the Mineral Mountains (Figure 5). The line traverses Salt Cove valley at the eastern end of Salt Cove Rd. (Figure 1). It crosses the Opal Mound fault between CDP 50 and 100. Injector well 12-35 is midway along and north of the line.

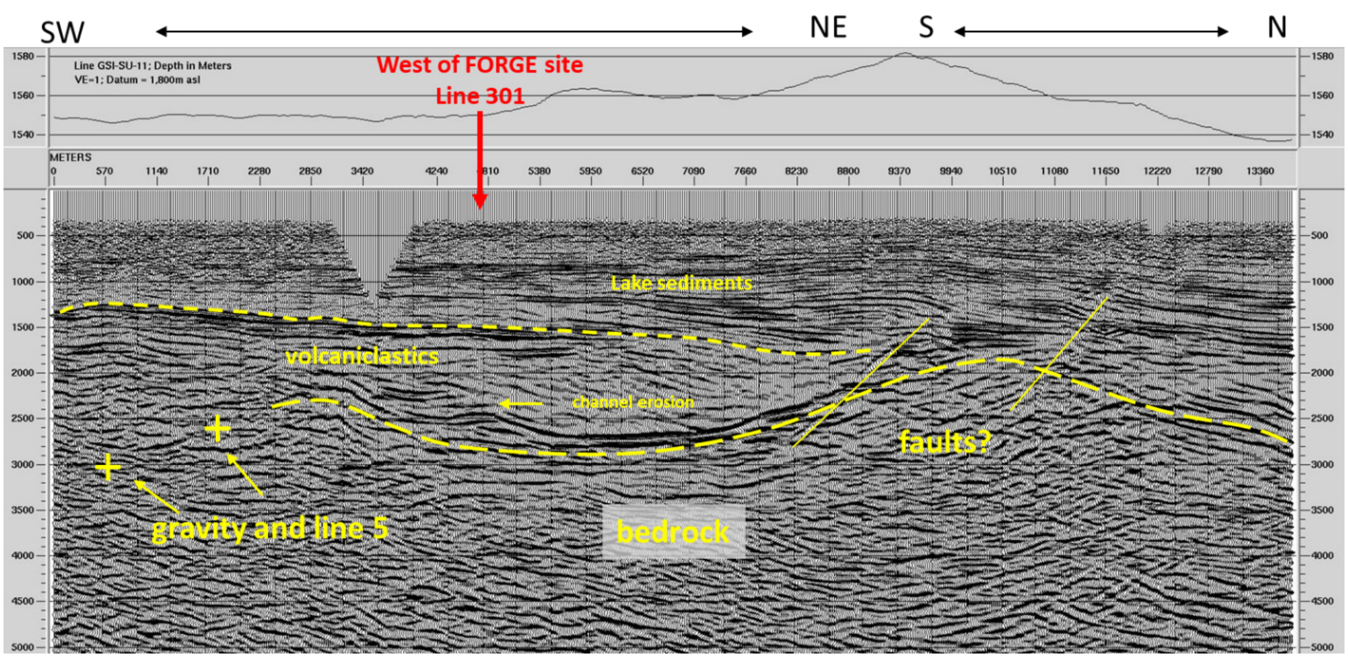

Figure 3. *Line 11 along Antelope Pt. Rd. The upper graph shows the surface topography (m asl), and the lower graph shows the reflection imagery in depth (m) below the datum of 1800 m asl. There is no vertical exaggeration. The west edge of the 3-D survey area is 0.5 km east of the profile at the 5-km mark. Acord-1 is 2 km west from where line 301 intersects the profile (refer to Figure 1). Seismic data are owned or controlled by Seismic Exchange, Inc.; interpretation is from this study for the FORGE project.*

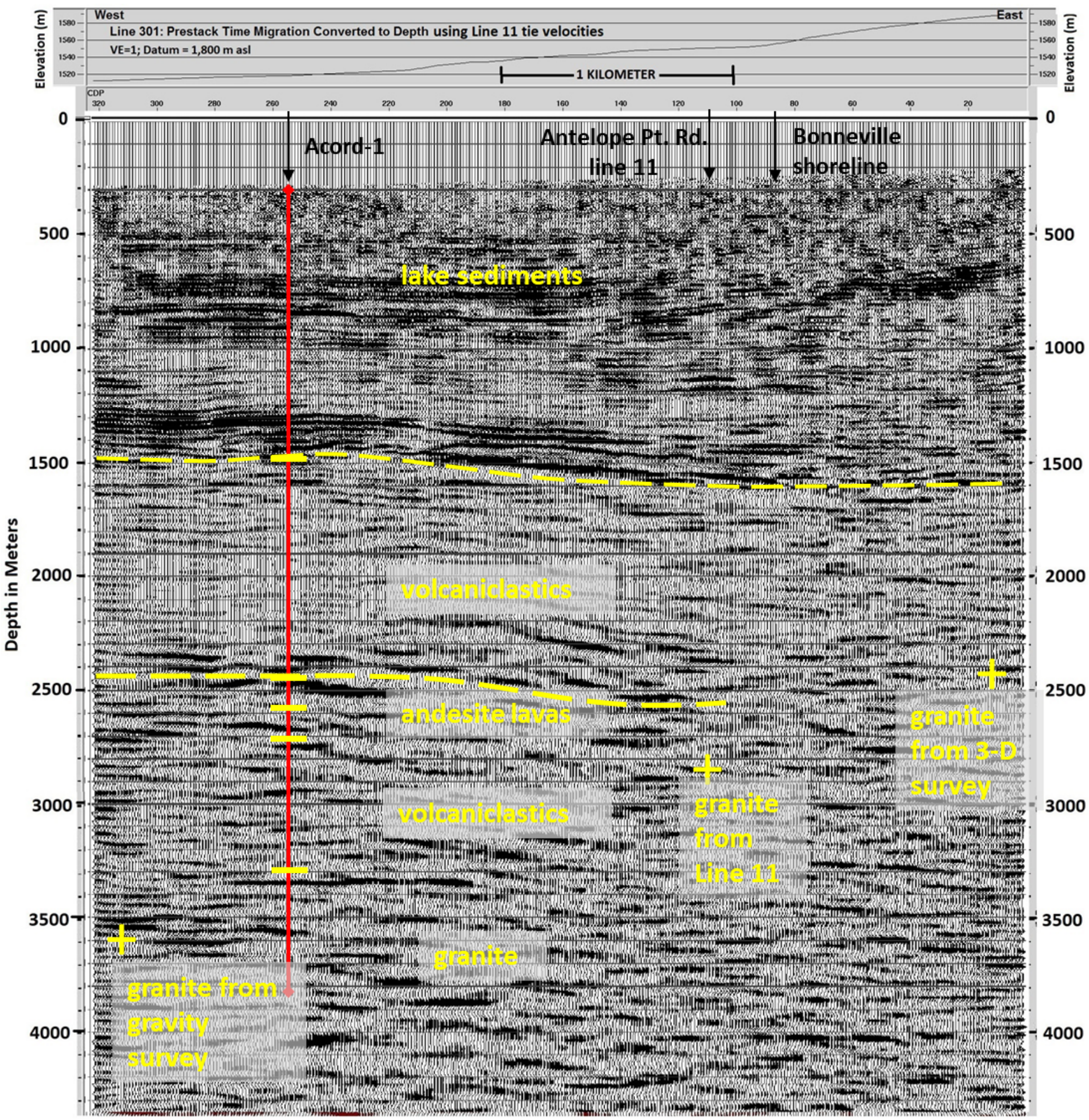

Figure 4. Line 301 with several reflectors highlighted. The upper graph shows the surface topography (m asl), and the lower graph shows the reflection imagery in depth (m) below the datum of 1800 m asl. There is no vertical exaggeration. Because zero-depth is at the 1800 m asl datum, 280 m needs to be subtracted from the depth axis to get depth below ground surface at Acord-1. Line location is shown on Figure 1.

An abandoned exploration well 24-36 is near east end of the line. These wells are near the north and south edges of the valley, respectively, and both penetrated granite at relatively shallow depth. Line 302 shows the granitic surface as an undulating reflector with the maximum depth at a two-way travel time of 400 ms. Assuming a near-surface velocity of 2 km/s (shallow velocity in GPC-15; Glenn and Hulen, 1979), this is a depth of about 400 m. This occurs where the valley is widest, being about 1.2 km at that point. It will be shown later that the dimensions of the infilled valley beneath line 302 are similar to the buried valley in the granite beneath the west FORGE site revealed by the 3-D survey. The granitic surface in the vicinity of the Opal Mound fault is too shallow to be imaged by seismic reflections.

We note here that line 302 is undergoing reprocessing and initial results indicate that the undulating nature of the granitic reflector may be an artifact of lateral velocity variations in the alluvium above the reflector.

Line 5, extending mostly west-east from Antelope Pt. Rd. to east of the Blundell production wellfield, images a reflector with a constant dip into the basin to the west. Early interpretations proposed that the granitic surface may be a low-angle detachment surface along which extensional movement occurred as the basin was formed (Barker, 1986; Smith et al., 1989; Figure 6). The

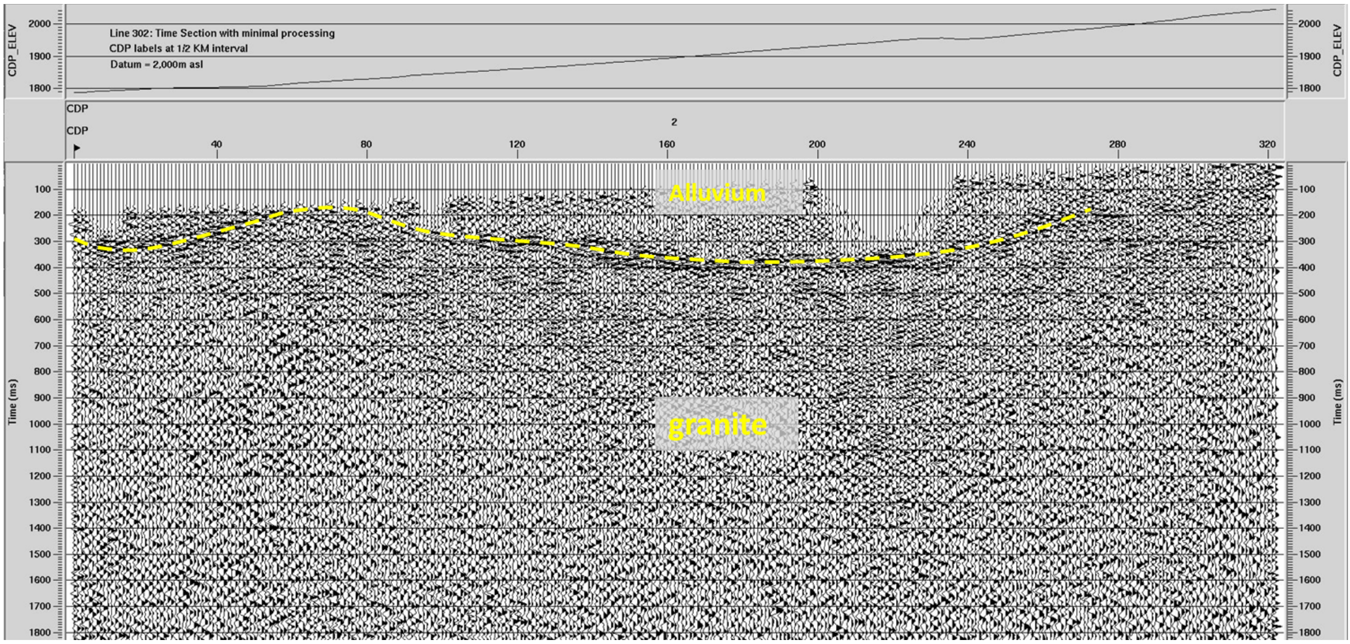

Figure 5. Time section of line 302 (location shown on Figure 1). The upper graph shows the surface topography (m asl), and the lower graph shows the reflection imagery in depth (m) below the datum of 2000 m asl. There is no vertical exaggeration. The maximum depth of the infilled valley around CDP 200 is about 400 m assuming a two-way travel time of 400 ms and velocity for the fill of 2 km/s. Note the elevation datum is 2000 m asl on this line because of the higher surface topography.

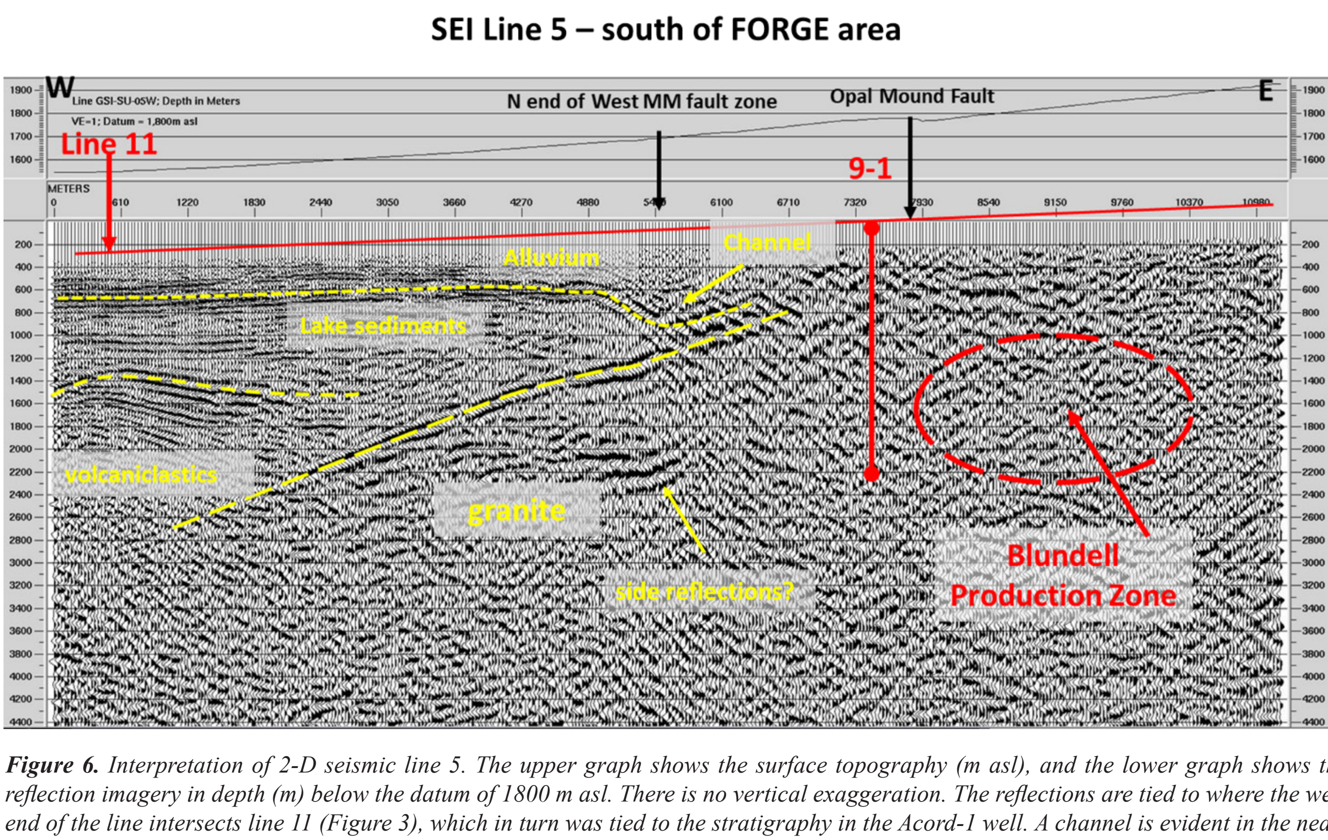

Figure 6. Interpretation of 2-D seismic line 5. The upper graph shows the surface topography (m asl), and the lower graph shows the reflection imagery in depth (m) below the datum of 1800 m asl. There is no vertical exaggeration. The reflections are tied to where the west end of the line intersects line 11 (Figure 3), which in turn was tied to the stratigraphy in the Acord-1 well. A channel is evident in the near-surface alluvium where the present-day Opal Mound fault wash occurs. The granitic surface is encountered at 230 m depth in well 9-1 (well 9-1 is 0.7 km northwest of the Opal Mound fault and line 5).

seismic interpretation presented here indicates that the granitic surface is likely erosional and not a fault surface. This is based on the valley and ridge morphology on the granitic surface revealed by the north-south crosslines in the 3-D survey discussed in the next section.

Line 5 does not show obvious offsets caused by faults in the granitic surface, or in surfaces identified in the basin fill. The north-trending West Mineral Mountains fault zone appears to diminish where it crosses Geothermal Plant Rd. (Kirby et al., 2019; Knudsen et al., 2019) and if present, would cross line 5 between 4900 and 5500 m from the west end of the line (Figure 6). Farther east, there is a lack of coherent reflectors both where the Opal Mound fault is crossed (7700 m), and even farther east where the line crosses the Blundell production wells (7800–10,000 m). Production wells tap into high-permeability fractures over a 1-km-wide zone east of the Opal Mound fault; these were not imaged in line 5.

3-D Imagery

Selected lines from the 3-D survey are now discussed to illustrate the character of the granitic surface and the basin fill beneath the FORGE site. Figure 2 shows the locations of the four north-south crosslines and the three west-east inlines that will be highlighted.

The reflection imagery from crossline 105, which runs north-south through FORGE well 58-32, is shown in Figure 7. The main feature is the strong reflector from the granitic surface with undulations between 1000 and 1200 m below the 1800 m asl datum. Checks from where inlines cross this line confirm the pick of the granitic surface. The uncertainty in this pick is about ± 50 m. In the vicinity of well 58-32 there are strong reflectors over a 300-m interval immediately above the granitic surface. The Formation Micro-Imager (FMI) log acquired in the open hole section of 58-32 below casing set at 670 m depth shows a matrix-supported boulder field in this depth interval above the granitic surface (Forbes et al., 2019). The seismic reflection imagery suggests the lateral dimensions of the boulder field is about 1 km in a north-south direction and centered close to 58-32. Figure 7 also shows the potential location of the future FORGE reservoir if it is constrained by 175°C and 225°C isotherms (Allis et al., 2019).

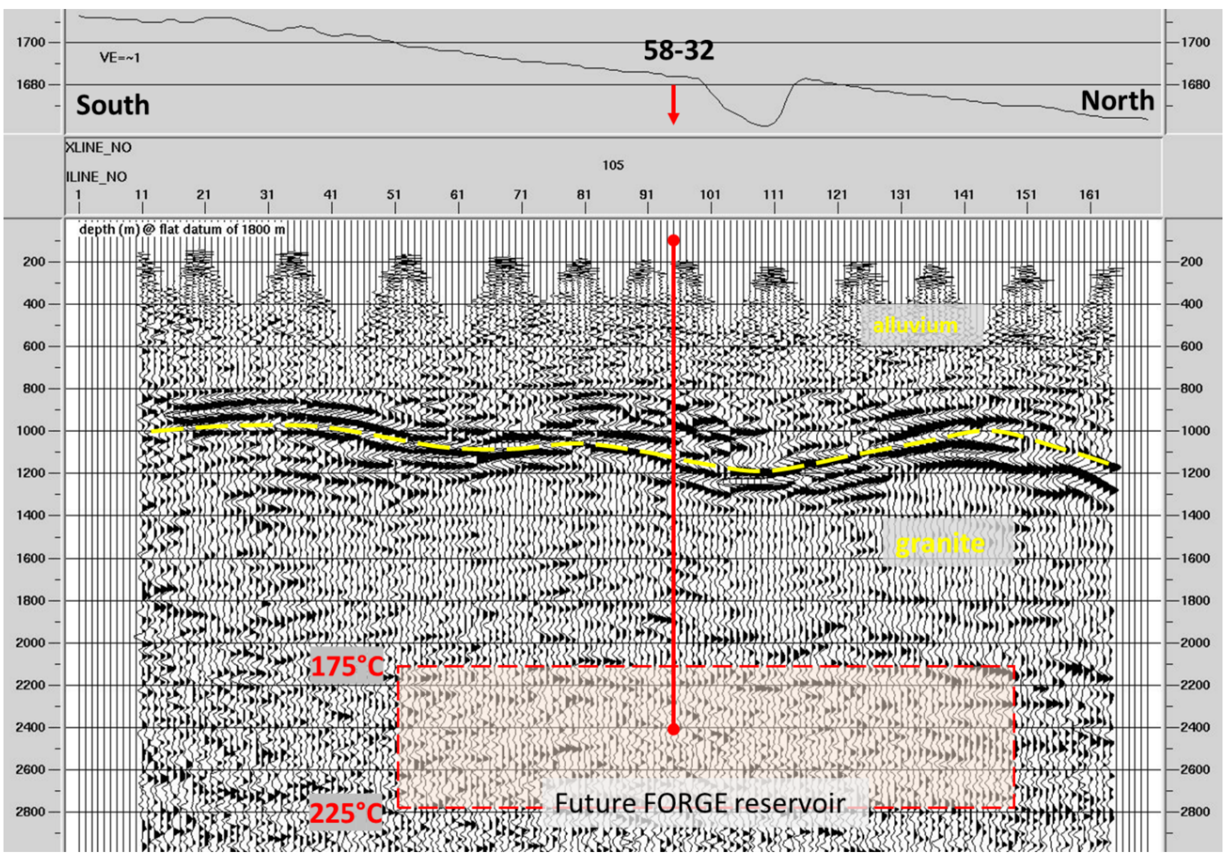

Figure 7. *Crossline 105 extends north-south through FORGE well 58-32. The upper graph shows the surface topography (m asl), and the lower graph shows the reflection imagery in depth (m) below the datum of 1800 m asl. There is no vertical exaggeration. NM Wash can be seen on the topographic profile about 250 m north of well 58-32. Yellow dashes are the geologic interpretation of the granitic surface. The red-dashed box outlines the location of the future reservoir beneath the FORGE site assuming temperature constraints of 175°–225°C.*

Inline 95 is a west-east section through well 58-32 (Figure 8). The granitic surface generally dips west at 20 ± 5 degrees, although near to 58-32 the dip steepens into what other lines confirm as a west-trending valley. The zone of strong reflectors above the granitic surface at 58-32 is only about 250 m wide in a west-east direction, suggesting that this boulder field was deposited against the west flank of the proto-Mineral Mountains. The upper surface of the volcaniclastic unit identified in line 301 mostly occurs at 900 m below the datum and laps against the boulder field just discussed. There is a valley, or broad channel, in this surface near the west side of the line that is about 1 km wide and about 200 m deep on this section. Reflections within the granite on the east side of the section are thought to be a combination of side reflections and multiples, and therefore spurious.

Crossline 120 runs north-south through the east side of the FORGE site (Figure 9). It is 375 m east of crossline 105 shown in Figure 7. The granitic surface is the only coherent reflector, and it undulates between 850 and 1000 m below the datum. The reflective boulder field seen in Figures 7 and 8 is not present on this line.

Crossline 90 is 375 m west of crossline 105 (Figure 10). This shows a major valley cutting across the section, with its axis at about 1500 m below the datum and located beneath the present-day NM Wash. This valley is about 1.5 km wide and 300–400 m deep. The scale of this valley is an order of magnitude larger than NM Wash, which is typically about 50 m wide and 30 m deep where is cuts across the FORGE site. The top of the volcaniclastic section overlying the granite is poorly imaged, but clearly has an undulating surface. The deepest point is in a channel (or wash) located in the same position as the valley in the granitic surface. As the basin filled with volcaniclastics and sediment eroded off the proto-Mineral Mountains to the east, it appears that a major drainage was located beneath the FORGE site for most of the depositional history (more than 20 million years).

Crossline 75 (Figure 11) extends parallel to the west side of section 32 in the FORGE site and crosses near the proposed drilling pad for drilling the deep, deviated wells during Phase 3 (Figure 2). This line shows the same valley imaged in Figure 7 (375 m to east), having similar dimensions and centered beneath the south side of NM Wash. The picks of the granitic surface from the inlines that cross this line confirm smooth sides and an erosional origin to the valley. The top of the volcaniclastic unit has the same characteristics as that seen in Figure 7, with a 100-m-deep channel present at about 900 m datum-depth beneath NM Wash (750 m true depth).

Two west-east lines across the north and south parts of the FORGE site are shown in Figure 12 for completeness. The main difference between these two lines is the increased dip and depth of the granitic surface beneath north FORGE. At crossline 50 the surface is at 1600 m below datum in the north compared to 1400 m beneath south FORGE. In both cases there are spurious reflections from within the granite.

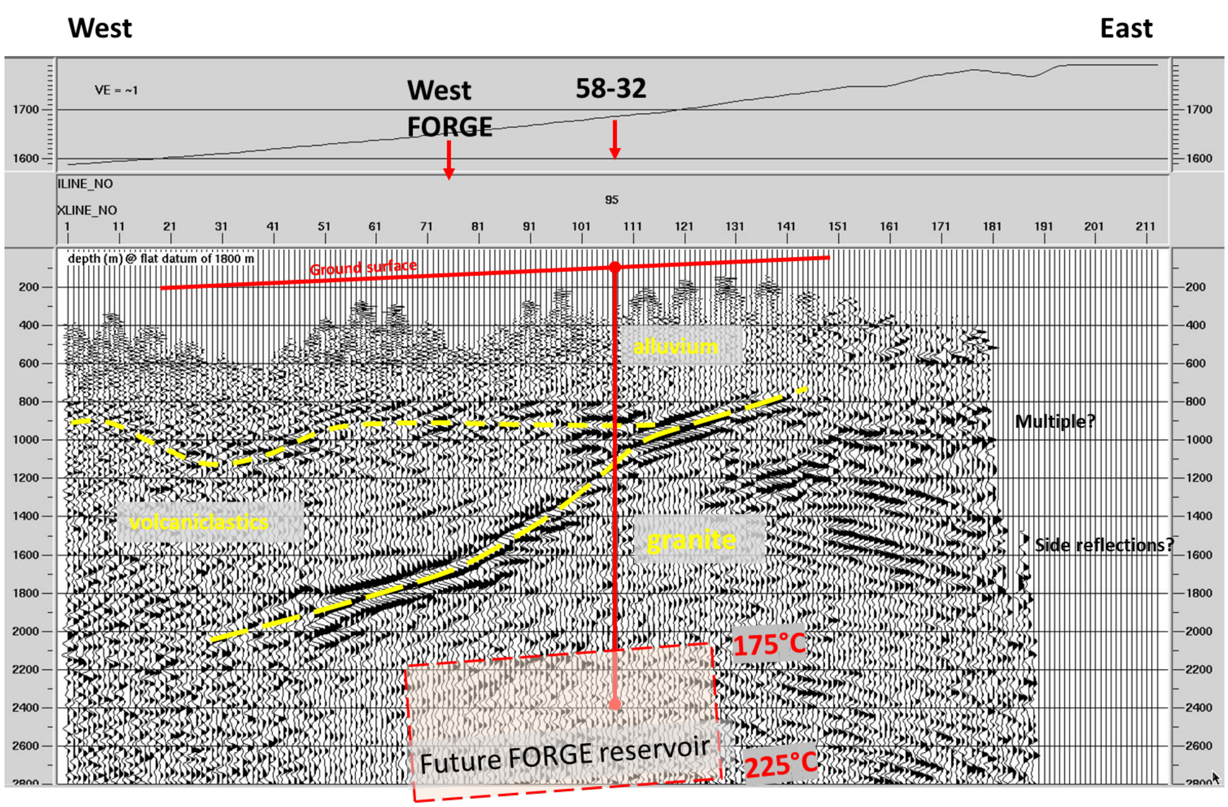

Figure 8. *West-east section through FORGE well 58-32 on inline 95. The upper graph shows the surface topography (m asl), and the lower graph shows the reflection imagery in depth (m) below the datum of 1800 m asl. There is no vertical exaggeration. Annotations are the same as in Figure 7.*

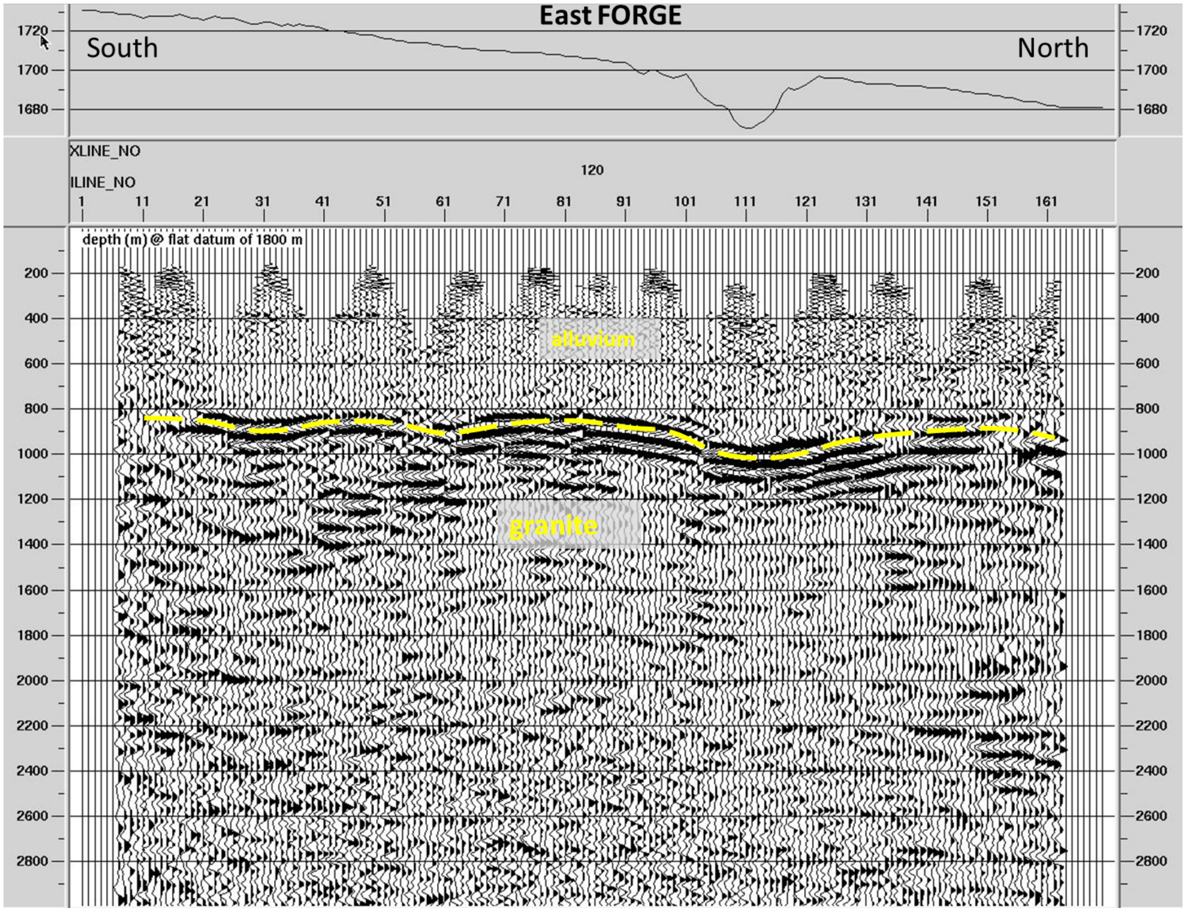

Figure 9. *Crossline 120, extending north-east through the east side of the FORGE site (location on Figure 2). The upper graph shows the surface topography (m asl), and the lower graph shows the reflection imagery in depth (m) below the datum of 1800 m asl. There is no vertical exaggeration.*

CONCLUSIONS

The identification of the reflections from the granitic surface in the 3-D survey area and the adjacent 2-D lines has been integrated with the gravity interpretations of basin-fill thickness (Hardwick et al., 2019) in Figure 13. Although the average westward dip of the granitic surface is 25 ± 5 degrees, the 3-D survey area reveals a valley and ridge structure. The westward orientation of the main valley, and high-resolution imagery of a truncated package of horizontal sedimentary layers on the south flank of the valley imaged beneath Antelope Pt. Rd. (line 11), indicate an erosional origin to most of the features. The scale of the valley is similar to those seen in the western flanks of the Mineral Mountains today, suggesting the buried topography represents earlier phases of uplift and erosion of the Mineral Mountains. Smaller-scale valleys and channels are also seen in the overlying basin-fill sediments, confirming an ongoing process of erosion of the Mineral Mountains and deposition of basin-fill deposits over the last 30 million years. This interpretation does not preclude detachment tectonics occurring during basin evolution as proposed by Bartley (2019), but the detailed 3-D image of the surface of the granite indicates that this feature is not of tectonic origin.

ACKNOWLEDGMENTS

This work was sponsored by the DOE EERE Geothermal Technologies Office project DE-EE0007080 Enhanced Geothermal System Concept Testing and Development at the Milford City, Utah FORGE Site (Managing PI, Joe Moore). We thank Paragon Geophysical Services, Inc. of Wichita, Kansas, for the data acquisition, and STAR Geophysics, Inc. of Oklahoma City, Oklahoma, for preliminary processing of the data. 2-D lines 5 and 11 were purchased from Seismic Exchange, Inc., Denver, with limited publication rights. Reviews by Lauri Burke, U.S. Geological Survey and Richard P. Mignogna, Renewable & Alternative Energy Management, LLC greatly improved earlier versions of the manuscript.

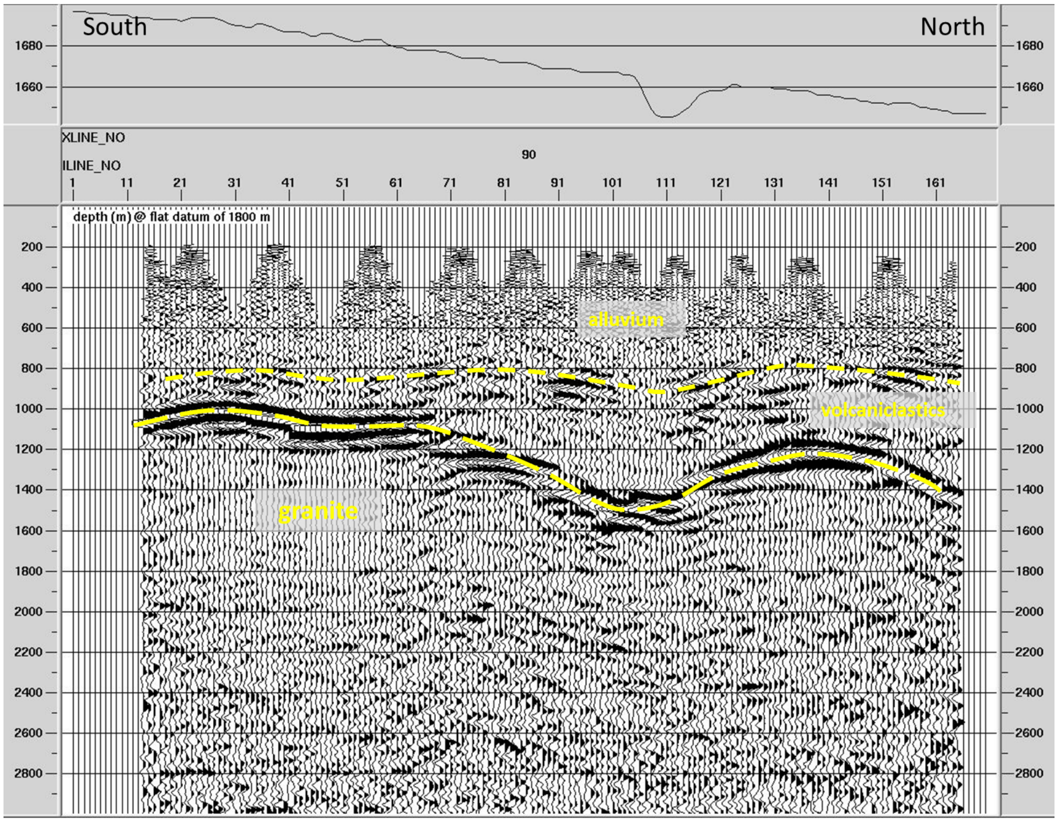

Figure 10. *Crossline 90, which extends north-south through the center of the FORGE site, 375 m west of well 58-32. The upper graph shows the surface topography (m asl), and the lower graph shows the reflection imagery in depth (m) below the datum of 1800 m asl. There is no vertical exaggeration.*

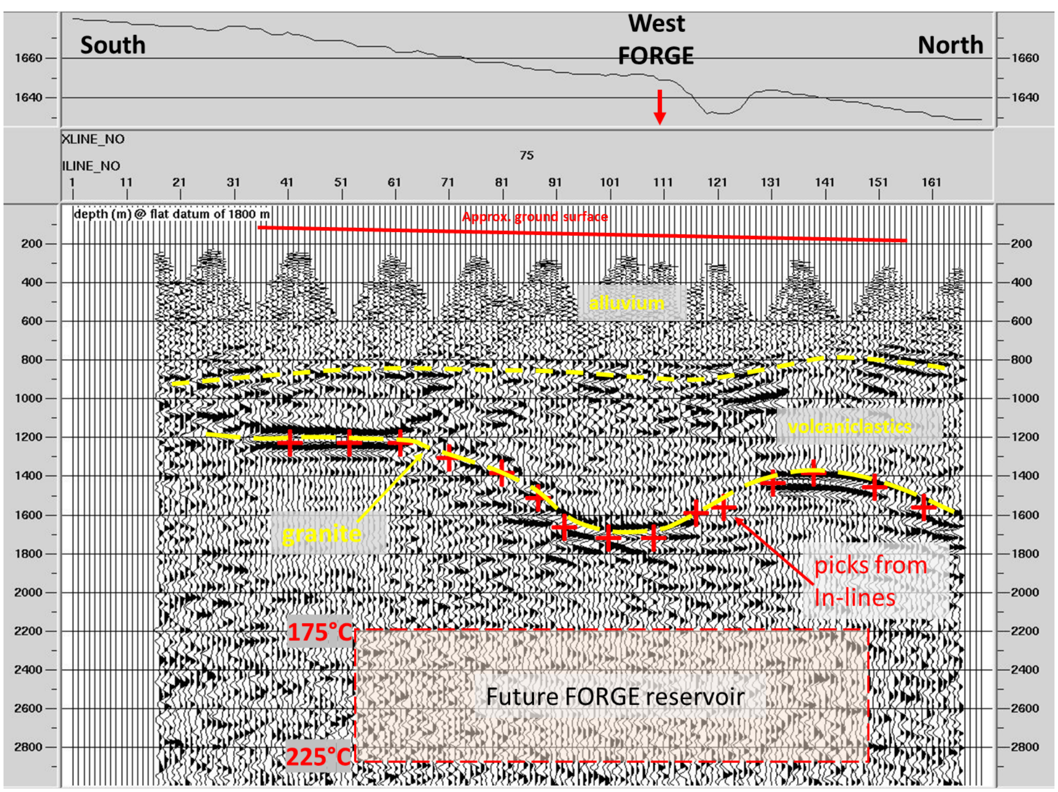

Figure 11. *Crossline 75, which extends north-south through the west side of section 32 in the FORGE site. The upper graph shows the surface topography (m asl), and the lower graph shows the reflection imagery in depth (m) below the datum of 1800 m asl. There is no vertical exaggeration. The red crosses are picks of the granitic surface from where the inlines intersect crossline 75. They confirm a smooth granitic surface to the buried valley beneath the west side of the FORGE site.*

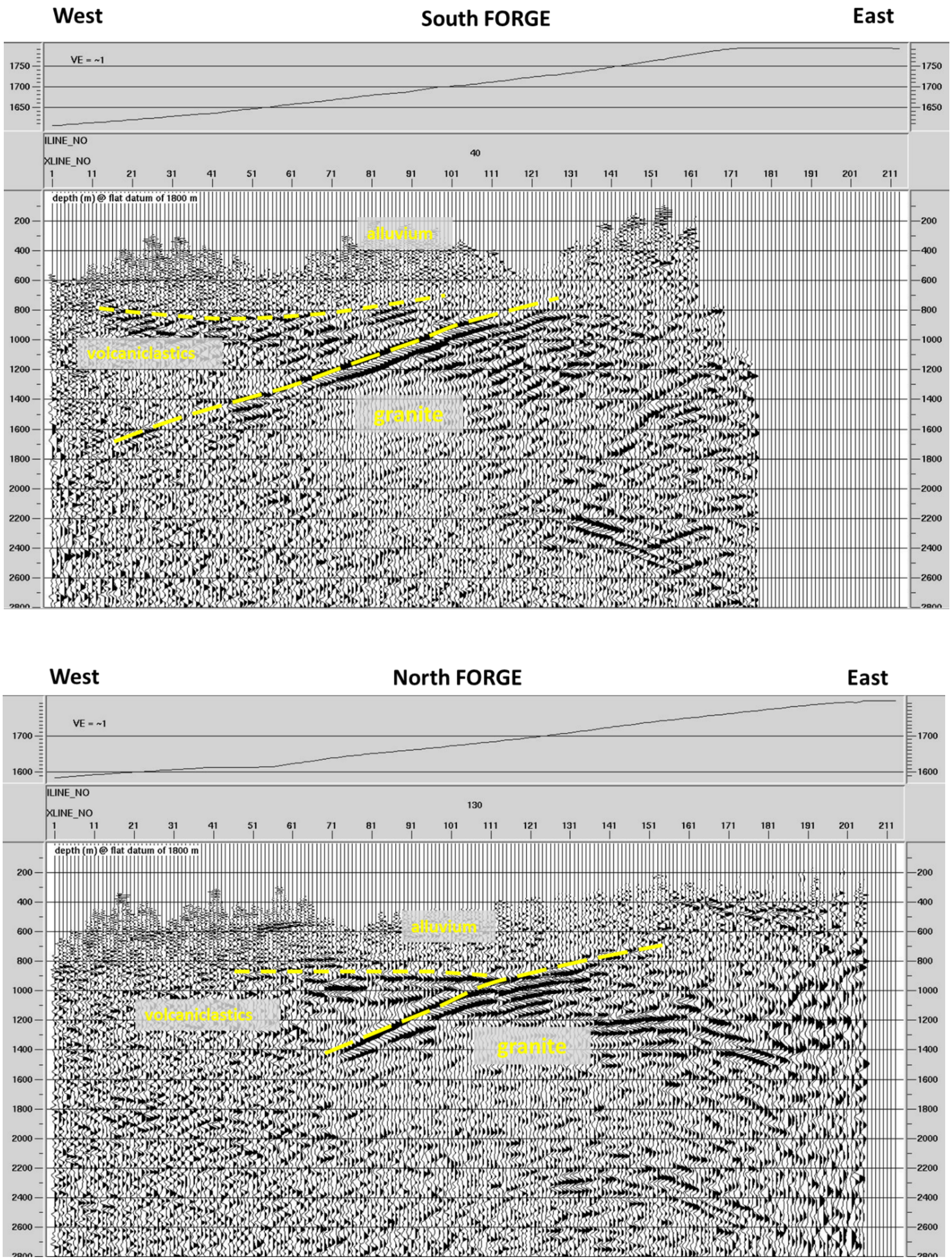

Figure 12. *Inlines 40 and 130. The upper graphs show the surface topography (m asl), and the lower graphs show the reflection imagery in depth (m) below the datum of 1800 m asl. There is no vertical exaggeration. Both lines have spurious reflections within the granite on the east side.*

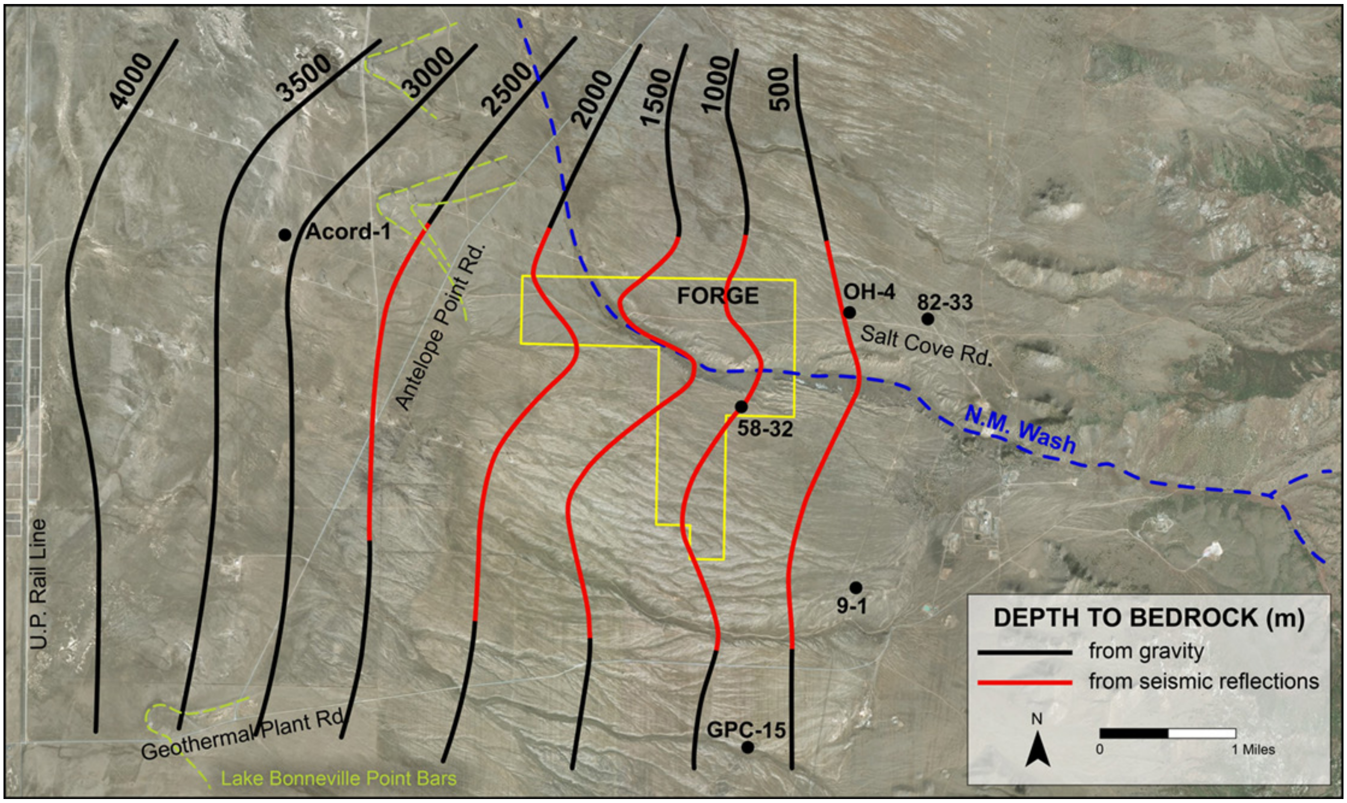

Figure 13. *Structural contours on the top of the granitic bedrock around the FORGE site. The contours are derived from integration of the picks from seismic reflection surveys and from gravity modeling by Hardwick et al. (2019).*

REFERENCES

Allis, R., Gwynn, M., Hardwick, C., Hurlbut, W., Kirby, S.M., and Moore, J.N., 2019, Thermal characteristics of the Roosevelt Hot Springs system, with focus on the FORGE EGS site, Milford, Utah, *in* Allis, R., and Moore, J.N., editors, Geothermal characteristics of the Roosevelt Hot Springs system and adjacent FORGE EGS site, Milford, Utah: Utah Geological Survey Miscellaneous Publication 169-D, 22 p., https://doi.org/10.34191/MP-169-D.

Barker, C.A., 1986, Upper crustal structure of the Milford Valley and Roosevelt Hot Springs, Utah region, by modeling of seismic refraction and reflection data: Salt Lake City, University of Utah, M.S. thesis, 101 p.

Barry, K.M., Cavers, D.A., and Kneale, C.W., 1975, Report on recommended standards for digital tape formats: Geophysics, v. 40, no. 2, p. 344–352, accessed January 26, 2016, at https://seg.org/Portals/0/SEG/News%20and%20Resources/Technical%20Standards/seg_y_rev0.pdf.

Bartley, J.M., 2019, Joint patterns in the Mineral Mountains intrusive complex and their roles in subsequent deformation and magmatism, *in* Allis, R., and Moore, J.N., editors, Geothermal characteristics of the Roosevelt Hot Springs system and adjacent FORGE EGS site, Milford, Utah: Utah Geological Survey Miscellaneous Publication 169-C, 13 p., 1 appendix, https://doi.org/10.34191/MP-169-C.

Forbes, B., Moore, J.N., Finnila, A., Podgorney, R., Nadimi, S., and McLennan, J.D., 2019, Natural fracture characterization at the Utah FORGE EGS test site—discrete natural fracture network, stress field, and critical stress analysis, *in* Allis, R., and Moore, J.N., editors, Geothermal characteristics of the Roosevelt Hot Springs system and adjacent FORGE EGS site, Milford, Utah: Utah Geological Survey Miscellaneous Publication 169-N, 11 p., https://doi.org/10.34191/MP-169-N.

Glenn, W.E., and Hulen, J.B., 1979, A study of well logs from Roosevelt Hot Springs KGRA, Utah, *in* Society of Professional Well Log Analysts 20th Annual Logging Symposium Transactions: p ZZ-1

Hardwick, C., Hurlbut, W., and Gwynn, M., 2019, Geophysical surveys of the Milford, Utah, FORGE site—gravity and TEM, *in* Allis, R., and Moore, J.N., editors, Geothermal characteristics of the Roosevelt Hot Springs system and adjacent FORGE EGS site, Milford, Utah: Utah Geological Survey Miscellaneous Publication 169-F, 15 p., https://doi.org/10.34191/MP-169-F.

Hintze, L.F., and Davis, F.D, 2003, Geology of Millard County: Utah Geological Survey Bulletin 133, 305 p.

Jones, C.G., Moore, J.N., and Simmons, S., 2019, Petrography of the Utah FORGE site and environs, Beaver County, Utah, *in* Allis, R., and Moore, J.N., editors, Geothermal characteristics of the Roosevelt Hot Springs system and adjacent FORGE EGS site, Milford, Utah: Utah Geological Survey Miscellaneous Publication 169-K, 23 p., 2 appendices, https://doi.org/10.34191/MP-169-K.

Kirby, S.M., 2019, Revised mapping of bedrock geology adjoining the Utah FORGE site, *in* Allis, R., and Moore, J.N., editors, Geothermal characteristics of the Roosevelt Hot Springs system and adjacent FORGE EGS site, Milford, Utah: Utah Geological Survey Miscellaneous Publication 169-A, 6 p., 2 plates, scale 1:24,000, https://doi.org/10.34191/MP-169-A.

Knudsen, T., Kleber, E., Hiscock, A., and Kirby, S.M., 2019, Quaternary geology of the Utah FORGE site and vicinity, Millard and Beaver Counties, Utah, *in* Allis, R., and Moore, J.N., editors, Geothermal characteristics of the Roosevelt Hot Springs system and adjacent FORGE EGS site, Milford, Utah: Utah Geological Survey Miscellaneous Publication 169-B, 21 p., 2 appendices, https://doi.org/10.34191/MP-169-B.

Murray, J.D., and vanRyper, W., 1996, Encyclopedia of graphics file formats, second edition: Sebastopol, O'Reilly Media, Inc., 1152 p.

Smith, R.B., Nagy, W.C., Julander, K.A, Viveiros, J.J., Barker, C.A, and Gants, D.G., 1989, Geophysical and tectonic framework of the eastern Basin and Range-Colorado Plateau-Rocky Mountain transition, *in* Pakiser, L.C., and Mooney, W.D., Geophysical framework of the continental United States: Boulder, Colorado, Geological Society of America Memoir 172, p. 205–233.

CARBON DIOXIDE FLUX AND CARBON AND HELIUM ISOTOPIC COMPOSITION OF SOIL GASES ACROSS THE FORGE SITE AND OPAL MOUND FAULT, UTAH

by Kristen Rahilly[1], Stuart Simmons[2,3], and Tobias P. Fischer[1]

[1] Department of Earth and Planetary Sciences, University of New Mexico, Albuquerque, New Mexico
[2] Energy & Geoscience Institute, University of Utah, Salt Lake City, Utah
[3] Department of Chemical Engineering, University of Utah, Salt Lake City, Utah

Link to supplemental data download: https://ugspub.nr.utah.gov/publications/misc_pubs/mp-169/mp-169-i.zip
Appendix

Miscellaneous Publication 169-I
Utah Geological Survey
a division of
UTAH DEPARTMENT OF NATURAL RESOURCES

This paper is part of *Geothermal Characteristics of the Roosevelt Hot Springs System and Adjacent FORGE EGS Site, Milford, Utah*. https://doi.org/10.34191/MP-169

Bibliographic citation:

Rahilly, K., Simmons, S., and Fischer, T.P., 2019, Carbon dioxide flux and carbon and helium isotopic composition of soil gases across the FORGE site and Opal Mound fault, Utah, *in* Allis, R., and Moore, J.N., editors, Geothermal characteristics of the Roosevelt Hot Springs system and adjacent FORGE EGS site, Milford, Utah: Utah Geological Survey Miscellaneous Publication 169-I, 16 p., 1 appendix, https://doi.org/10.34191/MP-169-I.

CARBON DIOXIDE FLUX AND CARBON AND HELIUM ISOTOPIC COMPOSITION OF SOIL GASES ACROSS THE FORGE SITE AND OPAL MOUND FAULT, UTAH

by Kristen Rahilly, Stuart Simmons, and Tobias P. Fischer

ABSTRACT

Surface measurements of soil carbon dioxide flux and isotopic composition across the Utah FORGE site and Roosevelt Hot Springs are used to assess the potential of hydrothermal activity west of the N-S trending Opal Mound fault. Carbon dioxide flux surveys were made in June 2017 and January 2018 using a PP Systems EGM 5 portable carbon dioxide analyzer. A total of 317 flux measurements were made across the FORGE site with 0.16 km spacing between points oriented along east-west and north-south grid lines. Additionally, 626 total flux measurements were made in east-west transects across the Opal Mound fault and across the Mineral Mountains West fault scarps approximately 2 km SW of the Opal Mound fault.

Individual flux points are categorized as either background vegetation or elevated values using the statistical Sinclair method. Interpolation of flux for both the FORGE site and across faulted areas outside the FORGE site is performed using Empirical Bayesian Kriging in the Geostatistical Analyst toolbox of ArcGIS. Variance above statistical background is then calculated to reveal regions with elevated carbon dioxide flux. The extrapolated soil flux map shows the FORGE site does not contain carbon dioxide flux values above regional vegetation background values, within analytical error. Regions of flux values elevated above statistical background occur near and to the east of the Opal Mound fault.

Soil carbon dioxide gas samples were collected in 1 liter Tedlar bags for measurement of $\delta^{13}C$ isotopic composition using a Thermo Fisher Delta Ray Isotope Ratio Infrared Spectrometer (IRIS) instrument. Samples of soil carbon dioxide were collected from both high and low flux points within the FORGE site as well as from vegetation points outside the FORGE site and across the Opal Mound fault. The isotopic composition of points taken on the FORGE site cluster with samples taken from vegetation points outside the FORGE site. Several soil carbon dioxide gas samples collected east of the Opal Mound fault may contain evidence of a magmatic source.

Finally, diffusion samplers were deployed in piezometers to characterize the helium isotope compositions of soil gases. Over the FORGE site, air corrected R/Ra values range between 0.1 and 1.0 whereas over Roosevelt Hot Springs, east of the Opal Mound fault, R/Ra values are up to 2.2. These He isotopic measurements along with flux measurements provide unambiguous geochemical evidence that the FORGE site is isolated from convective hydrothermal fluid flow and magmatic influences associated with the Roosevelt Hot Springs system.

INTRODUCTION

The Utah Frontier Observatory for Research in Geothermal Energy (FORGE) Enhanced Geothermal System (EGS) site is located in southwestern Utah (Figure 1) approximately 16 km northeast of Milford, Utah (e.g., Allis et al., 2016; Simmons et al., 2018). The site is west of the Mineral Mountains in the southeast part of the Basin and Range province, west of the transition zone into the Colorado Plateau province. The FORGE site is underlain by Quaternary through Tertiary-age basin fill overlying basement rock that includes Miocene granitoids and Precambrian gneiss. Beneath the FORGE site, depth to basement varies from 300 m to 1 km along a gentle west-dipping basement-basin fill contact (Hardwick et al., 2019; Miller et al., 2019; Jones et al., 2019).

Approximately 2 km east of the FORGE site lies the north-trending Opal Mound fault, a high-angle normal fault that was last seismically active during the late Pleistocene (Nielson et al., 1986; Knudsen et al., 2019). The Opal Mound fault has been the site of episodic discharge of deep thermal water. Discharge of thermal water has produced the silica sinter mound at the southern end of the Opal Mound fault as well as a series of sinter-cemented fan deposits along the trace of the fault (Moore and Nielson, 1994; Lynne et al., 2005). The Opal Mound fault forms the western boundary of the Roosevelt Hot Springs hydrothermal system (Nielson et al., 1986; Allis and Larsen, 2012; Allis et al., 2016; Simmons et al., 2018). Roosevelt Hot Springs is located within the Sevier thermal anomaly, a region of high heat flow that includes many of the geothermal systems within southwestern Utah (Blackett, 2007; Simmons et al., 2015). Roosevelt Hot Springs system reservoir fluids

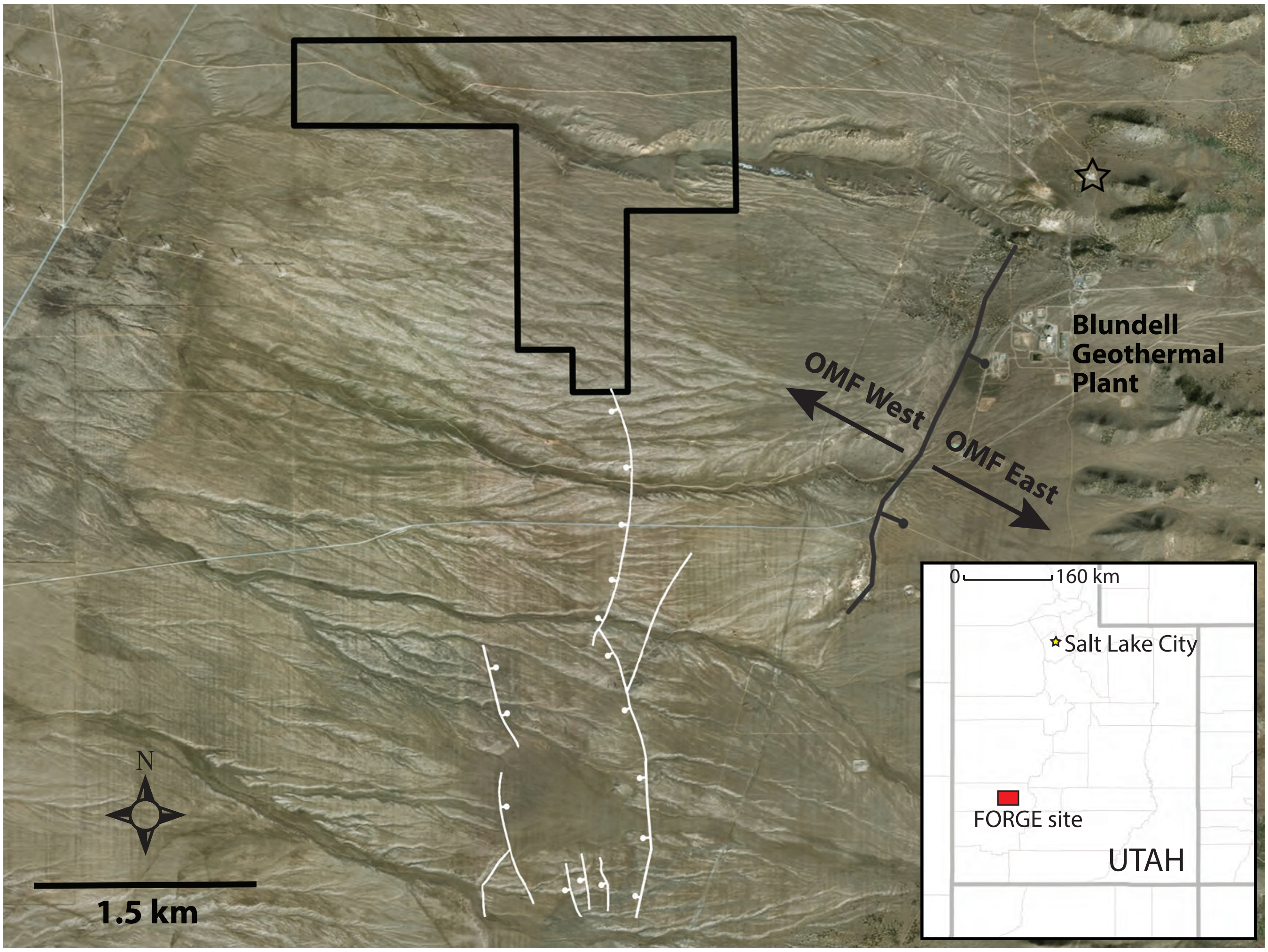

Figure 1. *Location of FORGE site (black polygon), Opal Mound fault (dark gray line), Mineral Mountains West fault scarps (white lines), and Roosevelt Hot Springs (black star). Opal Mound fault (OMF) West and East sampling areas indicated by black arrows. Location of FORGE site (inset map).*

have a maximum temperature of 260°C and are used to generate power at the Blundell power plant (33 MWe), which has operated continuously since 1984 (e.g., Faulder, 1991; Allis and Larsen, 2012). Fumarole gases from Roosevelt Hot Springs have high $^{3}He/^{4}He$ ratios with an air corrected value of R/Ra = 2.25, indicating a component of mantle helium (Kennedy and van Soest, 2007).

To better constrain deep-seated gas near the FORGE site, a soil gas carbon dioxide (CO_2) flux survey with accompanying soil gas $\delta^{13}C$ isotopic compositional analysis was performed in June 2017 and January 2018. In addition, a helium isotope soil gas survey was performed in November 2017, using diffusion samplers that are commonly used for sampling dissolved noble gases in the phreatic zone (e.g., Sanford et al., 1996; Gardner and Solomon, 2009; Dame et al., 2015). The goal was to constrain helium signatures, representing a range of values (i.e., radiogenic crustal R/Ra ~0.1, air R/Ra = 1, Roosevelt Hot Springs R/Ra ~2), in the shallow part of the vadose zone (e.g., Wannamaker et al., 2017).

SOIL CO_2 FLUX MEASUREMENTS

High rates of soil CO_2 flux have been consistently measured across a variety of active and quiescent volcanic areas as well as in geothermal reservoirs (Chiodini et al., 1998; Lewicki and Oldenburg, 2005). CO_2 is the most abundant non-condensable gas emitted by most geothermal systems and, due to its moderate solubility in water, is an ideal indicator of hydrothermal and magmatic activity at depth. In geothermal and volcanic regions, surficial measurements of CO_2 flux above background levels indicate sufficiently permeable pathways to allow transport of deeply-sourced CO_2 (Lewicki and Oldenburg, 2005). These pathways could include interconnected pore spaces or faults/fractures of various geometries and dimensions (Lewicki and Oldenburg, 2005; Peiffer et al., 2014; Lee et al., 2016). The CO_2 flux measured at the surface may be contributed by multiple sources and analyses should distinguish between background (biogenically or atmospherically-sourced CO_2) and magmatic/deeply-sourced CO_2 (Chiodini et al., 1998; Lewicki and Oldenburg, 2005). By combining flux measurements with $\delta^{13}C$ analyses, the sources for soil CO_2 can be identified (Chiodini et al., 2008; Parks et al., 2013; Lee et al., 2016). In geothermal or volcanic areas, CO_2 samples reaching the surface will be either purely magmatic, purely biogenic, or mixtures between the two based on isotopic composition and flux. For a prospective EGS reservoir with sealed, low-permeability basement rock, we expect surficial CO_2 to be within background values (Peiffer et al., 2014).

METHODS

We used a PP Systems Environmental Gas Monitor (EGM) 5 with soil respiration (accumulation) chamber to measure soil CO_2 flux with a 317-point gridded survey across the FORGE site and at an additional 626 points in transects across the Opal Mound fault and south of the FORGE site in June 2017 and January 2018 (Figure 2). Individual point measurements have a consistent spacing of 0.16 km in the FORGE site. Points outside of the FORGE site were acquired using an adaptive sampling technique as described by Werner and Brantley (2003). An adaptive sampling technique uses an initial coarser gridded survey but allows for smaller spacing between points if an anomalously high flux is measured (Werner and Brantley, 2003).

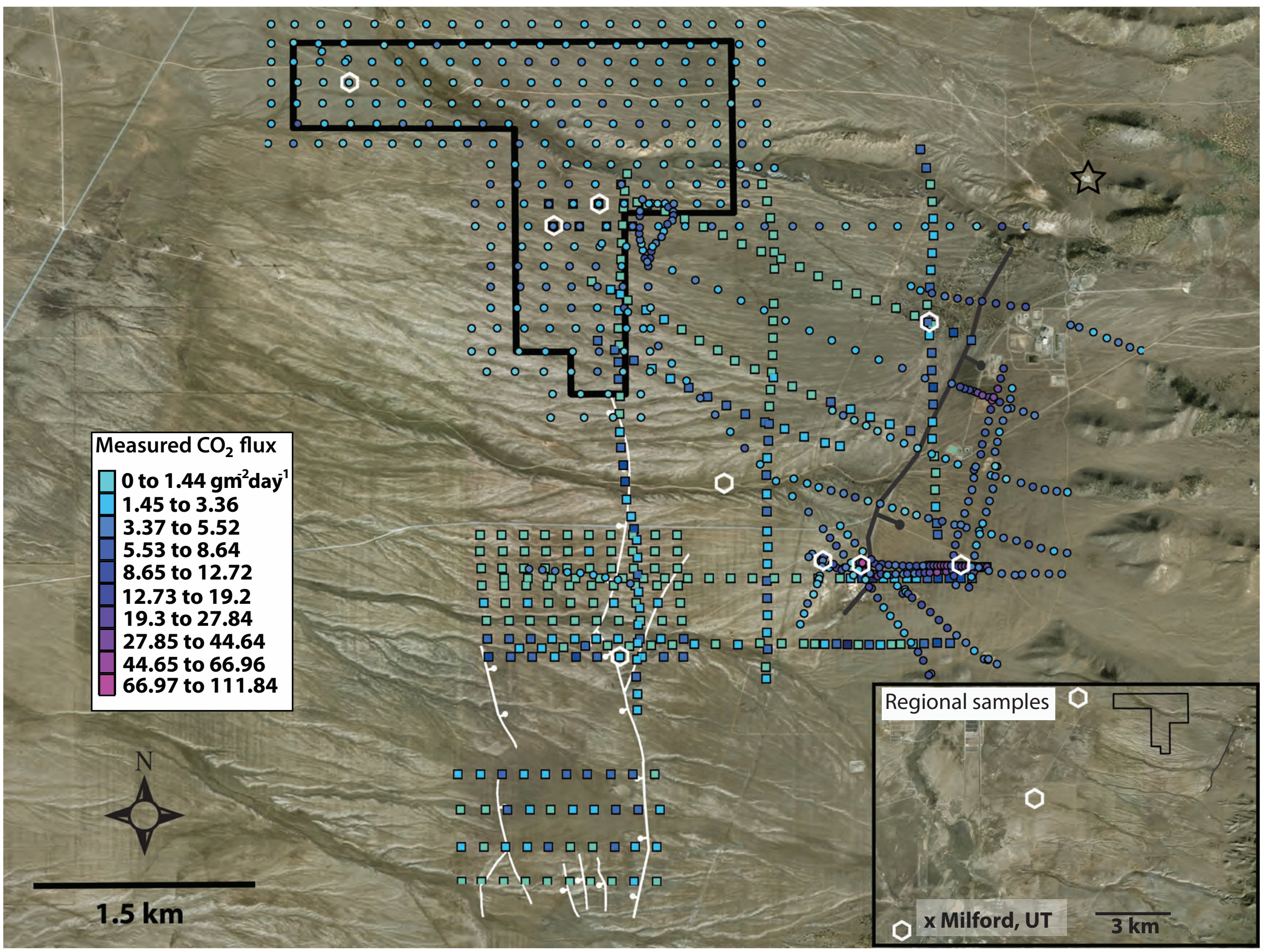

Figure 2. *Actual CO_2 flux measurements from June (circles) and January (squares) across the FORGE site (black polygon), Opal Mound fault (dark gray line), and Mineral Mountains West fault scarps (white lines). White hexagons are the locations of gas samples collected for $\delta^{13}C$ isotope composition analysis. The locations of regional gas samples are shown in inset. Roosevelt Hot Springs is the black star.*

To measure soil gas CO_2 flux, the EGM 5 with soil respiration chamber is placed securely on a soil surface, creating a seal (Figure 3A). Soil gas is then drawn up into the chamber from the soil surface using a rotary air sampling pump. The gas is passed through an infrared analyzer which measures the concentration of CO_2 and then pumped back into the chamber to create a closed system. The rate of change in CO_2 concentration over the entire 124 second measurement period is then determined using a linear fit calculation to obtain the CO_2 flux from that location (PP Systems, 2016). Once the measurement has been made, the flux value is recorded in g $CO_2/m^2/hr$.

For $\delta^{13}C$ isotope composition analyses, gas samples were collected from points with both high and low soil CO_2 flux (Figure 2). Soil gas samples were collected by connecting a 1 liter Tedlar® bag to the gas outlet of the EGM 5 analyzer (Figure 3B). In the FORGE site, soil gas samples were collected from both low flux and high flux points to evaluate whether higher flux rates are related to more deeply sourced CO_2.

Soil gas samples were also collected on both sides of the Opal Mound fault. Regional vegetation samples were also collected 1 to 15 km outside the FORGE site or Opal Mound fault areas (Figure 2 inset). Finally, three atmospheric gas samples were collected to determine the value of ambient air that may mix with our soil samples at the soil-air interface.

Tedlar bag gas samples were measured for $\delta^{13}C$ isotope composition of CO_2 the same day they were collected using a Thermo Fisher Delta Ray Isotope Ratio Infrared Spectrometer (IRIS) located at the field base station. The Delta Ray IRIS measures the infrared spectra of carbon isotopes to determine concentration and isotope composition (Rizzo et al., 2014; Fischer and Lopez, 2016). Samples of CO_2 can be measured from air-like concentrations up to pure CO_2. Gas samples above 3500 ppm CO_2 require dilution using the Thermo Fisher Xpand dilution box with incremented dilution capillaries.

CO_2 flux measured in June and January may be alternatively affected by weather and/or frozen ground and must be normalized to produce consistent data (Lewicki et al., 2003; Lewicki et al., 2005). For this reason, we plot variance above biogenic background flux rather than absolute flux. To do this, we have to calculate the background biogenic flux for both the June and January sets of measurements using the statistical population distribution method for geochemical data described by Sinclair (1974). This method calculates a maximum flux threshold for background CO_2 related to the processes associated with biogenically-sourced CO_2 (Chiodini et al., 1998). Any value above this maximum background is classified as anomalous and thus related to geothermal processes (Lewicki and Oldenburg, 2005).

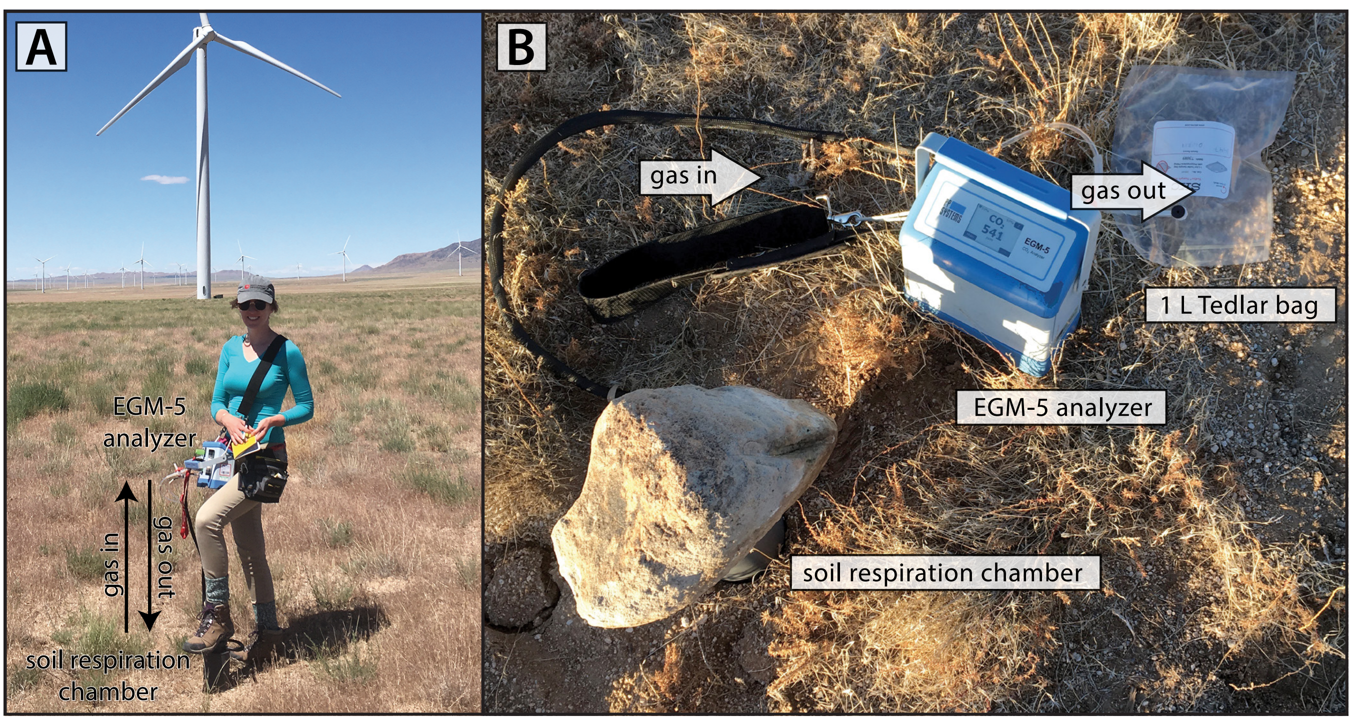

Figure 3. (A) *Field deployment of EGM 5 instrument with soil respiration chamber.* ***(B)*** *EGM 5 with Tedlar bag connected to gas out port for collection of soil gas samples.*

To normalize the flux measurements to variance above biogenic background using the Sinclair method, the cumulative probability distribution of both the June (Figure 4A) and January (Figure 4B) datasets was plotted separately against flux per day on a logarithmic plot. Based on the chosen inflection point along the distribution curve, the January dataset (Figure 4B) is composed of two populations: 1) 95% of the data are in a background (biogenic) flux population and 2) the remaining 5% are in an elevated (geothermal) flux population.

These values were chosen based on the inflection point at the cumulative probability of 5% and a check of the data was completed by adding flux measurements at defined probability intervals by using the following equation: (0.05*elevated) + (0.95*background) = mixture value (yellow triangles in Figure 4). If the dataset distribution has been correctly estimated, the mixture values will lie on the true data curve (gray points in Figure 4B). For the January dataset, the mixture values fit the true data and suggest that our proportions are correct (Figure 4B). The maximum threshold for biogenic CO_2 flux for the January dataset is 5.48 $gm^{-2}day^{-1}$ (green horizontal line in Figure 4B).

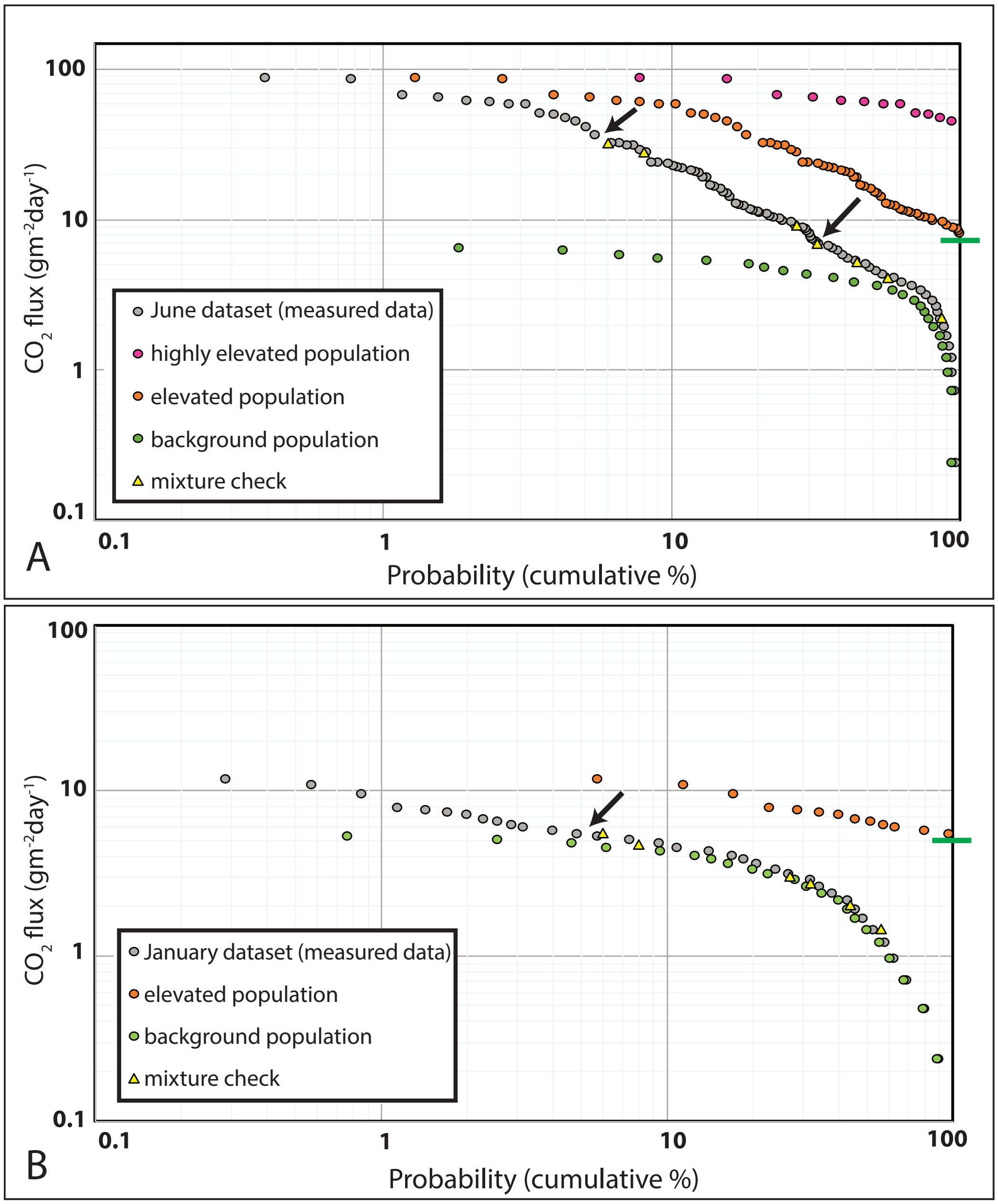

Figure 4. (A) *Population distribution of June 2017 CO_2 flux dataset across the FORGE site and Opal Mound fault.* ***(B)*** *Population distribution of January 2018 CO_2 flux dataset across the FORGE site, Opal Mound fault, and Mineral Mountains West fault scarps. Green horizontal lines indicate threshold between background population and elevated population (8.11 $gm^{-2}day^{-1}$ for June 2017; 5.48 $gm^{-2}day^{-1}$ for January 2018). Black arrows indicate chosen inflection points.*

The June flux dataset is more complicated (Figure 4A). A simple distribution of just two populations does not result in mixture check points that lie on the true data curve (gray points in Figure 4A). Therefore, the June dataset is likely comprised of three populations: 1) 65% is a background (biogenic) flux population, 2) 30% is an elevated flux population, and 3) 5% is a highly elevated flux population. The same mixture check was completed for the June dataset and a maximum background threshold of 8.11 $gm^{-2}day^{-1}$ was estimated (green horizontal line in Figure 4A). Note that the Sinclair Method of determining data distribution can be subjective and dependent on the selection of inflection points (Sinclair, 1974). Therefore, it is important to combine our determination of flux thresholds with isotopic analyses to evaluate the spatial distribution of biogenic soil CO_2 and geothermal (elevated) soil CO_2 (Chiodini et al., 2008).

Individual point soil CO_2 flux measurements were interpolated with the Geostatistical Analyst tool in ArcGIS across the entire measured area using Empirical Bayesian Kriging (EBK). EBK accounts for the spatial variance of measurements and is used here due to our use of both a gridded, evenly spaced survey as well as an adaptive survey (Krivoruchko, 2012). EBK is used to interpolate flux values between point measurements for full spatial coverage of the site. To do this, the June and January flux measurements are normalized by combining both datasets into one CO_2 flux map and reporting the variance from maximum background threshold. For the June flux dataset, the variance is calculated between the measured soil CO_2 flux value and the maximum background threshold of 8.11 $gm^{-2}day^{-1}$. For the January flux dataset, the variance is calculated between measured flux values and the calculated background threshold of 5.48 $gm^{-2}day^{-1}$. The variances from June and January are normalized to consider the 1% error of the EGM 5 instrument (PP Systems, 2016). This means that elevated point flux measurements are above statistical background outside analytical error. The variances between statistical background and the flux for each individual point are then combined to make one June-January dataset that is analyzed with the ArcGIS EBK tool. Due to the log-normal distribution of our flux data, we first performed a log-empirical transformation on the data to achieve a normal data distribution. However, before log-transforming our data we had to linearly shift all our data points by a constant value to account for the abundance of negative variance values. EBK analysis was then performed using 50-point subsets over 200 simulations in the Geostatistical Analyst toolkit. After an interpolated flux map was created, we removed the constant linear shift to get true variance above background values.

The helium isotope soil gas survey was performed in November 2017 using diffusion samplers (Figure 5). These samplers were placed into the bottoms of piezometers (2'–3' long and 1" diameter stainless steel tubes), which were inserted into holes dug with an auger tool and backfilled with compacted soil. The piezometer was sealed with a threaded galvanized steel cap. After 9–10 days, the samplers were retrieved and crimped within 1 minute of being exposed to atmosphere to seal the copper capsule. When retrieved, all the piezometers were dry. Three diffusion samplers were tarnished due to H_2S in areas of thermal ground. We also include one sample of deep thermal water from production well 45-3 in this study, collected in a long copper tube in 2015. All of the samples were analyzed for helium and neon isotopes at the University of Utah Dissolved and Noble Gas Lab on a magnetic sector field mass spectrometer, and the precision for these analyses is 1.5% and 2.0%, respectively.

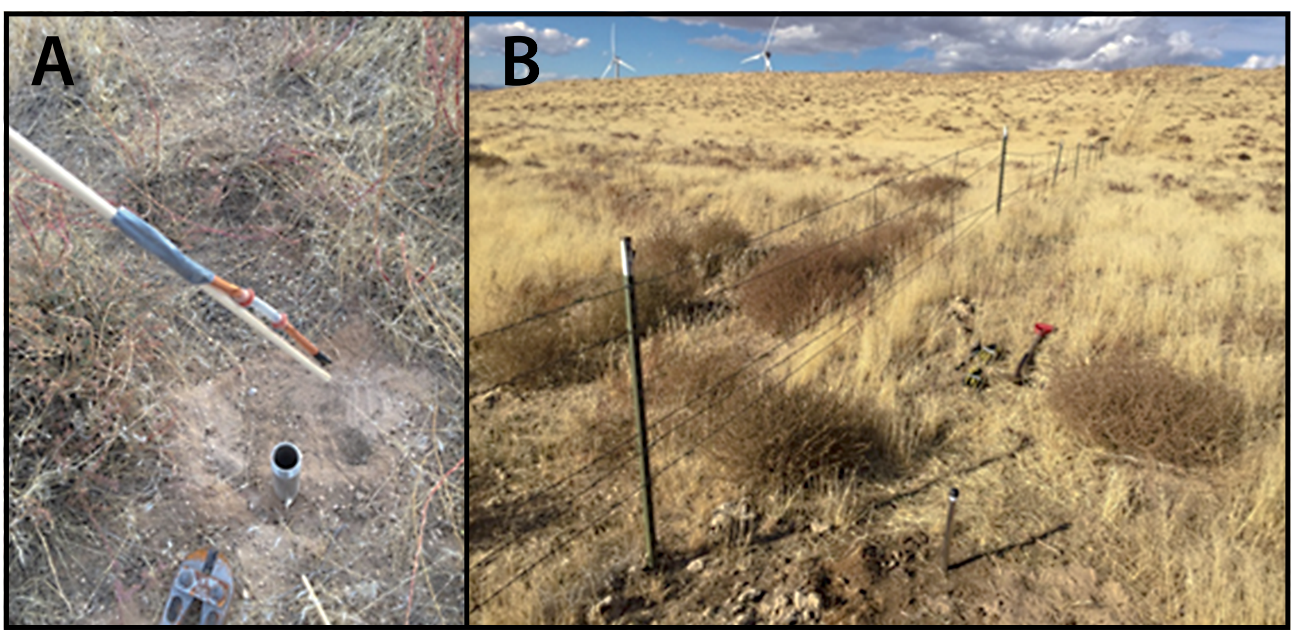

Figure 5. (A) *Copper diffusion sampler taped to the end of a wooden dowel before inserting into stainless steel piezometer tube buried in the ground.* ***(B)*** *Head of capped piezometer tube with copper diffusion sampler inside (not visible).*

Measured $^3He/^4He$ ratios are normalized using the atmospheric value (Ra = 1.386 x 10^{-6}, Ozima and Podosek, 1983). Using the atmospheric ratio of $^4He/^{20}Ne$ (air = 0.318, Ozima and Podosek, 1983), four soil gas samples were corrected for atmospheric contamination with the following expressions:

$$R/Ra \text{ corrected} = (R/Ra-r)/(1-r)$$

$$r = (^4He/^{20}Ne)_{air}/(^4He/^{20}Ne)_{measured}.$$

As the value of r approaches 1, the corrected values become very sensitive to analytical errors. Hence most of the soil gas samples were not corrected, and they have R/Ra values that are indistinguishable from air.

RESULTS

Soil CO_2 Flux Measurements

Individual soil CO_2 flux measurements made in June 2017 and January 2018 across the FORGE site and Opal Mound fault are shown in Figure 2 (see Appendix[1] for flux point measurements). A summary of dataset statistics is shown in Table 1. For the June dataset, the average and maximum CO_2 flux measured within the FORGE site is less than the average and maximum CO_2 flux measured outside the FORGE site. The maximum CO_2 flux for vegetation east of the Opal Mound fault is nearly 6 times greater than the largest flux measured west of the Opal Mound fault and nearly 14 times larger than the maximum CO_2 flux measured in the FORGE site. The average CO_2 flux for vegetation east of the Opal Mound fault is nearly 3 times larger than the average flux west of the Opal Mound fault and 5 times larger than vegetation measured in the FORGE site. The average CO_2 flux measured across the FORGE site in January is nearly identical to the average measured in June.

Overall, soil CO_2 flux measured in January was less than the CO_2 flux measured in June. This is most likely due to differences in meteorological conditions (Lewicki et al., 2003; Lewicki et al., 2005). During January, low temperatures produced frozen ground conditions (where the ground was observably frosted) during three out of seven field days at the FORGE and Opal Mound fault sites. If pore spaces were filled or partially filled with frozen water, this could decrease soil permeability for the passage of CO_2 to the surface as well as decrease the biogenic production of CO_2 (Elberling, 2003). Additionally, the average daily wind speed for field days in June was 6.6 kilometers per hour versus 4.2 kilometers per hour in January (Western Regional Climate Center, 2018). Lewicki et al. (2003) suggest that small changes in wind speed can result in rapid changes to soil CO_2 flux, possibly due to an increase in advective gas flow.

Compared to other volcanic or geothermal areas, the soil CO_2 flux measured across the FORGE site and Opal Mound fault is lower. Numerous soil CO_2 flux surveys were completed over areas associated with increased desert shrub die-off across the Dixie Valley Geothermal Field in west-central Nevada. These surveys showed a high flux population above 150 $gm^{-2}day^{-1}$ and a maximum flux of 570 $gm^{-2}day^{-1}$. At the Dixie Valley Geothermal Field, a statistical background threshold of 7 $gm^{-2}day^{-1}$ was calculated representing biogenic CO_2 flux across a dry sagebrush landscape similar to the Utah FORGE site (Bergfeld et al., 2001). At the Acoculco caldera hot dry rock geothermal system in Mexico, 95% of the soil CO_2 flux measurements fall within a background population with a mean flux of 18 $gm^{-2}day^{-1}$. The remaining 5% of the flux measurements fall within an elevated range with values up to 39,811 $gm^{-2}day^{-1}$ (Peiffer et al., 2014). The weighted average of these two populations across the entire Acoculco site is then approximately 150 times greater than the average for the FORGE site.

$\delta^{13}C$ Composition of Soil CO_2

Twelve soil CO_2 samples and three air samples were collected across the FORGE site, Opal Mound fault, and regionally in June and January for measurement of $\delta^{13}C$ isotope composition (Figure 2, Table 2). The average $\delta^{13}C$ composition of soil CO_2 within the FORGE site is -12.02‰ for June samples and -12.42‰ for January samples. Only one repeat sample was collected in both June and January for isotopic analysis (samples 3/7). These two samples are within 2% of each other when analytical error is considered. The January sample (sample 7) is heavier than the June sample (sample 3) at -11.876‰ and -12.079‰, respectively. Soil CO_2 collected in vegetation west of the Opal Mound fault has an isotopic composition of -10.41‰ in June and an average isotopic composition of -11.67‰ in January. East of the Opal Mound fault, soil CO_2 samples have an isotopic composition of -10.27‰ in June and -10.00‰ in January. Three regional soil CO_2 samples were collected from points located approximately 1 to 15 km outside of the FORGE site and Opal Mound fault area and have an average isotopic composition of -12.95‰ (Figure 2 inset).

Table 1. *Summary of CO_2 flux dataset statistics from June 2017 and January 2018 inside the FORGE site and across the Opal Mound fault (OMF) compared to other study areas.*

Site	Number of measurements	Maximum CO2 flux ($gm^{-2}day^{-1}$)	Average CO2 flux ($gm^{-2}day^{-1}$)	Background flux ($gm^{-2}day^{-1}$)	Reference
FORGE site 2017	288	8.16	2.02		This study
OMF west vegetation 2017	81	19.2	3.74		This study
OMF east vegetation 2017	226	111.84	10.88		This study
FORGE + OMF total 2017	595			≤ 8.11	This study
FORGE site 2018	29	5.04	2.03		This study
OMF west vegetation 2018	268	10.8	1.98		This study
OMF east vegetation 2018	51	12.24	3.92		This study
FORGE + OMF total 2018	348			≤ 5.48	This study
Dixie Valley Geothermal Field	558	570	32.5	≤ 7.00	Bergfeld et al. (2001)
Acoculco caldera HDR	200	39,811	294.25	mean for background population = 18	Peiffer et al. (2014)

Table 2. *Summary of isotopic and concentration measurements of CO_2 gas samples from June 2017 and January 2018.*

Sample number	Latitude (°N)	Longitude (°W)	$\delta^{13}C$-CO_2 ‰ (PDB)	Concentration CO_2 (ppm)	Description	Date collected
1	38.46982	112.85960	-9.997 ± 0.05	1,318.8 ± 43.2	Vegetation E of OMF	1/10/2018
2	38.49052	112.86332	-11.412 ± 0.05	637.1 ± 1.7	Vegetation W of OMF	1/12/2018
3	38.49865	112.89505	-12.079 ± 0.02	624.8 ± 0.01	FORGE vegetation	6/17/2017
4	38.39999	113.02161	-14.591 ± 0.03	587.1 ± 0.01	Regional vegetation	6/18/2017
5	38.47090	112.87240	-10.410 ± 0.03	583.3 ± 0.01	Vegetation W of OMF	6/25/2017
6	38.46222	112.88942	-11.924 ± 0.07	553.0 ± 0.4	Vegetation W of OMF	1/10/2018
7	38.49865	112.89505	-11.876 ± 0.11	549.2 ± 0.03	FORGE vegetation	1/13/2018
8	38.51275	112.92958	-11.331 ± 0.09	537.1 ± 0.04	Regional vegetation	1/13/2018
9	38.50056	112.89121	-12.966 ± 0.23	530.4 ± 0.02	FORGE vegetation	1/13/2018
10	38.51083	112.91233	-11.956 ± 0.03	507.6 ± 0.05	FORGE vegetation	6/17/2017
11	38.46569	112.95412	-12.92 ± 0.16	487.9 ± 0.09	Regional vegetation	1/14/2018
12	38.47019	112.86892	-10.268 ± 0.05	451.7 ± 0.0	Vegetation E of OMF	6/18/2017
13	38.46569	112.95412	-10.624 ± 0.11	417.0 ± 0.06	Air sample	1/14/2018
14	38.49865	112.89503	-10.635 ± 0.23	415.0 ± 0.04	Air sample	1/13/2018
15	38.47557	112.87965	-9.993 ± 0.03	409.0 ± 0.03	Air sample	6/18/2017

Helium Isotopic Composition

The majority of helium gas samples collected were not corrected for atmospheric contamination due to the high analytical error associated with correcting R/Ra values close to 1, as illustrated by the relatively high sigma value of 0.43 in sample 5 (R/Ra corrected = 1.19) (Table 3). For comparison, sample 13 has the highest corrected R/Ra value of 2.29 ± 0.06, representing an end-member composition. The four soil gas samples with elevated R/Ra (i.e., samples 4, 5, 6 and 13) have sufficiently high $^4He/^{20}Ne$ ratios to correct for air contamination, yielding values that range from R/Ra corrected = 1.19 to 2.29 (Table 3).

Table 3. *Helium isotope measurements on soil gases and a produced geothermal water.*

Sample	Elevation (m)	Latitude (°N)	Longitude (°W)	Setting	R/Ra	$^{4}He/^{20}Ne$	R/Ra corr
Diffusion samplers							
1	1680	38.49982	112.88811	Cold ground	0.98 ± 0.01	0.32 ± 0.01	---
2	1616	38.50782	112.89822	Cold ground	0.99 ± 0.01	0.33 ± 0.01	---
3	1633	38.51054	112.89820	Cold ground	1.00 ± 0.01	0.33 ± 0.01	---
4	1811	38.49818	112.85353	Hot steaming ground	1.42 ± 0.01	0.54 ± 0.01	2.03 ± 0.07
5	1855	38.49274	112.85237	Cold ground	1.01 ± 0.01	0.34 ± 0.01	1.19 ± 0.43
6	1814	38.48502	112.85885	Warm ground	1.13 ± 0.01	0.49 ± 0.01	1.37 ± 0.06
8	1675	38.47315	112.89625	Cold ground	0.99 ± 0.01	0.32 ± 0.01	---
9	1684	38.47303	112.89411	Cold ground	0.98 ± 0.01	0.32 ± 0.01	---
10	1795	38.46833	112.86491	Cold ground	1.02 ± 0.01	0.33 ± 0.01	---
11	1875	38.48771	112.84601	Cold ground	0.99 ± 0.01	0.31 ± 0.01	---
12	1737	38.47718	112.87658	Cold ground	1.00 ± 0.01	0.31 ± 0.01	---
13	1828	38.48997	112.85925	Warm ground	2.22 ± 0.01	5.95 ± 0.15	2.29 ± 0.06
Copper tube							
45-3		38.49062	112.85412	Production well	2.17 ± 0.01	30.20 ± 0.76	2.18 ± 0.06

DISCUSSION

Forge Site and West of the Opal Mound Fault

None of the 317 total individual CO_2 flux points measured across the FORGE site in June and January are greater than the calculated background flux thresholds when normalized for the instrumental error of 1% (Figure 6A). An interpolated flux map for the FORGE site and Opal Mound fault is shown in Figure 6A and Figure 6B. The main objective of this flux map is to determine where soil CO_2 flux is below the maximum threshold of biogenic values and where the flux is elevated above biogenic background. All of the green colors in Figures 6A and 6B represent CO_2 fluxes that are at (variance = 0) or below (variance less than zero) background. Figures 6A and 6B show that none of the interpolated flux measurements within the FORGE site are above calculated background values.

Just east of the FORGE site boundary, two point measurements are elevated above background outside the 1% error of the instrument. The highest flux of these points has a value of 12 ± 0.12 $gm^{-2}day^{-1}$ while the second point has a flux of 8.4 ± 0.08 $gm^{-2}day^{-1}$. Because these two points are discrete measurements surrounded by background values, the EBK flux map smooths out the slightly elevated higher values. These two values are aligned along a NW-SE line with one of the areas of high flux east of the Opal Mound fault. However, none of the other points measured along lines moving eastward are elevated above background until crossing the Opal Mound fault.

South of the FORGE site is a group of east and dominantly-west-dipping fault scarps that comprise the Mineral Mountains West fault (white lines in Figures 6A and 6B). This scarp system forms small grabens with a possible total offset in the overlying alluvium cover of less than 7 m (Knudsen et al., 2019). Four individual CO_2 flux point measurements elevated above background exist within this area. The highest flux measured in this area south of the FORGE site is 6.48 ± 0.064 $gm^{-2}day^{-1}$. This point is located along a line of three other points that may fall along a north-trending possible fault just south of the FORGE site.

Figures 7A and 7B show the isotopic composition and location of the 15 CO_2 gas samples collected across the FORGE site, the Opal Mound fault, and regionally (Figure 7B inset). The sample numbers used in Figure 7A correspond to Table 2 and Figure 7B. Shaded mixing regions have been drawn between average air $\delta^{13}C$ composition of the study area and typical global mantle (-6 ± 2.5‰; Sano and Marty, 1995), C4 vegetation, and C3 vegetation $\delta^{13}C$ compositions (Sharp, 2017). All of the soil gas samples inside the FORGE site clearly plot on average C4 vegetation-air or C3 vegetation-air mixing regions. This indicates that, in the FORGE site, all soil gas samples have a purely biogenic isotopic composition representative of the sage brush, desert grasses, and Juniper trees characterizing the vegetation across the area. Sample 3 was collected at flux point 569, the highest CO_2 flux point measured in June within the FORGE site with a value of 8.16 ± 0.082 $gm^{-2}day^{-1}$. This value

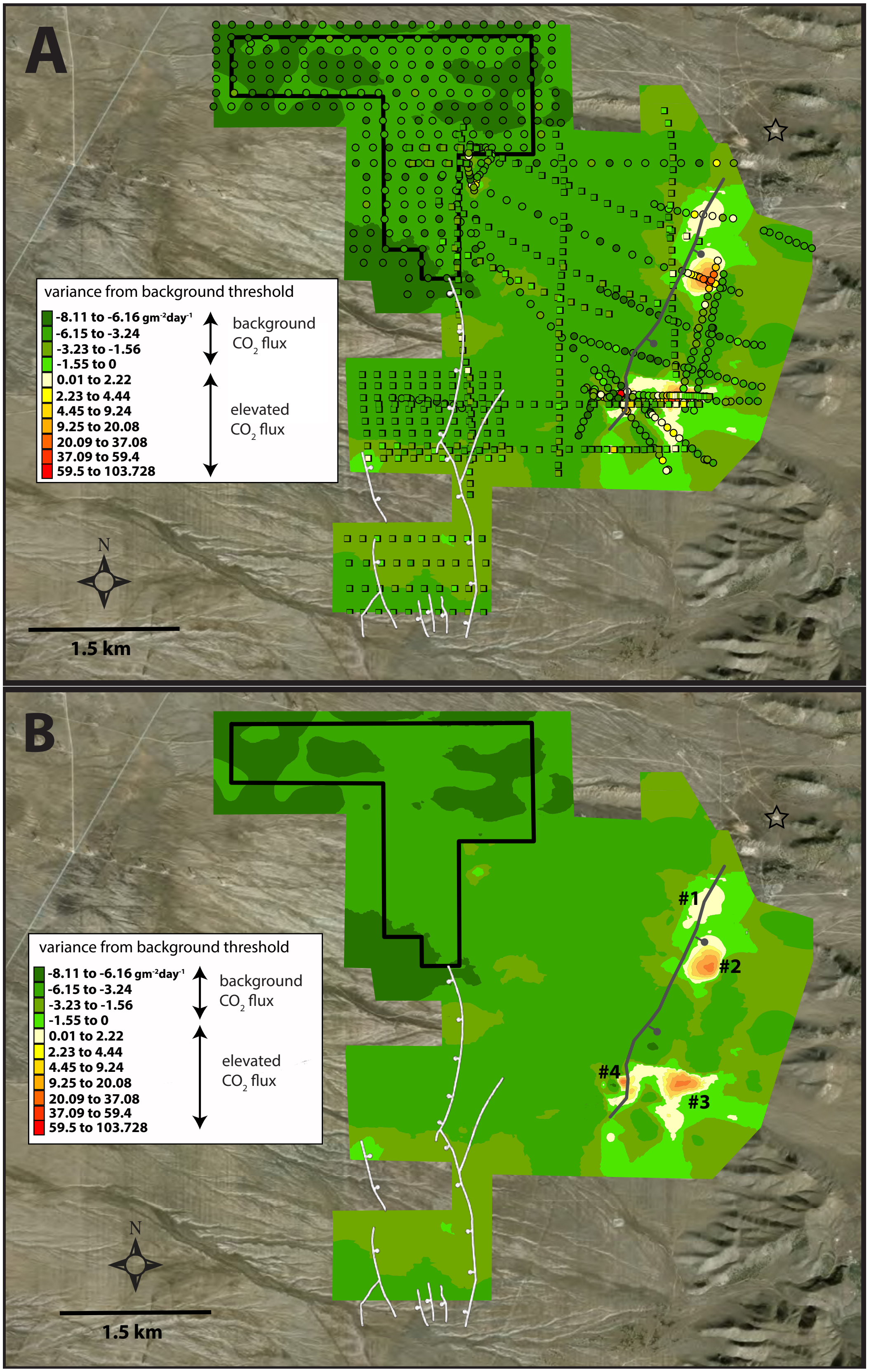

Figure 6. (A) *Empirical Bayesian Kriging flux map showing variance from background threshold overlain by individual point measurements of variance from background. Circle points are from June 2017 and square points are from January 2018.* ***(B)*** *Empirical Bayesian Kriging flux map showing variance from background threshold (individual point measurements removed for clarity). Regions #1, 2, 3, and 4 are elevated flux regions discussed in the text. FORGE site is the black polygon, Opal Mound fault is the dark gray line, scarps of the Mineral Mountains West fault are the white lines, and the black star is Roosevelt Hot Springs.*

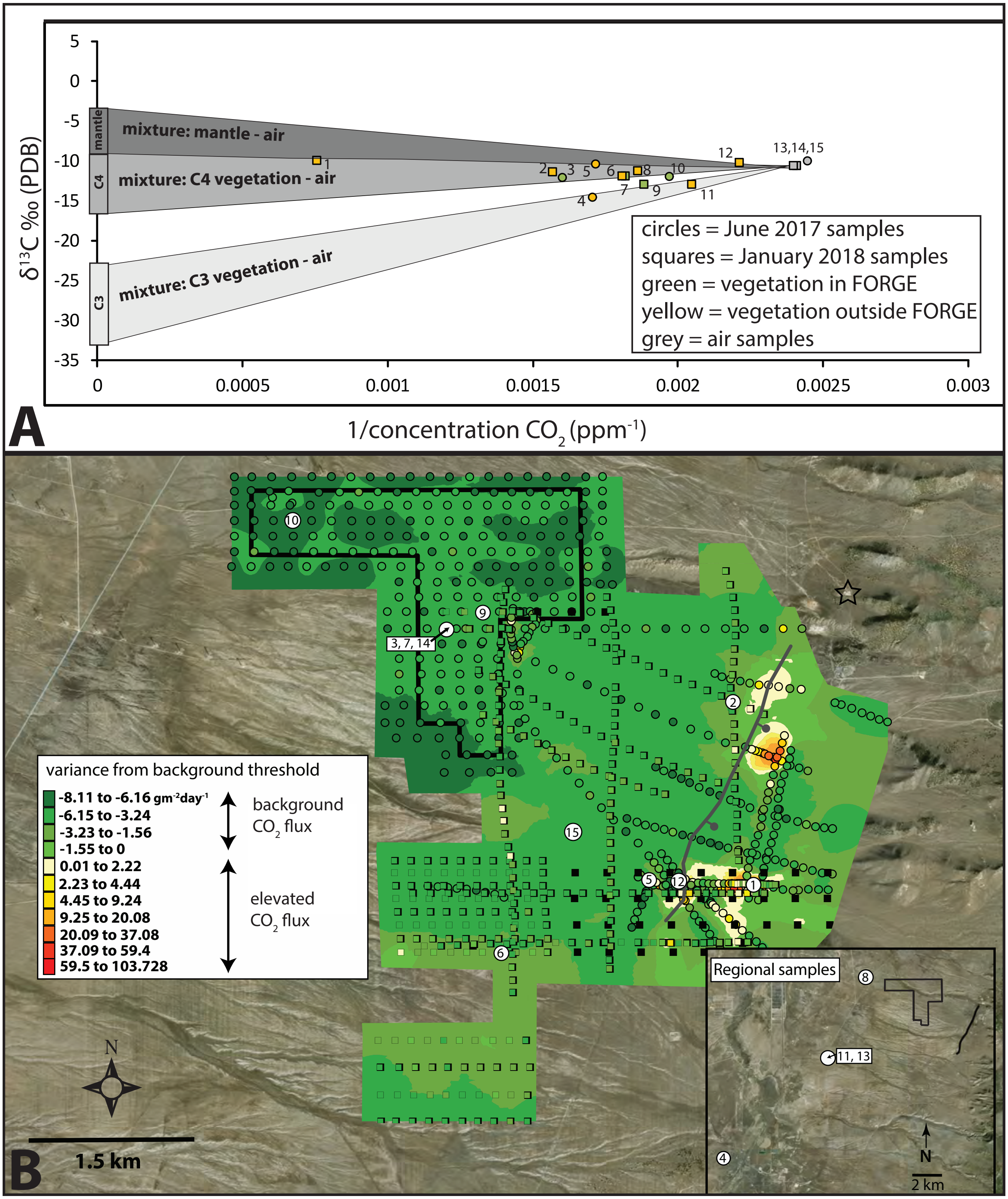

Figure 7. ***(A)*** *$\delta^{13}C$ composition versus 1/concentration for gas samples collected across the study area and regionally. Bars along the Y-axis indicate pure mantle (dark gray) (Sano and Marty, 1995), pure C4 vegetation (medium gray), and pure C3 vegetation (light gray) (Sharp, 2017). Shaded regions represent mixtures between air and end-member compositions. Sample numbers correspond to* ***(B)*** *Spatial distribution of gas samples across the FORGE site (black polygon), Opal Mound fault (dark gray line), Mineral Mountains West fault scarps (white lines), and regionally (inset) overlying Empirical Bayesian Kriging flux map of variance from background. Black star is Roosevelt Hot Springs.*

is just within the statistical background calculated for June when the 1% error of the instrument is considered. However, the $\delta^{13}C$ composition of point 569 lies well within the mixing region of C4 vegetation-air and therefore cannot be sourced from magmatic CO_2. This is also true for sample 6, collected from an elevated flux point along the Mineral Mountains West fault scarps south of the FORGE site.

Sample 6 also plots within the C4 vegetation-air mixing region and cannot be magmatically sourced. Gas sample 5 may be slightly heavier than the C4-air mixing region but has a low concentration, suggesting a purely biogenic source.

The isotopic composition of elevated flux values west of the Opal Mound fault suggests that the CO_2 source is not magmatic and therefore is sourced from near the surface rather than from rising hydrothermal fluids. This is consistent with the helium isotope analyses of soil gases. Furthermore, there is no evidence that the Mineral Mountains West fault scarps south of the FORGE site are pathways for deeply sourced CO_2.

East of the Opal Mound Fault

East of the Opal Mound fault, there are four regions (#1, #2, #3, and #4 in Figure 6B) of flux values elevated above background. These four regions are centered around the four highest individual flux values measured across the entire study area. Elevated flux region #1 intersects the northern sector of the Opal Mound fault, elevated flux region #2 is located approximately 1.5 km southwest of Roosevelt Hot Springs, elevated flux region #3 is located approximately 0.6 km east of the Opal Mound fault, and elevated flux region #4 intersects the southern portion of the Opal Mound fault. The highest individual CO_2 flux measurement within elevated region #2 is 50.16 $gm^{-2}day^{-1}$. The highest flux measurement within region #3 is 66.96 $gm^{-2}day^{-1}$. Elevated region #4 is located in soils directly adjacent to the siliceous sinter deposits of the Opal Mound fault and contains the highest flux value measured in the entire study area: 111.84 $gm^{-2}day^{-1}$. There is an additional region of elevated flux values along the northern trend of the Opal Mound fault, elevated region #1 (Figure 6B). However, the highest flux value for region #1 is much lower than the other three regions at only 11.52 $gm^{-2}day^{-1}$.

The only soil CO_2 gas samples that may possibly have a contribution of deeply-sourced, magmatic CO_2 are samples 1 and 12. Sample 1 was collected east of the Opal Mound fault in elevated region #3 where the measured flux was 2.55 $gm^{-2}day^{-1}$ in June 2017 and 0.45 $gm^{-2}day^{-1}$ in January 2018 with a $\delta^{13}C$ composition of -9.997‰. Even though sample 1 was collected in January when the overall CO_2 flux was lower, this gas sample has the highest concentration of all the samples collected (1,319 ppm). Furthermore, the isotopic composition of sample 1 may be heavier than the C4-air mixing region, suggesting a possible magmatic CO_2 component (Figure 7A). Soil gas sample 12 was collected from soil directly adjacent to the silica sinter on Opal Mound, and it appears to plot heavier than the C4-air mixing region (Figure 7A); however, the concentration of this particular sample is too close to the air-end member to resolve a magmatic CO_2 component with confidence.

The four soil gas samples with elevated R/Ra values over air (He soil gas samples 4, 5, 6, and 13) were collected east of the Opal Mound fault and represent mixtures in composition between air and thermal water collected from well 45-3 (Figures 8 and 9). Elevated R/Ra gas samples (13) and (6) were both collected within two of the previously discussed elevated CO_2 flux regions. No soil gas samples were collected for helium isotopic analysis within elevated flux region #4 intersecting the southern portion of the Opal Mound fault, where the highest soil CO_2 flux was measured (Figure 6B). However, in agreement with soil CO_2 data, the helium isotopic composition of all gas samples distinctly shows that R/Ra values elevated above air are located east of the Opal Mound fault. In summary, anomalous mantle helium is only detected in soil gases east of the Opal Mound fault and there is no evidence of mantle helium in samples from the vicinity of the FORGE site (Figure 9).

CONCLUSION

The FORGE prospective EGS site does not contain soil CO_2 flux values above statistical background, within analytical error. Soil CO_2 samples collected across the FORGE site have $\delta^{13}C$ compositions that plot with regional vegetation values along C3 vegetation-air or C4 vegetation-air mixing regions. At the intersection with and east of the Opal Mound fault, there are four regions of CO_2 flux elevated above background. The highest CO_2 flux values in these four regions vary from 11.52 to 111.84 $gm^{-2}day^{-1}$. Gas sample 1, collected from elevated region #3 east of the Opal Mound fault, may have a component of magmatic CO_2 based on $\delta^{13}C$ composition and CO_2 concentration. Gas sample 12, located at the intersection of the Opal Mound fault, may have a component of magmatic CO_2 as well but is too low concentration to determine with confidence. Elevated flux regions east of the Opal Mound fault are discrete and separated by regions of background flux values, suggesting that smaller-scale faults or fractures are creating pathways for deeply-sourced CO_2 to travel to the surface. The highest flux

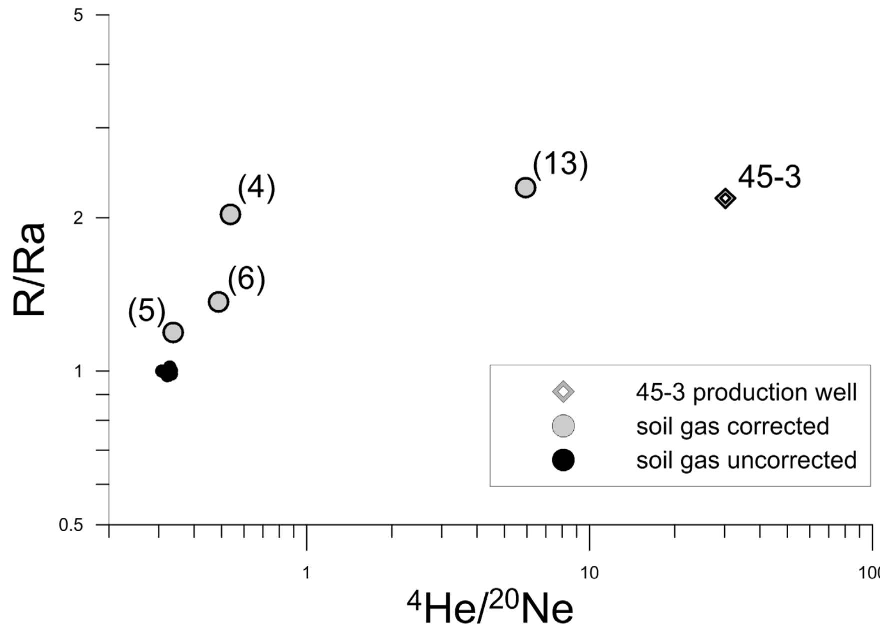

Figure 8. *R/Ra versus $^4He/^{20}Ne$ of soil gas samples collected across the FORGE site, Opal Mound fault, and Roosevelt Hot Springs region. Numbers in parentheses indicate sample sites shown in Figure 9.*

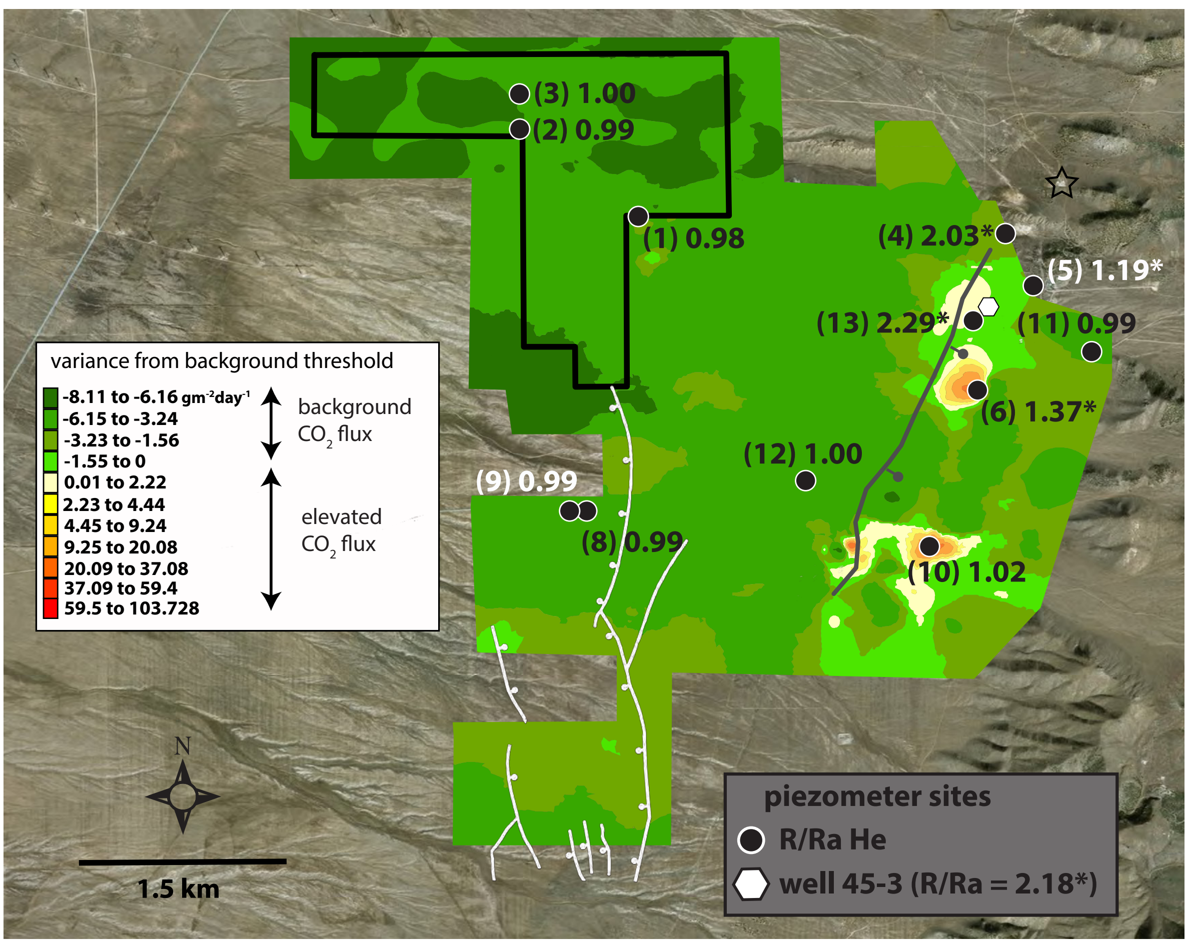

Figure 9. *Sample sites (black circles and white hexagon) with corresponding R/Ra helium isotope ratios overlying Empirical Bayesian Kriging flux map of variance from background. Asterisks indicate samples that have been corrected for air contamination. FORGE site is black polygon, Opal Mound fault is dark gray line, Mineral Mountains West fault scarps are white lines, and Roosevelt Hot Springs is the black star.*

value measured across the study area (111.84 $gm^{-2}day^{-1}$) was located on soils directly along the Opal Mound fault. However, the flow of deeply-sourced CO_2 appears to be centered around the remnants of siliceous sinter at the southern end of the fault, as flux values trending north along the fault return to background values. Soil gas samples with R/Ra values elevated above air are only located east of the Opal Mound fault. All samples collected within the FORGE site and west of the Opal Mound fault have air-like R/Ra values. Based on the spatial distribution of soil CO_2 flux, the $\delta^{13}C$ composition of soil CO_2, and the helium isotopic composition of soil gases, the Opal Mound fault serves as the western boundary of the Roosevelt Hot Springs system. Despite significant temperatures and thermal gradients, the Utah FORGE site has no evidence of deep-seated vertical gas permeability similar to the magmatic influences found east of the Opal Mound fault at Roosevelt Hot Springs.

ACKNOWLEDGMENTS

This work was sponsored by the DOE EERE Geothermal Technologies Office project DE-EE0007080 Enhanced Geothermal System Concept Testing and Development at the Milford City, Utah, FORGE Site. We thank Kent Smith for extensive field work assistance. We also thank Stefan Kirby and an anonymous reviewer for the reviews of an earlier draft of this report.

REFERENCES

Allis R.G., and Larsen, G., 2012, Roosevelt Hot Springs Geothermal field, Utah—reservoir response after more than 25 years of power production: Proceedings, 37th Workshop on Geothermal Reservoir Engineering, Stanford University, Stanford, California, 8p.

Allis, R., Moore, J., Davatzes, N., Gwynn, M., Hardwick, C., Kirby, S., McLennan, J., Pankow, K., Potter, S., and Simmons, S., 2016, EGS concept testing and development at the Milford, Utah FORGE site: Proceedings, 41st Workshop on Geothermal Reservoir Engineering, Stanford University, Stanford, California.

Bergfeld, D., Goff, F., and Janik, C.J., 2001, Elevated carbon dioxide flux at the Dixie Valley geothermal field, Nevada—relations between surface phenomena and the geothermal reservoir: Chemical Geology, v. 177, no. 1-2, p. 43–66.

Blackett, R.E., 2007, Review of selected geothermal areas in southwestern Utah: Geothermal Resources Council Transactions, v. 31, p. 111-116.

Chiodini, G., Cioni, R., Guidi, M., Raco, B., and Marini, L., 1998, Soil CO_2 flux measurements in volcanic and geothermal areas: Applied Geochemistry, v. 13, no. 5, p. 543–552.

Chiodini, G., Caliro, S., Cardellini, C., Avino, R., Granieri, D., and Schmidt, A., 2008, Carbon isotopic composition of soil CO_2 efflux, a powerful method to discriminate different sources feeding soil CO_2 degassing in volcanic-hydrothermal areas: Earth and Planetary Science Letters, v. 274, no. 3, p. 372–379.

Elberling, B., 2003, Seasonal trends of soil CO_2 dynamics in a soil subject to freezing: Journal of Hydrology, v. 276, no. 1-4, p. 159–175.

Faulder, D.D., 1991, Conceptual geologic model and native state model of the Roosevelt Hot Springs hydrothermal system: Proceedings, Sixteenth Workshop on Geothermal Reservoir Engineering, Stanford University, Stanford, California p 131–142.

Fischer, T.P., and Lopez, T.M., 2016, First airborne samples of a volcanic plume for $\delta^{13}C$ of CO_2 determinations: Geophysical Research Letters, v. 43, no. 7, p. 3272–3279.

Dame, B.E., Solomon, D.K., Evans, W.C., and Ingebritsen, S.E., 2015, Developing a new, passive diffusion sampler suite to detect helium anomalies associated with volcanic unrest: Bulletin of Volcanology, v. 77, no. 3, p. 1–17.

Gardner, P., and Solomon, D.K., 2009, An advanced passive diffusion sampler for the determination of dissolved gas concentrations: Water Resources Research, v. 45, no. 6, https://doi.org/10.1029/2008WR007399

Hardwick, C.L., Gwynn, M., Allis, R., Wannamaker, P., and Moore, J., 2016, Geophysical signatures of the Milford, Utah FORGE site: Proceedings, 41st Workshop on Geothermal Reservoir Engineering, Stanford University, Stanford, California.

Hardwick, C., Hurlbut, W., and Gwynn, M., 2019, Geophysical surveys of the Milford, Utah, FORGE site—gravity and TEM, *in* Allis, R., and Moore, J.N., editors, Geothermal characteristics of the Roosevelt Hot Springs system and adjacent FORGE EGS site, Milford, Utah: Utah Geological Survey Miscellaneous Publication 169-F, 15 p., https://doi.org/10.34191/MP-169-F.

Jones, C.G., Moore, J.N., and Simmons, S., 2019, Petrography of the Utah FORGE site and environs, Beaver County, Utah, *in* Allis, R., and Moore, J.N., editors, Geothermal characteristics of the Roosevelt Hot Springs system and adjacent FORGE EGS site, Milford, Utah: Utah Geological Survey Miscellaneous Publication 169-K, 23 p., 2 appendices, https://doi.org/10.34191/MP-169-K.

Kennedy, B.M., and van Soest, M.C., 2007, Flow of mantle fluids through the ductile lower crust: Helium isotope trends: Science, v. 318, no. 5855, p. 1433–1436.

Knudsen, T., Kleber, E., Hiscock, A., and Kirby, S.M., 2019, Quaternary geology of the Utah FORGE site and vicinity, Millard and Beaver Counties, Utah, *in* Allis, R., and Moore, J.N., editors, Geothermal characteristics of the Roosevelt Hot Springs system and adjacent FORGE EGS site, Milford, Utah: Utah Geological Survey Miscellaneous Publication 169-B, 21 p., 2 appendices, https://doi.org/10.34191/MP-169-B.

Krivoruchko, K., 2012, Empirical bayesian kriging: Esri, Redlands, California, USA.

Lee, H., Muirhead, J., Fischer, T., Ebinger, C., Kattenhorn, S., and Kianji, G., 2016, Tectonic degassing of mantle-derived CO_2 along faults in the East African Rift: Nature Geoscience, v. 9, p. 145–149.

Lewicki, J.L., Evans, W.C., Hilley, G.E., Sorey, M.L., Rogie, J.D., and Brantley, S.L., 2003, Shallow soil CO_2 flow along the San Andreas and Calaveras faults, California: Journal of Geophysical Research, Solid Earth, v. 108, no. B4, p. 14.

Lewicki, J.L. and Oldenburg, C.M., 2005, Near-surface CO_2 monitoring and analysis to detect hidden geothermal systems: Proceedings, Thirteenth Workshop on Geothermal Reservoir Engineering, Stanford University, Stanford, California.

Lewicki, J.L., Bergfeld, D., Cardellini, C., Chiodini, G., Granieri, D., Varley, N., and Werner, C., 2005, Comparative soil CO_2 flux measurements and geostatistical estimation methods on Masaya volcano, Nicaragua: Bulletin of Volcanology, v. 68, no. 1, p. 76–90.

Lynne, B.Y., Campbell, K.A., Moore, J.N., and Browne, P.R.L., 2005, Diagenesis of 1900-year-old siliceous sinter (opal-A to quartz) at Opal Mound, Roosevelt Hot Springs, Utah, USA: Sedimentary Geology, v. 179, no. 3, p. 249–278.

Miller, J., Allis, R., and Hardwick, C., 2019, Interpretation of seismic reflection surveys near the FORGE enhanced geothermal systems site, Utah, *in* Allis, R., and Moore, J.N., editors, Geothermal characteristics of the Roosevelt Hot Springs system and adjacent FORGE EGS site, Milford, Utah: Utah Geological Survey Miscellaneous Publication 169-H, 13 p., https://doi.org/10.34191/MP-169-H.

Moore, J.N., and Nielson, D.L., 1994, An overview of the geology and geochemistry of the Roosevelt Hot Springs geothermal system, Utah: Utah Geological Association Publication, v. 23, p. 25–36.

Nielson, D.L., Evans, S.H., and Sibbett, B.S., 1986, Magmatic, structural, and hydrothermal evolution of the Mineral Mountains intrusive complex, Utah: Geological Society of America Bulletin, v. 97, p. 765–777.

Ozima, M., and Podosek, F.A., 1983, Noble gas geochemistry: Cambridge University Press, 367 p.

Parks, M.M., Caliro, S., Chiodini, G., Pyle, D.M., Mather, T.A., Berlo, K., Edmonds, M., Biggs, J., Nomikou, P., and Raptakis, C., 2013, Distinguishing contributions to diffuse CO_2 emissions in volcanic areas from magmatic degassing and thermal decarbonation using soil gas ^{222}Rn–$\delta^{13}C$ systematics—Application to Santorini volcano, Greece: Earth and Planetary Science Letters, v. 377, p. 180–190.

Peiffer, L., Bernard-Romero, R., Mazot, A., Taran, Y.A., Guevara, M., and Santoyo, E., 2014, Fluid geochemistry and soil gas fluxes (CO_2–CH_4–H_2S) at a promising Hot Dry Rock Geothermal System—The Acoculco caldera, Mexico: Journal of Volcanology and Geothermal Research, v. 284, p. 122–137.

PP Systems, 2016, EGM-5 Portable CO_2 Gas Analyzer Operation Manual, Version 1.01, Amesbury, Massachusetts.

Rizzo, A.L., Jost, H.J., Caracausi, A., Paonita, A., Liotta, M., and Martelli, M., 2014, Real-time measurements of the concentration and isotope composition of atmospheric and volcanic CO_2 at Mount Etna (Italy): Geophysical Research Letters, v. 41, no. 7, p. 2382–2389.

Sanford, W., Shropshire, R., and Solomon, D., 1996, Dissolved gas tracers in groundwater—Simplified injection, sampling, and analysis: Water Resources Research, v. 32, no. 6, p. 1635–1642.

Sano, Y., and Marty, B., 1995, Origin of carbon in fumarolic gas from island arcs: Chemical Geology, v. 119, no. 1–4, p. 265–274.

Sharp, Z., 2017, Principles of stable isotope geochemistry, 2nd Edition, Albuquerque, University of New Mexico, doi:10.5072/FK2GB24S9F.

Simmons, S., Kirby, S., Moore, J., Wannamaker, P., and Allis, R., 2015, Comparative analysis of fluid chemistry from Cove Fort, Roosevelt and Thermo: Implications for geothermal resources and hydrothermal systems on the east edge of the Great Basin: 39th Geothermal Resources Council Annual Meeting-Geothermal: Always On, GRC 2015, Reno, Nevada.

Simmons, S.F., Moore, J.N., Allis, R., Kirby, S., Jones, C., Bartley, J., Kleber, E. Tyler, K., Milller, J., Hardwick, C., Rahilly, K., Gwynn, M., McLennan, J., Forbes, B., Podgorney, R., Pankow, K., Wannamaker, P., and Fischer, T., 2018, A revised geoscientific model of the FORGE Utah EGS laboratory: Proceedings, 43rd Workshop on Geothermal Reservoir Engineering, Stanford University, Stanford, California.

Sinclair, A.J., 1974, Selection of threshold values in geochemical data using probability graphs: Journal of Geochemical Exploration, v. 3, no. 2, p. 129–149.

Wannamaker, P.E., Faulds, J. E., and Kennedy, B.M., 2017, Integrating magnetotellurics, soil gas geochemistry and structural analysis to identify hidden, high enthalpy, extensional geothermal systems: University of Utah/EGI Technical Report to U.S. Department of Energy, Office of Energy Efficiency & Renewable Energy Geothermal Technologies Program.

Werner, C., and Brantley, S., 2003, CO_2 emissions from the Yellowstone volcanic system: Geochemistry, Geophysics, Geosystems, v. 4, no. 7, 27p.

Western Regional Climate Center – Desert Research Institute: Reno, Nevada Online, https://cemp.dri.edu/cgi-bin/cemp_stations.pl?stn=milu, accessed January 18, 2018.

LOCALIZED AMBIENT NOISE TOMOGRAPHY OVER THE FORGE UTAH SITE

by Andy J. Trow[1], Kristine L. Pankow[1], Yadong Wang[2], and Fan-Chi Lin[2]

[1]University of Utah Seismograph Stations, University of Utah, Salt Lake City, Utah
[2]Department of Geology and Geophysics, University of Utah, Salt Lake City, Utah

Miscellaneous Publication 169-J
Utah Geological Survey
a division of
UTAH DEPARTMENT OF NATURAL RESOURCES

This paper is part of *Geothermal Characteristics of the Roosevelt Hot Springs System and Adjacent FORGE EGS Site, Milford, Utah*. https://doi.org/10.34191/MP-169

Bibliographic citation:

Trow, A.J., Pankow, K.L., Wang, Y., and Lin, F.-C., 2019, Localized ambient noise tomography over the FORGE Utah site, *in* Allis, R., and Moore, J.N., editors, Geothermal characteristics of the Roosevelt Hot Springs system and adjacent FORGE EGS site, Milford, Utah: Utah Geological Survey Miscellaneous Publication 169-J, 15 p., https://doi.org/10.34191/MP-169-J.

LOCALIZED AMBIENT NOISE TOMOGRAPHY OVER THE FORGE UTAH SITE

by Andy J. Trow, Kristine L. Pankow, Yadong Wang, and Fan-Chi Lin

ABSTRACT

In December 2016 and August 2017 two geophone arrays recorded 30 days of seismic data near Milford, Utah, to perform ambient noise tomography, centered on the Frontier Observatory for Research in Geothermal Energy (FORGE) Utah project site. The initial deployment in December 2016 consisted of 93 5-Hz three-component geophones roughly centered on the FORGE project area but spanning across the Mineral Mountains and into the Milford Valley. The second deployment in August 2017 consisted of 49 densely spaced geophones centered about the FORGE deep test well site. Ambient noise cross-correlations were calculated using 10-minute windows for all station pairs. The individual correlation functions were then stacked in order to estimate the Green's functions for virtual source and receiver paths. For the initial 93-station deployment, clear Rayleigh wave signals were observed in the 3 to 10 second period range. During the August 2017 dense deployment, signals were observed between 0.5 and 1 seconds. Frequency-time analysis was used to obtain surface wave dispersion measurements from the cross-correlation functions for both arrays. Dispersion measurements were inverted for Rayleigh wave group velocity maps at 3, 5, and 7 second periods for the initial 93-station array. Sensitivity kernels indicate that these periods are sensitive to depths from 2.5 to 8 km. Group velocity maps show a general trend of higher velocities in the core of the Mineral Mountains with lower velocities in the alluvium of the Milford Valley. For the 3 to 7 second periods, group velocities range from 2 to 3.5 km/s, but show the top of a low-velocity layer beginning to develop at 5 to 8 km depth. This low-velocity zone is consistent with work from a previous teleseismic tomography study. For the dense array, a group velocity map was determined for the 0.67-second period, which roughly correlates to the upper 500 m. This map shows higher velocities (600 m/s) at the eastern portion of the array, closer to the Mineral Mountains consistent with the shallowing of a granitic reservoir unit and thinner alluvial cover.

INTRODUCTION

As part of site characterization efforts for the Utah Frontier Observatory for Research in Geothermal Energy (FORGE) project, two geophone seismic monitoring arrays were deployed over the FORGE project area in order to record both microseismicity and ambient noise for seismic imaging (Trow et al., 2018). The instruments are compact 5-Hz three-component Nodal geophones. Other studies using this instrumentation have proven its applicability to earthquake detection and crustal imaging studies (Bowden et al., 2015; Li et al., 2015, 2018; Hansen and Schmandt, 2015; Wang et al., 2017). Specifically, these geophone arrays facilitate high-resolution crustal imaging at periods below 10 seconds (e.g., Wang et al., 2017; Ward and Lin, 2017; Wu et al., 2017). For imaging we use ambient noise cross-correlation records to estimate the Green's function between a virtual source station and receiver (Shapiro and Campillo, 2004). Primarily, we extracted Rayleigh wave signals from the vertical-vertical noise cross-correlations.

The study area is located in southwestern Utah to the northeast of Milford, Utah, on the western flank of the Mineral Mountains (Figure 1). This area has undergone many investigations to understand its geothermal potential since the late 1970's (e.g., Ward et al., 1978; Robinson and Iyer, 1981), and geologic and thermal conditions have been summarized in more recent reports (Hardwick et al., 2016; Simmons et al., 2016; Allis et al., 2017). Overall, the region is characterized by high heat flow and Quaternary volcanism (Blackwell, 1983; Edwards and Chapman, 2013) with crystalline basement rock (Moore and Nielson, 1994). The high heat flow can be attributed to thinning crust in the Basin and Range Province along with an active volcanic history (e.g., Benz et al., 1990). Recent volcanism began in the Oligocene (Faulder, 1991) with emplacement of the granitic rocks beginning about 25 Ma, with the most recent rhyolite flows and domes occurring about 0.5 to 0.8 Ma (Robinson and Iyer, 1982; Faulder, 1991).

Structural interpretations (Smith and Bruhn, 1984; Barker, 1986) of seismic profiles across the project site, extending from the Mineral Mountains into the Milford Valley, highlight a major reflector dipping westward into the basin that could be a low-angle listric fault or a basement rock-sediment contact. In addition, teleseismic P-wave tomography indicates a low-velocity zone beneath the western portion of the Mineral Mountains (Robinson and Iyer, 1981). This zone has been identified in the upper crust below the study area at depths between 5 and 15 km (Robinson and Iyer, 1982; Barker, 1986) with up to a 7% reduced P wave seismic velocity indicating higher basement temperatures and the possibility of partial melt. Low-velocity anomalies and areas of elevated crustal temperatures are important for understanding the heat source of the Roosevelt Hot Spring System. We propose the use of ambient noise seismic tomography to look for and better constrain these along with other structures in the FORGE project area.

To map seismic velocities, continuous seismic data is used to perform noise cross-correlations between geophone stations. This allows an estimation of the Green's functions along the path between station pairs (Shapiro et al., 2005; Yao et al., 2008). Surface wave tomography is performed on a grid by inverting travel-time measurements (Barmin et al., 2001; Lin et al., 2008, 2013; Ward, 2015). This technique has been applied to the high-permeability zone in a geothermal reservoir in portions of Europe (Calò et al., 2013; Lehujeur et al., 2017) and has identified low-velocity regions in known geothermal fields that have been interpreted to be geothermal reservoirs (Calò et al., 2013). Repeated experiments that show mapped velocity changes can relate to changes in the reservoir of the geothermal system. Group velocity measurements from this study will serve as a base model to establish reservoir changes as the geothermal field evolves with development and production during the Utah FORGE project (Simmons et al., 2018).

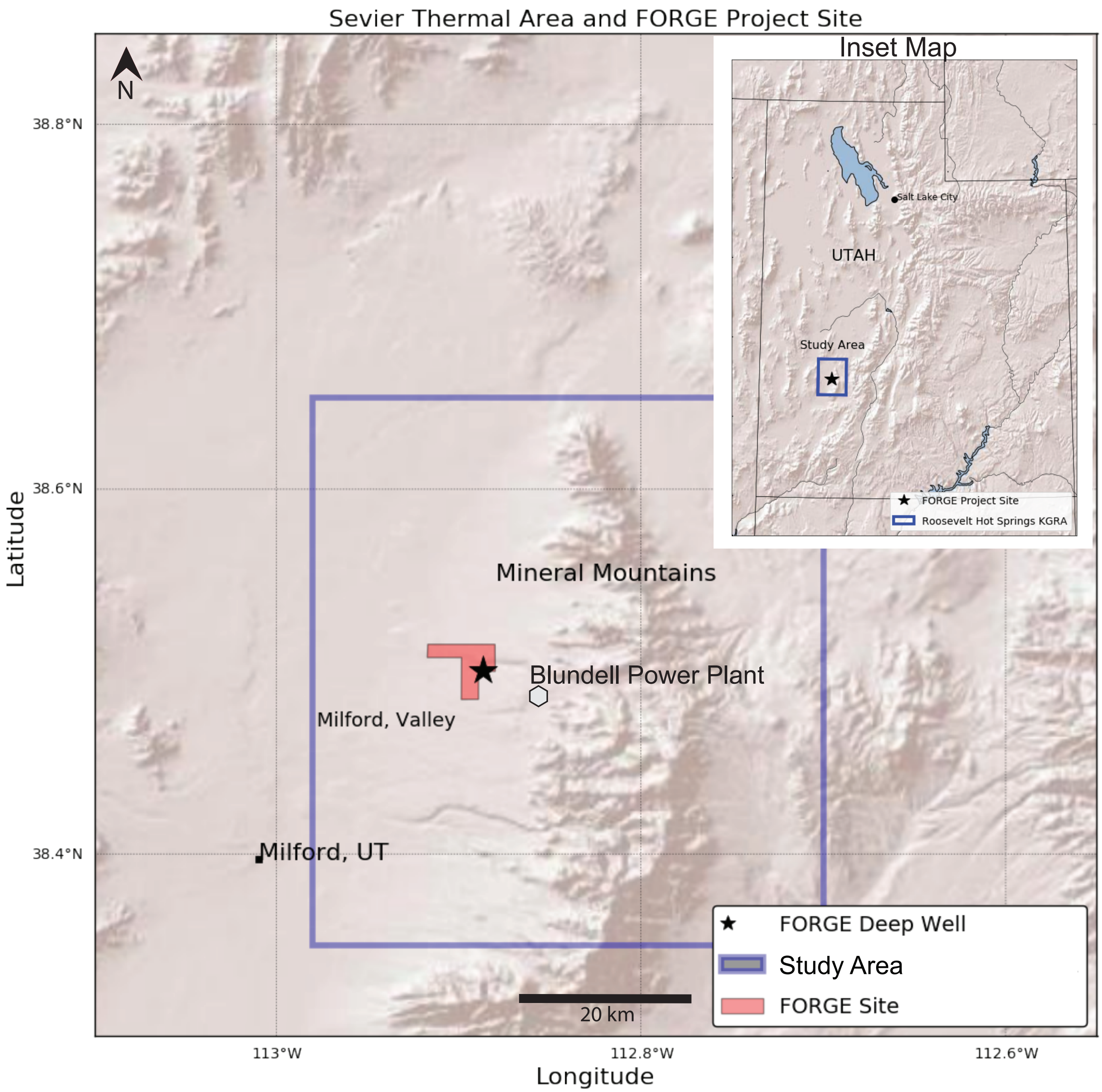

Figure 1. Overview Map of Utah FORGE project area and Roosevelt Known Geothermal Resource Area (KGRA). Inset map shows the Roosevelt KGRA (blue box) and FORGE site within the state of Utah. The detailed map shows the footprint of the proposed research facility, the deep well location, and location of the Blundell geothermal power plant.

DATA

Two seismic deployments were conducted in December 2016 and August 2017 (Figure 2) (Trow et al., 2018). Each experiment lasted ~30 days and consisted of 93 and 49 5-Hz three-component Nodal geophones, respectively. Array geometry was designed to maximize its aperture while maintaining equal station spacing in order to optimize crossing source-receiver ray paths. Recorded seismic waveforms were sampled at 250 Hz with a pre-amp gain of 18 dB. Deployments generated ~250 to 500 GB of time series data. Figure 1 shows the study area, Figure 2 gives the detailed array geometry.

The 2016 deployment included 44 geophones spaced at ~4 km, and a central dense grid of 49 geophones with 650 m station spacing. The dense portion of the array was centered over the proposed Utah FORGE geothermal research facility footprint (Figure 1) and the sparse grid covered the Milford Valley and spanned across the Mineral Mountains for seismic event detection and imaging. The full 93-station array (December 2016) was used to extract longer period surface waves that will sample deeper in the crust but will have lower lateral resolution.

During the 2017 deployment the central dense portion of the FORGE array (49 stations) was re-occupied during drilling of the test well. The dense grid has 650 m spacing, which enabled short-period surface waves to propagate between station pairs and show clear move-out in the cross-correlation functions (CCF). Surface wave records between 0.5 and 1 seconds were extracted allowing higher lateral resolution, and imaging of shallower structure due to near-surface sensitivity of the surface waves at these frequencies.

NOISE SOURCE ANALYSIS

Ambient noise seismic tomography is sensitive to azimuthal variations and frequency content of the noise source. Reliability of travel-time measurements is affected by source characteristics, which are important inputs of tomographic inversion problems (Snieder, 2004). Wang et al. (2017) show minor changes to tomographic inversion results at Mount St. Helens after imposing a correction to an azimuthally biased noise source distribution. Since inhomogeneous noise plays a minor role in final results, it is not corrected for in this study. The continuity of the frequency of persistent noise sources is another consideration, such that, depth resolution can be hampered due to restricted sensitivity from a limited bandwidth of noise sources. Data from the arrays showed promising move-out in two discrete ranges: 3 to 10 seconds and 0.5 to 1 seconds. The 2016 deployment of 93 stations showed coherent signal in the 3 to 10 second range. We do not consider signal

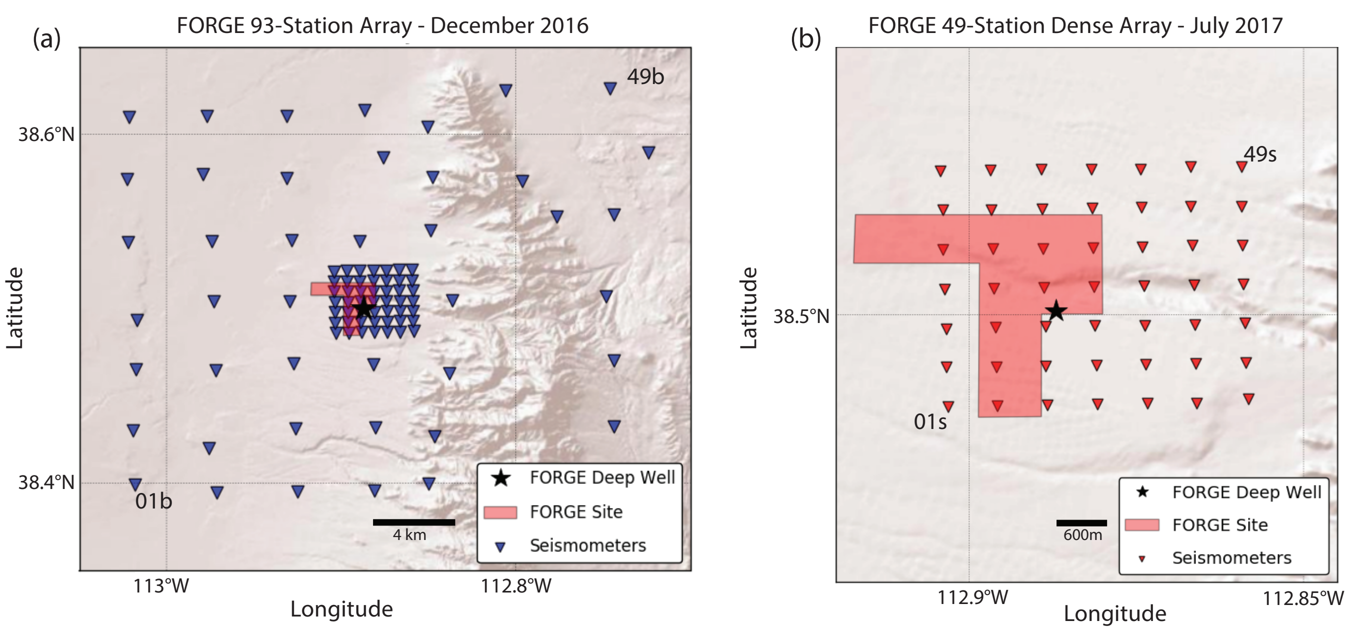

Figure 2. *Detailed array map of the two deployments.* ***(a)*** *The full 93-station deployment from December 2016. Outer grid has about 4 km spacing with a dense grid of 49 stations spaced at 650 m.* ***(b)*** *August 2017 re-occupation of 49-station dense grid. Close up of the 650-m-spaced dense array. Both maps have the footprint of the FORGE facility in red and the deep well location.*

beyond 10-second periods due to the limited aperture of the array (~30 km). The 3 to 10 second signal corresponds with the secondary oceanic microseismic peak (~8 sec) (Haubrich et al., 1963). At shorter periods the signal was strongly influenced by a near vertically arriving signal that did not propagate across the array as a surface wave. Body wave energy is strongest between 1 and 3 seconds and causes challenges for imaging 1 to 3 km depths.

The 2017 49-station dense array was re-occupied to measure small drilling-related seismic events and record ambient noise records during the summer. During re-occupation of the dense grid, we see a homogeneous signal between 0.5 and 1 seconds that was used to measure group velocity. Move-out was clear on positive and negative lags of record sections indicating a homogenous source. We compared the dense grid stations for both FORGE deployments to assess the higher frequency signal variation during different seasons as well as local variation in noise source distribution (Figure 3). The record section shows the cross-correlations from the furthest southwest station 01s as the virtual source to all other receivers. The re-occupied dense grid has a higher signal-to-noise ratio (SNR) and a more homogeneous noise distribution (Figure 3a), while the dense portion of the initial array deployed in December has weaker signals and stronger move-out only in the negative lags of the CCFs (Figure 3b).

METHODS

For crustal imaging we use ambient noise cross-correlation to establish Rayleigh wave group velocity structure beneath the array. This tomography process has been well documented by Bensen et al. (2007) and we follow the procedure described in Lin et al. (2013) to calculate the cross-correlations. This process is completed in three steps: (1) Prepare data for each station including spectral whitening, followed by calculation of the noise cross-correlation records from continuous seismic data and temporal normalization of each cross-correlation record. (2) Measure Rayleigh wave group travel-times through frequency-time analysis (FTAN) (Levishin et al., 1989; Bensen et al., 2007). (3) Invert travel-time measurements on a 2D grid (Barmin et al., 2001) to obtain smooth group velocity maps of the region for the periods where we see strong Rayleigh wave signals in the CCFs.

Data Preparation and Cross-Correlation

The aperture of the initial FORGE deployment in December 2016 consisting of 93 stations is approximately 30 km. The aperture of the re-occupied 49-station dense grid is approximately 6 km. Both experiments had a one-month duration, and we follow the same processing steps for each dataset. Time series data are cut into 10-minute segments for each array. Each segment is spectrally whitened based on the average of the horizontal components, and then for every station pair, we calculate

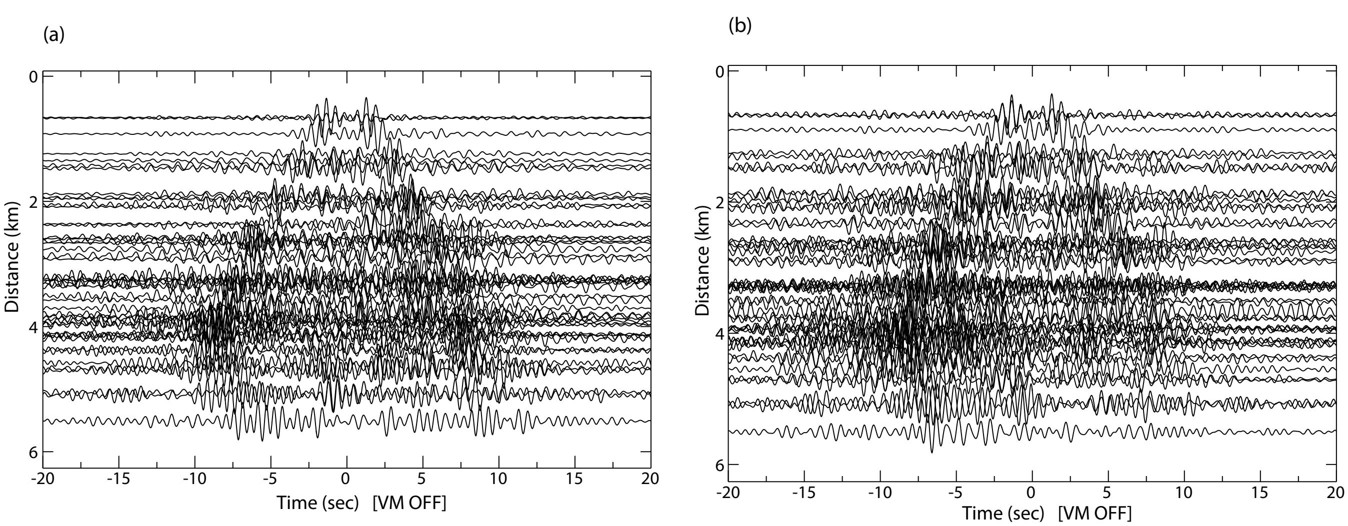

Figure 3. *Temporal variance in shorter period (0.5–1 second) signal illustrated by plotting the record sections of the CCF's bandpass filtered between 0.5 and 1 second for the dense portion of the FORGE array.* ***(a)*** *Record section for the July 2017 deployment when only the dense portion of the grid was occupied. Signal is more symmetric and has a higher SNR. This illustrates a more homogeneous and stronger noise source during this deployment.* ***(b)*** *Record section for only the dense portion of the grid for the December 2016 FORGE deployment. The signal is stronger on the negative lags of the CCF's and has azimuthal bias in the noise source distribution.*

the cross-correlation functions for each 10-minute time window. Resulting cross-correlation results are normalized in the time domain by running-absolute-mean normalization (Bensen et al., 2007). We stack the 10-minute-long window normalized CCF's to obtain a final interstation CCF, which approximates the Green's function between stations (Lin et al., 2013). The processing steps effectively remove transient earthquake signals and other large-amplitude signals including spurious noise spikes (Bensen et al., 2007; Lin et al., 2013).

We compute the cross-correlation for all nine components (EE, EN, EZ, NN, NE, NZ, ZE, ZN, ZZ). The horizontal component cross-correlation functions are rotated into radial and transverse components in order to isolate Rayleigh and Love wave energy and determine which components have the highest SNR. Figure 4 shows a comparison of rotated components of the CCF between station 01b and station 49b. It is clear that the vertical-vertical (ZZ) component result has the highest SNR. For this reason, we focus efforts on the ZZ component results. Using the ZZ component ensures that we extract predominantly Rayleigh wave energy.

The number of cross-correlations computed scales by a factor of $n^2/2$ where n is the number of stations. For the full FORGE array, over 4000 cross-correlations are calculated using the 93-station grid and 1,200 are calculated for the re-occupied dense array. Stacked CCFs can be evaluated for positive and negative time lag. Figure 5 is a record section of non-symmetric CCFs for the full FORGE array that is bandpass filtered from 4 to 7 seconds. The asymmetry in the records is due to a non-homogeneous azimuthal distribution of noise. At these longer periods we determine that the main surface wave energy directionality has a southwesterly back-azimuth. To improve SNR on the negative lag of the CCF, the positive and negative lags are averaged to produce a symmetric CCF.

Group Velocity Extraction

Group velocities are measured through frequency-time analysis (FTAN) over the ZZ component CCF's. FTAN has been used to estimate velocities of the fundamental mode Rayleigh wave (e.g., Levishin et al., 1989; Bensen et al., 2007). We use the automated process outlined in Bensen et al. (2007) and Lin et al. (2008) where each CCF is subject to a series of narrow band-pass filters each having a unique center frequency. After applying a Hilbert transform to the cross-correlation time series, the real portion is combined with the imaginary portion to obtain an envelope function. The max amplitude or peak of the envelope function is picked and corresponds to a time lag (t). This time lag is used with the interstation distance (d) and time (t) to compute the group velocity (V_g) via:

$$V_g = \frac{d}{t}$$

where V_g denotes group velocity, d is distance, and t is time (full details are given in Lin et al. (2008).

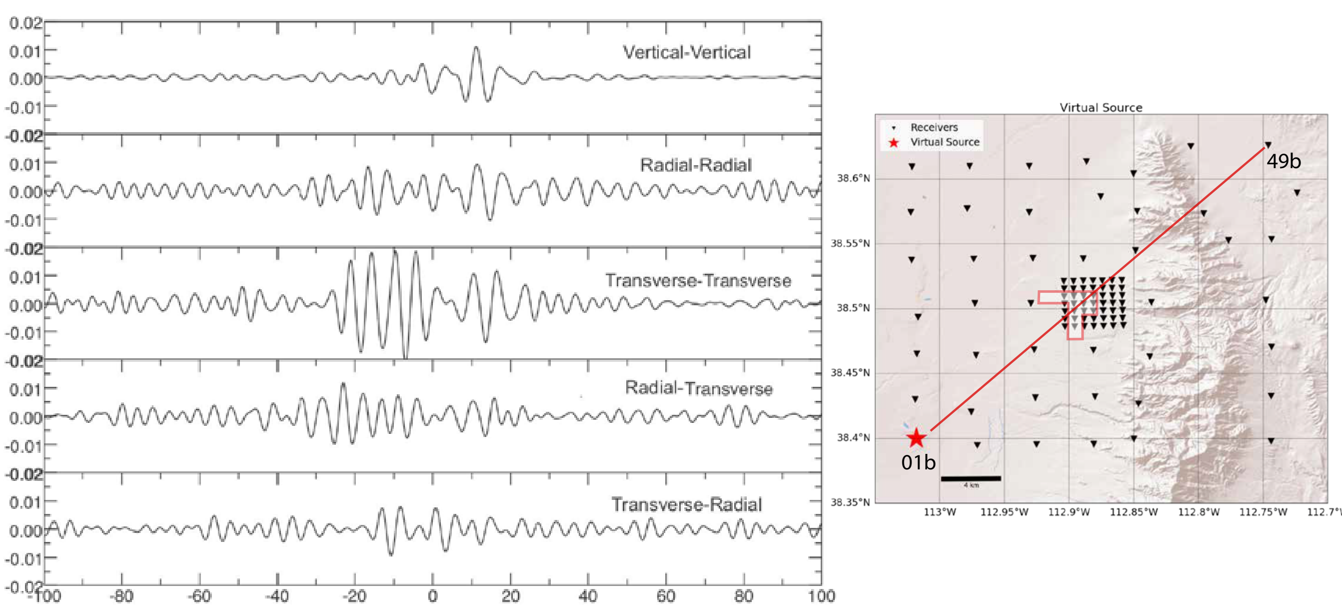

Figure 4. *Cross-correlation functions for station 01b-49b. The traces are bandpass filtered from 3 to 10 seconds and components are listed for each CCF. We note that the vertical-vertical component has the highest SNR. The strong signal on the vertical-vertical component shows that the signal is dominated by Rayleigh wave energy.*

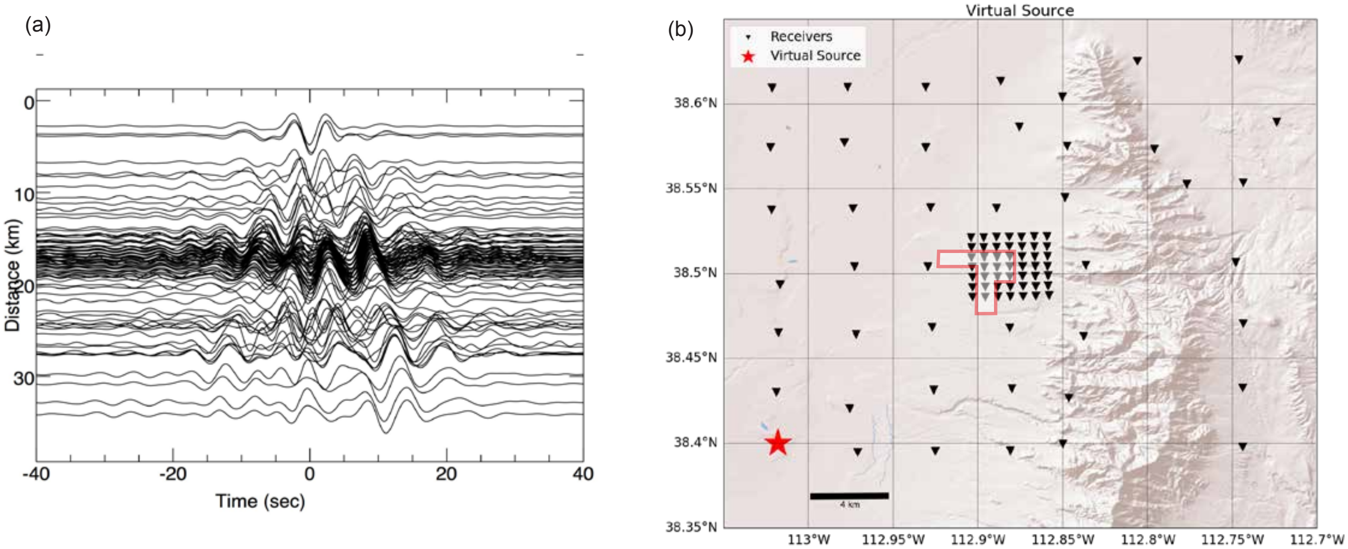

Figure 5. *Record section of FORGE cross-correlation functions (CCF). **(a)** The CCF's bandpass filtered from 4 to 7 seconds. Each trace is a one-month stack of 10-minute windows. **(b)** Map highlighting the virtual source (01b) and receiver map used to plot record section.*

To ensure reliable measurements we imposed a minimum distance criterium and a SNR criterium for every station pair. It has been shown that more reliable velocity measurements are obtained when the minimum distance between virtual source and receiver station is three wavelengths (Bensen et al., 2007), but more recent studies have produced robust phase velocity maps using only one wavelength as a minimum distance criterium (Wang et al., 2017). Our group velocity measurements may have bias due to the one wavelength as a minimum distance criterium but with the interstation spacing and limited period band where signal was clear, we were restricted to this shorter criterium. The dense geophone arrays in this study are best suited for a minimum distance criterium of one wavelength, rather than two or three wavelengths (Lin et al. 2008, 2013) because the array apertures are relatively small, and a shorter minimum distance criterium maximizes the number of crossing ray paths, which is a key element to generating robust velocity maps. For 3-second period signals we estimate an average velocity of 2 km/s, and a corresponding minimum distance of ~6 km. For the dense array we evaluate a 1-second period wave where we estimate an average velocity of 400 m/s, related to unconsolidated basin sediment, and therefore, we have a minimum distance of roughly 400 m. Additionally we require a SNR criterium of 4, which is measured after the FTAN pick window as defined by estimated crustal velocities and interstation distances. SNR is calculated as the maximum amplitude in the FTAN pick window divided by the root-mean-squared amplitude in the CCF following the FTAN pick window. Once travel-time measurements have passed the quality control criteria, they are stored in a matrix corresponding to each station pair in the array.

Tomographic Inversion

We use the fundamental-mode Rayleigh-wave group velocity measurements to produce tomographic velocity maps for 3, 5, and 7 second periods for the full 93-instrument grid and a 0.67 second map for the dense 49-station grid. We follow the surface wave inversion method outlined in Barmin et al. (2001) that performs a regularized inversion in two dimensions. We divide our model into an evenly spaced grid (0.001° x 0.001°). The inversion process minimizes the misfit of the travel-time residuals for all ray paths. Regularization includes both smoothing and damping of the function. The regularization is determined empirically, and a suite of inversion parameters are tested to obtain the best parameterization. A tradeoff curve showing the model misfit with smoothing parameters is plotted in Figure 6. The smoothing consists of a weighted smoothing parameter alpha (α), and a spatial smoothing parameter sigma (σ). Optimum smoothing parameters are determined when model residuals are minimized (Figure 6) and results do not contain sharp artifacts. A suite of parameters are tested while keeping the others fixed. We do not use damping, as ray path coverage is regular and well distributed. We look to reproduce smooth features consistent with geologic models when establishing the best model. We note that main high-velocity features remained consistent throughout testing of different parameters. We combine inversion results from the dense central grid at higher frequencies with longer period results from the whole array to improve resolution in the center of the array. Figure 7 shows ray path coverage for both arrays. High ray path density yields an overdetermined inverse problem. The number of ray paths decline as the period increases; this is due to the minimum distance and SNR criteria that are imposed after velocity measurements are made.

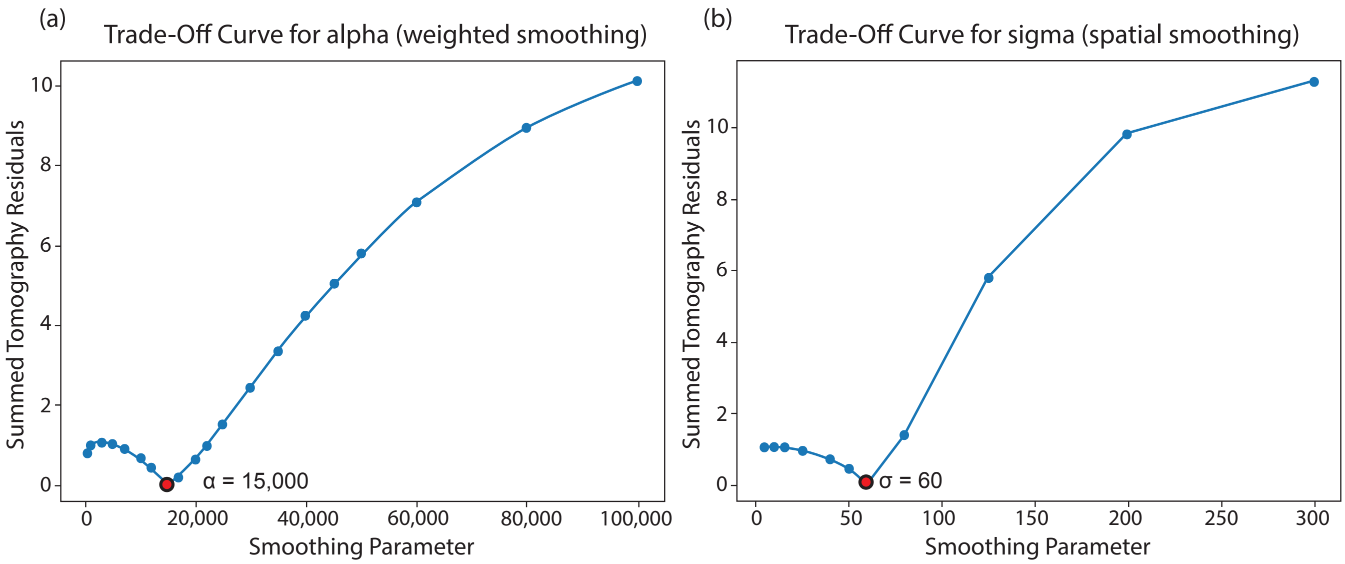

Figure 6. *Trade-off curves used in determining smoothing parameters during inversion process. Optimum smoothing was determined empirically and parameters were chosen when the inversion residuals are minimized.* ***(a)*** *Relationship between weighted smoothing parameters and the inversion residuals.* ***(b)*** *Relationship between the spatial smoothing parameters and inversion residuals. A red marker indicates the selected smoothing values.*

Depth Sensitivity Kernels

To better estimate the depth of the resulting velocity maps we calculate two-dimensional depth sensitivity kernels for the fundamental mode Rayleigh-wave group velocities at 3, 5, and 7 second periods (Figure 8a). This is done using a western U.S. (WUS) velocity model that was developed by Herrmann et al. (2011) and adopted for the Utah region in Whidden and Pankow (2012) (Figure 8b). Sensitivity kernels are calculated by calculation of the partial derivative of the predicted surface wave velocity with respect to shear wave velocity as outlined in Wang et al. (2017). Figure 8a shows that the inversion process produces maps that are most sensitive around 3 km depth for 3 seconds, 5 km depth for 5 seconds, and 7.5 km depth for 7 seconds. Sensitivity for the 0.67 period map was in the upper 500 m of the crust.

RESULTS

We performed cross-correlations between each possible source receiver pair. Move-out of the surface waves is observed in the record sections for both arrays but at different dominant periods; Figure 9 shows a record section for the 49-station dense array and Figure 5a is a record section for the full 93-station array. The signal is most clear and strongest in the 3 to 10 second period band for the entire FORGE array while on the dense array we see it most clear between 0.5 and 1 seconds. The record sections of the symmetric component CCF's show approximate group velocities of 2.3 km/s at 7 second period and 0.5 km/s at 0.67 second period. Based on the ray-path coverage maps, the models are well constrained at the location of the dense grid for both arrays with decreasing resolution towards the edges of the array. Velocity measurements in general are the most well constrained where there is a high density of crossing ray paths.

Figure 10 shows the results from the tomographic inversion. We inverted for group velocities at 0.67, 1, 3, 5, and 7 seconds, respectively. Note that as period increases, group velocities become most sensitive to increasingly deeper velocity structures.

Results from the broad 93-station array show, in general, higher velocities near and below the Mineral Mountains with lower velocities at the edges of the arrays where the basin-fill sediments are deeper and more prominent. However, areas of lower seismic velocities also tend to occur near the edges of the array where velocity measurements are not as well constrained. Figure 10a shows the 7 second Rayleigh wave group velocity map, where we see a prominent high-velocity anomaly (>3 km/s) coincident with the Mineral Mountains to the east of the dense grid. If we trace the outline of the mountain range from satellite imagery we see that the velocity anomaly correlates in space with the granitic Mineral Mountains (Figure 10).

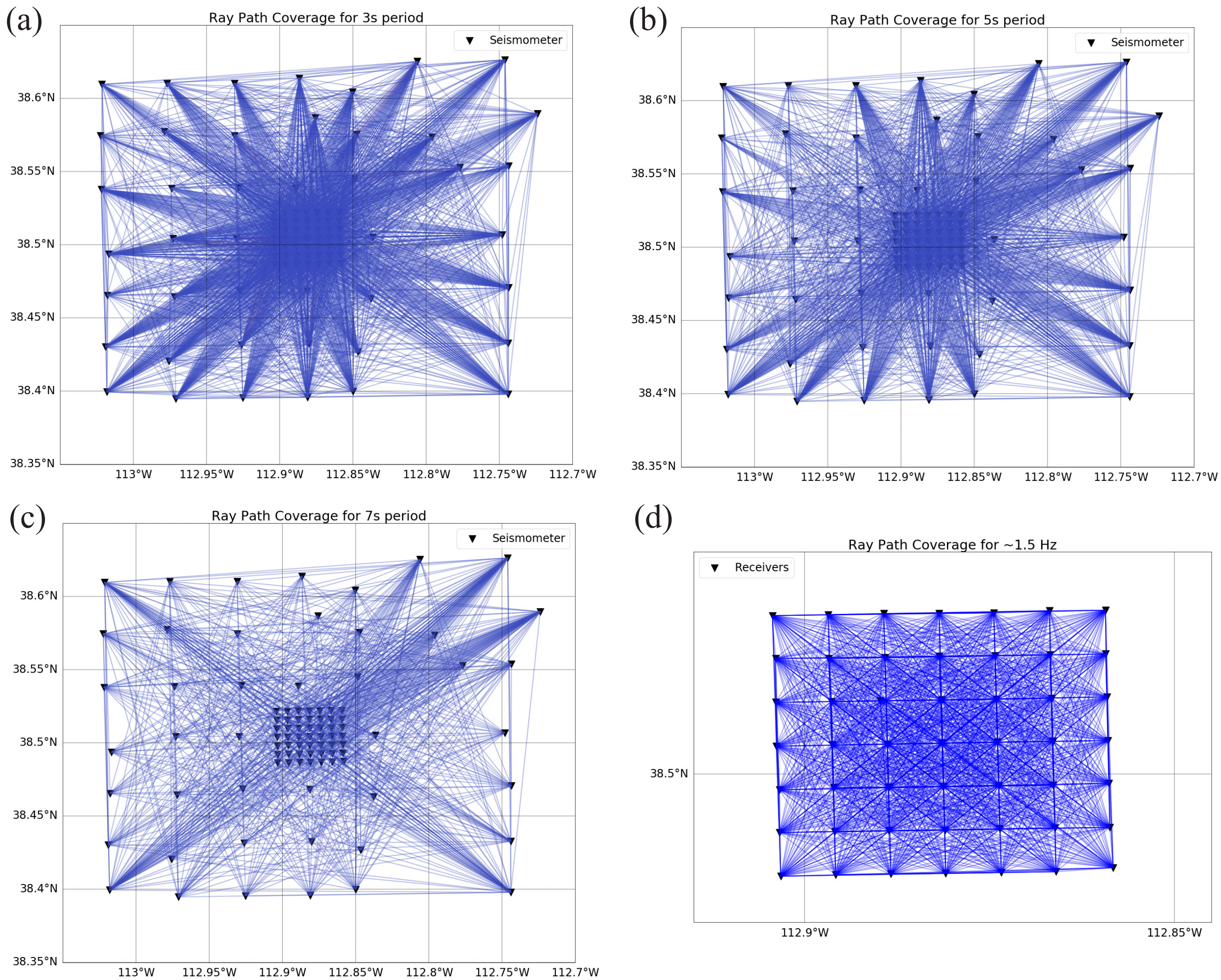

Figure 7. *Ray path coverage of main FORGE grid. Great circle paths are plotted between virtual source and receiver pairs showing approximate surface wave ray path. Note decreasing ray density as period increases; this is due to minimum distance criteria of one wavelength between virtual source and receiver.* ***(a)*** *3 second period,* ***(b)*** *5 second period,* ***(c)*** *7 second period,* ***(d)*** *0.67 second period map of dense 49-station grid deployed in July 2017.*

DISCUSSION

The tomographic method reproduces major geologic features in the region. In general, the Mineral Mountains are imaged as a high-velocity anomaly (>3 km/s) and the basins towards the edges of the arrays are relatively slower. Our results indicate as the period of the surface waves increase, and investigation depth increases, there is a reduction in group velocity values. Typically, seismic velocity increases with depth, but beneath the central portion of the Mineral Mountains it reverses. A typical model would show increasing group velocity with depth; however, ours begins to highlight decreasing velocities at roughly 8-km depth. We have plotted the velocity maps with a constant velocity scale (Figure 11) to illustrate this change rather than relative changes due to structure. The decrease in seismic velocity between 5 and 8 km depth corresponds spatially with the high-attenuation body outlined in Robinson and Iyer (1981) where a low-velocity, and highly attenuative body was identified at 5 to 15 km depth using teleseismic tomography. This low-velocity zone could have implications for the heat source of the geothermal basin and is likely related to recent magmatism and volcanism in the region. Depth sensitivity in our analysis is limited to 8 km so we cannot estimate the lower boundary of this low-velocity zone. It is also difficult to estimate the lateral extent of the low-velocity zone, because of poor ray coverage at the longer periods.

In the shorter period range (0.5–1 seconds), we measure seismic velocities of 400 to 500 m/s and we interpret this to be basin-fill sediment. At 0.67 seconds we estimate we are imaging the upper 500 m of the subsurface. The 400 m/s seismic velocities

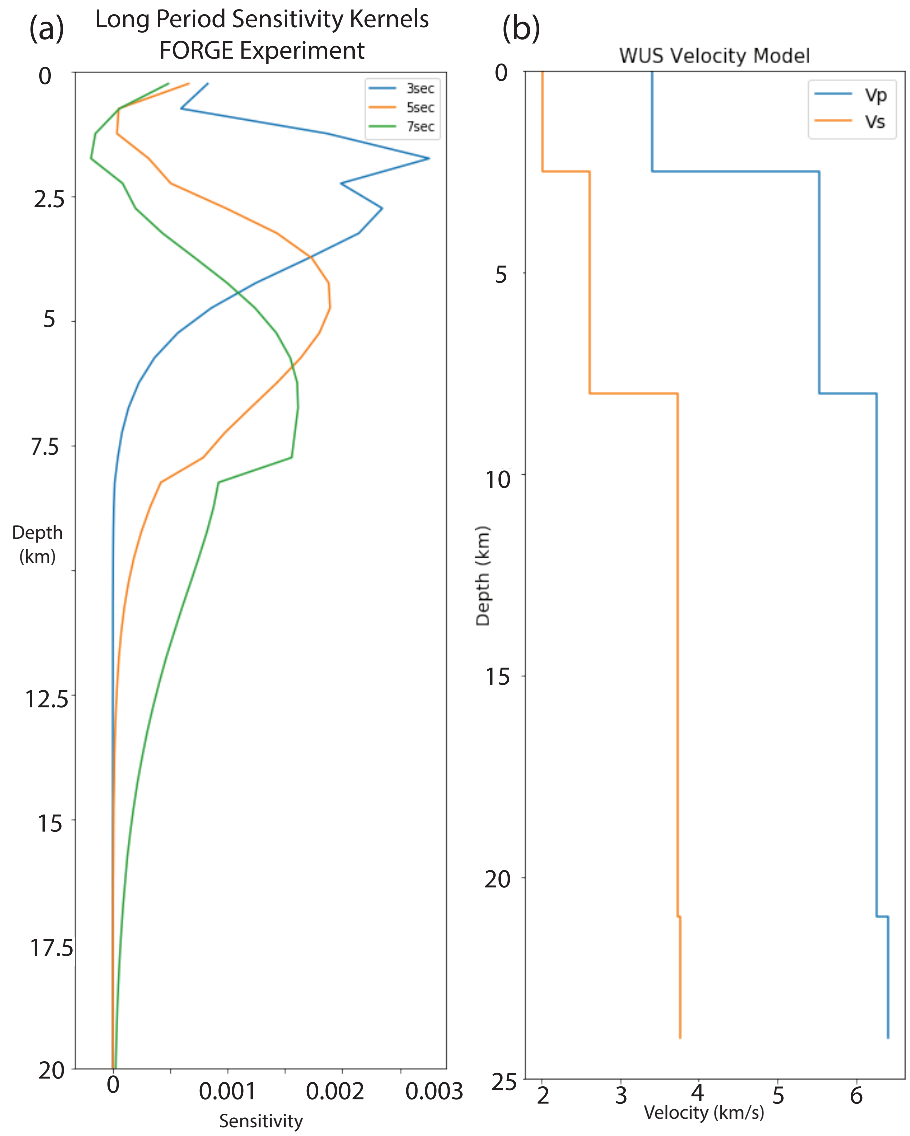

Figure 8. (a) *Sensitivity kernels for 3, 5, and 7 second period surface waves. We note that depth sensitivity for tomographic models is in the upper 10 km of crust with sensitivity near 2.5 km, 5 km, and 7.5 km, respectively. Western U.S. (WUS) velocity model (Hermann et al., 2011; Whidden and Pankow, 2012) was used in computation of sensitivity kernels and is plotted in* ***(b)****.*

are consistent with results from Spatial Autocorrelation (SPAC) VS30 results in the same region (Zhang and Pankow, 2018). The trend towards higher velocity in the eastern portion of the array, closer to the Mineral Mountains, reflects a shallowing of the alluvium-bedrock contact. This structure is consistent with a strong shallow to moderately dipping reflector identified by Smith and Bruhn (1984).

If looking at absolute group velocities rather than relative changes, there is a decrease of group velocity as period increases. There is a low-velocity zone beneath the western edge of the Mineral Mountains identified by Robinson and Iyer (1981) that has been mapped to similar depths as seen in the 7-second group velocity map.

When considering the dense 49-station grid, we see a general trend of higher velocities to the east, and slower velocities moving basinward to the west (Figure 10b). The dip of the basement rock-sediment interface in this region may affect group velocity measurements at short periods. As the contact becomes shallower towards the east, it is likely that our measurements are increasingly more sensitive to basement rocks. The short-period velocities (0.67 s, 400–500 m/s) are roughly five times slower when compared to measurements at the longer periods.

The tomographic method does not account for topographic changes. While the peaks of the Mineral Mountains are close to 900 m higher than the valley, the great circle distance between two stations on either side of the Mineral Mountains changes by a fraction of a percent between a path along surface topography versus a path assuming a spherical earth. Because inverted

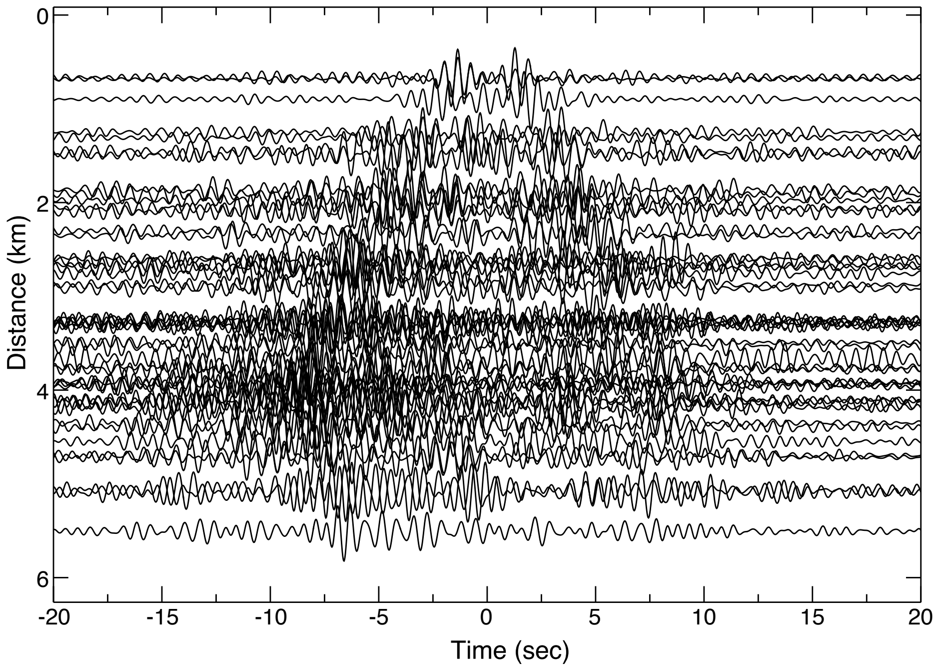

Figure 9. *Record section of FORGE dense array (49 stations) cross-correlation functions (CCF) bandpass filtered from 0.5 to 1 second. Each trace is the one-month stack of 10-minute windows. Virtual source (01s) is station in southwest corner of the dense array (Figure 5b) that is cross-correlated with all other stations in the dense array.*

surface wave group velocity measurements vary by up to 20%, we can assume the majority of travel-time residuals are due to seismic velocity changes, rather than differences in path length from the assumed spherical path that ignores topography used in this study. Previous work on volcanoes in the Pacific Northwest has shown there is very little travel-time bias due to topographic effects (Wang et al., 2017) when major geologic features are the contributing factor to travel-time anomalies.

Finally, our model results are not well constrained. We have limited periods where velocity measurements are made. This is due to noise sources recorded by the FORGE array that are limited between 3 to 10 seconds (full deployment) and 0.5 to 1 seconds (dense deployment). This gives us little depth sensitivity and therefore a full 3D model was not constructed.

CONCLUSION

Shallow crustal imaging has been performed within the Milford Valley at the FORGE Utah site using dense geophone arrays. One-month deployments generate sufficient ambient seismic noise records to estimate the Green's functions in the upper crust. Cross-correlations were calculated using data collected during the December 2016 93-station full deployment at surface wave periods between 3 and 10 seconds. ZZ component cross-correlations were used to determine fundamental mode Rayleigh wave velocities. These records were used to measure group velocities at 3, 5, and 7 second periods. The dense grid of 49 stations was re-occupied July 2017 during a drilling phase of the FORGE project and was used to extract higher frequency surface waves between 0.5 and 1 seconds. Dispersion measurements were obtained through automated frequency-time analysis of the stacked cross-correlation results and were inverted to produce smooth velocity maps over the FORGE project site. The velocity maps indicate regions of high seismic velocities in the central Mineral Mountains and slower velocities towards the edges of the arrays where basin fill is deeper. For the longer period inversion results, velocities in the Mineral Mountains reach 3.2 km/s whereas the slower basin velocities are ~ 2 km/s. This is due to sediment cover affecting the surface wave group velocity. The sediment cover is thinner or non-existent in the core of the mountains and therefore the surface waves are sampling bedrock, but when moving away from the mountains alluvial deposits are thicker and have slower surface wave velocities than pure bedrock. Shear wave velocities have not been calculated in this study but could be calculated using the sensitivity kernels and could be compared to the well logs of the FORGE well. A low-velocity zone exists below 5 km depth and is coincident with a high-attenuation, low-velocity zone identified by Robinson and Iyer (1981). This low-velocity zone could be related to the heat source of the geothermal system beneath the FORGE footprint. At higher frequency, we measure increasing velocities in the east portion of the dense array with seismic velocities of 400 to 600 m/s. The depth of investigation is estimated at the upper 500 m of the subsurface. This 400 m/s measurement is

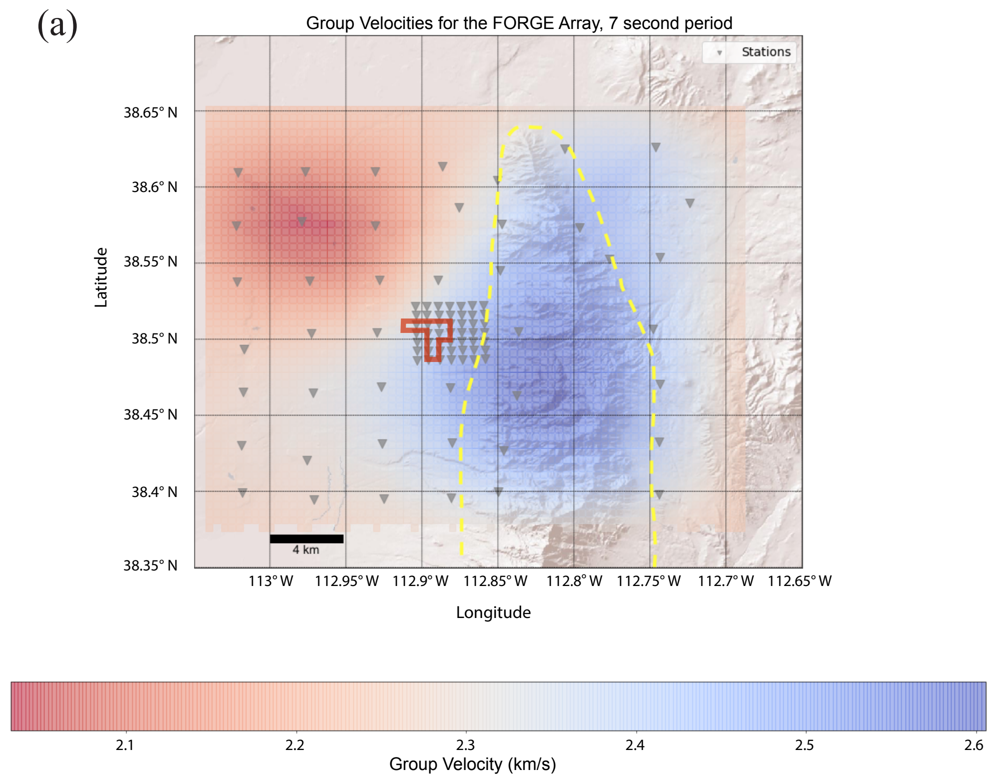

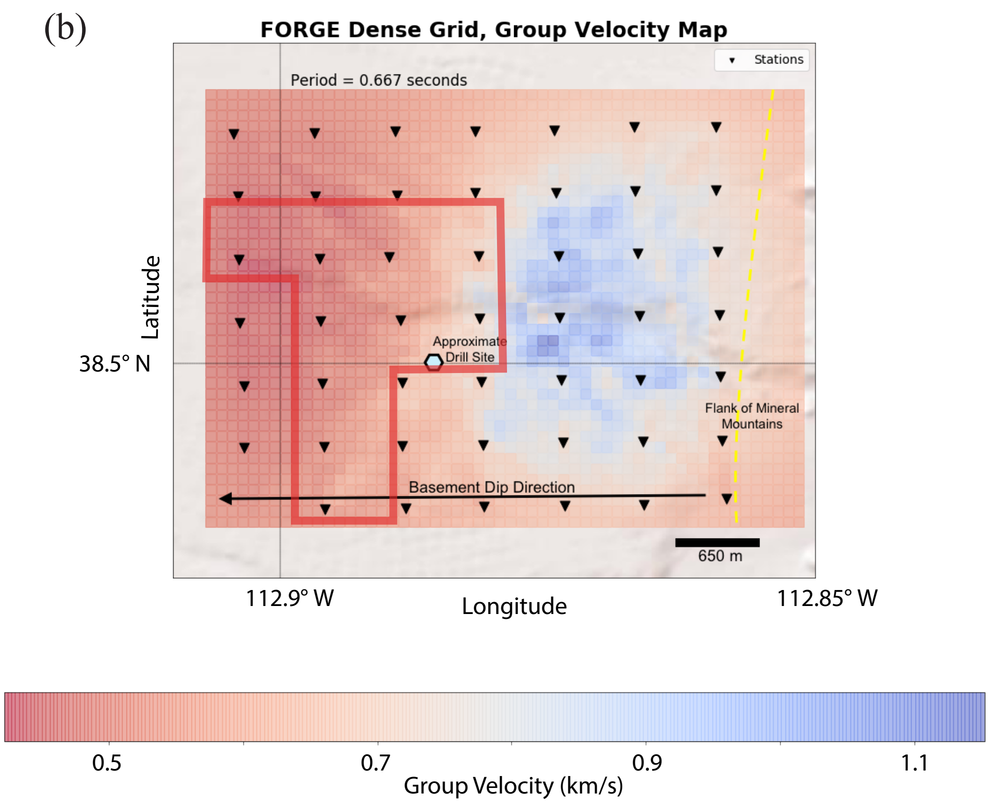

Figure 10. (a) *Tomographic model obtained using 7 second period data from 93-station array. The majority of the Mineral Mountains high-velocity anomaly remains consistent at different periods. Dashed yellow line outlines approximate boundaries of granitic basement outcropping in the Mineral Mountains. Smoothing here is based on values selected by plotting tradeoff curves (Figure 6), but we note that main high-velocity features are consistent through multiple sets of smoothing parameters.* ***(b)*** *Inversion results from dense 49-station array. Boundary of Mineral Mountains is outlined in yellow. Basement sediment contact dips to west. FORGE site is highlighted in red.*

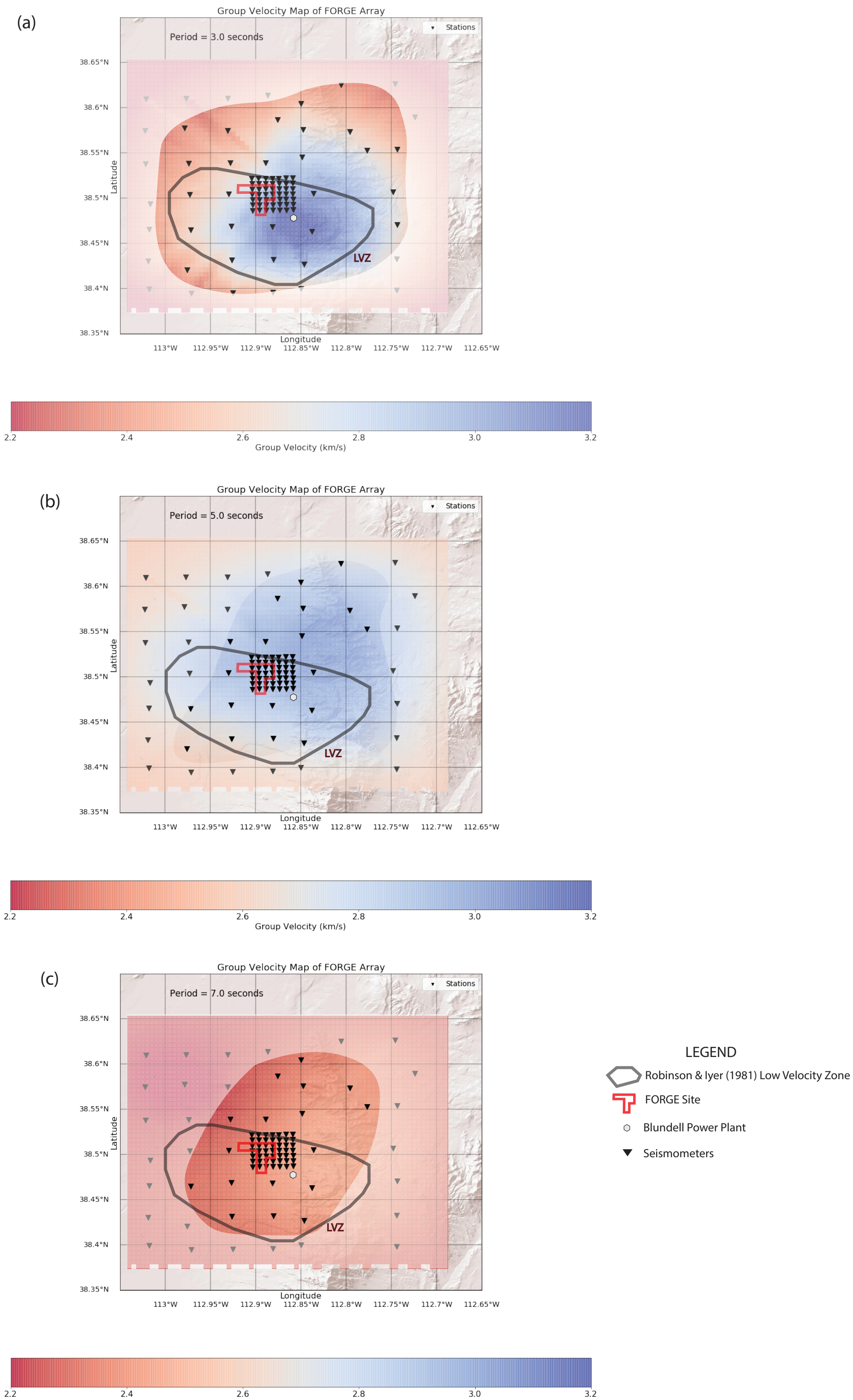

Figure 11. *Tomographic models for the Mineral Mountains from the FORGE array. Group velocity maps are plotted in 0.001 degree grid cells.* ***(a)*** *Group velocity map for 3 second period,* ***(b)*** *group velocity map for 5 second period,* ***(c)*** *group velocity map for 7 second period. Low-velocity zone (LVZ) identified by Robinson and Iyer (1981) is outlined. Masked region represents the approximate area that has enough crossing ray paths to resolve structure. Qualitatively, this is the region with the most constrained results.*

consistent with other shallow subsurface Vs30 studies in the area (Zhang and Pankow, 2018). We also note higher velocities towards the Mineral Mountains and interpret this to be a shallowing of the bedrock contact. Results from this study will form a baseline for future ambient noise studies that will be conducted in the region.

DATA AND RESOURCES

Seismic data used in this experiment are currently available from a University of Utah data server on request; send inquiries to andyjtrow@gmail.com. Seismic data were processed using Seismic Analysis Code (Helffrich et al., 2013). We operate within the Python framework and rely on existing toolboxes and numerical and plotting libraries, namely NumPy, Matplotlib, Basemap, and ObsPy (Beyreuther et al., 2010).

ACKNOWLEDGMENTS

We thank Jamie Farrell, Nathan Downey, Rick Allis and Stephanie Carney for thoughtful reviews of the manuscript.

REFERENCES

Allis, R., Gwynn, M., Hardwick, C., Kirby, S., Boweers, R., Moore, J.N., Wannamaker, P., and Simmons, S. 2017, Characteristics of the Cove Fort-Dog Valley-Twin Peaks thermal anomaly, Utah: Proceedings of the 42nd Workshop on Geothermal Reservoir Engineering, Stanford University, Stanford, California.

Barker, C.A., 1986, Upper-crustal structure of the Milford Valley and Roosevelt Hot Springs, Utah region, by modeling of seismic refraction and reflection data: Salt Lake City, University of Utah, M.S. thesis, 101 p.

Barmin, M.P., Ritzwoller, M.H., and Levshin, A.L., 2001, A fast and reliable method for surface wave tomography. Pure and Applied Geophysics, 158, 1351–1375.

Bensen, G.D., Ritzwoller, M.H., Barmin, M.P., Levshin, A.L., Lin, F., Moschetti, M.P., Shapiro, N.M., and Yang, Y., 2007, Processing seismic ambient noise data to obtain reliable broad-band surface wave dispersion measurements, Geophysical Journal International, 169, 3, 1239–1260.

Benz, H.M., Smith R.B., and Mooney W.D., 1990, Crustal structure of the Northwestern Basin and Range Province from the 1986 Program for Array Seismic Studies of the Continental Lithosphere Seismic Experiment, Journal of Geophysical Research., 95(B13), 21823–21842.

Beyreuther, M., Barsch, R., Krischer, L., Megies, T., Behr, Y., and Wassermann, J., 2010, ObsPy: A Python Toolbox for Seismology. Seismological Research Letters, 81(3), 530–533.

Bowden, D.C., Tsai, V.C., and Lin, F.C., 2015, Site amplification, attenuation, and scattering from noise correlation amplitudes across a dense array in Long Beach, CA, Geophysical Research Letters. 42, 1360–1367.

Blackwell, D.D., 1983, Heat flow in the northern Basin and Range province, *in* The Role of Heat in the Development of Energy and Mineral Resources in the Northern Basin and Range Province, edited by Geothermal Resources Council, Spec. Rep., 13, 81–93.

Calò, M., Kinnaert, X., and Dorbath, C., 2013, Procedure to construct three-dimensional models of geothermal areas using seismic noise cross-correlations: application to the Soultz-sous-Forêts enhanced geothermal site, Geophysical Journal International, 194, 3, 1893–1899.

Edwards, M.C., and Chapman, D.S., 2013, Geothermal resource assessment of the Basin and Range province in western Utah report and heat flow map: unpublished report to the Utah Geological Survey, 121 p.121.

Faulder, D.D., 1991, Conceptual geologic model and native state of the Roosevelt Hot Springs hydrothermal system. Proceedings of the 16th Workshop on Geothermal Reservoir Engineering, Stanford University, 1991. 131–142.

Hansen, S.M., and Schmandt, B., 2015, Automated detection and location of microseismicity at Mount St. Helens with a large-N geophone array, Geophysical Research Letters. 42, 7390–7397.

Hardwick C.L., Gwynn, M., Allis, R., Wannamaker, P., and Moore, J., 2016, Geophysical signatures of the Milford, Utah FORGE site: Proceedings, 41st Workshop on Geothermal Reservoir Engineering, Stanford University, Stanford, CA.

Haubrich, R.A., Munk, W.H., and Snodgrass, F.E., 1963, Comparative spectra of microseisms and swell. Bulletin of the Seismological Society of America, 53 (1) (1963), 27–37.

Helffrich, G., Wookey, J., and Bastow, I., 2013, The Seismic Analysis Code: A Primer and User's Guide. Cambridge: Cambridge University Press.

Herrmann R.B., Benz H., and Ammon C.J., 2011, Monitoring the earthquake source process in North America, *Bulletin of the Seismological. Society of America*, 101, 2609–2625.

Lehujeur, M, Vergne, J.,Maggi, and A., Schmittbuhl, J., 2017, Ambient noise tomography with non-uniform noise sources and low aperture networks: case study of deep geothermal reservoirs in northern Alsace, France, Geophysical Journal International, 208, 1, 193–210.

Levshin, A.L., Yanovskaya, T.B., and Lander, AV., 1989, Seismic Surface Waves in Laterally Inhomogeneous Earth, Kluwer Acad., Norwell, Mass.

Li, Z., Peng, Z., Hollis D., Zhu, L., and McClellan, J., 2018, High-resolution seismic event detection using local similarity for Large-N arrays, Scientific Reports 8:1646.

Li, Z., Peng, Z., Meng, X., Inbal, A., Xie, Y., Hollis, D., and Ampuero, J.P., 2015, Matched Filter Detection of Microseismicity in Long Beach with a 5200-station Dense Array, SEG Technical Program Expanded Abstracts 2015, Society of Exploration Geophysicists, 2615–2619.

Lin, F.-C., Moschetti, M.P., and Ritzwoller, M.H., 2008, Surface wave tomography of the western United States from ambient seismic noise: Rayleigh and Love wave phase velocity maps. Geophysical Journal International, 173, 281–298.

Lin, F.-C., Li, D., Clayton, R.W., and Hollis, D., 2013, High-resolution 3D shallow crustal structure in Long Beach, California: Application of ambient noise tomography on a dense seismic array. Geophysics, 78(4), Q45–Q56.

Moore J.N., and Nielson, D.L., 1994, An overview of the geology and geochemistry of the Roosevelt Hot Springs geothermal system, Utah: Utah Geological Association Publication 23, 25–36.

Robinson, R., and Iyer, H.M., 1981, Delineation of a low-velocity body under the Roosevelt Hot Springs geothermal area, Utah, using teleseismic P-wave data, Geophysics 46(10), 1456–1466.

Shapiro N.M., and Campillo, M., 2004, Emergence of broadband Rayleigh waves from correlations of the ambient seismic noise, Geophysical Research Letters, 31.

Shapiro, N.M., Campillo, M., Stehly, L., and Ritzwoller, M.H., 2005, High-resolution surface-wave tomography from ambient seismic noise. Science, 307(5715), 1615–1618.

Simmons, S., Moore, J., Allis, R., Kirby, S., Jones, C., Bartley, J., Kleber, E., Knudsen, T., Miller, J., Hardwick, C., Rahilly, K., Gwynn, M., McLennan, J., Forbes, B., Podgorney, R., Pankow, K., Wannamaker, P., and Fischer T., 2018, A reveised geoscientific model for FORGE Utah EGS Laboratory, Proceedings, 43rd Workshop on Geothermal Reservoir Enginnering, Stanford University, Stanford, CA.

Simmons, S., Kirby, S., Jones, C., Moore, J., and Allis, R., 2016, The geology, geochemistry, and hydrology of the EGS FORGE site, Milford Utah: Proceedings, 41st Workshop on Geothermal Reservoir Engineering, Stanford University, 10 p.

Smith, R.B., and Bruhn, R.L., 1984, Intraplate extensional tectonics of the Eastern basin-Range: Inferences on structural style from seismic reflection data, regional tectonics, and thermal-mechanical models of brittle-ductile deformation, Journal of Geophysical Research, 89(B7), 5733–5762.

Snieder, R., 2004, Extracting the Green's function from the correlation of coda waves: A derivation based on stationary phase, Physical Reviews E, 69, 046610.

Trow, A.J., Zhang, H., Record, A.S., Mendoza, K.A., Pankow, K.L., Wannamaker, P.E., 2018, Microseismic Event Detection Using Multiple Geophone Arrays in Southwestern Utah, Seismological Research Letters, 0895-0695.

Wang, Y., Lin, F.-C., Schmandt, B., and Farrell, J., 2017, Ambient noise tomography across Mount St. Helens using a dense seismic array, Journal of Geophysical Research, Solid Earth, 122, 4492–4508.

Ward, K.M., 2015, Ambient noise tomography across the southern Alaskan Cordillera. Geophysical Research Letters, 42(9), 3218–3227.

Ward, K.M., and Lin, F.C., 2017, On the Viability of Using Autonomous Three- Component Nodal Geophones to Calculate Teleseismic Ps Receiver Functions with an Application to Old Faithful, Yellowstone, Seismological Research Letters 88(5), 1268–1278.

Ward, S.H., Parry, W.T., Nash, W.P., Sill, W.R., Cook, K.L., Smith, R.B., and Bowman, J.R., 1978, A summary of geology, geochemistry, and geophysics of the Roosevelt Hot Springs thermal area, Utah, Geophysics 43(7), 1515–1542.

Whidden, K.M., and Pankow, K.L., 2012, A catalog of regional moment tensors in Utah from 1998 to 2011, Seismological Research Letters, 83, 775–783.

Wu, S.-M., Ward, K.M., Farrell, J., Lin, F.-C., Karplus, M., and Smith, R.B., 2017, Anatomy of Old Faithful From Subsurface Seismic Imaging of the Yellowstone Upper Geyser Basin, Geophysical Research Letters, 44, 10, 240–247.

Yao, H., Beghein, C., and Van Der Hilst, R.D., 2008. Surface wave array tomography in SE Tibet from ambient seismic noise and two-station analysis—II. Crustal and upper-mantle structure, Geophysical Journal International, 173, 205–219.

Zhang, H., and Pankow, K., 2018, A Bayesian Application of SPAC to Resolve Vs30 Using Nodal Seismic Instruments. Seismology of the Americas Meeting, May 14–17, 2018, Miami, FL.

PETROGRAPHY OF THE UTAH FORGE SITE AND ENVIRONS, BEAVER COUNTY, UTAH

by Clay G. Jones, Joseph N. Moore, and Stuart Simmons

Energy & Geoscience Institute, University of Utah, Salt Lake City, Utah

Miscellaneous Publication 169-K
Utah Geological Survey
a division of
UTAH DEPARTMENT OF NATURAL RESOURCES

This paper is part of *Geothermal Characteristics of the Roosevelt Hot Springs System and Adjacent FORGE EGS Site, Milford, Utah*. https://doi.org/10.34191/MP-169

Bibliographic citation:

Jones, C.G., Moore, J.N., and Simmons, S., 2019, Petrography of the Utah FORGE site and environs, Beaver County, Utah, *in* Allis, R., and Moore, J.N., editors, Geothermal characteristics of the Roosevelt Hot Springs system and adjacent FORGE EGS site, Milford, Utah: Utah Geological Survey Miscellaneous Publication 169-K, 23 p., 2 appendices, https://doi.org/10.34191/MP-169-K.

PETROGRAPHY OF THE UTAH FORGE SITE AND ENVIRONS, BEAVER COUNTY, UTAH

by Clay G. Jones, Joseph N. Moore, and Stuart Simmons

ABSTRACT

In this paper we focus on the characterization of core and cuttings recovered from geothermal wells 58-32 and Acord-1 using petrographic, X-ray diffraction (XRD) and scanning electron microscope (SEM) techniques. Well 58-32 was drilled to 7536 ft measured depth in 2017 as part of the Utah Frontier Observatory for Research in Geothermal Energy (FORGE) project. Acord-1 is a 12,650-ft-deep exploratory geothermal well drilled in 1979 in the central part of the Milford Valley. For comparison, samples have also been analyzed from outcrops in the Mineral Mountains and from geothermal wells 9-1, 52-21 and 14-2 drilled within and adjacent to the Roosevelt Hot Springs geothermal field.

Well 58-32 primarily penetrated two rock types: alluvium in the upper part of the well (0–3176 ft) and coarse-grained plutonic rocks in the lower portion (3195–7536 ft). Separating these two lithologies is a thin, sheared rhyolite (3176–3195 ft). Acord-1 penetrated a thick sequence of basin fill consisting of lacustrine sediments, evaporite deposits, volcaniclastic deposits, ash-flow tuffs, tuffaceous sediments and andesite lava flows before reaching the plutonic rocks of the Mineral Mountains Batholith at ~10,175 ft.

Formation Microscanner Image (FMI) logs of well 58-32, petrographic analyses and the results of a 3-D seismic survey provide no evidence that the sediments and volcanic rocks of the basin fill have undergone significant deformation or contact metamorphism. In contrast, the underlying plutonic rocks encountered in Acord-1 and well 58-32 are intensely sheared and brecciated. The contact between the basin fill and plutonic rocks dips at approximately 25° to the west. Westward-dipping, shallow bedding planes in the alluvium of well 58-32 are also observed in the FMI log. These observations suggest the basin fill was deposited on an exposed and rotated range front fault as discussed by Bartley et al. (2018).

In well 58-32, samples from >6500 ft, where measured temperatures exceed 347°F (175°C), are within the Enhanced Geothermal System (EGS) reservoir. At these depths the plutonic rocks consist dominantly of granite and quartz monzonite with minor granodiorite, quartz monzodiorite and fine-grained banded diorite. Except for relatively rare banded diorite, the plutonic rocks are composed of 90–97 wt% quartz, K-feldspar and plagioclase, with minor biotite, hornblende, titanite, apatite, magnetite/ilmenite and zircon. Alteration is weak and shows no clear relationship to temperature. The most common secondary minerals are the clay minerals, with illite > chlorite> interlayered illite/smectite > smectite and carbonates. Other secondary minerals include anhydrite, hematite, epidote, quartz and plagioclase.

INTRODUCTION

The Frontier Observatory for Research in Geothermal Energy (FORGE) has been envisioned by the U.S. Department of Energy as a dedicated site where scientists and engineers will be able to develop, test, and accelerate breakthroughs in Enhanced Geothermal System (EGS) technologies and techniques. In this paper we present petrographic, X-ray diffraction (XRD), and scanning electron microscope (SEM) analyses of well cuttings, core, and outcrop samples from the Utah FORGE site and wells drilled in the surrounding area (Figure 1), with emphasis on the plutonic rocks that comprise the EGS reservoir.

METHODS

Petrographic Analysis

Three hundred and fifty-four thin sections were analyzed to document rock type, primary and secondary mineral assemblages, evidence of brittle and ductile deformation, and the paragenetic relationships of open-space filling minerals.

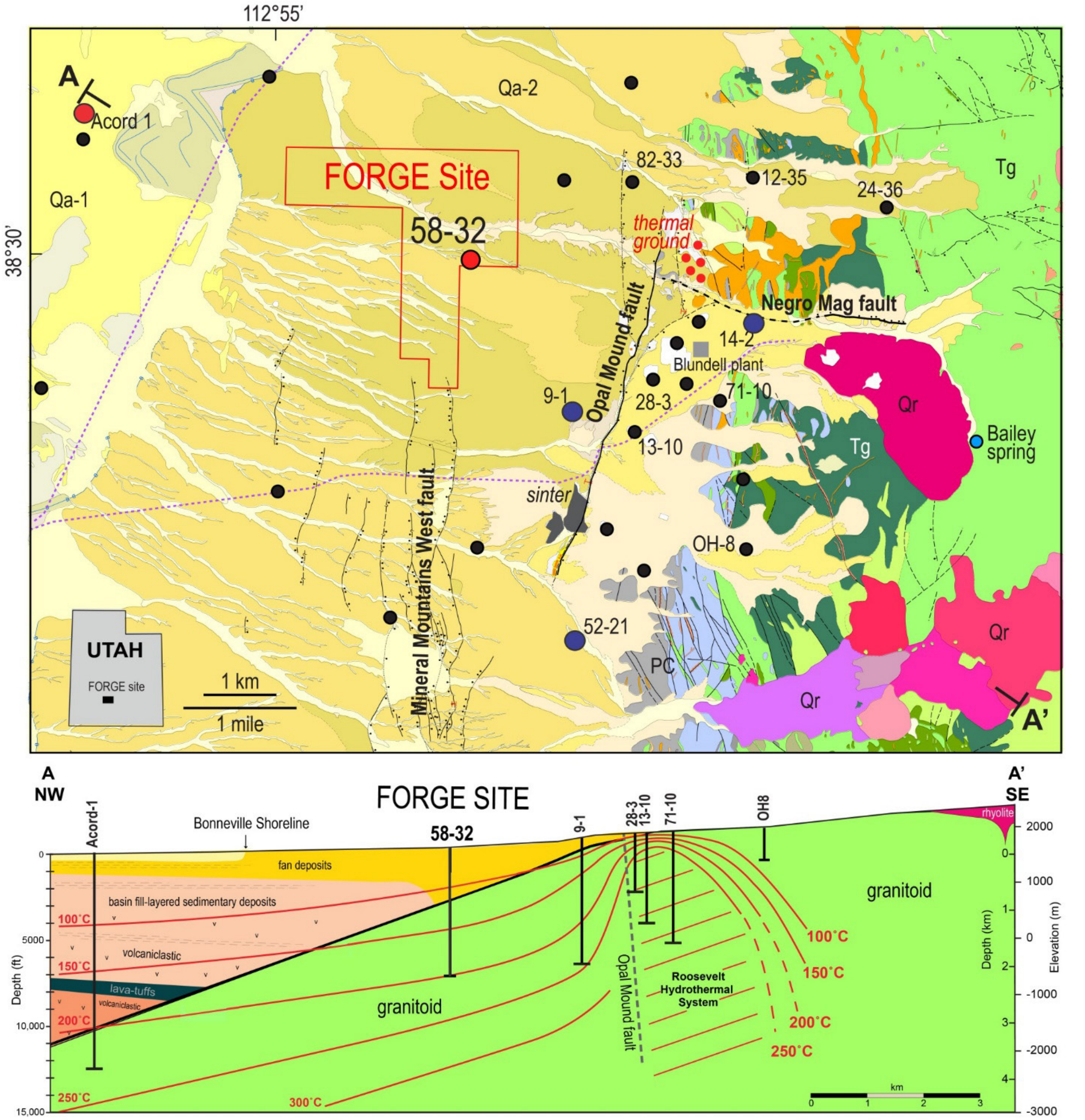

Figure 1. Geologic map and cross section (no vertical exaggeration) of the Utah FORGE site and environs (modified from Kirby et al., 2018). In the cross section the intrusive lithologies of the Mineral Mountains Batholith have been combined and are shown as simply "granitoid." Wells from which samples were selected for this study include Acord-1 and 58-32 (large red circles), as well as 9-1, 52-21 and 14-2 (large dark-blue circles). Other wells are shown as black circles. All outcrop samples analyzed come from within the bounds of this map.

X-Ray Diffraction (XRD)

Two hundred and forty-seven whole-rock and clay-sized (< 5 µm size fraction) XRD analyses were performed at the Energy & Geoscience Institute on a Bruker D-8 Advance XRD system. The following operating parameters were used: Cu-Kα radiation at 40 kV and 40 mA; 0.02°2θ step size; and a scan rate of 0.4 to 0.6 seconds per step. The clay-size fraction was examined from 2 to 45°2θ, and the whole-rock samples from 4 to 65°2θ. Phase quantification of whole-rock samples using the Rietveld method were performed using TOPAS software. Clay mineral species were identified by comparing the air-dried and glycolated clay-size fraction diffractograms using the techniques of Moore and Reynolds (1997). Results from all XRD analyses are provided in Appendix A.

Scanning Electron Microscopy (SEM)

SEM analyses were conducted on 11 polished thin sections of the two cored intervals of 58-32, as well as polished thin section billets from a handful of select cuttings samples from 58-32. SEM analyses were performed at the Energy & Geoscience Institute using a JEOL IT300 SEM.

DESCRIPTIONS OF THE LITHOLOGIES ENCOUNERED IN UTAH FORGE WELL 58-32

Analysis of core and cuttings from FORGE well 58-32 show that alluvium was penetrated in the upper part of the well (0–3176 ft), and coarse-grained plutonic rocks were encountered in the lower part (3195–7536 ft). Separating these two lithologies is a thin sheared and brecciated porphyritic rhyolite (3176–3195 ft) (Figure 2).

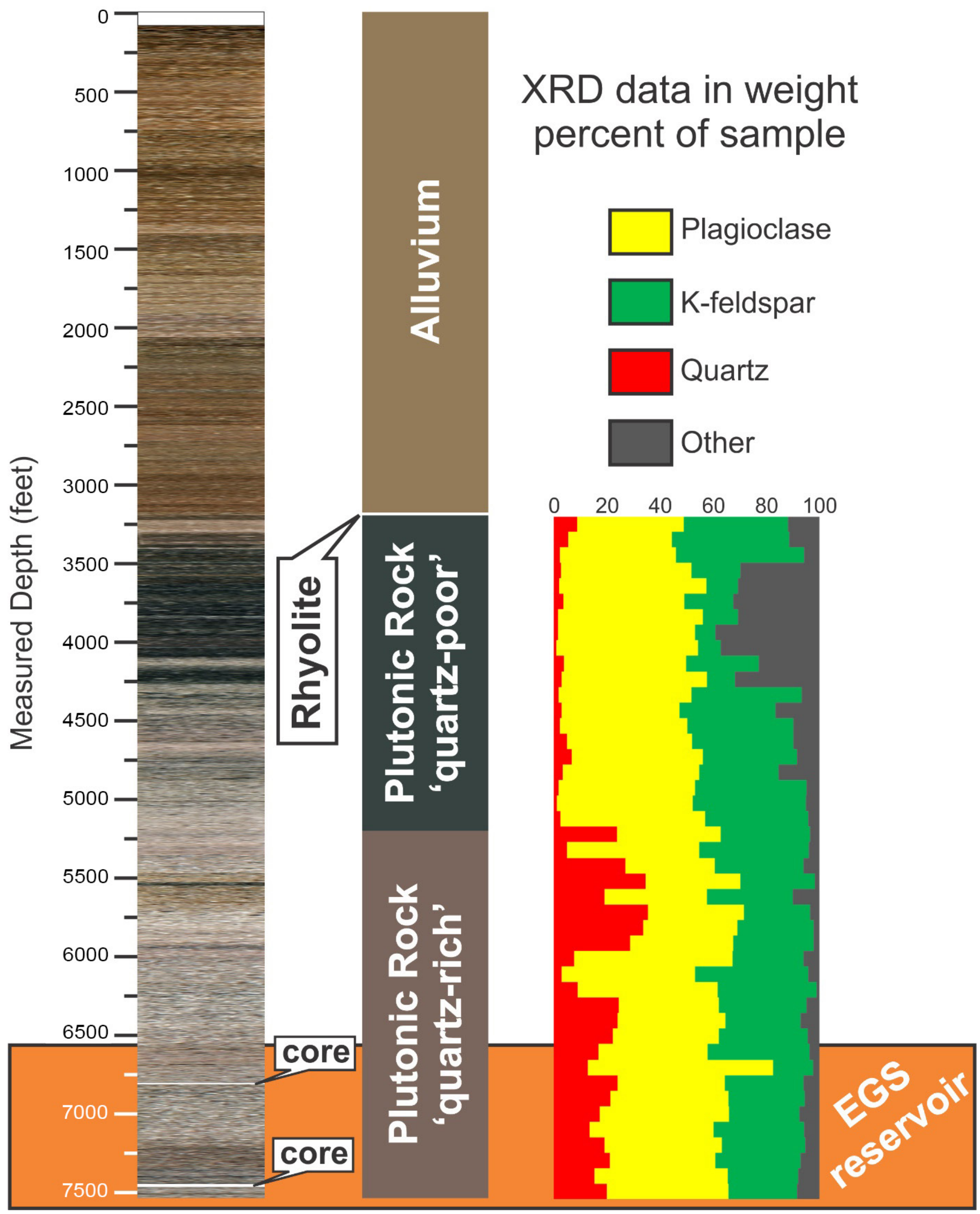

Figure 2. *At left is a lithologic column constructed from compressed images of the well cuttings from 58-32, with a simplified lithologic column at center. At right is XRD data from the plutonic rock analyzed at 100-ft intervals. Two cores were taken at the depths indicated. The proposed EGS reservoir (shown in orange) is at depths greater than 6528 ft where temperatures in excess of 347°F (175°C) have been measured.*

Alluvium (0–3176 ft)

The alluvial deposits in the upper part of the well (0–3176 ft) were clearly imaged in the FMI log as poorly sorted sediments containing boulders up to several feet in diameter with minor finer-grained deposits. The FMI log also shows bedding planes that dip predominantly westward, mimicking the topography of the Milford basin and the top of the underlying plutonic rocks. These are poorly-lithified sediments that have not experienced contact metamorphism, nor have they been indurated by hydrothermal fluids. Disaggregation of the sediments during drilling and washing of the cuttings removed much of the smaller than sand-size fraction, therefore the XRD data are skewed to reflect the composition of the clasts and larger mineral grains. The clasts consist of plutonic rock similar in both composition and texture to those outcropping in the Mineral Mountains to the east of the Roosevelt geothermal field and the plutonic rock encountered at deeper levels of well 58-32 ("quartz-rich" plutonic rocks of Figure 2). Secondary minerals compose 1 to 5 wt% of the cuttings and include illite, hematite, and smectite. No open-space filling mineralization was observed binding clasts together (i.e., cement). Hematite (up to 2 wt%) in the alluvium cuttings gives them a reddish-brown color compared to the cuttings of the plutonic rock below (Figure 2).

Rhyolite (3176–3195 ft)

An approximately 19-ft-thick zone of sheared and brecciated porphyritic rhyolite occupies a short vertical interval (3176–3195 ft) at the unconformity between the alluvium above and the plutonic rocks below. The rhyolite was initially identified as an area of interest in the FMI log, due to its distinct resistivity texture (Figure 3). Cuttings from this interval contain resorbed quartz (Figure 4) and less abundant alkali feldspar phenocrysts in a fine-grained equigranular groundmass composed of intergrown K-feldspar and quartz with minor spherulitic devitrification textures. The devitrification textures suggest that this lithology was originally glassy and cooled slowly, allowing these microstructures to form. It is not clear if this unit represents an extrusive rhyolite flow or a shallow intrusion.

Evidence of shearing and brecciation of the rhyolite includes cataclasites, silica-cemented breccias, and veining. The cataclasites contain vein fragments and are cut by veins (Figure 4). Paragenetic relationships suggest that there have been at least three episodes of brittle deformation and open-space mineralization (Figure 4): 1) early botryoidal chalcedony (subsequently recrystallized to quartz) followed by multiple generations of quartz ranging from fine-grained to coarse-grained and euhedral in texture; 2) an episode of feldspar dissolution and kaolinite precipitation in the resulting open space; and 3) late veins filled by calcite ± hematite. Similar evidence of high paleo-permeability was not observed in the alluvium above, nor the plutonic rock below. There was no evidence of modern permeability observed during drilling (i.e., no lost circulation).

The observed paragenetic relationships within the rhyolite documents changes in physical and chemical conditions with time. The transition from chalcedony to quartz may indicate an increase in temperature. In geothermal systems, chalcedony is the stable polymorph at temperatures less than ~180°C, and quartz is stable at higher temperatures (Fournier, 1985). Alternatively, the paragenetic relationship of chalcedony before quartz without a hiatus in deposition has been attributed to boiling resulting in supersaturation of silica and precipitation of chalcedony below its typical temperature stability field (e.g., Moore et al., 2008). Localized boiling could occur during a pressure drop caused by fault rupture. Measured temperatures at this depth are ~100°C, well below the stability of quartz, suggesting that the observed silica deposition occurred earlier under a different temperature regime. Following silica deposition was an episode of K-feldspar dissolution and kaolinite precipitation. It is not clear if this records an episode of extensive weathering or interaction of the rhyolite with an acidic hydrothermal fluid. The last open-space minerals to precipitate in the rhyolite are calcite and hematite. The co-precipitation of calcite and hematite is likely the result of downward percolation and heating of oxidized fluids.

Plutonic Rocks (3195–7536 ft)

The FORGE EGS reservoir is hosted by the plutonic rocks of the Mineral Mountains Batholith. The batholith is thought to have been emplaced in two pulses: 1) 25 ± 4 Ma (Aleinikoff et al., 1986); and 2) 18.2–17.5 Ma (Coleman, 1991; Coleman and Walker, 1992). These two periods of plutonic emplacement have been interpreted as the result of coeval intrusion and mixing of mafic and felsic magmas (Coleman, 1991; Coleman and Walker, 1992). Later events include coeval rhyolite and basalt dikes at ~11 Ma (Coleman and Walker, 1994) and the eruption of rhyolite domes along the crest of the range at 0.8–0.5 Ma (Lipman et al., 1978).

Within the plutonic rocks intersected by well 58-32, the most striking shift in bulk mineralogy was observed between 5100–5110 and 5200–5210 ft, with relatively "quartz-poor" plutonic rock above and "quartz-rich" plutonic rock below (Figures 2 and 5). The quartz-poor rocks (Figure 6) are finer grained, generally darker in color due to higher a proportion of ferromagnesian

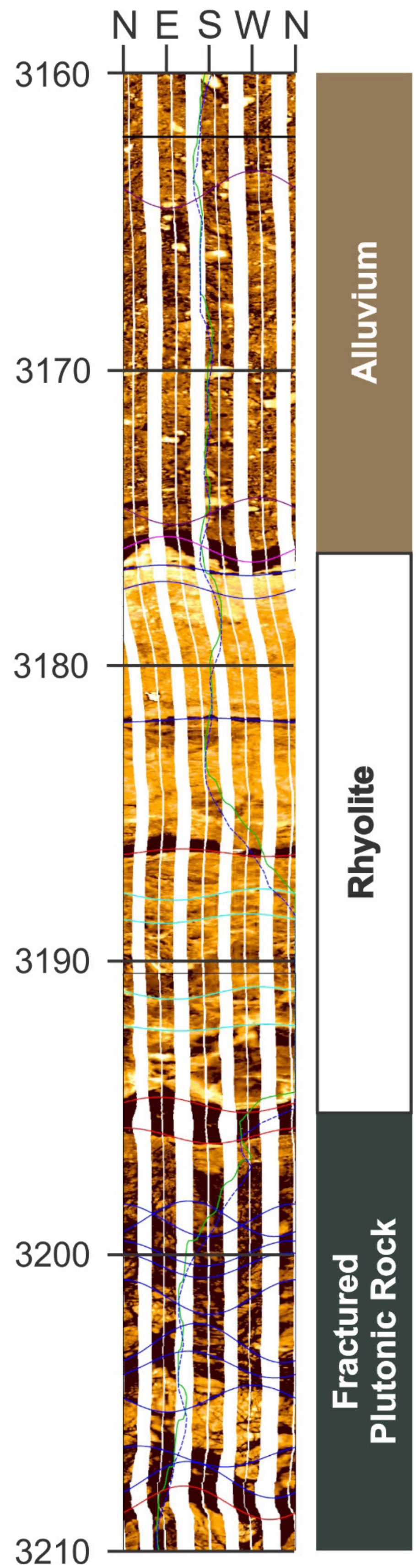

Figure 3. *A 50-ft interval of the FMI log run in well 58-32 that shows the transition from alluvium to plutonic rock. Rhyolite separates these two lithologies (3176–3195 ft). The sinusoidal lines on the FMI image are interpreted fractures and most are concentrated in the plutonic rock. The FMI image is a 2-D representation of the cylindrical borehole from north (0°) on the left, to south (180°) in the middle, back to north (360°) on the right. In this FMI log lighter areas are more resistive than darker areas.*

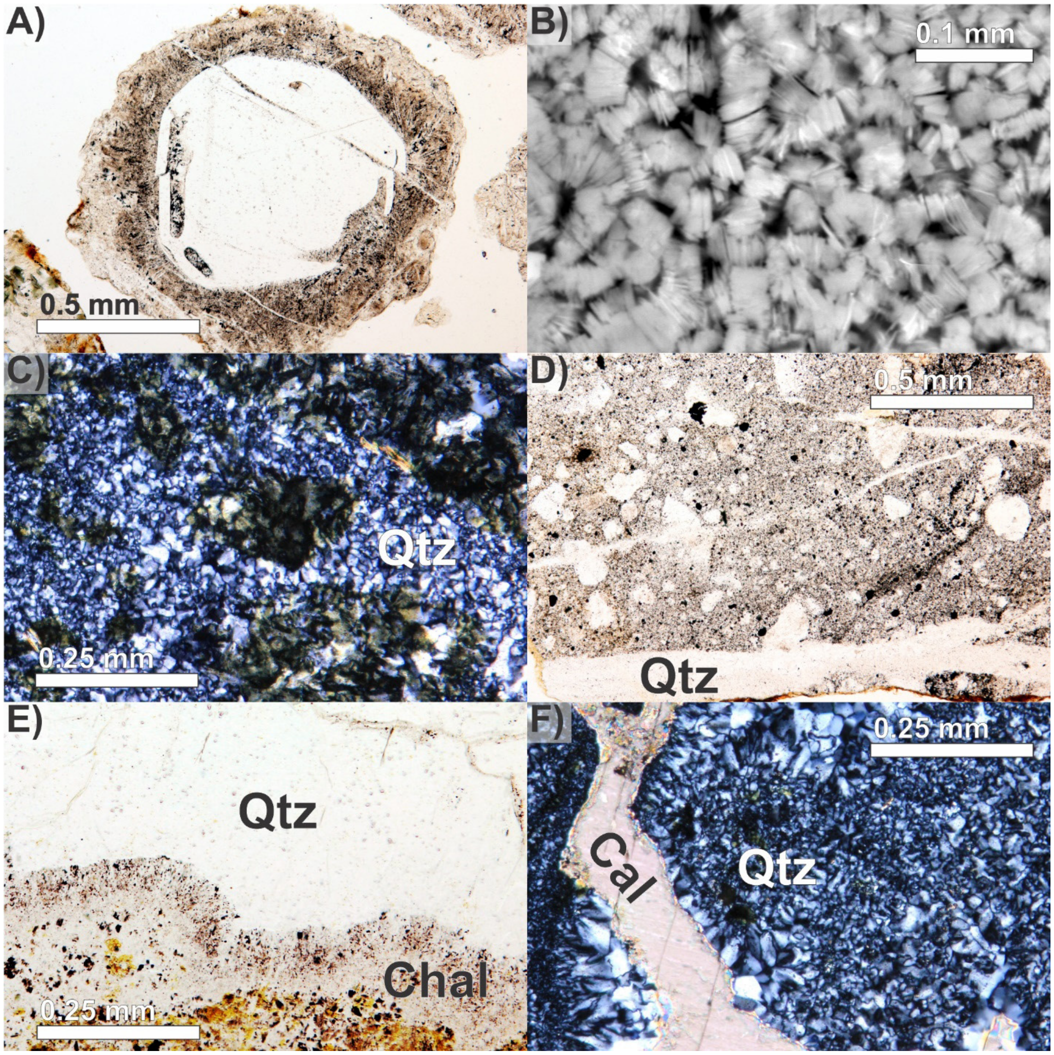

Figure 4. *Images of the rhyolite.* ***(A)*** *Plane-polarized light (PPL) photomicrograph of a partially resorbed quartz phenocryst.* ***(B)*** *Backscatter SEM image of kaolinite filling open space.* ***(C)*** *Crossed-polarized light (XPL) images of quartz- (Qtz) cemented breccia. The K-feldspar in the wall rock has been stained.* ***(D)*** *PPL photomicrograph of cataclasite cut by later quartz veins.* ***(E)*** *PPL photomicrograph of a vein filled by botryoidal chalcedony (Chal) before euhedral quartz. K-feldspar stained yellow in the wall rock.* ***(F)*** *XPL photomicrograph of a late calcite (Cal) vein cutting an earlier quartz vein.*

minerals (biotite + hornblende ± clinopyroxene), and can be compositionally banded. The quartz-rich lithologies (Figure 7) are coarser grained, contain fewer ferromagnesian minerals, and may exhibit a subtle foliation. Small-scale changes in texture and mineralogy are common. In both cored intervals of 58-32 changes in mineralogy and/or rock type were observed (Figure 8). Similar compositional variations were observed in outcrops of the Mineral Mountains.

Core and cutting samples at 6600 ft or deeper in 58-32 are within the FORGE EGS reservoir where temperatures exceed 347°F (175°C) and are composed primarily of granite and quartz monzonite with less-abundant quartz monzodiorite, granodiorite, and diorite (Figure 8). Except for the banded diorite in the lower core, the EGS reservoir rocks are composed of 90–97 wt% quartz, K-feldspar, and plagioclase, with the remainder of the primary minerals consisting of (in decreasing order of abundance) biotite, hornblende, titanite, apatite, and zircon. In contrast, the diorite in the cored section of well 58-32 contains 58–67 wt% quartz, K-feldspar and plagioclase; and 30–35 wt% biotite and hornblende.

To document the textures of the plutonic rocks within the EGS reservoir, SEM backscatter photomosaic images were made of 1.5-inch-diameter core plugs taken at horizontal and vertical orientations relative to the core (Figure 9). In these backscatter SEM images, minerals consisting of elements having higher average atomic numbers are relatively lighter gray in color. Lithologies 1, 2, and 4 in Figure 9 are coarse-grained compared to the banded diorite (lithology 3). The coarse-grained rocks in the upper core (lithologies 1 and 2) are equigranular with a subtle foliation, whereas the coarse-grained rock in the lower core (lithology 4) has a slightly porphyritic texture with large, rounded K-feldspar phenocrysts with no apparent foliation.

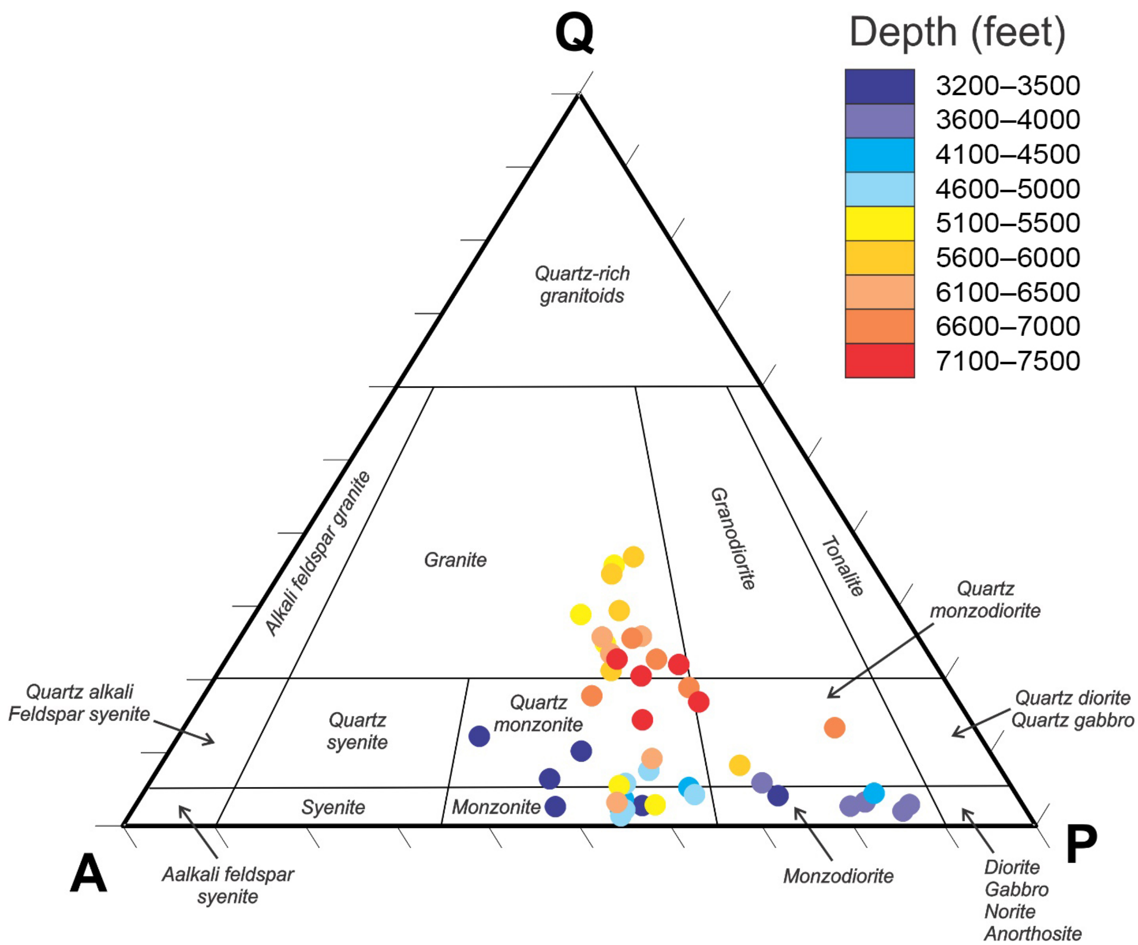

Figure 5. *XRD data from the plutonic rocks in well 58-32. The data have been normalized to 100 weight percent quartz (Q), K-feldspar (A), and plagioclase (P) and plotted on the IUGS classification diagram (Le Maitre et al., 1989). The samples have been color coded by depth. Cuttings from within the EGS reservoir at depths ≥ 6600 ft where temperature exceed 347°F (175°C) are shown in red and darkest orange and plot primarily in the granite and quartz monzonite fields.*

Alteration mineralogy in plutonic rocks

The abundance of alteration minerals is generally low in the plutonic rock from well 58-32 and decreases with depth (Figure 10), suggesting decreasing permeability. Three intervals in the upper basement that consisted of sheared/brecciated and veined rock contain higher abundances of alteration minerals; however, the vast majority of cutting samples contain less than 7 wt%, and within the EGS reservoir secondary minerals make up only a few wt% of the samples on average.

Clay minerals are the most common secondary minerals observed in 58-32 (Figure 10) and include smectite, interlayered chlorite/smectite, chlorite, illite, and kaolinite. Within the plutonic rocks, clay minerals replace primary minerals; plagioclase is dominantly altered to illite with less abundant smectite and chlorite (Figure 11A), and ferromagnesian minerals are dominantly altered to chlorite with less abundant interlayered chlorite/smectite and smectite. Other secondary minerals include carbonates (calcite > siderite > dolomite), epidote, quartz, hematite and anhydrite. Alteration of plagioclase to epidote (Figure 11B) was regularly observed; however, epidote abundances are low (< 1 wt% by XRD). Calcite and anhydrite also sporadically replace plagioclase in low abundances.

Open-space filling minerals in plutonic rocks

Open-space minerals in the plutonic rocks of well 58-32 are sporadically observed in low abundances (Table 1) filling veins and open space in sheared/brecciated rock. Carbonates are the most commonly observed open-space filling minerals, with calcite being the most abundant and widely distributed. Siderite and dolomite (± hematite) are locally concentrated in a few samples towards the top of the basement in sheared/brecciated rocks (Figure 11C) in abundances ranging from 3 to 6 wt%. Anhydrite and/or hematite may be found within carbonate veins.

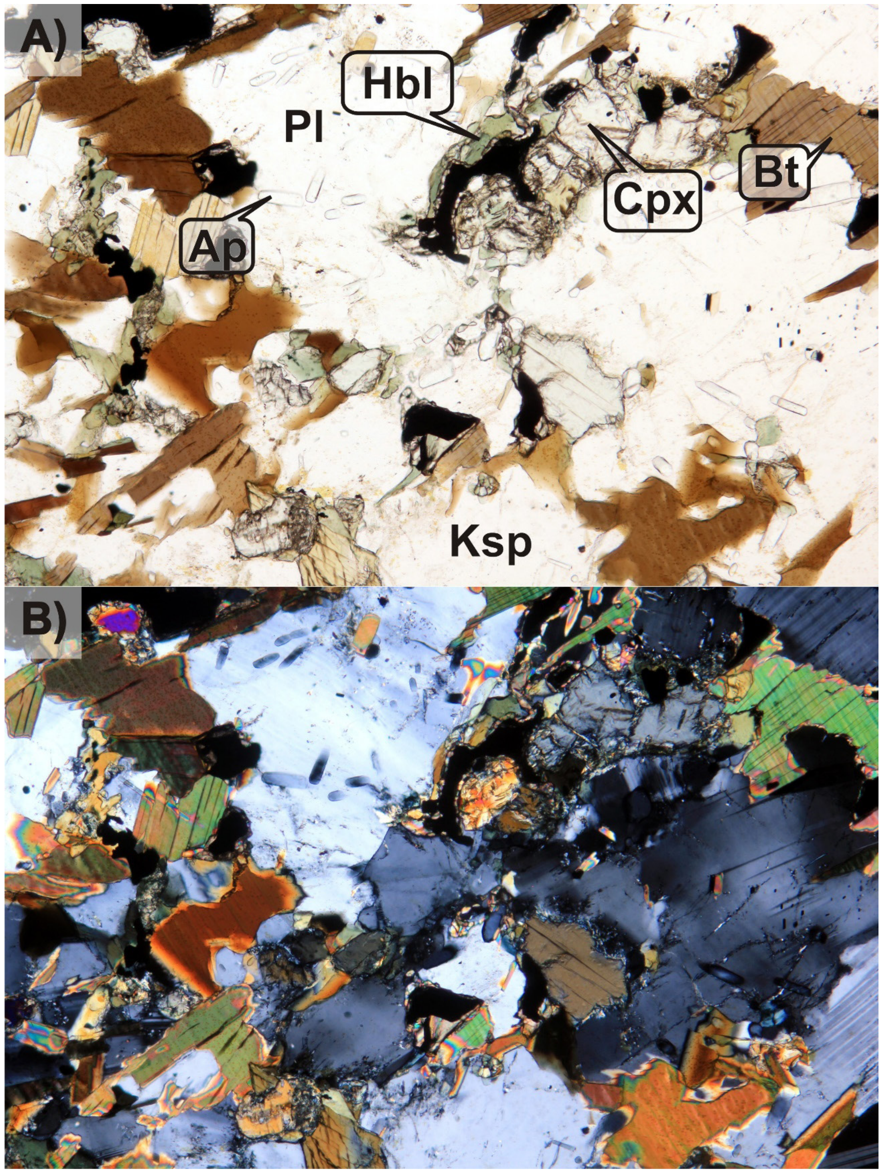

Figure 6. *Representative photomicrograph of a quartz-poor plutonic rock (monzodiorite) from 3700–3710 ft in well 58-32.* ***(A)*** *Plane-polarized light.* ***(B)*** *Crossed-polarized light. Field of view = 1.6 mm. Ap = apatite, Bt = biotite, Cpx = clinopyroxene, Hbl = hornblende, Ksp = K-feldspar, and Pl = plagioclase.*

Quartz, plagioclase, epidote, and chlorite locally fill open space; however, modern temperatures are below their respective stability ranges, suggesting that they formed during an earlier alteration event and are therefore older than the carbonate and/or anhydrite veins, which may be stable under modern in situ conditions.

Only a few mineralized fractures were observed in the approximately 22 ft of core recovered from 58-32. The upper core (6800–6810.25 ft) contained two steeply dipping mineralized fractures: one epidote + quartz lined, and partially sealed; the other filled by epidote. The lower core (7440–7452.15 ft) contained several mineralized fractures. Within the diorite there are multiple thin fractures sealed by plagioclase and epidote that cut across compositional banding. An epidote-filled fracture also cuts the lower granitic lithology and abruptly terminates within the diorite. Several other steeply dipping fractures in the core are likely to have been induced as they do not contain any secondary mineralization.

Microstructures in plutonic rocks

Microstructures within the plutonic rocks of 58-32 (Figure 12) provide a record of both plastic and brittle deformation. Table 1 shows microstructures observed during thin section petrographic analysis of the cuttings of 58-32 at 100 ft intervals. Observed microstructures that record plastic deformation within the EGS reservoir include mylonites, deformation twins, kink bands,

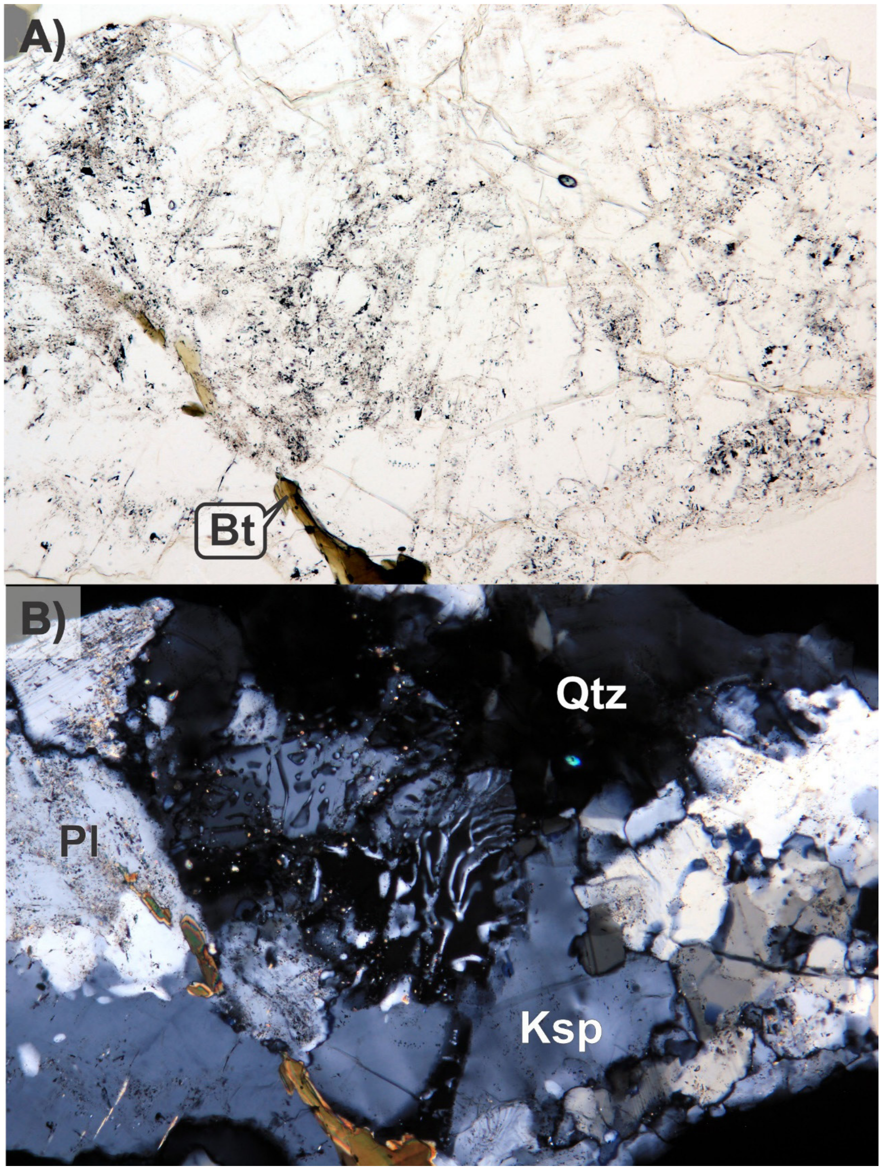

Figure 7. *Representative photomicrograph of a quartz-rich plutonic rock (granite) within the proposed EGS reservoir at 7200–7210 ft in 58-32. Myrmekite texture (Ksp replaced by worm-like Qtz in Pl) can be seen at center.* ***(A)*** *Plane-polarized light.* ***(B)*** *Crossed-polarized light. Field of view = 1.6 mm. Bt = biotite, Ksp = K-feldspar, Pl = plagioclase, and Qtz = quartz.*

deformation lamellae, dynamic recrystallization, transformation twinning, and undulatory extinction. Brittle deformation is recorded by cataclasite, shearing/brecciation, and veining. The proportion of cuttings in any given sample that display textures compatible with mylonite and/or cataclasite is generally minor and is interpreted to be the result of sampling relatively thin zones of deformation between larger blocks of more coherent plutonic rock.

Perthite (Figure 12A) and myrmekite (Figure 7) are pervasive within the EGS reservoir and the formation of both results in a net volume reduction. Perthite, the exsolution of plagioclase from alkali feldspar, leaves host grains with a turbid appearance due to the formation of micropores (Walker et al., 1995). The formation of myrmekite also results in a net volume loss (Simpson and Wintsch, 1989), but porosity within these domains is not as apparent in thin section.

Microstructures observed within the plutonic rocks of 58-32 record early plastic and later brittle deformation as the Mineral Mountains Batholith ascended from depth after emplacement to its current position at or near the earth's surface during Basin and Range extension. Microstructures can be pervasive and are likely to influence mechanical and physical properties of the EGS reservoir rock. Microstructures may locally influence the mechanical and physical properties of the rock, especially those that result in preferred mineral orientations (i.e., mylonites, dynamic recrystallization), reduced rock strength (i.e., cataclasite, brecciation), and/or increased porosity (i.e., perthite and myrmekite).

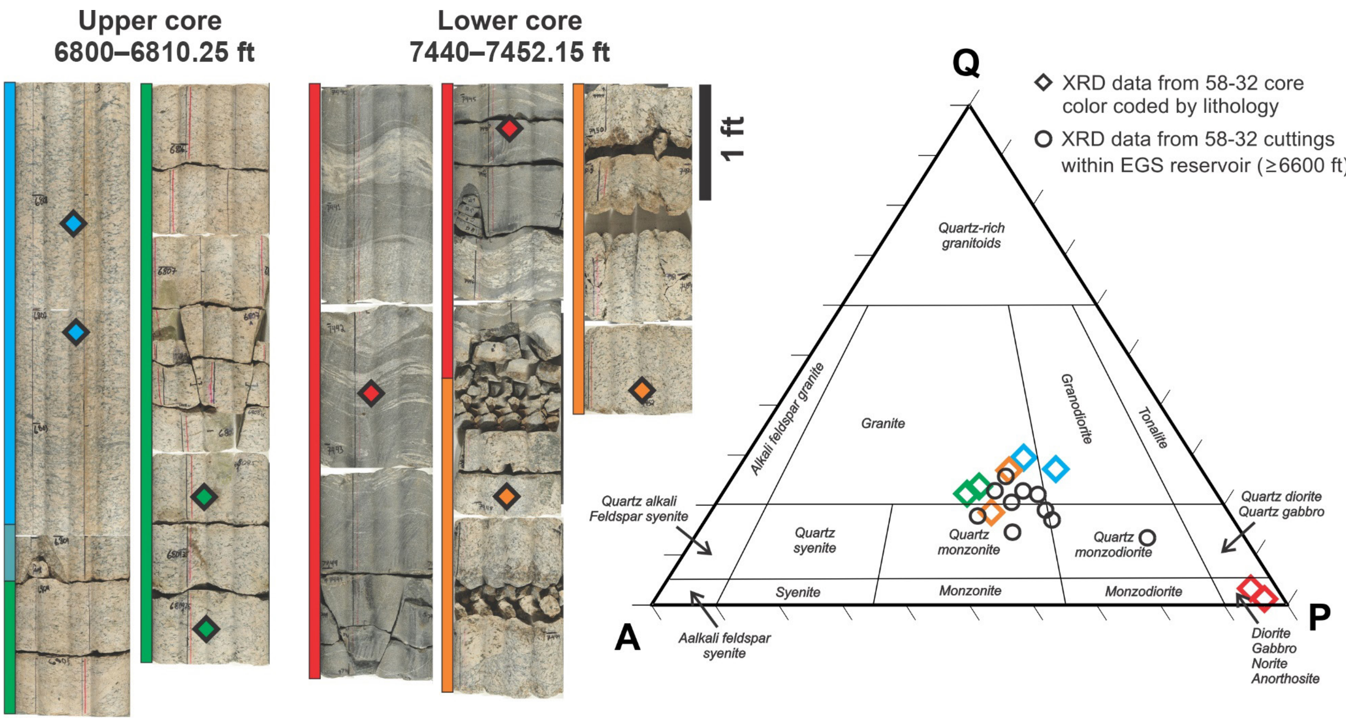

Figure 8. *Images on the left are of the two cores retrieved from well 58-32 at the depths indicated. These images are constructed from four separate images taken 90° apart that have been stitched together to give a 2-D representation of the entire cylindrical core. Colored bars next to the core indicate the four texturally distinct zones, with a subtle transition zone over less than 1 ft in the upper core (blue-green color). On the right is the XRD data from core and cuttings within the EGS reservoir, normalized to 100 weight percent quartz (Q), K-feldspar (A), and plagioclase (P) and plotted on the IUGS classification diagram (Le Maitre et al., 1989). The depths from which XRD samples were taken from the core are indicated and color-coded to the symbols on the IUGS ternary diagram.*

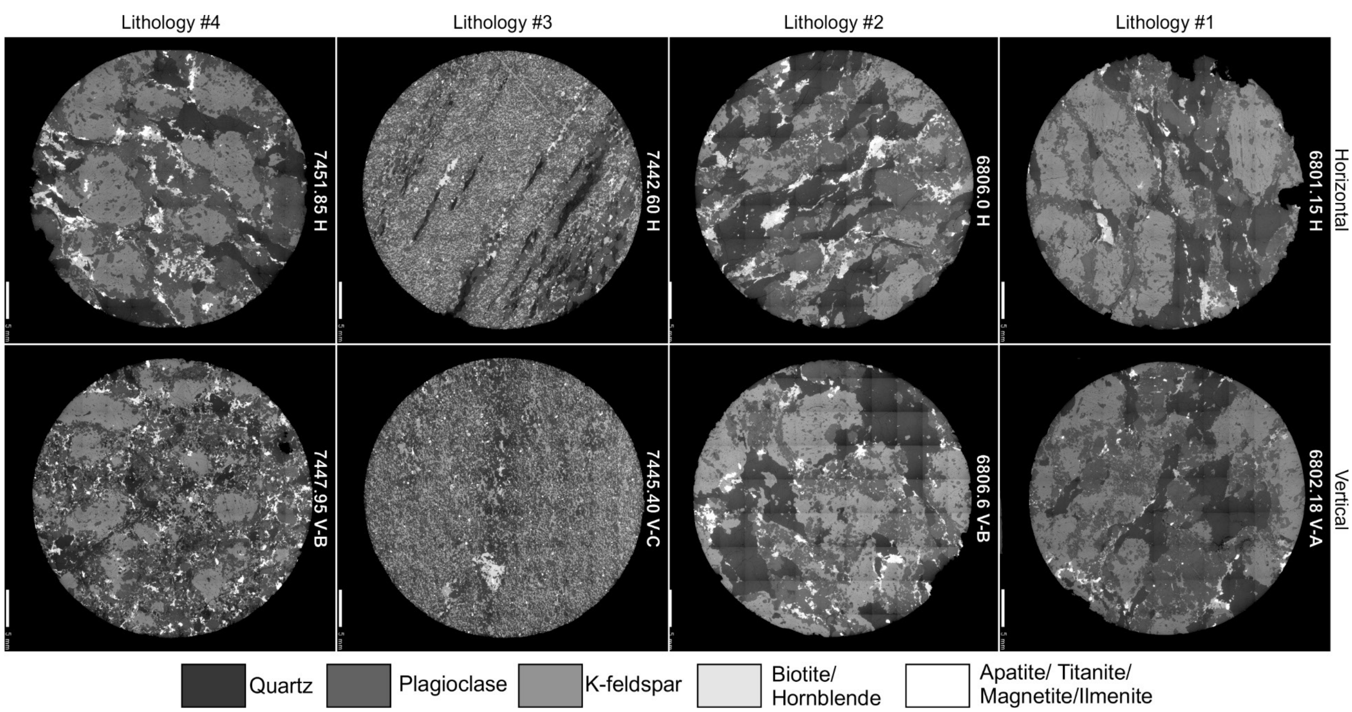

Figure 9. *Backscatter electron SEM photomosaic images of vertically and horizontally oriented 1.5-inch-diameter plugs from each of the four lithologies in the two cores from well 58-32. The approximate grayscale values by mineral are shown at right.*

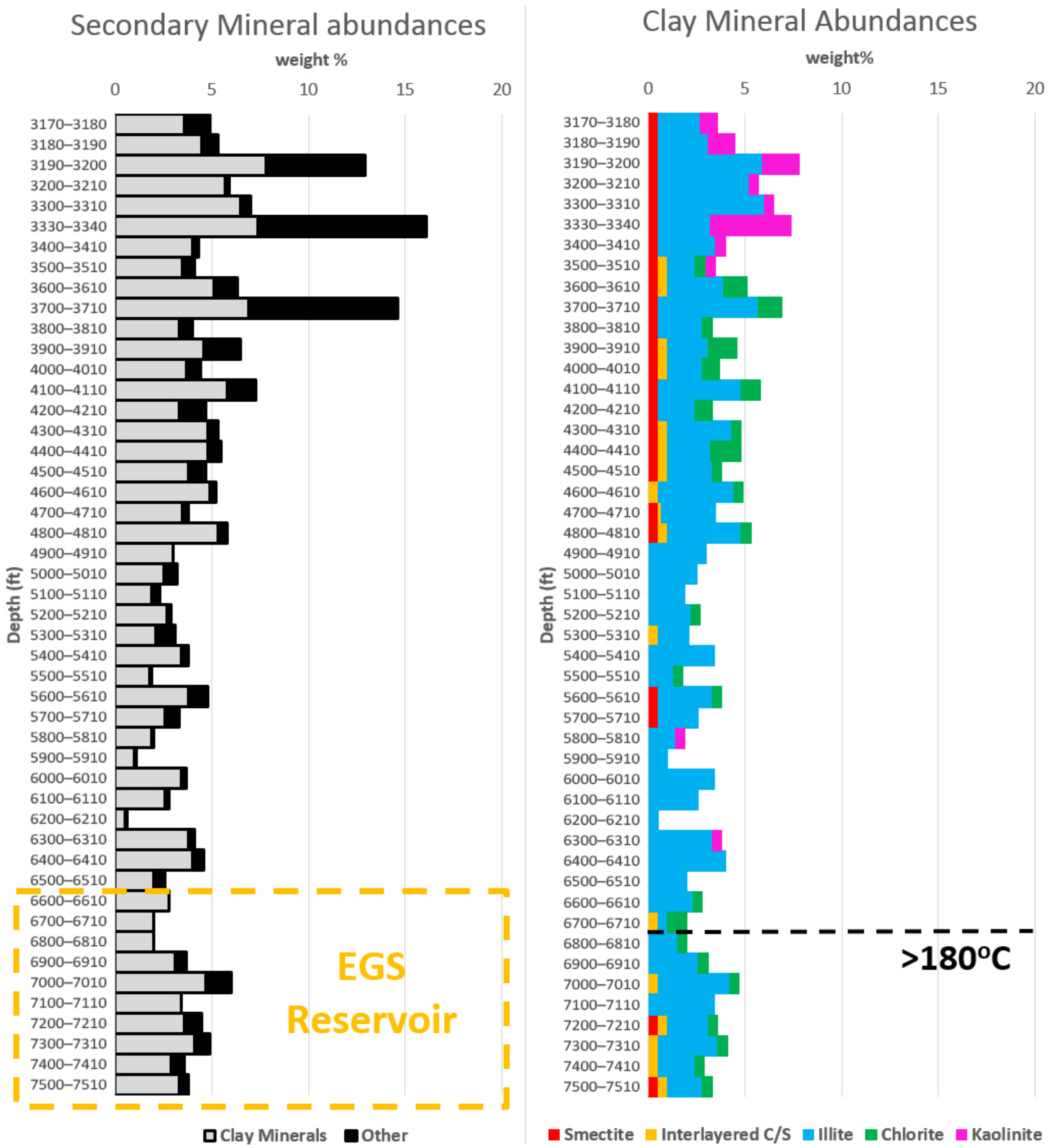

Figure 10. *Abundance of secondary minerals within the plutonic rocks of well 58-32 from XRD data. Secondary minerals observed in trace amounts during petrographic observation are shown as 0.5 wt% for visualization purposes,* possibly over-representing the total abundance of secondary minerals on this figure*. "Other" secondary minerals include: carbonates (calcite>siderite>dolomite), epidote, quartz, hematite, and anhydrite.*

DESCRIPTIONS OF THE LITHOLOGIES ENCOUNTERED IN WELL ACORD-1

Photomicrographs representative of each of the lithologies that comprise the basin fill are in Appendix B, with figure captions labeled to match the depths indicated in the subheadings below.

Basin Fill. Samples 70–100 to 10,140–10,150 ft

Acord-1 penetrated a thick sequence of basin fill consisting of lacustrine sediments, evaporite deposits, volcaniclastic deposits, ash -flow tuff and andesite lava flows before reaching the plutonic rocks of the Mineral Mountains Batholith at ~10,175 ft (Figure 13).

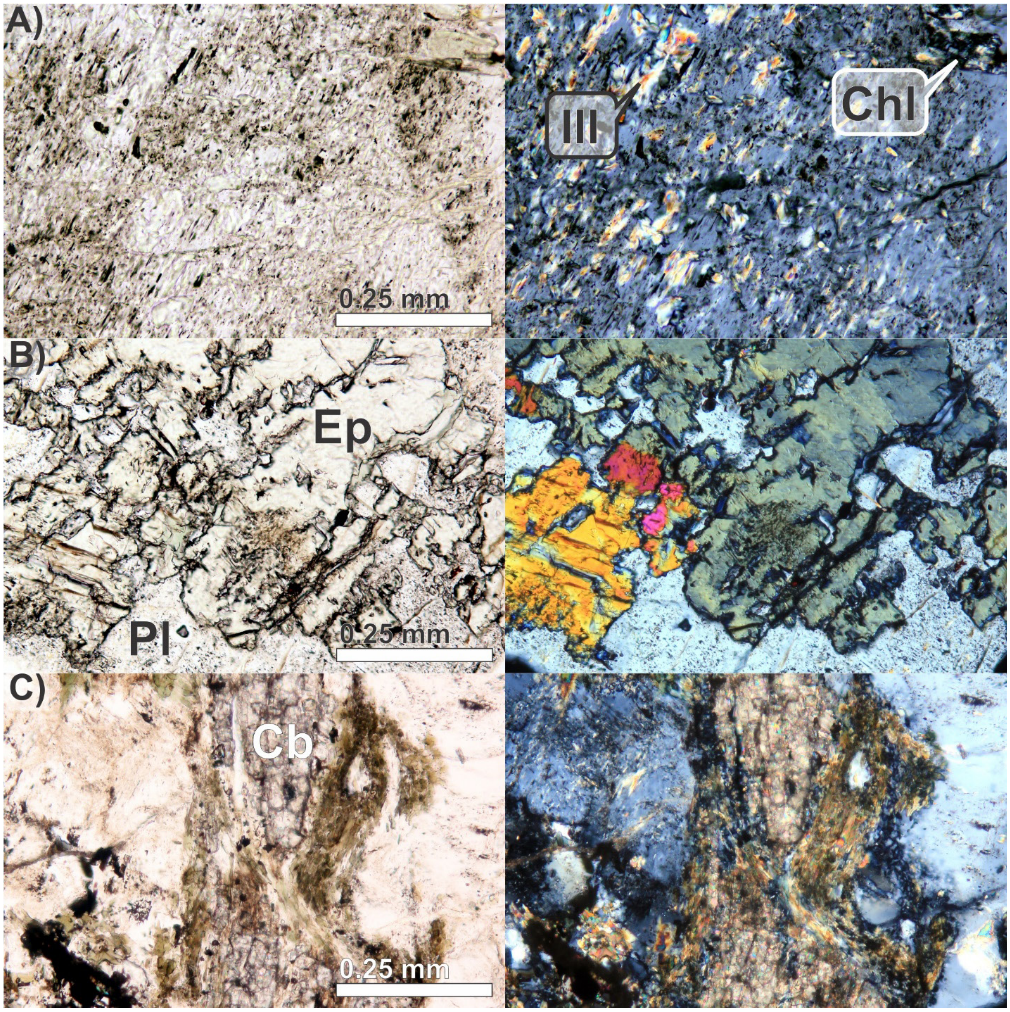

Figure 11. *Plane-polarized (left) and cross-polarized (right) photomicrographs of secondary minerals in the plutonic rock of well 58-32.* ***(A)*** *Illite (Ill) and chlorite (Chl) replacing plagioclase at 6700–6710 ft.* ***(B)*** *Epidote (Ep) replacing plagioclase (Pl) at 7400–7410 ft.* ***(C)*** *Carbonates (Cb = siderite>dolomite) filling open space and replacing sheared rock at 3700–3710 ft.*

Mixed sediments. Sample 70–100 ft

This sample contained sediments with variable grain sizes ranging from large clasts of plutonic rocks and lava flows that are at least gravel-size, to fine grained silt-size clasts predominantly composed of mineral grains. The siltstone has both clay-rich (illite and kaolinite) and fine-grained calcite matrix, and contains rare calcite-filled burrows (trace fossils). Sedimentary rip-up clasts are also incorporated into these sediments. The finer-grained fraction (siltstone and fine-grained sandstone) is generally matrix supported and the coarser-grained cuttings are cemented by calcite.

Lacustrine sediments and evaporite deposits. Samples 320–350 to 4240–4250 ft

The dominant lithology in the cuttings from this interval is siltstone, with less abundant sandstone and larger clasts of plutonic rock that are at least gravel-size. In general, the sequence becomes finer-grained towards the top of the unit. The sediments have a fine-grained matrix composed of variable proportions of clay minerals (illite and smectite ± kaolinite ± chlorite) and carbonate minerals (calcite ± dolomite). Anhydrite is intermittently observed as nodules, laths, and as thin beds with up to 35 wt% anhydrite in the sample from 3320–3350 ft. Trace fossils (burrows) are consistently observed in siltstone, whereas carbonate fossils (locally replaced by anhydrite) are more common in sandstone. Sedimentary rip-up clasts of siltstone are also a fairly consistent feature in this unit. Sandstone chips are dominantly matrix-supported, with less abundant grain-supported sandstone having calcite or anhydrite cement. The larger lithic clasts are derived primarily from plutonic rock with minor andesite lava flows and ash-flow tuffs. Rare and intermittent replacement of anhydrite by quartz and chalcedony is observed as shallow as 1340–1350 ft and minor occurrences of analcime are found from 1580–1610 to 2600–2630 ft. No evidence of brittle deformation is observed in these soft sediments.

Table 1. *Summary of microstructures and open-space minerals observed during thin section petrography of well 58-32 cuttings samples of plutonic rock. An "X" indicates that the microstructure was observed at that depth. A "?" indicates that there are some mineral textures that may be compatible with thin mylonite zones at these depths. Mineral abbreviations used to denote which open-space minerals were observed at each depth are: Cb = carbonate; Anh = anhydrite; Ep = epidote; Chl = chlorite; and Qtz = quartz.*

Depth (ft)	Mylonite	Perthitie	Myrmekite	Cataclasite	Shearing/	Veining	Open-space filling minerals
3200–3210		X		X	X	X	Cb
3300–3310		X	X	X	X	X	Cb & Qtz
3400–3410							
3500–3510	X			X	X		Cb
3600–3610	X		X		X	X	Cb & Ep
3700–3710	X			X	X	X	Cb
3800–3810						X	Cb &Anh
3900–3910							
4000–4010				X	X	X	Cb
4100–4110		X	X				
4200–4210	X						
4300–4310		X	X				
4400–4410	X	X	X			X	Cb & Qtz
4500–4510	X	X	X	X	X	X	Cb
4600–4610	X	X	X			X	Cb
4700–4710	?	X	X			X	Cb, Anh, & Qtz
4800–4810	X	X	X	X	X		
4900–4910	?	X	X				
5000–5010	?	X	X		X		
5100–5110	?	X			X		
5200–5210	X	X	X		X	X	Cb
5300–5310	X	X	X	X	X	X	Cb & Anh
5400–5410		X	X	X	X		
5500–5510		X	X		X		
5600–5610		X	X	X	X	X	Cb
5700–5710	?	X		X	X	X	Cb
5800–5810		X	X	X	X		
5900–5910		X	X	X	X	X	Cb
6000–6010	?	X	X	X	X	X	Cb
6100–6110		X	X	X	X	X	Cb
6200–6210	?	X	X		X	X	Cb
6300–6310		X	X	X	X		Cb
6400–6410		X	X		X	X	Cb
6500–6510		X	X	X	X	X	Cb
6600–6610		X	X	X	X	X	Cb, Anh, & Chl
6700–6710		X	X	X	X	X	Cb & Anh
6900–6910		X	X		X		
7000–7010		X	X	X	X	X	Cb
7100–7110		X	X		X	X	Cb
7200–7210		X	X		X		
7300–7310		X	X		X	X	Cb
7400–7410		X	X		X	X	Chl
7500–7510	X	X	X	X	X	X	Cb & Anh

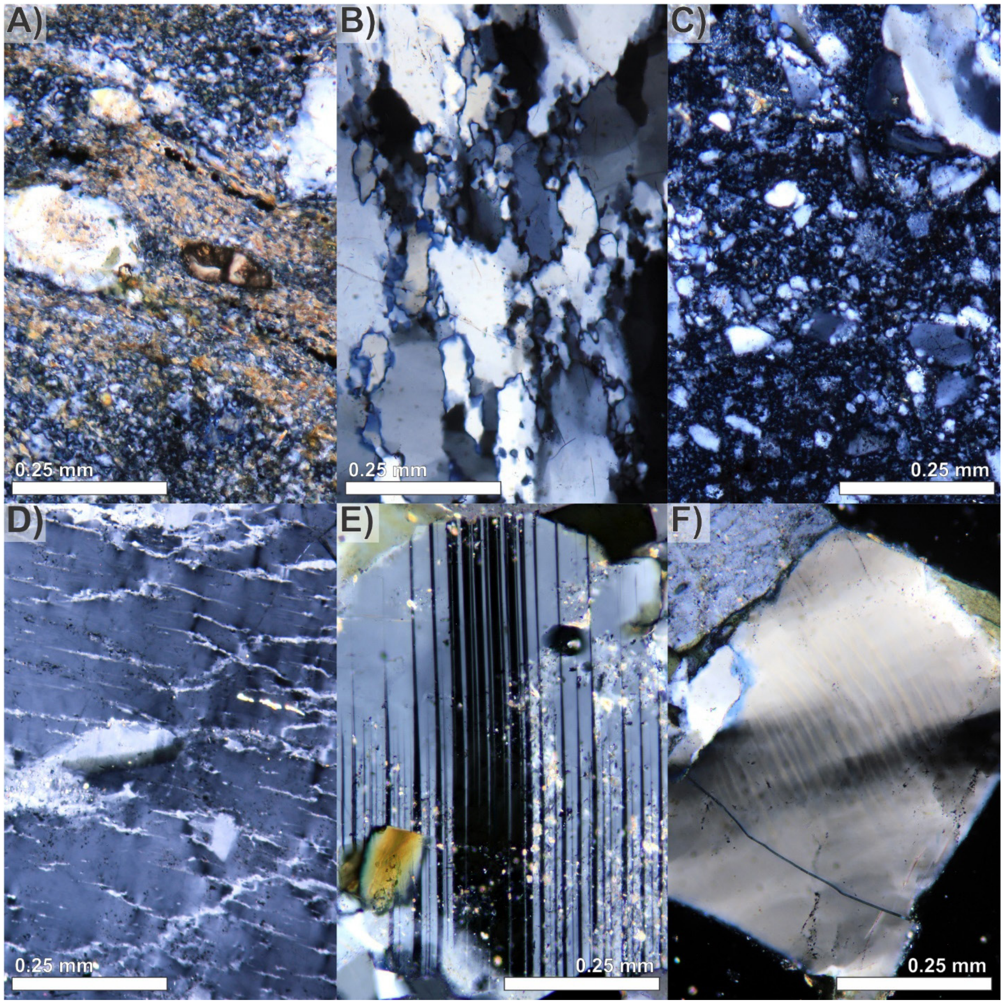

Figure 12. *Cross-polarized light photomicrographs of some of the microstructures observed in the plutonic rocks of well 58-32.* ***(A)*** *Mylonite at 4200–4210 ft.* ***(B)*** *Dynamically recrystallized quartz at 7500–7510 ft.* ***(C)*** *Cataclasite at 7500–7510 ft.* ***(D)*** *Perthite at 7400–7410 ft.* ***(E)*** *Deformation twins in plagioclase at 6300–6310 ft.* ***(F)*** *Quartz grain that displays both undulatory extinction and deformation lamellae at 3300–3310 ft.*

Alluvial deposits. Samples 4380–4400 to 5440–5450 ft

The cuttings from this interval are mostly composed of large (up to at least gravel-size) angular to sub-rounded lithic clasts. Lithic clasts are dominantly composed of plutonic rocks with variable textures, primary minerals and alteration assemblages, with less abundant andesite lava flow and ash-flow tuff clasts, as well as rare vein fragments. The fine-grained matrix is composed of variable proportions of clay (illite, chlorite and smectite) and carbonate (calcite ± dolomite) minerals. Minor carbonate cement is observed at the edges of the clasts or binding clasts together. This unit also contains minor siltstone and fine-grained sandstone with rare fossils, and anhydrite (as nodules and/or laths) with rare chalcedony replacement textures.

Rhyolite ash-flow tuff and tuffaceous sediments. Samples 5640–5650 to 6990–7000 ft

This unit is a mix of rhyolite ash-flow tuff and tuffaceous siltstone and sandstone. The lower part of this unit from 6440–6450 to 6990–7000 ft contains a higher proportion of ash-flow tuff cuttings while the upper part has a higher proportion of tuffaceous sediments.

The rhyolite ash-flow tuffs are moderately to densely welded, with few shard or pumice textures preserved. The cuttings are variable in texture and mineralogy ranging from crystal-rich to crystal-poor, with resorbed quartz, plagioclase and rare sanadine phenocrysts, and chlorite pseudomorphs of ferromagnesian phenocrysts. The groundmass contains variable proportions of quartz, illite, and K-feldspar most commonly as a fine-grained and equigranular groundmass, with less common spherulitic and granophyric devitrification textures.

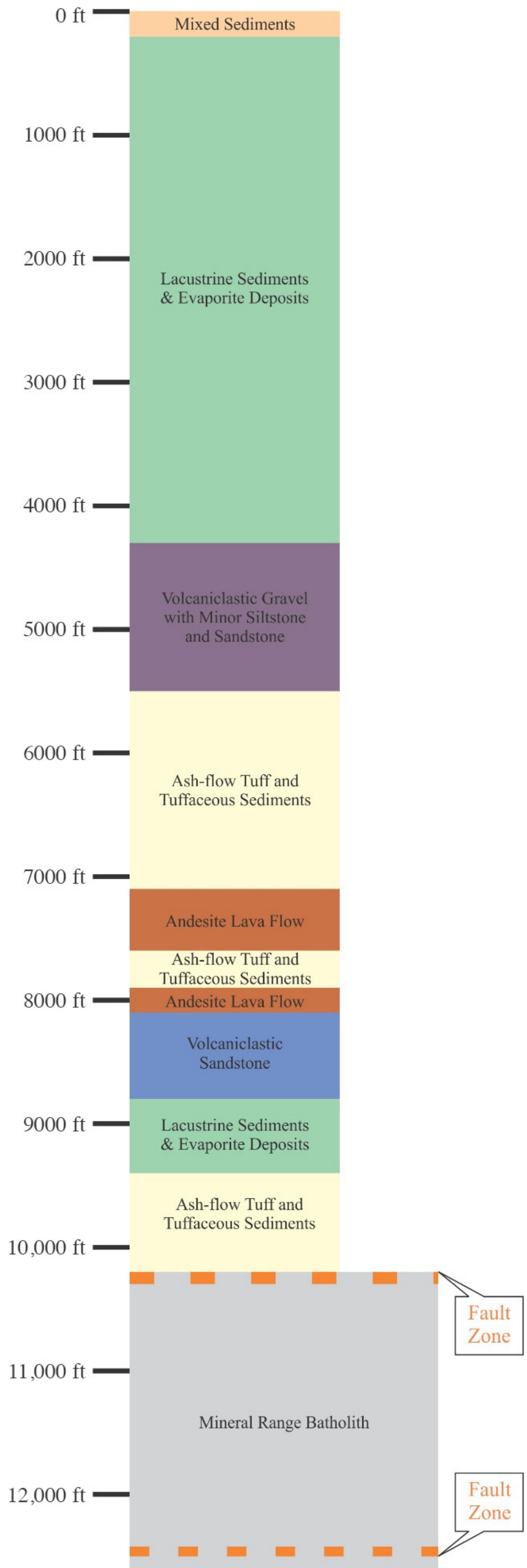

Figure 13. *Stratigraphic column of well Acord-1 constructed from petrographic analyses of cuttings collected at ~50 to 300 ft intervals.*

The sediments consist dominantly of siltstone with detrital quartz, feldspar, and mica grains (mica would have been classified as illite in XRD analyses) and lithic clasts dominantly composed of texturally variable ash-flow tuff with less abundant andesite lava flow and plutonic clasts in fine-grained clay (chlorite and illite ± interlayered illite smectite ± smectite) and/or carbonate (calcite ± dolomite) matrix that is commonly hematite stained. Minor anhydrite is observed as nodules in siltstone.

Silicification of tuff cuttings is commonly observed, but there was no direct evidence of in situ silicification after deposition (i.e., no silicification of fine-grained sedimentary matrix or open-space fillings of quartz or chalcedony that were not contained within a clast).

Andesite lava flow. Samples 7220–7250 to 7540–7550 ft

The samples from this unit consist of porphyritic fine- to medium-grained andesite lava flows with plagioclase, biotite, and clinopyroxene phenocrysts in a fine-grained groundmass composed of plagioclase laths with interstitial K-feldspar and clinopyroxene.

The rock itself is not very altered, there is not much clay in the sample (XRD) and the clinopyroxene grains are often preserved (usually the first mineral in this assemblage to alter/weather), but there is significant secondary silica precipitation in open spaces that resulted from brecciation. Open-space silica is observed as chalcedony, quartz after chalcedony, and anhedral to euhedral quartz. Calcite and rare prehnite are observed filling open space after earlier silica deposition. Calcite veins are also observed cutting earlier sheared/brecciated and silicified chips. Chips containing euhedral quartz growing into open space suggests remnant porosity in this lithology.

Plagioclase is partially altered to albite, K-feldspar, and quartz. Biotite is partially altered to interlayered chlorite/smectite and hematite. Clinopyroxene is partially altered to interlayered chlorite/smectite, quartz, titanite, calcite, and hematite.

Rhyolite ash-flow tuff. Sample 7740–7750 ft

This sample consists of moderately welded, crystal-rich, lithic-poor ash-flow tuff containing plagioclase, sanidine, biotite, and rare quartz phenocrysts, as well as fine-grained quartz pseudomorphs (± hematite) of a ferromagnesian phenocryst. Biotite is often partially altered to hematite. The groundmass contains abundant shards and pumice (fiamme). The shards have been altered to quartz (after chalcedony) and rare analcime. The fine-grained groundmass is K-feldspar- and quartz-rich with a mottled texture. Sparse lithic fragments were derived from andesite lava flows.

The sample contains abundant secondary quartz as replacement of minerals and volcanic glass, as well as open-space fillings. Anhedral quartz is most commonly observed in veins and is likely after chalcedony or opal (i.e., recrystallized). Rare analcime is the last mineral to be deposited in the veins.

Andesite lava flow. Sample 7990–8000 ft

This sample is composed of medium- to coarse-grained andesite flows that have sparse clinopyroxene phenocrysts in a mostly crystalline groundmass consisting of interlocking equigranular plagioclase laths and clinopyroxene, with interstitial K-feldspar and quartz. Plagioclase is partially altered to illite and calcite. Clinopyroxene is partially altered to smectite, hematite, and calcite.

Moderate shearing and minor veining are observed in this sample. Sheared chips are hematite stained. The majority of the open space in the sample appears to be primary including vesicles/amygdules. The sample is cut by several generations of veins: 1) early calcite (botryoidal to euhedral) ± hematite; 2) calcite without hematite; and finally 3) chalcedony followed by quartz. A similar succession of mineralization is recorded in amygdules with quartz precipitating last.

Volcaniclastic sediments. Samples 8240–8250 to 8740–8750 ft

This unit generally consists of volcaniclastic sandstone composed of mineral grains, texturally variable andesite lava flow clasts, and ash-flow tuff clasts in a clay-rich matrix and less commonly calcite cement. Fine-grained quartz with less abundant chalcedony and chlorite fill open pore space. Silicification is also observed. Calcite veins cut the silica deposition and alteration.

Lacustrine sediments and evaporite deposits. Samples 8940–8950 to 9340–9350 ft

This unit is dominantly composed of matrix-supported siltstone consisting of mineral grains and lithic fragments in a clay-rich (interlayered illite/smectite and chlorite ± illite) and/or fine-grained carbonate (dolomite>calcite) matrix. Lithic fragments are derived from ash-flow tuffs (clay altered pumice with remnant vesicular textures and glass shards), andesite lava flows, and plutonic rocks. Preserved shard textures are observed within the fine-grained clay- and/or carbonate-rich matrix. Less commonly anhydrite or calcite cement clasts. This unit contains abundant anhydrite (up to 39 wt% at 9340–9350 ft) as nodules, laths, and thin beds that are partially replaced by chalcedony and quartz. Euhedral rhombohedrons of dolomite are associated with quartz replacements of anhydrite.

Rhyolite ash-flow tuff and tuffaceous sediments. Samples 9540–9550 to 10,140–10,150 ft

The first sample above the granite is composed of equal parts extensively sheared and altered plutonic rock and densely welded ash-flow tuff with minor volcaniclastic sediments. The upper three samples in this unit are composed of ash-flow tuff and tuffaceous sediments.

Trace amounts of tourmaline and epidote are in the sample just above the granite, but they are exclusively within fine-grained plutonic rock chips with no evidence of high-temperature hydrothermal alteration or contact metamorphism observed in the tuff or tuffacous sediments that lie above the thick granite body.

The ash-flow tuff cuttings are densely to non-welded and contain resorbed quartz and plagioclase phenocrysts. The groundmass contains abundant illite-replaced fiamme in the upper part of this unit. In the lower samples, the groundmass is often silicified with a matrix composed of fine-grained quartz with minor illite and K-feldspar.

The volcaniclastic sediments range from silt to gravel-size and consist of mineral grains and lithic fragments in a fine-grained clay-rich matrix with less common fine-grained calcite matrix. The lithic clasts are dominantly composed of ash-flow tuff with less abundant lava flows and plutonic rocks. Pumice fragments are fairly common with preserved vesicular textures that have been extensively altered to interlayered illite/smectite and illite. Plagioclase in ash-flow tuff and lava flow clasts has been partially altered to calcite and anhydrite. Ferromagnesian minerals have been replaced by chlorite. Siltstone cuttings contain anhydrite nodules that may be partially replaced by quartz and/or chalcedony.

Mineral Mountains Batholith. Samples 10,190–10,200 to 12,640–12,650 ft

Cuttings from 10,140–10,150 to 12,640–12,650 ft are composed of plutonic rocks of the Mineral Mountains Batholith. The dominant lithologies encountered in Acord-1 are granite and granodiorite (Figure 14). The vast majority of these lithologies are coarse-grained and composed of equigranular, interlocking plagioclase, K-feldspar, and quartz with minor hornblende and biotite, as well as accessory magnetite/ilmenite, titanite, apatite and zircon (Figure 14A and B).

Minor occurrences of texturally distinct porphyritic intrusive rock with a fine-grained groundmass that range in composition from granite to diorite are observed in samples from 10,190–10,200 ft, 12,090–12,100 ft and 12,240–12,250 ft. Their localized occurrences, minor abundances within the cuttings samples, distinct textures, and relative lack of alteration and deformation compared to the coarser-grained lithologies suggest that these are younger dikes that cut the batholith.

Evidence of brittle deformation such as shearing and brecciation is commonly observed in the cuttings (Figures 15 and 16) and is interpreted to be the result of multiple episodes of tectonic activity. The most intensely deformed of these samples are interpreted as fault zones (Figure 13).

The upper contact between the plutonic rock and the ash-flow tuff/tuffaceous sediments is interpreted as an unconformity with volcanic and volcaniclastic rock deposited on a low-angle fault zone. There is comparatively little deformation in the overlying sedimentary/volcanic units. The lack of contact metamorphism in the lithologies overlying the thick sequence of plutonic rock precludes this as a plutonic contact. The uppermost granitic basement samples are sheared (10,190–10,200 ft) with abundant cataclasite, and a brecciated zone (10,290–10,300 ft) dominated by open-space fillings of quartz and calcite (69 wt% by XRD) with less abundant chlorite, illite, anhydrite, and fluorite (Figure 16A).

Near the bottom of the well at 12,440–12,450 ft another shear zone composed dominantly of cataclasite (Figure 15A) separates medium-grained granitic rock above from finer-grained, compositionally banded plutonic rock with more abundant ferromag-

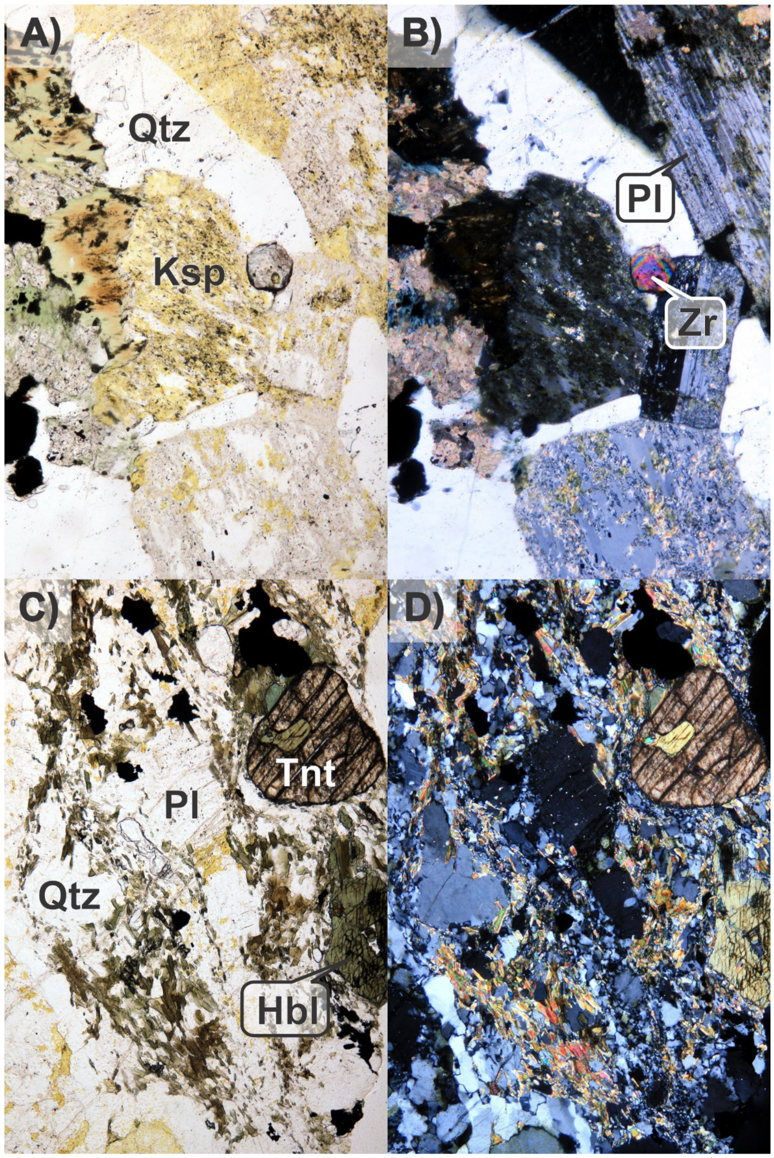

Figure 14. (A&B) *Representative photomicrographs of granite from 12,140–12,50 ft in Acord-1.* ***(C&D)*** *Representative photomicrographs of the finer-grained, compositionally banded granodiorite which contains more ferromagnesian minerals.* ***(A&C)*** *are in plane-polarized light,* ***(B&D)*** *are in crossed-polarized light. Vertical field of view is 1.6 mm in all.*

nesian minerals below (Figure 14B). The deeper, finer-grained plutonic rock displays fewer deformation textures and contains fewer alteration minerals than the medium-grained rocks above. Unlike the upper shear zone, alteration is less prominent and the overall mineralogy more closely resembles unaltered rock.

Secondary minerals in the plutonic rocks of Acord-1 are generally more abundant in cuttings that show evidence of brittle deformation. Plagioclase is variably altered to illite, calcite, K-feldspar, albite and quartz, as well as rare chlorite and epidote. The ferromagnesian minerals are also variably altered with only trace amounts (<1 wt%) remaining in some samples whereas others contain up to 4 wt% hornblende and/or 2 wt% biotite. Biotite is replaced by chlorite, rutile and hematite, and hornblende by chlorite, calcite and hematite. In contrast, K-feldspar, quartz, apatite, zircon, and titanite are relatively unaltered. However, in the most deformed and altered samples quartz is the only major primary phase without replacement textures (Figure 16C and D). In deformed cuttings, quartz often displays undulatory extinction and contains trains of secondary fluid inclusions along healed fractures.

Quartz and calcite are the most commonly observed open-space filling minerals in veins and brecciated rock (Figure 16A and B). Minor phases include chlorite, illite, and anhydrite. Rare open -pace filling of K-feldspar, pyrite, rutile, fluorite, epidote, and fine-grained, fibrous pseudomorphs of actinolite(?) are also observed.

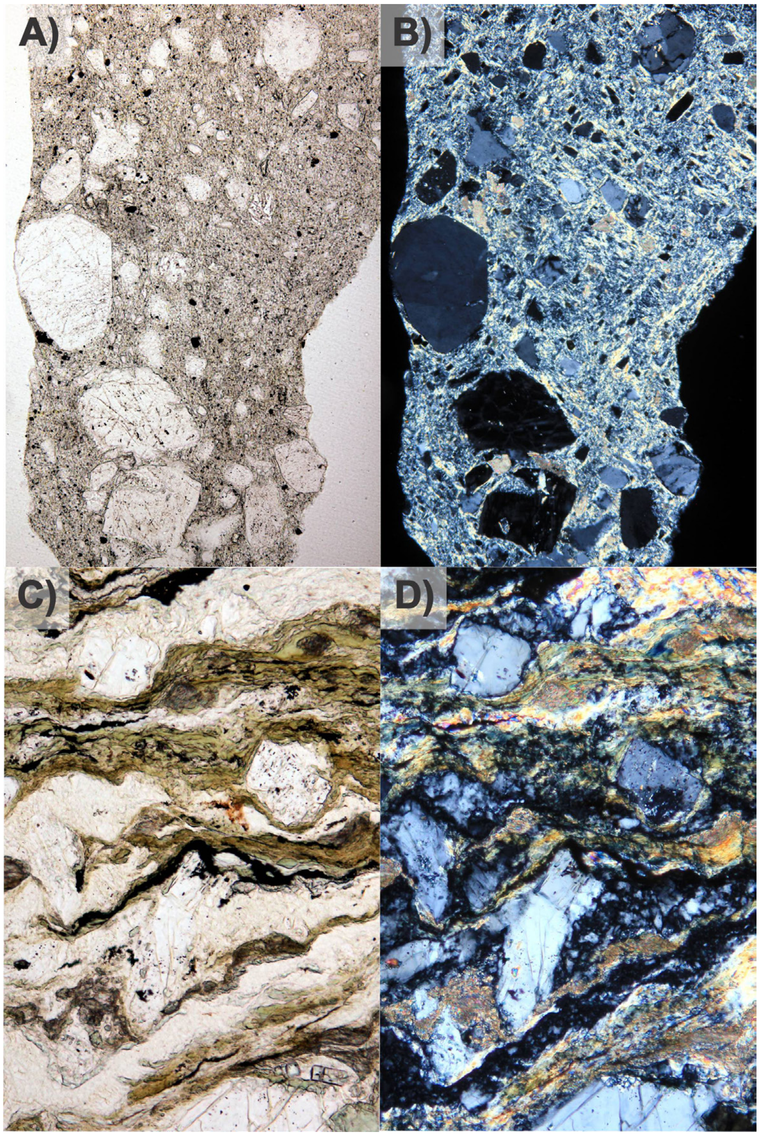

***Figure 15. (A&B)** Cataclasite from 12,440–12,450 ft in Acord-1. **(C&D)** Sheared rock from 10,890–10,900 ft in Acord-1. **(A&C)** are in plane-polarized light, **(B&D)** are in crossed-polarized light. Vertical field of view is 1.6 mm in all.*

Several episodes of tectonic deformation and accompanying hydrothermal alteration and open-space mineralization have affected the granitic rocks as evidenced by: 1) rare early epidote (and pseudomorphs of actinolite?) deposited in open space; 2) quartz replacing calcite and anhydrite in veins; 3) calcite and anhydrite veins cutting cataclasite, silica cemented breccia and silicified rock; 4) low abundances of interlayered illite/smectite (from XRD) indicating retrograde argillic overprinting (<225°C); 5) the incorporation of vein fragments in cataclasite; and 6) multiple dikes ranging in composition from granite to diorite that cut extensively deformed rocks.

COMPARISON OF THE PLUTONIC ROCKS IN 58-32 TO THOSE FROM OTHER WELLS AND TO THE ROCKS EXPOSED IN THE MINERAL MOUNTAINS

The Mineral Mountains Batholith, while potentially variable at a fine-scale (foot or meter scale), contains similar lithologies over a wide area, ranging from the deep Acord-1 well in the center of the Milford Valley, to the Mineral Mountains exposed to the east of the FORGE site and in all of the deep geothermal wells in between (Figure 1).

Plutonic rocks encountered in deep geothermal wells (Acord-1, 58-32, 52-21, 9-1 & 14-2) and those that outcrop in the Mineral Mountains have been classified using XRD data (Figure 17). The most common rock types are monzodiorite, quartz monzodio-

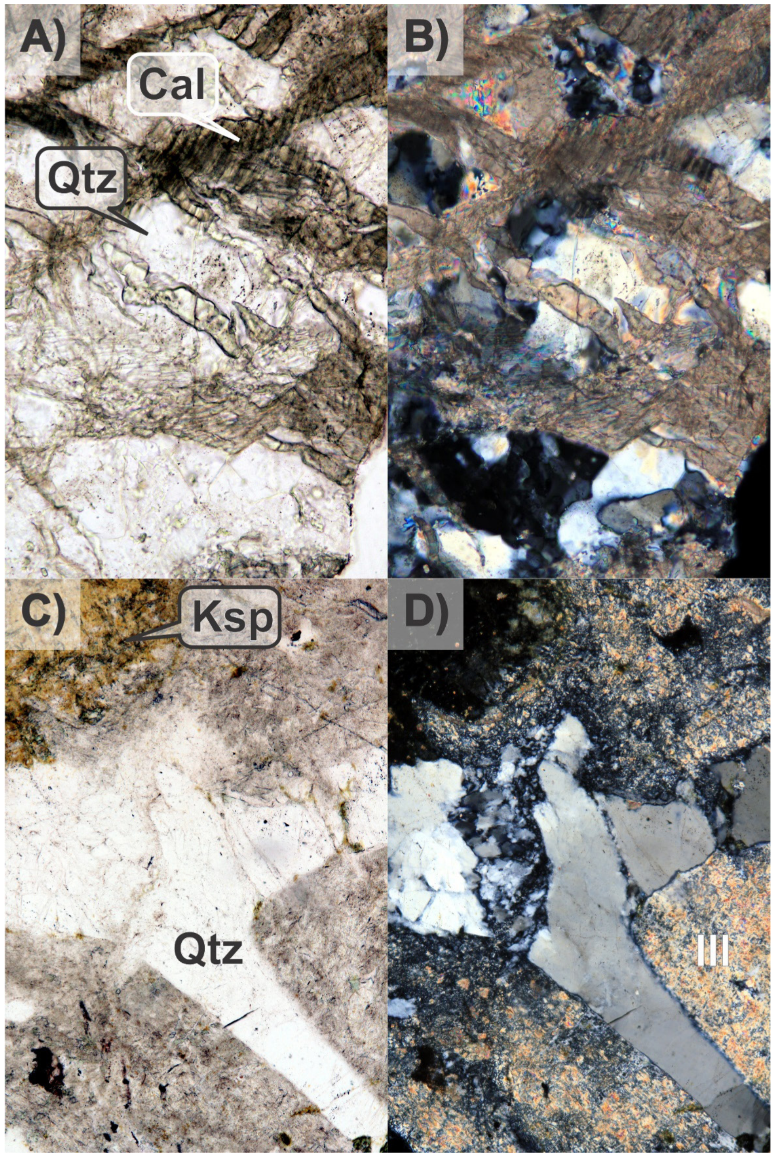

Figure 16. (A&B) *Brecciated quartz vein with open space filled by calcite from 10,290–10,300 ft in Acord-1. Vertical field of view is 0.8 mm.* ***(C&D)*** *Brecciated primary quartz and plagioclase that has been extensively altered to illite from 11,890–11900 ft in Acord-1. Vertical field of view is 1.6 mm.* ***(A&C)*** *are in plane-polarized light,* ***(B&D)*** *are in crossed-polarized light.*

rite, monzonite, quartz monzonite, granite, and granodiorite. The plutonic rocks are dominantly composed of quartz, K-feldspar, and plagioclase that constitutes 57 to 99 wt% of all of the samples analyzed, and average 86 wt%. Primary ferromagnesian minerals including biotite, hornblende, and clinopyroxene are locally abundant and can compose up to 35 wt% of a sample, or as little as <1 wt% (average = 8 wt%). Accessory minerals like titanite and apatite are ubiquitous in the plutonic rocks examined (Min = < 1 wt%, Max = 6 wt%, average = 1 wt%).

Secondary minerals are generally found in low abundance in the plutonic rocks and range from < 1 wt% up to approximately14 wt% with an average of 4 wt%. The highest abundances of secondary minerals were observed in the plutonic rocks of Acord-1. The most common secondary minerals are the clay minerals: smectite; interlayered illite/smectite; interlayered chlorite/smectite; illite; chlorite; and kaolinite. Clay minerals are dominantly observed replacing primary plagioclase, biotite, hornblende, and clinopyroxene. Epidote is sporadically observed replacing plagioclase but is often below the limit of detection by XRD analysis (< 1 wt%). Carbonates (calcite > siderite > dolomite) appear sporadically and are observed filling fractures, often with anhydrite and hematite.

The rocks within the FORGE EGS reservoir most closely resemble samples from outcrop just to the east of the Roosevelt geothermal field, and some of those in well 9-1, Acord-1 and 14-2.

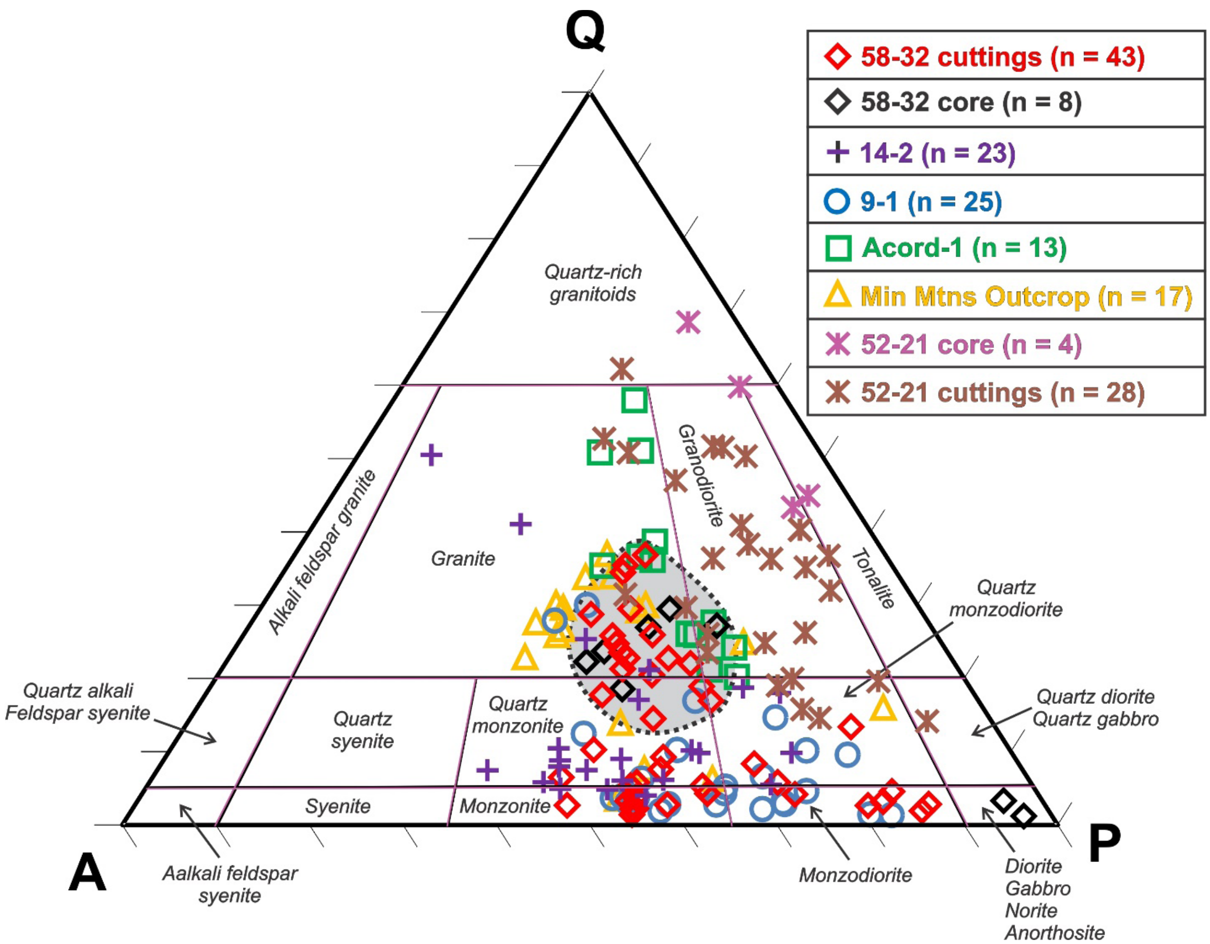

Figure 17. *XRD data from the plutonic rocks of the Mineral Mountains Batholith from deep geothermal wells and outcrop. The data have been normalized to 100 weight percent quartz (Q), K-feldspar (A), and plagioclase (P) and plotted on the IUGS classification diagram (Le Maitre et al., 1989). The majority (15 of 18) of the analyzed samples from within the EGS reservoir are within the gray shaded area and consist of granite, granodiorite, quartz monzonite, and quartz monzodiorite. XRD data from 14-2, 9-1, and Acord-1 come from cuttings.*

CONCLUSIONS

The FORGE site is located on the gently sloping east side of the Milford basin. From the surface to 3176 ft depth, well 58-32 encountered coarse-grained alluvial-fan deposits. To the west, in Acord-1, the basin fill consists of lacustrine sediments, evaporite deposits, volcaniclastic deposits, ash-flow tuff, tuffaceous sediments and andesite lava flows. In well 58-32, FMI logs indicate the basin-fill deposits are undeformed and dip gently to the west mimicking the topography of the plutonic rocks.

The contact between the basin fill and the Mineral Mountains Batholith is interpreted as an unconformity separating plutonic rocks exposed in the footwall of a normal fault from the overlying sediments and volcanic rocks of the basin fill (see Bartley et al., 2019). The absence of high-temperature secondary minerals in the sediments overlying the plutonic rocks precludes this as an intrusive contact. Strong brittle deformation is observed in the rhyolite that separates the alluvium above from the plutonic rock below in well 58-32. In Acord-1 where the unconformity is ~7000 ft deeper, minor brittle deformation is observed in the overlying sediments and volcanic rock when compared to the extensive shearing and brecciating that has impacted the upper portions of the plutonic basement. Coleman and Walker (1994) suggested 30° to 50° of eastward tilting has occurred since 8 to 9 Ma in the western Mineral Mountains which may account for the modern gentle dip of the unconformity beneath the Milford Valley.

The analyzed samples of the Mineral Mountains Batholith from deep geothermal wells and outcrop are composed of plagioclase, quartz, K-feldspar, biotite, hornblende, titanite, apatite, magnetite/ilmenite, and zircon ± clinopyroxene. Variations in bulk composition/mineralogy and texture are observed across the Mineral Mountains Batholith, within each well, and at the outcrop and core scale; however, the rocks within the EGS reservoir are fairly homogeneous and plot primarily within the granite and quartz monzonite fields of the IUGS classification diagram with minor granodiorite, quartz monzodiorite, and fine-grained banded diorite. With the exception of the diorite in the lower core of well 58-32, the vast majority of the EGS reservoir samples analyzed consist of 90 to 97 wt% coarse-grained, interlocking quartz, K-feldspar, and plagioclase.

Alteration minerals in the plutonic rocks of 58-32 are relatively sparse and decrease in abundance with depth, suggesting an accompanying decrease in permeability. Within the EGS reservoir, secondary minerals make up only a few wt% of the samples on average. Clay minerals are the most common secondary minerals observed in the plutonic rock, with illite and chlorite being most abundant. In geothermal systems, the expected temperature stability ranges of the clay minerals are as follows: at <180°C smectite is stable; at >180°C and <220°C interlayered clays are stable; and at >220°C chlorite and illite are stable (Henley and Ellis, 1983). Traces (<1 wt% by XRD) of smectite and interlayered chlorite/smectite where observed in the deeper part of the well at temperatures >180°C; however, expandable clay minerals are found outside of their expected stability range in low-permeability rocks. Illite and to a lesser extent chlorite are found throughout the batholith and are well below their stability range, suggesting that they are remnants of an earlier alteration episode.

Open-space mineralization was intermittently observed within the EGS reservoir. Observed open-space-filling minerals are calcite, anhydrite, epidote, quartz, chlorite, and plagioclase. Epidote is sporadically observed filling open space and replacing plagioclase. In geothermal systems, epidote typically forms at temperatures greater than 240° to 260°C (Browne, 1978; Reyes, 1990) far above the maximum recorded temperature in well 58-32 of 197°C. The occurrence of epidote, so far outside of its stability range, suggests it too is a remnant of an older episode of alteration.

Carbonates, anhydrite, and the expandable clay minerals would all be expected to form under in situ conditions. Calcite and anhydrite, the most common open-space-filling minerals in the EGS reservoir, both display retrograde solubility and precipitate on heating, suggesting that the fluids within the EGS reservoir are downward percolating.

REFERENCES

Aleinikoff, J.N., Nielson, D.L., Hedge, C.E., and Evans, S.H., 1986, Geochronology of Precambrian and Tertiary rocks in the Mineral Mountains, south-central Utah: U. S. Geological Survey Bulletin 1622, p. 1–12.

Bartley, J.M., 2019, Joint patterns in the Mineral Mountains intrusive complex and their roles in subsequent deformation and magmatism, *in* Allis, R., and Moore, J.N., editors, Geothermal characteristics of the Roosevelt Hot Springs system and adjacent FORGE EGS site, Milford, Utah: Utah Geological Survey Miscellaneous Publication 169-C, 13 p., 1 appendix, https://doi.org/10.34191/MP-169-C.

Browne, P. R. L. (1978). Hydrothermal alteration in active geothermal fields. Annual review of earth and planetary sciences, 6 (1), 229–248.

Coleman, D.S., 1991, Geology of the Mineral Mountains Batholith, Utah: Lawrence, University of Kansas, Ph.D. dissertation, 219 p.

Coleman, D.S., and Walker, J.D., 1992, Evidence for the generation of juvenile granitic crust during continental extension, Mineral Mountains Batholith, Utah: Journal of Geophysical Research, v. 97, no. B7, p. 11,011–11,024.

Coleman, D.S., and Walker, J.D., 1994, Modes of tilting during extensional core complex development: Science, v. 263, no. 5144, p. 215–218.

Fournier, R.O., 1985, The behavior of silica in hydrothermal solutions; *in* Berger, B.R., and Bethke, P.M., editors, Geology and geochemistry of epithermal systems: Reviews in Economic Geology, v. 2, p. 45–62.

Henley, R.W., and Ellis, A.J., 1983, Geothermal systems ancient and modern—a geochemical review: Earth-science reviews, v. 19 no. 1, p. 1–50.

Kirby, S.M., Knudsen, T.R., Kleber, E., and Hiscock, A., 2018, Geologic map of the Utah FORGE area: Utah Geological Survey Contract Deliverable for DOE project number DE-EE0007080, scale 1:24,000, 2 plates, 13 p.

Le Maitre, R.W., Dudek, P., Keller, A., Lameyre, J., Le Bas, J., Sabine, M.J., Schmid, P.A., Sorensen, R., Streckeisen, H., Woolley, A., and Zanettin, A.R., 1989, A classification of igneous rocks and glossary of terms—Recommendations of the International Union of Geological Sciences, Sub commission on the Systematics of Igneous Rocks: International Union of Geological Sciences. Blackwell Science, Oxford, p. 236.

Lipman, P.W., Rowley, P.D., Mehnert, H.H.S., Evans, S.H.J., Nash, W.P., and Brown, F.H., 1978, Pleistocene rhyolite of the Mineral Range, Utah—Geothermal and archaeological significance: U.S. Geological Survey Journal of Research, v. 6 no. 1, p. 133–147.

Moore, J.N., Allis, R.G., Nemčok, M., Powell, T.S., Bruton, C.J., Wannamaker, P.E., and Norman, D.I., 2008, The evolution of volcano-hosted geothermal systems based on deep wells from Karaha–Telaga Bodas, Indonesia: American Journal of Science, v. 308 no. 1, p. 1–48.

Moore, D.M., and Reynolds, R.C., 1997, X-ray Diffraction and the Identification and Analysis of Clay Minerals (p. 155). Oxford: Oxford university press.

Reyes, A.G., 1990, Petrology of Philippine geothermal systems and the application of alteration mineralogy to their assessment: Journal of Volcanology and Geothermal Research, v. 43, p. 279–309.

Sander, B., 1930, Gefugekunde der Geteine: Vienna, Springer, 352 p.

Simpson, C., and Wintsch, R.P., 1989, Evidence for deformation-induced K-feldspar replacement by myrmekite: Journal of Metamorphic Geology, v. 7, no. 2, p. 261–275.

Vernon, R.H., 2004, A practical guide to rock microstructure: Cambridge University Press, 594 p.

Walker, F.D.L., Lee, M.R., and Parsons, I., 1995, Micropores and micropermeable texture in alkali feldspars—geochemical and geophysical implications: Mineralogical Magazine, v. 59, no. 3, p. 505–534.

Appendix A: XRD Data Sets

Summary of XRD data from wells 58-32, Accord-1, 52-21, 9-1 and 14-2, as well as outcrop samples from the Mineral Mountains (Table A1). For each XRD data set presented in Table A1 the full XRD data are presented in Tables A2 through A9.

Table A1. *XRD data sets.*

XRD data set	Sample type	XRD analyses
58-32	cuttings	78
58-32	core	8
14-2	cuttings	23
9-1	cuttings	25
Accord 1-26	cuttings	62
52-21	core	4
52-21	cuttings	30
Mineral Mountains	outcrop/ hand sample	17
Total		***247***

Table A2. *XRD data acquired from cuttings of FORGE well 58-32. Sample depths are shown in the first column (drillers depth). XRD data are given in weight percent of sample, with values rounded to the nearest whole number. Fields marked with tr (trace) indicate that this mineral is present, but represents less than 1 wt% of the sample or that it was observed in the clay-sized fraction but not the bulk pattern, and/or it was observed in thin section. Where possible, the composition of interlayered chlorite/smectite was determined based on a comparison of air-dried and glycolated clay-size fraction diffractograms and is indicated in the column "% chlorite in C/S."*

58-32 Cuttings Depth (ft)	**Plagioclase**	**K-feldspar**	**Quartz**	**Biotite**	**Titanite**	**Hornblende**	**Apatite**	**Clinopyroxene**	**Smectite**	**Interlayered Chlorite-Smectite**	**% chlorite in C/S**	**Chlorite**	**Illite**	**Kaolinite**	**Epidote**	**Calcite**	**Dolomite**	**Siderite**	**Hematite**	**Anhydrite**
100–110	40	44	17						tr				tr							
200–210	42	33	20	tr					tr				4						tr	
300–310	39	34	26						tr				tr			2				
400–410	35	39	20	1					1				4						tr	
500–510	35	39	21	tr					tr				4						tr	
600–610	35	49	16						tr				tr						tr	
700–710	36	43	20						tr				tr						tr	
800–810	38	43	18						tr				tr						tr	
900–910	31	41	28						tr				tr						tr	
1000–1010	37	34	24	2					tr				3						tr	
1100–1110	40	36	24						tr				tr						tr	
1200–1210	36	39	25						tr				tr						tr	
1300–1310	37	37	25						tr				tr						tr	
1400–1410	38	35	26						tr				tr						tr	
1500–1510	34	38	27						tr				tr						tr	
1600–1610	35	38	26						tr				tr						1	
1700–1710	33	38	28						tr				tr						tr	
1800–1810	36	35	25	tr					tr				3						1	
1900–1910	34	41	20	tr					tr				3						tr	
2000–2010	34	40	21	tr					tr				4						tr	
2100–2110	37	33	22	3					tr				3						1	
2200–2210	35	34	25	1					tr				4						tr	
2300–2310	35	36	24	1					tr				3						tr	
2400–2410	42	37	15	4					tr				2						1	
2500–2510	35	34	26	2					tr				3						1	
2600–2610	38	37	19	1					tr				3						1	
2700–2710	38	40	18						tr				3						tr	
2800–2810	36	38	20	tr					tr				4						1	
2900–2910	38	37	19	1					tr				4						1	
3000–3010	37	37	20	2					tr				3						2	
3100–3110	38	39	18	1					tr				3						tr	
3170–3180	19	41	34	1					tr				2	1		1				
3180–3190	15	42	38	tr					tr				3	1		tr				
3190–3200	28	47	11	3			tr		tr				5	tr		tr		3	2	tr
3200–3210	40	39	9	3	tr		3		tr				5	tr		tr				
3300–3310	39	44	6	2	tr		3		tr				6	tr		tr				
3330–3340	43	32	2	8	tr		tr		tr				4	2		tr		6	2	tr

Table A2. *Continued.*

3400–3410	43	48	3	tr	tr		2		tr				3	tr		tr				
3500–3510	49	18	3	16	tr	3	3	5	tr	tr	50	tr	1			tr				
3600–3610	55	12	2	11	2	7	2	5	tr	tr	N/A	1.2	3		tr	tr				
3700–3710	45	18	4	12	tr	1	1	4	tr			1.2	5			tr	2	3	1	1
3800–3810	54	13	2	11	1	6	2	8	tr			tr	2			tr				
3900–3910	51	8	2	11	2	11	2	9	tr	tr	N/A	1.5	2		tr	1				
4000–4010	53	9	1	11	2	8	3	10	tr	tr	N/A	1	2			tr				
4100–4110	46	27	4	6	tr	4	1	5	tr			1	4			2				
4200–4210	54	11	3	15	1	6	1	5	tr			1	2		tr	1				
4300–4310	50	41	2	2	tr	tr	tr		tr	tr	N/A	tr	3			tr				
4400–4410	44	36	3	4	tr	4	tr	4	tr	tr	N/A	1.6	2			tr				
4500–4510	48	40	2	2	tr	2	tr	2	tr	tr	50	tr	2			1				
4600–4610	47	38	5	2	tr	2	tr	2		tr	N/A	tr	4			tr				
4700–4710	49	35	7	2	tr	2	tr	2	tr	tr	50		3			tr				
4800–4810	51	30	4	5	tr	2	tr	3	tr	tr	50	tr	4			tr				
4900–4910	51	42	2	tr	tr	1							3							
5000–5010	51	42	1	1	tr	tr	tr						3			tr				
5100–5110	54	39	3	tr	tr	1	tr						2			tr				
5200–5210	39	34	24	1	tr	tr	tr					tr	2			tr				
5300–5310	50	41	5	2	tr	tr	tr			tr			2		tr	tr				
5400–5410	34	33	27	1	tr	1	tr						3			tr				
5500–5510	35	28	35	tr	tr	tr	tr					tr	1			tr				
5600–5610	39	32	19	4	tr	1	1		tr			tr	3		tr	tr				
5700–5710	36	25	35	tr	tr	tr	tr		tr				2		tr	tr				
5800–5810	35	29	34	tr	tr	tr	tr						1	tr		tr				
5900–5910	39	30	29	tr	tr	tr	tr	tr					1			tr				
6000–6010	59	27	8	2	tr	tr	tr						3			tr				
6100–6110	50	42	3	1	tr	tr	tr						3			tr				
6200–6210	53	37	9	tr	tr	tr	tr						tr			tr				
6300–6310	38	33	25	1	tr	tr	tr						3	tr		tr				
6400–6410	41	28	24	2	tr	tr							4			tr				
6500–6510	40	33	22	1	tr	tr	tr						2			tr				
6600–6610	41	38	17	1	tr	tr	tr					tr	2							
6700–6710	69	15	13	tr	tr	tr	tr			tr	50	1	tr	tr						
6900–6910	44	29	21	1	tr	tr	tr					tr	3		tr					
7000–7010	48	26	17	1	tr	1	tr			tr	N/A	tr	4		tr	tr				
7100–7110	47	34	14	2	tr	tr	tr						3		tr					
7200–7210	44	31	19	2	tr	tr			tr	tr	50	tr	2		tr	tr				
7300–7310	40	32	21	3	tr	tr	tr			tr	50	tr	3		tr	tr				
7400–7410	50	26	16	3	tr	2	tr			tr	N/A	tr	2		tr	tr				
7500–7510	47	28	21	2	tr	tr	tr		tr	tr	50	tr	1			tr				

Table A3. *XRD data acquired from core of FORGE well 58-32. Sample depths are shown in the first column (drillers depth). XRD data are given in weight percent of sample, with values rounded to the nearest whole number. Fields marked with tr (trace) indicate that this mineral is present, but represents less than 1 wt% of the sample, or that it was observed in the clay-size fraction but not the bulk pattern, and/or it was observed in thin section. Where possible, the composition of interlayered chlorite/smectite was determined based on a comparison of air-dried and glycolated clay-size fraction diffractograms and is indicated in the column "% chlorite in C/S."*

58-32 Core Depth (ft)	**Plagioclase**	**K-feldspar**	**Quartz**	**Biotite**	**Titanite**	**Hornblende**	**Apatite**	**Smectite**	**Interlayered Chlorite-Smectite**	**% chlorite in C/S**	**Chlorite**	**Illite**	**Calcite**
6801.15 H	47	21	26	5	tr	tr	tr		tr	50		tr	
6802.18 V-A	40	25	27	3	tr	tr	tr		tr	N/A		3	
6809.00 H	37	34	22	3	tr	tr			tr	50		2	
6810.15 V-A	37	37	21	4	tr				tr	50		tr	
7442.60 H	62	3	2	15	2	16	1	tr				tr	tr
7445.40 V-C	56	2	1	12	1	24	2				3	1	tr
7447.95 V-B	38	27	24	4	tr	tr	tr		tr	50	1	4	
7451.85 H	42	36	18	3	tr	tr			tr	N/A	tr	tr	

Table A4. *XRD data acquired from cuttings of well 14-2. Sample depths are shown in the first column (drillers depth). XRD data are given in weight percent of sample, with values rounded to the nearest whole number. Fields marked with tr (trace) indicate that this mineral is present, but represents less than 1 wt% of the sample, or that it was observed in the clay-size fraction but not the bulk pattern, and/or it was observed in thin section. Where possible, the composition of interlayered illite/smectite was determined based on a comparison of air-dried and glycolated clay-size fraction diffractograms and is indicated in the column "% illite in I/S."*

14-2 Cuttings Depth (ft)	**Plagioclase**	**K-feldspar**	**Quartz**	**Biotite**	**Titanite**	**Hornblende**	**Apatite**	**Smectite**	**Interlayered Illite-Smectite**	**% Illite in I/S**	**Chlorite**	**Illite**	**Kaolinite**	**Calcite**	**Hematite**
590–600	42	48	5	3	tr		tr	tr				2		tr	
740–750	40	46	8	3	tr		tr	tr				2		tr	
1010–1020	32	33	22	8	tr	tr	tr	tr			1	3		tr	
1240–1250	34	54	7	2	tr			tr				2			
1520–1530	42	43	7	4	tr		tr	tr				2		1	
1720–1730	7	36	44	2				tr	tr	70–80		4	5	tr	tr
1995–2000	21	34	38	1	tr				tr	70–80		5			tr
2240–2245	40	29	19	5	tr		tr		tr	80	2	4			
2495–2500	51	30	9	4	tr		tr		tr	80–90	2	4		tr	
2755–2760	48	16	14	12	1	1	1				tr	5		2	
2955–3000	57	20	9	8	tr		tr				tr	2		1	
3245–3250	49	35	6	3	tr		tr				1	6		1	
3495–3500	37	43	9	1	tr		tr				2	5		tr	
3745–3750	49	38	4	tr	tr		tr				3	3		tr	
3995–4000	50	30	9	4	tr		tr				1	2		2	
4245–4250	39	45	7	2			tr				2	5		tr	
4495–4500	39	48	5	tr	tr		tr				2	4		1	
4745–4750	46	42	5	2	1						1	2		2	
4995–5000	38	29	14	5	1		tr				2	8		3	
5245–5250	54	23	5	10	tr	tr	1				tr	4		2	
5495–5500	46	40	6	2	tr	tr					tr	3		1	
5740–5745	45	39	8	4	tr	1	tr				tr	2		tr	
5995–6000	42	18	14	8	tr	10	tr				tr	4		2	

Table A5. *XRD data acquired from cuttings of well 9-1. Sample depths are shown in the first column (drillers depth). XRD data are given in weight percent of sample, with values rounded to the nearest whole number. Fields marked with tr (trace) indicate that this mineral is present, but represents less than 1 wt% of the sample or that it was observed in the clay-size fraction but not the bulk pattern, and/or it was observed in thin section. Where possible, the composition of interlayered illite/smectite was determined based on a comparison of air-dried and glycolated clay-size fraction diffractograms and is indicated in the column "% illite in I/S."*

9-1 Cuttings Depth (ft)	**Plagioclase**	**K-feldspar**	**Quartz**	**Biotite**	**Titanite**	**Hornblende**	**Apatite**	**Clinopyroxene**	**Smectite**	**Interlayered Illite-Smectite**	**% Illite in I/S**	**Chlorite**	**Illite**	**Calcite**	**Hematite**
760	50	27	4	11	3	tr	1		tr			1	3		
1010	32	33	28	4	tr				tr			tr	2		
1240	26	32	23	6	tr				2			tr	6	3	1
1480	43	34	5	10	1		tr		tr			tr	3	3	tr
1750	46	11	6	12	1	7	1	9	tr			tr	6	2	
2020	39	41	12	4	tr				tr			tr	2	tr	1
2250	42	15	10	10	tr	2	3	10	tr			tr	5	1	2
2500	45	29	9	8	tr	1	tr		tr			tr	3	2	1
2750	42	24	14	7	tr		tr		tr	tr	>90	4	6	2	
3000	48	21	5	13	tr	tr	3		tr			tr	8	2	
3250	46	25	4	13	tr	1	2		tr			tr	7	2	
3450	52	17	8	9	2	6	tr		tr			tr	3	2	
3700	47	41	4	4	tr		tr					tr	2	1	
4010	46	42	4	4	tr		tr		tr			tr	3	2	
4200	51	29	2	12	tr	1	1					tr	3	1	
4500	58	23	3	11	tr	tr	tr					tr	2	1	
4700	55	22	2	14	1	tr	tr					tr	2	2	
5000	47	35	2	7	tr	tr	tr					tr	4	2	
5240	46	32	2	10	1	tr	2		tr			tr	5	2	
5500	45	38	3	9	tr	1	tr		tr			tr	1	1	
5780	46	37	3	7	tr	tr	tr					tr	3	2	
6000	53	24	2	13	tr	3	1					1	1	1	
6200	55	11	1	21	tr	6	2						3	1	
6500	50	12	1	25	tr	4	3						3	tr	
6790	40	14	3	29	1	2	4						5	2	

Table A6*. XRD data acquired from cuttings of well Acord-1. Sample depths are shown in the first column (drillers depth). XRD data are given in weight percent of sample, with values rounded to the nearest whole number. Fields marked with tr (trace) indicate that this mineral is present, but represents less than 1 wt% of the sample, or that it was observed in the clay-size fraction but not the bulk pattern, and/or it was observed in thin section. Where possible, the composition of interlayered illite/smectite was determined based on a comparison of air-dried and glycolated clay-size fraction diffractograms and is indicated in the column "% illite in I/S."*

Acord-1 Cuttings Depth (ft)	Plagioclase	K-feldspar	Quartz	Biotite	Titanite	Hornblende	Apatite	Clinopyroxene	Magnetite	Smectite	Interlayered Illite-Smectite	% Illite in I/S	Interlayered Chlorite-Smectite	% chlorite in C/S	Chlorite	Illite	Kaolinite	Epidote	Calcite	Dolomite	Hematite	Anhydrite	Prehnite	Rutile	Pyrite	Aragonite	Bassanite	Halite	Analcime
70–100	17	11	28							tr						7	11		27										
320–350	7	7	32							2						7	16		19	10		tr							
590–620	7	11	15							tr						12	tr		21	21						12		1	
830–860	6	9	10							tr						11			14	36		4				7	3		
1070–1100	9	10	15							tr						9			20	25						12			
1340–1350	6	13	13							tr						15			12	20		2				15	5		
1580–1610	6	13	13							tr						15			14	26		5				8			1
1820–1850	4	12	9							tr					tr	13			10	19		13				5	10		4
2090–2120	16	18	27							tr					2	14			10	9						2			2
2330–2360	22	17	35							tr					4	4			13	3									2
2600–2630	17	20	25							tr					3	16			10	4		2				1			2
2840–2850	11	21	35							tr					9	10			14										
3080–3110	10	19	29							tr					3	21			12			6							
3320–3350	7	17	16							2					7	6			11	tr		35							
3590–3600	26	21	31							2					4	6			4	3	tr	2							
3840–3850	11	21	17							3					7	11			14	10	tr	6							
3990–4000	14	21	23							tr					3	17			14	5		4							
4240–4250	14	21	15							4					9	10			12	6	tr	8							
4380–4400	32	25	31							2					2	6			2			tr							
4640–4650	27	31	28							1					5	3			3		2	tr							
4840–4850	31	28	27							1					5	4			2		2	tr							
5040–5050	28	30	30							1					4	3			2		2	tr							
5240–5250	27	34	26							2					4	3			3	tr	1	tr							
5440–5450	20	28	24							3					7	8			8		2	tr							
5640–5650	21	26	25							6					6	6			9		1	tr							
5840–5850	21	30	32							tr	tr	90			6	6			4		2	tr							

Table A6. *Continued.*

6040–6050	16	39	28							tr	tr	90			6	4			2		2	2							
6240–6250	18	29	26							tr	tr	90			7	7			7	2	1	3							
6440–6450	22	26	37							tr	tr	90			6	6			2		1								
6640–6650	25	25	33							tr	tr	90			6	6			3		1	tr							
6840–6850	24	26	34							tr	tr	90			6	5			3		2	tr							
6990–7000	26	31	29							tr	tr	90			3	3			5		1	1							
7220–7250	46	31	10	tr	tr			2		1			1	50		1			4		3		tr						
7540–7550	50	27	15	tr				tr		tr			1	50		1			tr		4								tr
7740–7750	30	35	28	2							tr	50,90			tr	tr			tr		tr								3
7990–8000	41	9	12	tr				9		10						5			8		6								
8240–8250	36	10	23					tr		2	2	90			6	13			5		2								
8340–8350	25	8	27							7	19	90			9	tr			5	tr									
8540–8550	22	11	41								16	50,90			6	tr			4										
8740–8750	24	9	33								24	50,90			5	tr			2	2		tr							
8940–8950	25	9	25								22	50,90			6	tr			3	6		4							
9140–9150	10	9	19								26	50,90			7				5	13		12							
9340–9350	9	5	17								12	90			8				2	8		39							
9540–9550	20	7	26								27	50,90			8				4			7			tr				
9740–9750	23	8	23								4	50,90			9	24			4			5			tr				
9940–9950	18	18	24								3	50,90			13	16			2		1	4			1				
10,140–10,150	33	11	28				tr				tr	90			12	12		tr	1			1			1				
10,190–10,200	11	22	32	tr			tr	tr	tr		tr	50,90			12	12			9		tr	2							
10,290–10,300	6	9	34	tr			tr	tr	tr		tr	50,90			6	8			35		tr	tr							
10,490–10,500	26	18	25	tr	1		tr		tr		tr	90			13	10			5			1							
10,690–10,700	40	21	16	tr	tr	3	tr		1		tr	90			6	8		tr	3			tr							
10,890–10,900	19	12	32	tr	1	tr	tr		1		tr	50,90			11	13		1	7		tr	tr							
11,090–11,100	36	17	20	2	1	1	tr	tr	1		tr	50,90			14	4		tr	3		tr								
11,290–11,300	43	18	19	2	1	2	tr		1		tr	50			2	8		tr	3		tr	tr							
11,490–11,500	16	10	35	tr	tr	4	tr	1	tr		tr	90			8	11		tr	10	1	tr	1							
11,690–11,700	34	18	18	tr	tr	4	tr		tr		tr	90			11	9			5		tr				tr				
11,890–11,900	36	20	20	1	1		tr		1		tr	90			8	6			5		tr								
12,090–12,100	30	19	30	tr	tr		tr		tr		tr	90			6	7			4		tr	1		tr	tr				
12,140–12,150	17	15	33		2	tr	tr				tr	90			6	18			5	1		3		tr					
12,240–12,250	31	20	28	1	tr		tr		1						9	2			3	1		3							
12,440–12,450	25	23	26	tr	1		tr								5	11			1	4		3							
12,640–12,650	43	19	15	4	3	6	tr								4	6			tr			tr							

Table A7. *XRD data acquired from 52-21 core samples. Sample depths are shown in the first column (drillers depth). XRD data are given in weight percent of sample, with values rounded to the nearest whole number. Fields marked with tr (trace) indicate that this mineral is present, but represents less than 1 wt% of the sample, or that it was observed in the clay-size fraction but not the bulk pattern, and/or it was observed in thin section.*

52-21 Core Depth (ft)/ Sample ID	**Plagioclase**	**K-feldspar**	**Quartz**	**Biotite**	**Titanite**	**Hornblende**	**Apatite**	**Chlorite**	**Illite**	**Calcite**
3578-3583	46	6	40	6	tr	tr	tr	tr	tr	tr
GNS-5	25	5	66	3	tr	tr	tr	tr	tr	tr
GNS-6	35	4	58	3		tr	tr	tr	tr	tr
GNS-7	49	4	43	3	tr	tr	tr	tr	tr	tr

Table A8. *XRD data acquired from cuttings of well 52-21. Sample depths are shown in the first column (drillers depth). XRD data are given in weight percent of sample, with values rounded to the nearest whole number. Fields marked with tr (trace) indicate that this mineral is present, but represents less than 1 wt% of the sample, or that it was observed in the clay-size fraction but not the bulk pattern, and/or it was observed in thin section. Where possible, the composition of interlayered illite/smectite was determined based on a comparison of air-dried and glycolated clay-size fraction diffractograms and is indicated in the column "% illite in I/S."*

52-21 Cuttings Depth (ft)	**Plagioclase**	**K-feldspar**	**Quartz**	**Biotite**	**Titanite**	**Hornblende**	**Apatite**	**Clinopyroxene**	**Smectite**	**Interlayered Illite-Smectite**	**% Illite in I/S**	**Chlorite**	**Illite**	**Calcite**
230–240	41	32	14	1		3			tr			tr	8	
500–510	34	18	38	5	2	tr	tr		tr				3	
700–710	44	15	14	13	3	9	1		tr			tr	2	
1000–1010	49	13	11	11	2	5	1		tr			2	7	
1230–1240	46	14	11	12	3	9	1		tr			tr	3	
1490–1500	20	18	43	16	tr				tr			tr	3	
1790–1800	23	17	41	14	2				tr			3	tr	
2000–2010	33	10	46	7	tr	tr			tr			1	3	
2240–2250	17	12	47	19	2	1			tr			tr	2	
2490–2500	34	9	45	8					tr			tr	4	
2690–2700	32	16	43	3	tr				tr			1	4	
2990–3000	44	13	35	4	tr							tr	2	
3250–3260	51	9	32	5	tr				tr			tr	2	
3500–3510	48	7	37	4	tr		tr		tr			tr	2	
3730–3740	52	6	33	5	tr	1	tr		tr			tr	1	
3990–4000	49	12	34	3	tr							tr	1	
4240–4250	52	7	28	9	tr	2						tr	tr	
4520–4530	51	12	22	8	1	4	tr					tr	2	
4790–4800	48	4	9	9	1	25	1					tr	2	
4990–5000	46	23	21	4	tr	1			tr			1	3	
5290–5300	44	13	39	2		2			tr			tr	tr	
5490–5500	44	6	34	10	tr	4	tr		tr			tr	2	
5710–5720	53	7	15	4	tr	18	tr		tr			tr	tr	
5910–5920	36	29	29	4	tr	2			tr			tr	tr	
6210–6220	47	16	21	9	tr	2	tr					2	tr	2
6540–6550	40	22	26	7	tr	2	tr					tr	tr	
6740–6750	43	21	23	7	tr	1						tr	4	
6980–6990	39	16	31	6	tr	1			tr	tr	~90%	1	5	1
7260–7270	50	15	16	5	2	8	tr					tr	4	
7490–7500	35	7	42	14	tr							1	tr	

Table A9. *XRD data acquired from hand samples collected from outcrops in the Mineral Mountains by Mark Gwynn. Rock-type designation is based on mapping by Sibbett and Neilson (2017). XRD data are given in weight percent of sample, with values rounded to the nearest whole number. Fields marked with tr (trace) indicate that this mineral is present, but represents less than 1 wt% of the sample, or that it was observed in the clay-size fraction but not the bulk pattern, and/or it was observed in thin section. Where possible, the composition of interlayered illite/smectite was determined based on a comparison of air-dried and glycolated clay-size fraction diffractograms and is indicated in the column "% illite in I/S."*

Min Mtns Outcrop Sample ID	**Plagioclase**	**K-feldspar**	**Quartz**	**Biotite**	**Titanite**	**Hornblende**	**Apatite**	**Smectite**	**Chlorite**	**Illite**	**Calcite**
1 Tgr	32	38	25	1	tr				tr	2	tr
4 Ts	49	44	3	1	tr					2	tr
6A Tqm	32	28	35	1	tr					3	
7A Tgr	31	36	28	3	tr		tr			1	
7B Tgr	30	43	22	3	tr					2	
8 Xbg	35	25	26	10	1	tr	tr		1	1	tr
10 gd	32	38	24	1	tr					4	tr
11 gd	29	41	27	1						2	tr
12 hgn	34	25	24	2	tr	11	tr		tr	3	tr
13 Tgr	32	33	33	tr				tr		1	
14 Tg	53	30	5	5	1	1	tr			4	
15 Tbg	29	36	28	tr	tr		tr		2	4	
16 hgn	56	8	12	4	1	17	tr			tr	
17 Xbg	38	32	11	5	tr	11	tr			1	
18	37	29	5	2	tr		2	tr	11	10	3
19	33	29	32	2	tr			tr	1	3	
20	46	18	21	5	tr	6	tr	tr	1	1	

Appendix B: Representative photomicrographs of basin-filling lithologies encountered in Acord-1

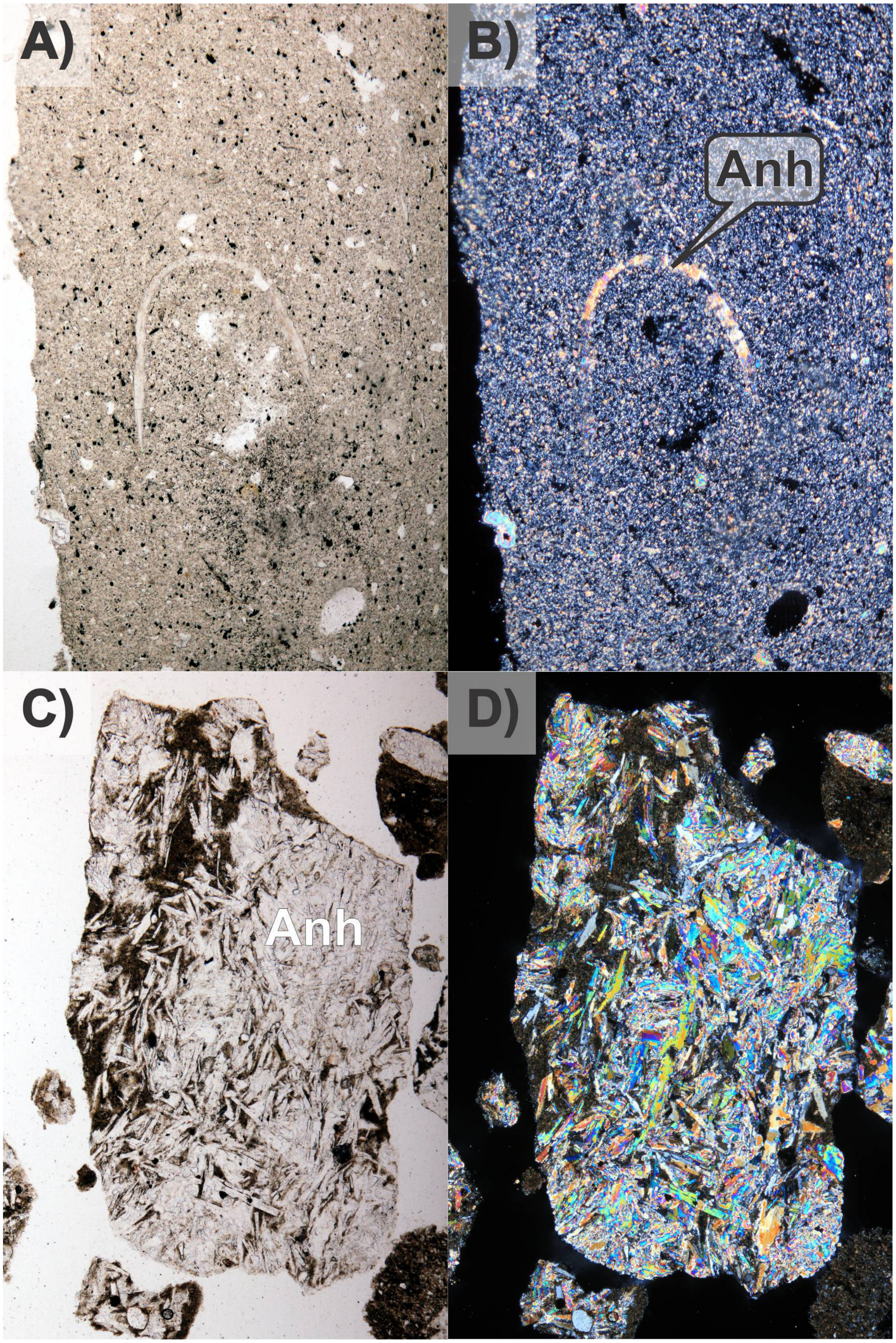

Figure B1. 320–350 to 4240–4250 ft: *Representative photomicrographs of lacustrine sediments and evaporite deposits.* ***(A&B)*** *Anhydrite replaced fossil in siltstone (1070–1100 ft). Vertical field of view is 1.6 mm.* ***(C&D)*** *Anhydrite laths in siltstone (3320–3350 ft). Vertical field of view is 3.2 mm.* ***(A&C)*** *are in plane-polarized light,* ***(B&D)*** *are in crossed-polarized light.*

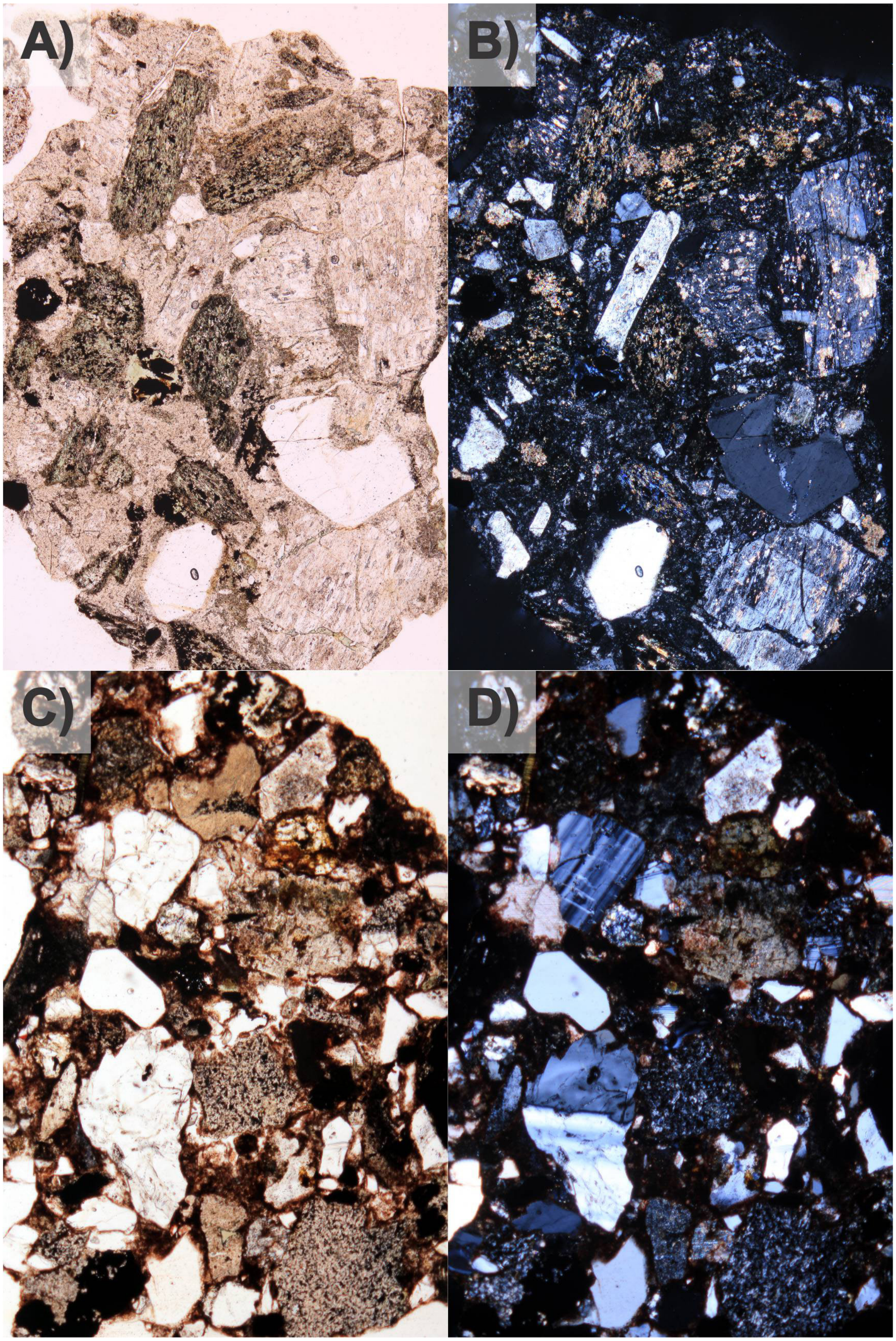

Figure B2. 4380–4400 to 5440–5450 ft: *Representative photomicrographs of alluvial deposits.* ***(A&B)*** *4840–4850 ft. Vertical field of view is 3.2 mm.* ***(C&D)*** *5240–5250 ft. Vertical field of view is 3.2 mm.* ***(A&C)*** *are in plane-polarized light,* ***(B&D)*** *are in crossed-polarized light.*

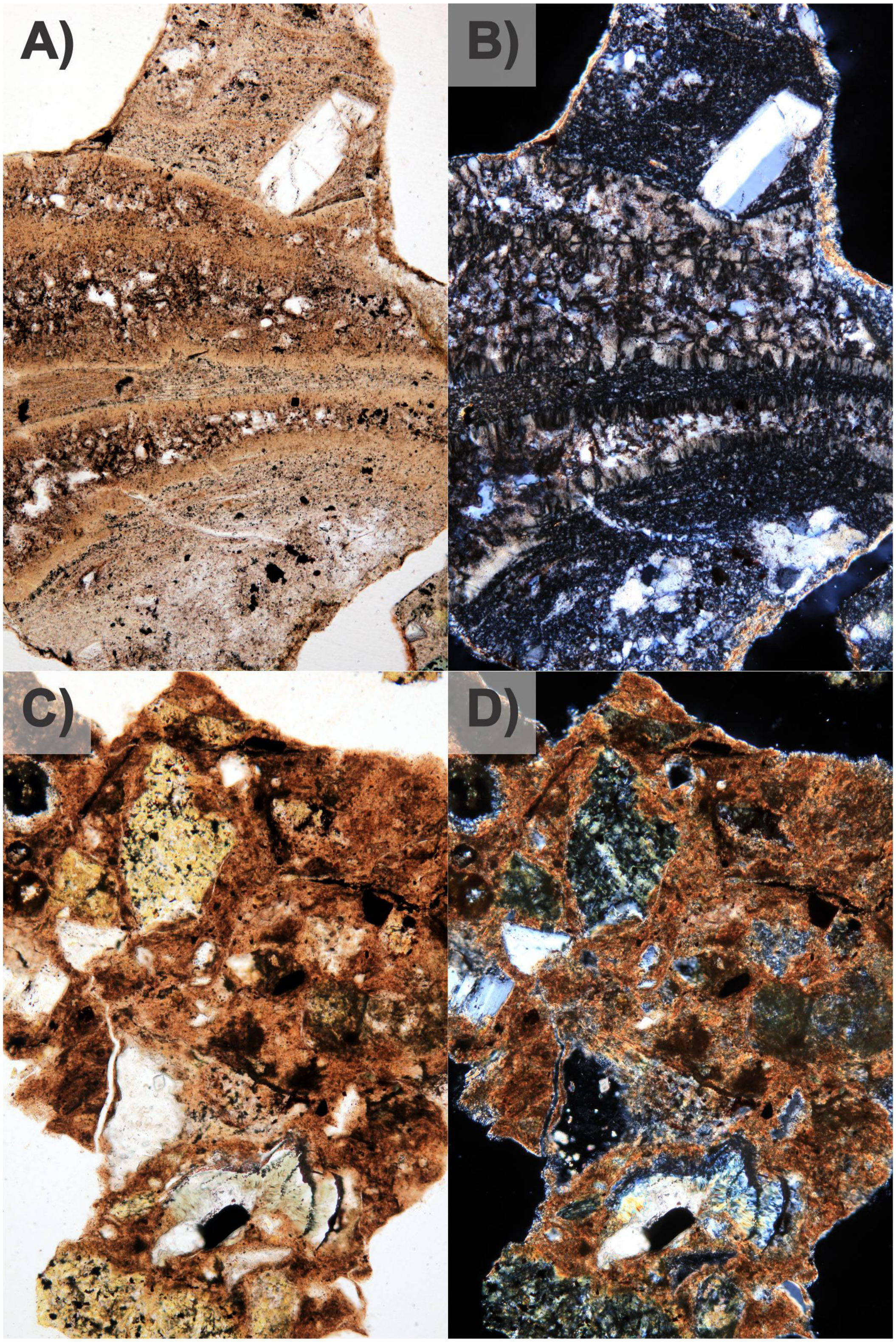

Figure B3. 5640–5650 to 6990–7000 ft: *Representative photomicrographs of rhyolite ash-flow tuff and tuffaceous sediments.* ***(A&B)*** *Devitrified ash-flow tuff with a sanadine phenocryst (5840–5850 ft). Vertical field of view is 1.6 mm.* ***(C&D)*** *Tuffaceous sediment (6040–6050 ft). Vertical field of view is 1.6 mm.* ***(A&C)*** *are in plane-polarized light,* ***(B&D)*** *are in crossed-polarized light.*

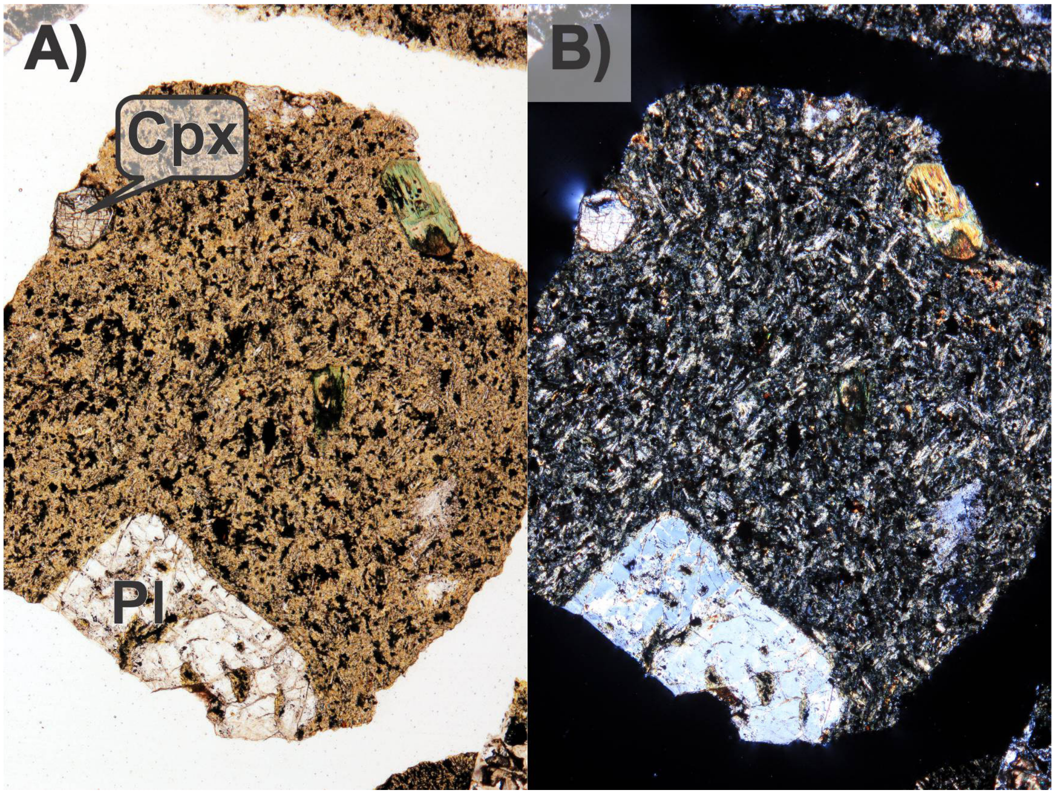

Figure B4. 7220–7250 to 7540–7550 ft: *Andesite flow with plagioclase (Pl) and clinopyroxene (Cpx) phenocrysts in a fine-grained groundmass (7540–7550 ft). Vertical field of view is 3.2 mm.* ***(A)*** *is in plane-polarized light,* ***(B)*** *is in crossed-polarized light.*

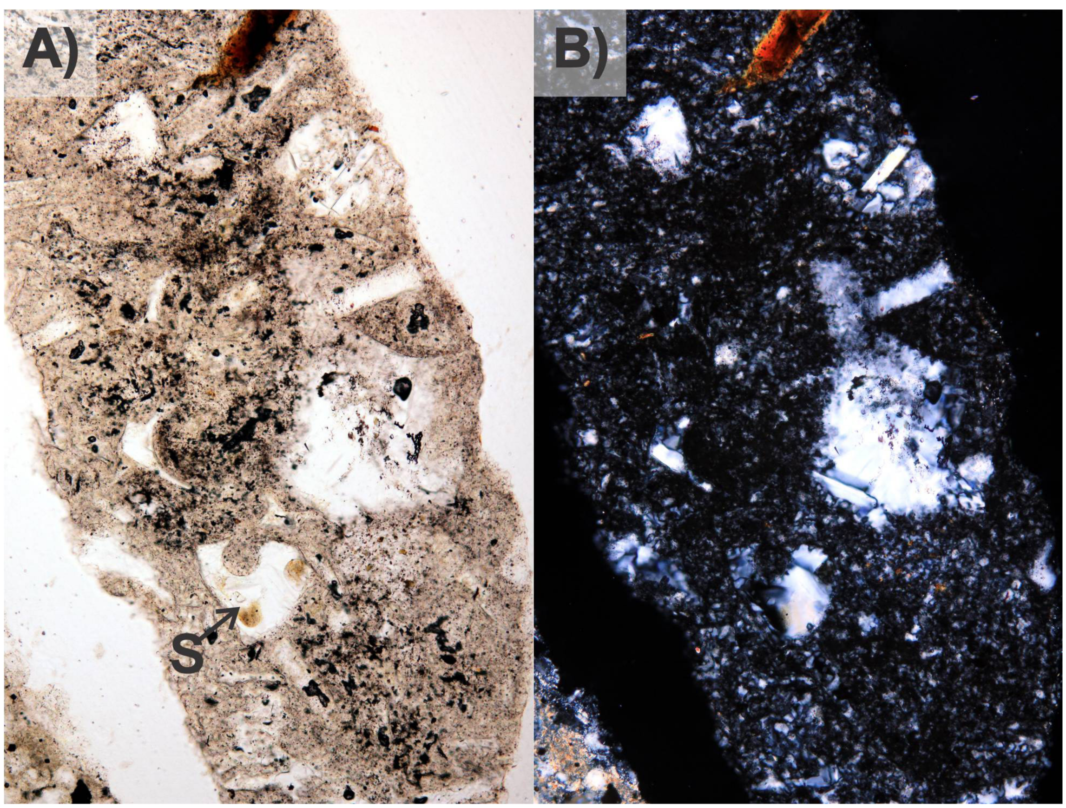

Figure B5. 7740–7750 ft: *Rhyolite ash-flow tuff devitrified shards (S) in a fine-grained matrix. Vertical field of view is 1.6 mm.* ***(A)*** *is in plane-polarized light,* ***(B)*** *is in crossed-polarized light.*

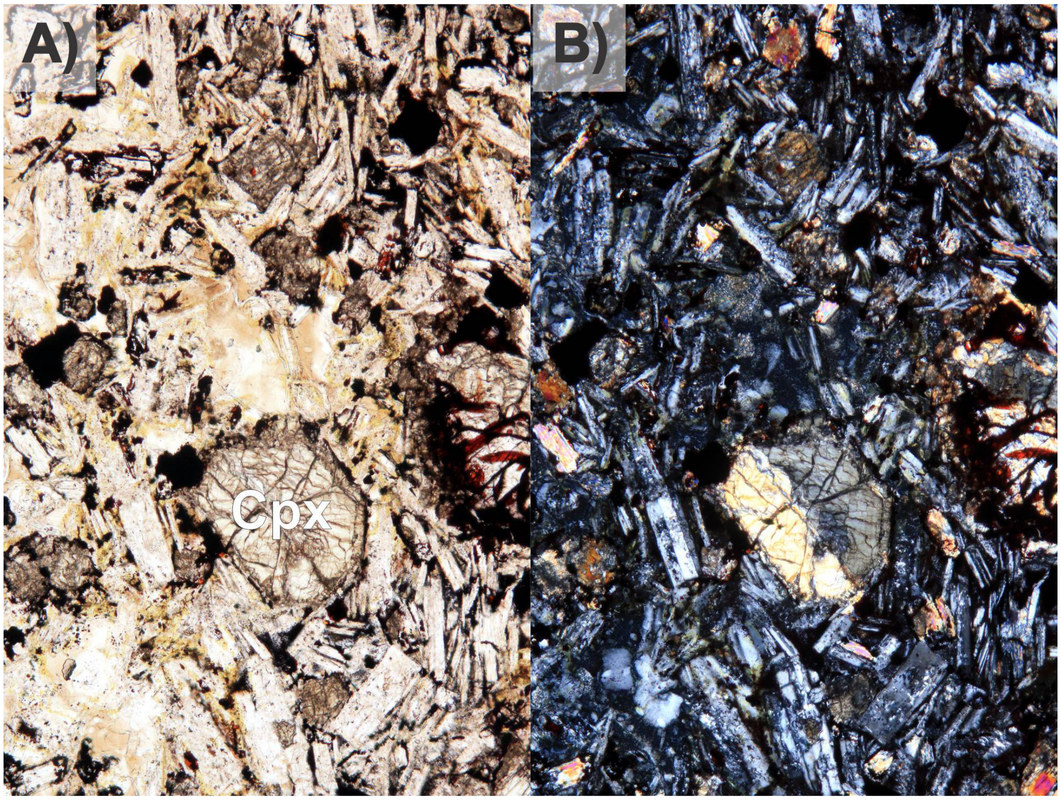

Figure B6. 7990–8000 ft: *Andesite flow with a clinopyroxene (Cpx) phenocryst in a groundmass of plagioclase laths. Vertical field of view is 1.6 mm.* ***(A)*** *is in plane-polarized light,* ***(B)*** *is in crossed-polarized light.*

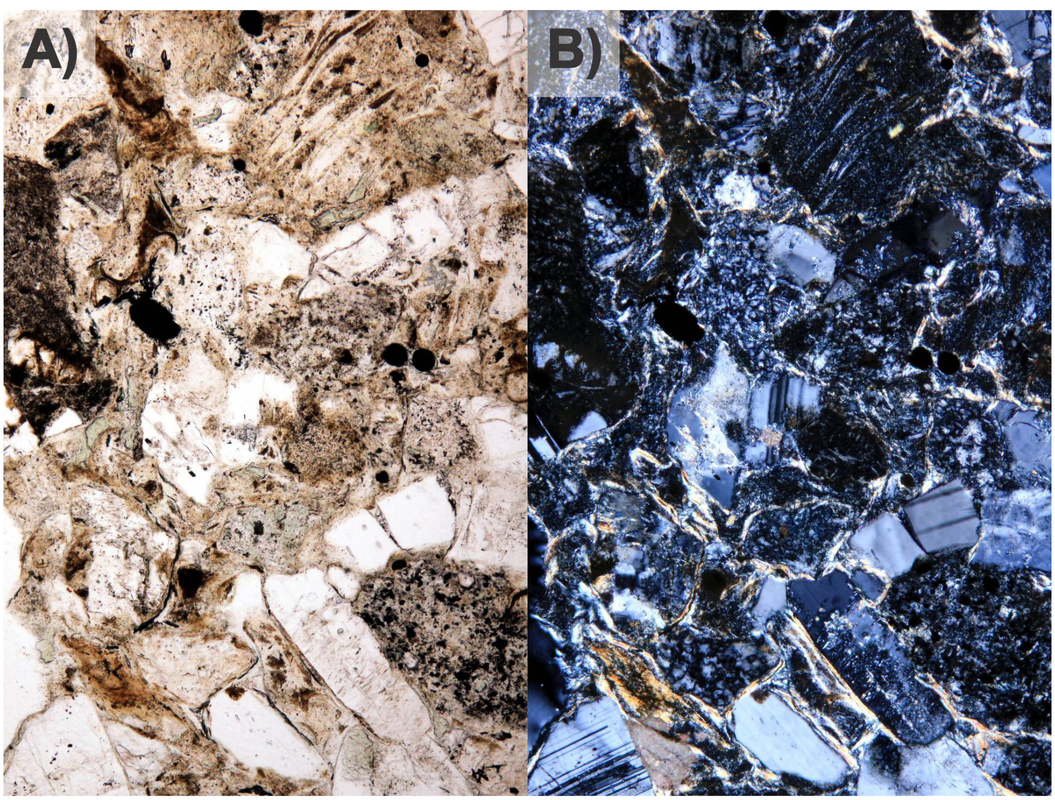

Figure B7. 8240–8250 to 8740–8750 ft: *Representative photomicrographs of volcaniclastic sandstone (8740–8750 ft). Vertical field of view is 1.6 mm.* ***(A)*** *is in plane-polarized light,* ***(B)*** *is in crossed-polarized light.*

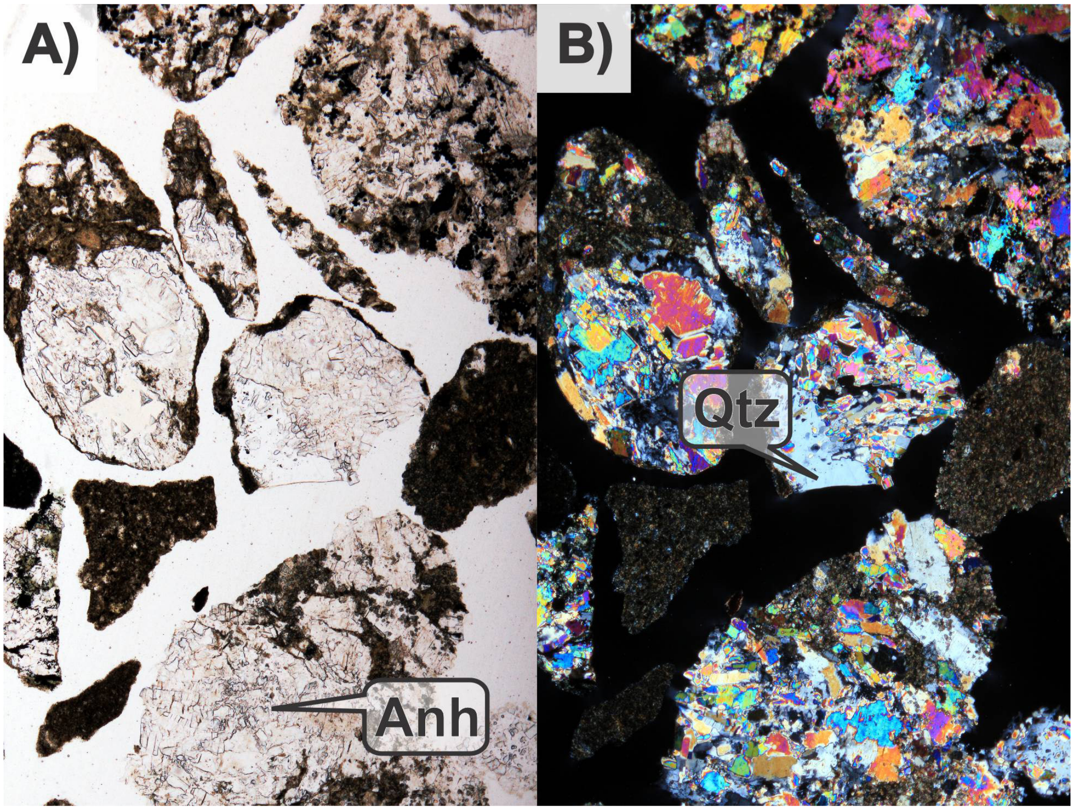

Figure B8. 8940–8950 to 9340–9350 ft: *Anhydrite nodules in siltstone 9340–9350 ft. This lithologic unit is composed of lacustrine and evaporite deposits. Vertical field of view is 3.2 mm.* ***(A)*** *is in plane-polarized light,* ***(B)*** *is in crossed-polarized light.*

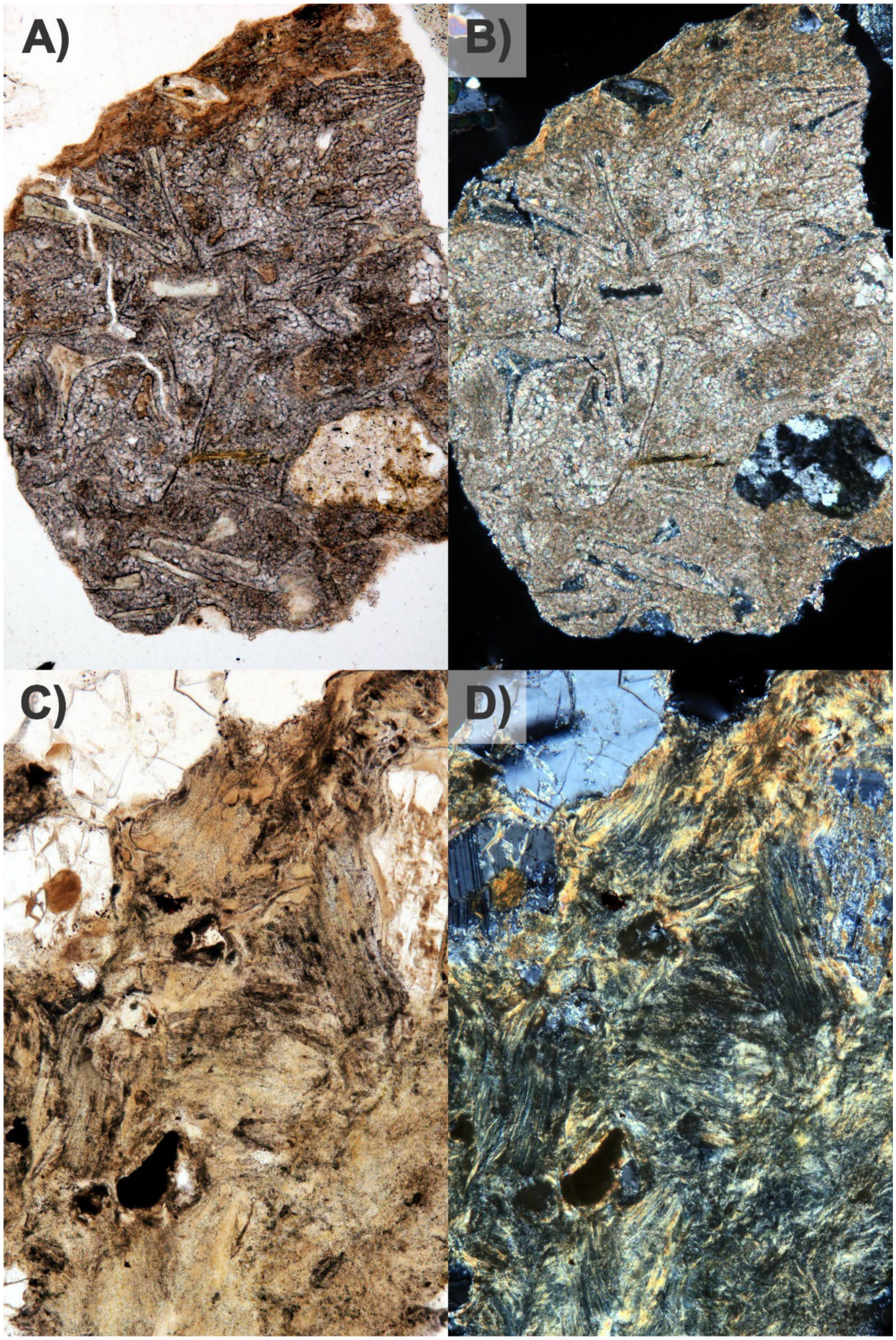

Figure B9. 9540–9550 to 10140–10150 ft: *Representative photomicrographs of rhyolite ash-flow tuff. This lithologic unit also contains tuffaceous sediments.* ***(A&B)*** *Shards in a carbonate matrix. Images of sample 9540–9550 ft. Vertical field of view is 3.2 mm.* ***(C&D)*** *Pumice (fiamme) textures in an ash-flow tuff. Images of sample 9940–9950 ft. Vertical field of view is 1.6 mm.* ***(A&C)*** *are in plane-polarized light,* ***(B&D)*** *are in crossed-polarized light.*

COMPILATION OF ROCK PROPERTIES FROM FORGE WELL 58-32, MILFORD, UTAH

by Mark Gwynn[1], Rick Allis[1], Christian Hardwick[1], Clay Jones[2], Peter Nielsen[1], and Will Hurlbut[1]

[1]Utah Geological Survey, Salt Lake City, Utah

[2]Energy & Geoscience Institute, University of Utah, Salt Lake City, Utah

Miscellaneous Publication 169-L
Utah Geological Survey
a division of
UTAH DEPARTMENT OF NATURAL RESOURCES

This paper is part of *Geothermal Characteristics of the Roosevelt Hot Springs System and Adjacent FORGE EGS Site, Milford, Utah*. https://doi.org/10.34191/MP-169

Bibliographic citation:

Gwynn, M., Allis, R., Hardwick, C., Jones, C., Nielsen, P., and Hurlbut, W., 2019, Compilation of rock properties from FORGE well 58-32, Milford, Utah, *in* Allis, R., and Moore, J.N., editors, Geothermal characteristics of the Roosevelt Hot Springs system and adjacent FORGE EGS site, Milford, Utah: Utah Geological Survey Miscellaneous Publication 169-L, 36 p., https://doi.org/10.34191/MP-169-L.

COMPILATION OF ROCK PROPERTIES FROM FORGE WELL 58-32, MILFORD, UTAH

by Mark Gwynn, Rick Allis, Christian Hardwick, Clay Jones, Peter Nielsen, and Will Hurlbut

ABSTRACT

Well 58-32 was drilled to a depth of 7536 feet in the Milford FORGE area during the summer of 2017 to confirm the reservoir characteristics inferred from over 100 existing wells and a wide variety of both new and legacy geologic and geophysical data. Drill cuttings were collected and described at 10-foot intervals and a robust suite of geophysical and image logs were run. Thermal conductivity, density, x-ray diffraction, magnetic susceptibility, and spectral gamma ray measurements were performed on the cuttings at least every 100 feet, and these analyses show that the basement rock within the FORGE area consists of a suite of intrusive rock types that are primarily granitic. Other mafic rock types were also encountered (mainly monzodiorite and a lesser volume of diorite), as was a significant volume of rock with a more intermediate composition. The laboratory analyses were used to calibrate gamma ray and density log responses, allowing foot-scale variations in rock type to be more accurately identified and interpreted throughout the well bore. Similar small-scale compositional changes can be seen in outcrop at many locations in the adjacent Mineral Mountains. The density of the granite and intermediate rock types typically ranges from 2.54 to 2.65 g/cm^3, but the higher gamma response of the granitic rock (140–290 gAPI) can often differentiate granitic compositions from intermediate compositions (70–210 gAPI). The higher density (2.65–2.90 g/cm^3) and lower gamma values (50–80 gAPI) of the dioritic compositions is more distinctive and greatly simplifies identification. The laboratory analyses and geophysical logs of the 58-32 well prove it was drilled into low porosity/low permeability intrusive rock with temperatures well within the U.S. Department of Energy-specified window of 175°–225°C. Despite small-scale compositional changes, the geomechanical characteristics throughout the reservoir zone are reasonably consistent and are suitable for testing the techniques and technologies required to develop enhanced geothermal reservoirs.

INTRODUCTION

Well 58-32 is the resource-proving well for the Milford Frontier Observatory for Research in Geothermal Energy (FORGE) project. The well was drilled in Section 32, Township 26 South, Range 9 West, Salt Lake Base Line and Meridian (SLB&M), in Milford Valley about 2 miles west of the Mineral Mountains (Figure 1). The 58-32 well was sometimes referred to as MU-ESW1 in earlier literature (Balamir and others, 2018). This report examines the physical properties of the rock in well 58-32 and several nearby wells to characterize the reservoir and to provide the criteria for recognizing intrusive rock-type variations using wireline logs in future FORGE wells. Many of the physical properties established in this report will provide a basis for the rock property assumptions required in future models and simulations of thermal, fluid flow, and geomechanical behavior.

The 58-32 well is located above the planned "toe" of the deviated wells that will be drilled in the final phase of the FORGE project. The Kenai Drilling crew, under the direction of Geothermal Resources Group, began assembling Rig 10 in late July and spudded the well at 23:30 on July 31, 2017 (Figure 2). A 17.5-inch bit was used to a depth of 342 feet, where 13-3/8-inch casing was set. A 12.25-inch bit was then used until 2180 feet was reached and 9-5/8-inch casing was set. Twelve 8.75-inch bits were then used to reach the final total depth (TD) of 7536 feet. Four temperature logs, run approximately 6 hours apart, were obtained at an intermediate depth of 6800 feet to ensure that the U.S. Department of Energy (DOE)-specified minimum temperature of 175°C would be met. A robust set of wireline logs and a Formation Micro-Imager (FMI) log were run from the shoe of the surface casing at 2173 feet to TD. The bottom of the hole was then filled with mud and gravel to protect the formation while 7-inch casing was run to 7378 feet and cemented. The shoe was subsequently drilled, and the hole was cleaned out, creating a 158 foot open-hole completion to facilitate a formation evaluation test. A second image log was then run to assess the results in the open-hole section after the formation evaluation test. Another temperature log was run 37 days after well completion to assess the near-equilibrium thermal regime prior to the end of the project phase in early 2018. A final temperature log was run slightly over one year later, during the next phase of the project, to assess the fully re-equilibrated formation temperature. Nadimi and others (2018) and Jones and others (2018, 2019) detail the formation evaluation testing, FMI logs, and the petrographic analyses of cuttings and core samples. Allis and others (2018a, 2018b) discuss the temperature logs and the FORGE thermal regime in detail.

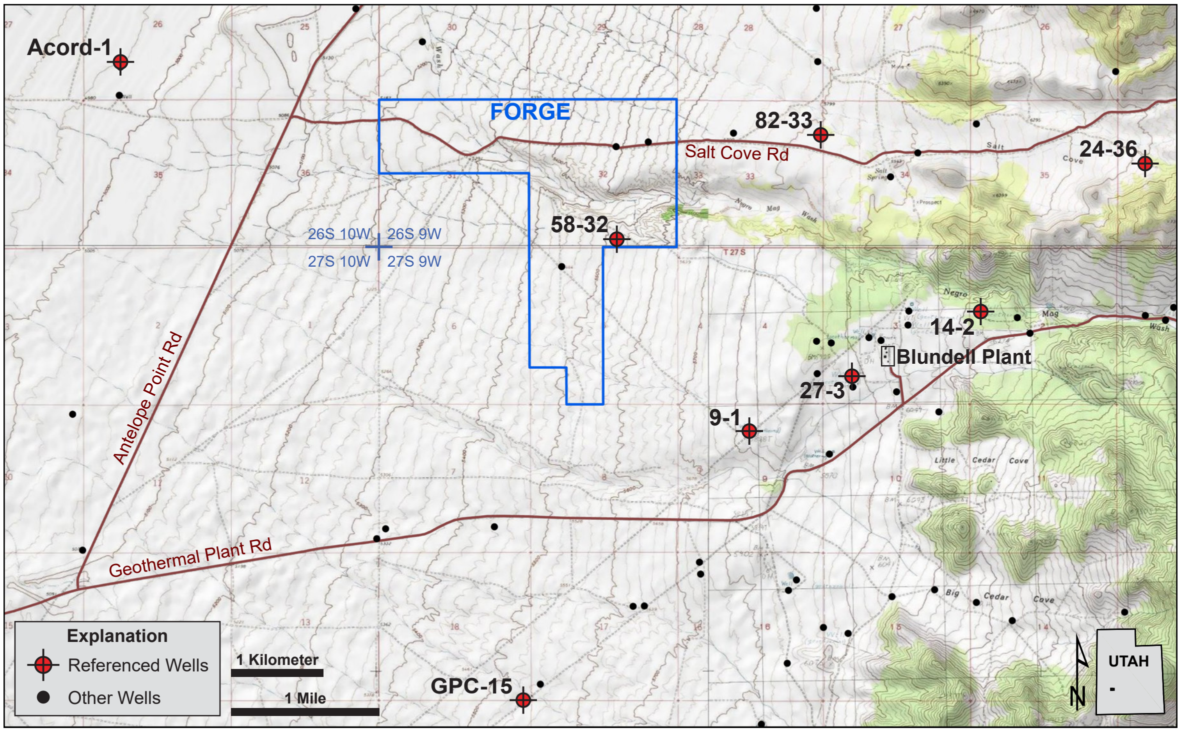

Figure 1. *Topographic base map showing the FORGE area and location of nearby wells. Well 58-32 was drilled as part of the FORGE program in the late summer of 2017. Other labeled wells are discussed in the text.*

Figure 2. *Kenai Rig 10 on the 58-32 well pad. Photograph taken on September 3, 2017, during the running of temperature logs at an intermediate depth of 6800 feet.*

FORGE WELL 58-32 DRILLING DATA

Drill Rate

The drilling rate greatly fluctuated in the near surface of the basin-fill section, sometimes approaching 1000 feet/hour for short durations, before decreasing through the rest of the section. The average drilling rate in the basin fill was 82 feet/hour. In the basement rock, below about 3176 feet, the drilling rate was less variable, and the average was around 14 feet/hour. In general, there was a steady decrease in drilling rate with increasing depth (Figure 3). However, some rate fluctuations were observed at many depths and the overall rate from about 4500 feet to TD slightly increased. Localized and sudden increases in drilling rate occurred at the transitions to smaller hole diameters (17.5-inch to 12.25-inch at 342 feet and 12.25-inch to 8.75-inch at 2180 feet). Some other increases can be correlated to changing out worn bits, as the worn bits often contributed to a decreasing trend in the drilling rate (all bit changes within a given size were in the lower part of the well where only 8.75-inch bits were used). Many other fluctuations, particularly those "spikes" of very short period (on the order of less than 10 feet of depth), may indicate small fracture zones, rock type variability, or other factors of diminishing effects. Other data show thin zones of differing rock types. Such zones may have had the greatest effect on localized drilling rates.

Weight on Bit

The trends shown for weight on bit (WOB) generally correlate to those of the drilling rate (Figure 3). The WOB occasionally exceeded 30,000 pounds in the basin-fill section, with an average of about 16,000 pounds. Weight on bit was much higher in the granitic basement section, sometimes exceeding 40,000 pounds, with an average of 28,000 pounds. The bottom part of the well, below about 4600 feet, required a much higher WOB to maintain optimal drilling rates. Weight on

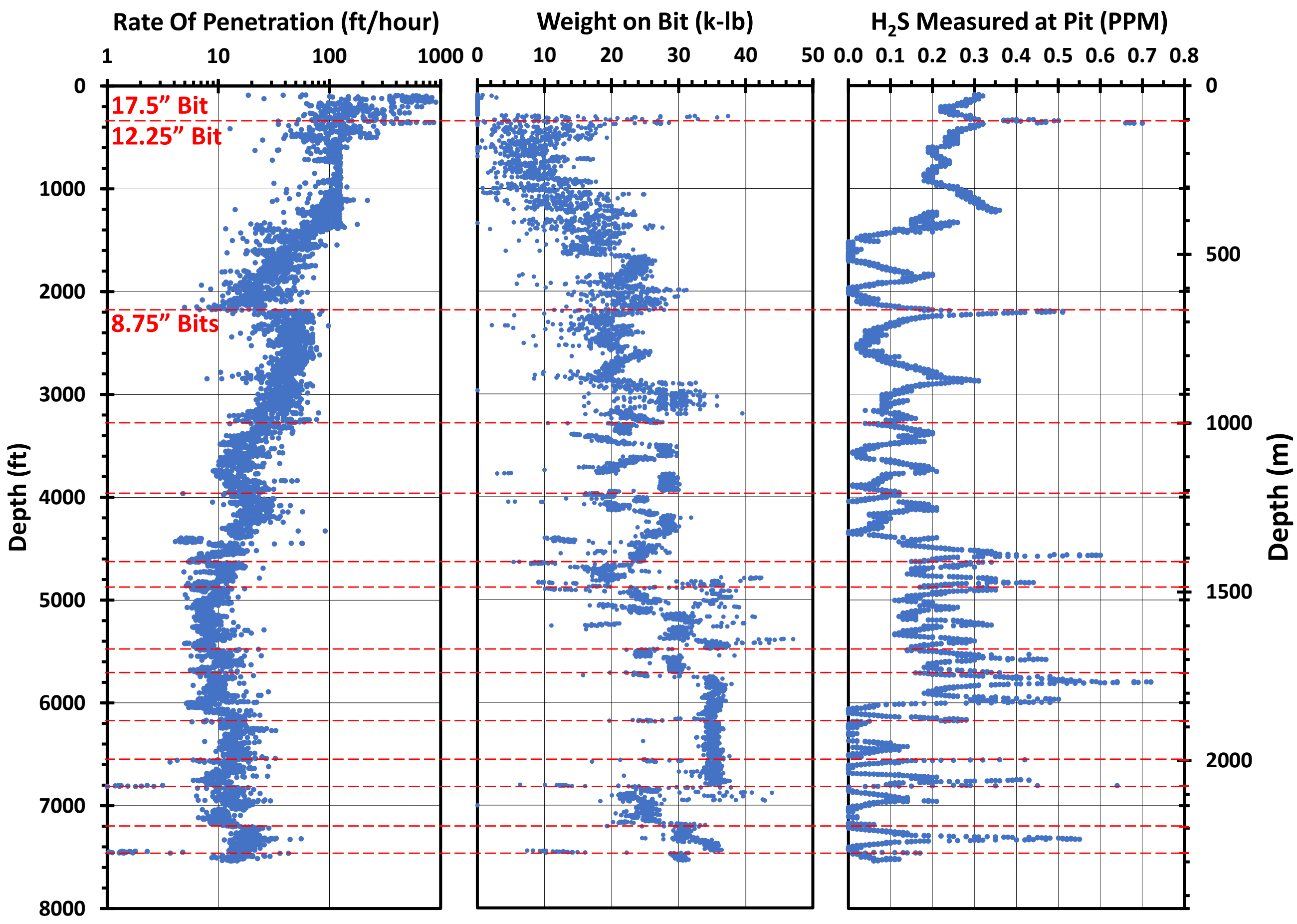

Figure 3. Drilling data consisting of the rate of penetration and the corresponding weight on the drill bit are shown in the two graphs to the left. Drilling rate was affected primarily by changes in bit size, bit condition, and rock type. The graph on the right shows the concentration of hydrogen sulfide (H_2S) gas detected in the pit. The concentration was well below safe limits and the spikes are typically related to periods of extended circulation without drilling, prior to deviation surveys or bit changes. Red dashed lines indicate bit changes except for short core intervals at 6800 feet and 7440 feet.

bit and rotational rate are major parameters that control the optimal drilling rate, although the use of a mud motor for much of the deeper drilling as well as the need to slide/rotate for directional control (keeping the wellbore relatively straight and vertical) are additional factors.

Hydrogen Sulfide

A low concentration of hydrogen sulfide (H_2S) gas was regularly detected in the cuttings pit, but the concentration was generally well below 0.5 parts per million (ppm) and never exceeded 0.73 ppm (the acceptable ceiling concentration for employee exposure is 20 ppm; OSHA, 2018). Hydrogen sulfide gas is a naturally occurring and colorless gas that can be trapped in sediments or dissolved in subsurface fluids, so it is commonly encountered during deep drilling operations (Cenovus Energy, 2014). Although drilling through fracture zones that contain H_2S can produce spikes, it appears that most of the spikes in Figure 3, particularly those with the greatest amplitudes, coincide with bit changes or periods of extended mud circulation (not active drilling) that allowed the H_2S concentration to build up. Additionally, fracture zones that could infuse the wellbore with H_2S might contribute to losses of drilling fluid, but no losses were recorded at any time during the drilling. Therefore, any fracture zones infusing H_2S gas into the wellbore are likely to have small apertures and poor connectivity. While localized increases in drilling rate may indicate fracture zones, they do not typically correlate with the H_2S spikes. A notable exception is the H_2S spike from about 7290 to 7360 feet. This interval was penetrated during a 12-hour period of continuous drilling and correlates with an increase in drilling rate. The FMI logs confirm that many moderately to steeply dipping fractures are present in this depth range, so it is possible that fractures in this zone were contributing H_2S. Because small quantities of H_2S are vented at the nearby Blundell geothermal plant (Figure 1), it is possible, though unlikely, that favorable wind conditions could artificially increase the detected concentration at the 58-32 well pad.

WIRELINE LOGGING DATA AND INTERPRETATIONS FROM EXISTING WELLS

Wireline logs from several existing wells were digitized and analyzed to help characterize the subsurface lithology in the FORGE area and provide insight to the lateral variability in rock properties. Examples for the Acord-1, 9-1, 14-2, and 82-33 well logs are shown in Figures 4 through 7 and well locations are shown in Figure 1.

Smoothed logs from the 82-33 and 9-1 wells (about 1.6 miles northeast and southeast of 58-32, respectively) reveal that several general rock types can be identified largely by characteristic responses of density and gamma log tools (Figures 8 through 10). In these cases, the gross lithology has been interpreted as granite, granodiorite, and diorite (or possibly monzodiorite), here called granitic, granodioritic, or dioritic. Granite will typically exhibit a high gamma response of around 150 gAPI or more and a density of about 2.67 g/cm^3. Granodiorite will have a density very similar to granite, but will show an intermediate gamma response of about 75–150 gAPI. In contrast, diorite will typically show low gamma responses of less than 75 gAPI and higher densities of around 2.8 to 3.0 g/cm^3. Sonic velocity also tends to be higher in diorite compared to the more granitic rock types, but also tends to increase with depth. Resistivity logs are less useful for identifying these intrusive rock types, but can reveal weathering and alteration zones.

The gross lithology identified at log-scale often fails to highlight small-scale, but significant, variations in rock type. For example, carefully examining the interval between 2300 and 2900 feet in the 9-1 well, which is well within the high density/low gamma "dioritic" zone, shows a large interval where the predominant diorite is interspersed with low density/high gamma granitic veins having thicknesses of less than about 30 feet, a uniform granite section of about 80 feet, and an interval that appears to be predominantly granodiorite that is about 40 feet thick (Figures 9 and 10). These small-scale variations can be seen in logs from many other wells and numerous outcrops where small intrusions of one or more rock types are present (Figure 11).

FORGE WELL 58-32 WIRELINE LOGGING DATA

Temperature Logs

Four temperature logs were run over a period of about 24 hours at an intermediate depth of 6800 feet prior to the first coring run. These logs were completed on September 3–4, 2017. A fifth logging run was made to the final TD of 7536 feet on November 2, 2017. A final logging run to TD was made on November 8, 2018. All temperature logging was accomplished by Di Drill Survey Services.

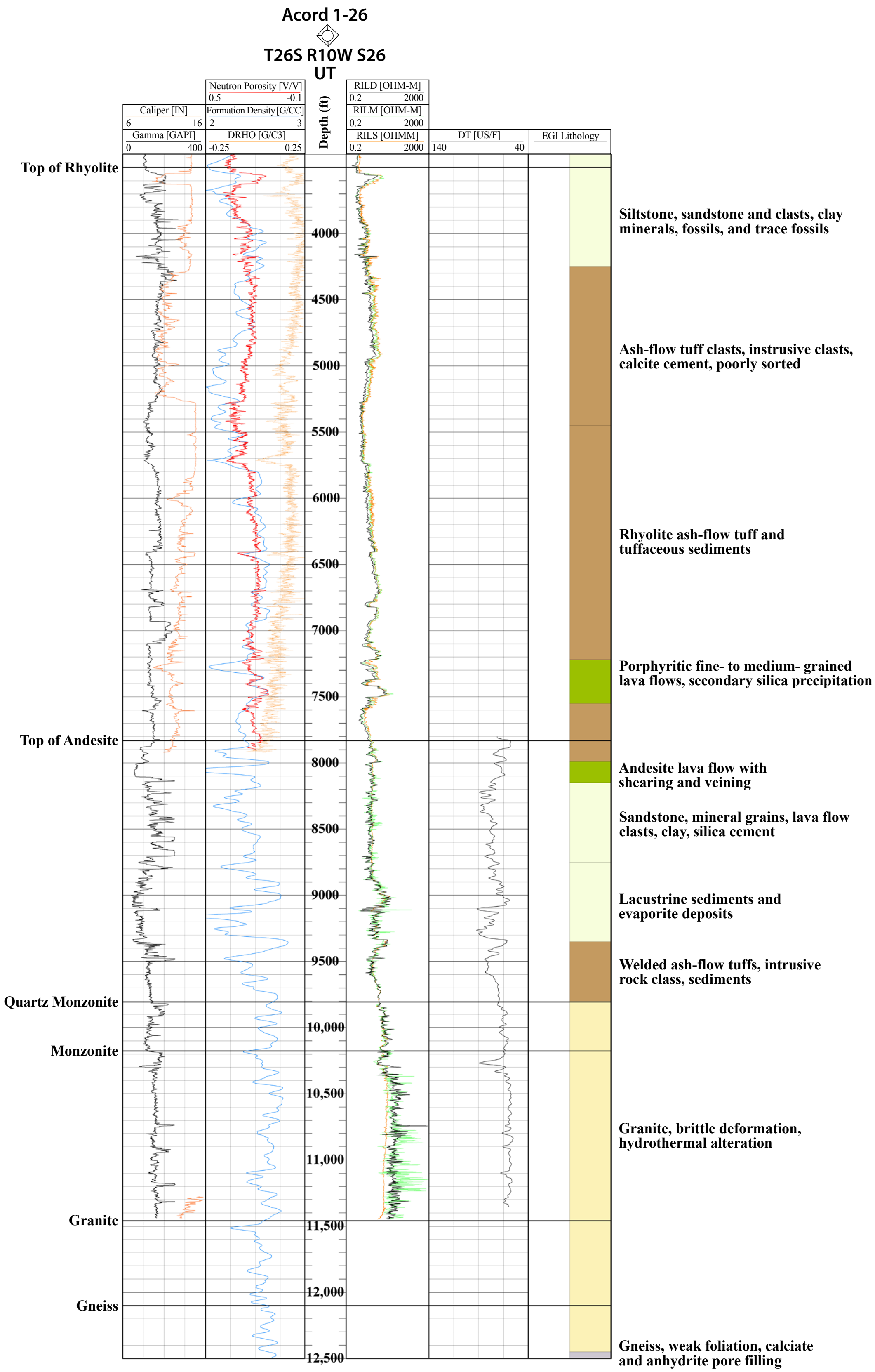

Figure 4. *Selection of wireline log responses for the Acord-1 well. "Caliper" indicates hole diameter, "Gamma" indicates natural gamma radiation, "Neutron Porosity" indicates rock porosity, "Formation Density" indicates rock density, "DRHO" indicates the quality of the density data, "RIL_" indicates rock resistivity, and "DT" indicates sonic properties of the formation. Interpreted lithology from x-ray diffraction and petrographic analyses (Jones and Moore, 2016) are shown on the right. Unlike other deep wells detailed in this report, Acord-1 has a thick sedimentary and volcanic sequence above the granitic basement.*

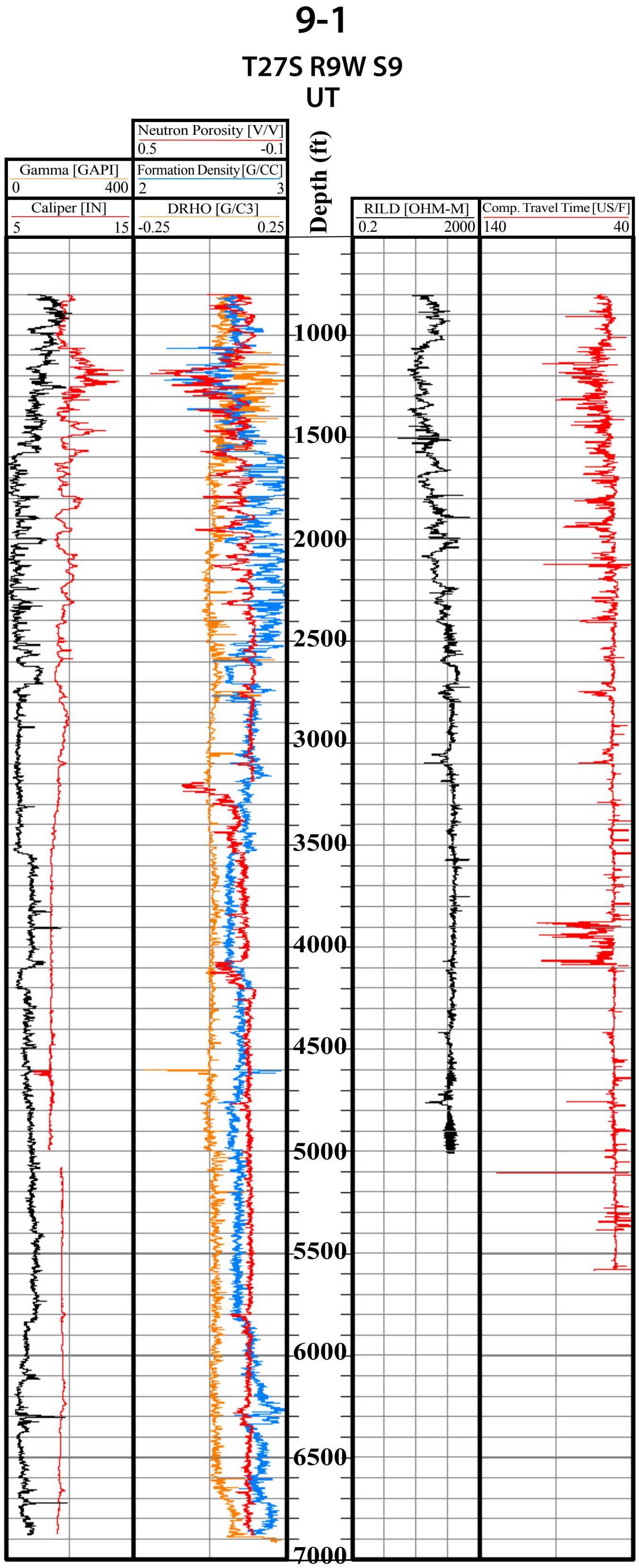

Figure 5. *Selection of wireline log responses for well 9-1. "Caliper" indicates hole diameter, "Gamma" indicates natural gamma radiation, "Neutron Porosity" indicates rock porosity, "Formation Density" indicates rock density, "DRHO" indicates the quality of the density data, "RILD" indicates rock resistivity, and "Comp Travel Time" indicates sonic properties of the formation. The gamma and formation density curves are the most useful for identifying intrusive rock types in the well. High gamma/low density responses are characteristic of granitic rocks while low gamma/high density responses are characteristic of dioritic rocks.*

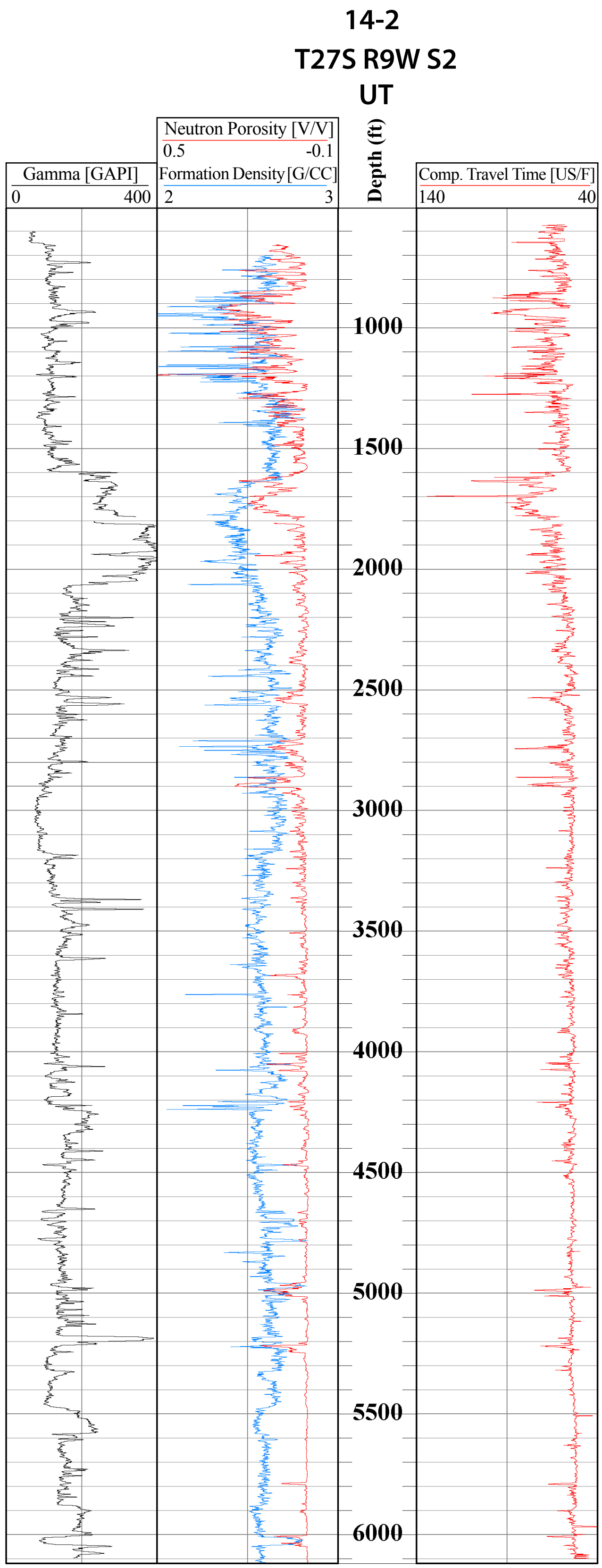

Figure 6. *Selection of wireline log responses for well 14-2. "Gamma" indicates natural gamma radiation, "Neutron Porosity" indicates rock porosity, "Formation Density" indicates rock density, and "Comp Travel Time" indicates sonic properties of the formation. The gamma and formation density curves are the most useful for identifying intrusive rock types in the well. High gamma/low density responses are characteristic of granitic rocks while low gamma/high density responses are characteristic of dioritic rocks.*

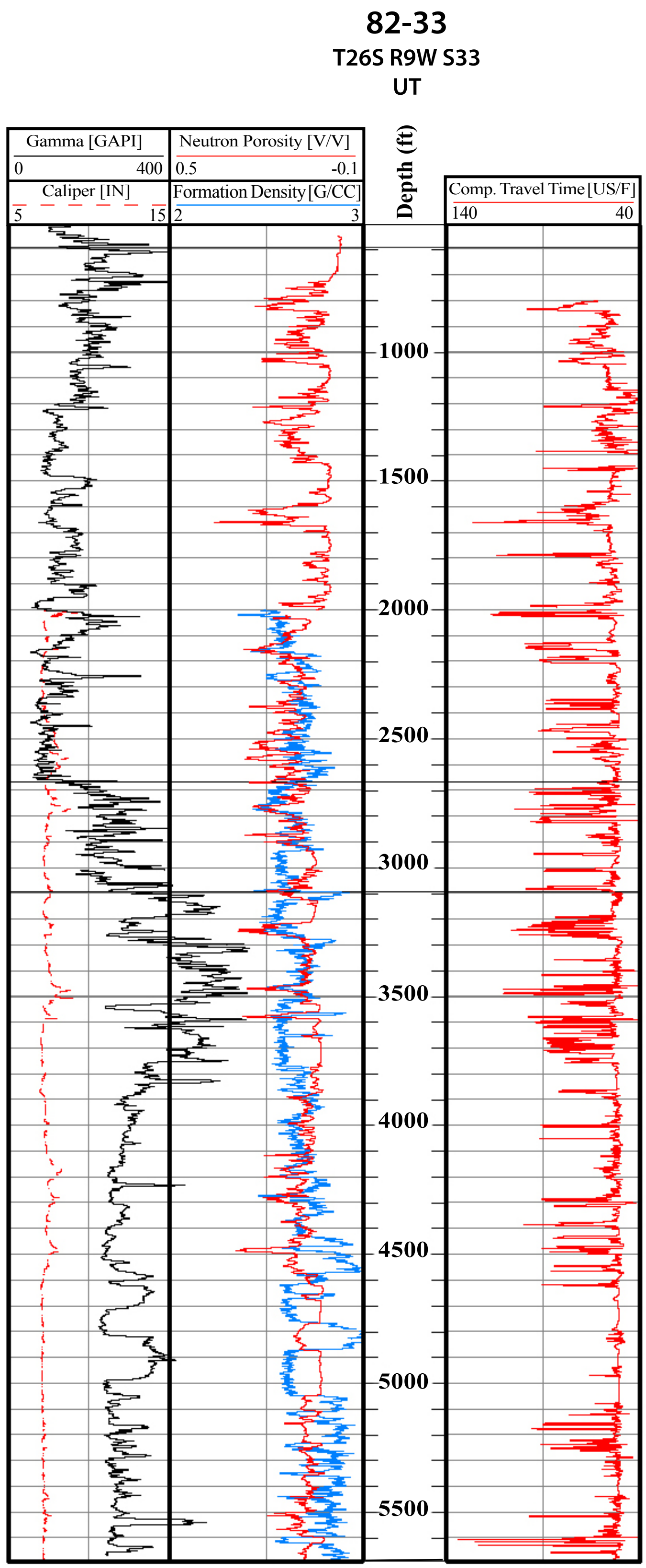

Figure 7. *Selection of wireline log responses for well 82-33. "Caliper" indicates hole diameter, "Gamma" indicates natural gamma radiation, "Neutron Porosity" indicates rock porosity, "Formation Density" indicates rock density, and "Comp Travel Time" indicates sonic properties of the formation. The gamma and formation density curves are the most useful for identifying intrusive rock types in the well. High gamma/low density responses are characteristic of granitic rocks while low gamma/high density responses are characteristic of dioritic rocks. Velocity logs are sensitive to borehole conditions, which is the cause of most of the "spikes" in the "Comp Travel Time" log.*

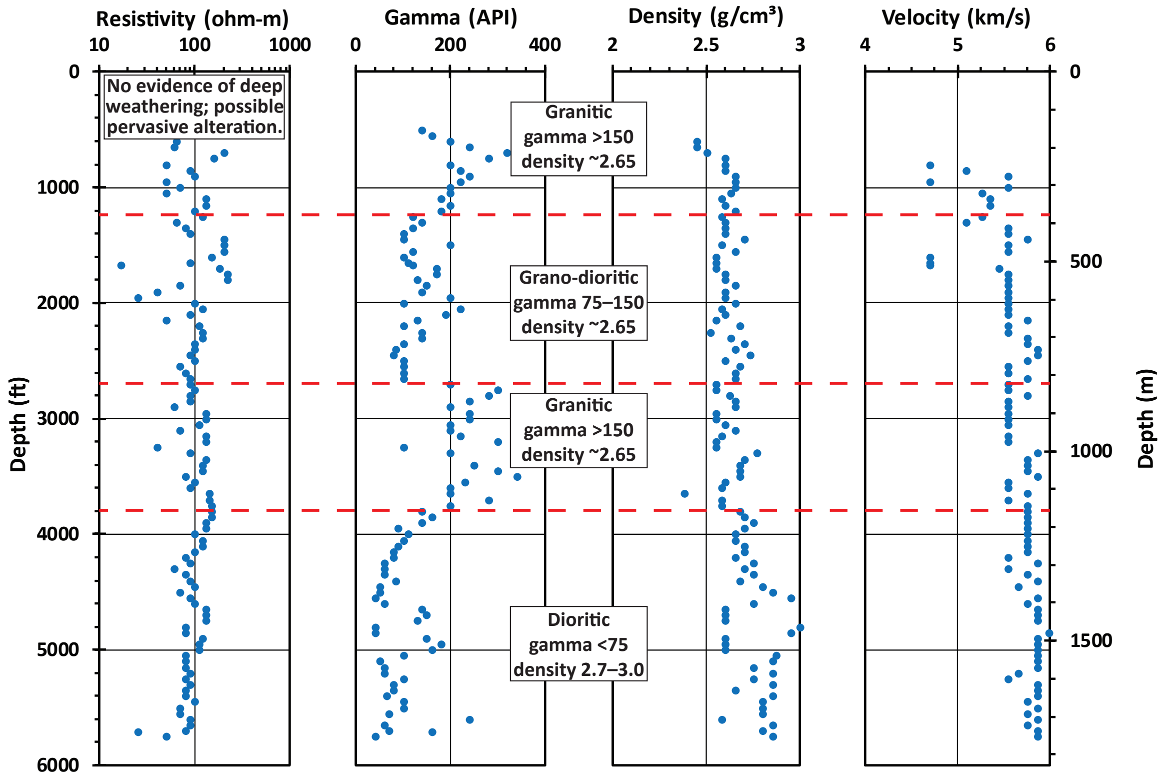

Figure 8. *Smoothed resistivity, gamma, density, and velocity log responses from well 82-33 located about 1.6 miles northeast of the 58-32 well. The well penetrated granite, granodiorite, and diorite that, outside of various analyses of cuttings or core, can typically be best identified by density and gamma logs.*

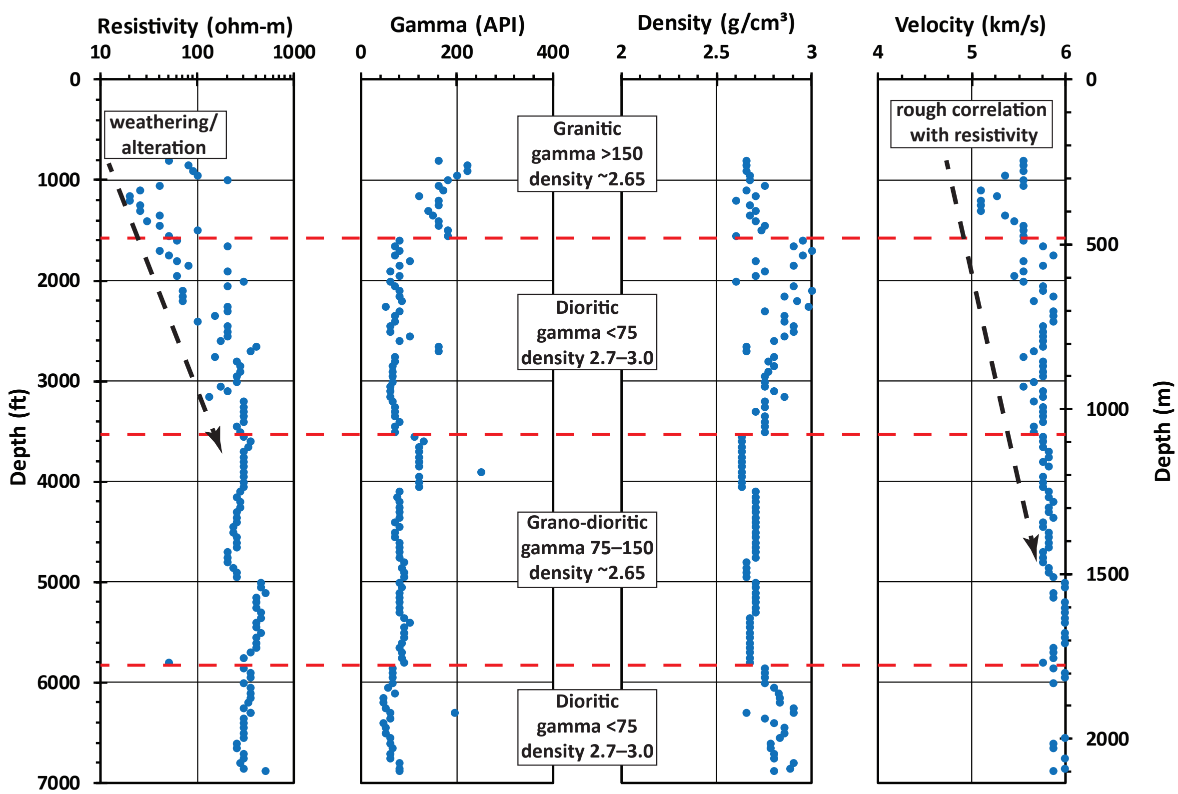

Figure 9. *Smoothed resistivity, gamma, density, and velocity log responses from well 9-1 located about 1.6 miles southeast of the 58-32 well. The well penetrated granite, granodiorite, and diorite that, outside of various analyses of cuttings or core, can typically be best identified by density and gamma logs.*

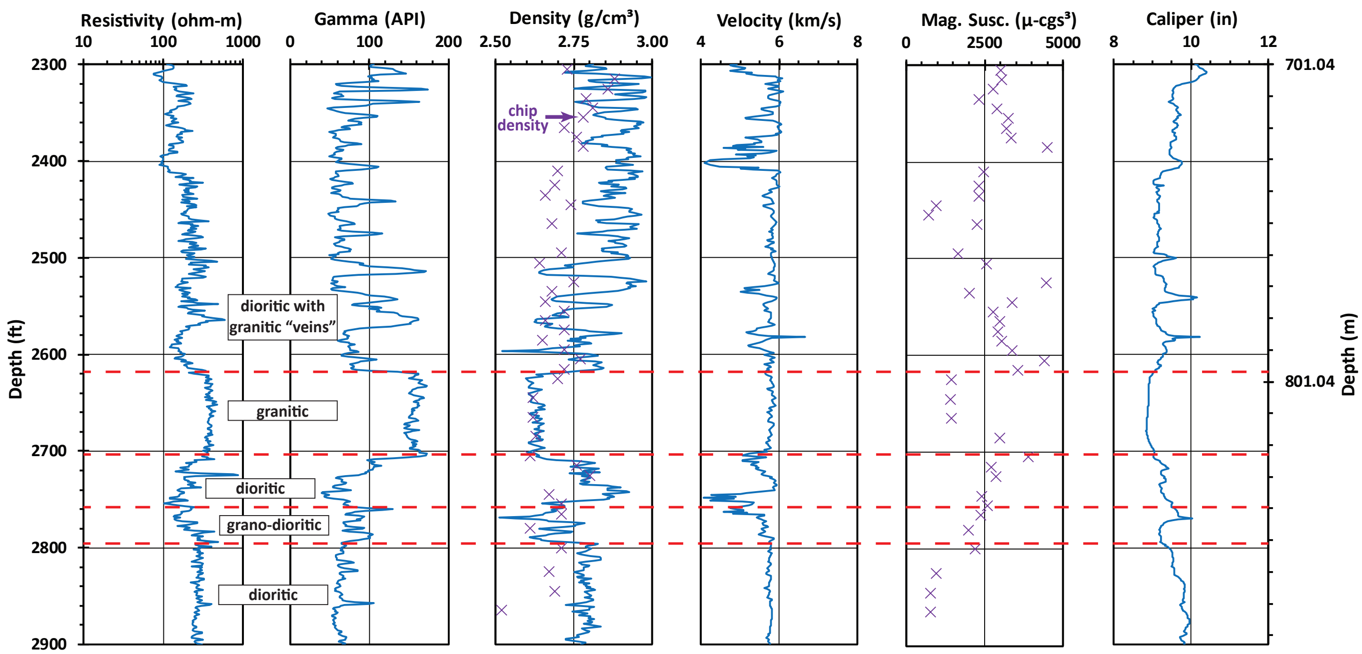

Figure 10. *Smoothed caliper, resistivity, gamma, density (logged and calculated from drill cuttings), sonic, and magnetic susceptibility (from cuttings) responses from a 600-foot section of well 9-1 (subset of "dioritic" interval on Figure 9). While this interval is located within a diorite zone, smaller veins and larger intervals of more granitic or granodioritic (intermediate) compositions are present. Increased magnetic susceptibility is generally correlative with more mafic (dioritic) compositions as these contain more iron-rich minerals.*

Figure 11. *Small-scale intrusions of lighter-colored granite and darker-colored diorite in an outcrop about 2.4 miles northeast of well 58-32. Similar small-scale lithologic variations can be seen at many other outcrop locations in the Mineral Mountains east of the FORGE site.*

The purpose of the first four runs (Figure 12) was to study the thermal recovery of the borehole to estimate the in situ formation temperature. This was necessary due to the thermal disturbance caused by drilling, particularly the circulation of relatively cool drilling fluids. Numerous studies have investigated the thermal effects of drilling, and some examples include Henrikson and Chapman (2002), Ascencio and others (2006), Goutorbe and others (2007), Edwards and Chapman (2013), and Gwynn and others (2014). Because the DOE requirements for FORGE specify a minimum resevoir temperature of 175°C (347°F) at 2 kilometers depth (6560 feet), it was important to estimate the equilibrium temperature at this depth (6800 feet) to ensure that suitable temperatures would exist at the final planned TD. Analysis of the temperature data from the 6800-foot runs suggested an equilbrium temperature of 181°C (358°F). The fifth run was accomplished after the wellbore was static for 37 days, allowing for a return to near-thermal equilibrium. The sixth, and final, temperature log was run after the well was static for over one year (408 days) to assess the undisturbed formation temperature. These logging runs confirm temperatures are suitable for the FORGE project (180°C at 2.0 kilometers and 199°C at the TD of 2.3 kilometers). Additional information on the thermal regime of the FORGE area is in Allis and others (2018a, 2018b).

Geophysical and Image Logging

Schlumberger wireline logs were run in the open-hole section of the well from the bottom of the 9-5/8-inch casing at 2173 feet to the total depth of 7536 feet on September 15, 2017. These logs included a FMI (image) log. A cement bond log was run on September 19–20, 2017, to assess the quality of the cementation of all the casing in the well. A second FMI run was made on September 24, 2017, to assess formation changes following a Diagnostic Fracture Injection Test (DFIT) in the open-hole segment below the 7-inch casing (see Nadimi and others, 2018). Figure 13 shows a selection of the wireline logs and the interpreted gross lithology from x-ray diffraction (XRD) data (Jones and others, 2018, 2019).

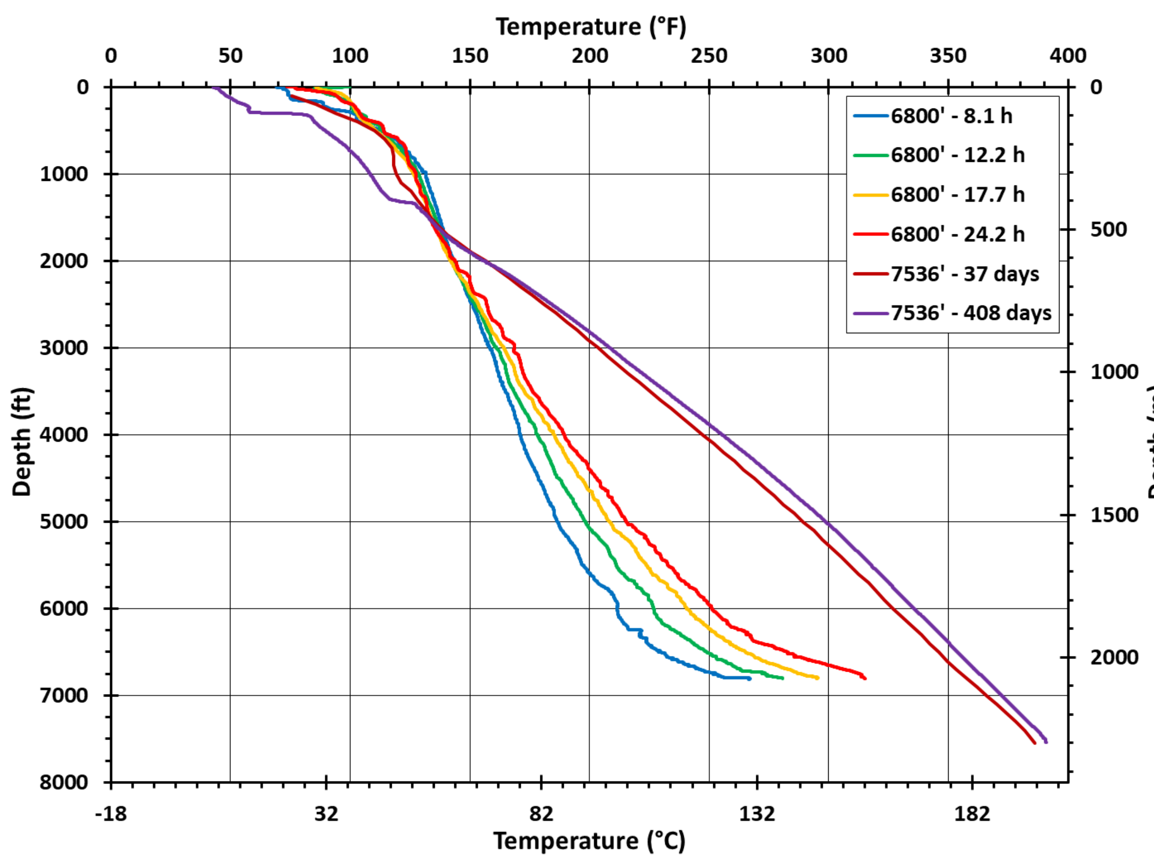

Figure 12. *Temperature-depth profiles from the four logging runs made while the bottom of the hole was at 6800 feet (September 3–4, 2017) and two additional runs to the final TD of 7536 feet (November 2, 2017 and November 8, 2018). The 6800-foot data were used to estimate an equilibrium temperature of 358°F (181°C) at this depth. The two runs to the final TD were made to obtain an initial assessment of the formation temperature after much of the drilling disturbance had been attenuated and then to determine the undisturbed formation temperature after the well had fully recovered. The final temperature at TD is 376 °F (191°C), well into the DOE-specified temperature-depth window. Cooler temperatures above 1300 feet shown in the 408-day log likely reflect groundwater flow.*

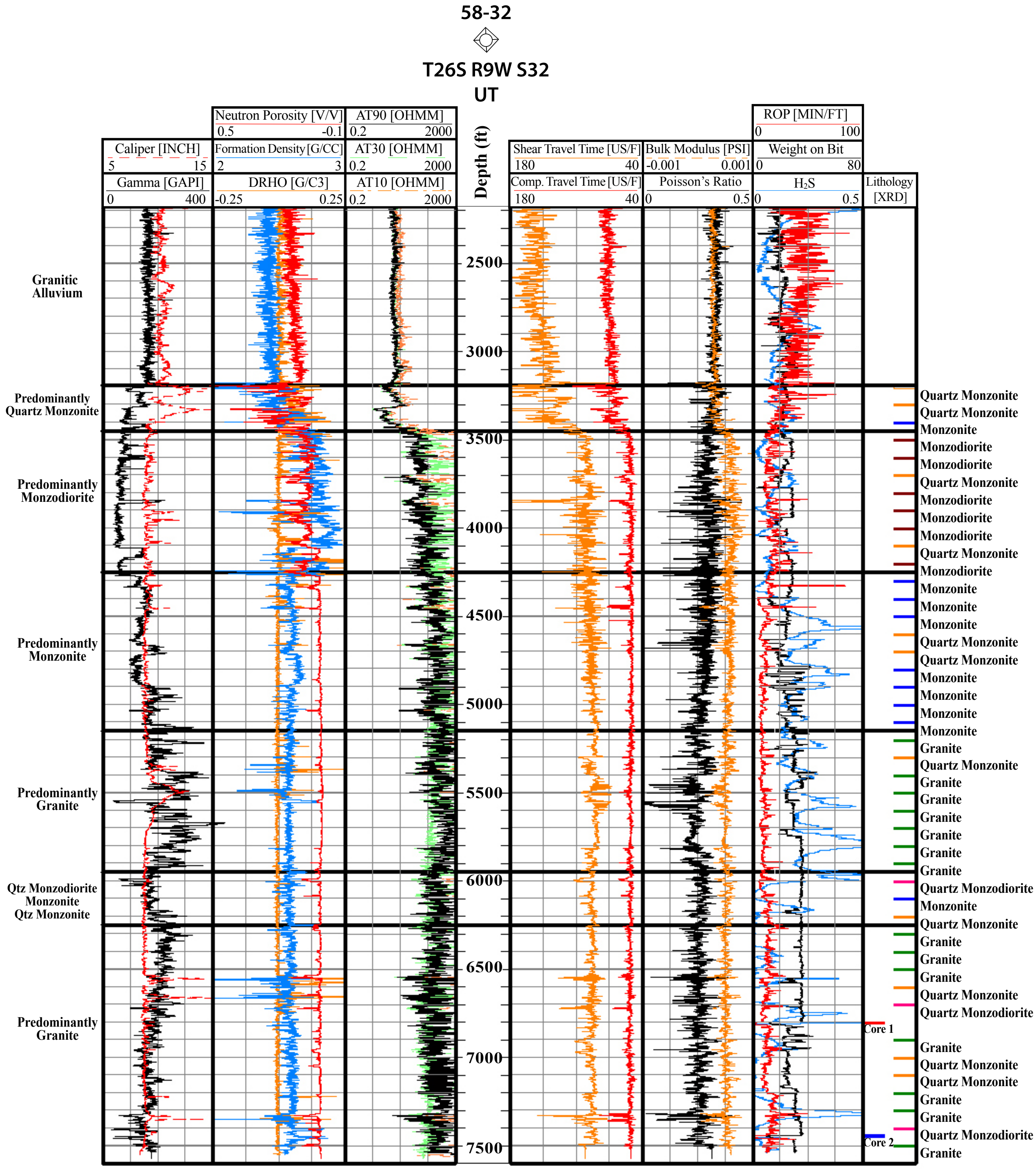

Figure 13. *Selection of wireline log responses for well 58-32 from the bottom of the surface casing at 2173 feet to TD. "Caliper" indicates hole diameter, "Gamma" indicates natural gamma radiation, "Neutron Porosity" indicates rock porosity, "Formation Density" indicates rock density, "DRHO" indicates the quality of the density data, "AT__" indicates rock resistivity, "Shear/Comp Travel Time" and "Poisson's Ratio" indicate sonic properties of the formation, "Bulk Modulus" is a measure of volumetric elasticity of the rock (a deformational characteristic), "ROP" and "Weight on Bit" indicate drilling parameters, and "H2S" is a measurement of hydrogen sulfide gas released from the formation while drilling. Rock-type "tops" on the left of the figure are defined primarily by XRD data (Jones and others, 2018, 2019) shown on the right. The gamma and formation density curves are the most useful for identifying intrusive igneous rock types. High gamma/low density responses are characteristic of granitic rocks while low gamma/high density responses are characteristic of dioritic rocks.*

FORGE 58-32 DRILL CUTTINGS AND CORE

Drill cuttings were collected at 10-foot intervals from 100 to 7500 feet (except for 6800 feet where the first core segment was obtained) by mud loggers from West Coast Geologic. Drilling fluids were rinsed from the samples, which were then bagged and dried. Two sets of samples were prepared; one set was sent to the Energy & Geoscience Institute at the University of Utah (EGI) and the other to the Utah Geological Survey (UGS). Thermal conductivity, density, spectral gamma, magnetic susceptibility, XRD, and optical analyses were performed on the samples at 100-foot intervals and some intermediate depths. Additional analyses were performed on core samples from 6800–6810.5 feet and 7440–7452 feet. Rock types determined from XRD and optical analyses are considered “ground truth” for this report and are shown or referenced in many figures herein.

Thermal Properties

Future modeling of the thermal-mechanical-fluid flow characteristics beneath the FORGE site will require knowledge of the thermal properties of the granitic host rock. Thermal properties such as thermal conductivity, specific heat, thermal diffusivity, and heat generation require laboratory measurements. Such measurements were performed on the core and selected cuttings recovered from the 58-32 well. Selected samples of outcropping bedrock from the adjacent Mineral Mountains were also collected for comparison with the 58-32 samples. The outcrop samples spanned a range of rock types based on the geologic maps of Sibbett and Nielson (2017) and Kirby and others (2018). X-ray diffraction analyses by Jones and others (2018, 2019) suggest some differences in rock types from those mapped by Sibbett and Nielson (2017).

Thermal Conductivity

Thermal conductivity measurements were made on the drill cuttings using divided bar-type equipment calibrated with fused quartz and water standards (see Allis and others, 2018a). The calibration checks showed that instrument accuracy was ±5%. The measurement cells were filled with the granular cuttings, then the air was removed under vacuum and the sample was saturated with water. Each cell was tested on each stack of the divided bar at least once, resulting in a minimum of two measurements per sample. The matrix thermal conductivity for the samples was then calculated after correcting for the mass of water in the measurement cells. The in situ thermal conductivity (at 25°C) was then calculated using porosity values from wireline logs (Gwynn and others, 2018). Both corrections used the geometric relationship for mixtures:

$$K_{mix} = K_1^{v1} \times K_2^{v2}$$

where: K is the thermal conductivity of the mixture and the two components, and v is the fractional volume of each component. Repeat measurements suggest that uncertainty is ±10%. Figure 14 shows the values and the differences between the matrix thermal conductivity and the corrected in situ (bulk) thermal conductivity.

Thermal conductivity was also measured on solid “pucks” cored and slabbed from the outcrop and well 58-32 core samples. The matrix density of the samples was calculated as part of the thermal conductivity measurements. Table 1 summarizes the results of the analyses on the outcrop samples.

Quartz has a relatively high thermal conductivity compared to many other silicate minerals, so plotting matrix thermal conductivity against weight percent quartz (Figure 15) reveals a linear relationship and two clusters of data. The low thermal conductivity cluster (2.1–2.6 W/m°C) occurs where quartz content is below 10% and corresponds to monzonite and monzodiorite compositions. The high thermal conductivity cluster (2.4–4.0 W/m°C) occurs where quartz content is above 13% and corresponds to more granitic compositions. The best-fit trendline through all the data extrapolates to a 100% quartz value of 7.5 W/m°C. This value is close to the 7.69 W/m°C average reported by Horai and Simmons (1969). Crystalline quartz can have a wide range of values but is often cited as ranging from 6 to 10 W/m°C, depending on crystal orientation (Birch and Clark, 1940; Robertson, 1988; Whittington and others, 2009).

The correlation between thermal conductivity and quartz content by depth and rock type is shown in Figure 16. Quartz content and thermal conductivity are relatively high (mainly around 18%–32% and 2.8–3.5 W/m·K respectively) in the alluvial section (above about 3200 feet), suggesting a granitic source. Values decrease to less than 12% quartz and thermal conductivities of less than 2.6 W/m·K in the zones characterized by more mafic rock (mainly monzodiorite). Thermal conductivity and quartz content increases again in the granite zone (19%–36% and 3.1–3.4 W/m·K), before decreasing in the (primarily) granitic-intermediate rock in the bottom section of the well.

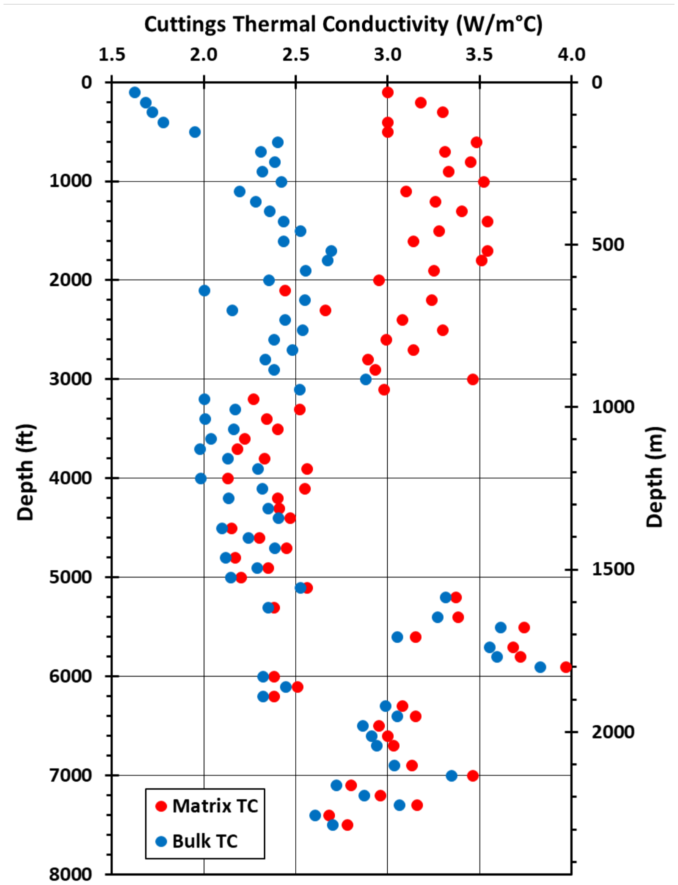

Figure 14. *Thermal conductivity data for well 58-32 based on cuttings measurements. Matrix thermal conductivity values are corrected for the effects of rock porosity using wireline geophysical logs (Gwynn and others, 2018). The variation in thermal conductivity is largely due to the quartz content of the rock. The transition from granitic basin fill to granitic bedrock occurs at about 3176 feet (Allis and others, 2018a).*

Specific Heat

Specific heat was measured with a calorimeter calibrated with water and fused quartz standards. Selected samples of cuttings and core from the 58-32 well were heated to 72°C and immersed in water at room temperature. The resulting temperature rise was measured with accuracy better than ±0.01°C. The measurement uncertainty was 0.08 kJ/kg°C, equating to about 10%. Measurements ranged between 0.7 and 1.0 kJ/kg°C. Specific heat typically increases from about 0.7 to 1.0 kJ/kg°C between 25° and 200°C (Whittington and others, 2009).

Thermal Diffusivity

Values determined from the thermal conductivity and specific heat measurements were used to calculate thermal diffusivity of the selected samples. This was done using the relationship:

$$\propto = \frac{K}{\rho \times \mathrm{c}}$$

where: $\propto$ is the thermal diffusivity, K is thermal conductivity, ρ is density, and c is specific heat. Values range from 0.7 to 1.7 mm^2/s, with an uncertainty of 15% (measurements at 25°C). Recent measurements suggest the typical crustal rock thermal diffusivity decreases from about 1.7 to 1.0 between 25° and 200°C (Whittington and others, 2009). Table 2 summarizes the results of these analyses.

Both thermal conductivity and thermal diffusivity decrease with increasing temperature. Based on the range of measurements shown in Figures 14, 15, and 16, and measurements of eastern U.S. granites at various temperatures (Robertson, 1988), the reservoir thermal conductivity will be about 15% lower than the laboratory measurements at room temperature.

Table 1. *Thermal conductivity and density measurements on outcrop samples from the Mineral Mountains (measurements at 25°C). T, Tertiary; Q, Quaternary; gr, fine-grained granite; rf, rhyolite flow; s, syenite; qm, quartz monzonite; Xbg, Precambrian banded gneiss; gd, granodiorite; hgn, hornblende gneiss; bg, biotite granite; d, hornblende biotite diorite; hd, hornblende granodiorite.*

Sample	Mapped Unit*	Thermal Conductivity (W/m°C)	Dry Density (g/cm^3)	Saturated Density (g/cm^3)	Porosity (%)
OC1	Tgr	2.75	2.54	2.56	2
OC2	Qrf	1.32	2.05	2.14	9
OC3	Qrf	1.49	2.12	2.21	9
OC4	Ts	2.10	2.50	2.53	3
OC6A	Tqm	3.21	2.54	2.56	2
OC7A	Tgr	2.66	2.59	2.60	1
OC7B	Tgr	2.42	2.50	2.53	3
OC8	Xbg	2.38	2.62	2.64	2
OC10	gd	3.01	2.53	2.55	3
OC11	gd	2.76	2.55	2.57	2
OC12	hgn	2.16	2.63	2.65	2
OC13	Tgr	2.64	2.55	2.57	2
OC14	Tgr	2.07	2.50	2.54	4
OC15	Tbg	2.69	2.55	2.58	3
OC16	hgn	2.24	2.66	2.68	2
OC17	Xbg	2.19	2.66	2.68	2
OC18	Td	1.75	2.70	2.73	3
OC19	Tqm	2.93	2.59	2.60	1
OC20	hd	2.30	2.69	2.70	1

*Sibbett and Nielsen (2017)

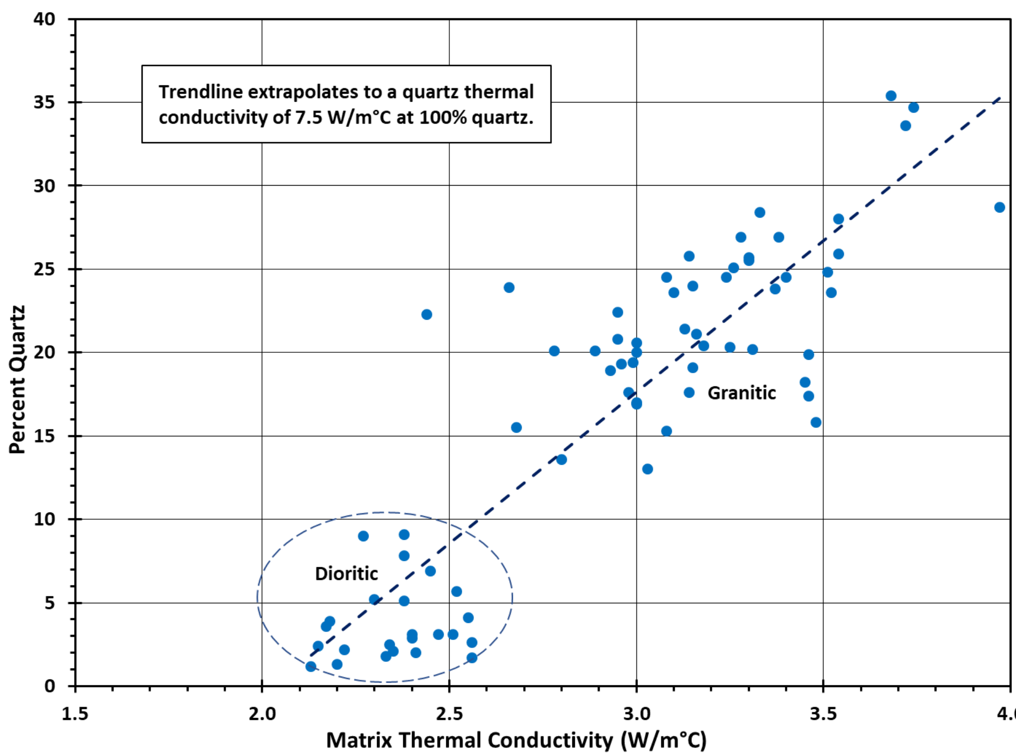

Figure 15. *Cross-plot showing the relationship between quartz content and matrix thermal conductivity in well 58-32 cuttings. The more-dioritic cuttings contain less quartz and therefore have lower thermal conductivity values than the more-granitic cuttings. The best-fit trendline projects to a thermal conductivity of 7.5 W/m°C for 100% quartz.*

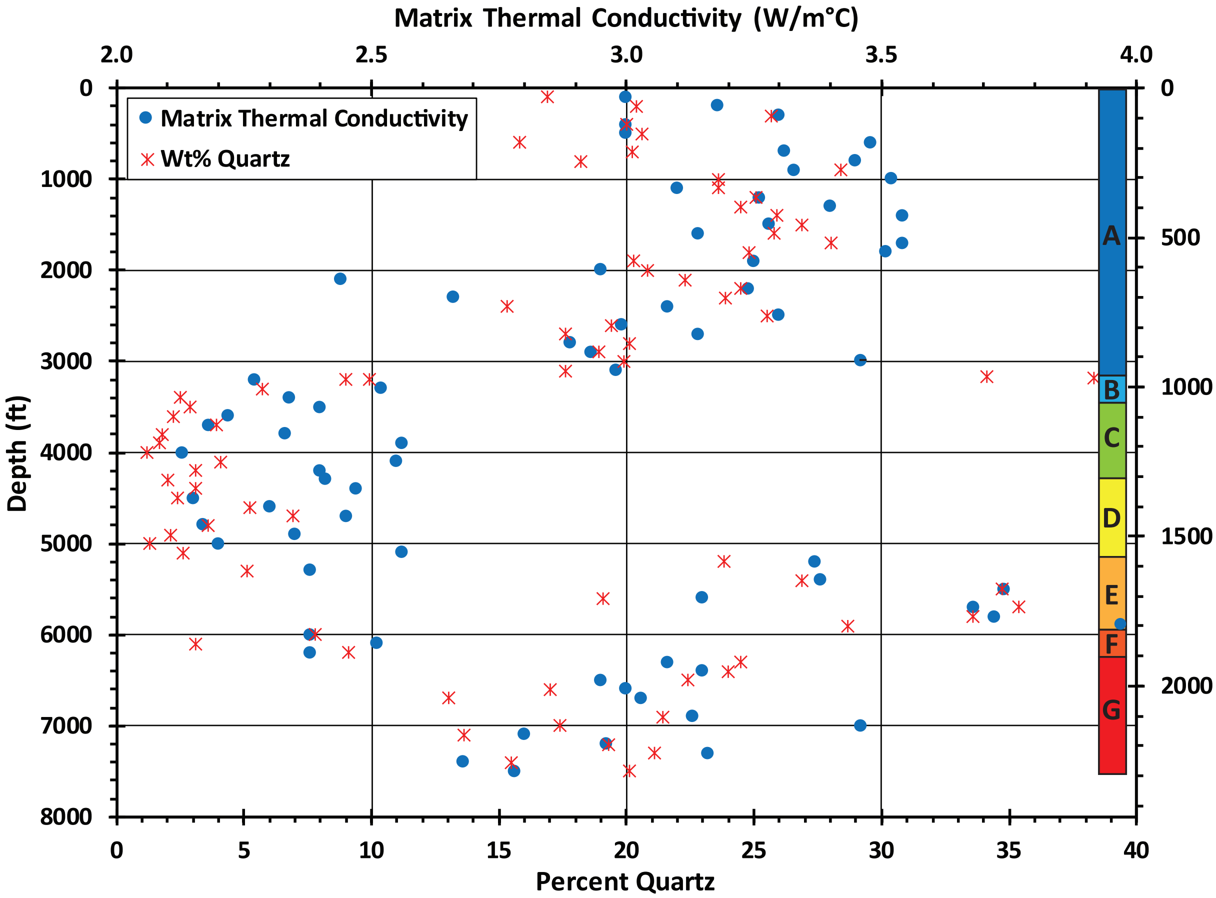

Figure 16. *Comparison of measured matrix thermal conductivity and weight percent of quartz (from cuttings at 100-foot intervals based on divided bar and XRD analyses) for well 58-32. Colored boxes on the right indicate rock types determined by XRD (Jones and others, 2018, 2019). A is mixed granitic alluvium; B is predominantly quartz monzonite; C is predominantly monzodiorite; D is predominantly monzonite; E is predominantly granite; F is a mix of quartz monzodiorite, quartz monzonite, and monzonite; G is predominantly granite with lesser amounts of quartz monzonite and quartz monzodiorite. Thermal conductivity in quartz is high compared to most minerals, so thermal conductivity is largely controlled by the quantity of quartz in these samples. The relatively high thermal conductivity and quartz content in the alluvial section (A) suggests a predominantly granitic origin. The relatively low thermal conductivity and quartz content from around 3000 to 5000 feet are typical of the monzodiorite and intermediate rock compositions through those zones. The high thermal conductivity and quartz content are consistent with the granite zone (E). Rock beneath the granite zone tends to be quartz-rich (granite, quartz monzonite, and quartz monzodiorite).*

Density

The matrix density of each sample is calculated as part of the thermal conductivity measurement and is shown in Figure 17. These data are useful for comparison with the wireline logs as well as gravity modeling (see Hardwick and others, 2018). Matrix density does not account for pore space within the in situ rock, so values need to be corrected using porosity data from other sources. The neutron porosity log for 58-32 was used for the correction below 2173 feet (bottom of surface casing/top of the log). Porosity in the deep alluvial section between the bottom of the surface casing and the top of the granitic basement at about 3300 feet shows a steady decrease from around 15% to 11% (Figure 18).

Porosity for most of this 900-foot interval varies from 6% to 9%. The rock is much tighter below 4300 feet, where porosity remains relatively constant at 1% to 2%. Because the 58-32 logs start below the surface casing, the formation density log from GPC-15 (3 miles south of 58-32) was used to calculate porosity in the shallow alluvial section. Porosity ranges from about 15% to 40% in the upper part of the alluvial section (decreasing with depth due to compaction). The bottom of the GPC-15 porosity data agrees well with the top of the 58-32 neutron porosity data. The higher porosity values cause the calculated bulk density to differ significantly from the measured matrix density in roughly the upper half of the well (alluvial and upper basement sections) compared to the low-porosity zones below. The bulk density of our granite cuttings (2.67 ± 0.08 g/cm^3) is 0.05 g/cm^3 higher than the formation density log values in granite (2.62 ± 0.08 g/cm^3).

Table 2. *Thermal properties from core and cuttings from 58-32. Measurements were made at 25°C. Thermal diffusivity was calculated from the other measured thermal properties.*

Depth (ft)	Thermal Conductivity (W/m°C)	Dry Density (g/cm^3)	Specific Heat (kJ/kg°C)	Thermal Diffusivity (mm^2/s)
Cuttings 3900	2.56	2.95	0.82	1.1
Cuttings 4500	2.15	2.71	0.79	1.0
Cuttings 7000	3.46	2.76	0.73	1.7
Cuttings 7300	3.16	2.72	0.73	1.6
Cuttings 7400	2.68	2.68	0.70	1.4
Core 6801.3	2.69	2.64	0.95	1.1
Core 6801.9	2.50	2.64	0.81	1.2
Core 6806.6	2.88	2.63	0.79	1.4
Core 6809.0	3.13	2.61	0.78	1.5
Core 7442.6	2.57	2.79	0.86	1.1
Core 7445.4	1.81	2.85	0.87	0.7
Core 7448.2	2.69	2.63	0.85	1.2
Core 7449.4	2.76	2.63	0.88	1.2
Average	**2.70**	**2.71**	**0.81**	**1.2**
Std. Dev.	**0.43**	**0.10**	**0.07**	**0.3**

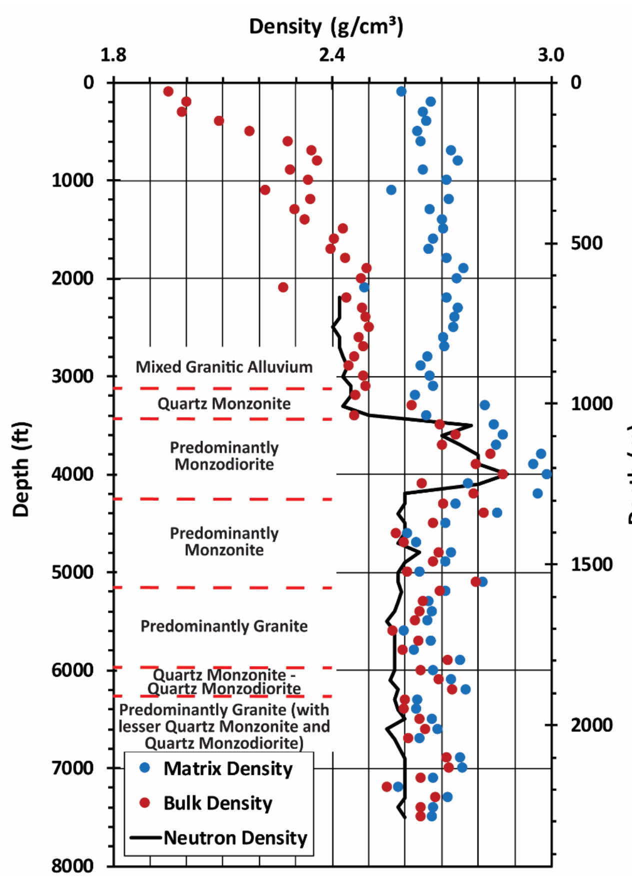

Figure 17. *Measured density values from drill cuttings at 100-foot intervals in well 58-32. Measurements taken as part of the thermal conductivity analyses yield matrix density values that must be adjusted for porosity to determine bulk density values. These measurements compare well with the wireline neutron density data starting at 2173 feet (bottom of the surface casing). Mafic minerals are the primary cause for density changes as shown by the dramatic increase between about 3500 and 4200 feet, which XRD data suggest are primarily monzodiorite. For cuttings in granite, the average bulk density is 2.67 ± 0.08 g/cm³, about 0.05 g/cm³ higher than the formation density log values in the granite zone (2.62 ± 0.08 g/cm³).*

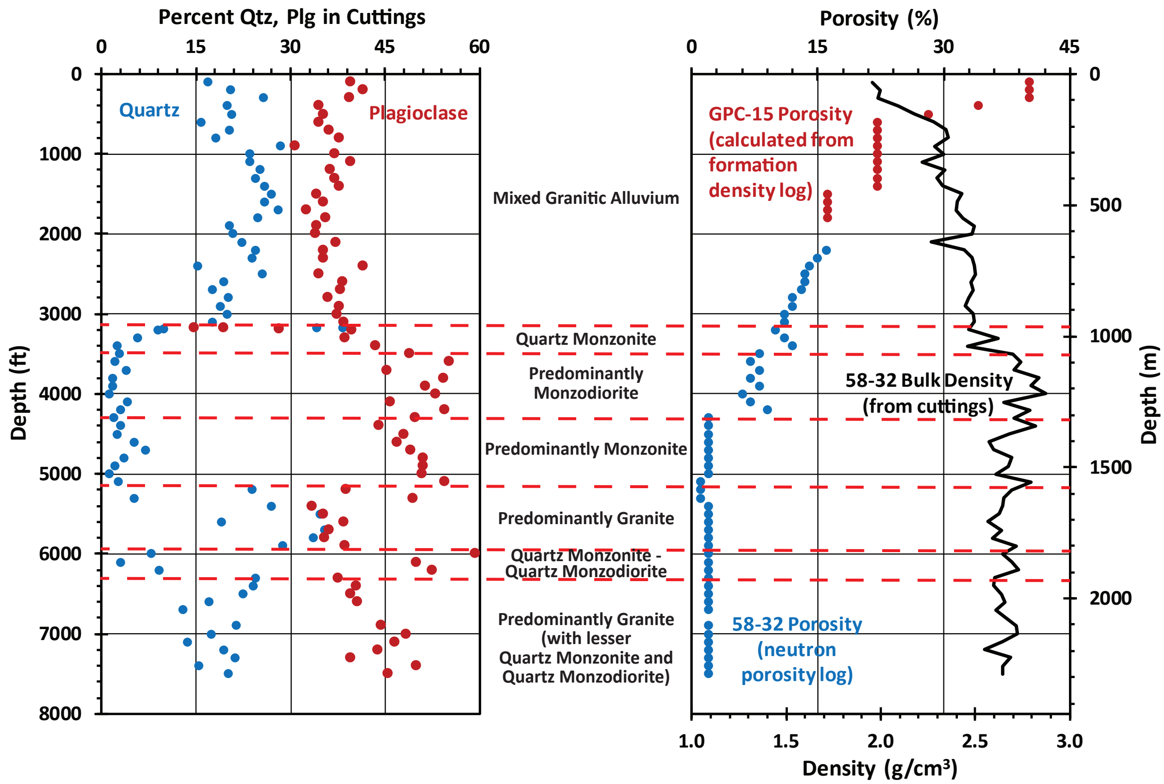

Figure 18. *Quartz and plagioclase in drill cuttings at 100-foot intervals show an inverse relationship, with low quartz and high plagioclase being diagnostic of more dioritic rock types (plot on left). The plot on the right shows porosity data (formation density logs from GPC-15 for the alluvium values above the level of the 58-32 casing, about 3 miles to the south) and well 58-32 neutron porosity log data that were used to determine bulk density from measured matrix density data. Note decreasing porosity with depth through the alluvial section, the very uniform and minimal porosity deeper in the granitic basement, and the high densities characteristic of the more dioritic zones. Except for "mixed granitic alluvium," all other rock types were determined from XRD analyses (Jones and others, 2018, 2019).*

Density changes in the well primarily correlate to compositional changes in the rock. For example, low quartz and high plagioclase in the zone characterized by monzodiorite is, to a degree, reflected by higher matrix densities as shown in Figure 19. Increasing concentrations of mafic minerals such as biotite, hornblende, titanite, apatite, and clinopyroxenes result in higher densities. Figure 19 shows that the matrix densities of granite and more-intermediate compositions typically vary between 2.58 and 2.82 g/cm^3 and have mafic compositions of less than 7% (by weight). In contrast, dioritic densities approach 3.0 g/cm^3, with mafic components ranging from about 12% to 34%. A linear correlation suggests that an ultramafic rock would have a matrix density of about 3.52 g/cm^3, and a complete lack of mafic minerals would yield a density of about 2.67 g/cm^3.

By using XRD as "ground truth" data with respect to rock types encountered in well 58-32 and comparing these data to density and other types of data, a general picture of what rock type causes a given response in the gamma and formation logs was developed. By comparing gamma and formation density logs (with the responses averaged over the same 10-foot intervals that were used for the various analyses performed on the cuttings, but only below 2200 feet where the logs start), a general identification trend develops (Figure 20). In general, density values (from formation density logs or bulk density from cuttings) below 2.5 g/cm^3 are almost certainly from alluvial sections, although the gamma values could shift depending on the source lithology (e.g., more dioritic parent rocks may produce alluvium with lower gamma signatures). Diorite (and monzodiorite) also have distinct gamma and density signatures (low gamma, high density) as do end-member granites (high gamma, low density). The intermediate rock can be reasonably discerned from the dioritic rock, but overlaps in both density and gamma with more intermediate granite. Identifying individual intermediate rock types is more challenging because gamma and density signatures for each type are less distinct and tend to overlap with one another. These characteristics can be applied to interpretations of log data for other wells in the FORGE area, but may be less diagnostic in other intrusive settings.

The XRD data show that most of the potassium content in well 58-32 is contained within potassium feldspar. Therefore, in a relative sense, potassium feldspar content reflects the potassium component of natural gamma radiation (Figure 21). This means that dioritic rocks, which are low in potassium feldspar, should have a lower gamma signal. Other data sources show this

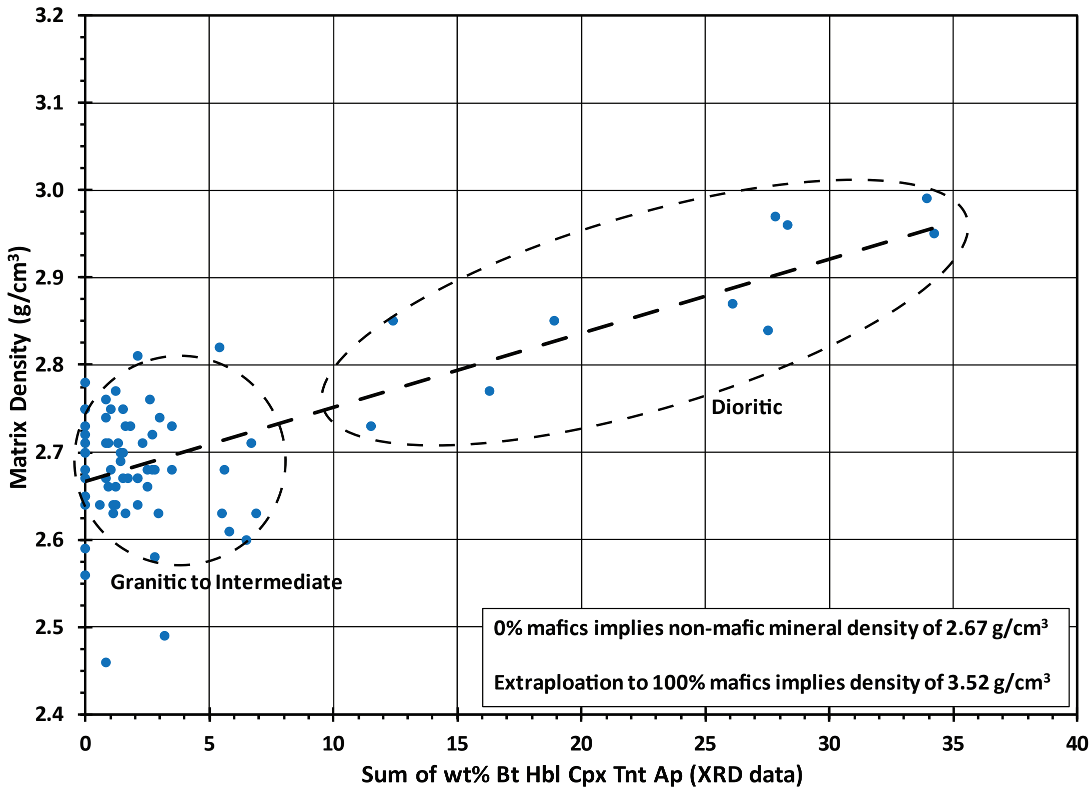

Figure 19. *Cross-plot of matrix density values and the sum weight percent of mafic minerals (biotite, Bt; hornblende, Hbl; clinopyroxene, Cpx; titanite, Tnt; and apatite, Ap) determined from XRD analyses of drill cuttings at 100-foot intervals from well 58-32 (Jones and others, 2018, 2019). The granite and more intermediate-composition rock have matrix density values of around 2.7 g/cm³ compared to more mafic (dioritic) rocks that approach 3.0 g/cm³. Extrapolation to 0% mafic minerals implies a density of about 2.67 g/cm³, compared to a 100% mafic composition where density should be about 3.52 g/cm³.*

to be true, but a quantitative value cannot be directly derived from potassium feldspar content. Potassium feldspar content in the other rock types found in the well overlap significantly and cannot be related to the total gamma signal due to the uranium and thorium components (e.g., the gamma signal is typically higher in granite than monzonite or quartz monzonite, but potassium feldspar content is generally less in granite; Figure 21). However, the same basic relationship between rock types along the x-axis in Figure 21 is present in spectral gamma plots of potassium, so there is a general relationship.

Gamma Ray Spectrometry

A Radiation Solutions, Inc. RS-230 spectrometer (Figures 22 and 23) was used to measure emitted gamma radiation from minerals containing potassium (K), uranium (U), and thorium (Th) in recovered 58-32 cuttings and core. The hand-held instrument uses a 103 cm^3 bismuth-germanium-oxide (BGO) detector. The characteristics of BGO detectors, particularly the high density (7.13 g/cm^3) and high atomic number (bismuth; 83), make the crystals very efficient gamma-ray absorbers that provide performance similar to commonly used and much larger (344 cm^3) sodium-iodide detectors (Saint-Gobain, 2016; Radiation Solutions, 2015).

Radioactive phenomena are discrete and random in nature, so statistical counting is an important part of their measurement (Blum, 1997). Therefore, accuracy and data quality are dependent on measurement duration. Three-minute assays were used to provide a good balance between data quality and measurement time, although Radiation Solutions (2015) considers two-minute assays to provide high-quality data under most conditions.

The wireline gamma logs for 58-32 are considered to be “ground truth,” but they only record total gamma rather than the proportions from K, U, and Th. The spectral components, especially K, can be diagnostic of mineral composition (and therefore rock type), so spectral gamma measurements were made to complement the wireline data. Gamma radiation from the core and cuttings at a given depth should not be expected to equal the gamma values from wireline logs at the same depth. However, the relative trends should be similar, and generally are, in well 58-32.

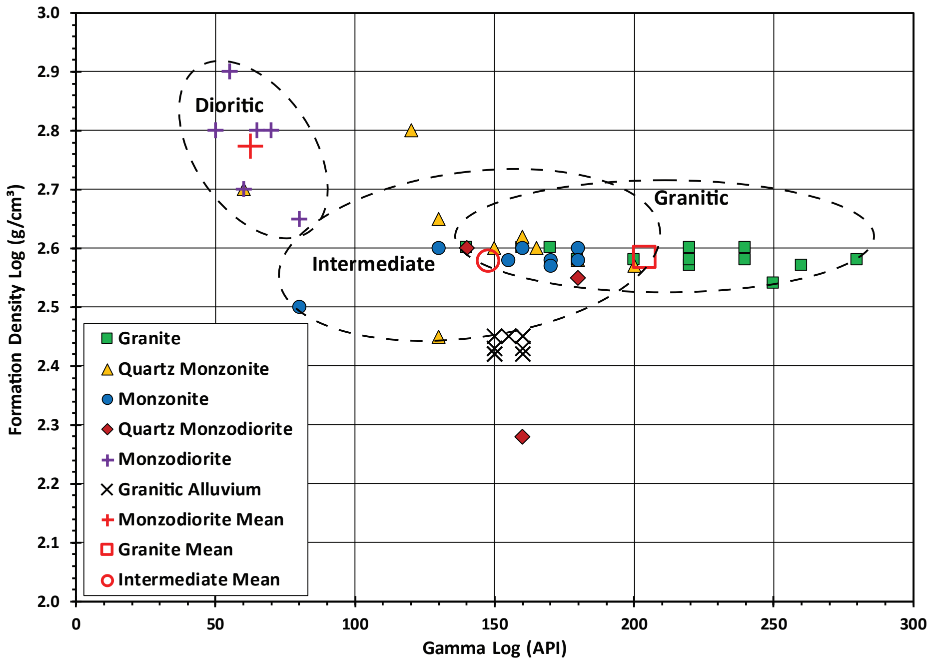

Figure 20. Rock types and associated geophysical characteristics from log data in well 58-32. Wireline log data were analyzed at 100-foot intervals within the lower part of the alluvial section and the rest of the wellbore. Potentially faulty data due to wellbore washouts were eliminated. Data are from most of the same 100-foot intervals used for analyses on the well cuttings, but only from below 2200 feet (top of the logged section). Dioritic (diorite and monzodiorite) rock can generally be discerned by density values greater than about 2.66 g/cm³ and gamma values of 50–80 gAPI (mean is 2.77 g/cm³ and 63 gAPI). Intermediate rock (quartz monzonite, monzonite, and quartz monzodiorite) and granite generally can be discerned from dioritic rocks, but have a large degree of overlap in density and gamma values. The mean density and gamma values for the intermediate types are 2.58 g/cm³ and 148 gAPI, compared to the mean values for granite of 2.58 g/cm³ and 204 gAPI. Density values below about 2.5 g/cm³ are almost certain to be alluvial in nature, but gamma values could vary greatly depending on parent rocks. Note that bulk density values measured in the laboratory tend to be about 0.05 g/cm³ higher than formation density values from logs, and the ellipses account for slightly greater possible density values.

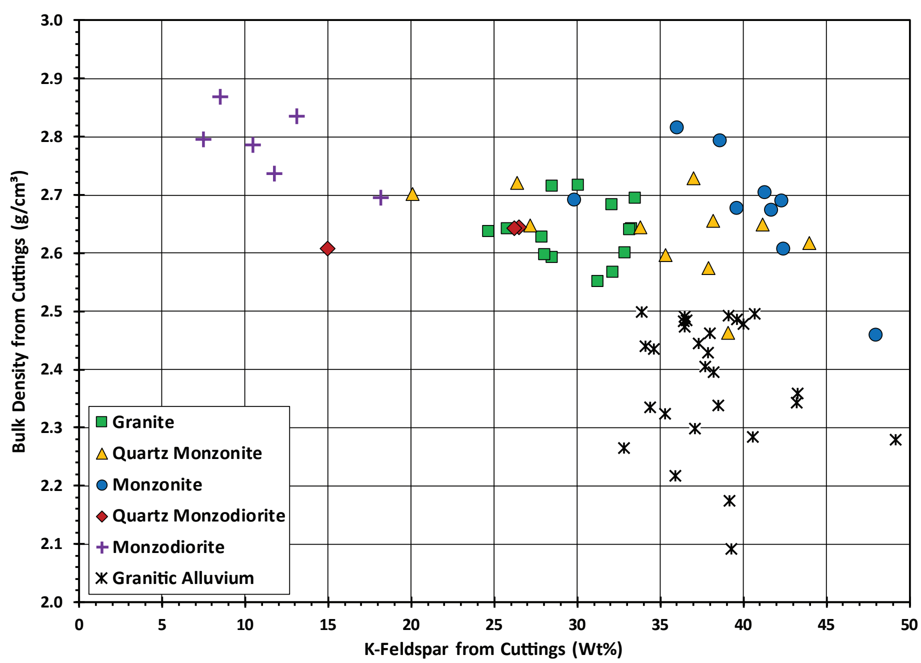

Figure 21. Rock types from well 58-32 cuttings in terms of potassium feldspar content and measured/calculated bulk density values. Potassium feldspar content (Jones and others, 2018, 2019) and bulk density were derived from cuttings at 100-foot intervals throughout the entire well. These data were then correlated to XRD-derived rock types. Dioritic (all monzodiorite in this case) samples have distinctively low potassium feldspar composition and high density. Potassium feldspar and density values are scattered for the granitic and intermediate (quartz monzonite, monzonite, and quartz monzodiorite) rock types. Lab-measured density values for these rock types vary more than those measured by wireline logs. Density for the granitic alluvium is universally low (below about 2.5 g/cm³).

Figure 22. *The RS-230 Gamma Ray Spectrometer in use on cuttings from well 58-32. Spectral gamma ray measurements were focused at 100-foot intervals, but due to limited sample mass, additional samples from above and below the target depth were needed to achieve a minimum mass experimentally determined from outcrop samples. Therefore, measurements were made using samples from an 80-foot interval with the spectrometer positioned over the targeted sample (photo on the right) so that the greater part of the gamma signal comes from the target depth. Measurements were made in a 5-mm-thick steel box (photo on the left) to attenuate a portion of the background gamma signal.*

Figure 23. *The RS-230 Gamma Ray Spectrometer (top center of photograph) in use on the lower core section (top at 7440 feet). Spectral gamma ray measurements were made at 3-inch intervals along the entire length of the reconstructed core. A second measurement was made on the opposite side of the core at each depth. The yellow instrument at the bottom of the photograph is the KT-10 Magnetic Susceptibility Meter that was used at the same measurement locations as the spectrometer.*

Uncertainty

Some variance in gamma readings was observed in the five gamma logs run in the 58-32 well. Such variance is due to logging speed (counting duration), logging tool calibration, and other factors, but the differences tend to be small. The gamma tools each recorded roughly 15,000 measurements and, while a few depths had large variations in recorded values, the average difference among all five tools at a given depth was about 21 gAPI with a standard deviation of 8.4 gAPI.

Spectral gamma measurements taken at the surface have some inherent deficiencies when compared to downhole measurements. Perhaps the most important is the presence of background atmospheric gamma radiation that is not present deep within the well bore. This effect was partially attenuated by making measurements on the cuttings in a 5-mm-thick steel box. No shielding was available for the core measurements, due to the length of many of the intact core segments.

To characterize the effect of background radiation on the cuttings and estimate the precision of the instrument, 20 measurements (3-minute assays) were made in the steel box without any samples. This testing showed K to be 0.58 ± 0.5%, U to be 1.99 ± 0.17 ppm, and Th to be 3.38 ± 0.25 ppm.

Although cuttings sample volumes collected in the 58-32 well are much larger than those commonly collected in deep wells, the initial spectral gamma ray measurements showed that the sample quantity was not sufficient to obtain reliable results. To determine how much granular material of granitic composition would be required to obtain reasonable measurements, 33 3-minute assays (three per location) were taken on a granitic outcrop sample from the Mineral Mountains. Measurements did vary between the 11 measurement locations (K: 1.4%–2.1%, U: 2.9–4.4 ppm, and Th: 8.2–13.4 ppm). The spectral components for the overall outcrop sample were: K: 1.7 ± 0.19%, U: 3.6 ± 0.41 ppm, and Th: 10.3 ± 1.1 ppm. The outcrop sample was then crushed and sieved to approximate the size of the cuttings obtained from the 58-32 well. These "pseudo cuttings" were placed in sample bags each weighing 700 grams and various combinations with respect to the number of bags (equating to the optimum sample mass) and their spatial arrangement were tested until results similar to the uncrushed rock were obtained. These results showed that an aggregate sample mass of about 5–6 kilograms, with the sample bags arranged so they create a volume of about 25x25x4 cm, provided the best results. This was used as a guideline for arranging the actual cuttings during the measurements.

Because the measurements are taken along the length of the cylindrical core with a 4-inch diameter, the flat surface of the 2.4-inch-diameter detector cannot be placed flat against the sample, leading to a decrease in detected gamma radiation (the top of the circular detector surface can be seen above the core in Figure 23). To assess this effect, about 5 kilograms of the "pseudo cuttings" were packed into a 4-inch-diameter cardboard cylinder and the gamma radiation was measured with the spectrometer. These results showed that core measurements may be decreased roughly 50%–70% due to detector-core geometry.

Measurements on cuttings

Measurements on the cuttings using 3-minute assays were performed on the same 100-foot intervals as used for other analyses (XRD, thermal conductivity, etc.), but due to limited sample mass additional samples from above and below the target interval had to be included (based on the sample mass testing described above). Available sample mass was still typically below the optimum of around 5.5 kilograms, but could not be increased without overlapping samples from one 100-foot interval to the next. The arrangement placed the samples closest to the target interval nearest to the detector, so that much of the spectral gamma signal was from close to the target interval. The results are shown in Figure 24. The relative lack of potassium, due to low quantities of potassium feldspar in the monzodiorite zone, is distinct, while the more granitic zones tend to be enriched with thorium. Total gamma was calculated from the spectral components for comparison with the wireline logs using the formula:

$$16K+8U+4Th = \mathit{Total\ Gamma\ Ray}\ (API)$$

where: K is potassium in percent, U is uranium in parts per million, and Th is thorium in parts per million. Figure 25 plots the calculated total gamma against wireline gamma (smoothed to the same 100-foot intervals as the cuttings). The calculated total gamma data and wireline gamma data follow the same trends; however, the calculated values are generally about one-third of the values from the wireline logs (Figures 25 and 26). This is likely due to most samples being at or below the calculated minimum mass threshold (also requiring material from above and below the target depth) and the lower density of loose cuttings compared to solid rock. Note that the intercept in Figure 26 is not at zero, which is probably an effect of background gamma and possibly some instrument bias.

While the absolute gamma values do not correlate well, the relative values appear correlative. Therefore, the ratios of spectral gamma components are likely accurate and useful to other calculations and interpretations. The large difference between the two data sets in the "C" zone (primarily monzodiorite) means that calculated and logged total gamma values are about 1:1 (i.e., about 50 gAPI). Comparing the potassium component from the spectral measurements and the total gamma from the logs against the potassium feldspar component from XRD analyses shows that there is excess scatter in the wireline total gamma log responses (due to differing ratios of K, U, and Th) compared to the reasonably linear correlation between cuttings-derived K-feldspar concentrations and spectral-gamma-measured percent K (Figure 27).

The radioactive decay of isotopes of K, U, and Th releases heat. Rocks with high concentrations of these elements can generate sufficient heat to be a significant factor augmenting surface heat flow when present in thicknesses of thousands of feet. The calculated total values from the spectral gamma measurements were scaled to match the API value for total gamma obtained at the same depth from the downhole logging, and the relative proportions of K, U, and Th were used to calculate heat generation. The resulting average for granitic rock in well 58-32 (granite, quartz monzonite, monzonite) and dioritic rock (quartz

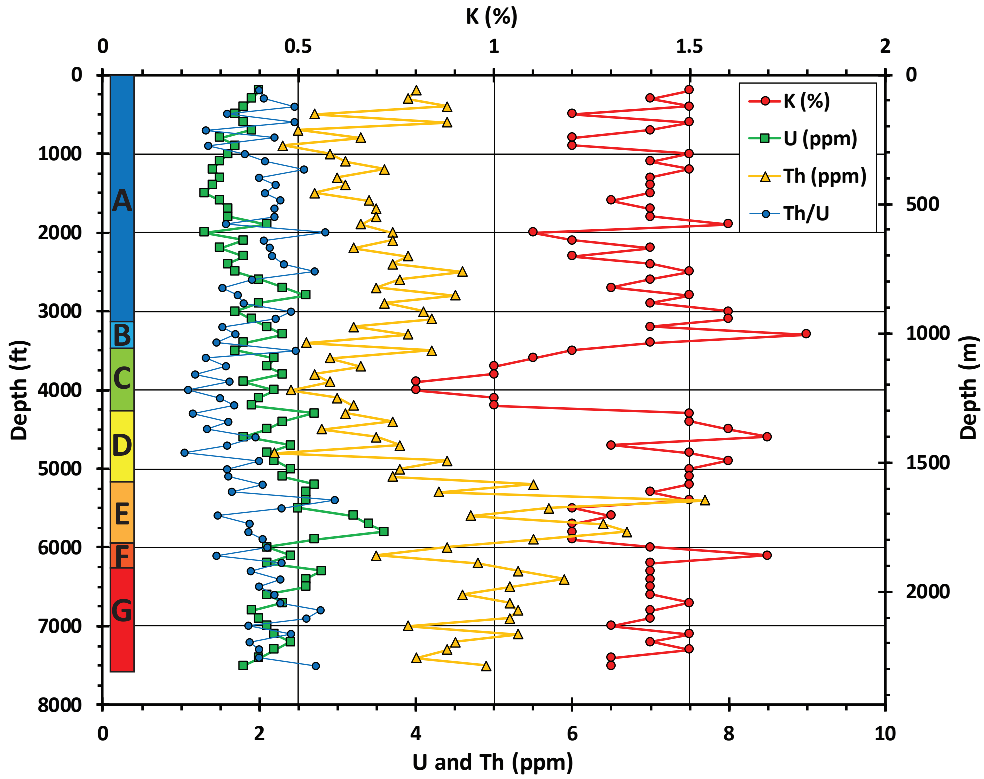

Figure 24. *Spectral gamma ray data from well 58-32 cuttings at 100-foot intervals. The spectrometer records the potassium (K) component as a percent, while uranium (U) and thorium (Th) components are recorded as parts per million (ppm). Due to limited sample mass of the cuttings at the test intervals, most measurements were made using samples from an 80-foot interval with the spectrometer positioned over the targeted sample so that the greater part of the gamma signal comes from the desired depth. Colored boxes on the left indicate rock types determined by XRD: A is mixed granitic alluvium; B is predominantly quartz monzonite; C is predominantly monzodiorite; D is predominantly monzonite; E is predominantly granite; F is quartz monzodiorite, quartz monzonite, and monzonite; G is predominantly granite with lesser amounts of quartz monzonite and quartz monzodiorite. Low K values correlate to decreased potassium feldspar (and increasing mafic minerals) in the zone that is mainly characterized as monzodiorite (about 3450–4250 feet). The more granitic zones (about 5250–5950 feet, and, to a lesser extent, 6250 feet to TD) show low to moderate K concentrations, but are relatively enriched in Th (primarily) and U (secondarily). Therefore, total gamma responses for the granitic zones are higher than for the other zones.*

monzodiorite and diorite) are shown in Table 3. A heat generation of 2–3 $\mu W/m^3$ is typical for granitic rock, but its effect on the geotherm in the upper crust is negligible because of the relatively high conductive heat flow at this site (the effect is a 2°C decrease in temperature over 5 km).

Measurements on cores

Two measurements were made at 3-inch intervals along the reconstructed length of the core, with the measurements made on opposite sides of the core (Figure 23). The measurement locations were picked to avoid fractures (natural and induced) or missing pieces of the core so that the maximum volume of rock would be adjacent to the spectrometer. Measurements on or near fractures were less reliable than those made in more competent sections of the core. These measurements show that compositional changes occur over small intervals in depth (feet or less). Distinct examples are at about 6805.5 feet in Figure 28 and in the felsic banding at about 7441.5 feet in Figure 29. This variation is not unlike that in the granitic outcrop sample used to generate the “pseudo cuttings.” The differences between the calculated total gamma and the wireline gamma logs are smaller than with the cuttings samples, but the calculated values are still around 50% that of the wireline values. Like the cuttings, though, the total gamma values in the more dioritic core sections are much closer to the down-hole log readings.

Magnetic Susceptibility

A Terraplus Inc. KT-10 Magnetic Susceptibility and Conductivity meter was used to measure the magnetic susceptibility (MS) of both core sections and the cuttings from well 58-32 (Figure 23). Increases in magnetic susceptibility are due to increasing quantities of iron-bearing minerals, which in this case are mafic minerals indicative of more dioritic rock compositions.

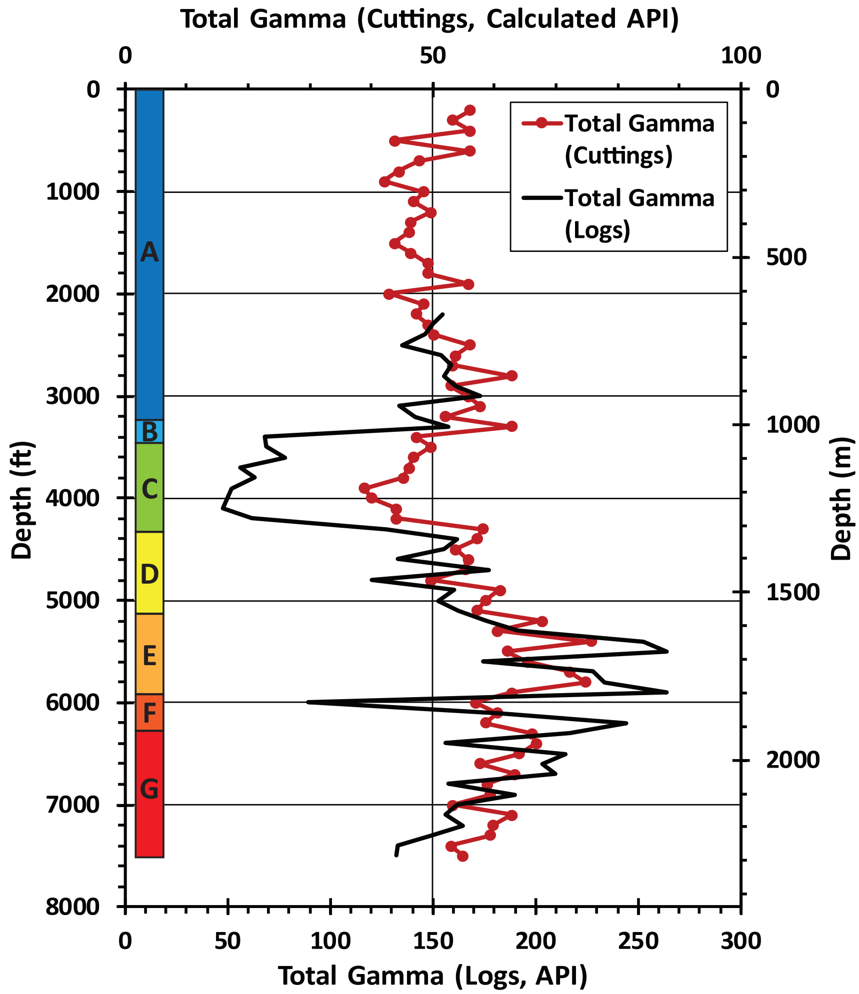

Figure 25. *Comparison of smoothed (data at 100-foot intervals) wireline gamma log and total gamma measurements (from the same intervals) for well 58-32. Measurements on the cuttings are spectral gamma (broken into contributions of potassium, uranium, and thorium), but were converted to total gamma. The wireline logs were run from 2173 feet (just below surface casing) to TD at 7536 feet. Due to limited sample mass of the cuttings at the sampled intervals, measurements were made using samples from 80-foot intervals with the spectrometer positioned over the targeted sample so that the greater part of the gamma signal comes from the desired depth. Colored boxes on the left indicate rock types determined by XRD: A is mixed granitic alluvium; B is predominantly quartz monzonite; C is predominantly monzodiorite; D is predominantly monzonite; E is predominantly granite; F is quartz monzodiorite, quartz monzonite, and monzonite; G is predominantly granite with lesser amounts of quartz monzonite and quartz monzodiorite. There is reasonable agreement in all sections of the curves except for the predominantly monzodiorite zone (about 3450–4250 feet). Logged API data are generally about three times higher than the total calculated API of the cuttings.*

Uncertainty

No accuracy specifications for the meter are supplied by the company. To help constrain measurement uncertainty, 20 measurements were made at the same location on each of two outcrop samples. The first was from outcrop mapped by Sibbett and Nielsen (2017) as Tertiary granite dikes (Tgr) and the second as Tertiary diorite (Td). Jones and others (2018, 2019) used XRD to confirm the Tgr sample is granite and classify the Td sample as quartz monzonite. The Tgr MS values range from 10.2 to 10.3 SI units with a standard deviation of 0.04. The Td MS values range from 36.3 to 38.6 SI units with a standard deviation of 0.58.

The KT-10 instrument is typically used to measure magnetic susceptibility on outcrop or on core samples. The instrument can be optimized for various core diameters ranging from 1 inch to 4.7 inches (2.54–12.00 cm) and for full diameter or split core. Therefore, the instrument is ideal for measuring the 58-32 core samples.

Because the meter is not optimized for use with cuttings, an effort was made to calibrate it using the same "pseudo cuttings" used to calibrate the spectral gamma meter. Prior to crushing the outcrop sample, five magnetic susceptibility measurements were made at 12 locations on the sample. Due to the heterogeneity of granitic rocks, the average magnetic susceptibility for each location varied from 5.51 to 9.67 SI units (variability at each location was minimal), yielding a "whole rock" average of 8.32 SI units.

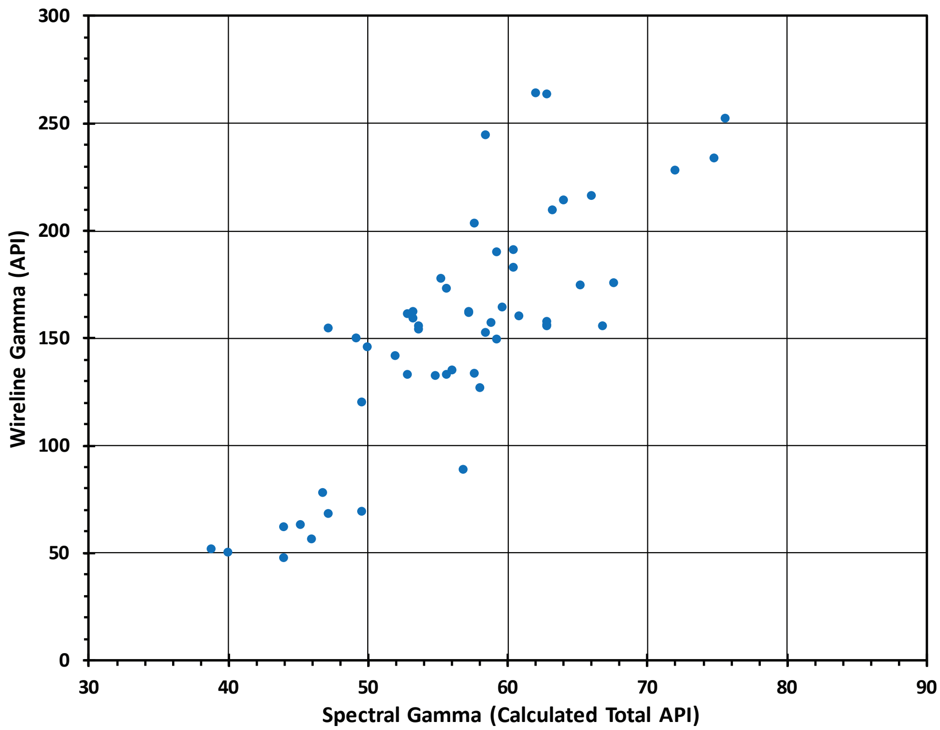

Figure 26. *Cross-plot of wireline gamma and total gamma calculated from spectral gamma data (at 100-foot intervals from 2200–7500 feet) in well 58-32. Measurements on the cuttings are spectral gamma (broken into contributions of potassium, uranium, and thorium), but were converted to total gamma. Wireline gamma values range from about 1.1 to 4.3 (2.64 average) times the calculated value from the spectral gamma measurements for a given depth. This is likely due to relatively small samples available from cuttings (2.3–5.7 kg, 4.1 kg average) despite using samples from an 80-foot interval with the spectrometer positioned over the targeted sample so that the greater part of the gamma signal came from the desired depth. A possible additional factor is that the cuttings were loosely packed in sample bags, compared to solid rock in the wellbore. However, the potassium, uranium, and thorium ratios are assumed to be reasonably accurate and useful to other analyses.*

The mass for each of the 58-32 cuttings samples (at the analyzed 100-foot intervals) varied from less than 300 to over 700 grams. Because the meter seemed to be sensitive to differences in sample mass, it was calibrated to a sample mass of 300 ± 1 grams using the "pseudo cuttings" (85% of the 58-32 samples surpassed this threshold). This was done by filling nine sample bags with 300 ± 1 grams of the "pseudo cuttings" and measuring the MS of each bagged sample five times using various meter configurations. The composite average of these measurements was then compared to the composite MS taken on the outcrop sample prior to crushing. The 2.4 inch (6.0 cm) split core configuration yielded an average magnetic susceptibility of 8.36 SI units compared to 8.32 SI units from the pre-crushed sample (measured with the meter optimized for outcrop samples). Other samples varied above and below the outcrop average by increasing magnitudes.

For cuttings samples with a mass over 300 grams, the cuttings were temporarily poured out and then 300 ± 1 grams were added back to the fabric sample bag and the MS was measured five times. For samples with less than 300 grams available, additional material from the next-deepest sample was measured along with the entire targeted sample (in separate sample bags) to create a composite sample of 300 ± 1 grams.

Measurements on cuttings

Magnetic susceptibility values generally correlate well with the XRD data from Jones and others (2018, 2019). Figure 30 compares the MS data with XRD-determined minerals that do, or may, contain iron. Comparisons were made with primary mafic minerals (biotite, hornblende, augite, titanite, and apatite) and then with the addition of other minerals that may contain iron (smectite, illite, chlorite, and epidote). Because these additional minerals are mainly found in the alluvial section, XRD differences in the granitic basement are less pronounced (MS values in the alluvial section are uniformly low). The most mafic section (predominantly monzodiorite) correlates to the highest MS values (about 18 to 47 SI units). Except for monzonite, MS values in the granitic and intermediate-composition rock fluctuate between about 2 and 10 SI units.

The measurement at 2200 feet is anomalously high and isolated compared to measurements directly above and below. The most likely explanation is that the sample is contaminated with steel particles from the drilling operation.

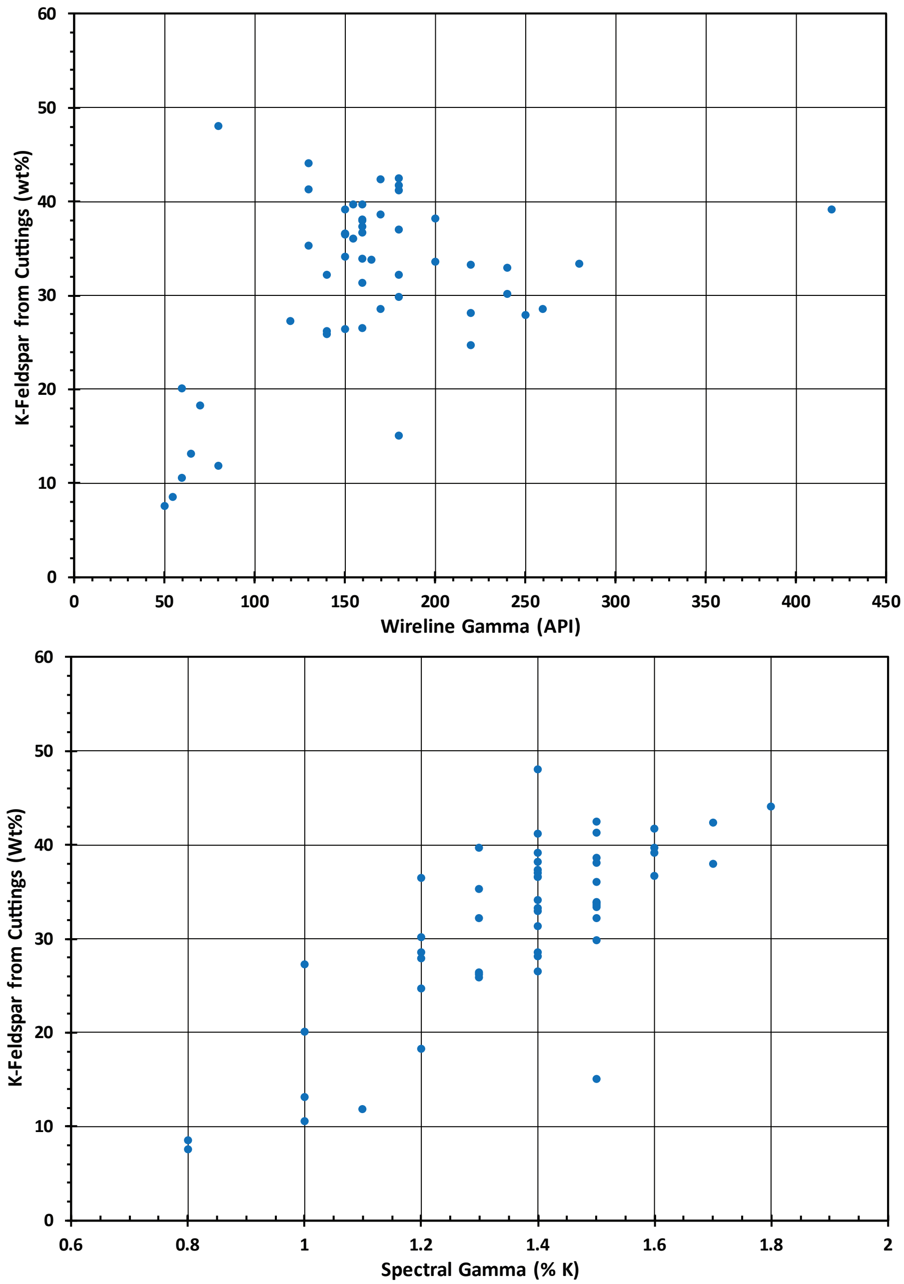

Figure 27. Potassium component of spectral gamma data from cuttings at 100-foot intervals and total gamma from wireline logs at the same intervals (all from 2200–7500 feet) plotted against concentrations of potassium feldspar from XRD data (Jones and others, 2018, 2019). Scatter is greater with the wireline logs due to varying concentrations of thorium (primarily) and uranium. Additionally, spectral gamma data suggest thorium plays a larger role in increasing total gamma levels in granitic rock than in other rock types.

Measurements on cores

The MS measurements were taken at the same locations as the spectral gamma measurements, with five measurements taken at each location for increased data confidence (Figures 31 and 32).

Roughly the top half of the upper core has been identified as granite-granodiorite based on XRD and petrographic analyses (Jones and others, 2018, 2019). The bottom half is granite, but closer to quartz monzonite in composition. Magnetic susceptibility in the top section ranges from near zero to about 22 SI units, whereas the bottom half is generally greater than 20 SI units. A pronounced boundary between the sections correlates with the visual and XRD-derived change in composition. The top half of the lower core has been identified as diorite, whereas the bottom half ranges from quartz monzonite to granite. Magnetic susceptibility varies widely (about 25–70 SI units) through most of the diorite, and correlates closely with several more-felsic bands within this section. The bottom half is compositionally more like the upper core and exhibits a similar range of MS values (about 20–40 SI units).

Table 3. *Heat generation characteristics of the granitic and dioritic rock encountered in well 58-32 (Allis and others 2018a).*

Rock Type	K (%)	U (ppm)	Th (ppm)	Density (kg/m3)	Heat Generation (µW/m3)
Granitic	4.0	6.7	12.4	2700	3.0
Diorotic	2.4	4.1	7.9	2800	2.0

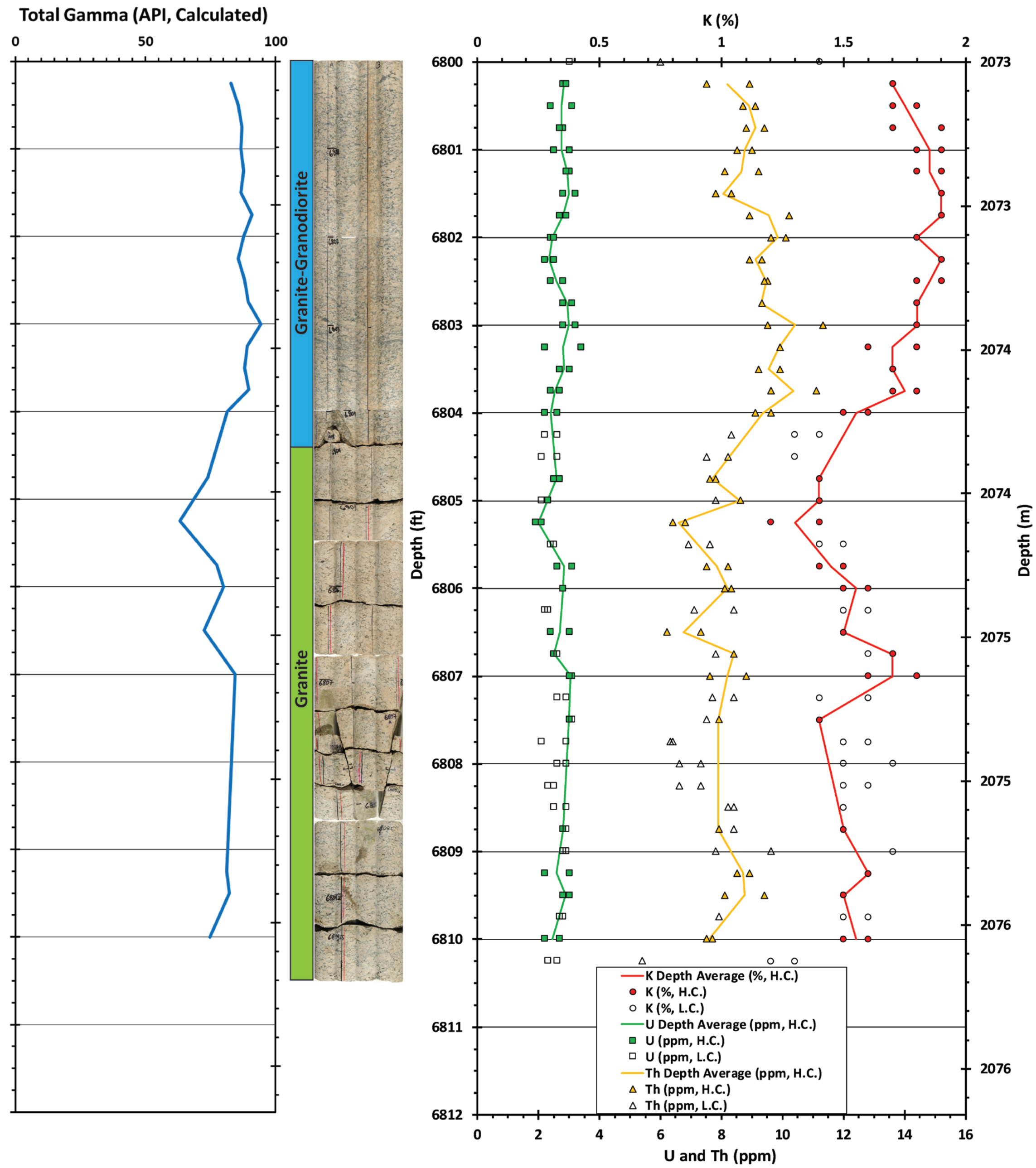

Figure 28. *Spectral gamma-ray measurements in the first cored section of well 58-32 (top at 6800 feet). Two measurements were taken at 3-inch intervals along the reconstructed core, with the measurements taken on opposite sides of the core. Measurements near, or on, fractures were lower confidence (L.C.) due to missing material. However, agreement with high-confidence (H.C.) data suggests the effects are generally moderate. The measurements at each location are plotted, as is the overall average per depth interval (high-confidence data only; colored trend lines). The core was photographed on four sides, and the photos were joined to create the composite photograph in the center. Colored boxes to the left of the photographs indicate rock type (granite-granodiorite and granite) based on XRD analysis of core plugs. Potassium, and to a lesser extent thorium, vary most with changing mineral composition (graph on right). Total gamma was calculated and is shown in the graph at the left. Lower total gamma (and potassium) indicate increasing concentrations of mafic minerals such as biotite, hornblende, augite, titanite, and apatite, and generally correlate with visible changes in lithology. Some areas show significant variation over small depth intervals.*

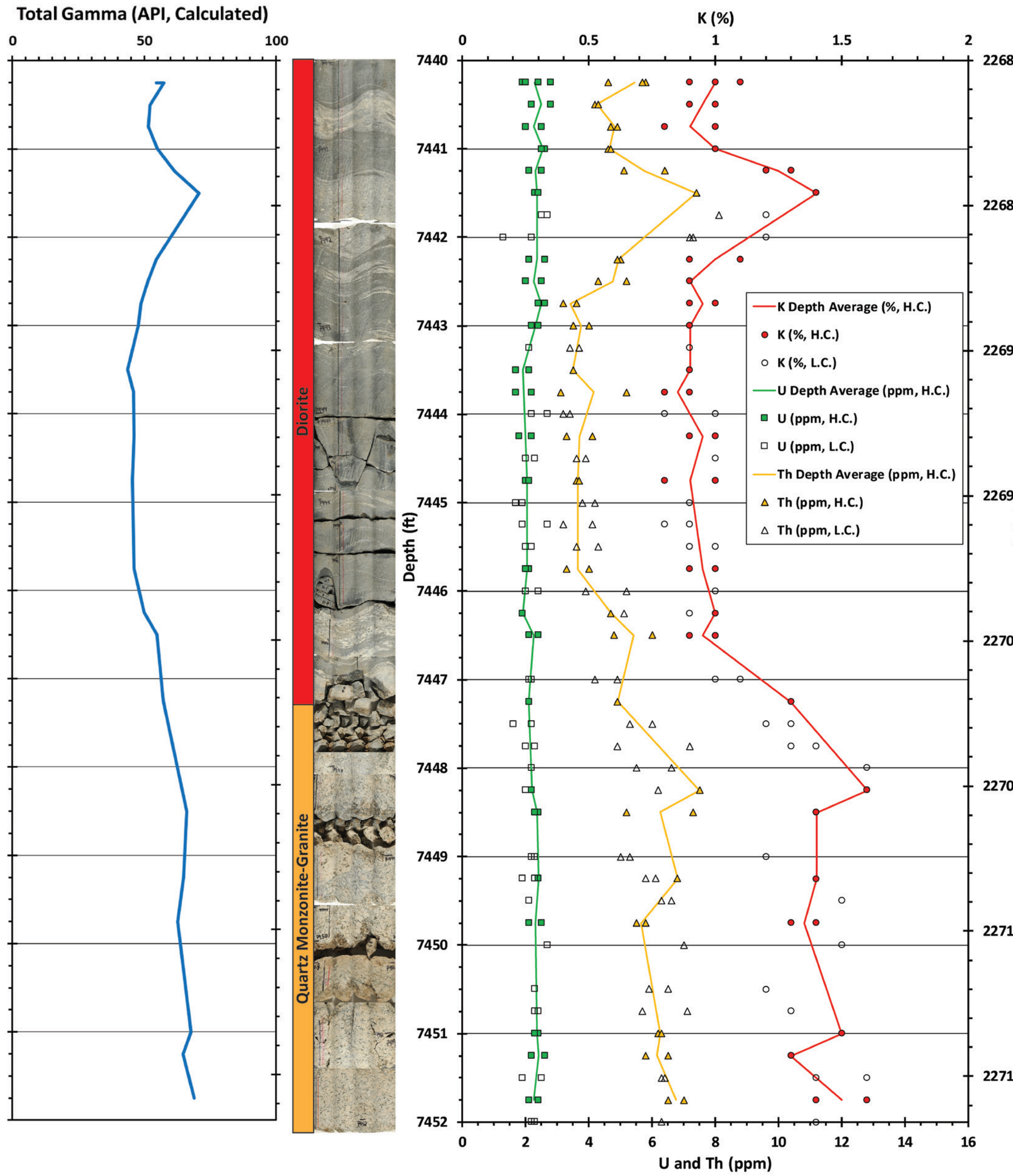

Figure 29. *Spectral gamma-ray measurements in the second cored section of well 58-32 (top at 7440 feet). Two measurements were taken at 3-inch intervals in the reconstructed core, with the measurements taken on opposite sides of the core. Measurements near, or on, fractures were lower confidence (L.C.) due to missing material. However, agreement with high-confidence (H.C.) data suggests the effects are generally moderate. The measurements at each location are plotted, as is the overall average per depth interval (high-confidence data only; colored trend lines). The core was photographed on four sides, and the photos were joined to create the composite photograph in the center. Colored boxes to the left of the photographs indicate rock type (diorite and quartz monzonite-granite) based on XRD analysis of core plugs. Potassium, and to a lesser extent thorium, vary most with changing mineral composition (graph on right). Total gamma was calculated and is shown in the graph at the left. Lower total gamma (and potassium) indicate increasing concentrations of mafic minerals such as biotite, hornblende, augite, titanite, and apatite, and generally correlate with visible changes in lithology (see felsic banding at 7441.6 feet and change from mafic to felsic at about 7446.2 feet). Some areas show significant variation over small depth intervals.*

The MS values in the cores tend to be higher than in the cuttings for a given lithology. Because the instrument is factory-calibrated to measure core of this diameter rather than cuttings, the core values are probably more accurate. The sensitivity of the meter is obvious in the changes from one closely-spaced measurement location to the next in the core. Some of the differences between core and cuttings, therefore, may stem from the cuttings being averaged over 10 feet. An additional factor is likely the decreased density in the cuttings samples, despite the effort to calibrate the instrument for these measurements. While less accurate in an absolute sense, the measurements in the cuttings seem to provide a reasonable representation of relative mineral composition. While there is some overlap, MS values above 30 SI units suggest a dioritic composition and those below that threshold likely have a granitic or intermediate composition.

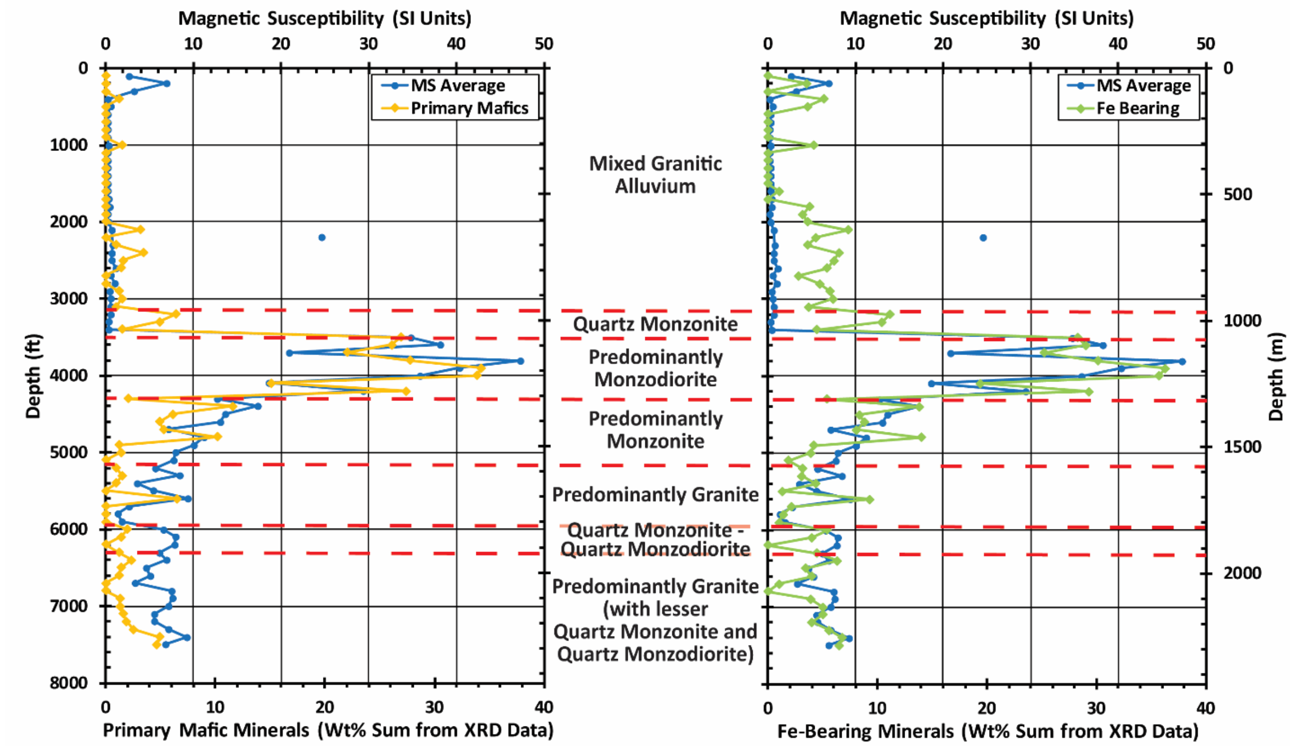

Figure 30. *Magnetic susceptibility (MS) and XRD data (Jones and others, 2018, 2019) for 58-32 well cuttings at 100-foot intervals. The XRD data in the left plot are the sum of the weight percent for primary mafic minerals (biotite, hornblende, augite, titanite, and apatite). The XRD data in the right plot add additional minerals that do, or may, contain iron (smectite, illite, chlorite, and epidote). Both are compared to the XRD-derived predominant rock types. The MS datum at 2200 feet is likely contaminated with steel particles from the drill rig, bit, or casing.*

DETAILED ANALYSIS OF FORGE WELL 58-32 WIRELINE LOGGING DATA

The general calibration of wireline log data (mainly gamma and density) determined by other analyses was used to gain a better understanding of rock characteristics in portions of the 58-32 well bore that were not subject to laboratory analyses. Figures 33 and 34 show the top and bottom halves of the logs shown in Figure 13 so important details can be more easily identified.

Note that the formation density is consistently less than 2.5 g/cm^3 in the alluvial section and that the neutron porosity log shows high (relative to the deeper parts of the well), but decreasing porosity in Figure 33. This is consistent with density measurements on the cuttings. Washouts, identified by spikes in the caliper trace, can significantly affect density calculations, resulting in abnormally low formation density responses (and a deflection of the DRHO trace, which is a measure of density measurement quality). The worst washout zones are highlighted in yellow in Figures 33 and 34. High density/low gamma are indicators of dioritic rock (mainly monzodiorite in Figure 33), which is more common in the upper half of the well.

However, many low density/high gamma peaks that suggest granite, or at least more granitic zones, are present (brown circles in Figure 33). These zones are typically less than 50 feet thick, and many are much thinner. These distinct changes could be the result of magmatic differentiation in the cooling magmas or the result of small intrusions of compositionally different magmas into fractures in existing rock.

The “more granitic” zone near the bottom (about 4200–4300 feet) of the “predominantly monzodiorite” zone, roughly correlates with the quartz monzonite cuttings sampled at 4100–4110 feet. However, most of the other “more granitic spikes” in Figure 33 tend to fall between the XRD-sampled intervals.

The bottom half of the well tends to be more granitic (Figure 34), but small-scale dioritic zones are present. The scale of these zones is generally like the granitic spikes in the upper half of the well. While the only XRD-derived diorite measurement occurred in the lower core (all other dioritic results were monzodiorite), several of the spikes probably reflect “pure” diorite rather than monzodiorite.

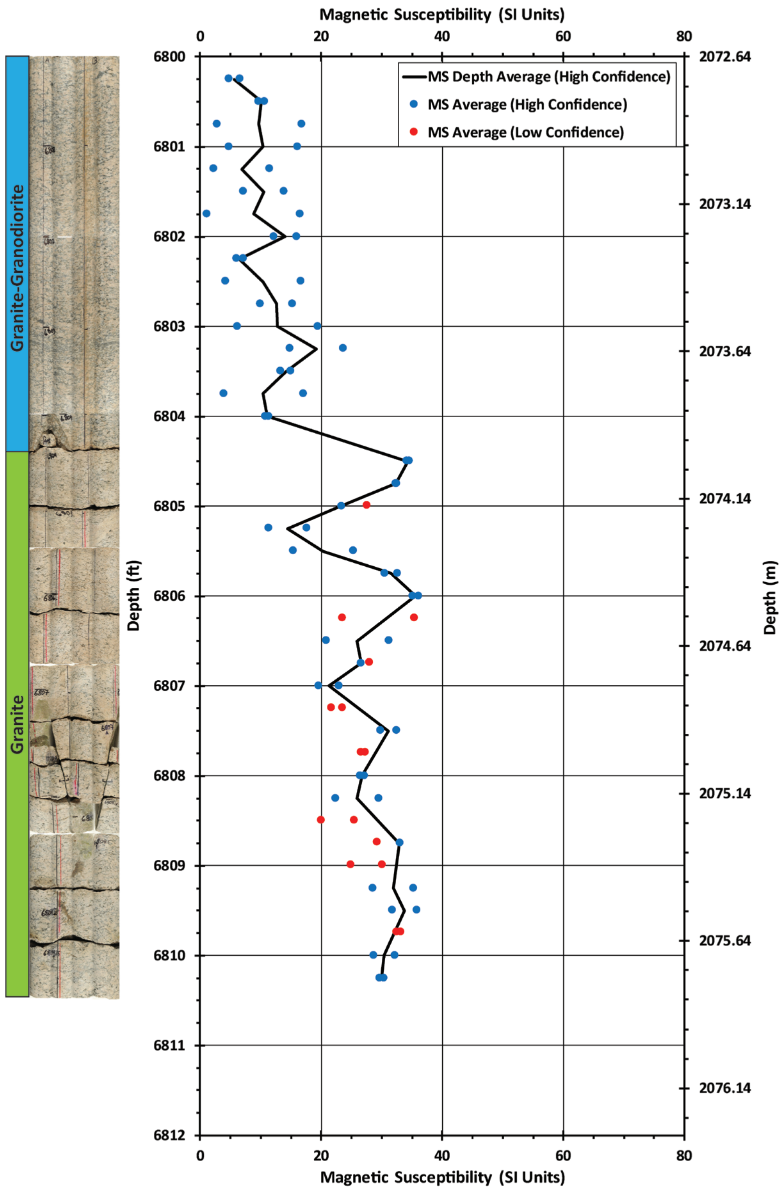

Figure 31. *Magnetic susceptibility (MS) measurements in the first cored section of well 58-32 (top at 6800 feet). Two measurements were taken at 3-inch intervals in the reconstructed core, with each measurement taken on opposite sides of the core. Five measurements were made at each location. Measurements near, or on, fractures were lower confidence due to missing material. However, agreement with high-confidence data suggests the effects are minimal. The average of the five measurements at each location is plotted, as is the overall average per depth interval (high-confidence data only; black trend line). The core was photographed on four sides, and these were joined to create the composite photograph on the left, showing the entire circumference of the core. Colored boxes to the left of the photographs indicate rock type (granite-granodiorite and granite) based on XRD and petrographic studies (Jones and others, 2018, 2019). Higher MS values indicate increasing concentrations of mafic minerals such as biotite, hornblende, augite, titanite, and apatite, and generally correlate with visible changes in lithology. Some areas show significant variation over small depth intervals.*

CONCLUSIONS

The diverse dataset discussed here, along with other data (FMI interpretations, XRD, petrographic studies, etc.) show that the basement rock within the FORGE area consists of a suite of intrusive rock types that are primarily granitic. However, significant quantities of rock with somewhat intermediate compositions (quartz monzonite, monzonite, quartz monzodiorite), and lesser quantities of monzodiorite and diorite are present. The XRD and petrographic data from Jones and others (2018, 2019) show considerable compositional variation with depth through the 58-32 well and reasonably characterize the well in terms of rock type over 100-foot intervals. Log interpretations (primarily based on rock density and the natural gamma signal),

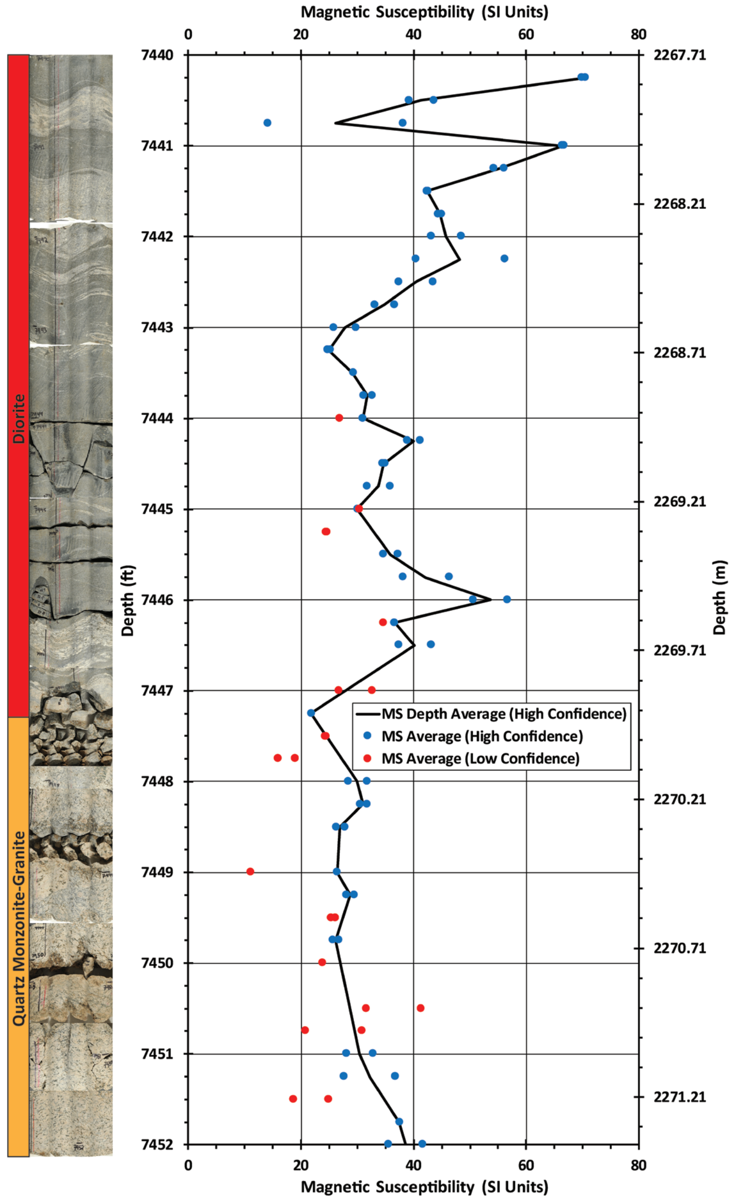

Figure 32. *Magnetic susceptibility (MS) measurements in the second cored section of well 58-32 (top at 7440 feet). Two measurements were taken at 3-inch intervals in the reconstructed core, with each measurement taken on opposite sides of the core. Five measurements were made at each location. Measurements near, or on, fractures were lower confidence due to missing material. However, agreement with high-confidence data suggests the effects are minimal. The average of the five measurements at each location is plotted, as is the overall average per depth interval (high-confidence data only; black trend line). The core was photographed on four sides, and these were joined to create the composite photograph on the left, showing the entire circumference of the core. Colored boxes to the left of the photographs indicate rock type (diorite and quartz monzonite-granite) based on XRD and petrographic studies (Jones and others, 2018, 2019). Higher MS values indicate increasing concentrations of mafic minerals such as biotite, hornblende, augite, titanite, and apatite, and generally correlate with visible changes in lithology. Some areas show significant variation over small depth intervals.*

spectral gamma measurements, thermal conductivity and density measurements, field investigations, and magnetic susceptibility measurements are all in general agreement with the XRD data. The XRD data were used to calibrate many of these other analyses to characterize their results with respect to the specifically identified rock types.

Distinct small-scale changes in rock composition do occur and many of these are missed when looking only at samples from 100-foot intervals. Similar small-scale variations are present in other nearby wells such as 9-1 and 82-33, confirming that such variations are characteristic of the intrusive complex in the FORGE area. These small-scale changes are primarily seen in the log interpretations and in the core analyses, since many of the other types of measurements were made at the same 100-foot intervals as the XRD analyses.

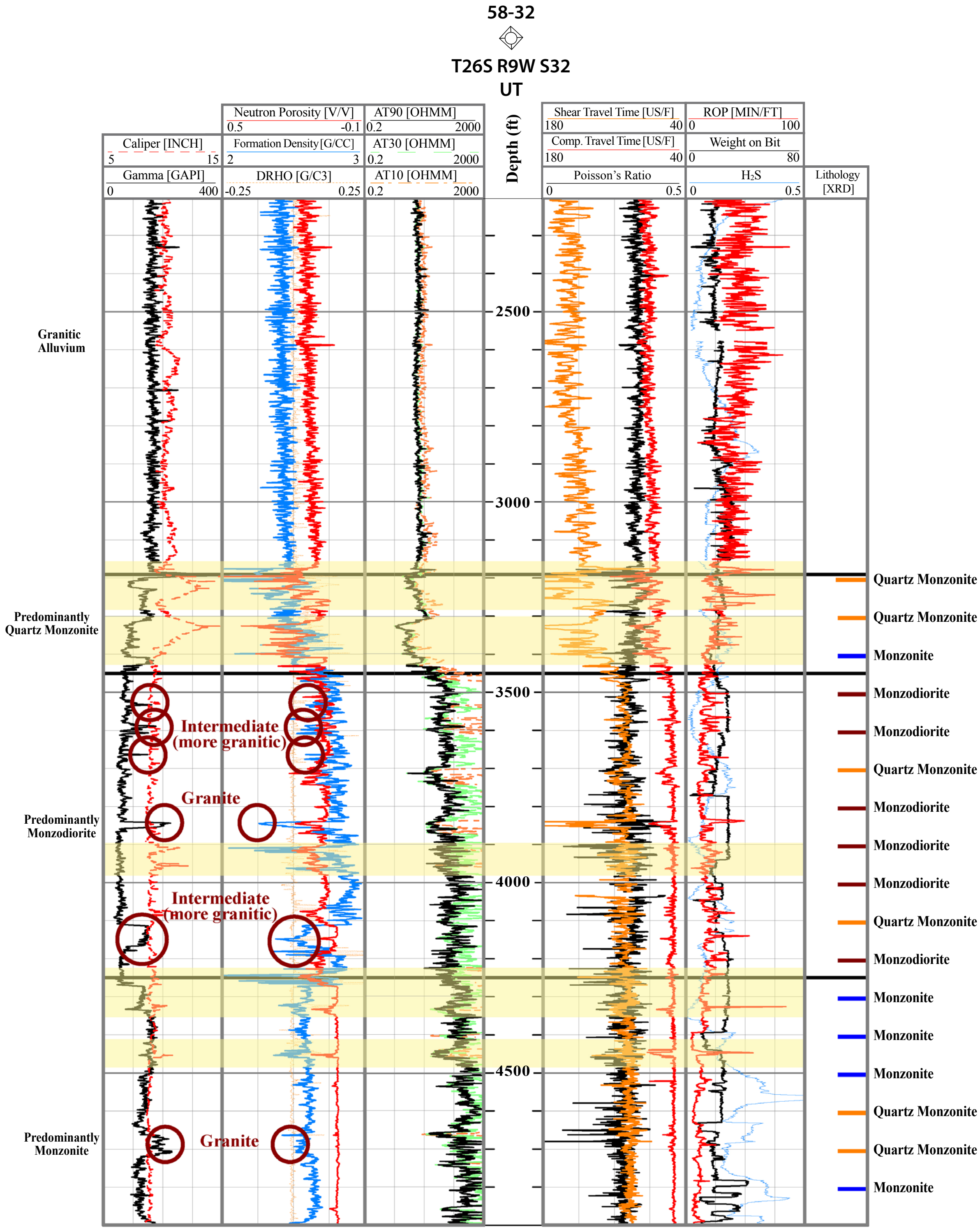

Figure 33. *Selection of wireline log responses for well 58-32 from the bottom of the surface casing at 2173 feet to 4900 feet. "Caliper" indicates hole diameter, "gamma" indicates natural gamma radiation, "neutron porosity" indicates rock porosity, "formation density" indicates rock density, "DRHO" indicates the quality of the density data, "AT__" indicates rock resistivity, "Shear/Comp travel time" and "Poisson's ratio" indicate sonic properties of the formation, "ROP" and "Weight on Bit" indicate drilling parameters, and "H2S" is a measurement of hydrogen sulfide gas released from the formation while drilling. Zones based on gross lithology on the left of the figure are defined by XRD data shown on the right (Jones and others, 2018, 2019). The gamma and formation density curves are the most useful for identifying rock types in the well. High gamma/low density responses are characteristic of granitic rocks while low gamma/high density responses are characteristic of dioritic rocks. Circled "spikes" indicate significant changes in rock composition over a short interval of depth. Most of these "spikes" occur between depths where cuttings were studied and were therefore missed by other analyses. Yellow highlighted zones show where washouts make formation density measurements unreliable (note that much of the "predominantly quartz monzonite" zone was badly affected by washouts). Increasing resistivity from 3300 to 4300 feet suggests weathering.*

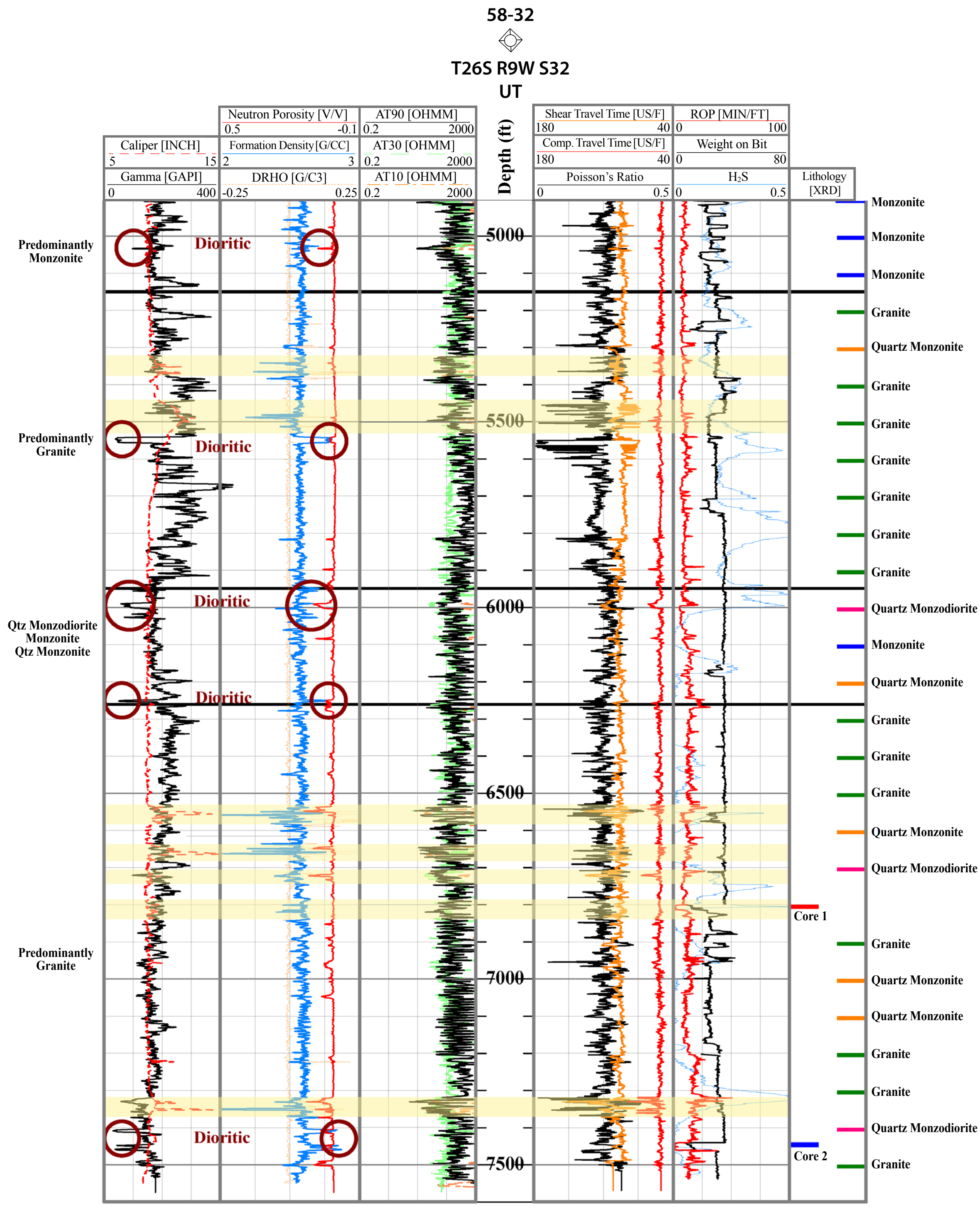

Figure 34. *Selection of wireline log responses for well 58-32 from 4900 feet to 7536 feet (TD). "Caliper" indicates hole diameter, "gamma" indicates natural gamma radiation, "neutron porosity" indicates rock porosity, "formation density" indicates rock density, "DRHO" indicates the quality of the density data, "AT__" indicates rock resistivity, "Shear/Comp travel time" and "Poisson's ratio" indicate sonic properties of the formation, "ROP" and "Weight on Bit" indicate drilling parameters, and "H2S" is a measurement of hydrogen sulfide gas released from the formation while drilling. Zones based on gross lithology on the left of the figure are defined by XRD data shown on the right (Jones and others, 2018, 2019). The gamma and formation density curves are the most useful for identifying rock types in the well. High gamma/low density responses are characteristic of granitic rocks while low gamma/high density responses are characteristic of dioritic rocks. Circled "spikes" indicate significant changes in rock composition over a short interval of depth. Most of these "spikes" occur between depths where cuttings were studied and were therefore missed by other analyses. Yellow highlighted zones show where washouts make formation density measurements unreliable.*

Thermal conductivity measurements provide data that is critical to understanding the thermal regime. These measurements can also help differentiate quartz-rich intrusive rock from other compositions due to the relatively high thermal conductivity of quartz. In 58-32, the matrix thermal conductivity of granite was generally greater than 3.1 W/m°C, while quartz-poor (plagioclase-rich) monzodiorite values were typically around 2.1 to 2.6 W/m°C. Matrix density values are also calculated when performing thermal conductivity measurements, and when adjusted for in situ porosity, may provide better estimates of rock density than density logs because the logs are sensitive to borehole conditions. Density is a major discriminator between dioritic rock (usually about 2.8–3.0 g/cm^3 due to increasing quantities of high-density mafic minerals) and more granitic rock types that are commonly about 2.65–2.75 g/cm^3. Density is not as useful for discerning individual rock types of intermediate composition because variations tend to be small and overlapping.

Spectral gamma measurements should be obtained from the bore hole with a wireline tool to eliminate the uncertainty shown using hand-held instruments at the surface. Wireline surveys with spectral gamma tools are more expensive than those measuring total gamma, but in an intrusive environment where potassium is a major indicator of changing rock type, the results may be worth the added cost. If spectral gamma is not measured as part of a logging package in future wells, the laboratory results could likely be significantly improved with larger cuttings samples, although it may still not be possible to obtain the optimum mass of around 5–6 kilograms. The mass of cuttings samples from the 58-32 well were typically between 300 grams and 700 grams. Because the samples were duplicated for EGI and the UGS, it follows that in wells of similar diameter, samples of around 1.4 kilograms, and possibly much greater, could frequently be collected over a 10-foot drilling interval. If the recovered samples were still below the optimum mass of 5 to 6 kilograms, at least the range of depths required to achieve the optimum mass could be tightened (i.e., maybe 30-foot intervals could be combined rather than the 80-foot intervals as described in this report). Despite the uncertainty of the gamma ray spectrometry measurements in 58-32 (especially in cuttings), Allis and others (2018b) found the relative ratios of potassium, uranium, and thorium to be useful for estimating heat production and differentiating between granitic and dioritic rock types. However, the greatest value of the spectral gamma study in 58-32 could be for the interpretation of down-hole spectral gamma logs if they are obtained in future wells.

Magnetic susceptibility measurements on core samples indicate that small (inch) depth-scale variations in mineral composition do occur. Increasing MS correlates well with increasing quantities of mafic minerals. Cuttings from granite and intermediate rock types that are more quartz-rich in the 58-32 well typically have MS values under 10 SI units, whereas more mafic rocks, particularly monzodiorite and diorite, show values that are typically between 20 and 50 SI units. Because sample measurements can be obtained quickly and inexpensively (now that a calibration has been established for granular materials), they could provide initial insight into rock compositions before more diagnostic analyses such as XRD are performed.

Wireline logs, particularly gamma and density, are key to characterizing the rock penetrated in an intrusive environment such as the FORGE area. They provide data well before laboratory analyses are completed and can highlight important compositional variations that may otherwise be missed by analyses at a coarser range of depths. Like density, total gamma values are less diagnostic of individual intermediate rock types due to overlap. These rock types have a “group” mean of about 150 gAPI, whereas granite has a mean of about 200 gAPI and diorite/monzodiorite has a mean of about 60 gAPI. Wireline spectral gamma logs may help to better differentiate the intermediate rock types in future wells. The log responses that are generally diagnostic of granitic, intermediate, and dioritic rock types are:

- Granitic: Gamma 140–290 gAPI; density about 2.54–2.62 g/cm^3
- Intermediate: Gamma 70–210 gAPI; density about 2.55–2.65 g/cm^3
- Dioritic: Gamma 50–80 gAPI; density 2.65–2.90 g/cm^3

The various analyses of the 58-32 well prove it was drilled into low porosity/low permeability rock that is generally granitic in composition with temperatures well within the DOE-specified window of 175°–225°C. Additionally, despite small-scale compositional changes in the rock, geomechanical characteristics throughout the reservoir zone are reasonably consistent and suitable for testing the techniques and technologies required to develop enhanced geothermal reservoirs.

ACKNOWLEDGMENTS

This work was sponsored by the DOE EERE Geothermal Technologies Office project DE- EE0007080 Enhanced Geothermal System Concept Testing and Development at the Milford City, Utah FORGE Site (Joe Moore, Managing PI). We thank Craig Morgan, David Tabet, Michael Vanden Berg, Kimm Harty, and Mike Hylland for their extensive reviews of this work.

REFERENCES

Ascencio, F., Samaniego, F., and Rivera, J., 2006, Application of a spherical-radial heat transfer model to calculate geothermal gradients from measurements in deep boreholes: Geothermics, v. 35, p. 70–78.

Allis, R., Gwynn, M., Hardwick, C., Hurlbut, W., and Moore, J., 2018a, Thermal characteristics of the FORGE site, Milford, Utah: Transactions, Geothermal Resources Council, v. 42, p. 1011–1025.

Allis, R., Gwynn, M., Hardwick, C., and Moore, J., 2018b, The challenge of correcting bottom-hole temperatures—an example from FORGE 58-32, near Milford, Utah: Proceedings, 43rd Workshop on Geothermal Reservoir Engineering, Stanford University, Stanford, California, SGP-TR-213, 8 p.

Balamir, O., Rivas, E., Rickard, W.M., McLennan, J., Mann, M., and Moore, J., 2018, Utah FORGE reservoir—drilling results of deep characterization and monitoring well 58-32: Proceedings, 43rd Workshop on Geothermal Reservoir Engineering, Stanford University, Stanford, California, SGP-TR-213, 7 p.

Birch, F., and Clark, H., 1940, The thermal conductivity of rocks and its dependence upon temperature and composition: American Journal of Science, v. 238, nos. 8 and 9, p. 529–558 and 613–635.

Blum, P., 1997, Physical properties handbook—a guide to the shipboard measurement of physical properties of deep-sea cores: Ocean Drilling Program Technical Note 26, http://www-odp.tamu.edu/publications/tnotes/tn26/TOC.HTM.

Cenovus Energy, 2014, Hydrogen sulfide (H_2S) Code of Practice, Version 2.0: Cenovus Energy Health and Safety Manual CEN-EHS143, 15 p., https://www.cenovus.com/contractor/health-and-safety-practices.html.

Edwards, M.C., and Chapman, D.S., 2013, Geothermal resource assessment of the Basin and Range province in western Utah—report and heatflow map: Utah Geological Survey unpublished report provided to Arizona Geological Survey under Contract DE-EE0002850, 121 p.

Goutorbe, B., Lucazeau, F., Bonneville, A., 2007, Comparison of several BHT correction methods—a case study on an Australian data set: Geophysical Journal International, v. 170, no. 2, p. 913–922, https://doi.org/10.1111/j.1365-246X.2007.03403.x.

Gwynn, M., Allis, R., Sprinkel, D., Blackett, R., and Hardwick, C., 2014, Geothermal potential in the basins of Northeastern Nevada: Transactions, Geothermal Resources Council, v. 38, p. 1029–1039.

Gwynn, M., Allis, R., Hardwick, C., Jones, C., Nielsen, P., and Hurlbut, W., 2018, Rock properties of FORGE well 58-32, Milford, Utah: Transactions, Geothermal Resources Council, v. 42, p. 1047–1070.

Hardwick, C., Hurlbut, W., Gwynn, M., Allis, R., Wannamaker, P., and Moore, J., 2018, Geophysical surveys of the Milford, Utah, FORGE site—gravity and TEM: Transactions, Geothermal Resources Council, v. 42, p. 1071–1083.

Henrikson, A., and Chapman, D.S., 2002, Terrestrial heat flow in Utah: Unpublished report, University of Utah, http://geology.utah.gov/emp/geothermal/pdf/terrestrialhf.pdf.

Horai, K., and Simmons G., 1969, Thermal conductivity of rock-forming minerals: Earth and Planetary Science Letters, v. 6, p. 359–368.

Jones, C. and Moore, J., 2016, Petrographic and x-ray diffraction analyses of 62 drill cutting samples from geothermal well Accord 1-26, Beaver County, Utah: Unpublished report, Energy & Geosciences Institute at the University of Utah, 23 p.

Jones, C.G., Moore, J.N., and Simmons, S.F., 2018, Lithology and mineralogy of the Utah FORGE EGS reservoir—Beaver County, Utah: Transactions, Geothermal Resources Council, v. 42, p. 1084–1096.

Jones, C.G., Moore, J.N., and Simmons, S., 2019, Petrography of the Utah FORGE site and environs, Beaver County, Utah, *in* Allis, R., and Moore, J.N., editors, Geothermal characteristics of the Roosevelt Hot Springs system and adjacent FORGE EGS site, Milford, Utah: Utah Geological Survey Miscellaneous Publication 169-K, 23 p., 2 appendices, https://doi.org/10.34191/MP-169-K.

Kirby, S.M., Knudsen, T., Kleber, E., and Hiscock, A., 2018, Geologic setting of the Utah FORGE site based on new and revised geologic mapping: Transactions, Geothermal Resources Council, v. 42, p. 1097–1114.

Nadimi, S., Forbes, B., Finnila, A., Podgorney, R., Moore, J., and McLennan, J., 2018, DFIT and fracture modeling of the Utah FORGE site: Transactions, Geothermal Resources Council, v. 42, p. 1144–1154.

OSHA, 2018, Occupational safety and health standards Table Z-2: Occupational Safety and Health Administration, U.S. Department of Labor, https://www.osha.gov/SLTC/hydrogensulfide/standards.html.

Radiation Solutions, 2015, RS-125/230 user manual: Radiation Solutions, Inc., 61 p.

Robertson, E.C., 1988, Thermal properties of rocks: U.S. Geological Survey Open-File Report 88-441, 106 p.

Saint-Gobain, 2016, BGO Bismuth Germanate Scintillation Material: Crystal specifications sheet, Saint-Gobain Ceramics and Plastics, Inc., 2 p., https://www.crystals.saint-gobain.com/products/bgo.

Sibbett, B.S., and Nielsen, D.L., 2017, Geologic map of the central Mineral Mountains, Beaver County, Utah (GIS reproduction of 1980 map): Utah Geological Survey Map MP-17-2dm, 1:24,000.

Whittington, A., Hofmeister, A., and Nabelek, P., 2009, Temperature-dependent thermal diffusivity of the Earth's crust and implications for magmatism: Nature, v. 458, p. 319–321.

WIRELINE LOG AND BOREHOLE IMAGE INTERPRETATION FOR FORGE WELL 58-32, BEAVER COUNTY, UTAH, AND INTEGRATION WITH CORE DATA

by David A. Handwerger[1] and John D. McLennan[2]

[1]Statistical Petrophysics, LLC, and Energy and Geosciences Institute, Salt Lake City, Utah

[2]Department of Chemical Engineering, University of Utah, Salt Lake City, Utah

Link to supplemental data download: https://ugspub.nr.utah.gov/publications/misc_pubs/mp-169/mp-169-m.zip

Appendices 1 & 2

Figures 4–7

Miscellaneous Publication 169-M
Utah Geological Survey
a division of
UTAH DEPARTMENT OF NATURAL RESOURCES

This paper is part of *Geothermal Characteristics of the Roosevelt Hot Springs System and Adjacent FORGE EGS Site, Milford, Utah*. https://doi.org/10.34191/MP-169

Bibliographic citation:

Handwerger, D.A., and McLennan, J.D., 2019, Wireline log and borehole image interpretation for FORGE well 58-32, Beaver County, Utah, and integration with core data, *in* Allis, R., and Moore, J.N., editors, Geothermal characteristics of the Roosevelt Hot Springs system and adjacent FORGE EGS site, Milford, Utah: Utah Geological Survey Miscellaneous Publication 169-M, 7 p., 2 appendices, supplemental data, https://doi.org/10.34191/MP-169-M.

WIRELINE LOG AND BOREHOLE IMAGE INTERPRETATION FOR FORGE WELL 58-32, BEAVER COUNTY, UTAH, AND INTEGRATION WITH CORE DATA

by David A. Handwerger and John D. McLennan

ABSTRACT

A series of wireline logs were collected in the Frontier Observatory for Research in Geothermal Energy (FORGE) well 58-32, which is located just west of the Mineral Mountains, northeast of Milford, Utah, to characterize the mechanical properties and stress framework of the rock and the fracture network. A baseline logging phase was carried out over the majority of the borehole (below surface casing) upon completion of drilling and coring operations, and included Triple Combo, Dipole Sonic (DSI) and Formation Micro-Imager (FMI) logs. A second logging phase was conducted after openhole injection and microhydraulic fracturing had been carried out in the bottom, uncased section of the wellbore (~150 ft). This second logging suite consisted of a repeat FMI run over the lowermost ~110 ft to observe the changes in the fractures following the injection.

Many drilling-induced natural fractures were observed, having an average azimuth of 219 degrees, but most common direction of around 206 degrees (N26E). This azimuth typically corresponds to the direction of maximum horizontal stress. Minor borehole breakouts, also identifiable from the FMI images and which typically occur in the direction of minimum horizontal stress, had an average azimuth of 297 degrees (NW-SE), as would be expected given the interpreted orientation of the orthogonal stress from the induced fractures. The breakouts suggest an average azimuth of the maximum horizontal stress of N27E (i.e., minimum horizontal stress of N53W).

Additional continuous mechanical properties were calculated from the P- and S-wave velocities measured by a dipole sonic log, and bulk density from conventional triple combo measurements. The dipole sonic data were calibrated to triaxial compression tests on samples taken from the two cored sections in the well. These procedures enabled conversion of the dynamically-derived log predictions to static-equivalent parameters required for true subsurface mechanical property calculations. Calibration to core also allowed for calculation of a continuous Biot's parameter over the logged interval. This parameter is useful for estimation of the in situ stresses. From the calibrated mechanical properties, independent assessment of the formation pore pressure, and a calculation of Biot's poroelastic parameter, the principal stress magnitudes were estimated over the majority of the borehole.

New methods were employed to interpret changes in the subsurface fracture state because this project was unique in recording two FMI logs at different times. The before and after images were carefully realigned and then digitally subtracted in order to highlight any changes associated with a moderately aggressive injection program. This comparison enabled identifying newly induced fractures as well as widening and lengthening of previously observed natural fractures. Additionally, non-planar vertical fractures, perturbed in response to small-scale textural heterogeneities in the granite, were observed, suggesting localized stress concentrations and associated complexities (relative to strictly planar features) in the induced fractures.

INTRODUCTION

Wireline logging is an important means to gather data on the geology and material properties of the subsurface. Logging is conducted by lowering a series of instruments down a borehole and recording the physical properties of the rock as the instruments are pulled back up the hole at a set speed, typically around 1800 ft/hr. Logs record multiple physical responses in the rock and are sensitive to mineralogy, porosity, fluid saturation, fluid type, mechanical properties and fracturing. Logging data are recorded continuously at discrete spacing along the logged section and have the advantage over seismic data in that they are higher resolution (less vertically smoothed) and less correlated to each other. This allows for easier interpretation and more unique solutions to various iterative models commonly employed to determine rock properties. Although acoustic logs record at higher frequency, they do not provide 3D subsurface data like seismic imaging does.

Data collected during two phases of logging conducted after the 58-32 (Figure 1) well was drilled were analyzed. Logging phase 1 (run 1) was conducted from the base of the surface casing at ~2172 ft logging depth to total depth (TD). Logging phase 2 (run 2) was conducted after production casing was run to 7374.9 ft measured depth (MD). Plugback TD in this hole is 7525 ft MD, leaving approximately 150 ft of open hole. This second logging campaign followed a series of injection tests in the barefoot region of the hole from the base of the production casing at ~7386 ft logging depth to TD. The production casing was run before the injection testing. The first logging phase consisted of a Triple Combo run, followed by a Dipole Sonic Imager (DSI) – Formation Micro-Imager (FMI) run. The second phase consisted of just a DSI – FMI run to canvas changes in the openhole section after the injection testing. The injection involved multiple cycles above fracturing pressure including two Diagnostic Fracture Injection Tests (DFITs), one step rate test (SRT) and a low rate (~9 barrels per minute, BPM, 2 L/s) injection cycle with 200 mesh $CaCO_3$ proppant, as well as a number of low-rate injection cycles for stress measurement (see, for example, Forbes et al., 2019).

The triple combo is a combination logging tool that includes three primary measurement sondes used for subsequent interpretation: gamma ray (natural radioactivity of the rock), electrical resistivity (or reciprocally, the electrical conductivity), and lithodensity (Schlumberger, 1989). The triple combo contains sensors which record data through physical contact to the borehole wall. The lithodensity measurements provide three measurements: the bulk density, the neutron porosity (essentially the hydrogen abundance, interpreted under the assumption that the amount of hydrogen in the formation reflects the amount of water and/or hydrocarbon [Schlumberger, 1989; Krygowski, 2003]), and the photoelectric cross section of the rock matrix, which is a function of constituent atomic numbers (Krygowski, 2003). The first two calculated values, the density and neutron

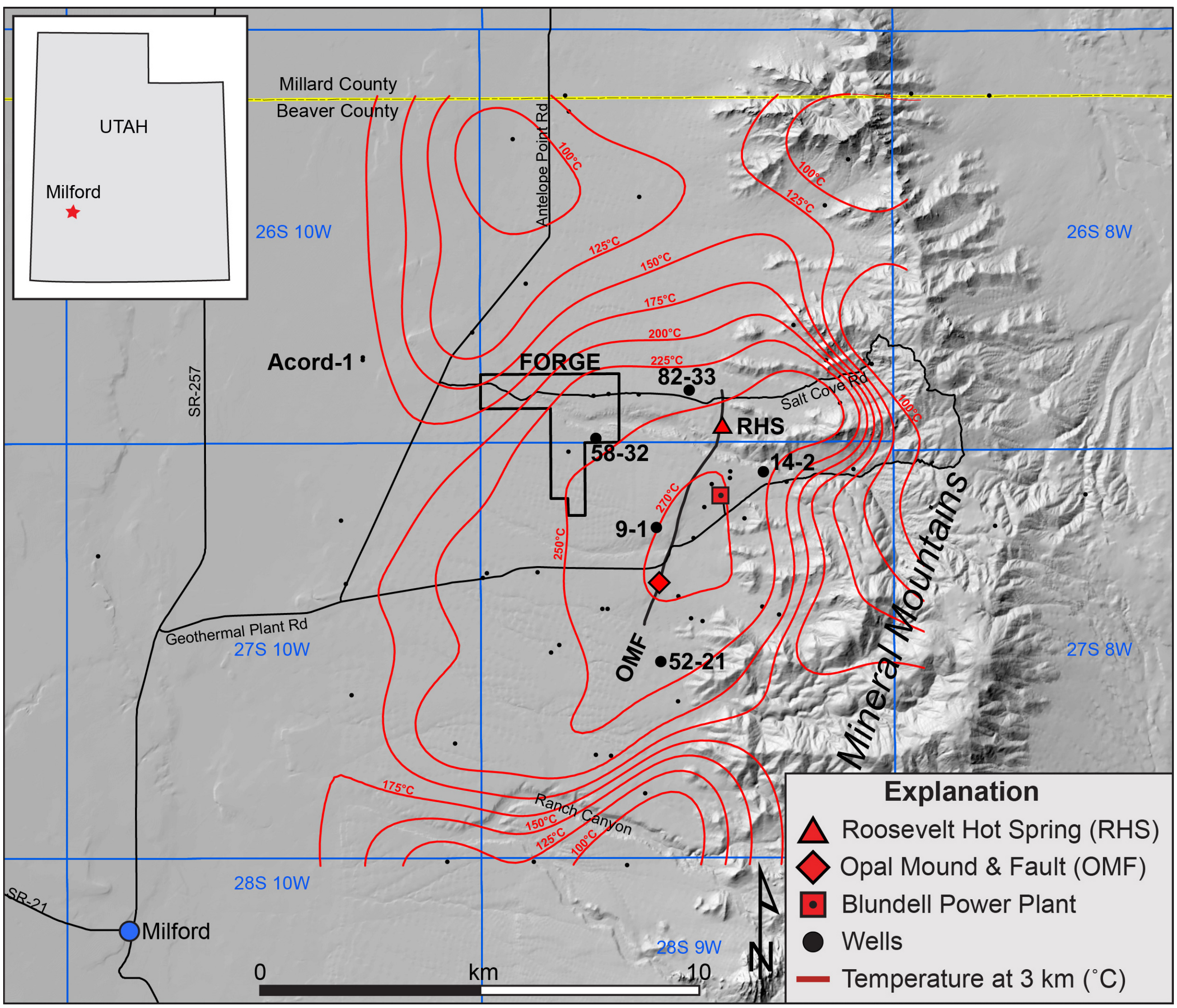

Figure 1. *Map showing the location of the FORGE 58-32 and nearby historical wells. Wells having data plotted in Appendix 2 are labeled. Other well locations shown are for historical thermal gradient wells. The isotherm contours displayed are from Allis et al. (2019).*

porosity, use fundamental measurements as proxies for formation porosity, liquid saturation, and fluid type. The gamma-ray count is a proxy for lithology (potassium, uranium, and thorium content; Schlumberger, 1989; Krygowski, 2003).

The DSI-FMI is a combination of two other logging tools. These were run concurrently but separately from the triple combo. A separate logging was required since these are run eccentrically in the borehole. The DSI log consists of a sonic source-receiver package to measure the velocity of acoustic waves in the rock, often viewed as a porosity proxy, but also fundamental for calculating geomechanical properties. The FMI records 192 short-spaced electrical resistivity measurements from a series of pads that contact about 80% of the borehole wall at any depth. Through these high-resolution measurements, an FMI survey returns an image of the borehole wall's features, particularly fractures (which are liquid filled and therefore much more conductive than the rock matrix) and pores. FMI images have millimeter-scale resolution (Schlumberger, 1989).

FRACTURE INTERPRETATION

Log analysis consisted of several steps. The first was interpretation and orientation of various fracture types and other planar features from the two FMI runs. An initial interpretation was provided by the logging contractor. We supplemented that interpretation, focusing on quality-controlling the initial interpretation and then adding additional important features that were overlooked. Numerous such features (tensile-induced fractures, breakouts, partially conductive fractures, conductive fractures, petal fractures, bedding planes, faults, etc.) were added to the initial interpretation, with particular attention to the lower 1000 ft of section, considered to be the thermal reservoir with in situ temperature exceeding 175°C. In the lowermost 1000 ft of the baseline FMI survey, only missed tensile-induced fractures, breakouts, and obvious bed boundaries were added to the fracture inventory developed by the logging contractor. Appendix 1 shows the baseline FMI image log with both the initial interpretation (left half) and the refined interpretation (right half). Figure 2 shows the distribution of tensile-induced (drilling induced) fractures from a merged set of the initial and refined interpretations. Figure 3 shows the merged breakouts. These data are important because tensile-induced fractures indicate the direction of the maximum horizontal stress and the borehole breakouts indicate the direction of the minimum horizontal stress. Each rose diagram shows the dip azimuth, with the average (solid arrow) and mode (dashed arrow) of the azimuths indicated. The drilling-induced fractures are oriented with a median azimuth of ~26° (NNE-SSW), and the breakouts are oriented with an average azimuth of ~297 degrees (NW-SE). Since some apparent breakouts were hard to conclusively identify as breakouts rather than induced fractures, feature orientation was used as a consideration for their interpretation in a number of cases.

The main interest in running an FMI log before and after the hydraulic fracturing in the barefoot section of the hole was to compare the two images and look for changes. We did this by taking the two static-processed FMI images and digitally subtracting one from the other. The static-processed images display the resistivity data with a color palette partitioned by the range of microresistivity values over the entire vertical recorded section, as opposed to a dynamically-processed image where the color palette is partitioned by microresistivity values within a small sliding window. Image subtraction required the use of the constant baseline imaging provided by the static processing.

To subtract the images as precisely as possible, they had to be depth-shifted relative to each other by refining the alignment of obviously identical features. Typically, each logging tool string contains a gamma-ray tool that provides a high-fidelity indication of lithology. As such, it is commonly used to depth-align the measurements from separate logging runs. In this case, the precision of this initial alignment of the two runs was not sufficient for the task of image subtraction. A refined, more precise alignment was made using like features in the FMI. Figure 4 shows the realigned and subtracted image logs.

Features present in the run-2 image that are not present in the run-1 image appear as black in the subtracted image, and features present in run 1, but not run 2 appear as white. While we were able to adjust the depths of the images to improve alignment, our software was unable to adjust the azimuth (left-right) alignment, so there are some thin wispy features in the subtracted image that result from very slight azimuthal misalignment. The background "zero" color signifying similar features in both images is the orange hue that makes up most of the area. Examples of vertical (induced) fractures that appear in run 2, but not run 1 can be found at 7452 ft, 7461.5 ft, 7468.5 ft MD. One can also note a widening of a fracture at 7509 ft and a long fracture from 7526 to 7532 ft, among others. All of these fractures are oriented approximately S-SW. A series of non-vertical fractures appears from 7537.5 to 7542.5 ft, predominantly dipping towards the east.

During propagation, a hydraulic fracture that is growing in a nominally homogeneous medium will minimize the expenditure of energy by aligning perpendicular to the least local stress. Around well 58-32, the in situ stress measurements have suggested that this minimum stress will likely act horizontally. Knowing the azimuth of that minimum horizontal principal stress allows for approximating the direction that hydraulic fractures will grow. Although this directionality can be locally varied by natural

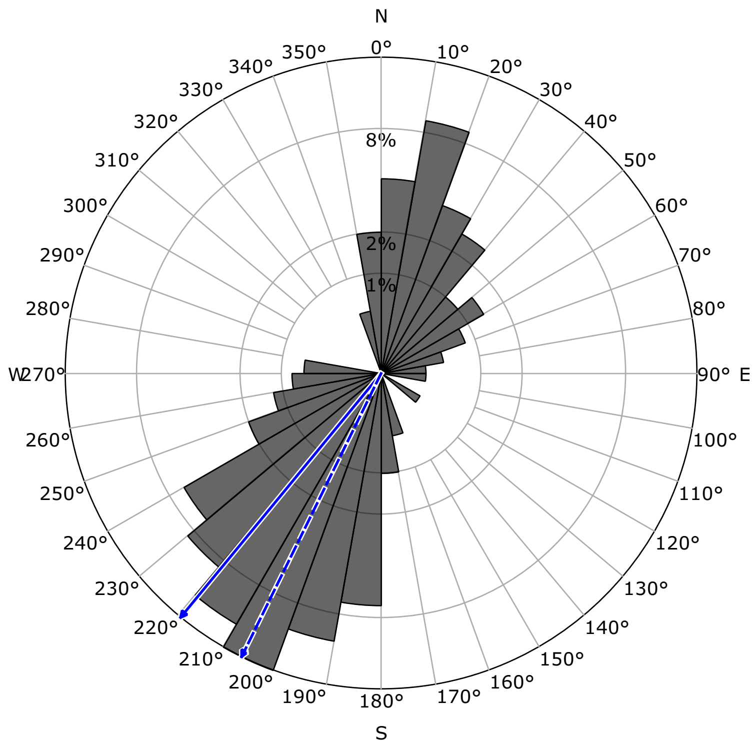

Figure 2. *Orientation of the tensile-induced natural fractures over the logged interval of the 58-32 well, including both those interpreted by the logging contractor and those that we added. Given that tensile-induced fractures are vertical to near-vertical, they do not appear as the sinusoids more gently dipping planes would, but as vertical traces on opposite sides of the borehole. To ensure that we did not identify the same feature twice, we only "picked" the most prominent trace. The traces, as identified, are shown rather than showing a reflection of one side to the other. This explains the lack of symmetry in the stereonet plot. We interpret the most common orientation as the direction of maximum horizontal stress.*

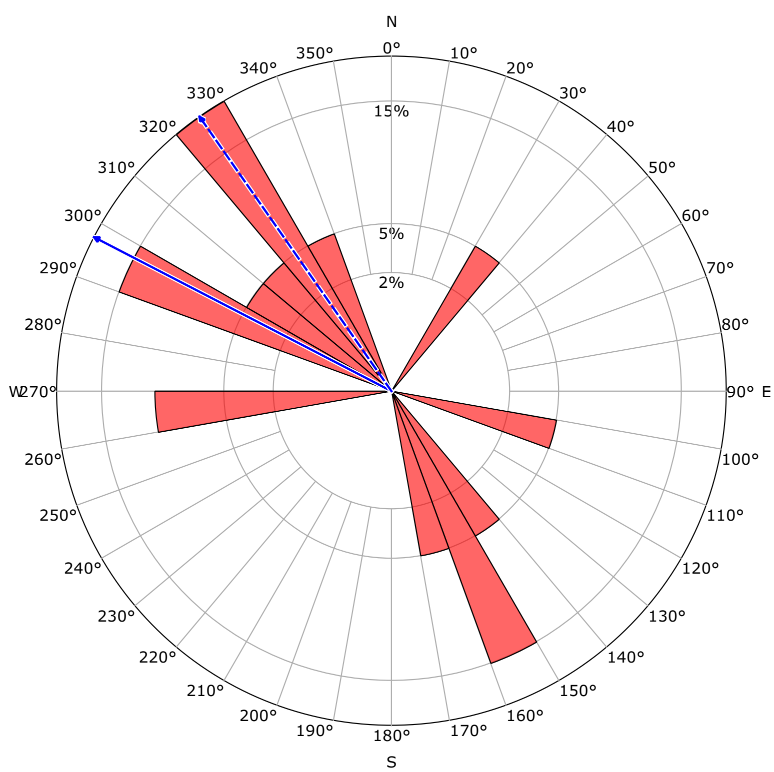

Figure 3. *Orientation of the borehole breakouts in the 58-32 well, following the same plotting guidelines as for the tensile-induced fractures in Figure 2. There were many fewer borehole breakouts than tensile-induced fractures, and they are much harder to interpret, accounting for the scatter in the data. The average orientation is approximately orthogonal to the tensile-induced fractures, suggesting this as the direction of minimum horizontal stress.*

discontinuities such as fractures, the propagation trend will be maintained at a large scale. If the propagation direction of hydraulically induced fractures in the vicinity of well 58-32 can be determined (that is, a vertical fracture, propagating in a plane containing the vertical stress and the maximum horizontal principal stress—perpendicular to the minimum horizontal principal stress), horizontal wellbores drilled in the minimum principal horizontal stress direction can ideally be stimulated multiple times to create a multitude of borehole-transverse horizontal fractures. As has been indicated, drilling-induced tensile fractures, tensile fractures created by hydraulic fracturing, and breakouts are all indicators of the directions of the horizontal stresses in the project area. In addition, if hydraulic shearing is a mechanism for growing a connective fracture network, then determination of the strike and dip of the most critically stressed, pre-existing fractures depends on the complete principal stress tensor (magnitude and direction of the three principal stresses as mentioned above).

GEOMECHANICAL INTERPRETATION

Using the dipole sonic data, we calculated the elastic parameters of the rock and then estimated the stresses (Figure 5). We calculated the dynamic Young's Modulus, E_D, dynamic Poisson's Ratio, v_D, and dynamic Bulk Modulus, K_D (not shown). The dynamic values of Young's modulus and Poisson's ratio were calculated from wave velocities following standard protocols (Jaeger et al., 2009). The vertical stress was calculated by integrating the bulk density over the entire true vertical depth. This calculation required extrapolating the bulk density from the first logging measurement to an estimated surface value.

Two sets of triaxial tests were conducted from samples collected in both cores that were acquired in the well. With measurements at different confining pressures, cohesion and the angle of internal friction were determined. Static values of Young's Modulus, E_S, Poisson's Ratio, v_S, and Bulk Modulus, K_S, were determined from these tests following accepted practices (Ulusay and Hudson, 2007). Those data are shown in Figure 5 in comparison to the log-based calculations (note, the core depths have been adjusted to align with log depth; see below). The core data represent static properties. The dynamic Young's Modulus was calibrated to the core data to provide a continuous static Young's Modulus curve. Since Poisson's ratios from the core generally align with the log-calculated values at and near the core point, Poisson's ratio was not further calibrated. This is accepted industry practice—correcting the dynamic moduli using the static data but not adjusting Poisson's ratio. The logging-based values of Poisson's ratio were used as-is for estimating the horizontal stresses.

Biot's poroelastic parameter was calculated using a constant bulk modulus of quartz of 5.3×10^6 psi, derived from published data on manufactured quartz (Crystran, 2018), and from there the minimum and maximum horizontal stresses were calculated. According to a variation of Eaton's model, stresses were estimated using a poro-uniaxial strain model; i.e., with the assumption of zero far-field lateral strain (Eaton, 1969). Biot's poroelastic parameter, α, is estimated in a conventional manner as one minus the ratio of the grain or solid compressibility to the static compressibility of the bulk medium (Detournay and Cheng, 1993). The grain compressibility was approximated as the reciprocal of the bulk modulus of quartz. Biot's poroelastic parameter was initially calculated using the dynamic bulk modulus, and then recalculated with a "calibrated" static bulk modulus derived from Poisson's ratio and the logging values that have been calibrated with the laboratory measurements. Figure 5 shows the minimum and maximum horizontal stresses (solid green and red curves in the stresses column) for the uncalibrated log data, and the minimum horizontal stress (dashed green curve) for the calibrated logging data. Both maximum and minimum horizontal stresses were further adjusted to match the stresses that had been measured by hydraulic fracturing (see Forbes et al., 2019). The inferred horizontal stresses are shown in Figure 5. Note that the measured horizontal stresses fall into a range, and a "likely" stress value was inferred. The calibrated minimum horizontal stress (from adjusted well logs) matches the DFIT range. Figure 6 shows the full section of log-derived geomechanics data from run 1, below the upper casing.

The stress magnitudes and their variation with depth are also important because they are needed for predicting the vertical and lateral growth of hydraulic fractures as well as their complexity. Hydraulic fracture complexity refers to the degree of branching and interactions with pre-existing natural fractures. The magnitudes of the three principal stresses also govern shearing along pre-existing discontinuities (Zoback, 2012). Reliable vertical profiling of the minimum principal stress allows for numerical simulation of the amount of upwards fracture growth. In an enhanced geothermal system, where an injection well needs to connect with a vertically displaced production well through fracture networks, predictions of the vertical extent of the fractured zone impact the trajectories and separation of the injection and production wells.

LOG-CORE DEPTH ALIGNMENT

The FMI image and the gamma-ray track from run 1 were used with a core gamma-ray measurement to align the two recovered cores to the well logs. The driller's depth (the depth estimated during drilling by tallying drillpipe) for the lower core was ~14 ft shallower than the equivalent section in the logs (estimated through the amount of wireline extended), and the driller's depth for the upper core was ~11 ft shallower than the equivalent section in the logs (this is possible because of cable stretch in the logging tool wireline). This is shown in Figure 7, where the core gamma-ray and core photos have been shifted to match the FMI and log gamma ray. The core-measured magnetic susceptibility (MS) is also plotted in a shifted position. The alignment of the upper core was based on a prominent igneous dike in the core that was also seen as a prominent sinusoid (the representation of a dipping plane on the unwrapped cylinder of the borehole wall) in the FMI at 6816.5 ft (MD on the log).

Available log data from other wells in the FORGE study area were also compiled. These data were digitized from paper copies and input into the interpretation software (Techlog). A selection of the wells is shown in Appendix 2. The cross section is flattened to the top of crystalline rock, below the alluvium. This boundary is recognizable in the FMI surveys in well 58-32 at ~3176 ft MD. By looking at the other log responses across this boundary in well 58-32 and comparing to those same logs in the other wells (since none had an FMI), we were able to modify the depths of the top of granite across the area. At the time the other wells were drilled, initial depth picks of the top of the granite were made from cuttings collected at the time of drilling and from the decrease in drilling rate, which is much less precise than picking through logs if the top is readily identified through log character.

CONCLUSIONS

Wireline logs are an important tool for characterizing subsurface rock properties in both hydrocarbon and geothermal systems. They provide a wellbore-scale characterization, unlike seismic which samples larger dimensions at a lower resolution. Logs are particularly important in geothermal settings where seismic exploration can be restricted by attenuation and lack of reflectors in the granite and where other measurements such as magnetotelluric and gravity surveys lack resolution. The logging data contain a more diverse set of measurements than seismic data, and at a higher resolution. Additionally, in geothermal systems, seismic imaging is particularly challenging as resolution of features below the basin-fill (in this case) contact is virtually impossible due to the strength of the reflector at the contact and subsequent ray dispersion. The main value of the seismic data at this location is in identifying gross subsurface structures and the depth to the top of the granite. Detection of smaller scale fractures and faults within granitic material is masked by the properties of the granite itself, leaving logs and core as the only viable, high-resolution detection tools, at least for deep granitic systems.

Given the need to hydraulically fracture the FORGE-type, enhanced geothermal systems to set up convective water circulation, geomechanical properties are critical data in addition to fracture detection. Both were obtained in well 58-32 with wireline logging. In addition, fracture system development was resolvable by comparing FMI images before and after the fracture hydraulic injection program.

Fracture identification shows a dominantly NE-SW oriented set of injection- or drilling-induced fractures, suggesting this as the direction of maximum horizontal stress. An orthogonal borehole breakout orientation confirms this. Additionally, after the hydraulic injection, there are numerous zones of increased fracture intensity, such as ~7490–~7505 ft MD and ~7522 –~7535 ft MD, in the section below casing where the FMI was run twice. Image subtraction of the post-fracture FMI from the pre-fracture FMI shows changes in fracture width and extent resulting from hydraulic pressure during the injection program.

Downhole testing, via the DFIT (Forbes et al., 2019), shows a minimum horizontal stress gradient of around 0.62 psi/ft. Log interpretation was able to confirm this individual measurement and estimate the stress gradient variation with depth along the borehole.

ACKNOWLEDGMENTS

Funding for this work was provided by the U.S. DOE under grant DE-EE0007080, "Enhanced Geothermal System Concept Testing and Development at the Milford City, Utah FORGE Site". We thank the many stakeholders who are supporting this project, including Smithfield Foods, Inc., Utah School and Institutional Trust Lands Administration, Beaver County, and the Utah Governor's Office of Energy Development. We would also like to thank Schlumberger for providing logging and interpretation services.

REFERENCES

Crystran, 2018, Quartz sample specification: Online, https://www.crystran.co.uk/optical-materials/quartz-crystal-sio2

Detournay, E., and Cheng A.H.-D., 1993, Chapter 5—Fundamentals of poroelasticity, *in* Fairhurst, C., editor, Comprehensive rock engineering—Principles, practice and projects, volume II—Analysis and design methods: Oxford, Pergamon Press, p. 113–171.

Eaton, B.A., 1969, Fracture gradient prediction and its application in oilfield operations: Journal of Petroleum Technology, v. 246, p. 1353–1360.

Jaeger, J.C., Cook, N.G.W., and Zimmerman, R.W., 2009, Fundamentals of rock mechanics, 4th Edition: Malden, Blackwell Publishing, 488 p.

Krygowski, D.A., 2003, Guide to petrophysical interpretation: Austin, Texas, 147 p.

Schlumberger, 1989, Log interpretation principles/applications: Sugar Land, Schlumberger Wireline and Testing, 241 p.

Ulusay, R., and Hudson, J.A., editors, 2007, The complete ISRM suggested methods for rock characterization, testing and monitoring—1974-2006:ISRM Turkish National Group, Ankara, Turkey, 628 p.

Zoback, M.D., 2012, Reservoir geomechanics, 7th printing: New York, Cambridge University Press, 449 p.

NATURAL FRACTURE CHARACTERIZATION AT THE UTAH FORGE EGS TEST SITE: DISCRETE NATURAL FRACTURE NETWORK, STRESS FIELD, AND CRITICAL STRESS ANALYSIS

by Bryan Forbes[1], Joseph N. Moore[1], Aleta Finnila[2], Robert Podgorney[3], Siavash Nadimi[4], and John D. McLennan[4]

[1]Energy & Geoscience Institute, University of Utah, Salt Lake City, Utah
[2]Golder Associates, Redmond, Washington
[3]Idaho National Laboratory, Idaho Falls, Idaho
[4]Department of Chemical Engineering, University of Utah, Salt Lake City, Utah

Miscellaneous Publication 169-N
Utah Geological Survey
a division of
UTAH DEPARTMENT OF NATURAL RESOURCES

This paper is part of *Geothermal Characteristics of the Roosevelt Hot Springs System and Adjacent FORGE EGS Site, Milford, Utah*. https://doi.org/10.34191/MP-169

Bibliographic citation:

Forbes, B., Moore, J.N., Finnila, A., Podgorney, R., Nadimi, S., and McLennan, J.D., 2019, Natural fracture characterization at the Utah FORGE EGS test site—discrete natural fracture network, stress field, and critical stress analysis, *in* Allis, R., and Moore, J.N., editors, Geothermal characteristics of the Roosevelt Hot Springs system and adjacent FORGE EGS site, Milford, Utah: Utah Geological Survey Miscellaneous Publication 169-N, 11 p., https://doi.org/10.34191/MP-169-N.

NATURAL FRACTURE CHARACTERIZATION AT THE UTAH FORGE EGS TEST SITE: DISCRETE NATURAL FRACTURE NETWORK, STRESS FIELD, AND CRITICAL STRESS ANALYSIS

by Bryan Forbes, Joseph N. Moore, Aleta Finnila, Robert Podgorney, Siavash Nadimi, and John D. McLennan

ABSTRACT

Natural fractures are pre-existing cracks in a rock created from changes in earth stresses over time. In oil, gas, and geothermal operations, natural fractures can dominate fluid flow patterns, lead to unanticipated stress shadowing effects, drilling stability issues, and complex interactions with hydraulically induced fractures. These challenges can have perverse production and fluid flow effects on a reservoir. All formations contain unique sets of natural discontinuities. Therefore, it is highly desirable to locate and characterize natural fractures to assist in determining their associated contributions or risks to producing a quality reservoir.

Well 58-32 in Milford, Utah, was drilled to a depth of 7550 ft to serve as the pilot well for the Utah Frontier Observatory for Research in Geothermal Energy (FORGE) site. Formation Micro-Imager (FMI) logs and outcrop maps were used as the primary measurement sources for characterizing natural fracture properties such as their type, orientation, geometry, conductivity, and connectivity. This paper describes three activities incorporating natural fractures to characterize the FORGE test site reservoir: 1) construction of a discrete fracture network (DFN) to stochastically characterize natural fractures away from well control, 2) determination of the field stresses, and 3) analysis of natural fracture critical stresses at the well borehole. This work describes initial tasks completed during FORGE Phase 2B and will be extended to further refine and improve the understanding of the test site during Phase 2C.

INTRODUCTION

The Utah FORGE (Frontier Observatory for Research in Geothermal Energy) site was chosen by the Department of Energy (DOE) as the winning location for testing and demonstrating new technologies that will advance geothermal heat extraction from naturally fractured, low-permeability host rocks—in particular, enhanced geothermal systems (EGS) energy development (Simmons et al., 2016). The test site is located 250 km south of Salt Lake City and 16 km north-northeast of Milford, Utah (Figure 1), between the Basin and Range and Colorado Plateaus. During Phase 2B of the FORGE project, a pilot well, 58-32, was drilled, completed, and tested. Tests and measurements from the well were used to characterize the reservoir and support the FORGE site as the best EGS development candidate.

A successful thermal reservoir incorporates hydraulic stimulation techniques to propagate tensile fractures and/or to reactivate pre-existing shear fractures that often reorient to favor extensile propagation (Ye and Ghassemi, 2018). All reservoirs contain unique sets of natural fractures. These naturally occurring discontinuities are often composed of complex networks that affect the rock conductivity, mechanical properties, and preferred fluid flow pathways (Elmo and Stead, 2010; Nadimi et al., 2016). Natural fractures can cause unanticipated interactions between hydraulic fractures, drilling stability issues, complex fluid paths, and contact interactions with hydraulically induced fractures. Natural fracture characterization is common in the oil, gas, and mining industries and is becoming frequently incorporated in geothermal systems to help predict, avoid, and mitigate drilling, completion, and reservoir development issues (Xia et al., 2017).

The importance of natural fractures in subsurface characterization has influenced the development of various natural fracture modeling tools (Herbert, 1996). Today, models can incorporate 3D stochastically-generated natural fracture networks that honor the measured parameter ranges compiled from data sets which can be 1D (e.g., well FMI data), 2D (e.g., outcrop data) or 3D (e.g., seismic data). A combination of data measured from well 58-32 was used to develop probabilistic representations of in situ fractures, known as a discrete fracture network (DFN) (Dershowitz et al., 2004; Meyer and Bazan, 2011). The rationale for developing a DFN in Phase 2B is to consider the mechanical effects natural fractures have on the granitic reservoir.

In this study, a stochastic DFN model of the FORGE site was built using data measurements from well 58-32. Formation Micro-Imager (FMI) logs and outcrops maps were used as the primary inputs in characterizing natural fracture properties such as their

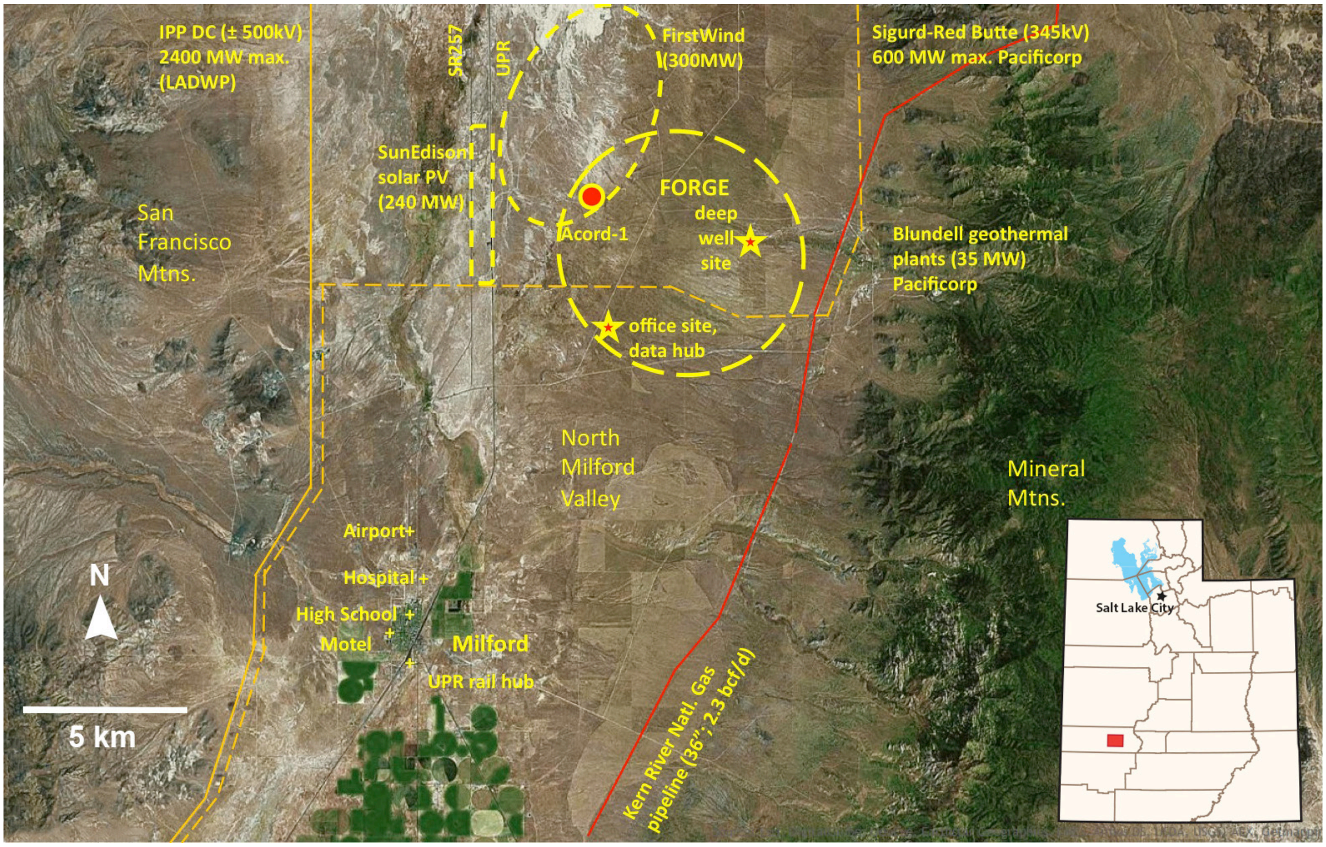

Figure 1. *Location of the FORGE deep well site near Milford, Utah (Allis et al. 2016).*

classification type, orientation, geometry, conductivity, and fracture connectivity. Additionally, various cycles of injection data were analyzed to determine the stress fields. The in situ stresses and wellbore fractures identified from the FMI logs were implemented in a stress analysis tool. The tool was used to identify fractures that were close to being critically stressed and likely to open first during hydraulic fracture stimulation. This information will be highly beneficial for designing optimal hydraulic fracture injection and reservoir management approaches for the wells planned to be drilled in Phase 2C of the FORGE project.

Discrete Fracture Network (DFN)

Well 58-32 was drilled, completed, and tested in 2017 to determine the crystalline granitic reservoir properties at the Utah Milford FORGE site. Outcrop mapping, seismic surveys, well logging, microhydraulic fracturing, pressure transient analysis, and core testing provided the intrinsic information for building a representative DFN. In particular, FMI data recorded in well 58-32 was processed. Each individual natural fracture was classified according to its orientation and fracture type. The FMI fractures were identified and categorized based on the resistivity differences observed along the rock as follows:

- Resistive continuous – partially open fractures filled with resistive materials such as calcite and quartz that limit fluid flow.
- Conductive continuous – an open conductive fracture around the borehole likely to be a preferred fluid flow path.
- Conductive partially resistive – partially open fractures with varying resistivity around the wellbore. Fracture fluid flow may be possible if calcite and quartz removal techniques are implemented (wellbore acid wash, for example).

Conductive partially resistive fractures constitute 97% of the natural fracture sample size. The fracture orientations from the image processing fall into three major groups with the following general strikes: N-S, E-W, and NE-SW groupings. Approximately 2000 natural features were identified over the entire logging interval of a baseline FMI run. Drilling-induced fractures were excluded from the imaged data, focusing the DFN construction on natural fractures. Natural fractures identifiable by the FMI are shown in rose and stereonet plots in Figure 2 from 3176 ft measured depth [MD] to 7550 ft total depth [TD].

Outcrop fracture mapping provided guidance in determining DFN properties such as the length, persistence, and terminations of the fractures around well 58-32 (Figure 3). From a nearby outcrop in the Mineral Mountains, natural fracture trace data

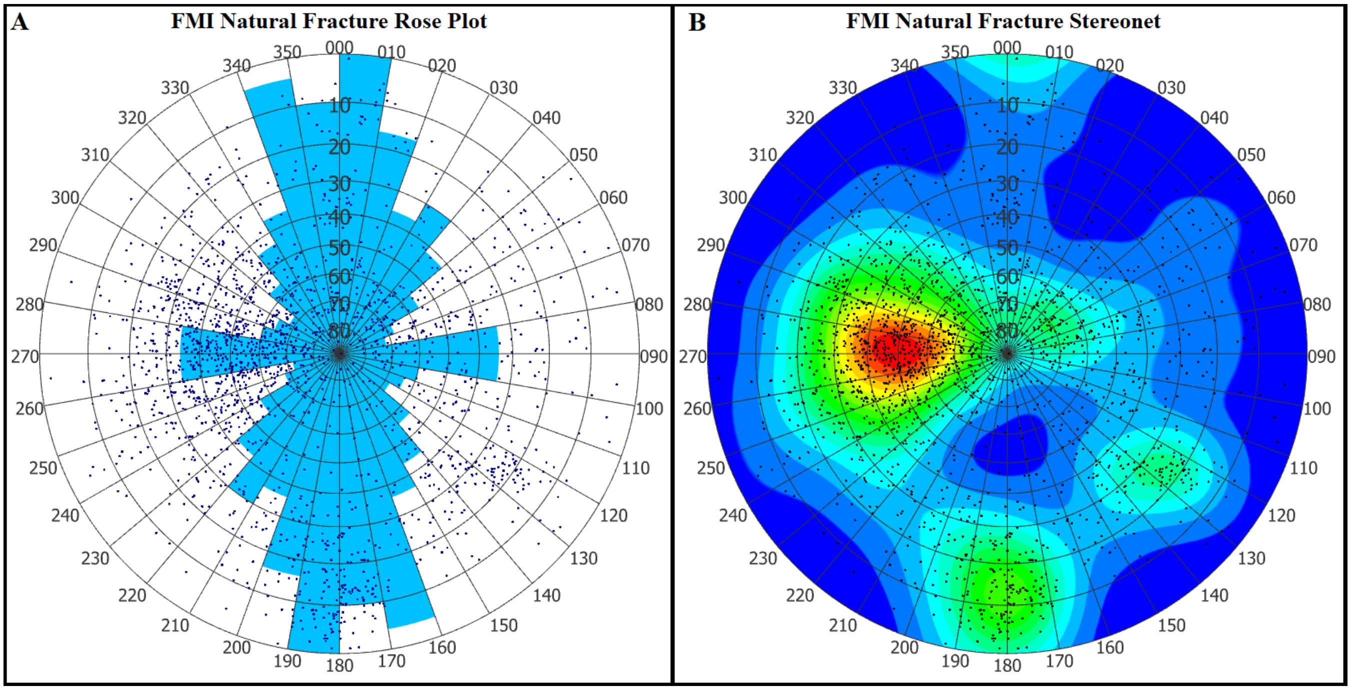

Figure 2. *Natural fractures identified from the FMI run from 3176 ft to 7550 ft TD in well 58-32.* ***(A)*** *The rose plot indicates the strike of the fractures.* ***(B)*** *The upper hemisphere, equal-angle stereonet plots the strike and dip of the natural fracture poles. Three general strike groups are identified: N-S, NE-SW, and a weak E-W group.*

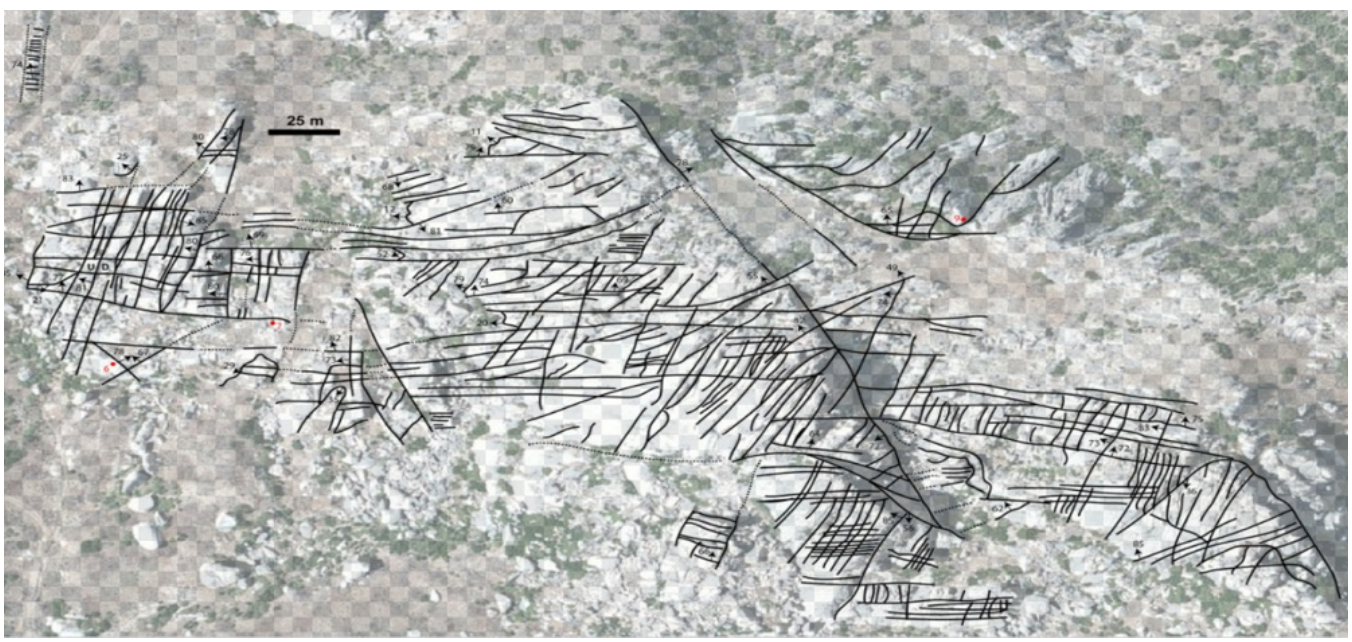

Figure 3. *Outcrop map from Salt Cove in the nearby Mineral Mountains where the target granite from the FORGE reservoir is exposed. The black lines represent mapped natural fractures superimposed on an aerial photograph. The strike, dip, and length of each fracture is recorded and used as one of the data sets for developing the FORGE site stochastic DFN. The surface location of well 58-32 is outside of this photograph (approximately 8 km west). Similar mapping was conducted for other outcrops, denoted as Bailey Springs, Negro Mag North, and Blundell SE.*

(strike, dip, and length) were fitted to the scale of the outcrop map, allowing determination of the equivalent fracture size corresponding to each exposed fracture trace. The fracture size is the radius of a circular fracture having the same area as the actual fracture shape. The measured fracture trace length will therefore be equal to or less than twice the fracture size (circular fracture diameter) depending on how the outcrop surface intersects the fracture. Figure 3 shows one of multiple outcrop maps used in determining DFN properties.

DFN models require inputs such as mean and standard deviation to generate statistically representable fracture properties. Fracture size can be estimated by constructing a cumulative frequency plot that shows the percentage of trace lengths that are less than or equal to particular values. A distribution curve is fit to the cumulative frequency plot that has the closest resemblance to the dataset (significance value). Figure 4 shows a cumulative frequency plot of the length data taken from the outcrop in Figure 3. A log-normal distribution gave the best match to the data (95% significance). The Salt Cove fracture size mean and standard deviation are 92 ft and 75 ft, respectively. This fitting procedure was also carried out for the other outcrop datasets. Note that while the trace length data best fit a log-normal distribution, this measured distribution can also represent data sets following an actual power law distribution that are truncated at both the low and high ends of the range.

Discrete fracture network models are not exact representations of all the actual fractures in the full 3D reservoir. A DFN can match the exact fracture locations and orientations measured in the wellbore or from outcrops. However, it is important to remember that DFNs also stochastically generate natural fractures away from measured areas using statistical inputs derived from direct field measurements.

Fischer distribution parameters were calculated for the N-S, E-W, and NE-SW fracture sets using the data provided from the FMI and outcrop evaluations. Table 1 shows the distribution data used to stochastically generate the fracture sets. The Fisher distribution in Table 1 is the analog of the Normal (Gaussian) distribution for a sphere, and is used to account for multiple uncorrelated variations in rock properties and stress conditions that can cause variations in the fracture orientation. The K1 value is a concentration parameter. An increasing K1value produces a higher distribution of fractures around the mean trend and plunge.

The vertical and areal dimensions of the DFN generation region were selected to cover the entirety of the FORGE site, resulting in an approximately 1 km^3 modeling domain. The stochastic natural fracture density and orientations were compared against the FMI fractures measured to determine the validity of the population datasets being generated. The statistical routine in FracMan™ generated approximately 350,000 fractures in the modeling domain. Each generated fracture set was filtered to only include approximately 2000 fractures directly intersecting the well. These filtered, intersecting fractures were compared with the fractures detected by the FMI survey before any injection tests were performed in the wellbore. The stochastic DFN models honored the FMI datasets and showed enough statistic similarity to represent the 1 km^3 region.

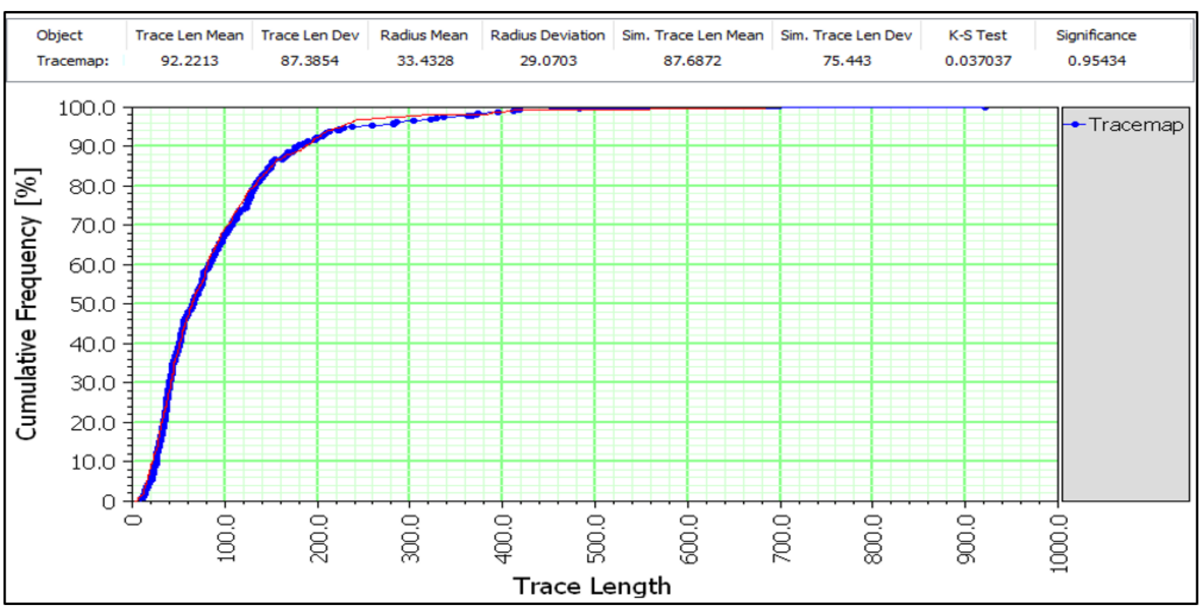

Figure 4. *Central Mineral Mountain cumulative frequency plot (trace lengths are displayed in meters). For example, 50% of the trace lengths measured are less than approximately 60 m. The blue points are the measured fracture lengths of natural fractures mapped in the Salt Cove outcrop in Figure 2. A line (red) is fit to the dataset and extracts mean and standard deviation values used to statistically represent the outcrop fracture lengths during DFN construction.*

Table 1. *Fracture set generation parameters and their distribution.*

	Orientation (fracture pole)			Fracture Radius (ft)		Fracture Intensity
Fracture Set	Fisher Distribution			Log Normal Distribution		(# Fractures / ft)
	Mean Trend (°)	Mean Plunge (°)	K1 Value	Mean	Standard Deviation	
NE/SW	331	1.0	.98	92	82	3.1
N/S	87	41.8	41.8	105	94	1.2
E/W	3	10.8	10.8	115	98	0.32

Field Stress Measurements

Stress and permeability measurements were made in late September 2017 in 147 ft of open hole below the 7-inch casing shoe. The 7-inch, 29-lb-per-ft, N80 casing was set at a total measured depth of 7374.9 ft kelly bushing (KB). After waiting on cement and a cement bond log (CBL), the hole was cleaned to 7525 ft (originally, drilled to 7536 ft). The purpose of leaving 10 ft of cement at the base of the well was to allow logging to total depth after injection. After the injection program, the cement was drilled out to allow full run of the FMI and dipole sonic imaging (DSI) logging tools.

Before injection, Baker Hughes ran a Retrievamatic™ compression packer into the hole. The setting depth covered 7244.7 to 7247.7 ft MD KB. A stinger was placed below the packer and communicated with the 4-inch drill pipe used to run the packer. At the bottom of the stinger was a gauge carrier for a pressure and temperature gauge, set to recover data every three seconds. Ports connecting to the openhole section were at 7426.8 ft MD (perforated sub). The stinger deployed a DiDrill™ pressure and temperature tool in the openhole section, allowing for a reliable bottomhole pressure and temperature measurement at 7426.8 ft MD, 7418.7 ft true vertical depth (TVD) KB. Tubing pressure, annulus pressure and injection rate were recorded by the pumping services company, Resource Cementing, and an auxiliary pressure transducer was provided by the mud loggers, West Coast Geologic. The drill pipe was tested successfully to 8000 psi. A rupture disk downhole was removed by progressively dropping a sinker bar. This disk allowed pressure testing of the drill pipe without pressurizing the formation.

Figures 5 and 6 show a surface pressure chronology for the injection measurements made over a two-day period. Table 2 shows the sequence of injection measurements made on September 22 and 23, 2017. The injection protocols were as follows.

September 22, 2017:

1) Injection/falloff test to assess permeability.
2) Three cycles of microfracturing for stress determination.
3) Diagnostic fracture injection test (DFIT) at ~5.8 and 8.7 barrels per minute (bpm) with an extended shut-in to determine permeability.

September 23, 2017:

1) One cycle repeating the microhydraulic fracturing for stress determination.
2) Step rate and DFIT with an extended shut-in to determine permeability.
3) DFIT followed by a proppant stage with 200-mesh calcium carbonate to prop the fracture and enhance differentiation between fractures identified with the pre- and post-fracturing FMI logging.

Table 3 summarizes the calculated stress gradients. The maximum stress gradient was determined using methods proposed by Haimson and Fairhurst (1967). Tensile strength is set to zero assuming pre-existing fracturing. Near-wellbore pore pressure was taken as hydrostatic (as determined from the near-static wellbore pressure, measured before injection began). Instead of using breakdown pressure, fracture reopening pressure was taken as the initial deviation from linearity during the injection phase of each cycle. All measurements were expressed as gradients based on the true vertical depth of the bottom hole pressure device (7429 ft KB MD, 7421 ft KB TVD) The depth can be corrected to ground level by subtracting 21.5 feet from the TVD value, but is inconsequential. The vertical stress was inferred by integrating the logging-based density values to the surface. The suggested stress field ranges are the following:

σ_{hmin}...0.58–0.63 psi/ft (best guess 0.62 psi/ft)

σ_{HMAX}...0.68–0.82 psi/ft (best guess 0.77 psi/ft)

σ_{v}...1.13 psi/ft

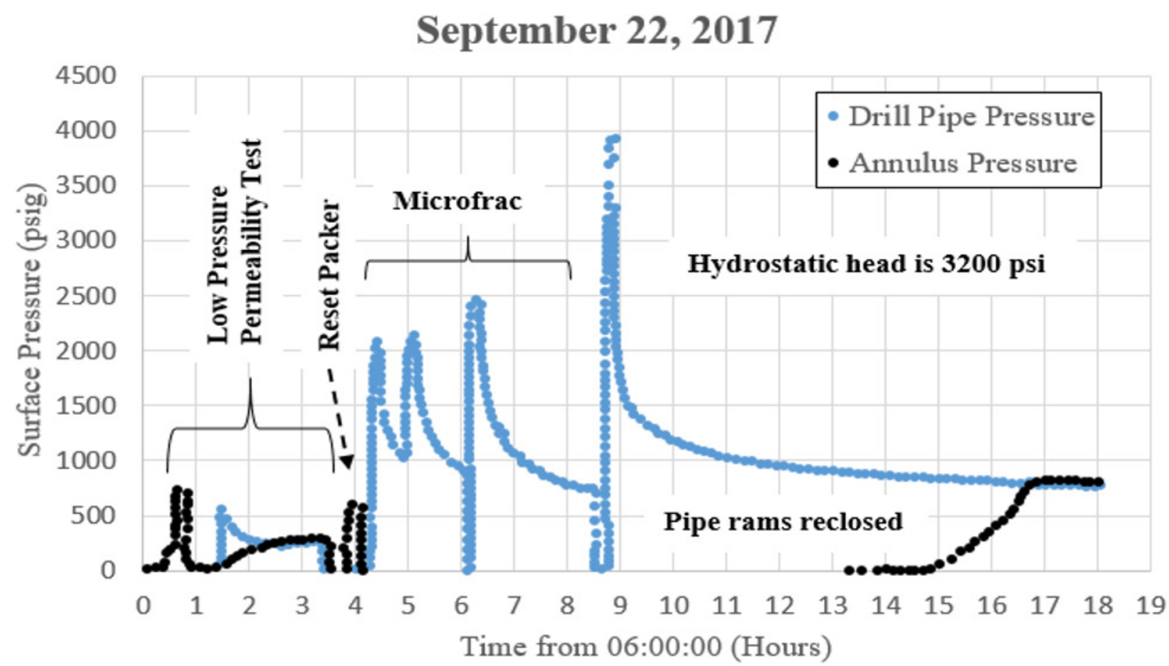

Figure 5. Surface pressure during the injection campaign. The plot shows the injection program on September 22, 2017. Five injection cycles are shown (cycles 1 through 5, chronologically increasing).

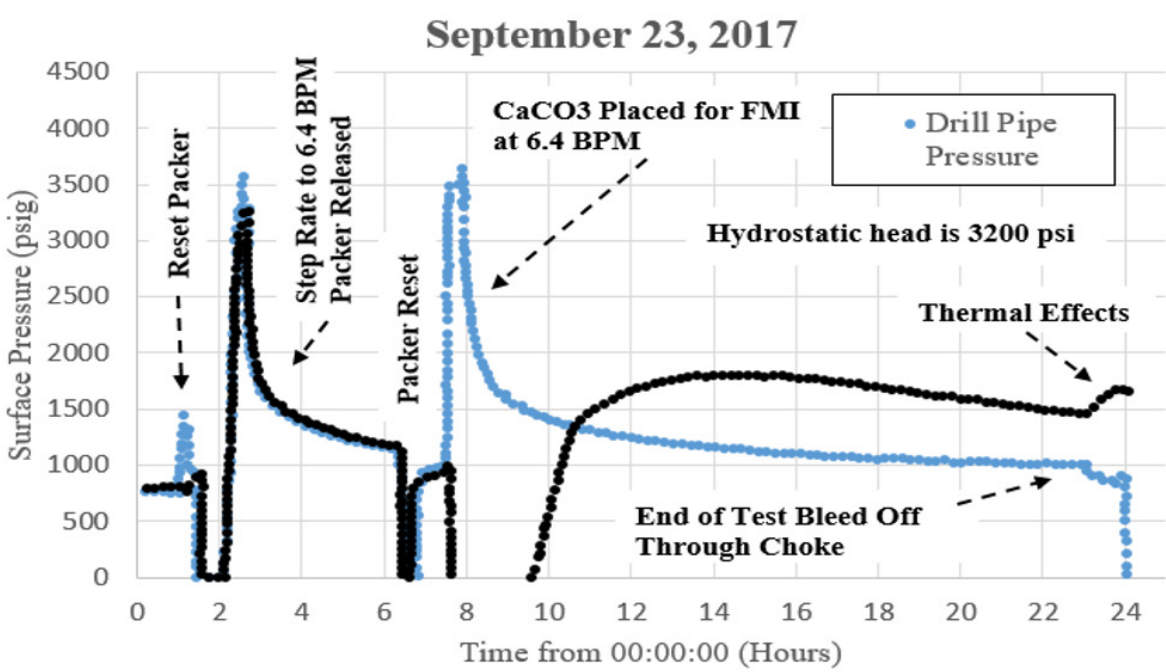

Figure 6. Surface pressure during the injection campaign. The plot shows the injection program on September 23, 2017. Three injection cycles are shown (cycles 6 through 8, chronologically increasing).

Table 2. *Summary of stress and permeability measurements.*

Cycle	Description	Purpose
1	Injection falloff. Pressure was increased to below the pressure required to hydraulically fracture the formation.	Assessment of native permeability before hydraulic fracturing testing
2	Microhydraulic fracture. 2.8 bbl were pumped at 0.4 bpm	Stress measurement
3	Microhydraulic fracture. 4.2 bbl were pumped at 0.4 bpm	Stress measurement
4	Microhydraulic fracture. 10.0 bbl were pumped at 0.8 bpm	Stress and permeability measurements
5	DFIT^{TM} pumped initially at 5.8 bpm and increased to 8.7 bpm for 5 minutes (67.2 barrels pumped). Prolonged shut-in.	Stress and permeability measurements
6	Repeat microhydraulic fracture test. 0.4 bpm and 3.8 bbl pumped	Stress measurement
7	76.9 bbl were pumped in a Step Rate Test (SRT) where rate was progressively increased • 0.4 bpm, 2.7 bbl pumped • 0.8 bpm, 4.1 bbl pumped • 1.6 bpm, 9.8 bbl pumped • 3.2 bpm, 16.1 bbl pumped • 6.3 bpm, 44.2 bbl pumped	An SRT is alternative method for evaluating minimum in situ stress as a function of injection rate. Shut-in pressure decline at the end of the SRT can be used to pick fracture closure with classic techniques. Permeability was also inferred.
8	DFIT^{TM} containing an 8 bbl slug of viscosified fluid carrying 200-mesh calcium carbonate proppant. 28.8 bbl of water at 6.4 bpm, followed by 8 bbl of viscosified xanthan with $CaCO_3$ at 6.4 bpm, displaced with 3 bbl of water at 6.4 bpm, and 8 bbl of water at 3 bpm to encourage screenout and fracture packing for subsequent logging.	Stress and permeability measurements

Table 3. *Summary of reopening data.*

Cycle	Description	Maximum Rate (bpm)	Volume Pumped (bbl)	Inflection (psi)	Inflection Gradient (psi/ft)	σ_{HMIN} Gradient (psi/ft)	σ_{HMAX} Gradient (psi/ft)	Temperature at Shut-In (°F)
1	Injection falloff							319
2	Micro-hydraulic fracture	0.4	3.8	4751	0.64	0.620	0.79	326
3	Micro-hydraulic fracture	0.4	4.2	4900	0.66	0.711	0.80	326
4	Micro-hydraulic fracture	0.8	10	5308	0.71	0.656	0.82	321
5	DFIT	8.7	67.2	4681	0.63	0.731	0.79	270
6	Micro-hydraulic fracture	0.4	3.8	4163	0.56	0.605	0.78	333
7	SRT	6.3	76.9	5205	0.70	0.75	0.82	280
8	DFIT with slug	6.7	86.6	5989	0.81	0.633	0.78	240

Critical Stress Analysis and Hydro-Shearing

The orientation of critically stressed fractures during hydro-shearing stimulation was studied using the Critical Stress Analysis functionality in FracMan™. The proposed approach is similar to Finnila et al. (2015). The analysis assumes shear failure occurs if the shear force,$|\tau|$ exceeds the shear strength, $f(\sigma)$, of a fracture if (Dershowitz et al., 1998):

$$|\tau| \geq f(\sigma) \tag{1}$$

If the fracture is critically stressed, its permeability may be enhanced. The Mohr-Coulomb criterion is used to calculate the fracture shear strength of fractures:

$$f(\sigma) = S_0 + \sigma \tan \phi_f \tag{2}$$

S_0 is the cohesion of the fracture, σ is the shear stress, and ϕ_f is the friction angle. Critically stressed fractures are typically oriented at a $(45° + \phi_f/2)$ angle from the minimum principal stress direction, σ_3 (Goodman, 1989).

The deepest 1000 ft of well 58-32 was analyzed from 6550 to 7550 ft to determine which fractures were critically stressed. The vertical, maximum, and minimum horizontal stress gradients considered were 1.13, 0.77, and 0.62 psi/ft, respectively (the basis for these stress gradients is explained in Section 3). Figure 7 shows the natural fracture stresses over the 1000 ft interval. Red colored fractures are less stable and should slip first. The first column in Figure 7 is the critical stress value calculated for each fracture at hydrostatic pore pressure (approximately 3200 psi). No fractures are critically stressed under static conditions. The next three columns show stable fractures in blue and critically stressed fractures in red for pressures of 200, 400 and 600 psi above hydrostatic pressure.

Predictions of which fractures will fail first can be tested by isolating and stimulating sections of the well. Stable sections (blue colors in the first column of Figure 7) remain closed and do not increase fracture conductivity after low-pressure stimulation (below the minimum principal stress). Conversely, sections containing fractures near to being critically stressed (red colors in the first column) are predicted to show an increase in fracture conductivity during low-pressure stimulation. The Mohr diagrams for the four different pore pressure cases are shown in Figure 8. A rose plot of critically stressed fractures at 600 psi excess pore pressure is shown in Figure 9. The critically stressed fracture directions from the rose plot suggest NE-SW-azimuth fractures are likely to be critically stressed first and could be considered as initial targets during hydraulic fracture stimulation.

CONCLUSIONS

Recent industry research has focused on incorporating natural fractures into reservoir characterization. The presence of natural fractures can cause challenges during drilling, completions, and production in an enhanced geothermal system. Outcrop and well 58-32 FMI data show that the FORGE granitic reservoir houses multiple, complex natural fracture sets.

A stochastic discrete fracture network model was constructed that honors the FORGE Phase 2B data and covers the entire test site boundaries. Injection tests were conducted and used to determine the local stresses in well 58-32. Stress values were used in critical stress analysis to predict natural fractures likely to fail first during hydraulic fracture stimulation. Results showed that NE-SW-azimuth fractures have the highest likelihood of re-opening first. This information will be important for future hydraulic fracture injection design and reservoir management tasks in Phase 2C.

In summary, this study provides: 1) initial stochastic natural fracture models of the FORGE site, 2) an approach for determining the granitic reservoir local stress field using well injection data, and 3) an analysis of critically stressed fractures near the 58-32 wellbore. As mentioned, caution must be taken when developing a DFN model. The fractures are not exact representations of all the actual fractures in the full 3D reservoir and are dependent on the data available. As Phase 2C progresses, the work described in this paper during Phase 2B will be refined to further characterize and develop the Utah FORGE EGS research site.

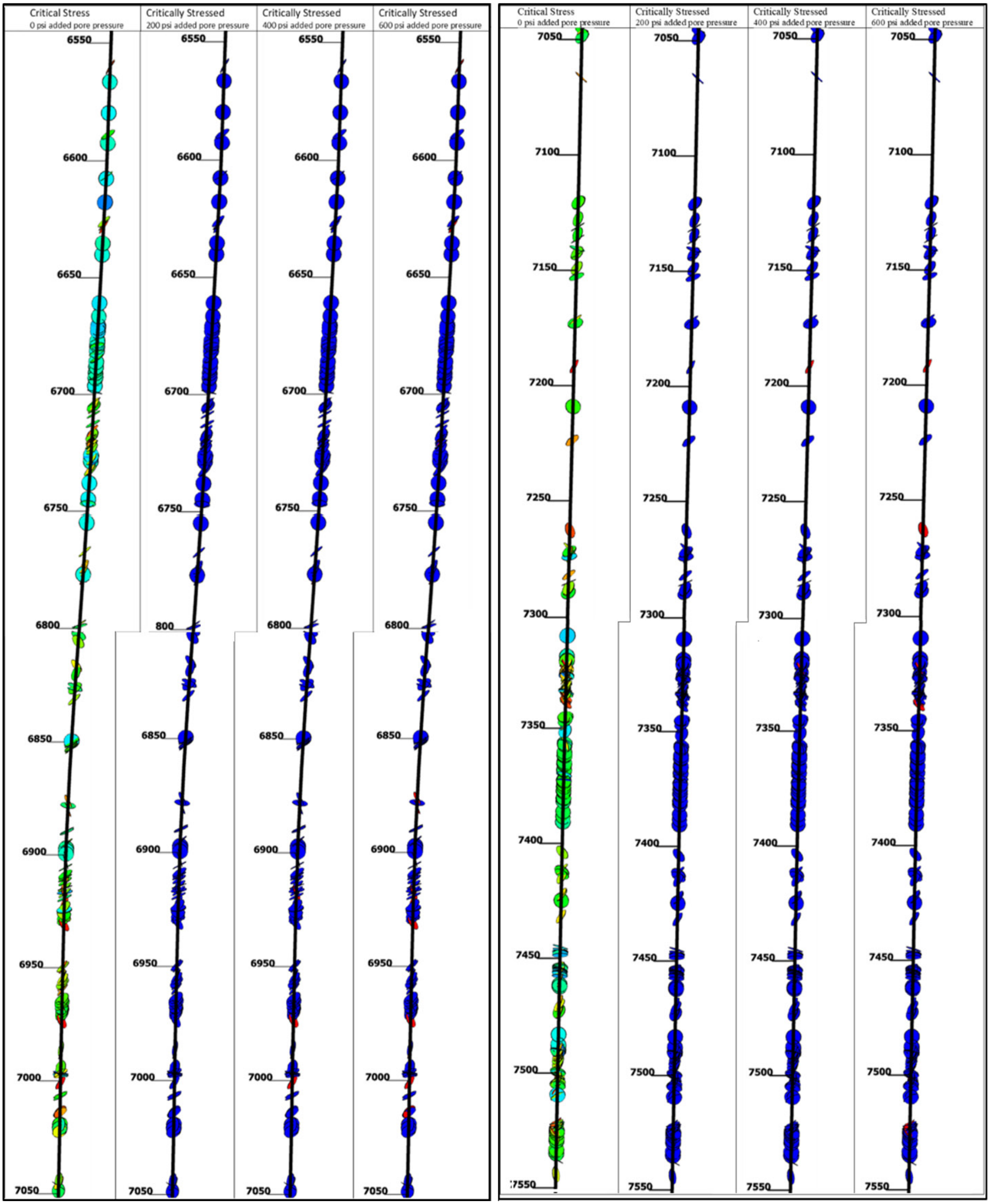

__Figure 7.__ The critical stress value calculated for each fracture identified from the FMI between 6550 ft to 7550 ft in the Utah 58-32 well. A hydrostatic and three overpressure instances were tested: 0 psi (hydrostatic ~3200 psi), 200 psi, 400 psi, and 600 psi. Red and orange highlighted fractures are under the highest degree of stress and most likely to open first during stimulation compared to the lower stressed blue fractures.

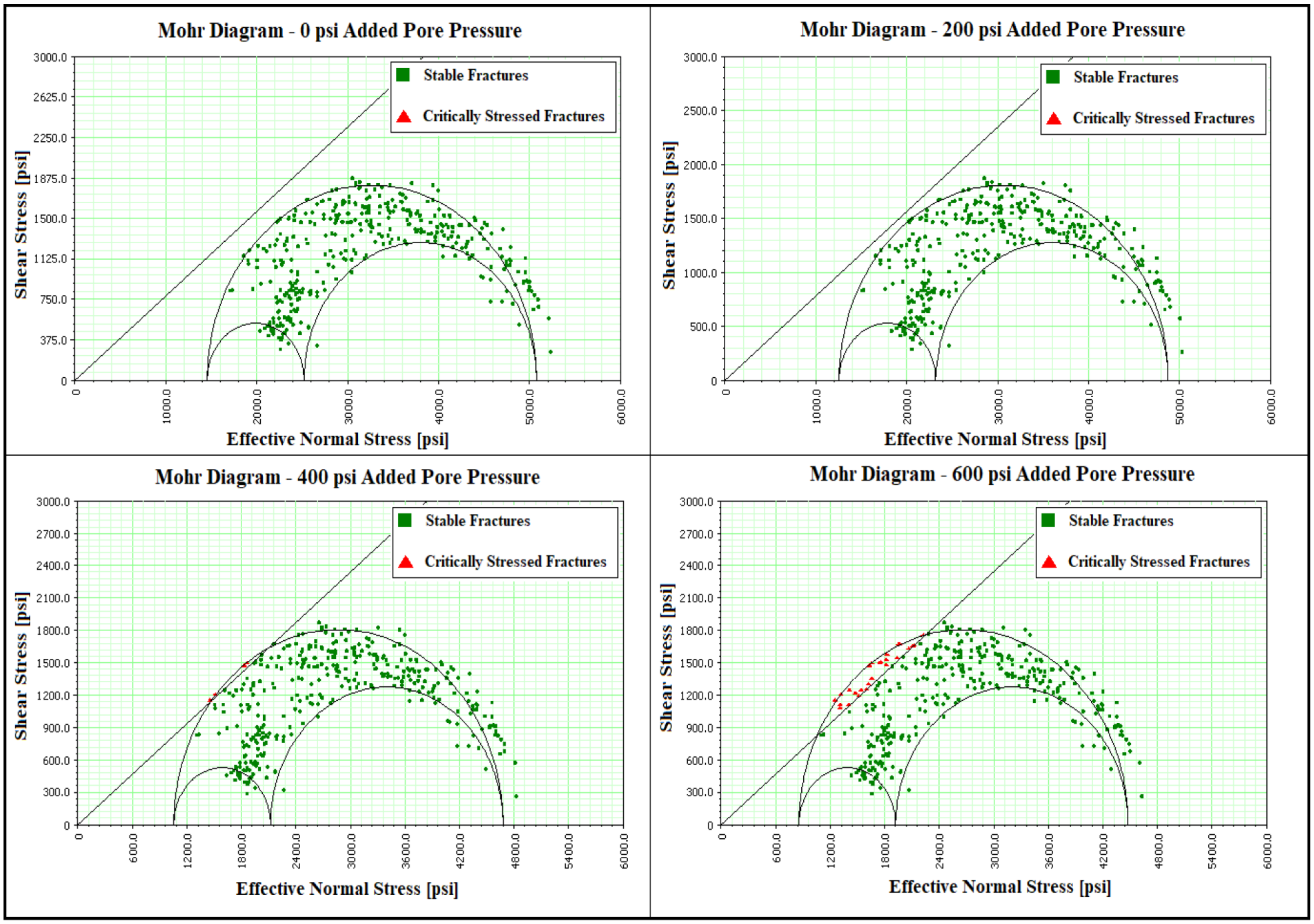

Figure 8. *Mohr diagram of the hydro-sheared system at varying pore pressure tests. Critically stressed fractures (red) are shown at a stimulation level between hydrostatic pore pressure and pore pressures approaching the minimum principal stress.*

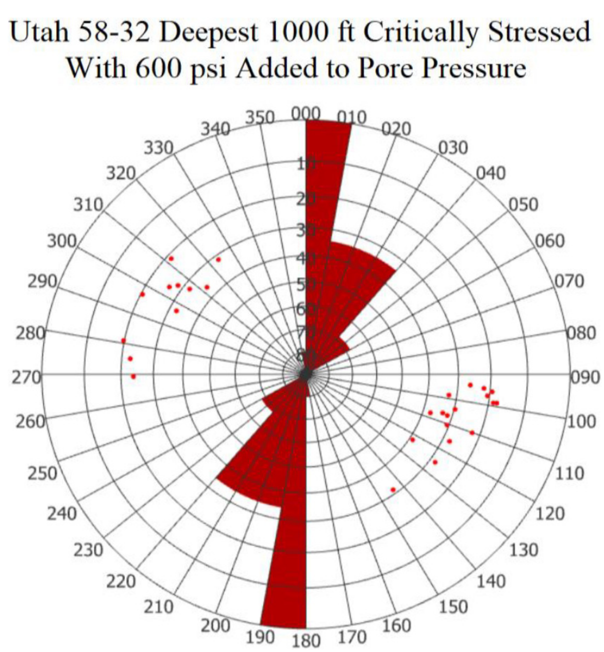

Figure 9. *Rose plot of critically stressed fractures at 600 extra psi pore pressure (fracture poles shown in upper hemisphere, equal angle stereonet). The majority of critically stressed fractures are oriented in the NE-SW direction that is approximate to the maximum horizontal stress direction.*

ACKNOWLEDGMENTS

Funding for this work was provided by the U.S. DOE under grant DE-EE0007080 “Enhanced Geothermal System Concept Testing and Development at the Milford City, Utah, FORGE Site”. We thank the many stakeholders who are supporting this project, including Smithfield (Murphy Brown LLC), Utah School and Institutional Trust Lands Administration, and Beaver County as well as the Utah Governor’s Office of Energy Development.

REFERENCES

Allis, R., Moore, J., Davatzes, N., Gwynn, M., Hardwick, C., Kirby, S., McLennan, J., Pankow, K., Potter, S., and Simmons, S., 2016, EGS concept testing and development at the Milford, Utah FORGE site. In Proceedings.

Dershowitz, B., LaPointe, P., Eiben, T., and Wei, L., 1998, Integration of Discrete Feature Network Methods with Conventional Simulator Approaches. Society of Petroleum Engineers, https://doi.org/10.2118/49069-MS.

Dershowitz, W.S., La Pointe, P.R., and Doe, T.W., 2004, Advanced in Discrete Fracture Network Modeling.

Elmo, D., and Stead, D., 2010, An integrated numerical modelling–discrete fracture network approach applied to the characterization of rock mass strength of naturally fractured pillars. Rock Mechanics and Rock Engineering, 43(1), p. 3–19.

Finnila, A., Dershowitz, W.S., Doe, T.W., and McLaren, R., 2015, Hydro-Shearing and Hydraulic Fracturing for Enhanced Geothermal Systems in Archetypical Normal, Strike-Slip, and Thrust Faulting Terrains, GRC, Geothermal Resources Council Annual Meeting. Vol 39, p. 303–314.

Goodman, R.E., 1989, Introduction to Rock Mechanics, Second Edition. John Wiley & Sons.

Haimson, B., and Fairhurst, C., 1967, Initiation and Extension of Hydraulic Fractures in Rocks, Society of Petroleum Engineers. https://doi.org/10.2118/1710-PA.

Herbert, A.W., 1996, Modelling approaches for discrete fracture network flow analysis, Developments in Geothechnical Engineering. Elsevier, Vol 79, p. 213–229.

Meyer, B.R., and Bazan, L.W., 2011, A discrete fracture network model for hydraulically induced fractures-theory, parametric and case studies, In SPE hydraulic fracturing technology conference, Society of Petroleum Engineers.

Nadimi, S., Miscovic, I., and McLennan, J., 2016, A 3D peridynamic simulation of hydraulic fracture process in a heterogeneous medium, Journal of Petroleum Science and Engineering, 145, p. 444–452.

Simmons, S., Kirby, S., Jones, C., Moore, J., Allis, R., Brandt, A., and Nash, G., 2016, The Geology, Geochemistry, and Geohydrology of the FORGE Deep Well Site, Milford, Utah, PROCEEDINGS, 41st Workshop on Geothermal Reservoir Engineering.

Xia, Y., Plummer, M., Mattson, E., Podgorney, R., and Ghassemi, A., 2017, Design, modeling, and evaluation of a doublet heat extraction model in enhanced geothermal systems, Renewable energy, 105, p. 232–247.

Ye, Z., and Ghassemi, A., 2018, Experimental study on injection-induced fracture propagation and coalescence for EGS stimulation, In Proc., 43rd Workshop on Geothermal Reservoir Engineering. Stanford, CA: Stanford Univ.

BIBLIOGRAPHY OF GEOTHERMAL CHARACTERISTICS OF THE ROOSEVELT HOT SPRINGS SYSTEM AND ADJACENT FORGE EGS SITE, MILFORD, UTAH

Miscellaneous Publication 169-O
Utah Geological Survey
a division of
UTAH DEPARTMENT OF NATURAL RESOURCES

This bibliography is part of *Geothermal Characteristics of the Roosevelt Hot Springs System and Adjacent FORGE EGS Site, Milford, Utah*. https://doi.org/10.34191/MP-169

BIBLIOGRAPHY OF GEOTHERMAL CHARACTERISTICS OF THE ROOSEVELT HOT SPRINGS SYSTEM AND ADJACENT FORGE EGS SITE, MILFORD, UTAH

This bibliography of papers on the RHS and the FORGE site has been compiled because of the "gray" literature, such as conference proceedings, of most of the work. The format of these references is not uniform because of the differing databases that they have been pulled from. Active links for almost all publications have been inserted. In the case of copyrighted material the link references the appropriate journal.

Allis, R.G., and Larsen, G., 2012, *Roosevelt Hot Springs Geothermal field, Utah—reservoir response after more than 25 years of power production*. Proc. 37th Workshop on Geothermal Reservoir Engineering, Stanford University, 8 p., https://pangea.stanford.edu/ERE/pdf/IGAstandard/SGW/2012/Allis.pdf.

Allis, R.G., Gwynn, M., Hardwick, C., Kirby, S., Moore, J., and Chapman, D., 2015, *Re-evaluation of the pre-development thermal regime of Roosevelt Hot Springs geothermal system, Utah*. Stanford Geothermal Reservoir Engineering Workshop. https://www.geothermal-library.org/index.php?mode=pubs&action=view&record=8019519.

Allis, R.G., 2014, *Formation pressure as a potential indicator of high stratigraphic permeability*. Proc. 39th Workshop on Geothermal Reservoir Engineering, Stanford University, 11 p., https://pangea.stanford.edu/ERE/pdf/IGAstandard/SGW/2014/Allis.pdf.

Allis, R.G., Gwynn, M., Kirby, S., 2017, *Pressure Trends at Cove Fort and Roosevelt Hot Springs Geothermal Systems Provide Insight to Their Flow Regime*, Geothermal Resources Council Transactions, http://pubs.geothermal-library.org/lib/grc/1033782.pdf.

Allis, R.G., Gwynn, M., Hardwick, C., and Moore, J., 2018, *The Challenge of Correcting Bottom-Hole Temperatures—an example from FORGE 58-32, near Milford, Utah*, Proc. 43rd Workshop on Geothermal Reservoir Engineering, Stanford University, 8 p., https://pangea.stanford.edu/ERE/pdf/IGAstandard/SGW/2018/Allis.pdf.

Allis, R.G., Moore, J., Davatzes, N., Gwynn, M., Hardwick, C., Kirby, S., McLennan, J., Pankow, K., Potter, S., and Simmons, S., 2016, *EGS Concept Testing and Development at the Milford, Utah FORGE Site*, Stanford Geothermal Workshop, 13 p., https://pangea.stanford.edu/ERE/pdf/IGAstandard/SGW/2016/Allis.pdf.

Allis, R.G., Gwynn, M., Hardwick, C., Hurlbut, W., and Moore, J., 2018, *Thermal Characteristics of the FORGE site, Milford, Utah*, Geothermal Resources Council Transactions, 42, p. 1011-1025, https://www.geothermal-library.org/index.php?mode=pubs&action=view&record=1033913.

Atkinson, D.J., 1981, *The Roosevelt Field: new model and geochemical evaluation*. Trans. GRC, 5, p. 149-152, https://www.geothermal-library.org/index.php?mode=pubs&action=view&record=1000757.

Balamir, O., Rivas, E., Rickard, W.M., McLennan, J., Mann, M., and Moore, J., 2018, *Utah FORGE Reservoir: Drilling Results of Deep Characterization and Monitoring Well 58-32*, Proc. 43rd Workshop on Geothermal Reservoir Engineering, Stanford University, 7 p., https://pangea.stanford.edu/ERE/pdf/IGAstandard/SGW/2018/Balamir.pdf.

Ballantyne, G.H., 1978, *Hydrothermal Alteration at the Roosevelt Hot Springs Thermal Area, Utah : Characterization of Rock Types and Alteration in Getty Oil Company Well Utah State 52-21*. Salt Lake City: Department of Geology and Geophysics, University of Utah, https://www.osti.gov/biblio/6579521.

Ballantyne, J.M., 1978, *Hydrothermal Alteration at the Roosevelt Hot Springs Thermal Area, Utah : Modal Mineralogy, and Geochemistry of Sericite, Chlorite, and Feldspar from Altered Rocks, Thermal Power Company Well Utah State 14-2*. Salt Lake City: Department of Geology and Geophysics, University of Utah, https://www.osti.gov/biblio/5754229.

Ballantyne, J.M., and Parry, W.T., 1978, *Hydrothermal Alteration at the Roosevelt Hot Springs Thermal Area, Utah : Petrographic Characterization of the Alteration to 2 Kilometers Depth*. Salt Lake City: Department of Geology and Geophysics, University of Utah, https://digitalcommons.usu.edu/govdocs/275/.

Ballantyne, J.M., 1980, *Geochemistry of Sericite and Chlorite in Well 14-2 Roosevelt Hot Springs Geothermal System and in Mineralized Hydrothermal Systems*. Salt Lake City, Utah: Dept. of Geology and Geophysics, University of Utah, https://www.osti.gov/biblio/5285752.

Bamford, R.W., 1978, *Geochemistry of Solid Materials from Two U. S. Geothermal Systems and Its Application to Exploration*. Salt Lake City: Earth Science Laboratory, University of Utah Research Institute, https://www.osti.gov/biblio/6779944.

Bamford, R.W., 1980, *Multielement Geochemistry of Solid Materials in Geothermal Systems and Its Applications : Part 1, the Hot-Water System at the Roosevelt Hot Springs KGRA, Utah*. Salt Lake City, Utah: Earth Science Laboratory, University of Utah Research Institute, https://www.osti.gov/biblio/5197458.

Bamford, R.W., Bowman, J.R., Brown, F.H., Cook, K.L., Chapman, D.S., Hohmann, G.W., Nash, W.P., et al., 1977, *Geothermal Research, Roosevelt Hot Springs KGRA*. Salt Lake City, Utah: University of Utah, https://www.osti.gov/biblio/896040.

Barker, C.A., 1986, *Upper-Crustal Structure of the Milford Valley and Roosevelt Hot Springs, Utah Region : By Modeling of Seismic Refraction and Reflection Data*. Thesis MS--Dept. of Geology and Geophysics, University of Utah, https://www.worldcat.org/oclc/14865881.

Becker, D.J., and Blackwell, D., 1993, *A Hydrothermal Model of the Roosevelt Hot Springs Area, Utah, USA, N.Z. Geothermal Workshop,* https://www.geothermal-energy.org/cpdb/record_detail.php?id=2105.

Becker D.J., and Blackwell, D., 1983, *Gravity and hydrothermal modeling of the Roosevelt Hot Springs area, southwest Utah.* Jl. Geophysical Research, 98, 17,787-17,800, https://onlinelibrary.wiley.com/doi/10.1029/93JB01231/abstract.

Benoit, W.R., and Butler, R.W., 1980, *A review of high-temperature geothermal developments in the northern Basin and Range Province.* Geothermal Resources Council Transactions, Special report No. 13, 57-80, https://www.geothermal-library.org/index.php?mode=pubs&action=view&record=1005447.

Benoit, D., 2013, *An empirical injection limitation in fault-hosted Basin and Range geothermal systems*. Trans. GRC, 37, 887-894, https://www.geothermal-library.org/index.php?mode=pubs&action=view&record=1030675.

Blackett, R.E., 2005, *Geothermal Utah — geology, resources and development in the Beehive State*: Bulletin - Geothermal Resources Council, v. 34, no. 2, p.78-83, https://www.geothermal-library.org/index.php?mode=pubs&action=view&record=7004995.

Blackett, R.E., and Moore, J.N., editors, 1994, *Cenozoic geology and geothermal systems of southwestern Utah*. Utah Geological Association Publication 23, 215 p., https://www.utahmapstore.com/uga23.html.

Blackett, R.E., and Ross, H.P., 1992, *Recent exploration and development of geothermal resources in the Escalante Desert region of southwestern Utah*, Harty, K.M., in: Engineering Geology of southwest Utah: Utah Geological Association Publication 21, 1992 Field Symposium, 261-280. http://archives.datapages.com/data/uga/data/063/063001/261_ugs630261.htm.

Blackwell, D.D., and Chapman, D.S., 1977, *Interpretation of geothermal gradient and heat flow data for Basin and Range geothermal systems*. Geothermal Resources Council Transactions, 1, 19-20, https://www.geothermal-library.org/index.php?mode=pubs&action=view&record=1000007.

Bowman, J.R., and Rohrs, D.T., 1981, *Light Stable Isotope Studies of Spring and Thermal Waters from the Roosevelt Hot Springs and Cove Fort/Sulphurdale Thermal Areas and of Clay Minerals from the Roosevelt Hot Springs Thermal Area*. Salt Lake City, Utah: Dept. of Geology and Geophysics, University of Utah, DOE/ID 12079-44, 36 p., http://www.osti.gov/biblio/5245145.

Bowman, J.R., 1980, University of Utah. Dept. of Geology and Geophysics, and United States. Dept. of Energy. Division of Geothermal Energy. *Management Assistance and Technical Support for the Programs in Exploration Technology : Final Report, for the Period December 1, 1978 - February 28, 1980*. Salt Lake City, Utah: Dept. of Geology and Geophysics, University of Utah, http://www.osti.gov/biblio/6509015.

Bowman, J.R., 1979, *Stable Isotope Investigation of Fluids and Water-Rock Interaction in the Roosevelt Hot Springs Thermal Area, Utah*. Salt Lake City: Department of Geology and Geophysics, University of Utah, http://www.osti.gov/biblio/5911506.

Bowman, J.R., Brown, F.H., Cook, K.L., Nash, W.P., Parry, W.T., Sill, W.R., Smith, R.B., Ward, S.H., and Whelan, J.A., 1976, *Geothermal Research, Roosevelt Hot Springs KGRA*. Salt Lake City, Utah: University of Utah, http://www.osti.gov/biblio/5665459.

Brown, F.H., 1977, *Attempt at Paleomagnetic Dating of Opal, Roosevelt Hot Springs KGRA*. Salt Lake City: University of Utah, Dept. of Geology and Geophysics, http://www.osti.gov/biblio/5754238.

Brumbaugh, W.D., 1977, *Gravity Survey of the Cove Fort-Sulphurdale KGRA and the North Mineral Mountains Area, Millard and Beaver Counties, Utah*. Salt Lake City: University of Utah, Dept. of Geology and Geophysics, http://www.osti.gov/biblio/893365.

Bruhn, R.L., Yusas, M.R., and Huertas, F., 1981, *Mechanics of low-angle faulting: an example from Roosevelt Hot Springs geothermal area, Utah.* Tectonophysics, 86, p. 343-361, http://www.sciencedirect.com/science/article/pii/0040195182901792.

Bryant, N.L., and Parry, W.T., 1977, *Hydrothermal Alteration at Roosevelt Hot Springs KGRA - DDH 1976-1*. Salt Lake City: Department of Geology and Geophysics, University of Utah, DOE/ID/01601-T9, 96 p., http://www.osti.gov/biblio/5815782.

Butz, J.R., 1980, *A case study of two-phase flow at the Roosevelt Hot Springs, Utah KRGA.* Trans. GRC, 4, p. 439-442, https://www.geothermal-library.org/index.php?mode=pubs&action=view&record=1000622.

Butz, J., Plooster, M., 1979, *Subsurface Investigations at the Roosevelt KGRA, Utah : Final Report*. Denver, CO: Denver Research Institute, DOE/ET/28389-1, 81 p., http://www.osti.gov/scitech/biblio/5592994-lPtGQs/.

Capuano, R.M., 1978, *Initial Investigation of Soil Mercury Geochemistry as an Aid to Drill Site Selection in Geothermal Systems*. Salt Lake City: Earth Science Laboratory, University of Utah Research Institute, http://www.osti.gov/scitech/biblio/5778808.

Capuano, R., and Cole, D.R., 1982, *Fluid-mineral equilibria in a hydrothermal system, Roosevelt Hot Springs, Utah*. Geochimica et Cosmochemica Acta, 46, p. 1353-1364, http://www.sciencedirect.com/science/article/pii/001670378290271X.

Carlston, K.J., 1982, *Electric Field Ratio Telluric Survey of the Roosevelt Hot Springs, Utah*. Thesis MS--Dept. of Geology and Geophysics, University of Utah, DE-AC07-78ET28392, 41 p., https://www.geothermal-library.org/index.php?mode=pubs&action=view&record=1019328.

Carter, J.A., 1978, *Regional Gravity and Aeromagnetic Surveys of the Mineral Mountains and Vicinity, Millard and Beaver Counties, Utah*. Salt Lake City: Department of Geology and Geophysics, University of Utah, 179 p., https://www.geothermal-library.org/index.php?mode=pubs&action=view&record=1020156.

Carter J.A., and Cook, K.L., 1978, *Regional gravity and aeromagnetic surveys of the Mineral Mountains and vicinity, Millard and Beaver Counties.* DOE/DGE Report volume 77-11, Contract EY-76-S-07-1601 with University, Salt Lake City, http://www.osti.gov/scitech/biblio/5665404.

Christensen, O.D., Moore, J.N., and Capuano, R.M., 1980b, *Trace element geochemical zoning in the Roosevelt Hot Springs thermal area, Utah.* Geothermal Resources Council Transactions, 4, p. 149-152. http://pubs.geothermal-library.org/lib/grc/1000549.pdf.

Chu, J.J., 1980, *Induced Polarization Data at Roosevelt Hot Springs Geothermal Area, Utah*. Thesis MS1980—Dept. of Geology and Geophysics, University of Utah, 55 p., http://ngds.egi.utah.edu/files/GL04031/GL04031.pdf.

Chu, J.J., Sill, W.R., and Ward, S.H., 1979, *Induced Polarization Measurements at Roosevelt Hot Springs Thermal Area, Utah*. Salt Lake City: Department of Geology and Geophysics, University of Utah, http://www.osti.gov/scitech/biblio/6564250.

Clement, M.D., 1981, *Heat Flow and Geothermal Assessment of the Escalante Desert, Southwestern Utah, with Emphasis on the Newcastle KGRA*. Salt Lake City, Utah: Dept. of Geology and Geophysics, University of Utah, http://www.osti.gov/scitech/biblio/6150551.

Cochrane, F., Tosaya, C.A., and Owen, J.L., 1988, *Evaluation of a site-specific commercial hot dry rock geothermal power prospect*. Geothermal Resources Council Transactions, 12, 375-382 p., https://www.geothermal-library.org/index.php?mode=pubs&action=view&record=1001731.

Cook, K.L., 1978, *Precision Leveling and Gravity Studies at Roosevelt Hot Springs KGRA, Utah*. Salt Lake City: Department of Geology and Geophysics, University of Utah, http://www.osti.gov/scitech/biblio/5696697.

Cook, K.L., 1980, *Detailed Gravity and Aeromagnetic Surveys of the Cove Fort-Sulphurdale KGRA and Vicinity, Millard and Beaver Counties, Utah*. Salt Lake City, Utah: Dept. of Geology and Geophysics, University of Utah, http://www.osti.gov/scitech/biblio/7044813.

Crebs, T.J., 1976, *Gravity and Ground Magnetic Surveys of the Central Mineral Mountains, Utah*. Salt Lake City: University of Utah, http://www.osti.gov/scitech/biblio/7211157.

Crecraft, H.R., 1980, *Petrology, Geochronology, and Chemical Evolution of the Twin Peaks Rhyolite Domes, Utah*. Salt Lake City, Utah: Dept. of Geology and Geophysics, University of Utah, http://www.osti.gov/scitech/biblio/5285924.

Dedolph, R.E., 1976, *A Thermodynamic Model of the Hydrolysis of Microcline in Acid Sulfate Solutions*. Salt Lake City: University of Utah, Dept. of Geology and Geophysics, http://www.osti.gov/scitech/biblio/5744970.

Earll, F.N., 1957, *Geology of the central Mineral Range, Beaver Co., Utah*. PhD thesis, Univ. Utah, 112 p., https://collections.lib.utah.edu/details?id=195429.

East, J., 1981, *Hot Dry Rock Geothermal Potential of Roosevelt Hot Springs Area : Review of Data and Recommendations*. Los Angeles, NM: Los Alamos National Laboratory, http://www.osti.gov/biblio/6349353.

Evans, S.H., 1980, *Compositional Gradients in Natural Silicic Liquids*. Salt Lake City, Utah: Dept. of Geology and Geophysics, University of Utah, http://www.osti.gov/scitech/biblio/6773738.

Evans, S.H., and Nash, W.P., 1978, *Quaternary Rhyolite from the Mineral Mountains, Utah, U. S. A.* Salt Lake City: University of Utah, http://www.osti.gov/scitech/biblio/5696814.

Evans, S.H., 1980, *Summary of Potassium/argon Age Dating, 1979*. Salt Lake City: Dept. of Geology and Geophysics, University of Utah, http://www.osti.gov/scitech/biblio/5166169.

Evans, S.H., and Nielson, D.L., 1982, *Thermal and tectonic history of the Mineral Mountains intrusive complex.* Trans. GRC, 6, 15-18. https://www.geothermal-library.org/index.php?mode=pubs&action=view&record=1000906.

Faulder, D.D., 1991, *Conceptual geologic model and native state model of the Roosevelt Hot Springs hydrothermal system*. Proc. 16th Workshop on Geothermal Reservoir Engineering, p. 131-142, https://pangea.stanford.edu/ERE/pdf/IGAstandard/SGW/1991/Faulder.pdf.

Faulder, D.D., 1994, *Long term flow test No. 1, Roosevelt Hot Springs*. Trans. GRC, 18, p. 583-590, https://www.geothermal-library.org/index.php?mode=pubs&action=view&record=1007044.

Finnila, A., Forbes, B., Podgorney, R., 2019, *Building and Utilizing a Discrete Fracture Network Model of the FORGE Utah Site*, Proc. 44th Workshop on Geothermal Reservoir Engineering, Stanford University, https://pangea.stanford.edu/ERE/pdf/IGAstandard/SGW/2019/Finnila.pdf.

Forrest, R.J., 1980, *Historical synopsis of the Roosevelt Hot Springs geothermal field, Utah, in D. L. Nielson, ed., Geothermal systems in central Utah*. Geothermal Resources Council Field Trip 7, 18-24,

Forrest, R.J., 1993, *Geothermal development at Roosevelt Hot Springs geothermal area, Beaver County, Utah, 1972-1993*. In: Cenozoic Geology and Geothermal Systems of southwest Utah: Utah Geological Association Publication 23, p. 37-44, http://archives.datapages.com/data/uga/data/065/065001/37_ugs650037.htm.

Frangos, W., 1980, *Bipole-Dipole Survey at Roosevelt Hot Springs Thermal Area, Beaver County, Utah*. Salt Lake City, Utah: Earth Science Laboratory Division, University of Utah Research Institute, https://www.osti.gov/scitech/biblio/5050398.

Geothermex, 1977, *Geothermal potential of the lands leased by Geothermal Power Corporation in the Northern Mineral Mountains, Beaver and Millard Counties, Utah*. Open File Rept., Univ. Utah Research Inst., Earth Science Lab., 43 p., http://ngds.egi.utah.edu/files/GL04423/GL04423_1.pdf.

Geothermex, 1982, *Geothermal reservoir assessment of Roosevelt Hot Springs, Geothermal power Company, Novato, CA*, DOE/ET/28406-1, 81 p., https://www.osti.gov/scitech/biblio/5045454.

Gertson, R.C., 1979, *Interpretation of a Seismic Refraction Profile across the Roosevelt Hot Springs, Utah and Vicinity*. Salt Lake City: Department of Geology and Geophysics, University of Utah, https://www.osti.gov/scitech/biblio/5814637.

Glenn, W.E., 1981, *A Comprehensive Study of LASL Well C/T-2, Roosevelt Hot Springs KGRA, Utah, and Applications to Geothermal Well Logging*. Los Alamos, NM: Los Alamos Scientific Laboratory, https://www.osti.gov/scitech/biblio/6600607.

Glenn, W.E., and Hulen, J.B., 1979, *Interpretation of well log data from four drill holes at Roosevelt Hot Springs KGRA*. Univ. Utah Research Inst., Earth Science Lab. Rept. 28, 74 p., https://www.osti.gov/scitech/biblio/5597946.

Goff, F., Decker, E.R., 1983, *Candidate sites for future hot dry rock development in the United States*, Jl. Volcanol. Geothermal. Research, 15, p. 187-221, https://www.sciencedirect.com/science/article/pii/0377027383901002.

Gwynn, M., Allis, R.G., Hardwick, C., Hill, J., and Moore, J., 2016, A New Look at the Thermal Regime Around Roosevelt Hot Springs, Geothermal Resources Council Transactions, 40, https://www.geothermal-library.org/index.php?mode=pubs&action=view&record=1032370.

Gwynn, M., Allis, R.G., Hardwick, C., Jones, C., Nielson, P., Hurlbut, W., 2018, *Rock Properties of FORGE Well 58-32, Milford, Utah.* Geothermal Resources Council Transactions, 42, https://www.geothermal-library.org/index.php?mode=pubs&action=view&record=1034058.

Halliday, M.E., 1978, *Gravity and Ground Magnetic Surveys in the Monroe and Joseph KGRA's and Surrounding Region, South Central Utah*. Originally published as thesis, University of Utah, https://www.osti.gov/scitech/biblio/5754069.

Hardwick, C., Gwynn, M., Allis, R.G., Wannamaker, P.E., Moore, J., 2016, *Geophysical Signatures of the Milford, Utah FORGE Site*, Stanford Geothermal Workshop, https://pangea.stanford.edu/ERE/pdf/IGAstandard/SGW/2016/Hardwick.pdf.

Hardwick, C., Hurlbut, W., Gwynn, M., Allis, R.G., Wannamaker, P.E., Moore, J., 2018, *Geophysical Surveys of the Milford, Utah, FORGE Site: Gravity and TEM.* Geothermal Resources Council Transactions, 42 p., https://www.geothermal-library.org/index.php?mode=pubs&action=view&record=1033944.

Hintze, L.F., and Davis, F.D., 2003, *Geology of Millard County, Utah.* UGS Bulletin 133, pp. 305, https://ugspub.nr.utah.gov/publications/bulletins/B-133.pdf.

Hirtz, P., and Lovekin, J., 1995, *Tracer dilution measurements for two-phase geothermal production: Comparative testing and operating experience*. World Geothermal Congress, 1881-1886, https://www.geothermal-library.org/index.php?mode=pubs&action=view&record=1010748.

Hulen, J.B., 1978, *Stratigraphy and Alteration, 15 Shallow Thermal Gradient Holes, Roosevelt Hot Springs KGRA and Vicinity, Millard and Beaver Counties, Utah*. Salt Lake City: Earth Science Laboratory, University of Utah Research Institute, https://www.osti.gov/scitech/biblio/5598309.

James, L.P., and Bamford, R.W., 1977, *An Evaluation of AIRTRACE in the Geothermal Environment*. Salt Lake City, Utah: Dept. of Geology and Geophysics, University of Utah, http://ngds.egi.utah.edu/files/GL01138/GL01138.pdf.

Johnson, E.H., 1975, *Resistivity and Induced Polarization Survey of a Basalt Flow in a Geothermal Environment, Western Utah.* Thesis MS 1975—Dept. of Geology and Geophysics, University of Utah, https://collections.lib.utah.edu/details?id=194214.

Kamali, A., Ghassemi, A., McLennan, J., and Moore, J., 2019, *Analysis of Forge DFIT Considering Hydraulic and Natural Fracture Interactions*, Proc. 44th Workshop on Geothermal Reservoir Engineering, Stanford University, https://pangea.stanford.edu/ERE/pdf/IGAstandard/SGW/2019/Kamali.pdf.

Katz, L., 1977a, *Seismic emissions study, Roosevelt Hot Springs, Milford, Utah (for Getty Oil Co,)*: Open-File Rept., Univ. Utah Research Inst., Earth Science Lab., 7 p., http://ngds.egi.utah.edu/files/GL04417/GL04417.pdf.

Katz, L., 1977b, *Seismic emission study, Roosevelt Hot Springs, Milford, Utah (for Union Oil Co.)*: Open-File Rept., Univ. Utah Research Inst., Earth Science Lab., 7 p.

Kennedy, M., and Soest, V., 2007, *A Systematic Regional Trend in Helium Isotopes Across the Northern Basin and Range Province, Western North America*. Science, 318, 1433-1436. http://escholarship.org/uc/item/124591jd.

Kerna, M.J., and Allen, T.S., 1984, *Roosevelt Hot Springs development,* Trans. GRC, 8, 75-77, https://www.geothermal-library.org/index.php?mode=pubs&action=view&record=1001153.

Kirby, S.M., Bartley, J., and Simmons, S., 2017, Revised geologic mapping and fracture analysis of bedrock adjoining the Utah FORGE site: Geothermal Resources Council Transactions, v. 41, 34 p.

Kirby, S.M., Knudsen, T., Kleber, E., and Hiscock, A., 2018, Geologic setting of the Utah FORGE site based on new and revised geologic mapping: Geothermal Resources Council Transactions, v. 42.

Kleber, E., Hiscock, A., Kirby, S., Allis, R.G., 2017, *Assessment of Quaternary Faulting near the Utah FORGE Site from Airborne Light Detection and Ranging (lidar) Data* Geothermal Resources Council Transactions, 41 p. 301-302, https://www.geothermal-library.org/index.php?mode=pubs&action=view&record=1033725.

Klusman, R.W., LeRoy, M.P., 1996*, Potential for use of gas flux measurements in surface exploration for geothermal resources.* Trans. GRC, 20, p. 331-338, https://www.geothermal-library.org/index.php?mode=pubs&action=view&record=1014753.

Lee, W., 1908, *Water resources of the Beaver Valley*. USGS Water Supply Papers 217, p. 5-60, https://pubs.er.usgs.gov/publication/wsp217.

Lenzer, R.C., Crosby, G.W., and Berge, C.W., 1976, *Geothermal exploration of Roosevelt KGRA, Utah: 17th U.S. Symposium on Rock Mechanics*, Site Characterization Volume, Univ. Utah Engineering Experimental Station, 3 p., BI-1, https://www.onepetro.org/conference-paper/ARMA-76-0283.

Lenzer, R.C., Crosby, G.W., and Berge, C.W., 1977, *Recent developments at the Roosevelt Hot Springs, KGRA*. Trans Am. Nuclear Soc. Topical Mtg., Golden, Colo., April 12-14, http://ngds.egi.utah.edu/files/GL01615/GL01615_1.pdf.

Lin, Y.T., 1981, The impact of bit performance on geothermal well cost. Geothermal Resources Council Transactions, 5, 253-256, https://www.geothermal-library.org/index.php?mode=pubs&action=view&record=1000784.

Lipman, P.W., Rowley, P.D., Mehnert, H.H., Evans, S.H., Nash, W.P., and Brown, F.H., 1978, *Pleistocene rhyolite of the Mineral Mountains, Utah geothermal and archeological significance*. U.S. Geol,Survey Jour. Research, v. 6, p. 133-147, https://www.researchgate.net/publication/236393864_Pleistocene_rhyolite_of_the_Mineral_Mountains_Utah-Geothermal_and_archeological_significance.

Lynne, B.Y., Campbell, K.A., Moore, J., and Browne, P.R.L., 2004, Siliceous sinter diagenesis at the Opal Mound Roosevelt Hot Springs, Utah, USA. Proc. 26th NZ Geothermal Workshop, 12-17, http://www.geothermal-energy.org/pdf/IGAstandard/NZGW/2004/Lynne_et_al.pdf.

McKinney, D.B., Brooks, C.A., 1978, *Annotated Bibliography of the Geology of the Roosevelt Hot Springs Known Geothermal Resource Area and the Adjacent Mineral Mountains, March 1978*. Salt Lake City: Earth Science Laboratory, University of Utah Research Institute, http://www.osti.gov/scitech/biblio/5514935.

Micro Geophysics, 1977, *Refraction Shooting near Roosevelt Hot Springs : Data*. Salt Lake City: University of Utah, http://ngds.egi.utah.edu/files/GL01141/GL01141.pdf.

Miller, C.D., 1976, *Alteration and Geochemistry of the Monroe Known Geothermal Resource Area*. Thesis MS1976—Dept. of Geology and Geophysics, University of Utah, http://www.worldcat.org/oclc/2600671.

Miller, J., Allis, R.G., Hardwick, C., 2018, Seismic Reflection Profiling at the FORGE Utah EGS Site, Geothermal Resources Council Transactions, 42, https://www.geothermal-library.org/index.php?mode=pubs&action=view&record=1034095.

Moore J.N., and D.L. Nielson, 1994, *An overview of the geology and geochemistry of the Roosevelt Hot Springs geothermal system. Utah Geological Association Publication*. 23, p. 25-36, http://archives.datapages.com/data/uga/data/065/065001/25_ugs650025.htm.

Moore, J., Allis, R.G., Pankow, K., Simmons, S., McLennan, J., Wannamaker, P., Rickard, W., and Podgorney, R., 2017, *The Utah Frontier Observatory for Geothermal Research (FORGE): a Laboratory for EGS Development.* New Zealand Geothermal Workshop, http://www.geothermal-energy.org/pdf/IGAstandard/NZGW/2017/007_Moore-Final.pdf.

Moore, J., McLennan, J., Allis, R.G., Pankow, K., Simmons, S., Podgorney, R., Wannamaker, P., and Rickard, W., 2018, *The Utah Frontier Observatory for Geothermal Research (FORGE): Results of Recent Drilling and Geoscientific Surveys*. Geothermal Resources Council Transactions, 42, https://www.geothermal-library.org/index.php?mode=pubs&action=view&record=1034044.

Moore, J., McLennan, J., Allis, R.G., Pankow, K., Simmons, S., Podgorney, R., Wannamaker, P., and Rickard, W., 2019, *The Utah Frontier Observatory for Research in Geothermal Energy (FORGE): An International Laboratory for Enhanced Geothermal System Technology Development.* Proc. 44th Workshop on Geothermal Reservoir Engineering, Stanford University, https://pangea.stanford.edu/ERE/pdf/IGAstandard/SGW/2019/Moore.pdf.

Mower, R.W., 1978, *Hydrology of the Beaver Valley area, Beaver County, Utah, with emphasis on ground water*. Utah Dept. Natural Resources Tech. Pub. 63, 90 p., http://www.waterrights.utah.gov/cgi-bin/docview.exe?Folder=TP20-5-530&Title=Technical+Publication+63.

Mower, R.W., and Cordova, R.M., 1974, *Water resources of the Milford area, Utah, with an emphasis on ground water*. Utah Dept. Natural Resources Tech. Pub. 43, 106 p., http://www.waterrights.utah.gov/cgi-bin/libview.exe?Modinfo=Viewpub&LIBNUM=20-5-140.

Mundorf, J.C., 1970, *Major thermal springs of Utah*. Utah Geological and Mineral Survey, Water resources Bulletin, 13, 60 p., http://ugspub.nr.utah.gov/publications/water_resources_bulletins/WRB-13.pdf.

Nadimi, S., Forbes, B., Moore, J., Ye, Z., Ghassemi A., and McLennan, J.D., 2019, *Experimental Evaluation of Effect of Hydro-Shearing on Fracture Conductivity at the Utah FORGE Site*. Proc. 44th Workshop on Geothermal Reservoir Engineering, Stanford University, https://pangea.stanford.edu/ERE/pdf/IGAstandard/SGW/2019/Nadimi.pdf.

Nash, W.P., 1982, *Evolution of the Quaternary Magmatic System, Mineral Mountains, Utah : Interpretations from Chemical and Experimental Modeling*. Salt Lake City, Utah: Dept. of Geology and Geophysics, University of Utah, http://www.osti.gov/scitech/biblio/893697.

Nash, W.P., and Evans, S.H., Jr., 1978, *Fluid Dynamic Properties of Rhyolitic Magmas, Mineral Mountains, Utah*. Salt Lake City: Department of Geology and Geophysics, University of Utah, http://www.osti.gov/scitech/biblio/890953.

Nash, W.P., 1976, *Petrology of the Quaternary Volcanics of the Roosevelt KGRA and Adjoining Area, Utah*. Salt Lake City: University of Utah, Dept. of Geology and Geophysics, http://www.osti.gov/scitech/biblio/7308985-uWl9gW/.

Nash, W.P., Crecraft, H.R., Evans, S.H., 1980, *Volcanism of the Black Rock Desert and Twin Peaks areas, west central Utah*, in Nielson, D.L. ed., Geothermal Systems in Central Utah, Guidelbook to Field Trip No. 7, GRC Annual Meeting, http://ngds.egi.utah.edu/files/GL04060/GL04060.pdf.

Neupane, G., Baum, J., Mattson, E., 2015, Mines, Gregory; Palmer, Carl; Smith, Robert: *Validation of Multicomponent Equilibrium Geothermometry at Four Geothermal Power Plants*, Proceedings: Workshop on Geothermal Reservoir Engineering, 40, https://www.geothermal-library.org/index.php?mode=pubs&action=view&record=8019444.

Nielson, D.L., 1978, University of Utah. Earth Science Laboratory, and United States. Dept. of Energy. Division of Geothermal Research. *Geology of Roosevelt Hot Springs KGRA, Beaver County, Utah*. Salt Lake City: Earth Science Laboratory, University of Utah Research Institute, https://www.osti.gov/biblio/5696785.

Nielson, D.L., 1978, *Radon Emanometry as a Geothermal Exploration Technique : Theory and an Example from Roosevelt Hot Springs KGRA, Utah*. Salt Lake City: Earth Science Laboratory, University of Utah Research Institute, http://www.osti.gov/scitech/biblio/5815672.

Nielson, D.L., 1989, *Stress in geothermal systems*, Geothermal Resources Council Transactions, 13, p. 271-276, https://www.geothermal-library.org/index.php?mode=pubs&action=view&record=1001789.

Nielson, D.L., and Moore, J.N., 1979, *The exploration significance of low-angle faults in the Roosevelt Hot Springs and Cove Fort-Sulphurdale geothermal systems*. Utah. Trans. GRC, 3, p. 503-506, https://www.geothermal-library.org/index.php?mode=pubs&action=view&record=1000431.

Nielson D.L., Evans, S.H., and Sibbett, B.S., 1986, *Magmatic, structural, and hydrothermal evolution of the Mineral Mountains intrusive complex, Utah.* Geol. Soc. America Bull., 97, p. 765-777, https://pubs.geoscienceworld.org/gsa/gsabulletin/article/97/6/765-777/203190.

Nielson, D.L., Sibbett, B.S., and McKinney, D.B., 1979, *Geology and structural control of the geothermal system at Roosevelt HotSprings, Beaver County, Utah* (abs.): AAPG Bull., v. 63, p. 836, http://archives.datapages.com/data/bulletns/1977-79/images/pg/00630005/0800/08360.pdf.

Nielson, D.L., Sibbett, B.S., McKinney, D.B., Hulen, J.B., Moore, J.N., and Samberg, S.M., 1978, *Geology of Roosevelt Hot Springs KGRA, Beaver County, Utah*. Univ. Utah Research Inst., Earth Science Lab. Rept. 12, 121 p., https://www.osti.gov/scitech/biblio/5696785.

Olson, T.L., 1976, *Earthquake Surveys of the Roosevelt Hot Springs and the Cove Fort Areas, Utah*. Salt Lake City: University of Utah, Dept. of Geology and Geophysics, http://www.osti.gov/scitech/biblio/7289667.

Olson, T.L., and Smith, R.B., 1976, *Earthquake surveys of the Roosevelt Hot Springs and the Cove Fort areas, Utah*. Final Rept. to Natl. Sci. Foundation, Univ. Utah, Dept. Geology and Geophys., 82 p. https://www.osti.gov/scitech/biblio/7289667.

Pankow, K.L., Potter, S., Zhang, H., and Moore, J., 2017, *Local Seismic Monitoring at the Milford, Utah FORGE Site*, Geothermal Resources Council Transactions, http://pubs.geothermal-library.org/lib/grc/1033727.pdf.

Parry, W.T, Cleary, M., Ward, S.H., and Geothermal Research Program (U.S.), 1978, *Na-K-Ca and SiO_2 Temperature Estimates for Utah Spring and Well Waters*. Salt Lake City, Utah: University of Utah, http://search.geothermaldata.org/dataset/na-k-ca-and-sio2-temperature-estimates-for-utah-spring-and-well-waters.

Parry, W.T., 1976, *Geochemistry and Hydrothermal Alteration at Selected Utah Hot Springs*. Salt Lake City: University of Utah, Dept. of Geology and Geophysics, https://www.osti.gov/scitech/biblio/5026993.

Parry, W.T., 1978, *Hydrothermal Alteration at the Roosevelt Hot Springs Thermal Area, Utah*. Salt Lake City: Department of Geology and Geophysics, University of Utah, http://ngds.egi.utah.edu/files/GL01132/GL01132.pdf.

Parry, W.T., et al., 1980, *Geochemistry of hydrothermal alteration at the Roosevelt Hot Springs thermal area, Utah*. Geochim. Et Cosmochim. Acta, v. 44, p. 95-102, https://www.sciencedirect.com/science/article/pii/0016703780901799.

Parry, W.T., Ward, S.H., Nash, W.P., 1977, University of Utah. Dept.. of Geology and Geophysics, and United States. Dept.. of Energy. Division of Geothermal Energy. *Geology and Geochemistry of the Roosevelt Hot Springs Thermal Area, Utah - a Summary*. Salt Lake City, Utah: Dept. of Geology and Geophysics, University of Utah, https://www.osti.gov/scitech/biblio/893367/.

Parry, W.T., Ballantyne, J.M., and Jacobs, D.C., 1980, *Geochemistry of hydrothermal sericite from Roosevelt Hot Springs and the Tintic and Santa Rita porphyry copper systems*. Economic Geology, 79, p. 72-86, https://pubs.geoscienceworld.org/economicgeology/issue/79/1.

Pelton, W.H., 1977, *Interpretation of Induced Polarization and Resistivity Data*. Thesis PhD1977--Dept. of Geology and Geophysics, University of Utah, https://www.worldcat.org/oclc/2972563.

Petersen, C.A., 1975, *Geology and Geothermal Potential of the Roosevelt Hot Springs Area, Beaver County, Utah*. Thesis MS1975--Dept. of Geology and Geophysics, University of Utah, https://collections.lib.utah.edu/details?id=194508.

Petrick, W.R., Sill, W.R., Ward, S.H., 1979, United States, Department of Energy, Division of Geothermal Energy, University of Utah, and Department of Geology and Geophysics. *Three-Dimensional Resistivity Inversion Using Alpha Centers*. Salt Lake City, Utah: Dept. of Geology and Geophysics, University of Utah, https://www.osti.gov/scitech/servlets/purl/6809531/.

Petrick, W.R., 1975, *Test Electromagnetic Soundings : Roosevelt Hot Springs KGRA*. Salt Lake City, Utah: University of Utah, https://www.osti.gov/scitech/biblio/7320342.

Podgorney, R., Finnila, A., McLennan, J., Ghassemi, A., Hunag, H., Forbes, B., and Elliott, J., 2019, *A Framework for Modeling and Simulation of the Utah FORGE Site*, Proc. 44th Workshop on Geothermal Reservoir Engineering, Stanford University, https://pangea.stanford.edu/ERE/pdf/IGAstandard/SGW/2019/Podgorney.pdf.

Qasim, I., Lynne, B.Y., 2018, *X-ray characterisation of siliceous sinter from Steamboat Springs and Roosevelt Geothermal Fields, USA*, Proc. 43rd Workshop on Geothermal Reservoir Engineering, Stanford University.

Rickard, W.M., McLennan, J., Islam, N., and Rivas, E., 2019, *Mechanical Specific Energy Analysis of the FORGE Utah Well*, Proc. 44th Workshop on Geothermal Reservoir Engineering, Stanford University, https://pangea.stanford.edu/ERE/pdf/IGAstandard/SGW/2019/Rickard.pdf.

Robinson R., and Iyer, H.M., 1981, *Delineation of a low-velocity body under the Roosevelt Hot Springs geothermal area, Utah, using teleseismic P-wave data. Geophysics, 46*, p. 1456-1466, https://library.seg.org/doi/abs/10.1190/1.1441152.

Rohrs, D.T., 1978, *Hydrothermal Alteration at the Roosevelt Hot Springs Thermal Area, Utah : Thermal Power Co. Well Utah State 72-16*. Salt Lake City: Dept. of Geology and Geophysics, University of Utah, http://www.osti.gov/scitech/biblio/6564287.

Rohrs, D.T., 1980, *A Light Stable Isotope Study of the Roosevelt Hot Springs Thermal Area, Southwestern Utah*. Salt Lake City: Dept. of Geology and Geophysics, University of Utah, https://www.osti.gov/scitech/biblio/5285736.

Ross, H.P., Nielson, D.L., Moore, J.N., 1982, *Roosevelt Hot Springs geothermal system, Utah – case study.* Amer. Assoc. Petroleum Geologists, 66, p. 879-902, http://archives.datapages.com/data/bulletns/1982-83/data/pg/0066/0007/0850/0879.htm.

Roxlo, K.S., 1980, *Uranium Geochemistry of the Roosevelt Hot Springs Thermal Area, Utah*. Thesis MS1980--Dept. of Geology and Geophysics, University of Utah, https://www.worldcat.org/oclc/6248087.

Rudisill, J.M., 1978, *A case history of a shallow, over-pressured geothermal well*. Trans. GRC, 2, p. 587-590, https://www.geothermal-library.org/index.php?mode=pubs&action=view&record=1000264.

Sandberg, S.K., 1980, *Controlled-Source Audiomagnetotellurics in Geothermal Exploration*. Thesis MS1980--Dept. of Geology and Geophysics, University of Utah, https://www.osti.gov/scitech/biblio/6749290-r1BMPL/.

Sawyer, R.F., 1977, *Gravity and Ground Magnetic Surveys of the Thermo Hot Springs KGRA Region, Beaver County, Utah*. Salt Lake City: Department of Geology and Geophysics, University of Utah, https://www.osti.gov/scitech/biblio/895548.

Schaff, C., 1981, *Seismic monitoring and potential for induced seismicity at Roosevelt Hot Springs, Utah and Raft River, Idaho*. Ann. Mtg., Seismological Soc. America, http://ngds.egi.utah.edu/files/GL01611/GL01611_1.pdf.

Serpa, L.F., 1980, *Detailed Gravity and Aeromagnetic Surveys in the Black Rock Desert Area, Utah*. Salt Lake City: Dept. of Geology and Geophysics, University of Utah, https://www.osti.gov/scitech/biblio/6773977.

Shannon, S.S., Goff, F., Rowley, J.C., Pettit, R.A., and Yuataz F.D., 1983, *Roosevelt Hot Springs/hot dry rock prospect and evaluation of the Acord 1-26 well.* Geothermal Resources Council Transactions, p. 541-544, https://www.geothermal-library.org/index.php?mode=pubs&action=view&record=1001123.

Sibbett, B.S., and Nielson, D.L., 1980, *Geology of the central Mineral Mountains, Beaver Co., Utah*. Univ. Utah Research Inst., Earth Science Lab. Rept. 33, 42 p., https://www.osti.gov/scitech/biblio/5040670.

Sill, W.R., 1978, *Electrical Energizing of Well Casings*. Salt Lake City: University of Utah, Department of Geology and Geophysics, https://www.osti.gov/scitech/biblio/6771882.

Sill, W.R. and John, D.S., 1979, *Self-Potential Survey, Roosevelt Hot Springs, Utah*. Salt Lake City: Department of Geology and Geophysics, University of Utah, https://www.osti.gov/scitech/biblio/6623737.

Sill, W.R., and Bodell, J., 1977, *Thermal Gradients and Heat Flow at Roosevelt Hot Springs*. Salt Lake City, Utah: University of Utah, http://www.osti.gov/scitech/biblio/5696712.

Simmons, S., Kirby, S., Moore, J., Wannamaker, P., Allis, R.G., 2015, *Comparative Analysis of Fluid Chemistry from Cove Fort, Roosevelt and Thermo: Implications for Geothermal Resources and Hydrothermal Systems on the East Edge of the Great Basin*, Geothermal Resources Council Transactions, 39, https://www.geothermal-library.org/index.php?mode=pubs&action=view&record=1032133.

Simmons, S., Kirby, S., Rahilly, K., Fischer, T., Moore, J., 2017, *Update on the Geochemistry and Geohydrology of the FORGE Deep Well Site, Milford, Utah*, Geothermal Resources Council Transactions, 313 p., https://www.geothermal-library.org/index.php?mode=pubs&action=view&record=1033728.

Simmons, S., Kirby, S., Bartley, J., Jones, C., Kleber, E., Knudsen, T., Miller, J., Rahilly, K., McLennan, J., Fischer, T., Moore, J., Allis, R.G., 2019, *Update on the Geological and Geochemical Understanding of the Utah FORGE Site*, Proc. 44th Workshop on Geothermal Reservoir Engineering, Stanford University, https://pangea.stanford.edu/ERE/pdf/IGAstandard/SGW/2019/Simmons.pdf.

Simmons, S., Moore, J., Allis, R.G., Hardwick, C., Kirby, S., Jones, C., Gwynn, M., Kleber, E., Miller, J., McLennan, J., and Bartley, J., 2018, *An Updated Geologic Model for FORGE Utah EGS Laboratory,* Proc. 43rd Workshop on Geothermal Reservoir Engineering, Stanford University, https://pangea.stanford.edu/ERE/pdf/IGAstandard/SGW/2018/Simmons2.pdf.

Simmons, S., Kirby, S., Allis, R., Moore, J., Fischer, T., 2018*, Update on the Production Chemistry of the Roosevelt Hot Springs Reservoir*, Proc. 43rd Workshop on Geothermal Reservoir Engineering, Stanford University, https://pangea.stanford.edu/ERE/pdf/IGAstandard/SGW/2018/Simmons3.pdf.

Simmons, S., Kirby, S., Jones, C., Moore, J., Allis, R.G., Brandt, A., Nash, G., 2016, *The Geology, Geochemistry, and Hydrology of the EGS FORGE Site, Milford Utah*, Stanford Geothermal Workshop, https://pangea.stanford.edu/ERE/pdf/IGAstandard/SGW/2016/Simmons2.pdf.

Smith, L., 1980, *A Model Study of the Regional Hydrogeologic Regime, Roosevelt Hot Springs, Utah*. Salt Lake City, Utah: Dept. of Geology and Geophysics, University of Utah, http://www.osti.gov/scitech/biblio/5231822.

Smith, R.B., 1977, *Long-Term Seismic Monitoring of the Roosevelt - Cove Fort KGRA's*. Salt Lake City: Department of Geology and Geophysics, University of Utah, https://www.osti.gov/scitech/biblio/893368.

Smith, R.B., and Bruhn, R.L., 1984, *Intraplate extensional tectonics of the eastern Basin and Range: Inferences on structural style from seismic reflection data, regional tectonics, and thermal-mechanical models of brittle-ductile deformation.* Jl. Geophysical Research, 9, p. 5733-5762, https://onlinelibrary.wiley.com/doi/10.1029/JB089iB07p05733/full.

Smith, R.B., and Arabasz, W.J., 1991, *Seismicity of the Intermountain seismic belt,* in Slemmons, D. B., Engdahl, E. R., Zoback, M. D., Zoback, M. L., and Blackwell, D., eds., Neotectonics of North America: Geological Society of America, Decade Map Volume 1, p. 185-228, https://rock.geosociety.org/Store/detail.aspx?id=DNAGCSMS7.

Stodt, J.A., Hohmann, G.W., and Ting, S.C., 1981, *The Telluric- Magnetotelluric Method in Two- and Three- Dimensional Environments.* Vol. 46. Salt Lake City, Utah: Dept. of Geology and Geophysics, University of Utah, http://ngds.egi.utah.edu/files/GL04094/GL04094.pdf.

Thangsuphanich, I., 1976, *Regional Gravity Survey of the Southern Mineral Mountains, Beaver County, Utah*. Thesis MS1976. Dept. of Geology and Geophysics, University of Utah, https://www.worldcat.org/oclc/2212382.

Ting, S.C., 1978, *Three Dimensional Magnetotelluric Modeling*. Salt Lake City: Department of Geology and Geophysics, University of Utah, http://ngds.egi.utah.edu/files/GL01154/GL01154.pdf.

Ting, S.C., and Hohmann, G.W., 1979, *Integral Equation Modeling of Three-Dimensional Magnetotelluric Response.* Department of Geology and Geophysics, University of Utah, https://www.osti.gov/scitech/biblio/6718866.

Tiwari, S., Simmons, S., McLennan, J., 2017, *A 2D HYDROTHERM Model of the Utah FORGE Site*, Geothermal Resources Council Transactions, http://pubs.geothermal-library.org/lib/grc/1033729.pdf.

Tosaya, C., Findikakis, A., Cochrane, F., 1988, *Preliminary reservoir design and screening for a commercial hot dry rock geothermal prospect*. Geothermal Resources Council Transactions, 12, p. 485-490, https://www.geothermal-library.org/index.php?mode=pubs&action=view&record=1001750.

Tripp, A.C., Ross, H.P., Stodt, J.A., and Wright, P.M., 1989, *Surface-to-borehole electromagnetic experiment at Roosevelt Hot Springs: a feasibility study*. Geothermal Resources Council Transactions, 13, p. 289-293, https://www.geothermal-library.org/index.php?mode=pubs&action=view&record=1001791.

University of Utah. Dept. of Geology and Geophysics, 1979, *Final Report: Work Performed under Contract No. EY-76-S-07-1601*. Salt Lake City, Utah: University of Utah.

University of Utah, Geology and Geophysics Department, and Geological Survey (U.S.), 1977, *Workshop on Electrical Methods in Geothermal Exploration.* Salt Lake City, Utah: University of Utah, https://www.osti.gov/scitech/biblio/892808.

Wannamaker, P.E., 1978, *Magnetotelluric Investigations at the Roosevelt Hot Springs KGRA and Mineral Mountains, Utah*. Salt Lake City: Department of Geology and Geophysics, University of Utah, https://www.osti.gov/scitech/biblio/6766105.

Wannamaker, P.E., Sill, W.R., and Ward, S.H., 1978, *Magnetotelluric observations at the Roosevelt Hot Springs KRGA and Mineral Mtns., Utah*. Geothermal Resources Council Transactions, 2, p. 697-700, https://www.geothermal-library.org/index.php?mode=pubs&action=view&record=1000292.

Wannamaker, P.E., Ward, S.H., Hohmann, G.W., and Sill, W.R., 1980, *Magnetotelluric Models of the Roosevelt Hot Springs Thermal Area, Utah*. Salt Lake City: University of Utah, Dept. of Geology and Geophysics, http://ngds.egi.utah.edu/files/GL01609/GL01609.pdf.

Wannamaker, P.E., Hohmann, G.W., Ward, S.H., 1982, *Magnetotelluric Responses of Three-Dimensional Bodies in Layered Earths*. Salt Lake City: Dept. of Geology and Geophysics, University of Utah, https://www.osti.gov/biblio/893412.

Ward, S.H., Parry, W.T., Nash, W.P., Sill, W.R., Cook, K.L., Smith, R.B., Chapman, D.S., Brown, F.H., Whelan, J.A., and Bowman, J.R., 1978, *A summary of the Geology, Geochemistry, and Geophysics of the Roosevelt Hot Springs thermal area, Utah*. Geophysics, 43, p. 1515-1542, https://library.seg.org/doi/abs/10.1190/1.1440912.

Ward, S.H., 1976, *Addendum to Proposal of January 20, 1976, Geothermal Research, Roosevelt Hot Springs KGRA*. Salt Lake City, Utah: University of Utah.

Ward, S.H., and Sill W.R., 1976, *Dipole-Dipole Resistivity Delineation of the near Surface Zone at the Roosevelt Hot Springs KGRA*. Salt Lake City: University of Utah, Dept. of Geology and Geophysics, https://www.osti.gov/scitech/biblio/6081571.

Ward, S.H., and Sill, W.R., 1976, *Dipole-Dipole Resistivity Surveys, Roosevelt Hot Springs KGRA*. Salt Lake City: University of Utah, Dept. of Geology and Geophysics, https://www.osti.gov/scitech/biblio/7255740.

Ward, S.H., 1980, *Induced Seismicity and Seismic Baseline Studies at Roosevelt Hot Springs and Cove Fort/Sulphurdale, Utah : Final Report for Period September 15, 1978 - March 31, 1980*. Salt Lake City, Utah: Dept. of Geology and Geophysics, University of Utah, https://www.worldcat.org/oclc/441497507.

Ward, S.H., and Crebs, Y.J., 1975, *Report on Preliminary Resistivity Survey, Roosevelt Hot Springs KRGA*. Salt Lake City, Utah: University of Utah, Dept. of Geology and Geophysics, https://www.geothermal-library.org/index.php?mode=pubs&action=view&record=1019327.

Ward, S.H., Ross, P., and Nielson, D.L., 1981, *Exploration strategy for high-temperature hydrothermal systems in the Basin and Range province*: AAPG Bull., v. 65, p. 86-102, http://archives.datapages.com/data/bulletns/1980-81/data/pg/0065/0001/0050/0086.htm?q=%2BtitleStrip%3Aexploration+titleStrip%3Astrategy+%2BauthorStrip%3Award.

Wechsler, D.J., 1979, *An Evaluation of Hypocenter Location Techniques with Applications to Southern Utah, Regional Earthquake Distributions and Seismicity of Geothermal Areas*. Salt Lake City, Utah: Dept. of Geology and Geophysics, University of Utah, https://www.osti.gov/scitech/biblio/6579471.

Whelan, J.A., 1977, *Thermal Gradient and Heat Flow Drilling by Dept. of Geology and Geophysics, University of Utah, Summer 1975*. Salt Lake City: University of Utah, Dept. of Geology and Geophysics, http://digitallib.oit.edu/cdm/ref/collection/geoheat/id/1108.

Wilson, W.R., 1980, *Thermal Studies in a Geothermal Area*. Thesis PhD 1980. Dept. of Geology and Geophysics, https://www.worldcat.org/oclc/7033941.

Wilson, W.R., 1980, *Three Topical Reports : Thermal Studies in a Geothermal Area*. Salt Lake City, Utah: Dept. of Geology and Geophysics, University of Utah, https://www.osti.gov/scitech/biblio/7015581.

Wilson, W.R., and Chapman, D.S., 1980, *Thermal studies at Roosevelt Hot Springs, Utah: Univ. Utah, Dept. Geology and Geophysics Rept*. DOE/ID/12079-19, 144 p., http://www.osti.gov/scitech/biblio/7015581.

Wright, P.M., and University of Utah, Research Institute, Earth Science Laboratory 1989, *Publications and Geothermal Sample Library Facilities of the Earth Science Laboratory, University of Utah Research Institute*. Rev 1.0. Salt Lake City, Utah: The Institute, http://www.osti.gov/scitech/servlets/purl/890978-Brm7HP/.

Yearsley, E., 1994, *Roosevelt Hot Springs reservoir model applied to forecasting remaining field potential.* Trans. GRC, 18, p. 617-622, https://www.geothermal-library.org/index.php?mode=pubs&action=view&record=1007049.

Yusas, M.R., 1979, *Structural Evolution of the Roosevelt Hot Springs Geothermal Reservoir*. Thesis MS1979--Dept. of Geology and Geophysics, University of Utah, https://www.worldcat.org/oclc/5778529.

Yusas, M.R., and Bruhn, R.L., 1979, *Structural Fabric and in-Situ Stress Analyses of the Roosevelt Hot Springs KGRA*. Salt Lake City, Utah: Dept. of Geology and Geophysics, University of Utah, https://www.osti.gov/biblio/6852810.

Zandt, G., University of Utah, Research Institute, Earth Science Laboratory, and United States. Dept. of Energy, Division of Geothermal Energy, 1982, *Final Technical Report : Seismic Baseline and Induction Studies, Roosevelt Hot Springs, Utah and Raft River, Idaho*. Salt Lake City, Utah: Earth Science Laboratory, University of Utah Research Institute, https://www.osti.gov/biblio/6396329.